STUDIES OF INTERACTION OF SMALL MOLECULES WITH WATER CONDENSED MEDIA

by
Sergey Mitlin

A thesis
presented to the University of Waterloo
in fulfillment of the
thesis requirement for the degree of
Doctor of Philosophy
in
Chemistry

Waterloo, Ontario, Canada, 2006

I hereby declare that I am the sole author of this thesis. This is a true copy of the thesis, including any required final revisions, as accepted by my examiners.

I understand that my thesis may be made electronically available to the public.

ABSTRACT

STUDIES OF INTERACTION OF SMALL MOLECULES WITH WATER CONDENSED MEDIA

The present work reports experimental and theoretical studies of the intermolecular interactions in condensed water media. The chemical objects comprise pristine ice and polar organic substances: acetone, acetaldehyde, methanol and chloroform and bi-component water-organic deposits. The experimental part of the studies includes the Fourier Transform Infrared Reflection Absorption spectral (FTIR RAS) examination of the processes of film growth by vapor deposition on cold metal substrate and subsequent annealing. The theoretical studies include *ab initio* (*MP2*) and semi-empirical (*B3LYP*) calculations on the small water and water-organic clusters and classical molecular dynamics simulations of the adsorption of inert guests (Xe/Rn) on the ice surface. The FTIR RA spectral studies reveal that depending on the deposition conditions condensed water media exist in two principal structural forms: noncrystalline and polycrystalline. The former is characterized by porous structure while the latter exists as a non-porous medium with smooth external interface. On annealing, characteristic spectral changes indicate on a rapid crystallization occurring at a certain temperature range. The initial adsorption of organic molecules is accompanied by the hydrogen-bonded coordination between the functional group of organic species and non-coordinated hydroxyl group of the ice surface, the topology of which depends on the electronic properties of the functional group. The computational studies of small water-organic clusters reveal, in particular, two major coordination minima for carbonyl group: a single hydrogen-bonded in-plane complex and a double hydrogen-bonded in-plane complex. The classical molecular dynamics of Xe/Rn species on the ice interface is consistent with two distinctly different surface adsorption sites: one that delocalized over the entire surface and one that confined to small opening in the top ice layer, disrupted by the thermal molecular motion. The penetration barrier is associated with van der Walls repulsion of guest species from the ordered water hexagonal arrangement. A thermo-disruption of latter leads to a rapid diffusion of guest species inside ice medium.

ACKNOWLEGMENTS

At the top of the list let me express my sincere thanks to the members of advisory committee Professors Tong Leung, James Sloan, Bruce Torrie and Dan Thomas for many helpful comments and suggestions during the long period of my studies. I am indebted to Professor Tong Leung who has supervised these studies for providing a rare opportunity to explore different scientific aspects of the water studies. Special thanks go to Professor Bruce Torrie for many hours of insightful discussions and advices.

I am grateful to Professors Peter Bernath, Marcel Nooijen, John Goddard, Tom Woo, Paul Rowntree and Dr. Nick Taylor for useful discussions and consultations. Contribution of Professor Victoria Buch to the computational part of this work is noted with special thanks.

I would like especially aknowlege that present studies are fundamentally based on the pioneer, thorough studies of Professor Paul Devlin on water media. Without his studies the present work would not be possible. I am also grateful to Professor Devlin, whose opinion I highly value, for reading and commenting on the present manuscript.

My sincere thanks go to Professor Robert Le Roy and members of his group, Douglas Weir and Yiye Huang, for providing access to the computation facilities and for constant help along the course of computational studies.

My appreciation is also extended to Sean McLeod, a member of Professor Peter Bernath's team, for sharing knowledge and kind help in conducting computational studies.

I would like also to thank all stuff members and secretariat of the Department of Chemistry and, especially, Catherine Van Esch and Scott Nicoll for their kind cooperation along my staying in the Department.

A unique UHV chamber used in the present studies has been manufactured by a rare craftsman and great man Richard Forgett, with whom I have a real pleasure to work on this project and with whom we became friends. Without his dedication and personal support this project would be impossible. I wish to express to Rick my deepest appreciation for his immerse help during the period of my studies.

My sincere thanks also go to the entire staff of the Science Electronic and Machine Shops at the University of Waterloo and, in particular, to Dave Reader, Krunomir Dvorski, Jacek Szubra, Mike Lang, Andy Colclough, Reg Graf, and Harmen Vander Heide. Their outstanding skills and workmanship are well known far beyond the University of Waterloo.

Many thanks should go to Drs. Tony Eng, Tim Rider and Tim Johnson from Bruker Canada, with whom I have a pleasure to collaborate on the experimental part of this project. They have provided us with exceptionally well-tuned FTIR instrument, certainly one of the best instruments of this class in the world, and have supported us in difficult moments by outstanding service going well beyond their direct duties. It is impossible to imagine successful spectral studies on Bruker machines without support of these people. I am grateful to share a merit for observing those unique surface features, which are reported in the present experimental studies, with the team of Bruker Canada.

I am sincerely grateful to Dr. Sasha Lemak and Dr. Galina Orlova for discussions of the practical aspects of molecular dynamic and quantum mechanical calculations. Their instructive help has been very useful for the theoretical part of the present studies. I wish also to thank Dr. A. M. Mebel for providing the data on optimized geometries of selected acetone-water clusters.

I would like to extent my thanks to the entire staff of the Library at the University of Waterloo, which provides us with exceptionally well-established bibliographic and information serves.

Specials thanks should go to my lab mates Dr. Qiang Li and Dr. Zhenua He, with whom I have shared the fascination and difficulty of the studies. I wish to especially thank Dr. Nina Heinig for proof reading of the thesis. Technical assistance of Qiang Gao in conducting certain experimental runs is appreciated.

Finally, I would like to acknowledge with my sincere thanks a personal support of the present studies by Professor Ranjana Bird, Dean of Graduate Studies Office, and senior advisor Mrs. Elaine Garner. Their help was of the vital importance for the present studies.

TABLE OF CONTENTS

LIST OF TABLES

LIST OF FIGURES

CHAPTER 1

Introduction

1.1 General Introduction

The present studies concern the fundamental physico-chemical processes in condensed water media using infrared spectroscopy and computational techniques. Infrared spectroscopy is among the most powerful tools for investigating the hydrogen bonded structures of low-density noncrystalline water and crystalline ices. The present work utilizes the infrared spectral method and computational techniques for studying the properties of water media and the guest-water interaction at cryogenic temperatures. Comprising adsorption, penetration of the medium surface, occlusion or enclathration, and chemical surface reactions, the physico-chemical processes in the condensed water media are part of the global matter circulation on Earth. In all spheres - biosphere, geosphere and atmosphere - the physico-chemical processes associated water media contribute significantly to and, in many cases, control the global chemical balance. The abundance of water media and their unique properties form ultimate foundation for all scientific studies on water in chemistry, geochemistry, atmospheric studies and ecology.

The mechanisms of adsorption, absorption, inside-host transport and interactions of the chemically different species with the ice micro-phases over the entire range of relevant temperatures remains the subject of intense investigations and debates primarily due to the important role that ice as the adsorbent and/or absorbent plays in atmospheric and stratospheric [1], biospheric [2, 3], cometary and interstellar chemistry [4, 5]. The important issue of the heterogeneous chemistry and physics on the surfaces of water objects is associated with those physico-chemical processes in the polar stratospheric clouds, which convert two most abundant inert reservoirs of chlorine, HCl and $ClONO_2$ into Cl_2. The latter species could be readily photo-decomposed to yield active chlorine, the known catalytic destroyer of ozone [6]. The penetration of surfaces confining a water medium is often a critical step in the inter-phase transport. Numerous experiments have shown that the chemical species belonging to the diametrically opposite classes, exemplified by the van der Waals particles on one side and Lewis acids and bases on the opposite, penetrate the ice and convert it to the corresponding

crystalline or noncrystalline hydrates [7, 8, 9, 10, 11, 12].

One of the ultimate goals in the spectral and structural studies of water media and the physico-chemical processes in condensed water resides in the explanation of the macroscopic properties of water and aqueous solutions, including IR and Raman spectra, in terms of the intermolecular forces. The understanding of these properties is mutually related to the concept of the hydrogen bond (*HB*, for short) between the molecular species in the system. Taking into account the conceptual importance of *HB* for the present studies, the hydrogen bonding between water molecules (specifically, *HB* in small water clusters) and that in the complexes of water with small oxygen-containing organic molecules is analyzed in Chapter 4. This analysis is based primarily on the quantum mechanical calculations performed in the present studies.

The present work explores both the experimental method of infrared spectroscopy and the computational techniques in an attempt to correlate the spectral and structural information. There is a double purpose associated with the present studies of bi-component (polar organic-water) systems: (i) to investigate the state of water media using a guest molecule as a probe, and (ii) to extract the structural information of the local hydrogen bond coordination between the organic and water molecules. For instance, the coordination of water molecules around carbonyl compounds remains to be a subject of intense studies [13, 14]. The present work provides a detailed quantum mechanical analysis of this problem in Chapter 4. The spectral information on the acetone-water and chloroform-water systems at cryogenic temperature is discussed in Chapter 5. In particular, the analysis of spectral data on acetone-water cryogenic deposits with parallel quantum-mechanical and molecular dynamic studies leads to establishing a fairly complete spectrum-structure correlation scheme. This scheme can most certainly be extrapolated on the liquid acetone-water solutions.

A very peculiar feature of the nucleation and crystallization processes taking place in the atmosphere is the appearance of metastable liquid water or liquid phases of the water solutions at temperatures below their freezing points. The filed observations and the laboratory experiments [15] on the formation of clouds indicate that the water droplets remain in the liquid state at temperatures far below 0 ºC. In this case metastable water is referred to as being in a supercooled liquid state. *In situ* measurements in the deep convective clouds reveal that the supercooled water droplets exist in liquid state at temperatures as low as −37.5ºC [16].

The nucleation processes in such supercooled liquid have found yet neither theoretical explanations nor a complete qualitative description. According to recent and somewhat "intuitive" thermodynamical arguments, the crystalline ice nuclei are expected to appear preferentially on the air-supercooled-liquid interface, which indicates the significance of interfacial properties for the kinetics of glaciation [17]. The underlying reasons for this remarkable property of forming supercooled liquid state and respective delay in the crystallization could be associated with the mismatch between a short range order anticipated in the supercooled state and the long range order of the hexagonal, *Ih*, or cubic ice, *Ic*. In other words, the supercooled state appears to be arrested within a certain area of the configurational space, corresponding to the aperiodic structures. A transition from this configurational subspace to the configurational area of crystalline packings is associated with the free energy barrier of the entropic nature. In aperiodic systems, there is a large number of different configurations (and conformations) of the water hydrogen bond network within a narrow energy range. The energy difference between these numerous aperiodic configurations and between the aperiodic configurations and the crystalline structures is typically very small. A high density of configurations on the energy scale is associated with the relaxed potential of water-water interaction as discussed in Chapter 4. The entropy of the aperiodic water state is apparently larger than that of the crystalline minima. Therefore, ordering of an aperiodic structure into a crystalline form most likely involves overcoming a free energy entropic barrier. In the present studies, the crystallization of aperiodic ice media at a low temperature boundary (see Chapter 2 for the partial phase diagram of water and the localization of boundaries of aperiodic amorph) has been investigated using infrared spectroscopy as discussed in Chapter 5. The structures and models of crystalline and noncrystalline media are discussed in detail in Chapter 2.

A fundamental structural problem in studying the noncrystalline water media resides in establishing the possibility of microscopic geometric description of an aperiodic system in question. If such a description is possible then the subsequent problem will be to find an algorithm for generating theses representative microscopic structures. These microscopic molecular ensembles form an inherent structure of the aperiodic medium. Pivotal for the concept of the inherent structure of noncrystalline media, the correlation between the topology of a multidimensional potential energy surface and the structural and dynamic characteristics

of an aperiodic system can be explored using a mapping procedure, which connects any available instant configuration to a parent local potential minimum that represents a stable arrangement. Such mapping, described in details by Stillinger and Weber [18], allows separating the vibrational motion within geometric boundaries of a potential minimum (the interior of the potential minimum is called a basin) and the transition (barrier hopping) between different neighboring potential minima. These two kinds of motion, i.e. the vibrational oscillations within a basin and the inter-basin hoppings, often display very different time characteristics as discussed by Eisenberg and Kauzmann in their fundamental book on the water structure and properties [19]. In the present work, quantum mechanical and classical potential energy minimization of small water clusters are performed in order to generate an ensemble of local minima that are part of the inherent structure. The physico-chemical properties of these minimized structures, including the IR spectra, can be readily calculated, which makes possible structure-property correlations. Furthermore, the computed properties (for very limited number of clusters in the present work), such as radial distribution functions and IR spectra, are found to be in reasonable accord with the experimental data. An account of these attempts is given in Chapter 4.

The configurations at distinct minima are temperature independent and, therefore, could be used for identifying an inherent structure of the molecular systems (even when these systems are in an aperiodic state). The topology of the potential energy surface (*PES*) is a complex function of the following parameters: (i) intermolecular forces; (ii) geometric forms attained by the water molecules under given external conditions; and (iii) the molecular density. In determining the topological features (critical and saddle points) of the *PES*, all the above-listed factors are practically independent of the temperature. This property of a molecular arrangement at a local minimum being temperature independence justifies the concept of inherent structure in the application to aperiodic systems. The *PES* features of a multi-molecule water system are closely related to the potential surface of the water dimer. However, the pairwise water-water potential is strongly affected by the presence of other water molecules surrounding a water dimer. This multi-body contribution in the hydrogen bond network is typically referred to as a cooperativity effect, which will be investigated in detail in Chapter 4. It should be noted at the very beginning that the cooperativity effect is responsible for specific IR spectral features in the acetone-water system.

Populated by the water system at temperatures above the melting point, a set of distinct local minima corresponds to the numerous homogeneous noncrystalline packings. These packings are thought to be characterized by a narrow distribution and relatively high values of the average potential energy per molecule. Furthermore, it could be assumed that the inherent structure of a water vapor deposition on metal substrates at cryogenic temperatures will be similar to that of liquid water. The difference between liquid and noncrystalline solid media resides in the rate of inter-basin hopping: in the case of liquid, the structural transitions are fast, whereas in the case of solid, structural changes are infinitely slow, i.e. the molecular mobility is insufficient for overcoming the free energy barriers. In contrast, a much smaller set of crystalline packings is associated with the deepest minima observed globally on the topological *PES* terrains. Peculiarly, in the case of water crystalline polymorphs, the energies of phase transitions are small in spite of significant conformational and configurational differences in their crystalline structures. However, the crystalline structures of ice maintain in their majority a coordination number *4*, which is characteristic to the water *HB* network. For example, the values of ΔU (hexagonal ice, *Ih* → ice two, *II*) = 19×10^{-3} kcal·mole^{-1} and ΔU (*Ih* → ice three, *III*) = 0.256 kcal·mole^{-1} [19] are indeed small in comparison with the maximum value of *HB* energy in *Ih* at ~5.1 kcal·mole^{-1} [19]. The small values of the enthalpy of phase transitions indicate the configurational flexibility of the crystalline packings in the *4*-coordinated *HB* networks. The flexibility of the *HB* contacts between water molecules self manifests, in particular, in the relaxed (smooth) shape of the energy profiles with respect to the geometric variables of the water dimer. This aspect of the *HB* between water molecules is discussed in detail in Chapter 4. In other words, the flexibility of *HB* networks is associated with relatively small variations of the potential energy with large changes in the geometrical parameters. In general, the flexibility of *HB* contacts is responsible for both the configurational and conformational packings and the dynamic properties of the water media, including the IR-spectral features.

An important question about the local structure of aperiodic water media is whether there is a geometric reproducibility (the common patterns) in the first or higher order coordination spheres at those local *PES* minima, which are part of a homogeneous set of the water replicas. Each water replica or, i.e. the configuration of a local *PES* minimum, can be characterized by distribution functions (for instance, the pairwise distribution functions for the

O···O, O···H and H···H pairs). If such a configuration is generated to represent a single water replica comprising of a large number of molecules, the computed distribution functions can be compared with the experimental data. In the present work, the generation of water replicas is demonstrated using examples of very small water clusters (4-26 molecule) as discussed in Chapter 4. In spite of this small size and the limited data on configurational and conformational space available for the clusters of a particular size, the computational results brings interesting information on the inherent structures of low- and high-density amorphs. It is established in the present studies that these small-size replicas can be used for obtaining both the average structural parameters and unique features.

The spatial 3-dimensional homogeneity of aperiodic water systems allows partitioning the system on molecular cells, each of which can be used as a representative model of the whole aperiodic system. This cellular structure of aperiodic media is different from a crystalline packing, where the whole structure is formed by the repetition of the exactly the same crystallographic cell. Of course, the spatial homogeneity in aperiodic (i.e. lacking crystalline long-range symmetry) system is fundamentally different from the lattice periodicity in crystalline packings, which is a source of the spatial heterogeneity in a crystal. In particular, if a local arrangement (molecular cell) exhibits symmetry incompatible with the Bravais symmetry, the repetition of these local patterns in the *3D*-space will lead either to the crystalline samples containing dislocation defects, or to the open-network (crystalline) packings, such as those taking place in clathrate-hydrates or zeolites. In this context, two experimental observations appear to be especially relevant. Firstly, the crystallization of noncrystalline water at 150 K proceeds to the microcrystalline cubic ice, *Ic*, and only at much higher temperatures (~210 K) to the hexagonal ice, which is the most stable crystalline phase at low temperature-low pressure section of phase diagram [20]. Secondly, the noncrystalline water at low temperatures exhibits two (or even more!) distinct *polyamorphous* forms classified according to their densities. The principal noncrystalline forms are low-density aperiodic and high-density aperiodic states [32]. The former observation appears to suggest frustration (mismatch between the local symmetry and the global symmetry of crystal) as the reason for the formation of the highly polycrystalline and metastable *Ic* (instead of *Ih*) on the crystallization of low-density noncrystalline water. Therefore, there are grounds to attribute the inherent structure of low-density noncrystalline species to that of *Ic*. Furthermore, the

presence of distinct amorphous water species allows consideration of distinct inherent aperiodic structures with different densities. In the light of the proposed relation between the inherent structures of aperiodic system and certain crystalline packings, one should attempt to establish such a correlation in the case of aperiodic and crystalline packings of the water. In particular, if a low-density aperiodic state is in the structural relation with the open-network ices *Ic* and/or *Ih*, a high-density aperiodic state was found to be in the structural relation with the high pressure ices such as ice *VII* and ice *VIII* [21], which are characterized by cubic symmetry lattice with a coordination number *8* in a dramatic contrast with the coordination number *4* in the *Ic*/*Ih* open-network systems. However, among these *8* nearest neighbors only *4* of them are hydrogen-bonded so the coordination number for hydrogen-bonded molecules still remains at *4*. It should also be noted that the crystallization of the high-density aperiodic structure proceeds at 77 K with the formation of the orientationally proton-disordered ice *VII* whereas at more elevated temperatures near 160 K the formation of proton-ordered ice *VIII* was observed [21], which is similar to the crystallization events taking place with the low-density aperiodic water system [20 and references therein].

On a structural level, the departure of a spatial arrangement of the structural units from periodicity occuring in a noncrystalline liquid and glass phase, creates a possibility for the formation of the finite-size clusters of a non-crystallographic symmetry with a deep potential-energy minimum such as the tridecan (12+1) icosahedron with one of the molecules located in the center of the regular pentagonal dodecahedron proposed by Frank [22]. By studying the local motifs with icosahedral and fivefold symmetry, Baker and Hoare [23] have found a considerable variety of the locally symmetric structures, which suggests the existence of the non-periodic networks characterized by self-limiting growth patterns. The present studies attempt to follow Hoare's proposal to generate plausible geometrical structures on an *a priori* basis followed by the testing of their properties. The icosahedral symmetry group operations on the "elementary" structural units of water such as bicyclo-octamer (tied by the directional hydrogen bonds) leads to the 280-molecular complex as one possible candidate for the structural unit of aperiodic water (see Chapter 2). Use of an icosahedral symmetry for the generation and classification of finite-size molecular assemblies appears to be successful. Indeed, such experts in the field of water structure as Pauling [24], Bernal [25, 26], Frank [27], Franks [28], Angell [15], Stillinger [29, 30] and many others [22, 31, 32 and references

therein] have strongly asserted the geometric or topological representations of the water medium as a powerful, if not unique, tool for the interpreting and predicting of the water properties. The illustration of a geometrical aspect of the studies on the water can be readily achieved by referring to a fundamental concept of the tetrahedral form, which single water molecule can attain in a condensed state. It should be again clarified that the tetrahedral form of the neighborhood of a water molecule in the multi-particle medium is not a rigid arrangement completely predefined by the properties of the individual water molecule, but rather a result of the cooperative interactions within the medium. An assembly of these molecular tetrahedrons creates a network, in which a number of nearest neighbors around a structural unit approaches a value of four. In the structural studies on water, Bernal [26], in particular, had widely employed a geometric analogy between the structures of solid water phases and that of crystalline silicate phases. While in his and Fowler's [25] original model, liquid water had been described as a dynamic "mixture" of the tridymite-like ice (ordinary *Ih* hexagonal ice) and the quartz-like ice, Bernal associated in his later model the structure of liquid water with the disordered keatite packing (structurally unique crystalline polymorph of SiO_2 containing pentagonal rings of silicon-oxygen tetrahedrons). Extending this comparative structural analysis by including the structures of clathrate-hydrates and those of carcass alumosilicates (zeolites) could be useful in designing those finite-size clusters, which would be generally common to tetrahedral networks regardless of the particularities of chemical bonding in the latter.

1.2 Research Objectives

The major goals of the present experimental and theoretical studies include: (i) design, construction and testing of the ultra-high-vacuum (UHV) chamber coupled optically with the Fourier Transform Infrared spectrometer for performing infrared reflection-adsorption spectral experiments (abbreviated by FTIR RAS or RAS through the rest of the thesis) on thin films of ice and/or volatile organic substances at cryogenic temperatures; (ii) FTIR RAS investigation of the adsorption and absorption complexes formed by small molecules of environmental significance on the ice micro phases; (iii) spectral investigation of the phase composition and/or phase transitions in the vapor deposited and thermo-annealed pristine water and organic films; and finally (iv) computer simulations and theoretical studies of the model systems in

order to provide a description of the fundamental surface processes on ice and an adequate interpretation for the spectral data.

The FTIR RAS is known to be a useful tool for the examination of the chemical and physical processes on the surfaces of metals and on dielectric thin films deposited on metals. Therefore, the choice of technique for the experimental studies was to a large degree predetermined by such attractive feature of the FTIR RAS method as sensitivity down to the sub-monolayer coverage of the film surfaces. However, as it usually happens, the advantages in one area bring disadvantages and complications in other areas. Among the latter, the most serious are (i) the inapplicability of the Beers-Lambert law directly to the analysis of RA spectra, and (ii) the significant distortion of the spectral RA features in comparison with the transmittance spectra, which makes impossible a direct comparison of the RA spectra with analogous transmittance spectra. An alternative experimental method for the spectral studies of the surface processes on the ice nano-particles has been established by Devlin [33] and is based on the transmittance spectroscopy of a 3-D ensemble of ice particles collected in a collisional-cooling cylindrical double-wall FTIR cell. The IR transmittance spectra obtained from the ensemble of nanoparticles also will vary substantially from that of the corresponding thin film, particularly for the vibrational modes of large transition dipole moment. Therefore, both the RA spectra of thin ice films and the transmittance spectra of nanoparticles impose serious difficulties for their interpretations. For example, during the experimental studies of pristine ice films [34] the present author has discovered that the spectra of polycrystalline ice obtained in the RA mode and those in the transmittance mode are incompatible (although the properties of polycrystalline ice medium studied in different labs are very likely to be identical). Moreover, an attempt of direct comparison will inevitably lead to wrong conclusions regarding the structure of ice films because the information encoded in these spectra is fundamentally different, particularly with respect to the strongest vibrational bands such as the OH stretching mode. In the ideal case of infinitely thin and optically perfect film, the transmittance IR band is given by the imaginary part of dielectric function, $\mathrm{Im}(\varepsilon) = \varepsilon'' = 2 \cdot n \cdot k$, where a dielectric function, ε, is defined as $\varepsilon' - i \cdot \varepsilon''$, and $\varepsilon = (n - i \cdot k)^2 = n^2 - k^2 - 2i \cdot n \cdot k$, and n and k are refractive and absorption indexes of the medium, respectively. The same band in the reflection-absorption spectra is given by an energy loss function or a Berreman's profile [35] defined as $\mathrm{Im}(-\varepsilon^{-1}) = \varepsilon''/(\varepsilon'^2 + \varepsilon''^2) = 2 \cdot n \cdot k / (n^2 + k^2)^2$. From an analysis of the simple

dispersion curve for a damped harmonic oscillator, it follows that at the resonance frequency $\omega = \omega_0$, the absorption index k reaches its maximum while n and ε' become equal *1*, which typically corresponds to the case when the absorbance maximum of transmittance mode, i.e. $2 \cdot n \cdot k$ reaches its maximum. On the other hand, in the case of reflection-absorption spectra, $\mathrm{Im}(-\varepsilon^{-1})$ reaches maximum at a frequency given by the following expression: $\omega = \omega_0 \cdot (\varepsilon_0 / \varepsilon_\infty)^{1/2}$ [35], where ε_0 is the dielectric constant and ε_∞ is a value of the dielectric function at high frequency. Therefore, in the transmittance spectra the maximum of absorption band is located at the frequency of the transverse optical (*TO*) mode, whereas in the RAS the same fundamental transition appears at the frequency of the longitudinal optical (*LO*) mode. The stronger the oscillator strength of the fundamental vibration, the stronger is the *LO/TO* split and consequently the larger difference between the observed transmittance and RA spectra. In the present experiment, the strong *LO/TO* splits were found for the OH stretch mode in the pristine ice films and for the carbonyl stretching mode in the pristine acetone film. Moreover, the RA character of the light-matter interaction in the thin films leads to the appearance of interference optical features, the frequency positions and intensities of which are dependent on the film thickness. Similar effects of the light interference could be observed also in the transmittance experiment performed in a thin optical cell. In addition to these optical interference patterns, the RA spectra of the ice films with rough surface could show additional spectral features originated from light scattering from the surface or bulk irregularities, which further complicates the interpretation of the spectra. The necessity of the spectral simulations on the basis of simple optical model becomes evident. A choice has been given to a Fresnel optical model for the three-layer stratified media: vacuum-dielectric film- metal substrate. A similar optical model has been previously employed in the studies of ice films by RAS technique and appears to provide an acceptable agreement between simulated and experimental spectra [36]. A detailed description of the Fresnel model is given in Chapter 3. In contrast to the strong vibrational fundamental modes that are subject to dielectric effects described above, there are surface-localized vibrations such as vibrations of OH dangling bonds in the water media, which are much less affected by the dielectric optical effect. For these spectral features, the comparison between transmittance and RA modes is valid.

An independent proof of the validity of the present experimental procedures and spectral data treatment comes from the FTIR RAS studies of Mate *et al.* [37], who performed

detailed RAS studies of pristine ice films and corroborate with the present RAS results.

The computer simulations were performed using UNIX on 64- multiprocessor and 32-bit single processor computers. The Gaussian [38] set of programs has been used for quantum mechanical *ab initio* and semi-empirical *B3LYP* computations whereas the CHARMM [39] set of programs has been employed for classical molecular dynamic simulations. The *ab initio* results obtained in the present work for single water molecule have been compared with those published previously [40] and there was good numerical agreement between the results of different laboratories. The comparison of the computed and experimental IR spectra allows one to predict the structures of distinctly different hydrogen-bonded and non-coordinated complexes that carbonyl compounds such as acetone and acetaldehyde form on the surface and in the bulk of ice films. The structure of distinct complexes for acetone and chloroform species in the ice can also be inferred on the basis of the present studies. The classical *MD* simulations of the Xe/Rn-ice (the results of Rn/ice simulations are not presented because they are qualitatively similar to those of the Xe-ice system) systems reveal two distinct adsorption complexes on the ice surface, one of which is mobile and localized atop the surface water layer whereas another is confined within the first water layer. The latter localized complex appears to be a precursor to the further penetration inside the water media. The penetration process of the guest species appears to be associated with the mobility of the water molecules in the media and in the present case leads to the partial loss of water crystallinity.

Apart from their necessity for extracting structural information from the RAS data, the computer experiments were also found to be useful in providing a molecular-level representation of the structural and dynamical features of the systems under investigation.

1.3 Thesis Organization

The present thesis comprises 7 Chapters. An introduction to the subject and general problematics of the water studies are discussed in the present first Chapter. The second Chapter provides a bibliographic review on the major results in understanding the structural and spectral properties of the water media with an emphasis on the water phase diagram as the main reference tool. The water phases, their structures and models are the main topics reviewed in Chapter 2. Chapter 3 describes in detail the content of the present experimental work and a method of the treatment of spectral data. Chapter 4 deals with the theoretical

analysis of the hydrogen-bonded systems with an emphasis on the water and acetone-water complexes, and outlines the major results of quantum mechanical simulations undertaken in order to extract relevant structural information from the spectral data. Furthermore, Chapter 4 provides a necessary theoretical background on the vibrational spectroscopy for the following Chapter 5, which deals with analysis of the RA spectral information of pristine water and organic films and the bi-component organic-water systems. Theoretical analysis of the penetration of guest molecules in the water media is represented in Chapter 6, where particular attention is given to the computational studies of a model Xe/ice systems. Finally, Chapter 7 summarizes the main results of the present work.

References:

1. B. J. Finlayson-Pitts, J. H. Pitts, "Chemistry of upper and lower atmosphere." 2000, Academic press, and references therein.
2. A. L. Sumner, P. B. Shepson, Nature ***398*** (1999) 230.
3. T. L. Couch, A. L. Sumner, T. M. Dassau, P. B. Shepson, R. E. Honrath, Geophys. Res. Letters ***27*** (2000) 2241.
4. G. Notesco, A. Bar-Nun, Icarus ***148*** (2000) 456.
5. M. P. Bernstein, S. A. Sandford, L. J. Allamandola, J. S. Gillette, S. J. Clement, R. N. Zare, Science ***283*** (1999) 1135.
6. M. J. Molina, "The Probable Role of Stratospheric Ice Clouds: Heterrogeneous Chemistry of the Ozone Hole" in "The Chemistry of t he Atmosphere: Its Impact on Global Change", ed. J. G. Calvert (1994) Blackwell Scientific Publications.
7. R. M. Barrer, A. V. J. Edge, Proc. Roy. Soc. London ***A300*** **(**1967) 1.
8. A. W. Adamson, B. R. Jones, J. Colloid Interface Sci. ***37*** (1971) 831.
9. J. Ocampo, J. Klinger, J. Colloid Interface Sci. ***2*** (1982) 377.
10. M. J. Molina, T-L. Tso, L. T. Molina, F. C.-Y. Wang, Science ***238*** (1987) 1253.
11. L. Delzeit, K. Powell, N. Uras, J. P. Devlin, J. Phys. Chem. A ***101*** (1997) 2327.
12. K. L. Foster, M. A. Tolbert, S. M. George, J. Phys. Chem. A ***101*** (1997) 4979.
13. A. K. Soper, E. W. Castner, A. Luzar, Biophys. Chem. ***105*** (2003) 649.
14. J.-J. Max, C. Chapados, J. Chem. Phys. ***120*** (2004) 6625.
15. A. Angell, in "Water: A Comprehensive Treatise" ***7*** (1972), 1, ed. F. Franks, Plenum Press, New York.
16. D. Rosenfeld, W. L. Woodley, Nature ***405*** (2000) 440.
17. A. Tabazadeh, Y. S. Djikaev, H. Reiss, Proc. Nat. Acad. Sci. ***99*** (2002) 15873.
18. F. H. Stillinger, T. A. Weber, Phys. Rev. A ***25*** (1982) 978.
19. D. Eisenberg, W. Kauzmann, "The Structure and Properties of Water" (1969), Clarendon Press, Oxford.
20. P. V. Hobbs, "Ice Physics", (1974) Clarendon Press, Oxford.
21. R. J. Hemley, L. C. Chen, H. K. Mao, Nature ***338*** (1989) 638.
22. M. R. Hoare, J. Non-Cryst. Sol. ***31*** (1978) 157.

23. M. R. Hoare, Ann. N. Y. Acad. Sci. ***279*** (1976) 186.
24. L. Pauling, "Hydrogen Bonding" (1959) ***1***, ed. D. Hadzi, Pergamon Press, New York.
25. J. D. Bernal, R. H. Fowler, J. Chem. Phys. ***1*** (1933) 515.
26. J. D. Bernal, "The Geometry of the Structure of Liquid" (1963) 25, in "Liquids: Structures, Properties, Solid Interactions", (1965), ed. T. J. Hughel, Elsevier Publishing Company, New York.
27. H. S. Frank, Science ***169*** (1970) 635.
28. F. Franks, ed. "Water: A Comprehensive Treatise" ***1-7*** (1982) Plenum Press, New York.
29. F. H. Stillinger, Science ***209*** (1980) 451.
30. F. H. Stillinger, T. A. Weber, J. Phys. Chem. ***87*** (1983) 2833.
31. A. H. Narten, H. A. Levy, Science ***165*** (1969) 447.
32. O. Mishima, H. E. Stanley, Nature ***396*** (1998) 329.
33. J. P. Devlin, V. Buch, "Ice Nanoparticles and Ice Adsorbate Interactions: FTIR Spectroscopy and Computer Simulations", in " Water in Confined Geometries", ed. V. Buch and J. P. Devlin, (2003) Springer, Berlin.
34. S. Mitlin, K. T. Leung, J. Phys. Chem. B ***106*** (2002) 6234.
35. D. W. Berreman, Phys. Rev. ***130*** (1963) 2193.
36. M. A. Zondlo, T. B. Onasch, M. S. Warshawsky, M. A. Tolbert, G. Mallick, P. Arentz, M. S. Robinson, J. Phys. Chem. B ***101*** (1997) 10887.
37. B. Mate, A. Medialdea, M. A. Moreno, R. Escribano, V. J. Herrero, J. Phys. Chem. B ***107*** (2003) 11098.
38. Gaussian 03, Revision C.02, M. J. Frisch, G. W. Trucks, H. B. Schlegel, G. E. Scuseria, M. A. Robb, J. R. Cheeseman, J. A. Montgomery, Jr., T. Vreven, K. N. Kudin, J. C. Burant, J. M. Millam, S. S. Iyengar, J. Tomasi, V. Barone, B. Mennucci, M. Cossi, G. Scalmani, N. Rega, G. A. Petersson, H. Nakatsuji, M. Hada, M. Ehara, K. Toyota, R. Fukuda, J. Hasegawa, M. Ishida, T. Nakajima, Y. Honda, O. Kitao, H. Nakai, M. Klene, X. Li, J. E. Knox, H. P. Hratchian, J. B. Cross, V. Bakken, C. Adamo, J. Jaramillo, R. Gomperts, R. E. Stratmann, O. Yazyev, A. J. Austin, R. Cammi, C. Pomelli, J. W. Ochterski, P. Y. Ayala, K. Morokuma, G. A. Voth, P.

Salvador, J. J. Dannenberg, V. G. Zakrzewski, S. Dapprich, A. D. Daniels, M. C. Strain, O. Farkas, D. K. Malick, A. D. Rabuck, K. Raghavachari, J. B. Foresman, J. V. Ortiz, Q. Cui, A. G. Baboul, S. Clifford, J. Cioslowski, B. B. Stefanov, G. Liu, A. Liashenko, P. Piskorz, I. Komaromi, R. L. Martin, D. J. Fox, T. Keith, M. A. Al-Laham, C. Y. Peng, A. Nanayakkara, M. Challacombe, P. M. W. Gill, B. Johnson, W. Chen, M. W. Wong, C. Gonzalez, and J. A. Pople, Gaussian, Inc., Wallingford CT, 2004.

39. B. P. Brooks, P. E. Bruccoleri, B. D. Olafson, D. J. States, S. Swaminathan, M. Karplus, J. Comput. Chem. ***4*** (1983) 187.

40. D. Feller, J. Chem. Phys. ***96*** (1992) 6104.

CHAPTER 2

Bibliographical Review and Modeling of the Non-Crystalline Water Media

The main purpose of the present review is to outline the current status in the understanding of the relationship between the structures of solid water micro-phases and those physico-chemical processes of environmental significance that occur on the surface or in the bulk of these micro-phases. The present author has found that a literature review of this subject does not provide the opportunity to represent the structural data on the crystalline and non-crystalline water media. Therefore, for analytical purposes the present author has constructed and analyzed 3-dimensional computer models of selected crystalline and non-crystalline structures using the literature data. The main difficulties reside, of course, in finding an algorithm for designing non-crystalline water models. The first four sections deal with the subjects of solid water phases, their structures and morphologies. The subsequent section will give the necessary technical details and outline the recent results in the application of infrared spectroscopy and computer simulations to the investigation of physico-chemical processes on the ice surfaces. The last section of the present Chapter reviews the bibliographical data on the interaction of the adsorbates of different chemical properties with ice media.

A search for the inherent structure of aperiodic water media leads to a set of relatively small, compact water polyhedra, which can be used as structural units for constructing large-scale water clusters of the icosahedral symmetry. Following Chaplin's approach [1], the present author shows the model structures that are suitable for further computer studies on the large water systems. These models provide a convenient starting point for the theoretical and computational studies of liquid and noncrystalline water systems including aqueous solutions and clathrate-hydrates. The present classical molecular dynamics simulations on Xe-ice systems (reported in Chapter 6) demonstrate that the pentagon-dodecahedron unit with 20 water molecules corresponds to the "natural" coordination sphere for small molecules. The large water clusters can be constructed on the basis of the pentagon-dodecahedron unit acting as the first inner shell.

2.1 Solid and Liquid Water: Structures and Models

A general review of the ice phases is necessary for further discussions on both crystalline and non-crystalline water structures and their bulk and surface properties. Among the latter, the disorder in the proton and oxygen sub-networks should be noted as a very interesting example specific to the water *HB* network, which manifests itself, in particular, in the corresponding IR spectra of the corresponding media. Moreover, the theories of noncrystalline (nc for short) water media at ambient and sub-zero temperatures are mutually related to the crystallographic structures observed in the solid crystalline phases such as the low-density open-work hexagonal (*Ih*) ice, and the cubic (*Ic*) ice, and the high-density ices (including the ice *II* or *III*/*IX* phases). For example, the mixed model of the liquid water developed by Robinson and coworkers [2, 3] is based fundamentally on the two-state outer-neighbor bonding configurations, which correspond to two distinct non-nearest-neighbor (i.e. non hydrogen bonded) O···O distances observed in the *Ih* and the ice-*II* phases. A key element of Robinson's approach resides in the modeling of the non-crystalline water structure as a special ensemble of hexagonal rings. Liquid water is explicitly considered as a dynamic mixture of two types of the hexagonal packing: the *Ih*- and ice-*II* packings, which transform into each other on a picosecond timescale such that the relative statistical weight of each packing depends on the pressure and temperature. If the temperature rises, the structural composition shifts dynamically from the low-density and more rigid *Ih*-type configuration characterized by a 1···3 (non-hydrogen-bonded nextneighbor) intermolecular distance of ~ 4.5 Å (see Figure 2.3.1) to the high-density and more fragile ice-*II* configuration with the outer-neighbor 1···3 intermolecular distances of 3.4 Å (see Figure 2.3.4 and Figure 2.3.5). The authors of this theory have also suggested that the aforementioned polymorphic transformation proceeds through bending of the inner-neighbor hydrogen bonds (within *HB* chain of 1–2–3 molecules) without significant alteration of the equilibrium O–O nearest-neighbor distances at ~ 2.8 Å and the equilibrium coordination number of water molecules, *4*. This approach is based on the early ideas of Kamb, who suggested that the density and X-ray structure of the liquid water near 0 °C could be understood and represented within the framework of the dynamic mixing between the normal ice *Ih* structure and that of ice *II*- and/or ice *III*-type [4]. It should be also noted with this respect that, in attempt to augment the original Bernal-Fowler [5] theory of the liquid water, Bernal has also proposed a model that associates the inherent

structure of the liquid water with the keatite structure of silica belonging to the tetragonal symmetry group $P4_12_12$. The keatite structure bears close resemblance to the ice *III* structure (shown on Figure 2.3.6), which also belongs to a space group of the tetragonal symmetry, $P4_32_12$ [6]. In the original 1933-version of the Bernal-Fowler theory, there were postulated three different intermolecular arrangements, which could take place in the liquid water: (i) tetrahedrally-coordinated, open-work tridymite packing below 4 °C; (ii) tetrahedrally-coordinated, quartz packing of high density between 4-200 °C; (iii) random close-packing (the coordination number above *4*) at higher temperatures. These structural forms are "not distinct" [5] (i.e. other structural packings (unspecified) are not excluded from the picture) and exist in an instant transformation into each other. In the modified theory, Bernal has conceived the liquid water as a totally disordered pseudo-keatite structure, therefore associating the crystalline packing in keatite with the inherent structure of liquid water. A key structural element of the keatite and ice *III* structures is a puckered pentagonal ring of silicon-oxygen tetrahedrons or water molecules, respectively, which contrasts with the hexagonal ring pattern observed in the low-density ices *Ih* and the *Ic* or in the high-density ice *II*. Related essentially to the Bernal's keatite model of water (the keatite model has been subsequently discarded according to Finney's correspondence to Walrafen [7]) a different model of liquid water been developed by Walrafen and coworkers [7] and employed for the interpretation of the Raman spectra of water media at different temperatures including the subzero range. The key element of Walrafen's model [7] is the coexistence of hexagonal as well as pentagonal rings. Both models consider a pentagonal five-member ring of water molecules as an essential structural element of the liquid water, in order to prevent the system from attaining a long range order [6]. Walrafen [7] has also argued that this group of water models conform most closely to the liquid water at supercooled state at subzero temperatures. Regrettably, Walrafen *et al.* [7] has provided only a verbal description of their model that does not allow to construct an appropriate water structure by computer or other means and use this model effectively. The present author has therefore undertaken the task of building, whenever possible, the computer models of the water structures to facilitate a discussion about these issues. The presence of both pentagonal and hexagonal rings in the noncrystalline water is consistent with co-equilibrium between the liquid water, the *Ih*, and ices *II* and *III* at a triple point ~ −20 °C and ~ 2 kbar (see Figure 2.2.1 below for the phase diagram). Within the framework of these models,

the structure of noncrystalline water could be conceived as a dynamic composition of hexagonal and pentagonal rings that are puckered in different degrees and interconnected in different ways.

Undoubtedly, the assumption of the flexibility of hydrogen bond network in water is an essential element of this class of theoretical models. An open space provided by the interior of pentagonal and hexagonal rings is significantly different, which should influence the diffusional parameters of the water media with respect to the foreign probe particles. The puckering of the individual rings includes primarily an angular distortion of the *HB* network whereas the coordination number in the first coordination sphere, *4*, remains unchanged, which holds true for a majority of the crystalline and perhaps noncrystalline phases at low and moderate pressures (< 2 GPa). The small energy changes for the high-pressure ice transitions indicates that the tetrahedral coordination of the water molecules appears to be not very sensitive to the angular distortion as large as 30° from the optimal 109.47° tetrahedral angle. Subcritical water therefore is not a closely packed system in which a coordination number in the first coordination sphere should be either *12* for a closely packed crystalline structure or close to *8* for a random closely packed structure [6]. This fundamental deviation of the water structure from the close packing arrangement is most definitely due to the contribution of the hydrogen bonds to the local molecular arrangement. Using the X-ray diffraction measurements, Narten and Levy [8] found that the average number of the nearest neighbors is ~ 4.4 at 4-200 °C confirming the average tetrahedral geometry of the water molecule. Similar experimental techniques give very different numbers of nearest neighbors for simple liquids: for neon and argons, for example, 8.6 and 10.5 nearest neighbors were found, respectively [9]. Another interesting idea regarding the properties of the *HB* network resides in the attributing a high flexibility to this network. This property is in agreement with a large distribution of the O–O–O angles observed for the crystalline ice phases (see Table 2.2.1 below). In other words, upon external thermodynamic force a *HB* network undergoes a reconstruction in order to preserve the time-averaged continuity of the hydrogen bonds, which is achieved by the conformational transitions of a deformational type. This idea will be demonstrated below in using the example of the expanded-to-collapsed cluster transition. The flexibility of the water *HB* network helps to explain the density variations of the liquid water induced by external forces in general and, in particular, consolidates the ideas on relationship between the open

work clathrate-hydrate structures and higher-density structures of ambient and supercooled liquid water.

Concerning the life-time of a particular instantaneous or time-averaged configuration relevant to a certain macroscopic property in the solid or liquid water, it is possible to establish three distinct levels according to fast molecular oscillations and slow molecular rotations and translations: (i) instantaneous configuration or snapshot; (ii) vibrational τ_V time scale and the corresponding averaged configuration (*V*-configuration); (iii) translational τ_D (rotational) time scale and the corresponding diffusionally-averaged *D*-configuration [9]. In particular, τ_V can be estimated as the average period of a molecular vibrational mode, which is in the case of *Ih* is the hindered translational mode at ω = 200 cm^{-1}. Accordingly, the characteristic vibrational time $\tau_V \sim 1/(\omega \cdot c)$ of water molecule in *Ih* is ~ 0.2 ps (1ps = 1×10^{-12} sec), (*c* designates the speed of light in vacuum). Therefore, a structure observed at a time scale smaller than τ_V should be considered as an instantaneous configuration, whereas the structure observed at time scale $\tau_V < t < \tau_D$ is a vibrationally averaged *V*-configuration. The frequency dependence of the dielectric function provides the estimation for the period of rotational rearrangement of the water molecules in *Ih*, which is ~10 μsec (i.e. 1×10^{-5} sec). Therefore, the structure observed over a period larger than τ_D (*Ih*) ~10 μsec is considered as a *D*-configuration. In liquid water, W_L, the molecular motions could be still divided between the fast oscillations within the same molecular cage and relatively slow rotational and translational rearrangements towards a new local environment. Indeed, spectroscopic studies revealed that the hindered translation band in liquid water is at 193 cm^{-1} [9], which is very close to 200 cm^{-1} of *Ih*, giving essentially similar value of τ_V (W_L) at 0.2 ps. In sharp contrast to the coincidence in the frequency of the molecular vibrational modes for the liquid and solid water, the dielectric relaxation time for liquid water at 0 °C is of the order of 10 ps that also sets the value of τ_D (W_L) to ~10 ps. which is by six orders of magnitude smaller than that for solid *Ih* but still significantly larger than the corresponding period of a molecular vibration. In accord with the aforementioned data, the thermal motion of water molecules in the solid and liquid phases can be regarded as being of two types: the rapid oscillations about a temporary position within the molecular cage and the slow inter-minima hoppings, which are of course much faster in the case of normal liquid state in comparison with that in the solid or supercooled liquid states. There are peculiar data with reference to the nearly identical values of the relaxation time and the activation energy for

different response processes in the water media such as self-diffusion (τ_{Diff} (*Ih*) ~1.7 μsec at −2 °C and 0.63 eV=14.482 kcal·mole^{-1}), dielectric relaxation (τ_{Debay} ~ 2.2 μsec at −2°C and 0.58 eV=13.333 kcal·mole^{-1}) and the average time-of-stay of a molecule at a given orientation of proton-proton vector (τ_{H-H} ~ 0.6 μsec and 0.61 eV=14.023 kcal·mole^{-1}) [10 and References therein]). The mechanism of molecular reorientation in hexagonal ice is primarily associated with valence faults and molecular vacancies. In particular, migration of non-deal vacancies is found to be equally effective in all relaxation processes in the ice lattice such as molecular diffusion, dielectric and elastic relaxations and spin-lattice relaxation [10].

The IR and Raman spectroscopy and inelastic neutron scattering provide information about the *V*-configuration for the liquid and solid states. In particular, it means that if there are different molecular complexes of the guest molecule embedded in the water matrix (assuming the presence of the activation barrier between nearest local minima) the corresponding vibrational bands will be fundamentally resolvable by the IR spectroscopy even though a guest molecule can change its vibrational status by walking from one distinct cage to the different arrangement. The lifetime of *V*-structure depends strongly on the temperature and phase state of the water medium. Considering a noncrystalline state of water, it should be noted that τ_D ascends significantly as the temperature decreases below 0 °C.

2.2 Crystalline and Non-Crystalline Solid Phases: General Description

Water demonstrates a fascinating range of crystalline phases, in which molecular packing varies from an open-work *4*-coordinated hexagonal architecture in *Ih*/*XI*/*Ic* system to high-density *8*-coordinated cubic packing of the two interpenetrating *HB* sub-networks in *VII* and *VIII* ice system. Traditionally, the ice phases are labeled with the Roman numerals *I*-*XII* in the order in which they were synthesized experimentally. This latter circumstance leads unfortunately to an absence of a relationship between a numerical identifier and an ice structure. Each of the crystalline phases, except ices *IV*, *IX*, *XII*, and *Ic*, is stable over a certain range of the (*T*, *P*) parameters, but it is a fundamental feature of the water *HB* network that many ice phases protrude inside a region of stability of another neighboring phase. Furthermore, some phases such as ice *Ic* or ice *XII* [11] are considered to be metastable over the entire thermodynamic (*T*, *P*) space. The partial phase diagram of water in the low pressure range is given below on Figure 2.2.1.

The structural properties of crystalline and non-crystalline ice phases have been investigated by a variety of techniques, including X-ray diffraction [12, 13], electron diffraction and microscopy [14, 15], neutron diffraction and inelastic scattering [16, 17], helium diffraction [18], calorimetry [19], and IR and Raman spectroscopies [20, 21, 22, 23, 24]. These studies have shown in particular that condensation of water vapor on a cold substrate at low pressure may lead to, depending upon the deposition conditions, the formation of different non-crystalline structures below 130 K and of polycrystalline ice (pc-ice for short) polymorphs, *Ic*, and *Ih* at a more elevated temperature. The metastability of cubic ice is especially important for the present studies because it is shown that the low-density nc-ice, formed initially by water vapor deposition at temperatures below ~135 K, crystallizes upon annealing firstly into the polycrystalline cubic ice, *Ic*, at 150-160 K. The transformation of the latter metastable phase into thermodynamically stable hexagonal ice, *Ih*, occurs only at much higher temperatures near 230 K [13]. It could be suggested that these kinetic properties of "extended" metastability and coexistence of different phases indicate the presence of a network of flexible intermolecular hydrogen bonds. These bonds are responsible for the peculiar properties of water phases.

As just mentioned, apart from the thirteen crystalline phases, solid water can exist at low temperatures in a supercooled state and in a number of noncrystalline solid forms, the existence of which and the peculiarity of their properties pose some interesting questions in condensed matter physics. Among them, the following issues should be highlighted: the nature of the sharp increase in isothermal compressibility, the isobaric heat capacity, and the magnitude of the thermal expansion coefficient upon supercooling; the nature of non-crystalline forms of solid water and the transitions between them; the relationship between liquid, supercooled, and solid water below and above glass-liquid transition temperature, T_g. To date, there are known to be, at least, three amorphous solid phases, which are distinctly different by the density, low-density amorph (*LDA*)(ρ ~ 0.94 g·cm^{-3} at P = 1 bar [11]), high-density amorph (*HDA*)(ρ ~ 1.17 g·cm^{-3} at P = 1 bar [11]), and very high-density amorph (*VHDA*)(ρ ~ 1.25 g·cm^{-3} at P = 1 bar [25]). The *LDA* is of special interest for the present studies because it is formed by the vapor water deposition on a cooled metal surface. The other polyamorphous high-density non-crystalline modifications are less relevant because they only exist at a high pressure range.

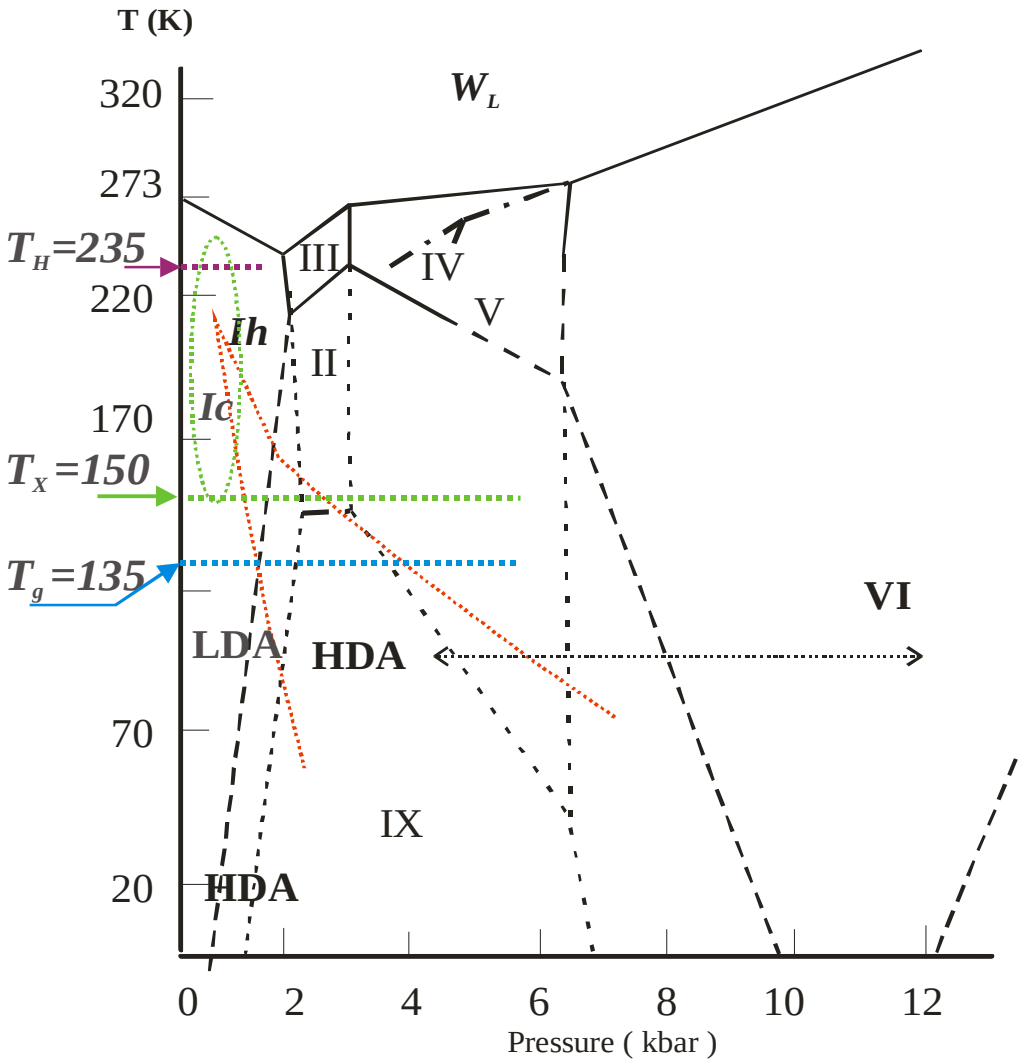

Figure 2.2.1. Schematic partial phase diagram of water [12]. Together with the crystalline ice phases, the regions of existence of non-crystalline low and high-density polyamorphs are also shown. T_H is the temperature for homogeneous nucleation of water; T_X is the temperature of crystallization to *Ic* of the amorphous water obtained by annealing of the low-density amorph; T_g is the glass transition temperature. Stable equilibriums are shown in continuous black lines; measured metastable equilibriums - dash black lines and estimated equilibriums - short dash lines. The approximate *T* region of kinetic stability for cubic ice, *Ic*, is indicated by a green oval. The dotted red lines represent the approximate equilibrium between the *LDA* and the *HDA* (left line) phases and the equilibrium between the *HDA* and the ice *VI* (right line).

Table 2.2.1. Structures of the crystalline phases of water. Parameters are given at the temperature *T* and the pressure *P* stated.

Ice	Crystal System	Space Group	Molec. per cell /*H.Ord.*	T (K)	P (GPa)	Density ($g \cdot cm^{-3}$) /*Mol.V.* ($Å^3$)	Coord. N. /*NN Dist.* (*Å*)	O–O–O Angles (Deg)/ *Str. El.*	Cell Par. (Å), (Deg)	References
Ih	Hex.	$P6_3/mmc$	4 *N*	250	0	0.920 *32.52*	4 *2.74*	$109^{\circ}_{\pm 0.2}$ *Hex.*	a = 4.518, c = 7.356	Kuhs and Lehmann [26]
Ic	Cubic	$F\bar{4}3m$	8 *N*	78	0	0.931 *32.13*	4 2.75_{148}	109° *Hex.*	a = 6.358	Kuhs *et al.* [27]
II	Rhomb.	$R\bar{3}$	12 *Y*	123	0	1.170 *25.57*	4 *2.75-2.84*	80-128°	a = 7.78, α = 113.1°	Kamb [28]
III	Tetrag.	$P4_12_12$	12 *N*	250	0.28	1.165 *25.68*	4 *2.76-2.80*	87-141° *Pent.*	a = 6.666 c = 6.936	Londono *et al.*[29]
IV	Rhomb.	$R\bar{3}c$	16 *N*	110	0	1.272 *23.52*			a = 7.60 α = 70.1°	Engelhard and Kamb [30]
V	Mon.	*A2/a*	28 *N*	98 223	0 0.53	1.231 *24.30* 1.283 *23.32*	4 *2.76-2.87*	84-128°	a = 9.22 b = 7.54 c = 10.35 β = 109.2°	Kamb *et al.* [31]
VI	Tetrag.	$P4_2/nmc$	10 *N*	225	1.1	1.373 *21.79*	4 *2.80-2.82*	76-128°	a = 6.181 c = 5.698	Kuhs *et al.* [32]
VII	Cubic	*Pn3m*	2/*N*	295	2.4	1.599 *18.71*	8 *2.95*	109.5°	a = 3.344	Kuhs *et al.* [32]
VIII	Tetrag.	$I4_1/amd$	8 *Y*	10	2.4	1.628 *18.38*	8 *2.96(HB); 2.80; 3.15*	109.5°	a = 4.656 c = 6.775	Kuhs *et al.* [32]
IX *III*	Tetrag.	$P4_12_12$	12 *Y*	165	0.28	1.194 *25.06*	4 *2.76-2.80*	87-141° *Pent.*	a = 6.692 c = 6.715	Londono *et al.* [29]
X	Cubic	*Pn3m*	2	300	62	2.79 *10.72*			a = 2.78	Hemley *et al.* [33]
XI *Ih*	Ortho.	$Cmc2_1$	8 *Y*	5	0	0.934 *32.03*		$109^{\circ}_{\pm 0.2}$ *Hex.*	a = 4.465 c = 7.858 a = 7.292	Line and Whitworth [34]
XII *IV*	Tetrag.	$I\bar{4}2d$	12 *N*	260	0.50	1.292 *23.15*			a = 8.304 c = 4.024	Lobban *et al.* [35]

There is an apparent similarity between the processes of crystallization of metastable supercooled media above T_g=135 *K* and below T_X =235 *K*. The former process is much slower than the latter because takes place at lower temperatures, which allows experimental observation of the crystallization in the time domain. In the present studies the FTIR RAS

investigation of the crystallization of the vapor deposited *LDA* has been undertaken and reported in Chapter 5. There are premises for assuming that these results could be useful also for studying the nucleation mechanism at upper limit of the liquid stability.

Among the twelve known crystalline phases of water today, the hexagonal ice *Ih* (space group $P6_3/mmc$) is the normal form of ice obtained by freezing water at atmospheric pressure or by direct condensation of vapor above ~170 K. At temperatures below 273 K and at pressures equal to or lower than 1 atm, *Ih* is assumed to be the thermodynamically most stable phase of solid water. Its metastable polymorph of a locally similar structure, the ice of cubic symmetry, *Ic*, with space group $F\bar{4}3m$ can be formed, in particular, by the heating of either vitrified states of water [12 and references therein,13], any of the high-pressure ices (*II* to *IX*) [36], or the pressure-amorphized cubic and the hexagonal ices [37]. The direct transition from the liquid water to cubic ice $W_L \rightarrow Ic$ was observed in the experiments on the hyperquenching of the micrometer water droplets down to 170-220 K [11], and on the evaporative cooling of the water clusters of $4\text{-}6\times10^3$ molecules down to 200 K [38]. These observations are thought to be in accord with the Ostwald cascade rule [38, 39], which could be formulated in the following statement: if several different crystalline phases exist, a metastable non-crystalline material will transform through a number of intermediate metastable forms to a crystalline state of the next-lowest free energy, which is the least stable one. In other words, under certain thermodynamical conditions, the formation of the cubic ice nuclei appears to be more favorable kinetically than that of the hexagonal polymorph. Therefore, the cubic ice will be formed first, instead of the hexagonal ice, if the crystallization process is governed by the kinetics, which requires a certain level of supersaturation. This possibility is of a special significance for the atmospheric physics and the chemistry because the cubic ice phase could be involved in the formation of icy particles in the clouds and of snowflakes [40, 41, 42]. The recent observation and computer modeling of the atmospheric halo over Northern Chile in the vicinity of the persistently steaming Lascar volcano provide further support for the possibility of the presence of the cubic ice together with *Ih* in the atmosphere in the form of spatially oriented octahedral *Ic* crystals in the cirrus clouds at temperature as low as 187 K [43]. The rareness of such observations could be interpreted in such a way that only in some rare and unique cases the crystallization of water droplets occurs under such supersaturation that would be high enough to cause the crystallization of cubic ice. The formation of *Ic* could be

considered, therefore, as an indicator of the crystallization that occurs in a deeply supercooled media. In the particular case [43], there are grounds for further speculation that the hot stream rising up from the volcano becomes highly supersaturated with respect to the liquid and solid water or $H_2O/H_2SO_4/NH_3$ systems after deep adiabatic cooling and especially after sharp and deep cooling by the very cold air masses at high elevations. Other atmospheric features, such as the noctilucent clouds, could also contain ice crystals in the cubic form [44].

2.3 Structures of Selected Solid Ice Phases

The structures of crystalline water phases play a fundamental role for understanding the structural and dynamical properties of the bulk and the surface of non-crystalline water microphases. Any model of non-crystalline water is constructed either on the basis of the known crystalline structure of one or a few coexisting phases or by applying symmetry operations incompatible with the continuous crystalline lattice.

2.3.1 Structure and Properties of Hexagonal Ice, *Ih*, and its Proton Ordered Structural Analog Ice *XI*

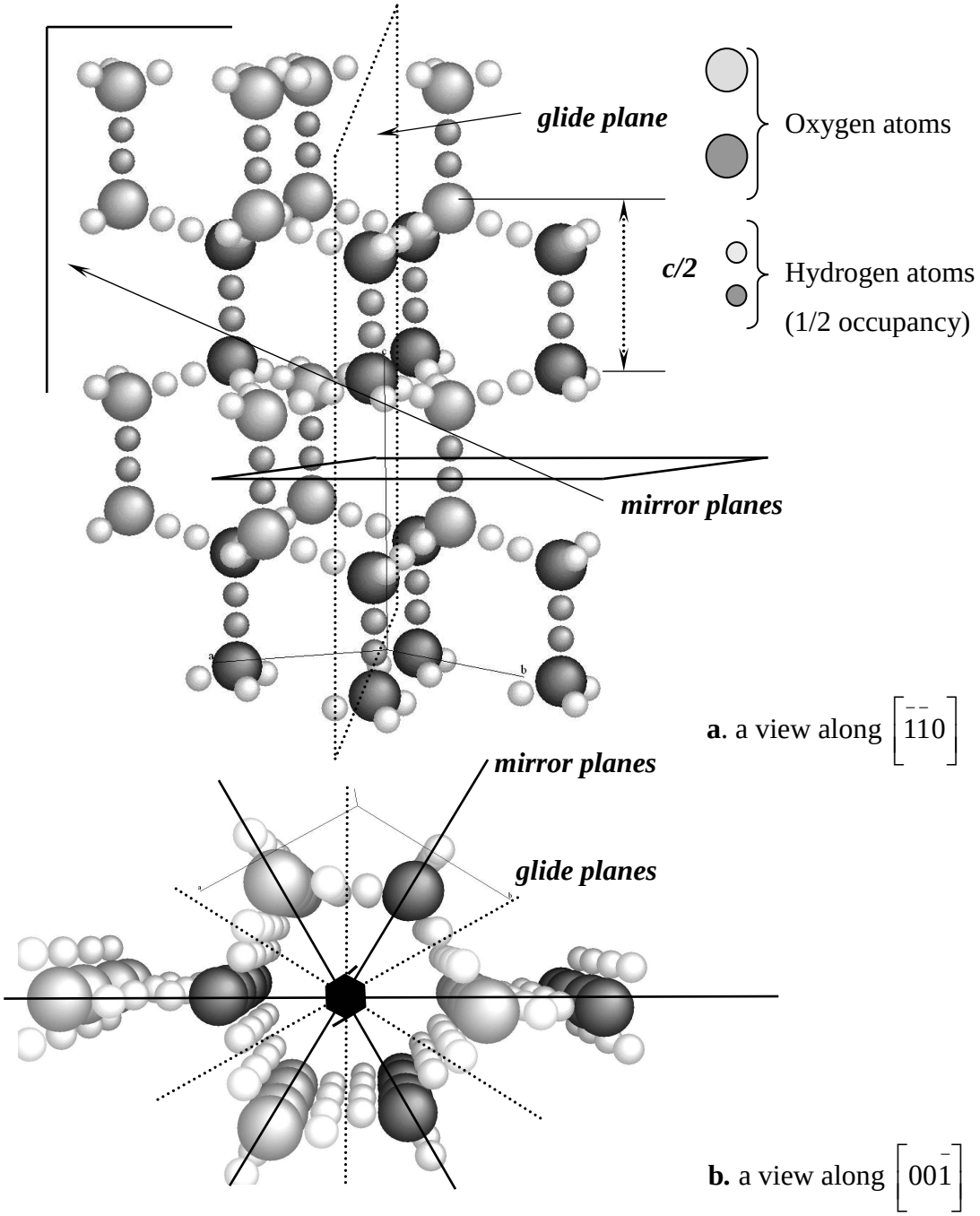

Figure 2.3.1. Crystallographic structure of the proton-disordered hexagonal ice, Ih [26]. Oxygen subnetwork belongs to the hexagonal space group $P6_3/mmc$**.**

There are *4* water molecules in the $P6_3/mmc$ hexagonal unit cell with the following lattice parameters: a = 4.4969 Å and c = 7.3211 Å at 10 K and 4.519 Å / 7.357 Å, respectively, at 253 K [11]. The ordered oxygen subnetwork displays a hexagonal-ring packing characterized by the 6_3 screw axis passing through the center of hexagons (i.e. the origin of the unit cell, Figure 2.3.1, *b*) and a set of three mirror and three *c/2* glide planes passing through the screw axis. Two adjacent layers of the puckered but otherwise close to ideal hexagons are related by the mirror plane (Figure 2.3.1, *a*). The fundamental features of the oxygen packing in the hexagonal ice, *Ih*, reside in the close-to-ideal tetrahedral configuration of the first coordination sphere, which assumes the presence of four nearest neighbors around an oxygen atom and the closeness of the O–O–O angles to the tetrahedral value of 109.5°. Unlike the crystalline closest packing, which assumes *12* nearest neighbors and is driven primarily by the dispersion forces, the present tetragonal arrangement exists as a network of the hydrogen bonded water molecules, in which the dispersion contribution to the lattice energy could be even negative. At 253 K, the mean value of the O–O *HB* distance is 2.764 Å, which is much shorter than 2.980 Å [45] for a water dimer in the gas phase, indicating a *very strong contraction* and, certainly, an energy gain in the *HB* contact between neighboring water molecules due to condensation. Unlike the ordered oxygen subnetwork, the hydrogen atoms appear to be in a disordered state, the average arrangement of which is shown in Figure 2.3.1. As a result of the proton disorder in the *Ih*, the hydrogen atoms are randomly distributed over the crystal. The most significant structural feature of the *Ih* structure is the nearly ideal tetrahedral first coordination sphere for a water molecule. The tetrahedrality of the first coordination sphere is a main topological element in the hydrogen bonding of water molecules.

(a) Fragment of the proton ordered ice *XI* structure at a orthorhombic space group $Cmc2_1$.

(b) Fragment of the proton disordered *Ih* structure with the O-subnetwork at a hexagonal space group $P6_3/mmc$.

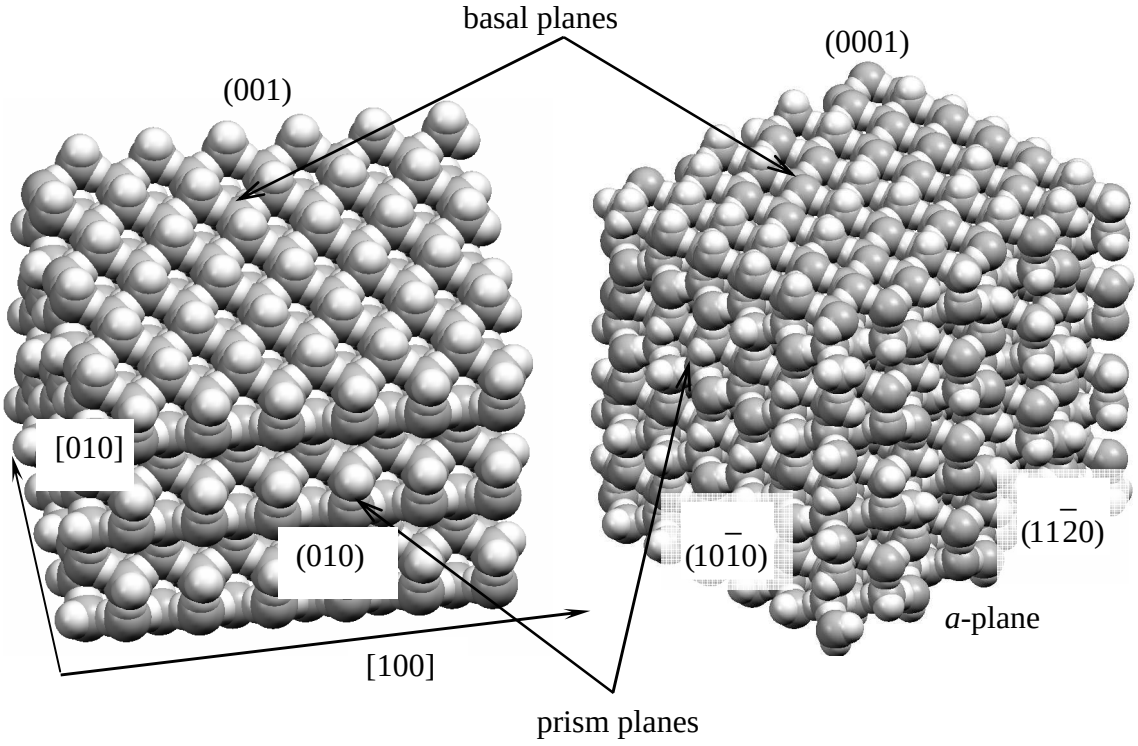

Figure 2.3.2. Crystallographic models of (a) the proton-ordered ice XI and (b) the hexagonal ice**,** ***Ih*****.**

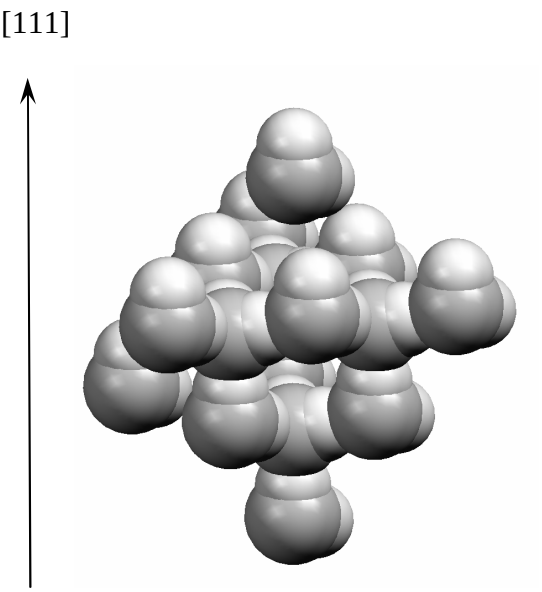

Figure 2.3.3. Fragment of the crystalline cubic structure. Cubic ice *Ic* $F\bar{4}3m$, a = 6.37 Å, (fragment of the structure). A vertical line is parallel to the [111] direction.

Similarly to the structure of *Ih*, the crystal structure of proton ordered ice *II* shown on Figure 2.3.4 can be constructed from the water hexagons, which are less puckered in this case. Kamb [28] described the crystallographic relationship between these two phases in a following way: hexagonal columns of *Ih* are detached from one another and shifted relatively up and down in the [111] direction in order to give a rhombohedral stacking pattern, and then rotated by ~ 30° around their axis ([111]) such that a more closely packed system can be generated by reconnecting those hexagons. The hexagonal rings within each column are twisted by 15° relative to one another as it is shown below on Figure 2.3.5. The *HB* connectivity of the hexagonal rings and the arrangement of the columns is shown on panels *a* and *b* of Figure 2.3.5, where the length of *HB's* (shown in wire lines) binding the nearest neighbors within the rings is 2.78 Å (light spheres, panel *a*) and 2.80 Å (dark spheres, panel *a*). The *HB's* between rings within the columns and between the columns are at 2.77 Å and 2.84 Å, which is shorter and longer than that in the rings, respectively. The overall length of the *HB* contacts in the ice *II* structure appears to be slightly larger than that in the *Ih* and *Ic* structures, which finds corresponding manifestation in the IR spectra: ν_{OH} (HDO in D_2O) appears at 3277 cm^{-1} in *Ih* and at 3373 cm^{-1}, 3357 cm^{-1}, and 3323 cm^{-1} in ice *II* [46].

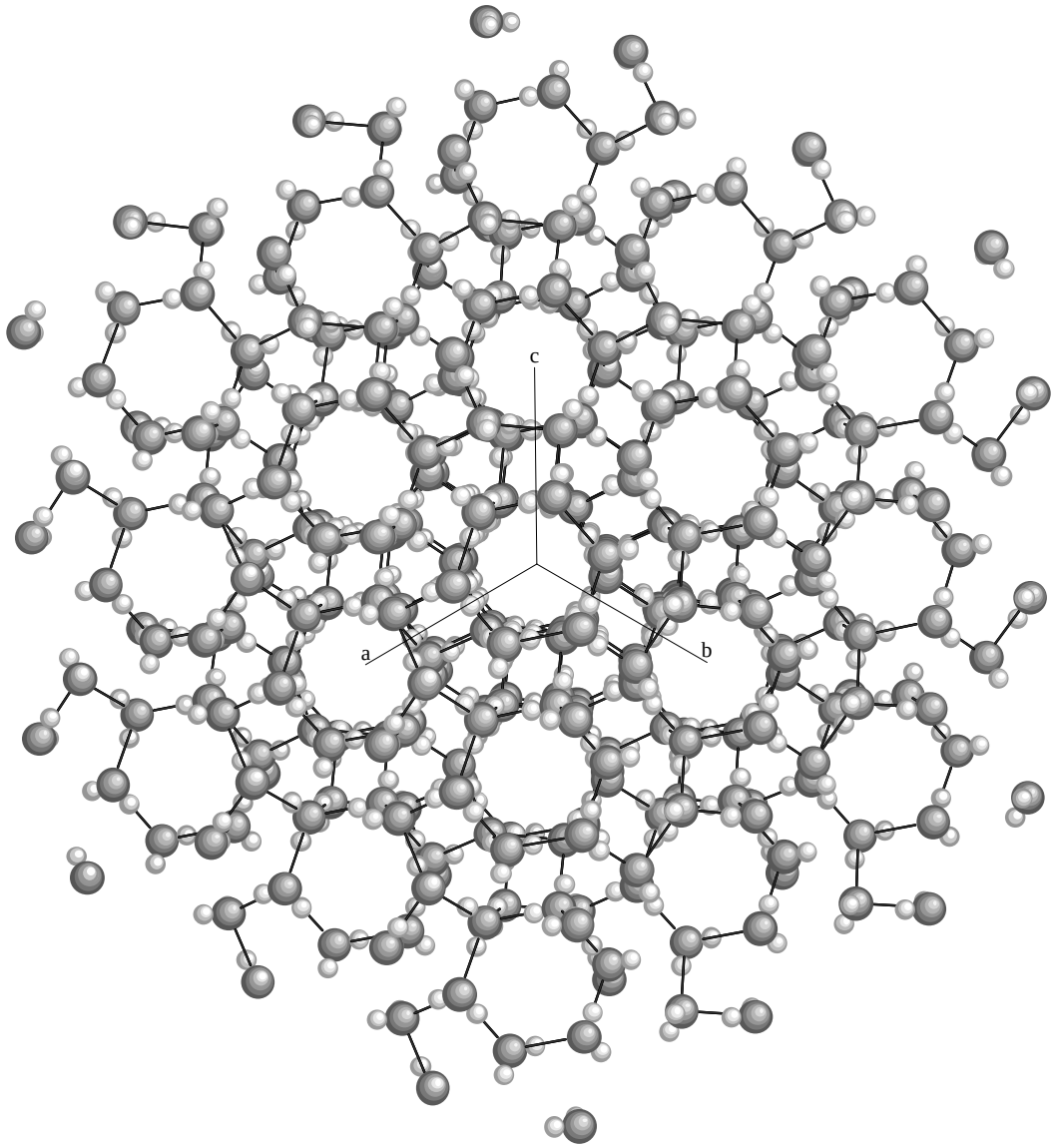

Figure 2.3.4. Crystallographic structure of proton ordered ice II. Rhombohedral lattice, space group, after Kamb *et al.*[28]. Oxygen and hydrogen atoms are represented by dark (larger) and light (smaller) spheres, respectively. The picture contains 27 unit cells.

The internal energy of ice *II* of $R\bar{3}$ space group is larger than that of hexagonal ice only by 19×10^{-3} kcal·mole^{-1} , which indicates minor weakening of the *HB* network due to the distortion of the "perfect" hexagonal packing in *Ih* [9]. However, in contrast to the proton disorder *Ih*, hydrogen atoms in the ice *II* are ordered in a way that facilitates a cooperativity

effect, which in turn strengthens the bonding in *HB* systems. With respect to the distances between third-neighbors (1⋯4) O··O, there is a remarkable difference between *Ih*/*Ic* and ice *II*. This structural difference resides in the appearance of the non-*HB* molecular pairs at distances between 3.24 Å to 4.76 Å (see panel *c* on Figure 2.3.5 for the ice *II*), whereas in the *Ih*/*Ic* structures the 1⋯3 neighbors are separated by ~ 45 Å. The hexagonal rings within columns are flatter in comparison with the *Ih*/*Ic* packing, which leads in particular to considerable shortening of the 1⋯4 between-ring distance from4.6 Å in *Ih* to 3.7 Å in ice *II*. These circumstances are reckoned for the density of ice *II*, 1.18 $g \cdot cm^{-3}$, which is higher than density of *Ih*/*Ic*, 0.93 $g \cdot cm^{-3}$ [11]. This structural feature of ice *II* arises from the high pressure force on the *HB* network causing such deformation of the latter, which allows decreasing of the molecular volume without disruption of the hydrogen-bonded network.

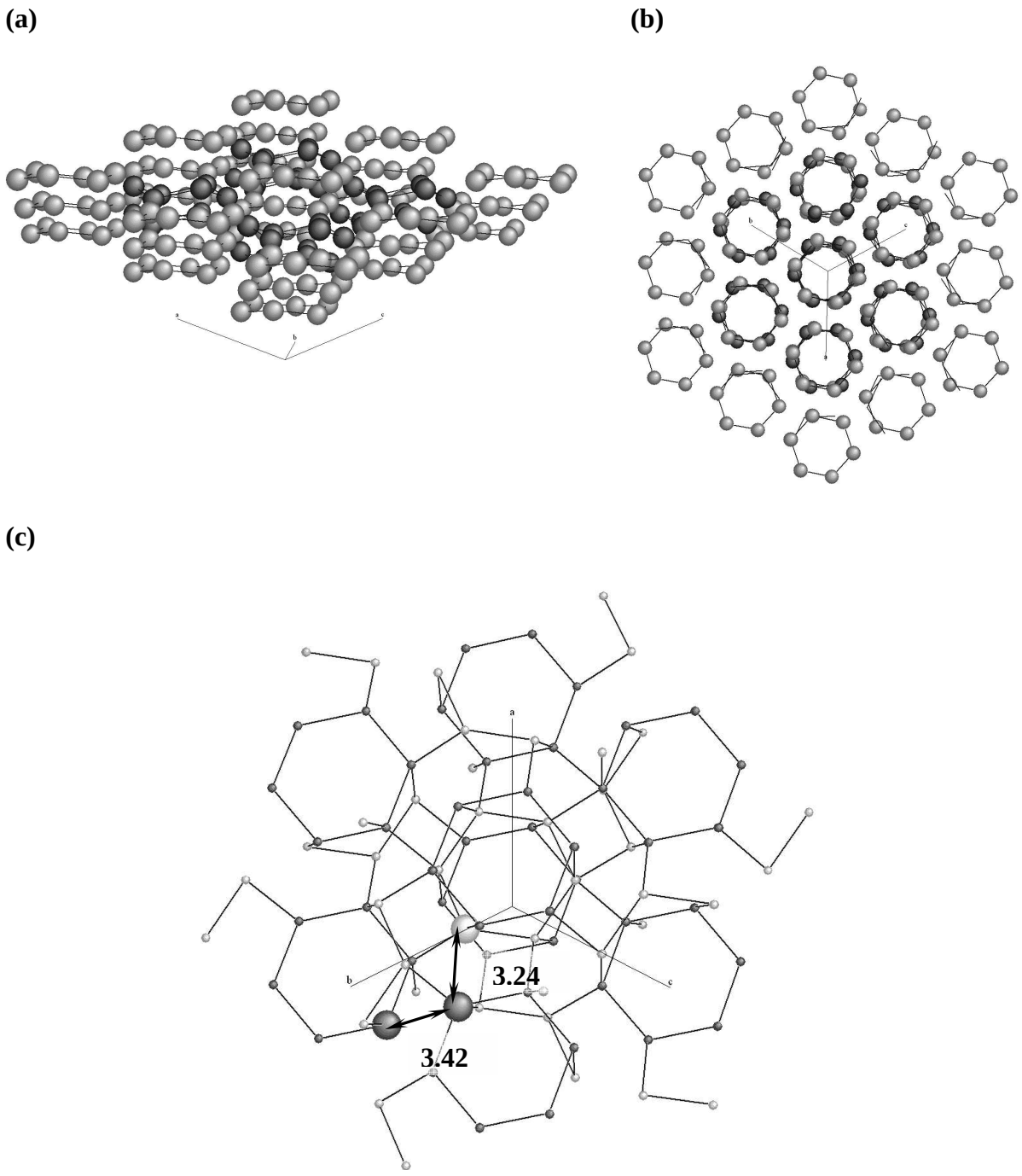

Figure 2.3.5. The oxygen subnetwork arrangement in ice *II*. (a) a side view (perpendicular to the [111]); (b) a top view (parallel to [111]) on the oxygen subnetwork of the ice *II* structure; (c) complete connectivity of the oxygen subnetwork in ice *II*. Two non-equivalent hexagonal rings are represented in dark and light grey color.

The ice *III* phase exhibits a proton disorder while ice *IX* phase is a crystallographically analogous proton-ordered phase. Unlike *Ih*, in which water molecules are arranged in hexagons, ices *III* and *IX* contain water molecules arranged in pentagons. As has been mentioned in the section 2.1, the Bernal and Walrafen models of non-crystalline water are based on the combination of hexagonal and pentagonal rings. Ice *III/IX* shown on Figure 2.3.6 is that crystalline phase, which provides support for such models.

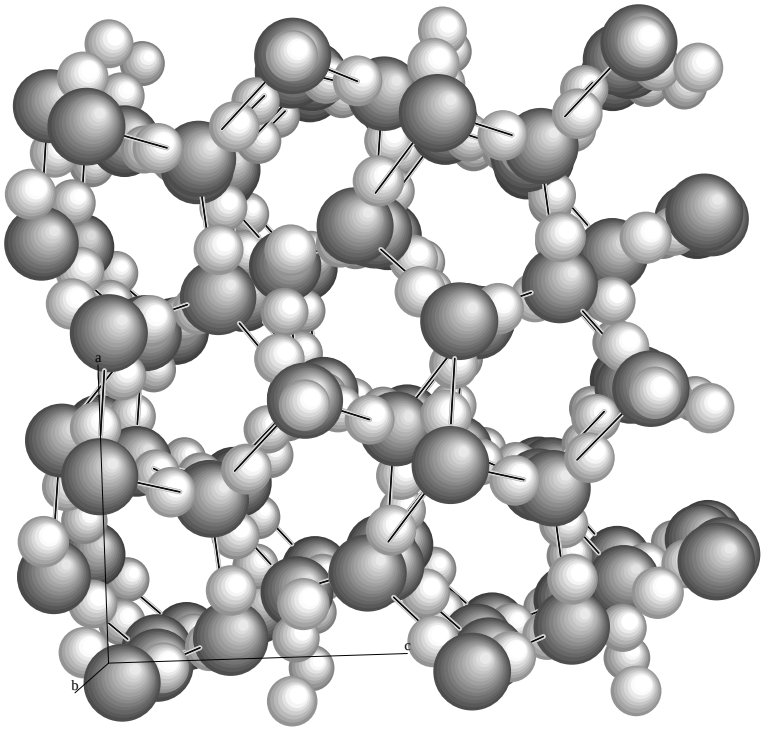

Figure 2.3.6. The structure of ices III and IX. Positions of the oxygen atoms (dark) in the crystallographic structure common for both ice phases are shown.

2.4 Structure and Properties of Non-Crystalline Water

Low-temperature micro-phases of ice have attracted intense interest over the past decade primarily due to their important role as a common medium for organic and inorganic chemical processes at different temperature regimes in the biosphere (220-273 K) [47], atmosphere (190-220 K) [48, 49], and interstellar space (10 K) [50]. The interaction of polymorph phases with the impinging molecules could lead to adsorption, clusterization and chemical modification, and diffusion in the original or modified forms into the bulk of the ice phase. The mechanisms of the interaction between the adsorbates and ice are therefore expected to depend on the bulk structure, and the surface properties and dynamics of the specific complexes of the micro-phases that exist under different temperature and other conditions.

Despite many sometimes controversial observations, there is a general consensus among the early studies [12, 51, 52, 53, 54] that condensation of water vapor on a cold substrate at low pressure under the appropriate deposition conditions can lead to the formation of different non-crystalline structures below 130 K and of polycrystalline polymorphs *Ic* and *Ih* at a higher temperature. In the case of nc-ice, the low-density amorphous ice is commonly described as a highly porous open network with nanoscale pores and therefore a significant concentration of non-compensated surface OH groups [23, 55]. For the more compact high-density amorphous ice, its structure has been proposed to be similar to the low-density amorphous ice, particularly in terms of the oxygen-oxygen radial distribution function but with additional water molecules occupying interstitial sites [53]. Non-crystalline structures are metastable with respect to crystalline phases *Ic* and *Ih* and consequently their formation and existence are kinetically controlled. Upon annealing to a higher temperature, nc-ice transforms irreversibly to *Ic* over 140-160 K [56], which in turn undergoes a further irreversible phase transition to *Ih* over 160-240 K. The wide transition temperature range of the *Ic*-to-*Ih* transition is thought to be the result of dependence of the crystallization temperature on the size of cubic ice crystals [56]. This series of crystallization processes, which begin at a temperature just above the glass-to-liquid transition, is found to be incomplete in the sense that fragments of non-crystalline micro-phases can coexist metastably with *Ic* over 140-210 K and with both *Ic* and *Ih* above 160 K. The nature of these non-crystalline micro-phases remains a subject of intense debate [13, 53, 54, 56]. These observations suggest that the ice phase

between 135 K (the onset of the glass-to-liquid transition) and 240 K (the completion of the *Ic*-to-*Ih* transformation) consists of non-crystalline and crystalline micro-phases in dynamic equilibrium, with increasing proportion of the latter phase with increasing temperature. The structural evolution of these ice micro-phases with temperature involves morphological and interfacial processes in which rearrangement of hydrogen bonds at multiple internal and external interfaces plays a key role. The reconstruction processes that accompany the phase transformations are believed to be responsible for the kinetically controlled nature of the phase transformations [56]. Clearly, the nature and composition of the ice micro-phases (the substrate) at a particular temperature induce a noticeable effect on the types of adsorbates and their interactions with the ice structure itself. On the other hand, molecules adsorbed on the surface or trapped into the bulk of such a complex, could in turn, affect the dynamics of the phase transformation and especially the progress of reconstruction. Indeed, very little is known about the surface complexes of the ice micro-phases over the temperature range 140-210 K.

The surface area of ice micro-phases may vary greatly from 240-500 m^2/g for vapor-deposited low-density amorphous ice (due to the abundance of nanoscale pores in a highly open network) [57] to 5-12 m^2/g corresponding to film structures without pores [58]. By comparing the amounts of surface areas of nc-ice and pc-ice deposited at 22-145 K by effusive beam dosing at different incident angles and by ambient dosing, Stevenson *et al.* showed that the surface area of the nc-ice deposits increases with a larger incident angle (from the normal direction) in qualitative accord with the predictions of the ballistic deposition model [59]. This model takes into general account of the interplay between roughening caused by randomness of deposition, smoothing by surface diffusion, and non-local effects generated by shadowing [60]. The unusually large values of surface area obtained by ambient dosing at 22 K (2700 m^2/g) and 77 K (640 m^2/g) along with the linear increase of the surface area with deposition time led Stevenson *et al.* to propose that the internal surface is directly connected to the external surface of the film. This observation is consistent with a grass-like or a dendrite-like model for the morphology of the ice film. Furthermore, the adsorbate uptake by the ice films deposited by beam dosing at different incident angles above 90 K was found to be the same as that by the pc-ice films deposited at 145 K [59], which can be explained by enhanced surface diffusion at a higher temperature. With increasing deposition temperature, the surface area of

the ice film was also found to be greatly reduced [59], suggesting isolation of the internal surface from the impinging gas molecules while the areas of the external surfaces of nc-ice and pc-ice films remain the same.

2.4.1 3-Dimensional Structural Units for the Non-Crystalline Water Hydrogen-Bonded Network

Spacefill model (left) and connection graph (right) of the bicyclo-octamer (*BO*) structural unit are shown on the Figure 2.4.1 below.

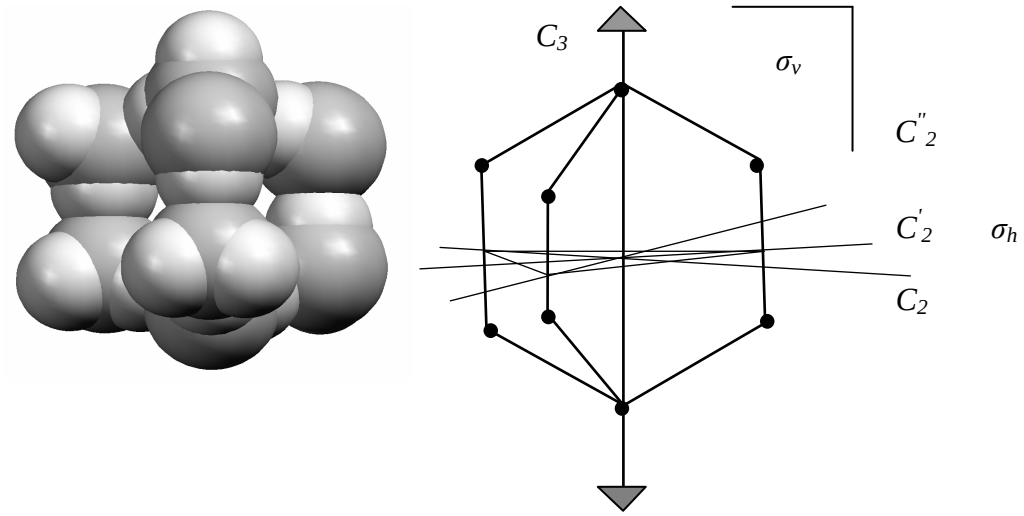

Figure 2.4.1. The structure of bicyclo-octamer unit.

The essential symmetry element of the oxygen subnet structure is a C_3 rotation axis and a set of three symmetry planes σ_v passing through two apical molecules of water and three C_2 axes in the plane of symmetry σ_h, which is perpendicular to C_3 and passing through the centers of three edges parallel to C_3. The oxygen subnet forms a molecular basis for the D_{3h} point group representation. However, disorder in the hydrogen subnet effectively reduces this symmetry to either C_s, such as shown on the next cartoon, or to E.

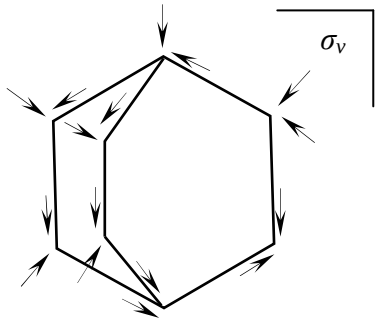

It turns out that, the *BO* packing pattern appears in the structure of the hexagonal ice *Ih*,

which can be assembled from the *BO* units sharing common edges within the hexagonal (basal) planes and common vertexes in the *c*-direction. In contrast, the *Ic* does not exhibit the *BO* arrangement pattern. On the other hand, the tricyclo-decamer and tetradecimal tetrahedral units, the structure and symmetry of which closely resembles that of *Ic* ice, can also be used for constructing larger scale symmetric water clusters. The core element of these two units is the adamantane-type water cluster, the oxygen subnet of which belongs to the tetrahedral point group T_d.

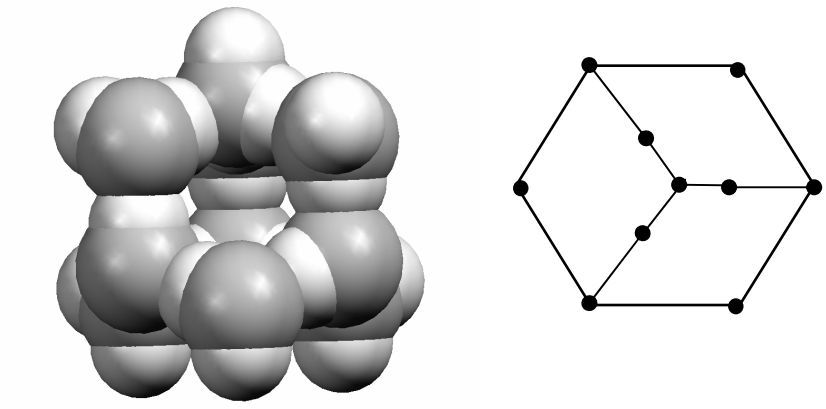

Figure 2.4.2. Structure and connectivity graph of the tricycle-decamer unit (10 H_2O).

The essential symmetry elements of the oxygen subnet for this decamolecular unit are: a set of 4 C_3 rotational axes passing through the apical molecules of water and the centers of opposite hexagons, three mutually perpendicular C_2 axes, and six σ_d planes. The oxygen subnet of this unit belongs therefore to the tetrahedral, T_d, point group. The *TD* structural unit resembles closely the structural pattern of *Ic*.

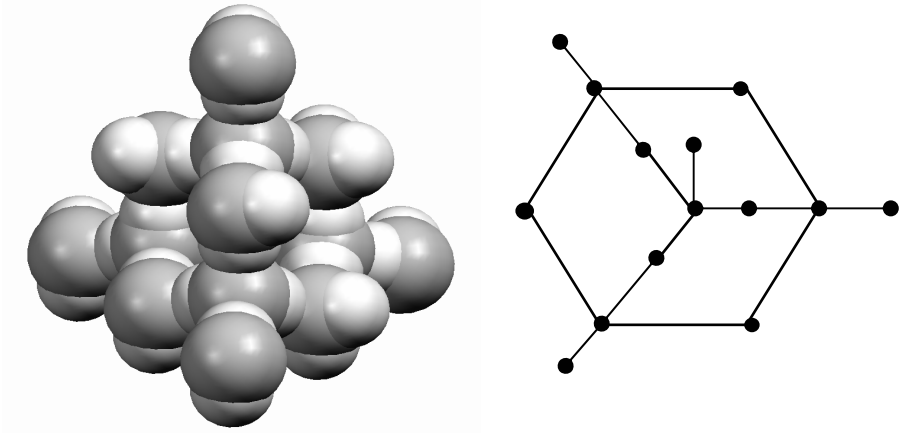

Figure 2.4.3. The structure and connectivity of tetradecimal structural unit (14 H_2O).

The oxygen sub-network belongs to T_d symmetry similarly to the tricyclo-decamer, which is a parent structure to the tetradecimal structural unit.

2.4.2 Icosahedral 280-mer Model of Non-Crystalline Water

Among possible spatially periodic and aperiodic structures, the icosahedral symmetric model is suggested by Chaplin [1] on the basis of pentagon-dodecahedron (5^{12}) central unit, which acts as a central core element. If the core unit remains non-deformed, an expanded structure can be generated with the average density of 0.94 $g \cdot cm^{-3}$. If, on the other hand, the core shell is deformed, so-called collapsed clusters can be obtained with the densities close to 1 $g \cdot cm^{-3}$ or higher. The equilibrium between expanded and collapsed structures is in accord with the concept of Frank and Wey on the flickering cluster representation of liquid water [61].

2.4.2.1 Expanded Cluster

Spacefill structure of the expanded 280-molecule cluster is shown below on Figure 2.4.4:

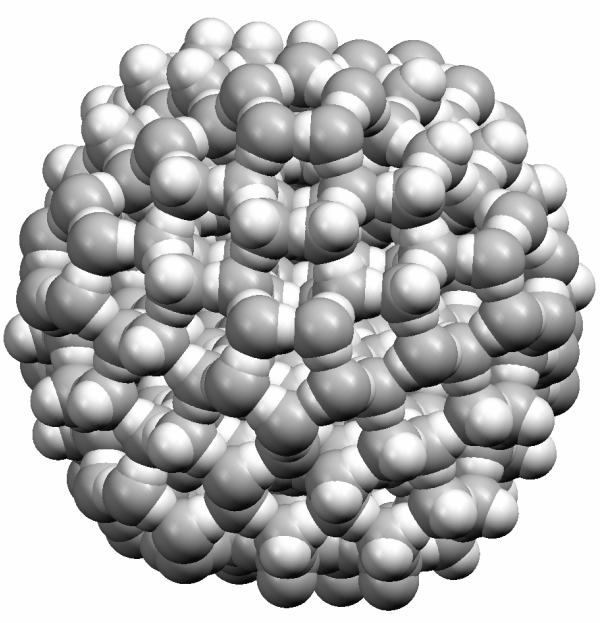

Figure 2.4.4. The spacefill 3-dimensional structure of expanded 280-molecule water cluster of icosahedral symmetry.

This expanded cluster with ~ 24.3Å of maximum radius consists of the three shells, which are enclosed one into another and defined according to the distance from the center of cluster. The molecular distribution in the expanded cluster as a function of the distance from the center of pentagon-dodecahedron central core and spherical coordinates (θ (0 – 360º)– angle between projection of radius-vector on *XY* plane and *X*–axis; φ (0 – 180º)– angle between radius-vector and *Z*–axis) are shown on Figure 2.4.5. While the first peak of density at ~3.88 Å designates the pentagon-dodecahedron core shell, two following peaks at 6.64 Å and 7.96 Å represent the second shell, which contains 80 water molecules. The third shell of 180 water molecules begins at 10.7 Å and spreads up to 12.4 Å.

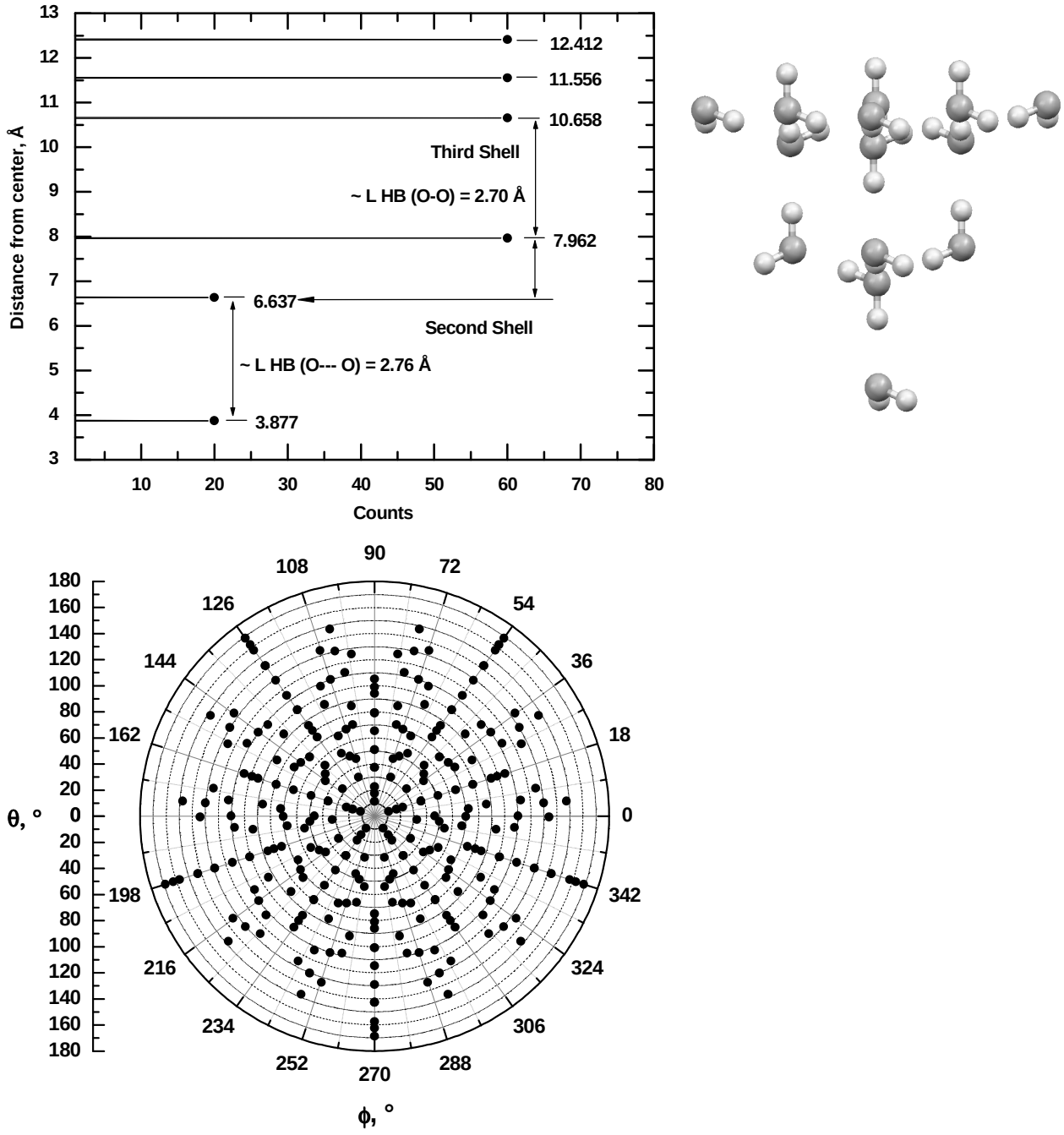

Figure 2.4.5. The representation of the expanded cluster in the spherical coordinates.

The position of each shell from the center can be associated with the molecular layers in the tetradecimal tetrahedral units as is clear from a right panel on Figure 2.4.5. It means that the overall radius of the icosahedral is determined by the height of the tetradecimal tetrahedral unit. The geometry representation in the spherical coordinate clearly reveals the 5-fold

rotational symmetry of the expanded cluster, which is in accord with the symmetry of the first shell.

The structures of individual the first and the second shells are visualized below on Figure 2.4.6 and Figure 2.4.7, respectively:

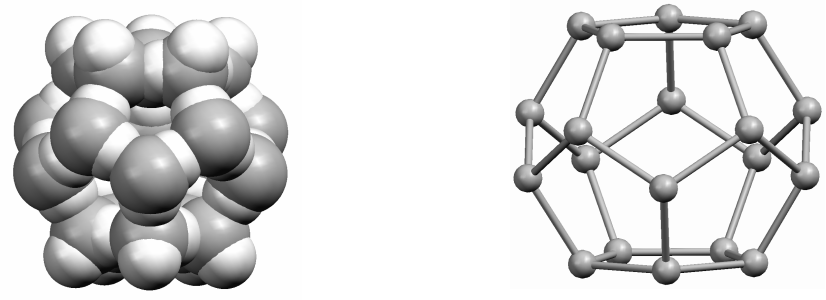

Figure 2.4.6. The pentagon-dodecahedron first shell (5^{12}): 20 water molecules, a key structural element of expanded cluster and the Chaplin's model of liquid water.

It is evident that in this well-defined 5-fold symmetry shell there are three nearest-neighbors at distance of ~ 2.8 Å for each water molecule, whereas the corresponding hydrogen-bonded fourth neighbor belongs to the second shell. The number of nearest neighbors for each molecule from the first shell is four, and they are hydrogen bonded in accord with the Bernal-Fowler rules. From a stoichiometric perspective it is possible to construct the dodecahedron shell from three pentagonal rings and five individual water molecules, which is however less probable in pristine water because such a regular arrangement would be of low configuration entropy. Pentagonal rings are thought to be a part of the structure of the liquid water network. The pentagon-dodecahedron shell of the expanded cluster provides the inherent cavity with a radius of ~ 3.9 Å, which can be occupied by the guest molecules of appropriate dimensions. From a structural perspective, the guest molecule could be considered as a pattern-forming entity, which acts as a nucleus around which assembling the pentagonal rings and individual water molecules assemble. Indeed, the pentagon-dodecahedron unit is a core structural element of clathrate-hydrates of type I and II, where they are occupied by the guest molecules with van der Waals diameters not exceeding ~5.2 Å, such as Ar, CH_4, Kr, Xe, H_2S and CO_2. These guest molecules appear to act as nucleation centers for the formation of pentagon-dodecahedral core unit, which in turns acts as

a motif for further growth of the clathrate hydrate lattice. It should be noted that the above mentioned guest molecules exhibit primarily hydrophobic properties, which cause such a configuration of the hydrogen bonds network such that there are exclusively hydrogen bonds directed outwards from the dodecahedron and no bonds directed inwards the core unit (as it can be seen on the right part of the picture above). Furthermore, it is possible that a certain arrangement of the hydrogen bonds within the first shell would be more energy favorable than others, which would lead to a specific rather than random polarization of the dodecahedron units. In this particular arrangement, given on Figure 2.4.6, ten oxygen atoms of the equatorial belt of the pentagon-dodecahedron are in the acceptor positions whereas two sets of five atoms on the "top" and the "bottom" are in the donor positions for the hydrogen bonding with the second shell.

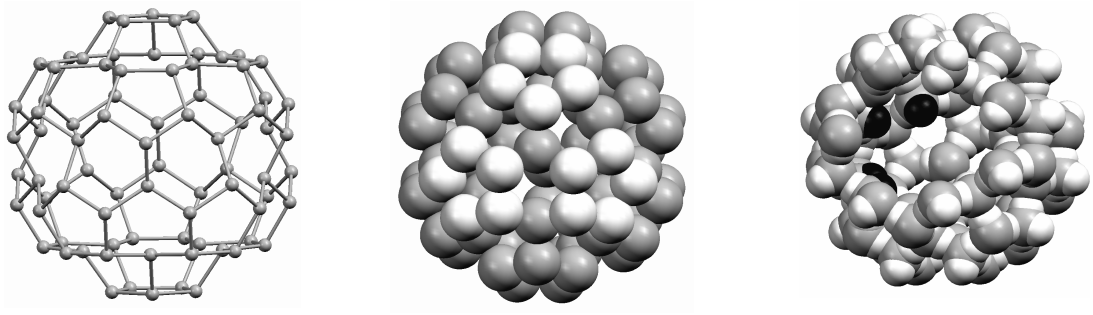

Figure 2.4.7. Second Shell: 80 water molecules.

Similarly to the first shell, the second shell consists of a two-dimensional mesh of hydrogen bonded water molecules with three nearest neighbors within the shell. The shell could be constructed from 12 pentagonal rings (three of which are shown in light gray color on the central panel of Figure 2.4.7) and 20 individual water molecules. A quarter of the molecules are hydrogen bonded with the first shell (on the right panel 4 hydrogen atom in black color are those pointing inwards and therefore acting as a donors in the hydrogen bonding with the oxygen atoms of the first shell, which are at the equatorial belt), whereas remaining three quarters are hydrogen bonded to the third shell. There are total of 20 hydrogen bonds between the first and second shells.

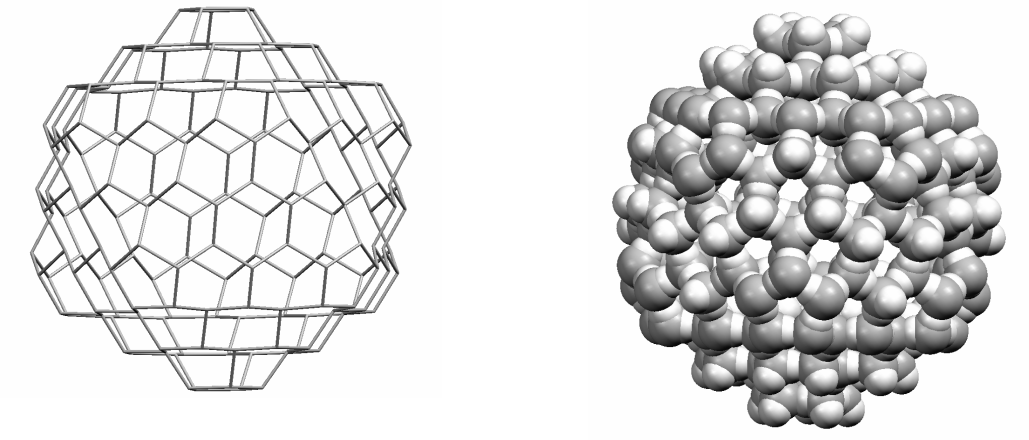

Figure 2.4.8. Third shell: 180 water molecules.

In contrast with two smaller inner shells, the third outer shell of the expanded cluster can be constructed exclusively from the pentagonal and hexagonal rings. Linked together, 12 pentagonal and 20 hexagonal rings form an uninterrupted hydrogen bonded mesh with diameter of ~ 24 Å. The hexagonal rings exhibit both chair and book configurations. This third shell shows a variety of the *HB* acceptor and donor configurations (see right panel in Figure 2.4.7) towards the interior and the exterior water or guest molecules. From a standpoint of the hydrogen bonding this shell therefore represents a heterogeneous *HB* structure (although it is not completely random) due to the irregular arrangement of the *HB* donor and acceptor "surface" fragments.

2.4.2.2 Construction of the 280-mer Molecule Expanded Cluster from the Structural Units

The icosahedral extended cluster can be constructed [1] from three above-mentioned 3-dimensional structural units as shown Figure 2.4.9 and Figure 2.4.10.

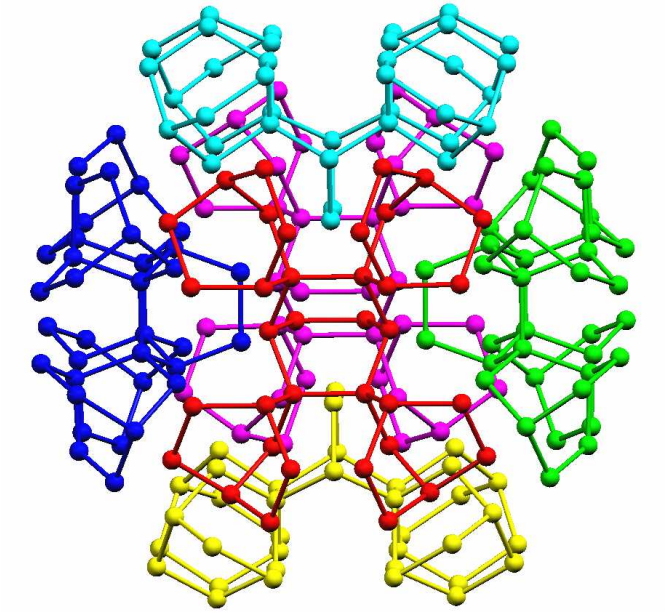

Figure 2.4.9. Construction of the 280-mer expanded cluster from the 22 bicyclo-octamer units. 64 H_2O or 8 *BO* units are removed for clarity.

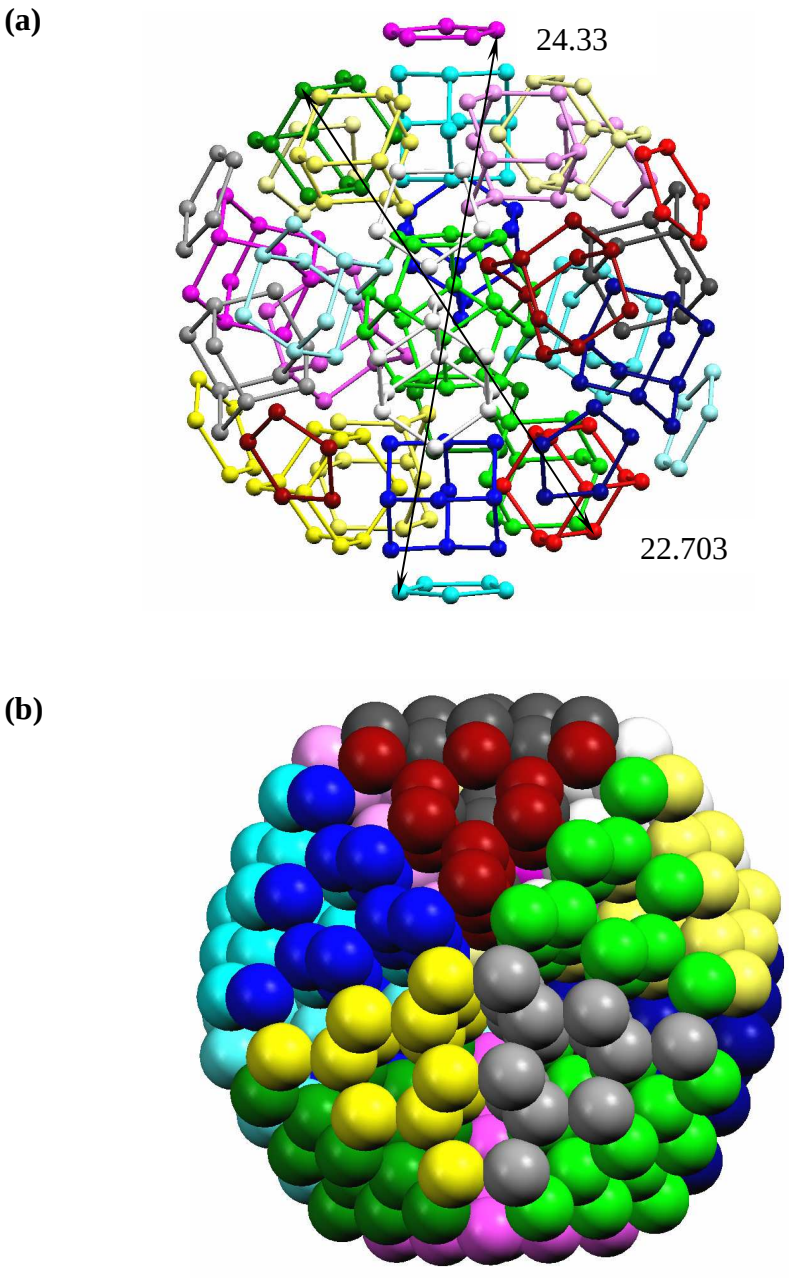

Figure 2.4.10. Construction of the expanded cluster from the primitive strucutral units.

(a) combination of 20 tricyclo-decamer units, 12 pentagonal units and a pentagon-dodecahedron unit (green color) in the center of cluster (water hexagons in the "book" conformation occur at the connections of two decamers); (b) construction of the expanded cluster from tetradecimal units.

The radial distribution function of O···O in the expanded cluster is shown on the separately for each shell.

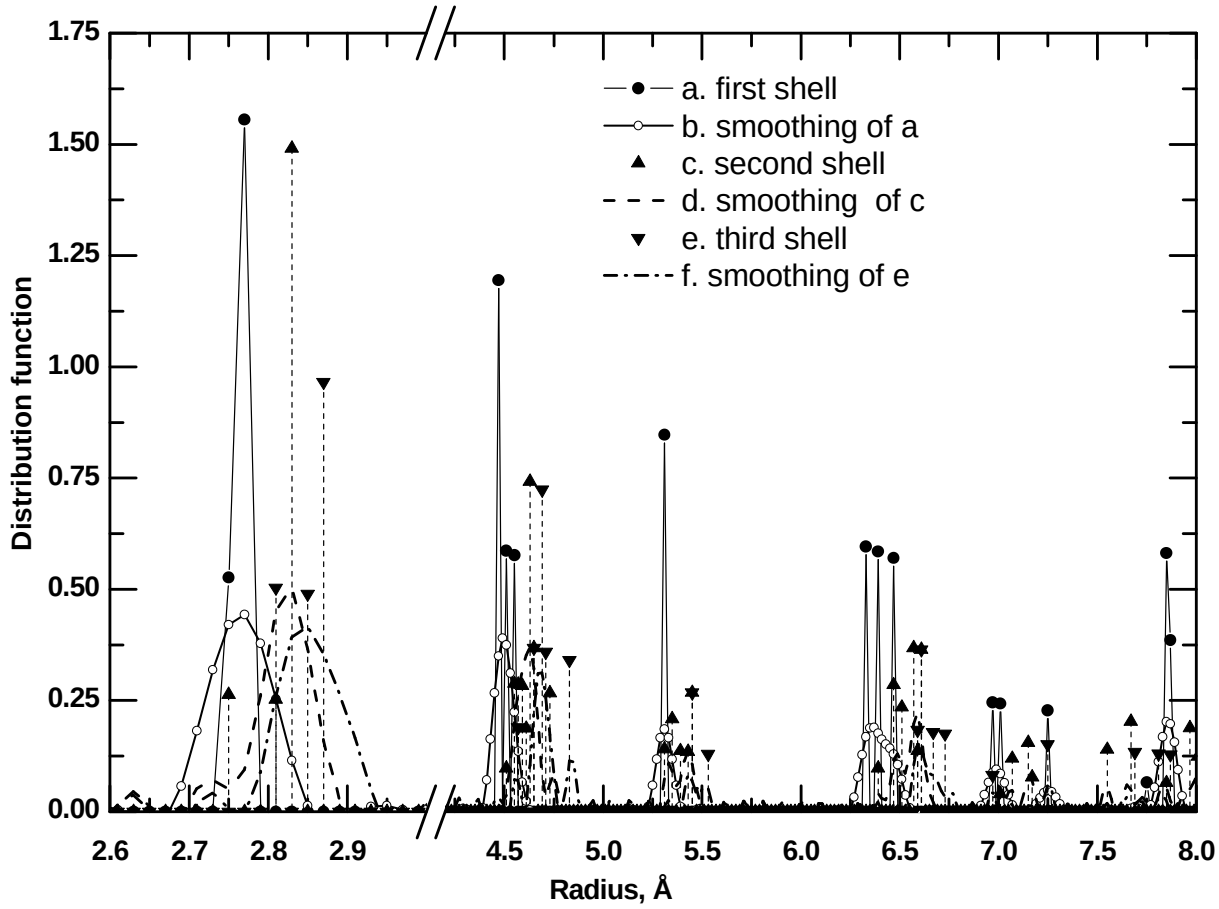

Figure 2.4.11. The radial O···O distribution functions for water molecules in the expanded cluster shown separately for the first, the second, and the third shells.

The first coordination sphere at ~2.75 Å contains 4 molecules, which are connected by hydrogen bonds in accord with the Bernal-Fowler ice rules. The second coordination sphere at ~4.5 Å contains 12 water molecules.

2.4.2.3 Collapsed Cluster

The first shell is more complex and could be classified among three categories in accord with the symmetry of the inner cavity residing inside the dodecahedron, which is used to represent a first shell. In the case of a cubic cavity, the pentagonal dodecahedron is deformed inwards such that two apexes of each pentagonal face are moved inside the shell to form a cubic sub-shell with edges of 2.91 Å and diameter of 5.05 Å. The coordination number of each molecule among those forming a cube (green-colored on Figure 2.4.12 above) is seven, as shown below on Figure 2.4.13. For each water molecule forming the cubic shell there are *3 HB* neighbors, *3* non-hydrogen-bonded neighbors (shown in green) from the cubic shell and *1* non-hydrogen-bonded neighbor from the subsequent shell (shown in purple).

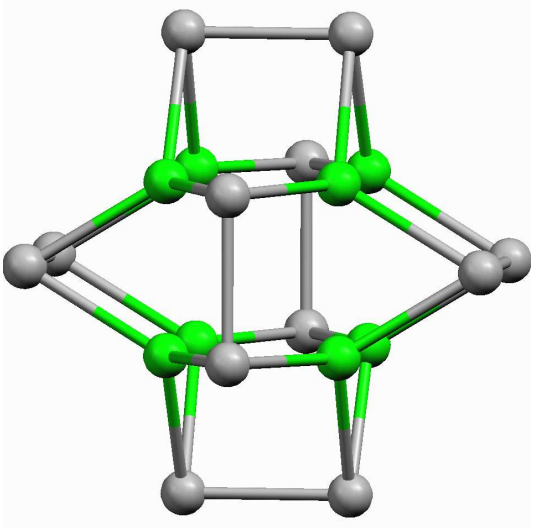

Figure 2.4.12. The inner cavity of the collapsed cluster of cubic symmetry.

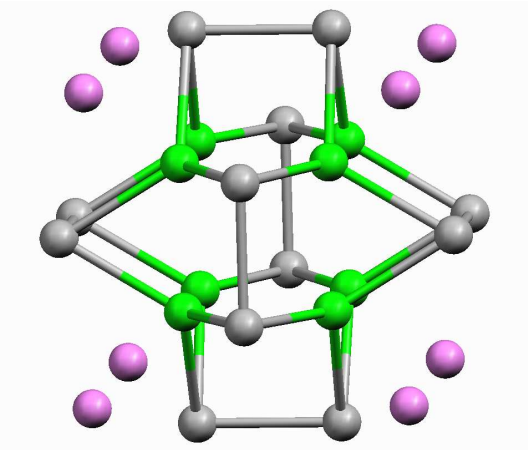

Figure 2.4.13. The inner cubic cavity with additional 8 H_2O molecules from the second shell. The water molecules of the second shell are shown in purple color.

The radial distribution functions for the expanded and collapsed clusters shown on and Figure 2.4.14, respectively, indicate that in the expanded cluster with pentagon-dodecahedron central unit the coordination shells are substantially better organized in comparison with the collapsed cluster. In the latter case the deformation of the central unit, which protrude into the subsequent shells, is manifested in the diffuse radial distribution function.

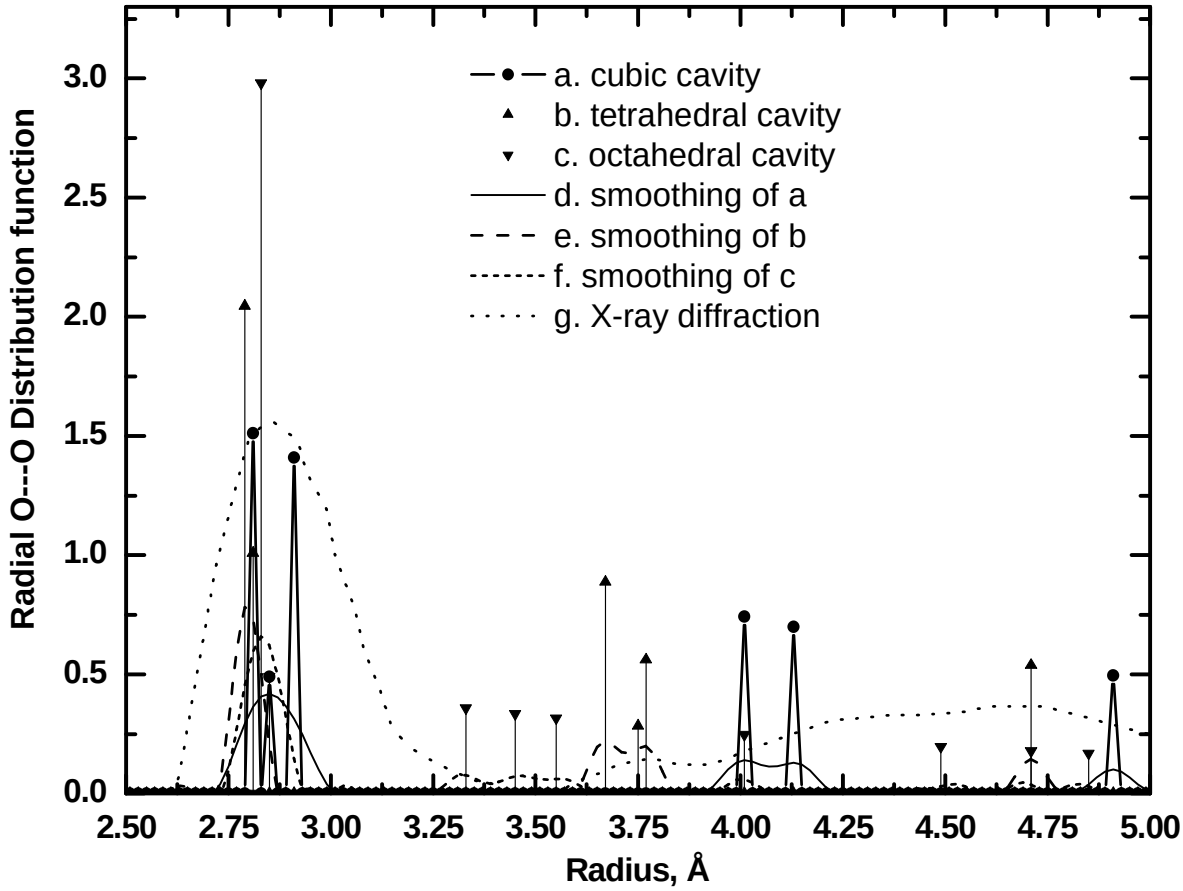

Figure 2.4.14. The radial O···O distribution function for the molecules in the collapsed cluster for different central cavities: cubic, tetrahedral, and octahedral.

2.5 Ice Adsorbate Interactions: IR Spectroscopy and Computer Simulations

This section outlines major results on the interaction of chemically different adsorbates with ice media. The ice media is classified among the polycrystalline and the noncrystalline structures.

Of particular interest is the microstructure of internal and external surfaces of low-density amorphous ice micro-phases. IR spectroscopy, with and without grazing-angle RA (reflection-absorption) technique, has been applied successfully for studying the surface properties of micro-clusters and vapor-deposited ice films. Transmittance IR measurements of low-temperature (10-15 K) amorphous micro-clusters of H_2O and D_2O, together with molecular dynamic simulations of their surfaces, obtained by Devlin and coworkers [23, 24, 54] have

shown that the external and internal surfaces of these materials contain two- and three-coordinated water molecules. Part of these molecules has a non-compensated OH dangling bonds (*DB's*), whereas others have an oxygen atom as a non-compensated site. Annealing the clusters at 60 K and further to 120 K led to complete disappearance of the *DB* features associated with two- and three-coordinated surface molecules, respectively. These observations were explained in terms of reduction in the amount of the internal surface [23, 24, 54]. Using FTIR RAS, Callen *et al.* [62] detected OD *DB's* on the outer surface of a 1.5-monolayer (ML) D_2O film at 130 K and OH *DB's* (at 3699 cm^{-1}) on the surface of a 5-ML H_2O film deposited above the D_2O film. The OD *DB* feature located at 2731 cm^{-1} was attributed to three-coordinated surface molecules. Its intensity was found to increase with increasing water exposure and become saturated at 3 ML's, above which coverage this signal was overwhelmed by the neighboring main peak of the OD stretch. The absence of the *DB* features corresponding to two-coordinated molecules shows that near 130 K newly adsorbed water molecules have sufficient energy for local surface reconstruction giving rise to the production of triply coordinated sites. Similar behavior of the OD *DB* was also observed by Horn *et al.* [63] on a much thicker D_2O amorphous ice film deposited at 110 K. Both these studies [62, 63] have suggested that the OD/OH *DB's* are most likely located on the outer surface of the ice films, after taking in to account the aforementioned signal behavior as a function of film thickness. On the other hand, a detailed investigation of the behavior of OH *DB* in the vapor-deposited ice samples between 94 K and 120 K by Zondlo *et al.* has shown that the majority of the OH *DB* are most likely located on the surface of micropores inside the bulk of amorphous ice [64]. The intensity of the OH *DB* feature was found to increase almost linearly with increasing film thickness up to 200-250 nm at 94 K, and to level off at 0.03-0.05 integrated absorption unit upon further film growth to 500 nm. This spectral saturation occurs as the result of the physics of RA and is not related to the amount of the OH *DB's*. Furthermore, the *DB* feature appeared to weaken at a higher deposition temperature. At 120 K and deposition pressure below 1×10^{-6} Torr, the peak intensity became very small (below 0.01 integrated AU) and decreased with a further increase in the film thickness. Zondlo *et al.* further concluded that the lower substrate temperature and faster deposition rate favored the production of an open water network with abundance of micropores covered by the OH *DB's* [64]. These FTIR-RAS studies [62, 63, 64] are consistent with a model that for thin (< 50 nm) amorphous

ice film (obtained by slow vapor deposition above 110-120 K) where the internal surface is small, in which case the *DB* signal, if detectable, comes predominantly from the OH/OD groups located on the smooth external surface. Faster deposition rate at these temperatures most likely leads to the production of a porous water networks with relatively well-developed internal surfaces. Under these growth conditions, the db signal originates primarily from the free OH/OD groups located on the surfaces of the micropores [64].

The low-density nc-ice deposits prepared by the vapor condensation on cold surfaces exhibit a high absorption capacity towards N_2 and other inert gases, which exemplifies by more than 200 $m^2 \cdot g^{-1}$ of specific surface area for the samples prepared at 77 K (according to Ghormley's [65], and Keyser and Leu [66]). On the other hand, Adamson *et al.* [67] and Ocampo and Klinger [68] have reported much smaller values in the range of 4-12 $m^2 \cdot g^{-1}$ for the surface area of the ice samples also prepared at 77 K and, furthermore, the former authors have found that the adsorption characteristics of the ice samples kept at liquid nitrogen temperature did not change over the period of two weeks [67]. These differences in the specific surface area and have been related, in particular, by Mayer and Pletzer [69], to the condensation mechanism and, specifically, to whether the condensation of water vapor occurs in the gas phase under supersonic flow giving highly convoluted and morphologically heterogeneous media, composed of an assembly of water clusters, or directly on the cold surface, producing much more compact continuous solid. By varying the direction of the incident flux of water molecules, Stevenson at el. [59] have observed a systematic change in the morphology of vapor-deposited low-density ice films, which at glancing angles of the flux exhibits the nitrogen uptake corresponding to as much as 2700 m^2/g at 22 K and to 640 m^2/g at 77 K. Obtained recently by Dohnalek *et al.* [70], the similar results on large uptakes of argon and methane species by the *LDA* indicate a fractal grass-like structure of the low-temperature vapor-deposit, which appear to be in agreement with the earlier views of Mayer and Pletzer [71], and Laufer *et al.* [72] on the low-density amorph as a morphologically porous media. These experimental results as well as well as the results of the computer simulations [73, 74, 75, 76] indicate, therefore, that the fractal structure of the low-density noncrystalline ice samples is highly heterogeneous with a significant variation in the local density over the space occupied by this metastable media, however the characteristic size of an intrinsic "building block", or cluster, although certainly very small (this case is similar to a glass), remains, as far

as we are aware, unknown. The hetero-/homogeneity of *LDA* clearly self-manifests on different spatial scales as it would be in any fractal, which suggestively spread from ~ 10 Å for the cross-sections of the typical fractal regions of self-similar elements of the *HB* network [74] to the unknown, but probably larger, size of micropores (~ 20Å? in diameter [71, 77]), and to much larger morphological macro-features [72]. It is note-worthy that the intrinsic hetero-/homogeneities in *LDA* obtained in the *MDS* [74] appears to be of the typical size of micropores in the solid adsorbents like active carbons.

The micropores in the *LDA* ice media were found to be accessible for small chemically inert non-polar species such as H_2, N_2, O_2, Ar, Kr, CH_4, or low-polar CO [24, 66, 70, 71, 78]. Larger and chemically more active species such as acetylene, SO_2, HCN, and NH_3, do not readily access the micropores independently on the temperature of an adsorption experiment. This effect can be attributed to the low mobility of adsorbed species or to the collapse of pores at more elevated temperatures [78].

Concerning the surfaces of crystalline ice samples, there is a large corpus of convincing evidences provided primarily by the studies of Devlin, Buch and collaborators [78, 86] that the surface of the samples prepared under "generic" experimental conditions is structurally disordered in the entire range of environmentally relevant temperatures. In contrast, the surface of the ultra-thin crystalline ice films carefully prepared by vapor deposition at low temperatures on the single-crystal metal substrates is stable and exhibits either a well-ordered hexagonal structure with a large-amplitude vibration of the water molecules in the topmost half-bilayer [79], or the reconstructed structure [80]. Using the IR technique, Devlin has identified the onset temperature of the molecular rotation of the triply-coordinated surface molecule on the surface of crystalline nanocrystals to be about 60 K, while the motions involving the molecular interchange on the surface, which likely involves overcoming of the activation barrier for translational motion and certain type of diffusion, appeared to be frozen below 130 K on the time scale of 10^5 sec [81].

Infrared spectroscopy has been extensively used for study reaction of molecules with ice surfaces [82, 83, 84, 85]. These studies have shown that the molecular adsorbates can be classified among three categories based on the interaction strength between the adsorbates and the water molecules. In particular, weak adsorbates such as ozone, carbon monoxide, and nitrogen were found to desorb rapidly into a vacuum at $T < 100$ K, and the spatial extent of

their interaction with the ice is limited only to the surface water molecules. The second category includes such adsorbates as H_2S and acetylene, which form relatively strong hydrogen bonds with the ice surface and also interacts with the subsurface water molecules. The interaction of species from the second category with subsurface water molecule alters the subsurface ice spectrum [86]. The third category represents those molecules which are capable penetrating the ice to form hydrates. This category includes hydrochloric acid, ammonia, and ethylene oxide. In the present studies, the interaction of ice surface with HCl (at 130-150 K) was found leading to the protonation of water media with formation of the Zundel ions as discussed in Chapter 4. Strong proton donor/acceptor properties (a capability of forming strong *HB's*) of adsorbate are considered critically important for transformation of ice structure to hydrate [87].

The mechanism of interaction of molecules from the environment with the ice micro-phases was found to be strongly dependent upon both the physico-chemical properties of adsorbate and the microstructure of the ice surface [88]. In particular, the molecular properties of an adsorbate such as an ability to establish the *HB* (electrophilic-nucleophilic) bonding with ice surface, the charge density distribution over a molecule, the molecular size and geometry, and the ionization ability play a leading role in the adsorption process and in the evolution of adsorbate complexes. In the adsorption of those polar molecules, which are capable of forming hydrogen bonds with water molecules, a pivotal role in the anchoring of adsorbate on the ice surface can be attributed to the hydrogen bonding between adsorbate and surface water molecules with either H or O atoms in dangling position. These atomic species, OH *DB* and O_d, form the adsorption sites on the ice surface for the polar organic molecules [82, 87]. Accordingly, the polar molecule may be subdivided functionally into two parts: the functional group, which carries a strong dipole and is involved in the "strong" hydrogen bonding with the ice surface and the remainder, which is usually almost electro-neutral and, thus, is bounded to the ice surface by van der Waals forces or weak electrostatics. In the case of acetone, the carbonyl group (functional group), which carries a significant dipole moment (μ= 2.88 D), is expected to establish the hydrogen bond with the positively charged hydrogen atom in the dangling position on the ice surface, whereas the contribution of two methyl groups (remainder) in adsorption energy is expected to be significantly smaller. However, the geometry of adsorption complex of many molecules at sub-monolayer coverage may be

determined by these "second order" interactions between the remainder and the adsorbent. In general, the qualitative mechanism of the surface-induced orientation of unsymmetrical molecules in adsorbate layers is well understood and was termed by Langmuir as the "principle of independent surface action" [89] or the "force field" as it was stated by Hardy [90].

In the case of acetone, and most likely other ketones and probably aldehydes, the adsorption centers are H atoms in dangling positions. The geometrical distribution of these centers on the ideal Ih (0001) basal surface is random, which suggests that this ideal surface and, consequently, the surfaces of real ice behave as a random heterogeneous surface for these classes of organic compounds. In the general case, however, the heterogeneity of the ice surface is also a function of the adsorbate, and for alcohols, which are amphoteric compounds in terms of hydrogen bonding, the ice surface is expected to be more homogeneous. The two kinds of hydrogen bonds $(O\text{-}H)_{Alc}\cdots O_{ice}$ and $(O\text{-}H)_{Ice}\cdots O_{Alc}$ are expected in the case of alcohol adsorption on ice surface. Although these two *HB* structures are not equivalent, the binding energy of the donor and acceptor configurations are expected to be close to each other. This prepositions leads to classification of the ice surface as a homogeneous structure in the case of alcohol adsorption. In the case of methanol on Ih (0001), Picaud *et al.* [91] have shown by optimizing classical potential (Coulomb and Lennard-Jones) at 0 K that the adsorption energy for complex where methanol behaves as a donor of OH group is larger only by 0.344 $kcal\cdot mole^{-1}$ than corresponding value of ~ 9.8 $kcal\cdot mole^{-1}$ for the complex where the methanol molecule is OH acceptor. Therefore, there are convincing grounds to suggest that the adsorbent properties of ice surface depend on the physico-chemical properties of an adsorbate.

The adsorbate-adsorbate attraction can be substantial in magnitude with relatively long-range spatial extent in the group of polar molecules with a large dipole moment, to which acetone belongs. This interaction is known to be of importance in the determination of the behavior of the adsorption isotherm and the properties of adsorbed phase [92]. The inter-adsorbate interaction becomes predominant at close to and above the monolayer coverage even for those molecules, which are capable to strong hydrogen bonding with ice surface. For instance, the acetone-acetone interaction is evident in the RA spectra as reported in Chapter 5.

In contrast with the picture described above, the adsorption of non-polar molecules or molecules with a low ability to donor-acceptor bonding does not occur on H/O dangling positions on the surface water molecules. Adsorption processes in this case are similar to the

condensation on the ice surface, where the ice surface could be considered as the provider of van der Waals potential. This adsorbate-ice interaction is expected to be much less sensitive to the ice surface structure on the atomic scale than the strong electrostatics between functional group and H or O dangling positions in the case of polar molecule. This, however, does not assume the absence of the influence of adsorbate on the energy of dangling groups [99]. The suitable candidates for the class of "weak" organic adsorbates, except hydrocarbons, are halogen tetra-substituted methanes and even chlorofluorocarbons. In fact, Graham *et al*. [93] have shown that adsorption of fluoroform on Ih (0001) ice surface at temperatures less than 75 K can lead, despite its significant dipole moment of 1.65 D, to the formation of ordered complete monolayer (coverage $\theta \sim 0.9$), in which fluoroform molecules occupy the "free space" at the centers of each water hexagon with the C-H bond pointing inside. The ice surface is expected to behave itself as a homogeneous site surface in similar cases. The present studies report the interaction of chloroform with ice surface accompanied with two hydrogen bond coordinations, OD···Cl−CCl_2H and Cl_3C−H···O−OH, as reported in Chapter 5.

The large-scale structure of the ice near-surface region, e.g. the microporous structure of the ice films deposited below ~120 K [64] or its large-scale disordering at temperatures above ~ 190 K [94], obviously will affect the time evolution of adsorption complexes by facilitating the trapping and the penetration of adsorbate into ice.

Local organization and energetic parameters of the adsorbate complex on the surface could remain, however, independent from the large-scale structure of the ice surface. The occluded guest species also form the complexes with water molecules inside the adsorbent medium. The structure of these complexes inside the host medium could be different from that on the surface but the principle hydrogen bonding coordination most likely is similar for both the surface and the occluded complexes. For instance, the present spectral studies reveal that the acetone-water complexes are different on the surface and in the bulk of the ice condensate but the principle *HB* configurations are most likely the same for the surface and the bulk complexes.

Another aspect of cryogenic adsorption on the ice surface is associated with the adsorbate-induced ordering of the originally disordered near-surface region of noncrystalline and polycrystalline ices. The kinetics and extent of the adsorbate-induce ordering is a function of temperature and adsorption energy. In fact, adsorption of molecules that are capable of

forming relatively strong hydrogen bonding with surface water molecules such as hydrogen sulfide and acetylene was found to cause noticeable reconstruction of near-surface region towards a more crystalline arrangement [95]. In contrast, weakly bonded adsorbates with small dipole moment or quadrupolar molecules such as carbon monoxide and nitrogen do not influence the ice near-surface region [95]. Therefore, it is expected that polar organic adsorbates will cause strong reconstruction of the subsurface ice region by the formation of hydrogen bonds with the surface water molecules.

Next part of this section reports a detail analysis of the spectral data on the adsorption complexes of cyanoacetylene, thiophene and acetone with a focus on the adsorbate-water and the adsorbate-adsorbate interactions and the adsorbate-induce reconstruction of the near-surface region of ice. These three chemical moieties are expected to exhibit different behavior upon adsorption on the ice surface. In contrast to acetone, which is evidently an acceptor of hydrogen bonds (with no or very minor donor capacity), cyanoacetylene, N≡C−C≡C−H, is expected to exhibit both a donor and an acceptor *HB* properties. Thiophene is expected to be a weak *HB* acceptor. In the case of cyanoaetylene, the strong adsorbate-adsorbate interaction is expected because of a large dipole moment of this molecule. It turns out, that, in spite of significant differences in the physico-chemical properties, all the abovementioned species exhibit similar adsorption behavior on the ice surface. This circumstance clearly underscores the water property to average the individual characteristics of guest species.

FTIR spectroscopy was used in transmittance mode to study the adsorption complexes of cyanoacetylene (μ= 3.72 D) [96] and in the reflection-absorption mode for acetone (μ= 2.88 D) [97], and thiophene (μ= 0.55 D) [98] complexes on polycrystalline and non-crystalline ice films. In particular, Borget *et al.* [96] have shown that solid cyanoacetylene pre-deposited on ice at 15 K begins to interact with OH *DB's* after becoming mobile at 25 K with formation of the acceptor C−N···H−OH complex, which was found tobe stable between 25 and 45 K. The formation of this adsorption complex was accompanied by a 25 cm^{-1} red shift in the frequency position of OH *DB* signal. Further annealing of this adsorbate-ice structure to 80 K led to progressive restoration of the original OH signal, which was interpreted in terms of the transformation of the acceptor complex to the donor C−H···O complex. The last was found to be stable in the temperature range 45-110 K. The cyanoacetylene desorption was observed between 110 and 140 K with activation energy of 39 $kJ \cdot mole^{-1}$ estimated from the TPD data.

The *DFT* calculations showed that the length of hydrogen bond is shorter in the donor complex (2.057 Å) than a corresponding value for the acceptor complex (2.189 Å), which suggests domination of the nucleophilicity over electrophilicity for water molecules. The donor adsorption complex is expected, according to *DFT* calculations, to flatten on the ice surface due to the weak hydrogen bonding (3Å) between dangling hydrogen atom and π-system of the adsorbate unlike the acceptor complex, the predicted geometry of which allocates the adsorbate to be perpendicular to the ice surface [96]. Such interaction between the π-system and the OH *DB*, which is critical for geometry of the adsorption complex, seems to be in contradiction with the spectral observations, which showed that the frequency position of OH *DB* is identical for bare ice and for the adsorbate-ice system at 80 K. In particular, Rowland *et al.* [99] have shown, using a differential IR spectroscopy method, that saturated adsorption of N_2, CH_4, and CO at 80 K on non-crystalline and crystalline nano-particles cause a noticeable red shift in the frequency position of OD/H *DB's*. Consequently, we can expect to observe significant red shift for the OH *DB's* peak on ice surface covered by polar molecule such as cyanoacetylene independent of particular structural details of the adsorption complexes due to the long-range electrostatic interaction between adsorbate and ice surface. Furthermore, Delzeit *et al.* [95] have demonstrated that molecules such as acetylene, which may be considered as a non-polar "analog" of cyanoacetylene with much lower ability to hydrogen bond, introduces ordering in the subsurface area of non-crystalline ice particles due to hydrogen bonding with surface dangling groups. No such reconstruction was reported by Borget *et al.* [96] for the adsorption of cyanoacetylene. The present author has also found unexpected similarity can be reported for the effect of partial reemergence of the free OH dangling features in N_2 covered non-crystalline ice upon annealing the system from 50 K to 80 K, which was observed and attributed by Rowland *et al.* [24] to the desorption of nitrogen from the pores of specific sizes, and the analogous desorption behavior of cyanoacetylene [96], despite the apparent difference in the chemical nature of adsorbates. Borget *et al.* [96], unfortunately, have not discussed the influence of adsorbate-adsorbate interaction on the structure and the temperature evolution of adsorption complexes, which can be significant and even predominant over the adsorbate-ice interaction due to large dipole moment of cyanoacetylene. Indeed, the activation energy of adsorption complex desorption at 39 kJ/mol appears to be close to the sublimation enthalpy of solid cyanoacetylene found at 42.3kJ/mol

[100].

The FTIR-RAS studies of thiophene adsorption on Pt (111) and ice surfaces at cryogenic temperatures by Haberkern *et al.* [98] have shown that adsorption on metal and crystalline ice surfaces proceeds with consecutive formation of a compressed monolayer, a disordered phase and a crystalline adsorbate film. The thiophene growth mode was found to be largely determined by adsorbate-adsorbate interactions. In contrast with this, thiophene adsorption on non-crystalline ice at 125 K (unlike 85 K) revealed the formation of ice-specific adsorption complexes, the appearance of which was attributed to a large number of OH dangling groups on the surface of non-crystalline ice and to a certain mobility of adsorbate at this temperature. The geometry of these adsorption complexes was found to be different from previous cases and suggests that the orientation of the molecule ring is much closer to the surface normal than in the compressed monolayer [98]. In the last case, the combination of the surface heterogeneity and adsorbate mobility allows adsorbate-specific adsorption complexes to be formed. Independently from the ice structure or the exposure temperature, Haberkern *et al.* [98] have found that the intensity of the IR signal corresponding to the OH *DB's* decreases upon thiophene exposure. Moreover, the thiophene deposition causes characteristic changes in the shape of main peak of OH stretching band, which is in agreement with observations of Rowland *et al.*[23], and Delzeit *et al.*[95].

In a series of two papers, Schaff and Roberts have shown, using FTIR-RAS and TPD, that acetone adsorbs on the surface of the amorphous D_2O and H_2O ices giving two distinct adsorption complexes [82, 97]. The first complex is referred to as acetone bounded to surface O-D/H *DB* by the hydrogen bond, whereas the second complex is described as physisorbed acetone. TPD experiments with the amorphous ice covered by adsorbate revealed two desorption peaks at 133 K and 157 K, which were related respectively to the physisorbed and hydrogen-bonded complexes. The surface concentration of the last complex was observed to achieve saturation at ~ 1.2 L (1 L = 1×10^{-6} Torr×sec), after which point the exclusive growth of the physisorbed complex continues. The activation energy of desorption of the hydrogen-bonded complex was estimated as 39 ± 2 kJ/mol, the value which appears to be slightly larger than the sum of the enthalpies of vaporization and fusion of acetone at 34.8 kJ/mol. In contrast to this, in the case of the desorption from crystalline ice, the hydrogen-bonded complex was almost completely absent and the physisorbed complex was predominant. This observation

was explained by qualitative difference in the surface concentration of OD/H dangling bonds on the non-crystalline and polycrystalline ices. However, in the partial contradiction to this, the FTIR-RA peak associated with the OD/H *DB's* was completely attenuated at the same intensity level by ~1L of acetone adsorption on non-crystalline ice and by less than 0.25 L on polycrystalline ice at 95 K. The spectral feature of the carbonyl stretching mode in the FTIR-RA spectra of acetone on non-crystalline ice was reported to be at ~1703 cm^{-1} for very low coverage and at 1716-1717 cm^{-1} for the condensed multilayer of adsorbate. The first peak was attributed to hydrogen-bonded acetone complex based on the red-shifted frequency position of the band and its intensity saturation with acetone exposure. The relative intensities of IR-RA spectral bands of adsorbed acetone complex were found to be coverage-independent for adsorption on nc-ice with the C=O stretch as the most intense one, whereas on pc-ice these intensities varied strongly with acetone exposure. These data were interpreted in terms of a nearly constant orientation of acetone with the respect to surface normal in the adsorbate complexes on nc-ice in contrast to adsorption on pc-ice, which was accompanied by distinct coverage-dependent orientational regimes [97]. There is an interesting similarity with the Haberkern *et al.* [98] data on thiophene adsorption since in both cases the adsorption complexes at low coverage on nc-ice revealed the preferential orientation of the adsorbate with the molecular plane to be closer to the surface normal than in adsorption on pc-ice. At this point, we can suggest that these results contain information about the large-scale structure of adsorbate and depend upon the heterogeneity of the ice surface structure. Molecular dynamics simulations of acetone adsorption on Ih (0001) ice surface done by Picaud and Hoang [101] show that the hydrogen-bonded acetone molecule is oriented almost parallel to the ice surface (75º from the normal at 125 K) at low coverages. This orientation is the result of van der Waals attraction or "weak" hydrogen bonding of the remainder to the surface. The same arguments can be used to justify a plausible preposition about similar orientation of thiophene adsorption complex at the same coverage range. If this is the case, the near-to- perpendicular (with respect to the normal to the substrate surface) orientation of the molecular plane observed by Haberkern *et al.* [98] and Schaff and Roberts [97] at low coverage on nc-ice can be explained by the preferential adsorption of organic molecules on the micropores surface, which is most likely to be perpendicular to the substrate surface.

The bibliographic analysis presented in this section reveals that polar organic substances can

be effectively used for probing the state of condensed water media on different spatial and time scales. All the above-mentioned adsorbates interact with the dangling bonds of ice surface, which can be observed in the differential IR spectra. Not only the local configuration of the adsorbate-water complexes can be determined from these IR spectra but also tentative conclusions regarding the lager-scale structure of the ice deposit can be drawn. The spectral part of the present studies follow this path by using such polar organic molecules as acetone, acetaldehyde, methanol and chloroform for analysis of the surface state and the dynamics in ice deposits.

References:

1. M. Chaplin, "Water Structure and Behavior", 2005, http://www.lsbu.ac.uk/water/.
2. J. Urquidi, C. H. Cho, S. Singh, G. W. Robinson, J. Mol. Struct. ***485-486*** (1999), 363.
3. G. W. Robinson, C. H. Cho, J. Urquidi, J. Chem. Phys. ***111*** (1999), 698.
4. B. Kamb, "Structural Chemistry and Molecular Biology", (1968), 507, ed. A. Rich and N. Davidson, W. H. Freeman, San Francisco.
5. J. D. Bernal, R. H. Fowler, J. Chem. Phys. ***1*** (1933) 515.
6. J. D. Bernal, "The Geometry of the Structure of Liquids", (1963) 25 in the "Liquids: Structure, Properties, Solid Interaction", (1965), ed. T. J. Hughel, Elsevier Publishing Company, New York.
7. G. E. Walrafen, W.-H. Yang, Y. C. Chu, "Raman Evidence for the Clathratelike Structure of Highly Supercooled Water" (1996) 287 in the "Supercooled Liquids" (1997), ed. J. T. Fourkas, D. Kivelson, U. Mohanty, K. A. Nelson, ACS Symposium Series 676, ACS, Washington DC.
8. A. H. Narten, H. A. Levy, Science ***165*** (1969) 447.
9. D. Eisenberg, W. Kauzman, "The Structure and Properties of Water", (1969) Clarendon Press, Oxford.
10. M. Kopp, "Molecular Motions in Ice", Dissertation, (1972) Swiss Federal Institute of Technology, Zurich, Verlag Zurich.
11. V. F. Petrenko, R. W. Whitworth, "Physics of Ice", (1999) Oxford University Press, Oxford.
12. P. V. Hobbs, “Ice Physics”, Clarendon Press, Oxford (1974); and references therein.
13. I. Kohl, E. Mayer, A. Hallbrucker, Phys. Chem. Chem. Phys. ***2*** (2000) 1579.
14. P. Jenniskens, S. F. Banham, D. F. Blake, M. R. S. McCoustra, J. Chem. Phys. ***107*** (1997) 1232.
15. N. Materer, U. Starke, A. Barbieri, M. A. Van Hove, G. A. Somorjai, G.-J. Kroes, C. Minot, Surf. Sci. ***381*** (1997)190.
16. J.-C. Li, J. Chem. Phys. ***105*** (1996) 6733.
17. A. I. Kolesnikov, J.-C. Li, S. Dong, I. F. Bailey, R. S. Eccleston, W. Hahn, S. F. Parker, Phys. Rev. Lett. ***79*** (1997)1869.

18. J. Braun, A. Glebov, A. P. Graham, A. Menzel, J. P. Toennies, Phys. Rev. Lett. ***80*** (1998), 2638.
19. A. Hallbrucker, E. Mayer, G. P. Johari, J. Phys. Chem. ***93*** (1989) 4986.
20. J. E. Bertie, H. J. Labbe, E. Whalley, J. Chem. Phys. ***50*** (1969) 4501.
21. W. Hagen, A. G. G. M. Tielens, J. M. Greenberg, Chem. Phys. ***56*** (1981) 367.
22. B. Rowland, J. P. Devlin, J. Chem. Phys. ***94*** (1991) 812.
23. B. Rowland, N. S. Kadagathur, J. P. Devlin, V. Bush, T. Feldman, M. J. Wojcik, J. Chem. Phys. ***102*** (1995) 8328.
24. B. Rowland, M. Fisher, J. P. Devlin, J. Chem. Phys. ***95*** (1991)1378.
25. T. Loerting, C. Salzmann, I. Kohl, E. Mayer, A. Hallbrucker, Phys. Chem. Chem. Phys. ***3*** (2001) 5355.
26. W. F. Kuhs, M. S. Lehmann, "The structure of ice-*Ih*" in the Water Science Reviews ***2*** (1986) 1, Cambridge University Press, Cambridge.
27. W. F. Kuhs, D. V. Bliss, J. L. Finney, J. de Physique ***48*** (1987) 631.
28. B. Kamb, W. C. Hamilton, S. J. LaPlaca, A. Prakash, J. Chem. Phys. ***55*** (1971) 1934.
29. J. D. Londono, W. F. Kuhs, J. L. Finney, J. Chem. Phys. ***98*** (1993) 4878.
30. H. Engelhard, B. Kamb, J. Chem. Phys. ***75*** (1981) 5887.
31. B. Kamb, A. Prakash, C. Knobler, Acta Cryst. ***22*** (1967) 706.
32. W. F. Kuhs, J. L. Finney, C. Vettier, D. V. Bliss, J. Chem. Phys. ***81*** (1984) 3612.
33. R. J. Hemley, A. P. Jephcoat, H. K. Mao, C. S. Zha, L.W. Finger, D. E. Cox, Nature ***330*** (1987) 737.
34. C. M. B. Line, R. W. Whitworth, J. Chem. Phys. ***104*** (1996) 10008.
35. C. Lobban, W. F. Kuhs, J. L. Finney, Nature ***391*** (1998) 255.
36. J. E. Bertie, L. D. Calvert, E. Whalley, J. Chem. Phys. ***38*** (1964) 840.
37. G. P. Johary, A. Hallbrucker, E. Mayer, Science ***273*** (1996) 90.
38. J. Huang, L. S. Bartell, J. Phys. Chem. ***99*** (1995) 3924.
39. G. P. Johari, Phil. Magazine B ***78*** (1998), 375.
40. E. Whalley, Science ***211*** (1981) 389.
41. E. Whalley, J. Phys. Chem. ***87*** (1983), 4179.
42. T. Takahashi, T. Kobayashi, J. Cryst. Growth ***64*** (1983) 593.

43. M. Riikonen, M. Sillanpää, L. Virta, D. Sullivan, J. Moilanen, I. Luukkonen, App. Opt. ***39*** (2000), 6080.
44. M. A. Zondlo, P. K. Hudson, A. J. Prenni, M. A. Tolbert, Annu. Rev. Phys. Chem. ***51*** (2000) 473.
45. J. R. Reimers, R. O. Watts, M. L. Klein, Chem. Phys. ***64*** (1982) 95.
46. J. E. Bertie, E. Whalley, J. Chem. Phys. ***40*** (1964) 1646.
47. A. L. Sumner, P. B. Shepson, Nature ***398*** (1999) 230.
48. S. Solomon, R. R. Garcia, F. S. Rowland, D. J. Wuebbles, Nature ***321*** (1986) 755.
49. M. J. Molina, L. T. Molina, C. E. Kolb, Ann. Rev. Phys. Chem. ***47*** (1996) 327.
50. S. A. Sanford, in "Polarimetry of the interstellar medium", Astron. Soc. Pac. Conf. Series ***97*** (1996) 29.
51. A. H. Hardin, K. B. Harvey, Spectrochim. Acta. ***29A*** (1973) 1139.
52. W. Hagen, A. G. G. M. Tielens, J. M. Greenberg, Chem. Phys. ***56*** (1981) 367.
53. P. Jenniskens, D. F. Blake, Science ***265*** (1994) 753.
54. P. Jenniskens, S. F. Banham, D. F. Blake, M. R. S. McCoustra, J. Chem. Phys. ***107*** (1997) 1232.
55. D. E. Brown, S. M. George, C. Huang, E. K. L. Wong, K. B. Rider, R. S. Smith, B. D. Kay, J. Phys. Chem. ***100*** (1996) 4988.
56. G. P. Johari, Phil. Mag. B ***78*** (1998) 375.
57. J. A. Ghormley, J. Chem. Phys. ***46*** (1967) 1321.
58. A. W. Adamson, L. M. Dormant, J. Am. Chem. Soc. ***88*** (1966) 2055.
59. K. P. Stevenson, G. A. Kimmel, Z. Dohnálek, R. S. Smith, B. D. Kay, Science ***283*** (1999) 1505.
60. A.-L. Barabási, H. E. Stanley, "Fractal Concepts in Surface Growth" 1995, Cambridge, Cambridge University Press.
61. H. S. Frank, W.-Y. Wen, Disc. Faraday Soc. ***24*** (1957) 133.
62. B. W. Callen, K. Griffiths, P. R. Norton, Surf. Sci. Lett. ***261*** (1992) L44.
63. A. B. Horn, M. A. Chesters, M. R. S. McCoustra , J. R. Sodeau, J. Chem. Soc. Faraday Trans. ***88*** (1992) 1077.
64. M. A. Zondlo, T. B. Onasch, M. S. Warshawsky, M. A. Tolbert, G. Mallick, P. Arentz,

M. S. Robinson, J. Phys. Chem. B ***101*** (1997) 10887.

65. J. A. Ghormley, J. Chem. Phys. ***46*** (1967) 1321.
66. L. F. Keyser, M.-T. Leu, J. Colloid Interface Sci. ***155*** (1993)137.
67. A. W. Adamson, L. M. Dormant, M. Orem, J. Colloid Interface Sci. ***25*** (1967) 206.
68. J. Ocampo, J. Klinger, J. Colloid Interface Sci. ***2*** (1982) 377.
69. E. Mayer, R. Pletzer, J. Chem. Phys. ***80*** (1984) 2939.
70. Z. Dohlanek, G. A. Kimmel, P. Ayotte, R. S. Smith, B. D. Kay, J. Chem. Phys. ***118*** (2003) 364.
71. E. Mayer, R. Pletzer, Nature ***319*** (1986) 298.
72. D. Laufer, E. Kochavi, A. Bar-Nun, Phys. Rev. B ***36*** (1987) 9219.
73. V. P. Shpakov, P. M. Rodger, J. S. Tse, D. D. Klug, V. R. Belosludov, Phys. Rev. Lett. ***88*** (2002) 155502.
74. V. P. Voloshin, E. A. Zhelegovskaya, G. G. Malenkov, Yu. I. Naberukhin, J. Struct. Chem. ***42*** (2001) 794.
75. H. Tanaka, J. Chem. Phys. ***105*** (1996) 5099.
76. J. P. Devlin, V. Buch, J. Phys. Chem. ***99*** (1995) 16534.
77. M. S. Westley, G. A. Baratta, R. A. Baragiola, J. Chem. Phys., ***108*** (1998) 3321.
78. J. P. Devlin, J. Geophys. Res. ***106(E12)*** (2001) 33333.
79. N. Materer, U. Starke, A. Barbieri, M. A. Van Hove, G. A. Somorjai, G.-J. Kroes, C. Minot, Surf. Sci. ***381*** (1997)190.
80. D. E. Brown, S. M. George, J. Phys. Chem. ***100*** (1996) 15460.
81. J. P. Devlin, J. Chem. Phys. ***112*** (2000) 5527.
82. J. E. Schaff, J. T. Roberts, J. Phys. Chem. ***98*** (1994) 6900.
83. H. Ogaswara, N. Horimoto, M. Kawai, J. Chem. Phys. ***112*** (2000) 8229.
84. Borget, F.; Chiavassa, T.; Allouche, A.; J. P. Aycard, J. Phys. Chem., B ***105*** (2001) 449.
85. A. Allouche, P. Verlaque,; J. Pourcin, J. Phys. Chem., B ***102*** **(**1998) 89.
86. V. Buch, J. P. Devlin,eds., "Water in Confining Geometeries", 2003, Springler, Berlin.
87. L. Delzeit, K. Powell, N. Uras, J. P. Devlin, J. Phys. Chem. ***101*** (1997) 2327.
88. C. Girardet, C. Toubin, Surf. Sci. Reports. ***44*** (2001) 59.

89. A. W. Adamson, A. P. Gast, "Physical Chemistry of Surfaces.", 6th edition, 1997, J. Wiley, New York.
90. W. D. Harkins, "The Physical Chemistry of Surface Films", 1952, Reinhold Pub. Corp., New York.
91. S. Picaud, C. Toubin, C. Girardet, Surf. Sci. ***454-456*** (2000) 178.
92. W. Rudzinski, D. H. Everett, "Adsorption of Gases on Heterogeneous Surfaces", 1992, Academic Press, London.
93. A. P. Graham, A. Menzel, J. P. Toennies, J. Chem. Phys. ***111*** (2000) 1169.
94. Y. A. Mantz, F. M. Geiger, L. T. Molina, M. J. Molina, B. L. Trout, J. Chem. Phys. ***113*** (2000) 10733.
95. L. Delzeit, M. S. Devlin, B. Rowland, J. P. Devlin, V. Buch, J. Phys. Chem. ***100*** (1996) 10076.
96. F. Borget, T. Chiavassa, A. Allouche, F. Marinelli, J-P. Aycard, J. Am. Chem. Soc. ***123*** (2001) 10668.
97. J. E. Schaff, J. T. Roberts, Langmuir ***14*** (1998) 1478.
98. H. Haberkern, S. Haq, P. Swiderek, Surf. Sci. ***490*** (2001)160.
99. B. Rowland, N. S. Kadagathur, J. P. Devlin, V. Buch, T. Feldman, M. J. Wojcik, J. Chem. Phys. ***102*** (1995) 8328.
100. R. M. Stephenson, S. Malanowski, "Handbook of the Thermodynamics of Organic Compounds",1987, Elsevier, New York.
101. S. Picaud, P. N. M. Hoang, J. Chem. Phys. ***112*** (2000) 9898.

CHAPTER 3

Experimental

3.1 Experimental Objectives

The present experiment consists of Fourier Transform Infrared Reflection-Absorption Spectroscopy (FTIR RAS) measurements performed on the films deposited under ultra-high vacuum conditions at cryogenic temperatures. The chemical objects of these FTIR RAS measurements comprise of: (i) crystalline *Ic*/*Ih* and noncrystalline phases of the pristine ice vapour-deposited on the copper support; (ii) crystalline *Ic*/*Ih* ice films obtained by annealing the pre-deposited non-crystalline samples; (iii) pristine deposits of acetone, C_3H_6O, acetaldehyde, CH_3CHO, methanol, CH_3OH, and chloroform, $CHCl_3$; (iv) the aforementioned organic species adsorbed on the crystalline and noncrystalline ice substrates; (v) water-organic solids prepared by a co-deposition of the vapors of water and an organic component; (vi) noncrystalline ice films treated by hydrochloric acid, HCl, and subsequently exposed by acetone or acetaldehyde. The present author decided to limit a discussion to the detail description of the interaction of acetone and chloroform species with the ice surface. A wide focus of the present studies does not allow reporting a complete volume of the experimental and computational results.

Although spectral observations on the ice films under constant external conditions, i.e. when the temperature of the Cu support and the chamber pressure are maintained at an approximately constant level for a period of 1-2 hours, have been performed in an attempt to obtain spectral information from an object at a steady state, the present experiment should be considered dynamic. In other words, during the spectral observations including the collection of a single spectral sample (the shortest sample time is ~20 sec) the physico-chemical state of the object in question is in the process of irreversible change. This latter circumstance resides, on the one hand, in the dynamical properties of *HB* network of ice and, on the other hand, in the large surface-to-volume ratio of the materials studied in the present work. The former is primarily applied to the noncrystalline ice micro-phases, which exhibit a "strong dynamics" at a temperature range above ~130 K when the crystallization to *Ic* occurs (see Chapter 2 for details). Furthermore, the cubic ice itself is a metastable substance, which converts to the

hexagonal structure at a rate, which becomes noticeable on the laboratory scale at temperatures near 230 K. It is evident therefore that within the entire temperature range accessible by the present experimental setup, i.e. 125-180 K, the ice substrate remains in metastable state. However, since the rate of inter-basin hopping is generally small under cryogenic conditions, at certain temperature intervals a quasi-equilibrium state could take place for a sufficient period, while at other temperatures a faster dynamic is expected such that there is a little hope of observing a sample at steady state. The small dimension of the objects, i.e. ultra thin films and/or nano-crystals, also plays a significant role in promoting dynamical processes because the characteristic length of the inter-basin hopping (see Chapter 1 and Chapter 2) is nearly comparable with the characteristic size of the object, and, therefore, the surface effects are very significant. The latter circumstances are of fundamental importance for studying the penetration, diffusion, and phase transitions in solid water media.

Among others, one of the most important experimental requirements for this kind of experiments resides in attaining the high spectral sensitivity and background stability (i.e. high signal to noise ratio), which are necessary for observing very weak spectral features associated with the vibrational motion of the surface molecules of water phases or organic moieties. The extraction of topological and dynamical information from the spectral data necessitates the utilization of computer models on different physical and chemical levels. Specifically, handling the reflection-absorption spectra requires modeling of the reflection-absorbance optical phenomenon, which originates from the out-of-normal radiation of the dielectric sample on the metal substrate. Ignoring the dielectric effects introduced by the RA method of the spectral experiment, which often lead to a significant frequency shift and deformation of the adsorption bands, could cause a misinterpretation of spectral features. Although a general theory of the RAS exists, in each particular experimental case a special attention is necessary to differentiate between the optical manifestation of the fundamental vibrations in the films in question and those optical features, which appear as a result of the RA mode.

Regarding molecular modeling, determination of a possible structure for a particular adsorbate-ice complex requires building a set of atomistic classical and/or quantum-mechanical models. From this latter set of models, the most realistic representation can be chosen by comparing the measured and calculated IR frequencies. Despite their primarily experimental appeal within the framework of the present studies, the computer models and

calculations are described separately in Chapter 4. The experimental results are discussed in Chapter 5.

3.2 UHV/FTIR RAS Chamber: Design and Construction

The home-designed and constructed UHV chamber for the present experiment is shown in Figure 3.2.1. The main components of this UHV chamber include: (i) the main chamber for the spectral experiment atop of the supporting 6-way cross chamber, to which a horizontal stainless steel appendix supporting the leak valves and gas/liquid sample handling system is attached; (ii) titanium-sublimation and turbo-molecular pumps mounted on the supporting chamber and on the horizontal appendix, respectively; (iii) sample holder with the heating element on the back side mounted on the X-Y-Z manipulator; (iv) liquid-N_2 dewar and two copper brazes to the sample holder for cooling; (v) two differentially-pumped optical windows (CaF_2 or KRS-5) for the IR beam entrance and exit. The Bruker FTIR Equinox-55 Spectrometer with air-cooled globar source is used for the spectral analysis of the films vapor deposited on the sample holder made of copper disk. From the standpoint of optics, the copper disk acts as a mirror, which reflects the incident IR beam hitting the sample at grazing angle from the sample holder towards the liquid-N_2 cooled MCT (mercury-cadmium-telluride) detector mounted on the optical table on the opposite side of the vacuum chamber.

A: main chamber; 19 ports; Ø 17'', h 15''.
B: supporting chamber; six-way cross.
C: X-Y-Z manipulator.
D: titanium sublimation pump.
E: turbomolecular pump (250 l/s) and gate valve.
F: supporting moveable platform.
G: multiport accessory flanges.
H: variable leak valve.

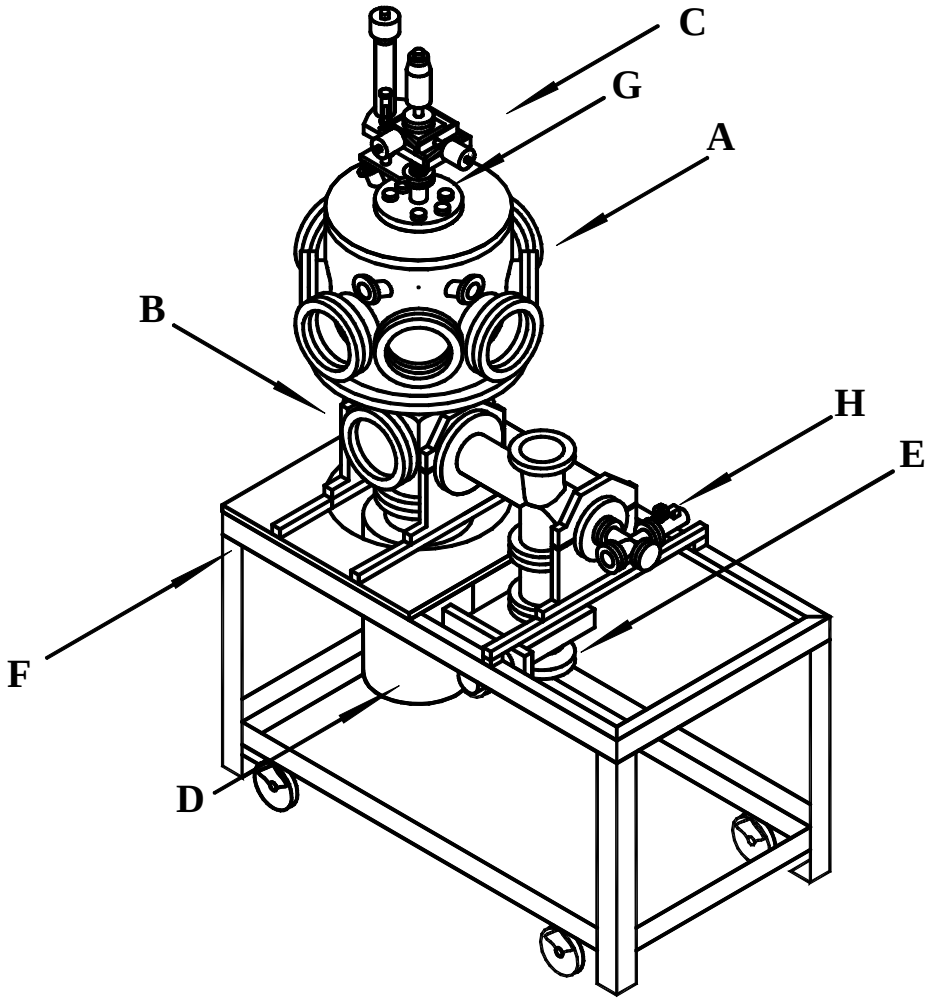

Figure 3.2.1. Schematic layout of the UHV chamber. Only three of the 19 ports of the central ultrahigh vacuum chamber (with a base vacuum better than 3×10^{-9} Torr) relevant to the present experiment are shown. Two of the ports that are used to house the CaF_2 windows are pumped differentially. The FTIR spectrometer (Bruker Equinox 55) and the two aluminium boxes that enclose the light-stirring optics and the MCT detector are purged with the dry N_2 gas continuously to minimize ambient contaminations.

The FTIR-RAS experiments were conducted in a home-built UHV chamber evacuated by a 250 l/sec turbo-molecular pump to a base pressure of better than 5×10^{-9} Torr. Ice was condensed from water vapor onto an optically flat polycrystalline Cu disk (2.25-inch diameter) mounted on a four-motion manipulator. Figure 3.2.2 shows schematically the glancing-incidence optical arrangement of the experiment, which allows signal optimization at zero path difference by easy adjustment of the position of the target with respect to the optical path of the infrared beam. The 1.5-inch diameter infrared beam from a Bruker Equinox 55 FTIR spectrometer equipped with an air-cooled Globar source was directed onto the Cu disk at ~83º from the surface normal by a focusing 90º parabolic mirror with a 16-inch focal length. The specularly reflected light was collected by a second identical 90º parabolic mirror of a 16-inch focal length positioned on the opposite side of chamber, and finally focused by a 1.7-inch focal-length parabolic mirror onto a liquid-nitrogen-cooled Mercury-Cadmium-Telluride (MCT) detector (energy range: 7000-600 cm^{-1}; sensitivity $>2.5\times10^{10}$ cm $Hz^{1/2}$/W). Two CaF_2 optical windows mounted on differentially pumped 8-inch conflat flanges were used to provide passage of the infrared beam onto the sample inside the UHV chamber. Enclosed in two aluminium boxes, the entire optical path outside the UHV compartment is purged with dry N_2 gas in order to remove water vapors, which otherwise will interfere with the useful signal from the condensed water phases by introducing absorption peaks of the gas phase water molecules at frequencies close to that of condensed phase. The stability of the dry N_2 gas flux into the external enclosure and the spectrometer contributes very significantly to the opportunity of obtaining the IR spectra free from water vapor interferences, which in the present case must be eliminated.

Two copper braids directly welded to a liquid-nitrogen-cooled stainless steel/copper container inside the UHV chamber facilitate the cooling of the Cu disk. During cooling, the liquid-nitrogen reservoir functions as a cryo-pump by reducing the pressure in the vacuum chamber to 3×10^{-9} Torr. A deposited film can be annealed at temperatures above the lowest achievable in the present setup value of ~125 K, by resistive heating of the backside of the Cu disk while the annealing regime was monitored manually by the reading of the temperature controller. The substrate temperature was measured by two K-type thermocouples mechanically fastened to the front face of the Cu disk. The precision of relative temperature measurement is ± 2 K, whereas the uniformity of temperature across the sampling area on the

Cu disk has been found to be 5 K. The latter non-uniformity is due to the heat transfer from the mounting accessory, which is at ambient temperature (18-25 °C), to the Cu disk at 125 K. Furthermore, the temperature of ice sample could be slightly higher than that of the Cu disk, and the difference will increase with the thickness of ice films because of radiation energy from the walls of chamber.

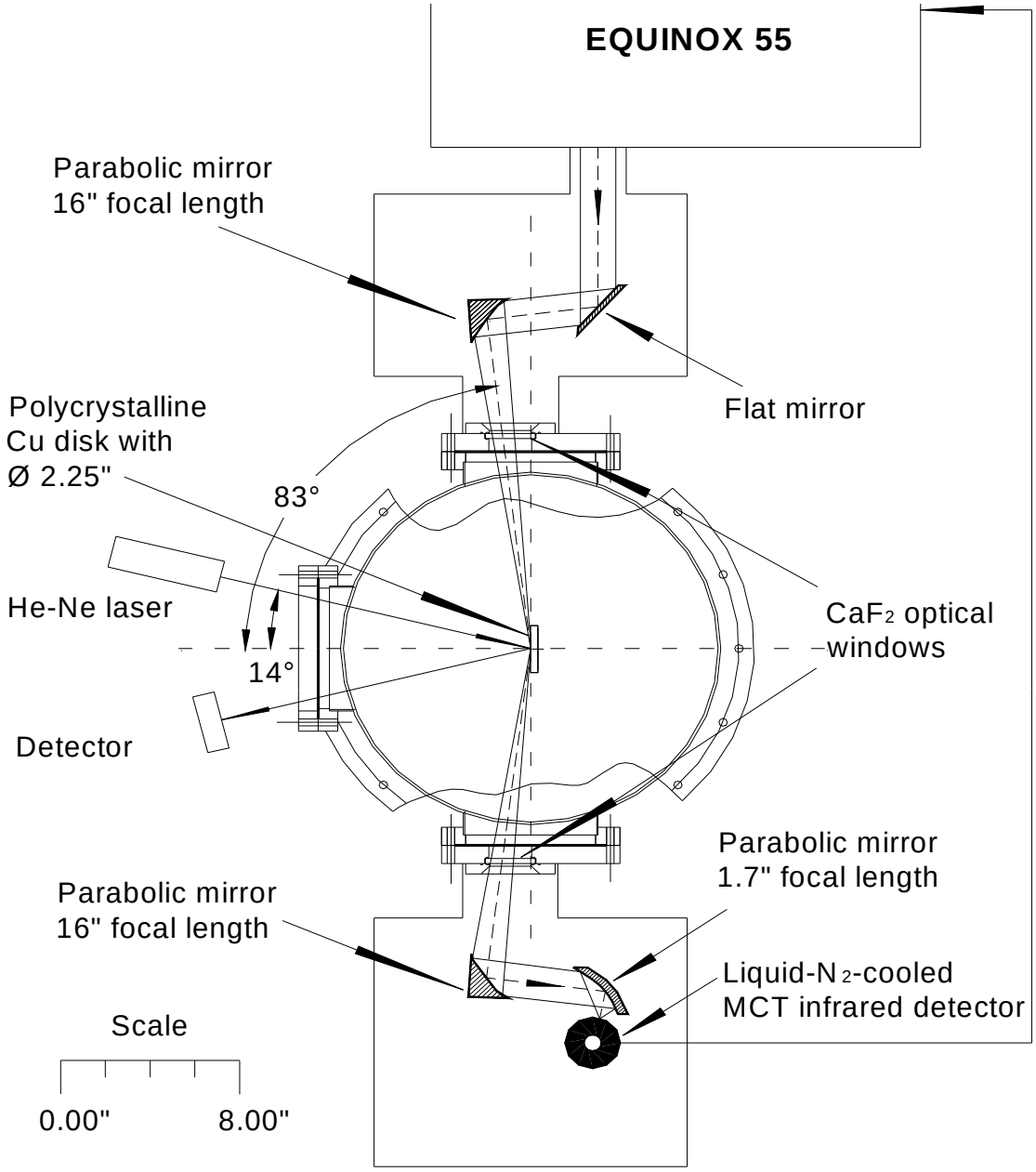

Figure 3.2.2. Schematic layout of the optical arrangement.

3.3 Samples and Accessories Preparation and Manipulation

In the present studies, the following chemical reagents have been used:

1) Acetone $_{Liq}$ (Fisher Scientific, 99.6% purity).
2) Acetaldehyde $_{Liq}$ (99.5+% purity) Aldrich.
3) Methanol $_{Liq}$ (Fisher Chemicals, Acetone free)
4) Chloroform $_{Liq}$ (Fisher Chemicals, preservation C_2H_5OH ~0.75%).
5) Hydrogen Chloride $_{Gas}$ (Technical Grade, Matheson Gas Products Inc.)
6) D_2O (99.9 atomic % of Deuterium, Iosotec Inc, Matheson). Due to periodic contacts with the ambient atmosphere, the D_2O sample became discernibly enriched by the HDO species.
7) H_2O, Millipore.

All substances have been used without further purification. The outgassing of liquid samples was performed in the external gas handling system through repeated freeze-pump-thaw cycles immediately prior dosing.

For ion sputtering and flushing of the external gas handling system, Ar gas (Praxair, Ultra pure grade) has been used.

The IR spectra of selected liquid and gaseous samples have been measured in the gas IR Cell (ICL international crystal Laboratories) with KRS-5 windows and 10 cm optical length and in the liquid IR cell (ICL international crystal Laboratories) with the KRS-5 windows and 0.015 mm thickness.

The ZnSe polarizer (1200 wires/mm, SpectraTech) with a spectral window in interval 20000-500 cm^{-1} has been used for the polarization FTIR RAS experiments.

3.4 FTIR RA Spectral Acquisition

Ice film samples with thicknesses up to 1.5 μ have been deposited by backfilling the entire UHV compartment with water vapour using a precision leak valve (Varian). Liquid water (Millipore) and organic liquids, which are kept in separate quartz ampoules attached to the gas handling system outside the UHV compartment, has been purified by multiple repeating of a freeze-pump-thaw cycle immediately prior to use. Pressure measurements were obtained by an uncorrected ionization gauge. The thickness of the ice film and the corresponding deposition rate have been estimated by observing the optical interference fringes of a He-Ne laser beam reflected off the sample using a phototransistor as the detector.

The laser interference patterns are shown below on Figure 3.5.2. It should be noted that the laser interference method provides information about the film thickness for a relatively small area (typically 1-2 mm diameter as defined by the illuminating laser spot size) in comparison with the total surface covered by ice, from which the FTIR-RA spectra are taken. Using a laser source with an adjustable beam size (1-10 mm diameter), Brown *et al.* showed that the thickness of the ice film deposited on Ru (001) was uniform over this area range [1]. In our experiment, the substrate surface was polycrystalline and relatively rough on a microscopic scale, which could introduce thickness non-uniformity. Since the sampling area was quite large (approximately the size of the target or 25 cm^2), the resulting spectra of the as-grown ice film represent the signal averaged over the entire area of the ice film with the possibility of a non-uniform thickness. With the sample held at 131 K, the initial deposition rate (after a typical induction period of 1 minute) was estimated to be 0.43 nm/sec at 1×10^{-6} Torr ambient pressure or 2 nm/sec at 5×10^{-6} Torr. The deposition rate was found to decrease slightly with increasing film thickness. It should be noted that the sensitivity of the optical interference method is limited in the case of very thin films and for films with thickness that satisfies the conditions of constructive and destructive interference (see Figure 3.5.2). During deposition of the ice film at a selected temperature, FTIR-RA spectra of the growing film were collected, unless stated otherwise, over a 20-second period by averaging 10 scans at 10 kHz (or 40 scans at 40 kHz) at a preset spectral resolution of 1 cm^{-1}, or alternatively 12 scans at 80 kHz at 0.5 cm^{-1} resolution. Background spectra over 5000-1000 cm^{-1} were collected immediately before the water exposure for the bare Cu surface with 1000 scans at the respective resolution settings. Spectral data are presented in the dimensionless absorbance unit, $AU = -log(R/R_0)$, where R/R_0 is the ratio of reflectance of the Cu substrate with and without the ice film.

3.5 Fresnel Method for Simulating the FTIR RA Spectra of Polycrystalline and Noncrystalline Ice Films

In general, the film thickness affects significantly the shape, frequency position and spectral intensity of the RA bands, and these dielectric effects have been discussed in detail by Greenler [2] and Decius and Hexter [3]. McIntyre and Aspens have used the Fresnel equations for reflection coefficients for parallel- and perpendicular-polarized light to simulate the RA spectra of an absorbing dielectric film [4]. First derived for a homogeneous dielectric film,

these equations have been extended and written in modified form to describe reflection-absorbance of light in a vacuum-absorbing dielectric film-metal system [5]. A classical Fresnel model for the reflection coefficients of σ- and π- polarized components of IR light on the interface of vacuum-ice-metal phases have been applied in the present work for modeling the RA spectra of growing non-crystalline and polycrystalline ice micro phases. The model describes the evolution of OH stretch band and interference patterns as functions of the ice optical indexes and film thickness:

$$
\begin{aligned}
&\zeta_j = \hat{n}_j \cos(\varphi_j) = \left(\hat{n}_j^2 - \sin^2(\varphi_1)\right)^{1/2} \\
&r_{\sigma\_jk} = \left(\frac{\mu_k \zeta_j - \mu_j \zeta_k}{\mu_k \zeta_j + \mu_j \zeta_k}\right) \\
&r_{\pi\_jk} = \left(\frac{\hat{\varepsilon}_k \zeta_j - \hat{\varepsilon}_j \zeta_k}{\hat{\varepsilon}_k \zeta_j + \hat{\varepsilon}_j \zeta_k}\right) \\
&r_{\sigma\_123} = \left(\frac{r_{\sigma\_12} + r_{\sigma\_23} \cdot \exp(-2i\beta)}{1 + r_{\sigma\_12} \cdot r_{\sigma\_23} \cdot \exp(-2i\beta)}\right) \\
&r_{\pi\_123} = \left(\frac{r_{\pi\_12} + r_{\pi\_23} \cdot \exp(-2i\beta)}{1 + r_{\pi\_12} \cdot r_{\pi\_23} \cdot \exp(-2i\beta)}\right) \\
&\beta = \left(\frac{2\pi \cdot d \cdot \zeta_2}{\lambda}\right),
\end{aligned}
\tag{3.1}
$$

where φ_1 and n_1 are the real angle of incidence (83º) and index of refraction of the vacuum phase (1) on Figure 3.5.1, while n_j is the complex refractive index of phase j. Parameters r_{σ_jk} and r_{π_jk} are the Fresnel coefficients of the interface between the two phases j and k for perpendicular and parallel polarized radiation. The symbols, μ_k , μ_j and ε_k , ε_j stand, respectively, for the magnetic permeabilities and complex dielectric constants of the two condensed 2 and 3 phases. Parameters r_{σ_123} and r_{π_123} are the Fresnel coefficients for reflection in three-phase system vacuum (1)-ice (2)-metal (3). β is the change in phase of the beam during one traversal of the ice film of thickness d. This algorithm has been implemented in Math CAD and C/C++ programs written for simulating of RA spectra of noncrystalline and polycrystalline ices of given thickness.

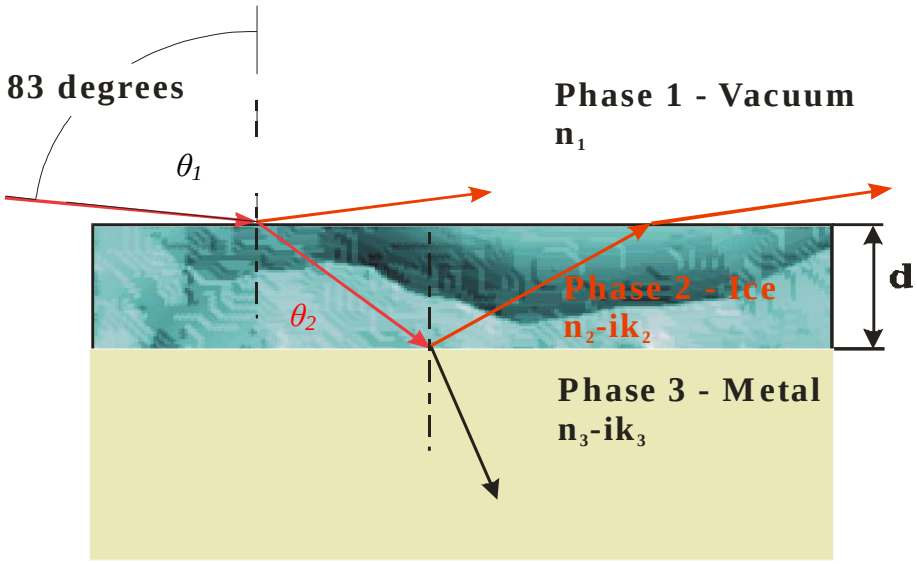

Figure 3.5.1. The geometry of IR beam passage through the ice media. Phase 1- vacuum, characterised by refractive index $n = 1$; Phase 2- ice, characterised by a set of the frequency dependent refractive and absorption indexes specific to the amorphous or polycrystalline deposits and combined in complex optical index; Phase 3- metal, characterised by a set of the frequency dependent optical indexes. The incident angle, θ_1, is near 83 °, which is close to the optimal angle for the present system as shown below on Figure 3.5.3. The angle θ_2 stands for the real refraction angle of the beam in the ice phase.

As an example, the time evolution of a laser interface pattern from an ice film grown at 131 K and water pressure of 1×10^{-6} Torr is shown Figure 3.5.2.

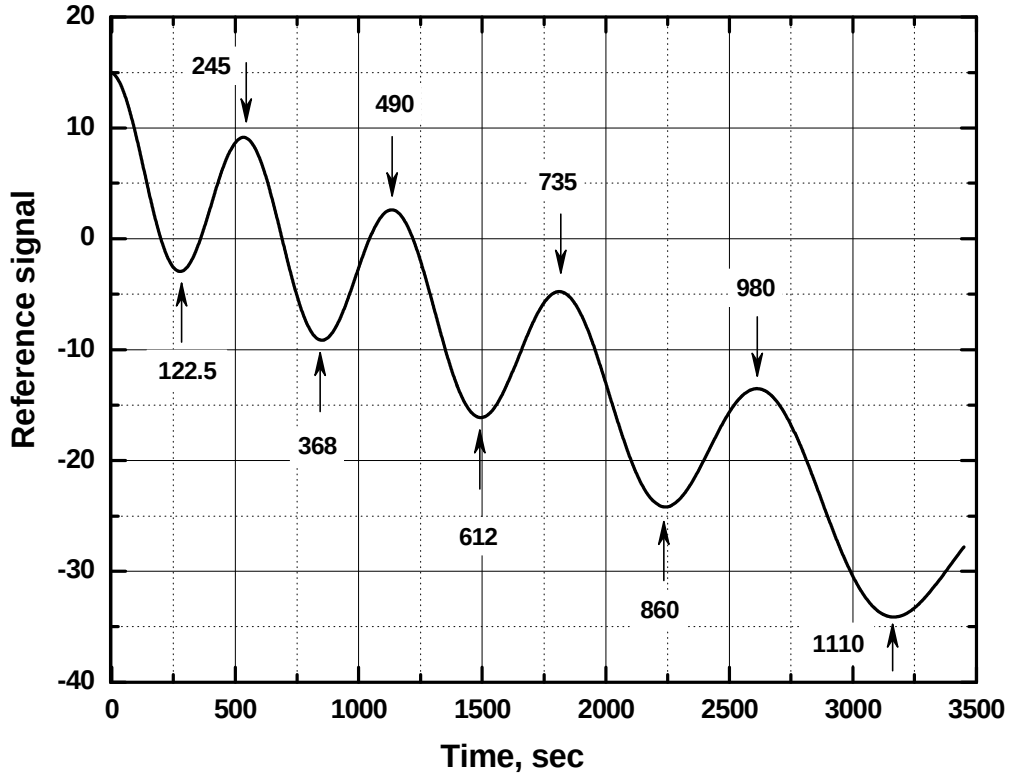

Figure 3.5.2. The He-Ne laser interference patterns for the growing pristine ice film. The approximated film thicknesses are indicated by arrows.

The thickness of ice film can be approximated at the maxima and minima on the interference curve in accord with the following equation (note that the He-Ne laser operated on λ = 632.8 nm, the incident angle, θ_1, is 14°):

$$\frac{2\cdot n_2\cdot d}{\cos\theta_2}-2\cdot d\cdot \sin\theta_1 \tan\theta_2 = m\lambda\,; \tag{3.2}$$

θ_2 stands for the refraction angle of the laser beam in the ice phase.
The d=245 nm for constructive interference.

For the spectral region of 6962-482 cm^{-1}, the values of real n and imaginary k parts of the complex refractive index of the ice layer ($\tilde{n}_{ice} = n_{ice} - ik_{ice}$) used in the present simulation for pc-ice are those derived by Toon *et al.* for ice films deposited at 163 K over a wide range

of thickness from 500 nm to 30 μ [6]. For nc-ice, Fresnel simulations are carried out using the corresponding values of *n* and *k* for amorphous ice films deposited at 77 K reported by Leger *et al.* [7]. Optical constants of Cu at room temperature compiled by Palik *et al*. [8] are used to generate the (*n*, *k*) constants of Cu at the same wavenumbers as the set of complex refractive indexes $\tilde{n}_j$ of the ice reported in the literature. Given the very small value of the magnetic susceptibility for Cu (-5.5×10^{-6} cgs) [9], the magnetic permeability of Cu is set to unity in our calculations. The calculated spectra are plotted as absorbance unit (*AU*) versus wavenumber (cm^{-1}), where *AU* is defined in an expanded form as: $AU = log\ [(R_{0\,\sigma} + R_{0\,\pi})/(R_{\sigma} + R_{\pi})]$ with $R_{0\,\sigma,\,\pi}$ and $R_{\sigma,\,\pi}$ as the reflectance of σ- or π-polarized light from the vacuum-Cu system (i.e. the bare substrate without ice) and vacuum-ice-Cu system (the substrate deposited with ice), respectively. These calculated spectra are referred to as Fresnel spectra in the present work.

As in the Fresnel notation, the σ- and π-polarizations are defined with respect to the plane of incidence (which corresponds to the plane perpendicular to the metal surface that contains the propagation vectors of the incident, reflected and refracted waves). If the electric field vector of the incidence wave is normal to the plane of incidence (i.e., parallel to the metal surface), such a polarization is denoted as σ-polarization. On the other hand, when the electric field vector of the incidence wave is parallel to the plane of incidence (i.e., normal to the metal surface), π-polarized wave is obtained. To illustrate the importance of the reflection geometry, we show in Figure 3.5.3 the calculated RA spectra of the OH stretch region for a 1-nm-thick pc-ice film as a function of the incident angle based on the Fresnel model. Because the normal incidence spectrum is analogous to the transmittance IR spectrum, Figure 3.5.3 shows in effect the changes in the spectral features from the transmittance mode to RA mode. In particular, the normal incidence spectrum shows three discernible features at 3145, 3205 and 3335 cm^{-1} (Figure 3.5.3, Curve A) to be in good agreement with the experimental transmittance spectrum reported by Buch and Devlin [10]. While there is essentially no changes in the reflectivity of the vacuum-ice interface in this spectral region and in the absorption profile of the σ-polarized component (Figure 3.5.3, Curve A), dramatic changes in the absorption profile of the π-polarized component are observed (Figure 3.5.3, Curves D and E), which accounts for the changes in the shape of the overall band from 0° to 15°. The evolution of the absorption profile is due to excitation of the longitudinal lattice modes by the electric field component of the incoming radiation perpendicular to the surface as a function of the near-normal incident

angle [11]. This excitation occurs at higher frequencies than the transverse excitation and is clearly absent in the transmittance (or normal incidence) mode [3]. Furthermore, increasing the incident angle above 15° (towards more glancing-angle incidence) significantly increases the intensity of the spectrum without affecting the general shape (Figure 3.5.3, Curves F-K) [2]. Evidently, the shape of the spectrum (determined predominantly by longitudinal excitations) is not particularly sensitive to the incident angle in the glancing incidence regime, and the experimental sampling angle (83°) used in the present work provides near optimal spectral intensity.

In the case of a thin ice film on the metal surface, the Fresnel model shows that reflection-absorption of the σ-polarized light is negligible for a film thickness up to 200 nm, which also suggests that vibrational modes with transition dipole moment parallel to the metal surface would remain undetectable until this critical thickness has been reached. This conclusion is particularly important for spectral observation of the OH *DB's*, because any OH *DB* oriented parallel to the metal surface is undetectable by RA spectroscopy in the case of thin films (see Figure 3.5.4 d below). In contrast, the absorbance of π-polarized light by thin films is strongly enhanced due to significant amplification of the electric field in the vicinity of the metal surface. In addition, the interference patterns in the transparent spectral region of ice away from the observed resonances can be described by two-beam interference produced by reflection from two parallel interfaces [5, 12]. In the case of relatively thick films, the interference patterns are observed over the entire spectral region of 5000-1000 cm^{-1}, and the corresponding absorption maxima are seen to travel from higher to lower frequencies with increasing film thickness. As shown by Robinson *et al.* [12], there are two sets of interference patterns, which are associated with destructive interference of σ- and π-polarized components of the infrared light. The present work shows that the σ-patterns in the 5000-1000 cm^{-1} optical window exhibit absorption maxima starting with film thicknesses of 350 nm, while the corresponding features of the π-patterns appear at thicknesses above 750 nm. Moreover, the emergence of an interference pattern in the optical region of any vibrational mode of ice causes considerable amplification in the intensity of the band.

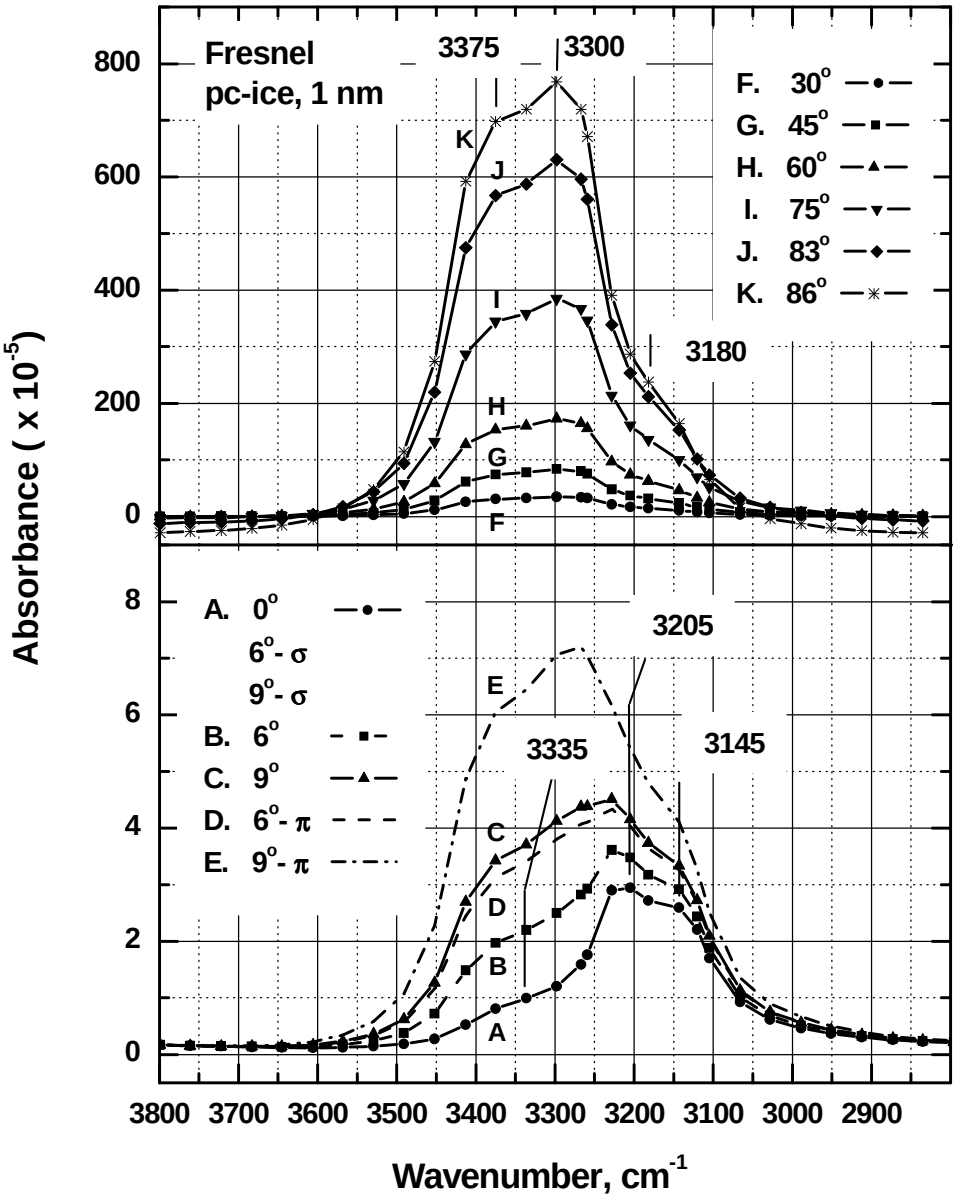

Figure 3.5.3. Fresnel spectra of the 1-nm pc-ice film at different incident angles. The simulations were performed using optical constants obtained for films deposited at 163 K [6]) for non-polarized light at different incident angles. (A) 0º or normal incidence, (B) 6º, (C) 9º, (F) 30º, (G) 45º, (H) 60º, (I) 75º, (J) 83º and (K) 86º. The σ-polarized components of the Fresnel spectra for incident angles of 6º and 9º are the same as Curve A, while the corresponding π-polarized components are shown as Curves D and E respectively.

In order to simulate the dependence of the integrated intensity of the OH *DB's* on the film thickness, the optical indexes of the crystalline ice obtained by Toon *et al.* [6] was modified by inclusion of the OH *DB* vibrational mode at $\nu_{OH} = 3690\ cm^{-1}$ with a damping constant γ of 15 cm^{-1}. Furthermore, the OH *DB* intensity is artificially enhanced by arbitrarily setting the integrated absorptivity ($\rho\pi^2 = 6.86\times10^3\ cm^{-2}$) to 0.1% of the integrated Lambert absorptivity of the OH stretching mode obtained from Bertie *et al.* [13]. This simulation treats the OH *DB's* as an integral part of the ice structure and the amount of OH *DB's* is proportional to the ice film thickness. The modified dielectric function ε of the resulting ice structure was calculated in accordance with Klein and Furtak [14] as follows:

$$\varepsilon = \varepsilon_0 + \frac{\rho\left(\frac{\varepsilon_0 + 2}{3}\right)^2}{\nu_{OH}{}^2 - \left(\frac{\varepsilon_0 + 2}{3}\right)\left(\frac{\rho}{3}\right) - \nu^2 + i\,\nu\,\gamma}, \tag{3.3}$$

where $\rho = \frac{1}{\pi^2}\int K(\nu)d\nu$, and *K(ν)* is the Lambert absorptivity. ε_0 is the dielectric function of pc-ice calculated from the data of Toon *et al.* [6].

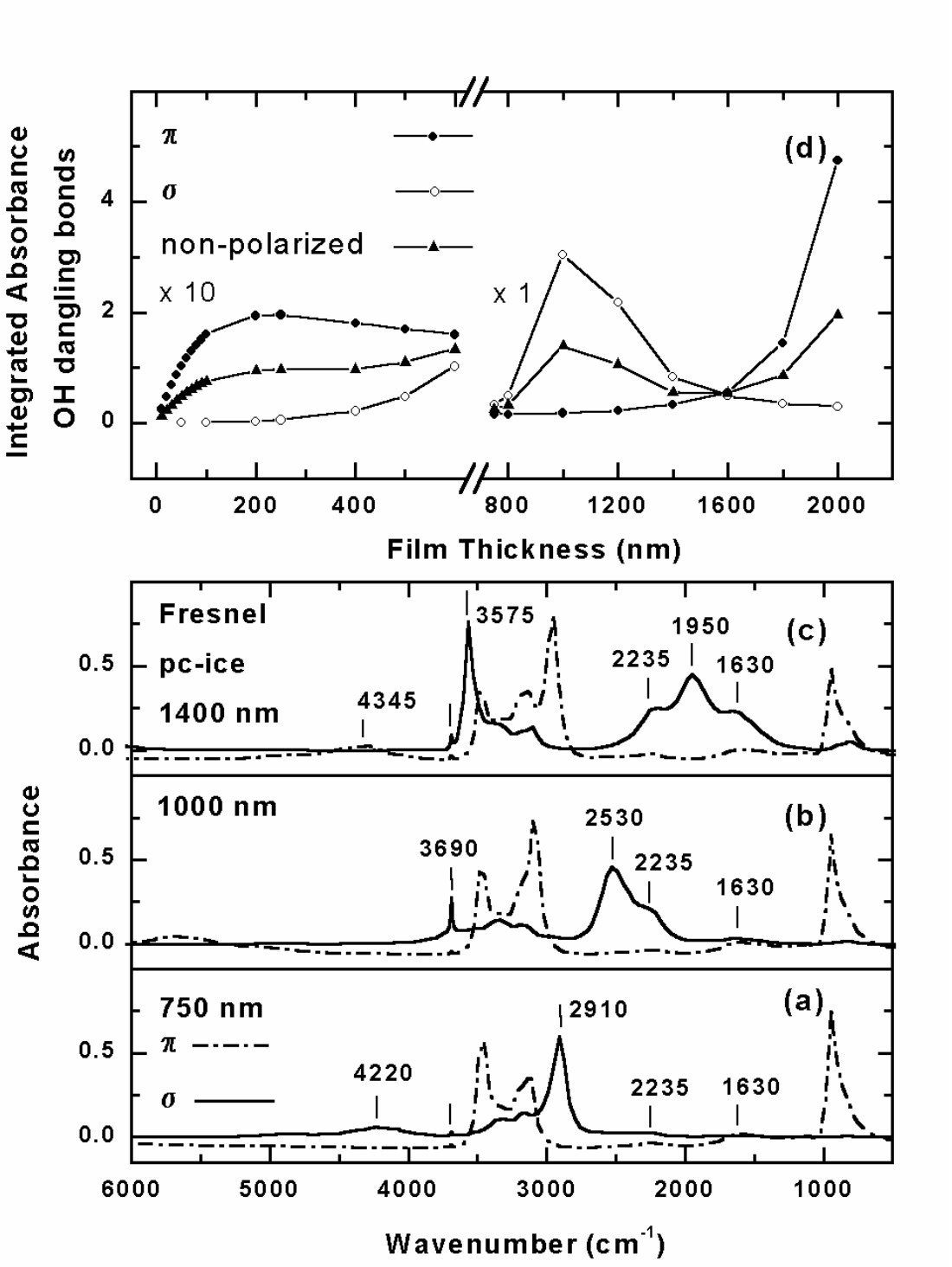

Figure 3.5.4. Fresnel spectra of pc-ice films as function of film thickness. Thickness parameter is (a) 750 nm, (b) 1000 nm, and (c) 1400 nm. The dependence of the integrated absorbance of the OH *DB* signal on the thickness is summarized in (d).

The calculations show that the destructive σ-polarized interference feature travels from 4220 cm^{-1} (Figure 3.5.4 a) to 3575 cm^{-1} (Figure 3.5.4 c) as the thickness is increased from 750 nm to 1400 nm. The passage of this σ-polarized feature over the optical window of the OH *DB* band at 3690 cm^{-1} (Figure 3.5.4 b) causes the amplification in the integrated intensity of the OH *DB* signal as summarized in Figure 3.5.4 d. Once the σ-interference feature passes over, the OH *DB* signal returns to its normal intensity. Furthermore, the passage of a second destructive σ-polarized interference feature, which travels from 2910 cm^{-1} (Figure 3.5.4 a) to 1950 cm^{-1} (Figure 3.5.4 c) over the same thickness range, causes significant amplification in the intensities of the combination band (at 2235 cm^{-1}) and bending band (at 1630 cm^{-1}). Figure 3.5.4 d also shows that the integrated intensities of the OH *DB* feature for the π-polarized and non-polarized waves increase linearly with the film thickness up to 100 nm and level off at greater thickness due to the physics of reflection-absorbance. This spectral dependence on the film thickness is in agreement with the experimental data of Zondlo *et al* [15]. The integrated intensity of the OH *DB* feature for π-polarization remains nearly constant in the thickness range 200-1200 nm, in spite of the increase in the amount of the OH *DB's* assumed in the model. The marked increase in the integrated intensity for thickness above 1600 nm (Figure 3.5.4 d) is evidently caused by the emergence of a destructive π-polarized interference pattern, which travels from 4345 cm^{-1} to a lower frequency (Figure 3.5.4 c).

References:

1. D. E. Brown, S. M. George, C. Huang, E. K. L. Wong, K. B. Rider, R. S. Smith, B. D. Kay, J. Phys. Chem. ***100*** (1996) 4988.
2. R. G. Greenler, J. Chem. Phys. ***44*** (1966) 310.
3. J. C. Decius, R. M. Hexter, "Molecular Vibrations in Crystals", McGraw-Hill, New York (1977).
4. J. D. E. McIntyre, D. E. Aspens, Surf. Sci. ***24*** (1971) 417.
5. M. Born, E. Wolf, "Principles of Optics", $6^{\underline{th}}$ edition, (1996) Pergamon, New York.
6. O. B. Toon, M. A. Tolbert, B. G. Koehler, A. M. Middelebrook, J. Geophys. Res. ***99*** (1994) 631.
7. A. Leger, S. Gauthier, D. Deforneau, D. Rouan, Astron. Astrophys. ***117*** (1994) 164.
8. E. D. Palik (Ed.) "Handbook of the optical constants of solids", (1985) Academic, Toronto.
9. R. C. Weast (Ed.) "Handbook of Chemistry and Physics", $64^{\underline{th}}$ edition, (1983-1984) CRC Press, Florida, page E-110.
10. V. Buch, J. P. Devlin, J. Chem. Phys. ***110*** (1999) 3437.
11. L. Schriver-Mazzuoli, A. Schriver, A. Hallou, J. Mol. Spect. ***554*** (2000) 289.
12. M. S. Robinson, G. Mallick, J. L. Spillman, P. A. Carreon, S. Shalloo, App. Optics ***38*** (1999) 91.
13. J. E. Bertie, H. J. Labbe, E. Whalley, J. Chem. Phys. ***50*** (1969) 4501.
14. M. V. Klein, T. E. Furtak, "Optics", J. Wiley & Sons, New York (1986).
15. M. A. Zondlo, T. B. Onasch, M. S. Warshawsky, M. A. Tolbert, G. Mallick, P. Arentz, M. S. Robinson, J. Phys. Chem. B ***101*** (1997) 10887.

CHAPTER 4

Theoretical Analysis and Computer Simulations of the Interaction of Small Polar Molecules with Water Media

4.1 Quantum Mechanical Analysis of the Hydrogen Bonding in Water Media

A key concept for understanding the structure of water medium and their interaction mechanisms with guest molecules of different chemical classes resides in hydrogen bonding (*HB*). It is generally established [1, 2, 3, 4, 5, 6] that there is a specific attraction between a molecular system containing electropositive hydrogen atoms, which are usually covalently bonded to a strongly electronegative neighbouring atom, and an electronegative molecular counterpart, which comprises of electronegative atoms (such as oxygen, nitrogen, halogens etc.) carrying lone electron pairs. In other words, a particular stable molecular configuration is classified among hydrogen-bonded systems if the hydrogen atom is directly involved in the bonding between two subsystems. A geometric manifestation of hydrogen bond in such a stable configuration resides in the localization of a hydrogen atom in the proximity of a line connecting the two atomic centres. Two hydrogen-bonded molecular counterparts are designated as a donor and an acceptor of the *HB*. The former is a molecular subsystem, which bears the electropositive hydrogen atom directly involved in the bonding, whereas the electronegative acceptor provides an electron density coordinated against that hydrogen atom. As any other chemical bond, *HB* can be characterized by its directionality and saturability, i.e. one electropositive hydrogen atom could form a single hydrogen bond or, in other words, the linear configuration is a global minimum, whereas a *HB* structure with a bifurcated hydrogen atom, which coordinates with two acceptors, corresponds to a transition state or to a less stable local minimum. In the context of weak hydrogen bonds these characteristics are especially important for distinguishing between the *HB* and such intermolecular forces as pure electrostatics between charged or dipole-carrying counterparts on the one side and the dispersion interaction, which exhibits different distance and orientational dependence and is non-saturable, on the other side. It should be noted that the unique properties of hydrogen atoms are evident and play a fundamental role in the formation of a hydrogen bond. At first

glance, the absence of a core electron shell is the most distinct relevant feature of the hydrogen atom, which makes it smaller than all other elements. With reduced electron density readily achievable by covalent bonding with a more electronegative counterpart, the hydrogen atom becomes mobile and can penetrate an adjacent basin of electron density supplied by the *HB* acceptor. Therefore, a capability of penetrating the electron density of *HB* acceptor should be highest in the case of hydrogen atom, which is free from the inner shell electrons. Being the dominant contribution to the total electron energy in the overlap region for van der Waals complexes by increasing the kinetic energy of electrons, the repulsive part of the electron exchange is expected to be less pronounced in the case of hydrogen. This view is supported by the observation that the more electropositive the hydrogen atom is the stronger is the hydrogen bond. In other words, the classical electrostatic interaction between electrical multipoles, which brings two *HB* counterparts together, leads to hydrogen bonding, because there is no significant repulsion originated from the Pauli exclusion for the electron densities on the *HB* acceptor and hydrogen atom.

The present section attempts to show that quantum mechanical calculations of isolated water clusters at different levels of theory are useful (even necessary) for interpreting experimental spectral and structural data on the aqueous and pristine water systems. In particular, spectrum-structure correlation could be adviced on the basis of a computational analysis restricted to relatively small, finite ensembles of water molecules. In some cases, such a spectrum-structure correlation scheme can be examined by comparing the computational and experimental results. By comparing computational and experimental data on isolated water clusters and protonated water system, the present author illustrate different aspects of hydrogen bonding in water media such as bifurcated hydrogen bond, strong and weak hydrogen bonds and their spectral manifestations. From technical perspective, this section provides detailed information on the structure and properties of 26-mer water cluster, the largest pristine water cluster considered in the present studies. It appears that even this system of very small size could provide interesting and clear insight in the structural and vibrational properties of such complex systems as acidic aqueous solutions. As this section will show, there are reasonable grounds for suggesting that the information obtained by the computational analysis of small water clusters is also useful for understanding real water

media with enormous number of water molecules, which are often computationally inaccessible. The key problem of this Chapter is hydrogen bonding in the network of water molecules.

In a majority of cases, the electropositive hydrogen atom participates only in a single hydrogen bond, and the preferential location of the hydrogen atom appears to be in the proximity of a line connecting two functions, *HB* acceptor and *HB* donor. This specific spatial localization of the hydrogen atom can be viewed as a geometric criterion for the presence of the hydrogen bond. However, in organic crystals, such as glycine [7] and crystalline hydrates, [8] hydrogen atoms were found in a bifurcated position, i.e. a hydrogen atom is locked at approximately equal distances from two neighbouring electronegative atoms. For water media, Giguere [9] has adopted this notation of a bifurcated hydrogen atom, which originates from crystallographic studies, and further suggested that the bifurcated *HB*'s (*bHB*) play a discernible role in the hydrogen bonding network in liquid water and fill a gap between linear hydrogen bonds and free non-hydrogen bonded species. Giguere proposed the following geometry for the bifurcated hydrogen bond in the tetrahedral *HB* network:

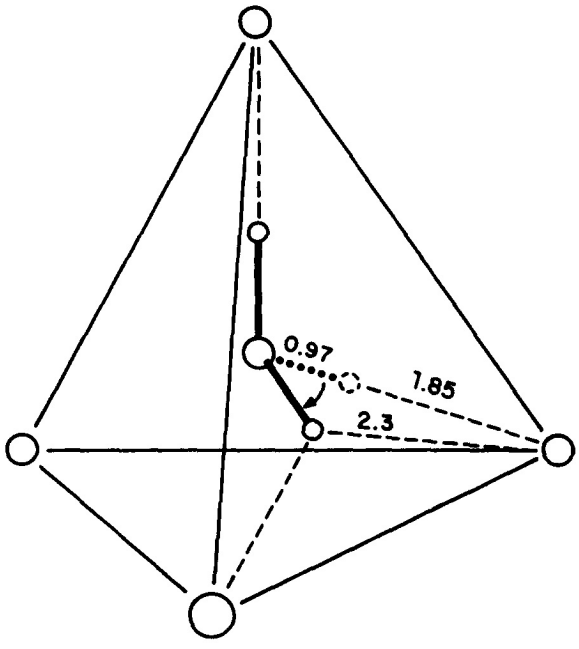

Figure 4.1.1. The configuration of bifurcated hydrogen bond in the tetrahedral water network. Reproduced from Giguere [9].

It is not immediately obvious from Giguere's original work [9] whether this structure represents a local minimum or a transition state between two neighboring minima with classical linear hydrogen bonds. Based on this work, Geiger and Mausbach [10], in particular, treat the arrangement in Figure 4.1.1 as a "transient structure", which, however, is "characteristic for the liquid water and responsible for the structural and dynamical distinction from amorphous solids". It is of interest to note that in the course of the present work on *ab initio* and semiempirical quantum mechanical and classical calculations, the *bHB*'s have been found in fully optimized water clusters comprising of 26 molecules. The configuration of the *bHB* appears to be quite different from that given by Giguere and corresponds to a coordination number of *5* for a central molecule as shown in Figure 4.1.2. The *bHB* configuration is characterized by a central molecule bonded to three neighbours with linear *HB*'s whereas the fourth neighbour, expected in the ideal tetrahedral configuration (Figure 4.1.1), is replaced by a pair of molecules to which a central molecule donates the hydrogen atom, leading to the formation of an additional bifurcated *HB* characterized by larger $H_d \cdots O_{Ac}$ distances. The difference in the bond lengths is evident and is in accord with Giguere's prediction, while the configuration of *bHB* observed in the present studies is different from that in Figure 4.1.1.

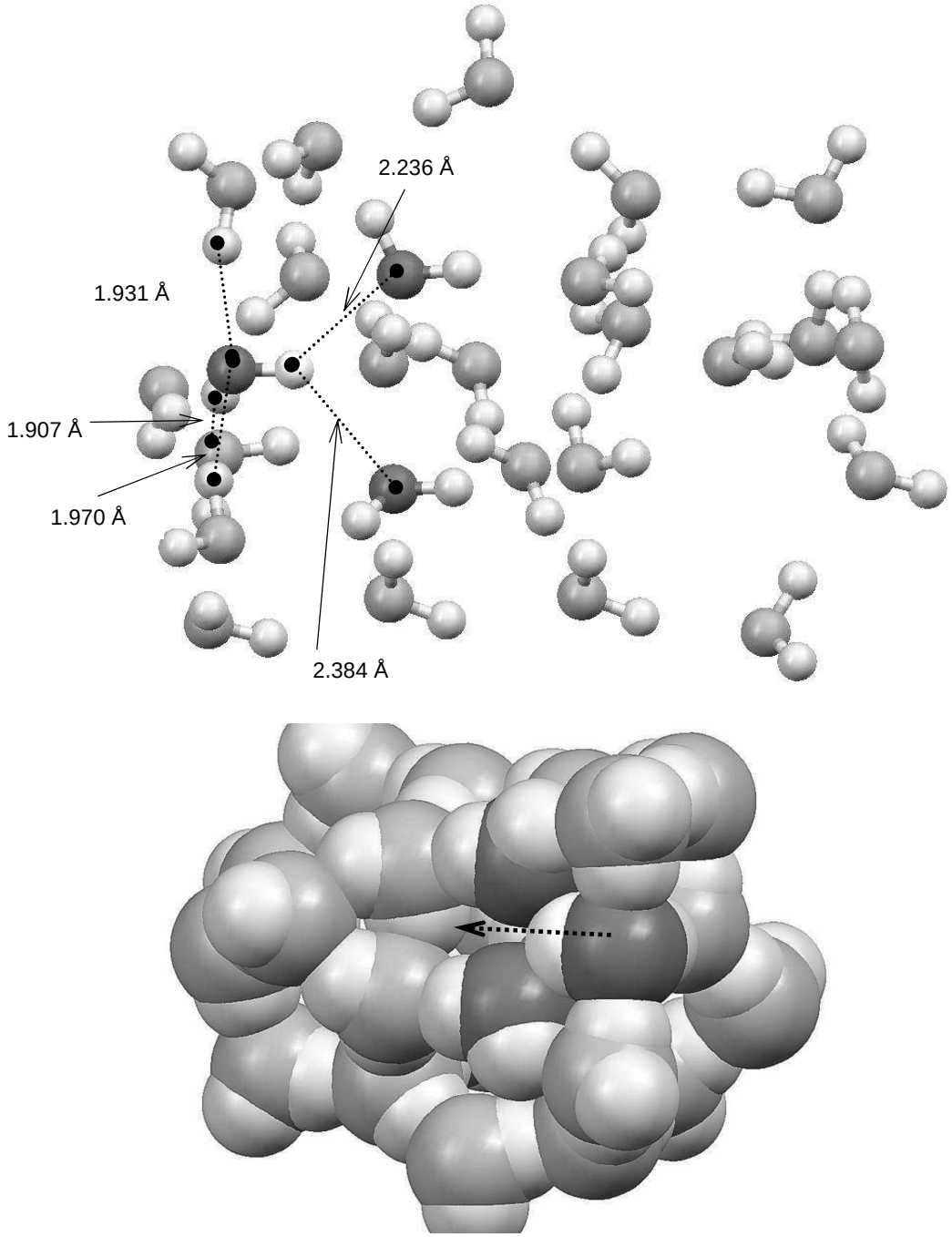

Figure 4.1.2. Structure of 26-mer water cluster optimized at the *HF/6-31g(d,p)* level. Bifurcated *HB*'s are an integral part of the local minimum at this level of theory. The arrow indicates the direction of bifurcated hydrogen bond.

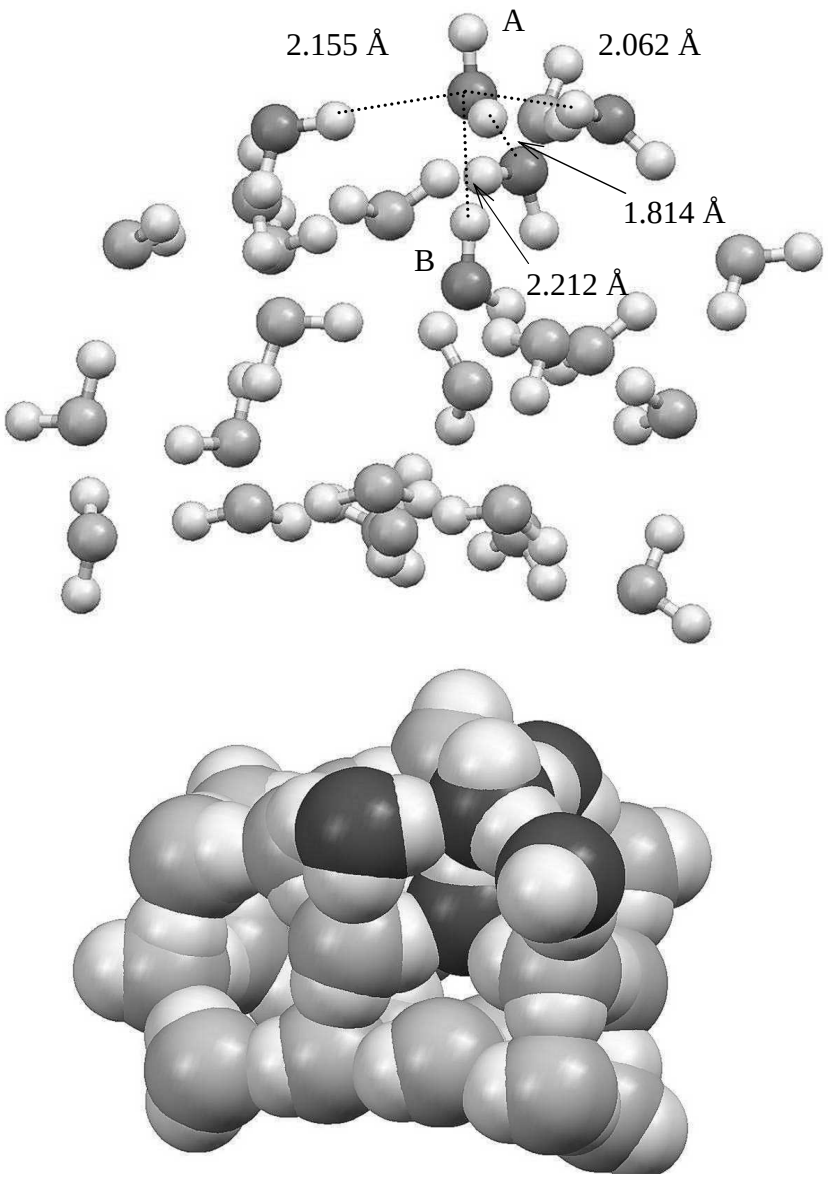

Figure 4.1.3. Molecular neighborhood of the water molecule that acts as a triple acceptor in the 26-mer cluster optimized at *HF/6-31g(d,p)* level.

In the example in Figure 4.1.2, the central molecule is located on the edge of cluster and is potentially accessible for additional acceptor coordination from the top, which could lead to even higher coordination numbers. A word of caution should be said about the bifurcated hydrogen bond, because it is not obvious whether the specific features of the hydrogen bond *per se* present in this (or similar) local arrangement(s) and indeed whether the

bifurcation is a leading factor in this arrangement or it is a result of other stronger intermolecular interactions among neighbours (*B3LYP* for instance shows no bifurcated *HB*'s). In this particular case, the delocalization energy of the electron density transfer from the lone pair orbitals of two O_{Ac} to the antibonding σ^*(O−H) of *bHB* donor are 2.9 kcal·mole^{-1} and 4.9 kcal·mole^{-1} (as calculated by the *NBO* program [11]), whereas the average value of delocalization energy for all 43 *HB*'s found in this cluster is 12.5 kcal·mole^{-1} with the maximum value at 24.8 kcal·mole^{-1}. This noticeable difference between the average delocalization energy for the cluster and the delocalization energies for the *bHB* indicates that the covalence of *bHB* is on the low side of the covalence of hydrogen bonds in water medium and, therefore, dipolar (purely electrostatic) forces could play a leading role in the formation of bifurcated hydrogen bonds. The same cluster also shows a local arrangement where a central water molecule A in Figure 4.1.3 serves as an acceptor of three and as a donor of a single *HB* with unused additional donor capacity.

The extra molecule B in an interstitial position is coordinated with the acceptor A by a linear hydrogen bond, bringing a total number of acceptor *HB*'s of molecule A to three. Such an acceptor configuration is apparently impossible in a proper tetrahedral network, but is found in this distorted network indicating that the acceptor capacity of the water molecule in not necessarily two. This unique structural feature is expected to contribute to the physical properties of this cluster in an unusual way (in comparison with a regular tetrahedral network). The IR spectrum is among the observable physical properties of the water media, in which the presence of structural features different from typical tetrahedral arrangements should be evident. This matter will be considered in some details following a discussion on the distribution functions. The *HB* network in this cluster therefore exhibits significant local deviations from a tetrahedral pattern. There are all possible kinds of close small rings in the cluster: three-, four-, five- and six-member cycles are evident. The starting configuration of this cluster contains two interconnected layers of three adjoined, nearly ideal hexagons. During the optimization the edges of the cluster collapse into a sequence of the book configurations of hexagonal rings as a result of the 1−4 intermolecular attraction. It should be noted that *bHB*'s and triple acceptor structural features were found in *HF* and *TIP4P* clusters whereas *B3LYP* cluster shows no sign of bifurcated *HB*.

The O-O, O-H and H-H pairwise radial distribution functions for this cluster are in surprisingly good correspondence with those of liquid water and low- and high-density noncrystalline solids reported by Finney *et al.* [12] and reproduced below in Figure 4.1.4 and Figure 4.1.5.

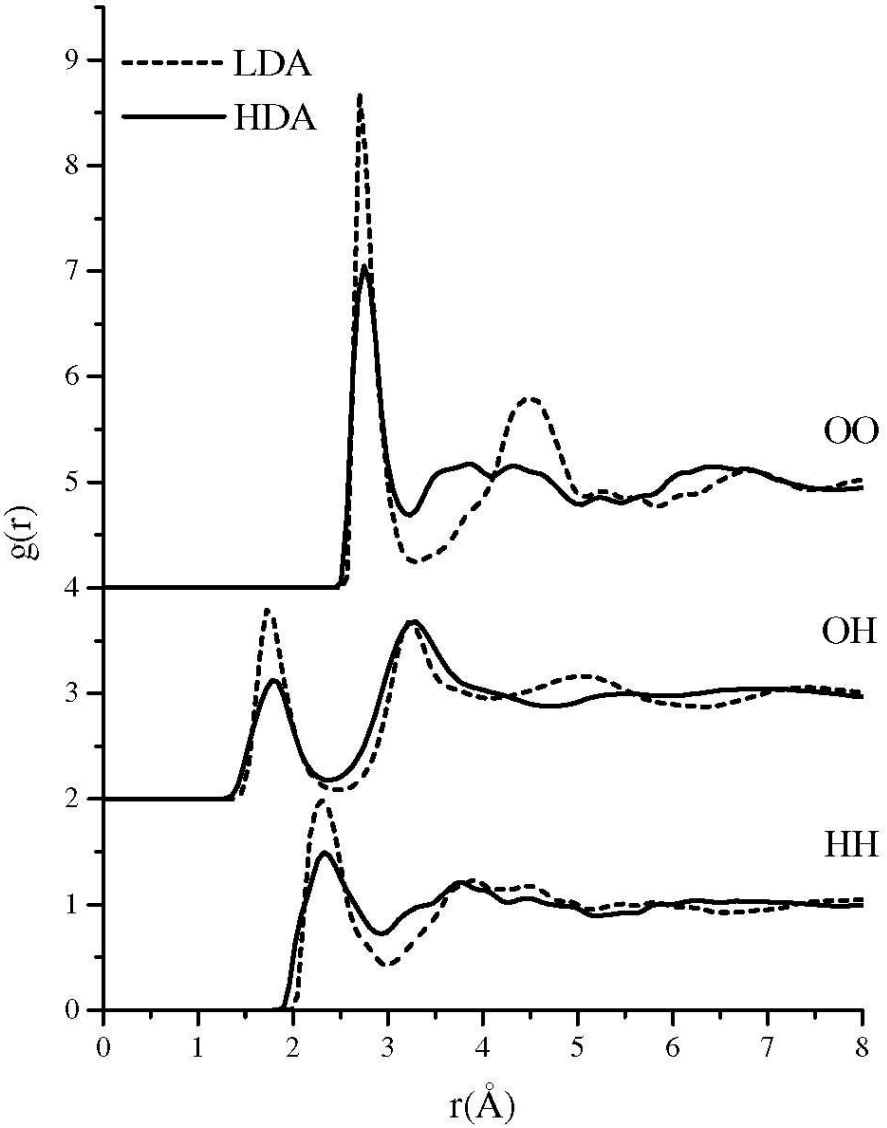

Figure 4.1.4. Radial distribution functions for the low-density and high-density amorphous solids at 80 K. Reproduced from Finney *et al.* [12].

(a)

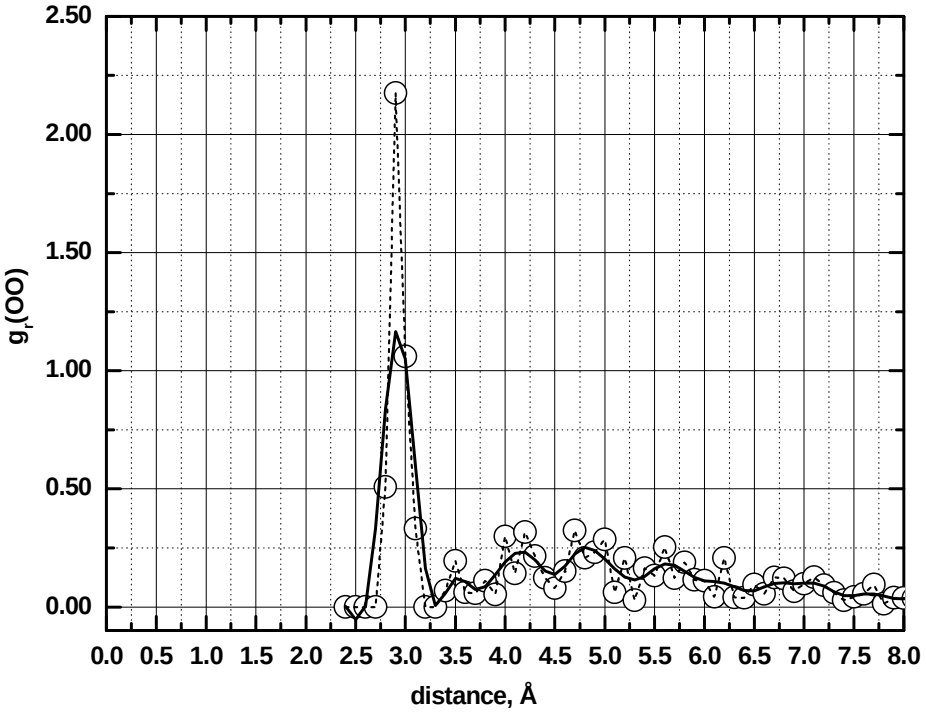
2.50
2.00
1.50
1.00
0.50
0.00
g_r(OO)
0.0 0.5 1.0 1.5 2.0 2.5 3.0 3.5 4.0 4.5 5.5 6.0 6.5 7.0 7.5 8.0
distance, Å

(b)

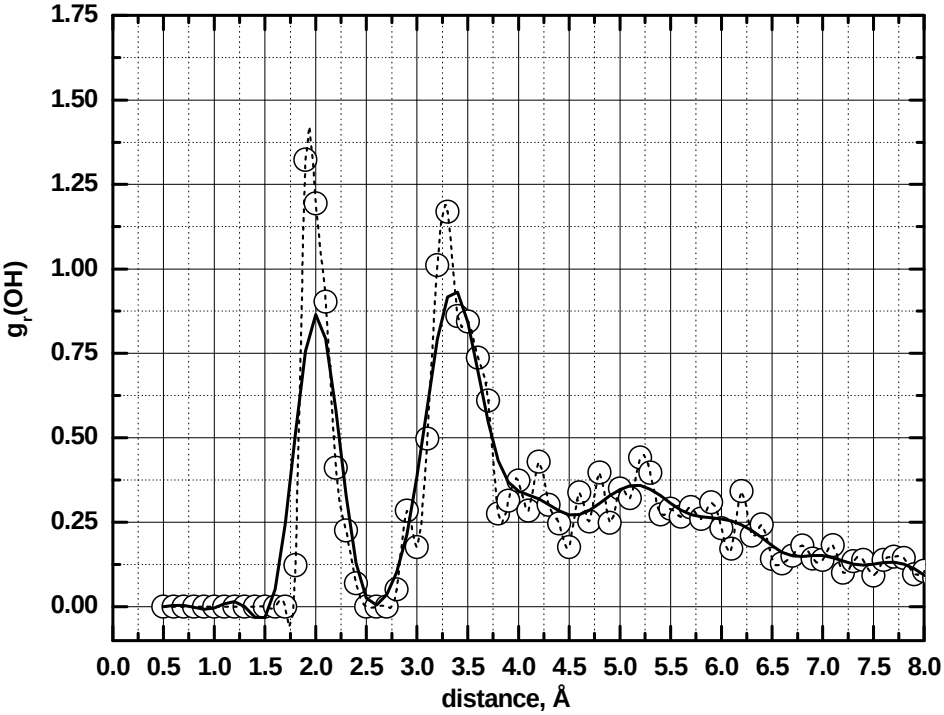
1.75
1.50
1.25
1.00
0.75
0.50
0.25
0.00
g_r(OH)
0.0 0.5 1.0 1.5 2.0 2.5 3.0 3.5 4.0 4.5 5.0 5.5 6.0 6.5 7.0 7.5 8.0
distance, Å

(c)

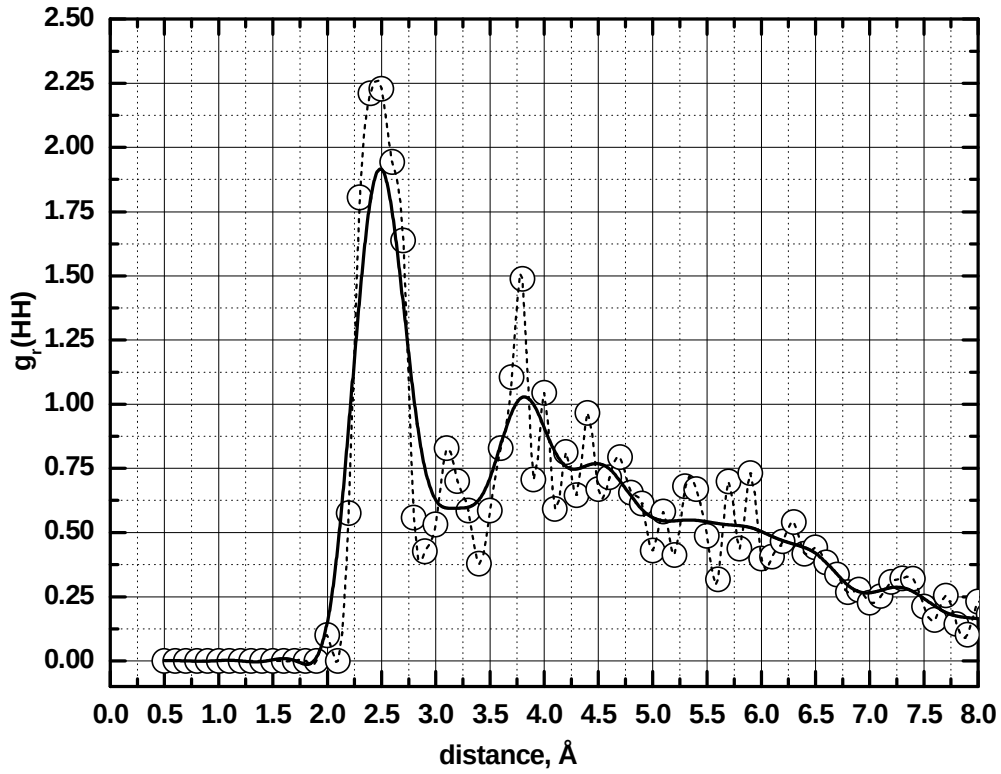

Figure 4.1.5. Distribution functions of the 26-mer cluster at the *HF/6-31g(d,p)* level. (a) O···O; (b) O···H and (c) H···H pairwise distribution functions. The solid lines represent the FFT (Fourier transform) smoothing of the data points performed by the OriginPro program [13].

The main features of the O···O radial distribution function include the position and intensity of the first peak, which represent the nearest neighbours of a water molecule, and those of subsequent peaks, which correspond to the second and the third coordination spheres. For the O···O data, Finney *et al.* [12] have shown that the integration between 2.3 and 3.3 Å (i.e. the first coordination shell) gives 3.9 ±0.1 nearest neighbours for the low-density amorph, which nearly coincides with that of crystalline ice at 220 K. The liquid water value of 4.3 ±0.12 nearest neighbors is discernibly larger than *4* whereas there are *5* nearest neighbours in the high-density amorph, suggesting the presence of an additional water molecule in the first coordination shell. A comparative analysis of the small water clusters in Section 4.3.3

indicates that compact water clusters exhibits the spatial characteristics that are in accord with Finney *et al.* [12] data for the *HDA* media, whereas open monocyclic water structures are more appropriate for the *LDA* media. The O···H distribution function (Figure 4.1.4 for the Finney's experiment [12] and Figure 4.1.5 (b) *HF* results) shows two distinct maxima at ~ 1.8 Å (2 Å in the *HF* cluster) and 3.25 Å, which correspond to $(O-H^{*})_{d}\cdots O^{*}_{Ac}\ 1^{O}{:}2^{H}$ (the figures enumerates the sequence of atoms along a chain of hydrogen bonds whereas the superscripts label elements) hydrogen-bonded and $(H^{*}-O-H)_{d}\cdots O^{*}_{Ac}\ 1^{O}{:}4^{H}$ configurations, respectively. The O···H density at larger separations originates from remote H···O pairs such as $(H^{*}-O-H^{*})\cdots(H-O-H)\cdots O^{*}_{Ac}\ 1^{O}{:}5^{H}$ and $1^{O}{:}7^{H}$. Finally, the H···H distribution function (Figure 4.1.4 for the Finney's experiment [12] and Figure 4.1.5 (b) for the *HF* results) exhibits a distinct first peak at ~2.4 Å (2.5 Å in the *HF* cluster) for the $(H-O-H^{*})_{d}\cdots(O-H^{*})_{Ac}\ 1^{H}{:}3^{H}$ configurations, whereas the second diffuse peak most likely describes the $(H^{*}-O-H)_{d}\cdots(O-H_{1,2}{}^{*})_{Ac}\ 1^{H}{:}5^{H}$ configurations (Figure 4.1.4 and Figure 4.1.5). In spite of all the obvious differences in the techniques and objects used by Finney *et al.*[12] and by the present author, the good accord between the experimental [12] and calculated *ab initio* distribution functions indicates the applicability of direct quantum mechanical simulations of small water clusters for the interpretation and, perhaps, prediction of the properties of real systems. In particular, the observation of *bHB*'s in this *HF* cluster (and also in the *TIP4P* cluster) shows that bifurcated bonds are an integral part of the network corresponding to a given local minimum. The present quantum mechanical analysis provides evidences that the covalence character of bifurcated hydrogen bonds is much less pronounced than in the average hydrogen bond in water media, which suggests the electrostatic (dipolar) origin of the bifurcated configuration.

If a set of minima are obtained in the course of computer simulations, then the comparison of their properties and structural characteristics could lead to practically relevant, property-structure correlations. The sizes of the water clusters for such simulations should not necessarily be very large because the main features of water media are rooted to a larger degree in the properties of a single water molecule, water dimer and in details of the tri-body interaction. The aperiodicity of present clusters and the large surface-to-volume ratio could be considered as inadequate for the description of continuous water media because in the finite

clusters a significant number of water molecules are in the asymmetric force field. With respect to this concern, it should be pointed out that noncrystalline water media exhibits a high degree of heterogeneity and the correlation volume could be small. Therefore, it is plausible that in real noncrystalline water media a large number of molecules exist in a spatially heterogeneous force field and a signature of this could be found in the vibrational IR spectra. The comparison between the 26-mer cluster optimized at the *HF* level and with the *TIP4P* classical Lennard-Jones and electrostatic potential clearly shows differences, which are to be expected from a general viewpoint on hydrogen bonding in the water media. In particular, both the *HB* cooperativity of the water network and the electron correlation lead to additional molecular polarization, which in turn should result in the compression of the medium. Indeed, optimized for an infinite water media and therefore effectively augmented with the multi-body and electron correlation effects, the *TIP4P* potential leads to more compressed finite structures than that obtained with *HF* that does not treat the electron correlation beyond the Pauly exclusion. The *B3LYP* results are comparable with the *TIP4P* as demonstrated in Figure 4.1.6 for the same 26-mer cluster that tentatively indicates the adequacy of the *B3LYP* functional in handling the electron correlation in the water media. Firstly, a surprisingly good agreement between the *TIP4P* and *B3LYP* distribution functions shows that despite fundamentally different force fields two clusters exhibit nearly identical spatial characteristics. Secondly, the mismatch between *HF* and *B3LYP* results is most likely due to differences in the treatment of exchange-correlation interactions in the system. The *B3LYP* functional overestimates the lengths of covalent bonds and correspondingly underestimates the lengths of hydrogen bonds (i.e. it overestimates the energies of *HB*'s). Such a computational property of *B3LYP* leads to interesting spectral features, analysis of which is closely associated with the polarization and spectral properties of short hydrogen bonds. These bonds in turn play a fundamental role in the pressure-induced dynamics of the ice *VIII*→ice *VII*→ice *X* conversion and possibly in the surface properties of water media. In contrast, *HF* underestimates the lengths of covalent bonds and correspondingly overestimates the lengths of hydrogen bonds.

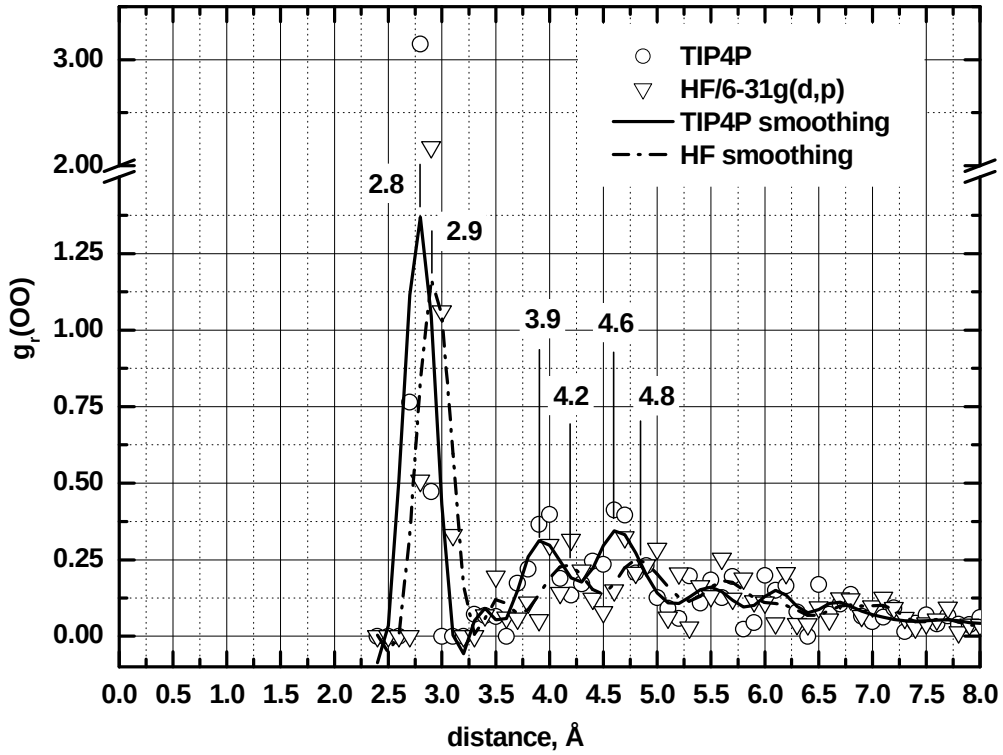
TIP4P
HF/6-31g(d,p)
TIP4P smoothing
HF smoothing
2.8
2.9
3.9
4.6
4.2
4.8
g_r(OO)
distance, Å

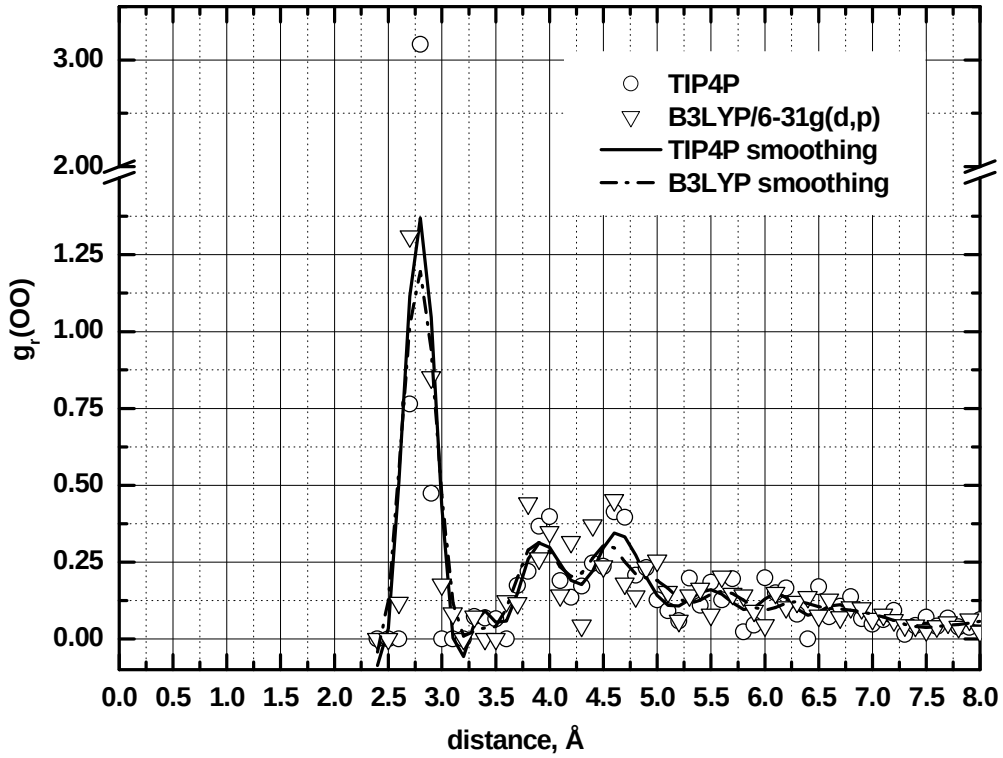
TIP4P
B3LYP/6-31g(d,p)
TIP4P smoothing
B3LYP smoothing
g_r(OO)
distance, Å

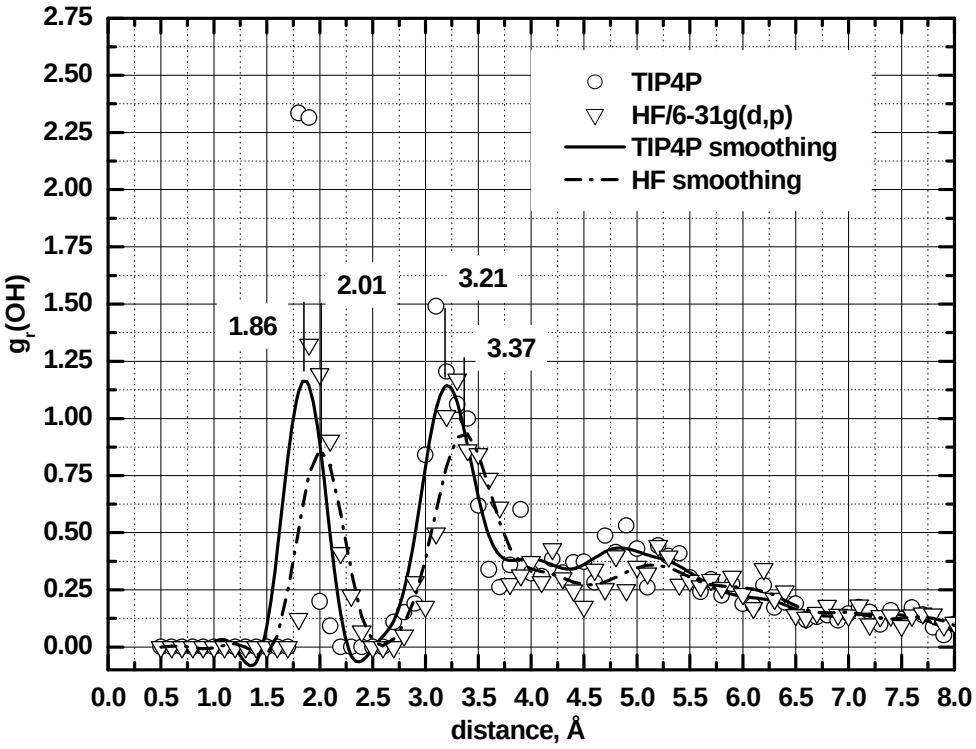
TIP4P
HF/6-31g(d,p)
TIP4P smoothing
HF smoothing
1.86
2.01
3.21
3.37
g_r(OH)
distance, Å

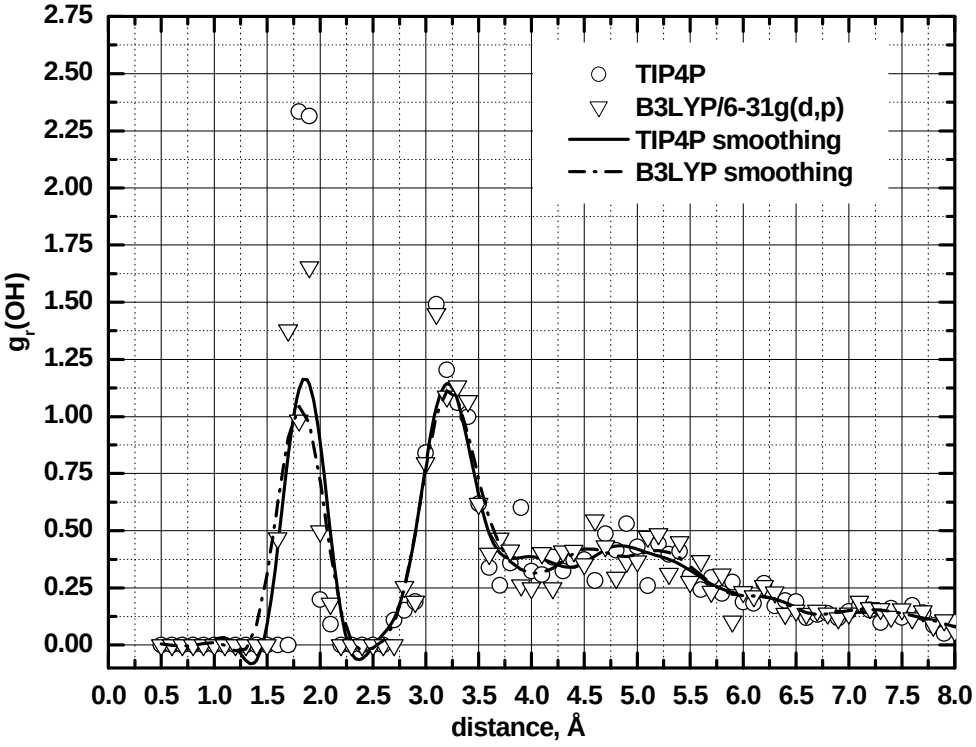
TIP4P
B3LYP/6-31g(d,p)
TIP4P smoothing
B3LYP smoothing
g_r(OH)
distance, Å

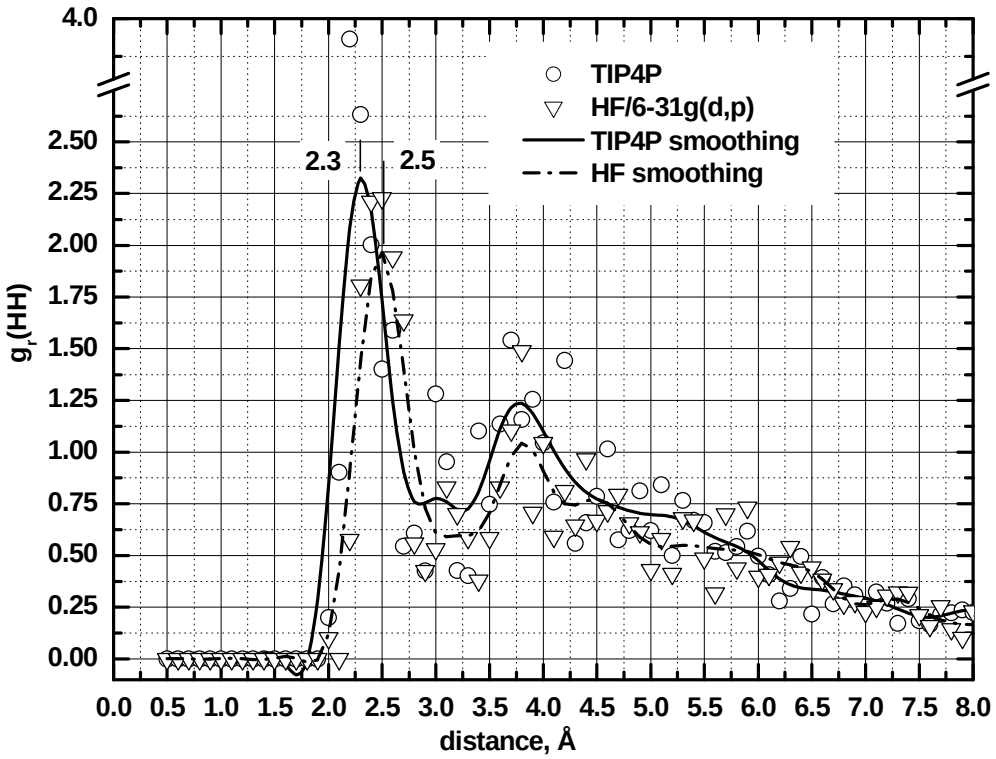
TIP4P
HF/6-31g(d,p)
TIP4P smoothing
HF smoothing
2.3
2.5
g(HH)
distance, Å

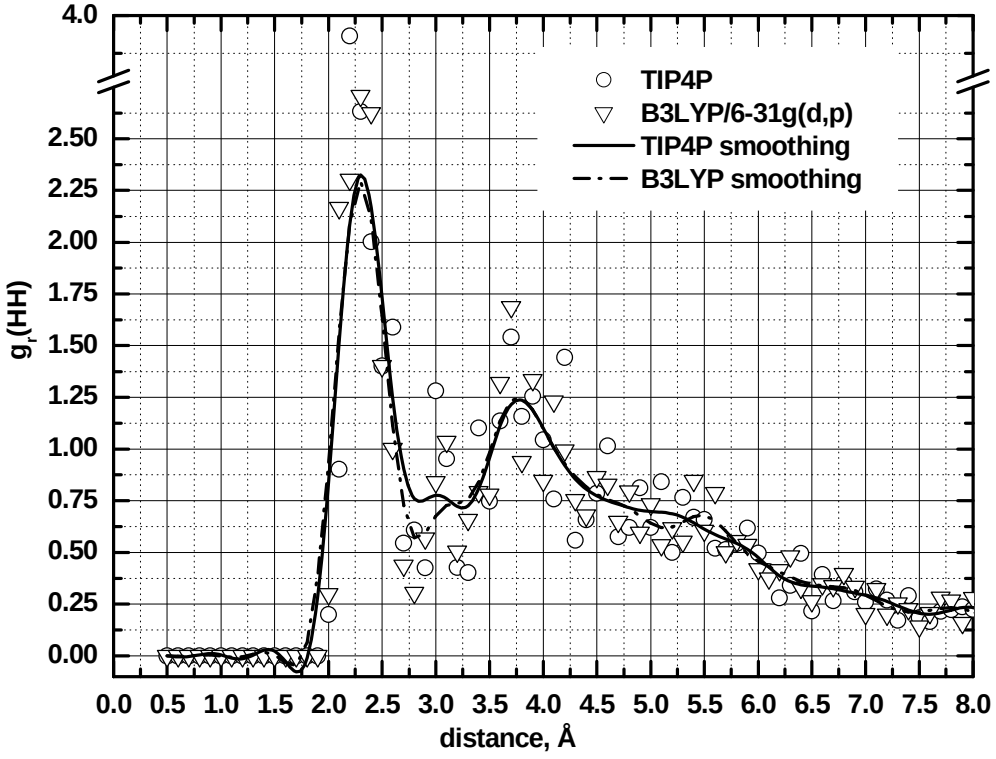
TIP4P
B3LYP/6-31g(d,p)
TIP4P smoothing
B3LYP smoothing
g(HH)
distance, Å

Figure 4.1.6. Distribution functions of the 26-mer cluster at *HF*, *B3LYP* and *TIP4P* levels. The quantum-mechanical calculations have been done with the *6-31g(d,p)* basis set. The lines represent the FFT smoothing of the computed points.

The quantum mechanical treatment of the 26-mer cluster reveals the configurations including a bifurcated hydrogen bond and those with a triple *HB* acceptor, which suggests that these hydrogen bonds are a part of the structure at the given local minimum. Furthermore, simulated IR spectra exhibit unusual features associated with the vibrational stretch mode of the water molecule acting as an acceptor of three *HB*'s and as a single donor. The combined induction effect of three acceptors causes an additional polarization of the OH bond coordinated against the oxygen atom of the fourth neighbour, which consequently becomes more ionic than those in more regular tetrahedral configurations. At the same time, the hydrogen bond itself becomes more covalent. Consequently, it could be expected that the corresponding stretching mode exhibits a red-shift and a strong intensity gain. Indeed, such an unusually red-shifted and very strong stretching mode at 2649 cm^{-1} associated with the stretching vibration of the triple *HB* acceptor can be clearly seen on the *B3LYP* spectra displayed in Figure 4.1.7(a). The main OH stretching mode is located above 3000 cm^{-1} while the non-coordinated OH_{free} groups exhibit a separate peak at 3870 cm^{-1}, which is close to the ν_3 mode of isolated water molecule found at 3913 cm^{-1}. Moreover, there is a separate OH stretch band at 3797 cm^{-1}, which is associated with the long *HB*'s in the cluster. The experimental spectral studies by Devlin and coworkers and computational studies by Buch and coworkers reveal the presence of such bands in the IR spectra of ice nanoparticles, which are associated with the disrupted *HB*'s [14, 15 and references therein]. Therefore, there is an apparent connection between the structure of cluster and its IR spectra, calculated in the present static model (in the sense that the system Hamiltonian is uncoupled from the bath) within a harmonic approximation. The *HF* IR spectrum of this cluster shown in Figure 4.1.7(b) demonstrates a noticeable distinction from that at *B3LYP*, which reveals no distinct IR features for the triple acceptor mode and for the free OH groups. Such a spectral difference is associated with the stronger structural compression and higher bond polarization observed with *B3LYP* in comparison with the *HF* calculations (see Figure 4.1.6). The more the structure is

compressed, the more the OH bond becomes ionic (at the expense of its covalence) while the *HB*'s gain the covalence. The spectral consequence of these structural changes is a red shift and strengthening of the stretching modes. The frequencies of the OH_{free} stretch band for the *HF* cluster are found near 4223 cm^{-1} whereas the frequency of ν_3 mode for an isolated H_2O is 4265 cm^{-1}, i.e. both frequencies are very close, which suggests similar bonding properties of the OH groups in isolated water molecules and on the surface of water media. In real water spectra, the ν_3 vibration is located at 3756 cm^{-1} [16], whereas the same vibration for dangling bonds on ice films is located at 3698 cm^{-1} (present studies), i.e. there is only a minor medium-induced shift for this mode, which therefore appears to be isolated and decoupled from the vibrational pool in the water media. Overall, the simulated IR spectra reproduce the main spectral features observed for condensed water: a broad and intense stretching band at higher frequencies, a weaker bending band at the intermediate frequency range and the libration and translational modes at the low frequency range (Figure 4.1.7).

(a) *B3LYP/6-31g(d,p)*, 26-mer H_2O cluster

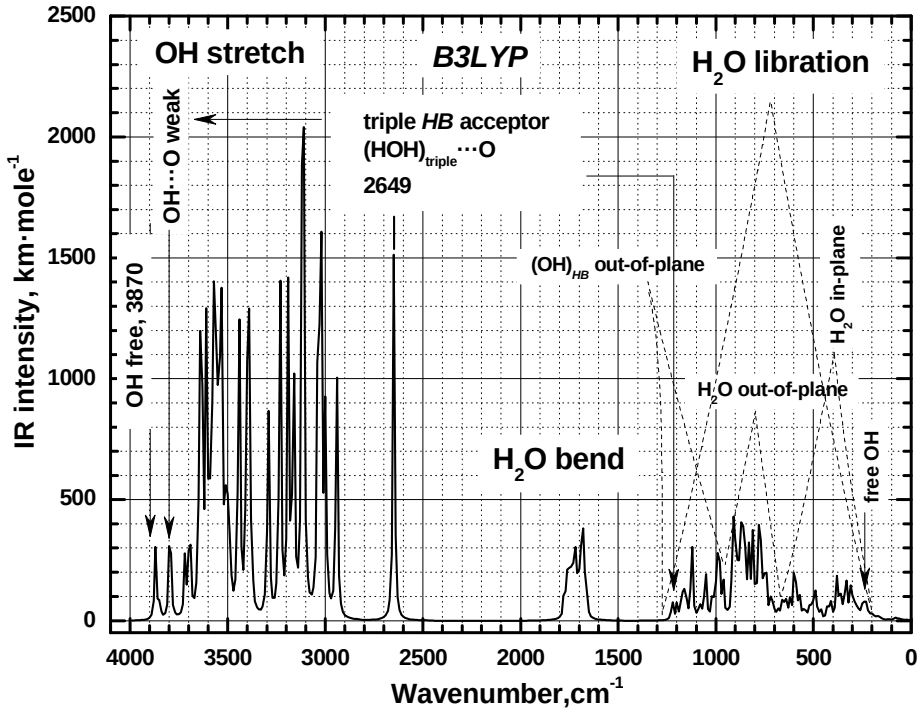

(b) *HF/6-31g(d,p)*, 26-mer H_2O cluster

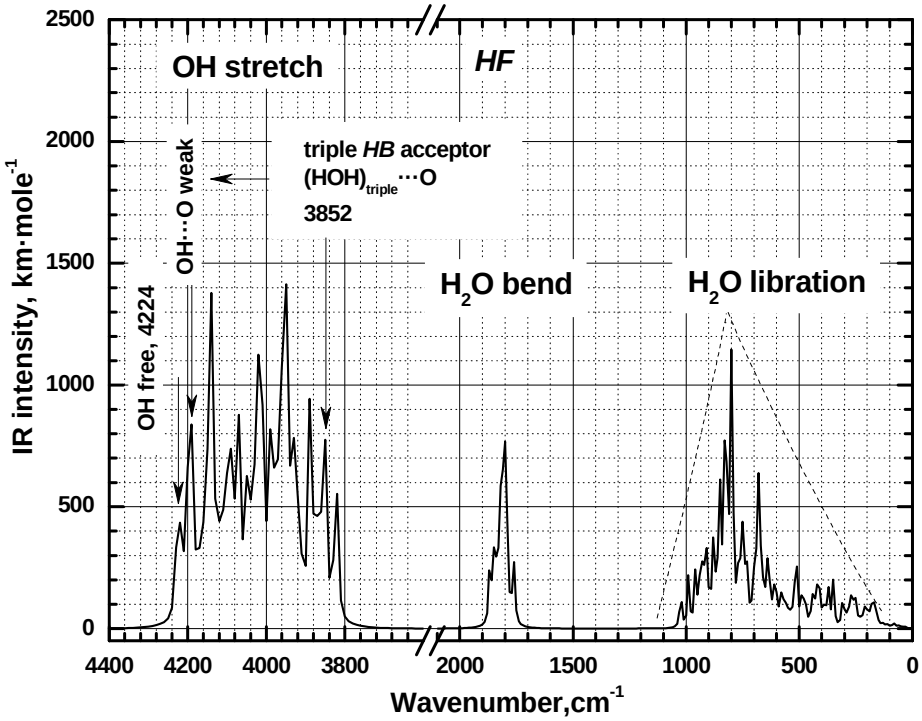

Figure 4.1.7. Calculated IR spectra for the 26-mer cluster at (a) *B3LYP* and (b) *HF* levels. The calculations were performed with the *6-31g(d,p)* basis set. The frequency lines are given with the Lorentzian profile generated by the Gaussian View program. The spectral feature at 2649 cm^{-1} in (a) corresponds to O−H···O unit with O···O and O−H distances at 2.565 Å and 1.031 Å, respectively.

The OH_{free} (non-hydrogen-bonded OH group in water molecule) spectral features at frequencies around 3690 cm^{-1} (3870 cm^{-1} and 4224 cm^{-1} in Figure 4.1.7 (a) and (b) respectively) are observed in spectra of any condensed water madia as a relatively sharp band on the high-frequency side of the main stretching band. In contrast, distinct peaks that are associated with the highly *HB*-coordinated water molecules with short hydrogen bonds (like a 2649 cm^{-1}-peak of the triple *HB* acceptor in Figure 4.1.7 (a)) are rarely observed. A unique example is given in the experimental studies of Buck and Huisken [17] using the infrared laser depletion spectroscopy of size-selected water clusters and explored in a theoretical work by Sadlej *et al.* [18]. The IR depletion spectra of selected water clusters are reproduced in Figure 4.1.8 and show that the heptamer spectrum includes two distinct lines at ~2950 cm^{-1}, which are attributed by Sadlej *et al.* to the stretching modes of two donor-acceptor-acceptor (*daa* ≡ da^2) hydrogen bonded water molecules with short hydrogen bonds in two the most stable isomers. It should be stressed that the appearance of short *HB*'s is a direct result of cooperative enhancement of the intermolecular *HB* interaction in a chain of hydrogen bonded molecules. (The question of cooperativity of the hydrogen bonds is discussed in the section 4.2.2.) It is instructive to compare the histograms of nearest neighbour O···O distances between pairs of hydrogen bonded molecules obtained by Sadlej *et al.* [18] for 6-9 molecule water clusters at the *MP2/DZP1* level (reproduced in Figure 4.1.9) with those obtained in the present work for the hexamer prizm at *B3LYP/LBS* and *SBS*, and 26-mer structures described above at the *HF/6-31g(d,p)*, *B3LYP/6-31g(d,p)* and *TIP4P* levels.

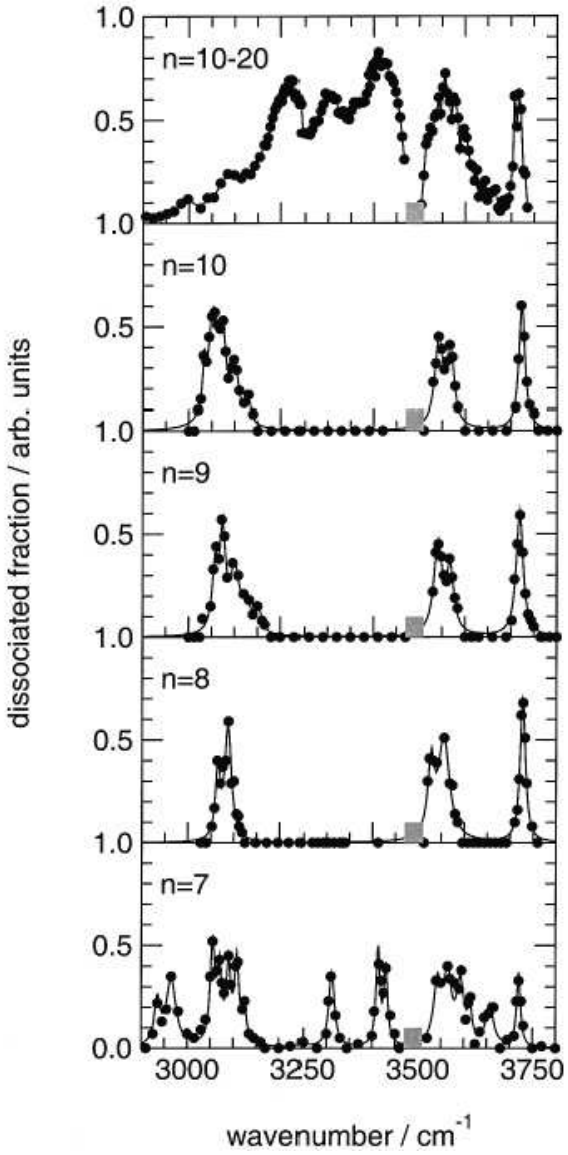

Figure 4.1.8. The experimental IR depletion spectra of size-selected water clusters with 7, 8, 9, 10 molecules and mixture of 10-20-mer clusters. Reproduced from Buck and Huisken [17].

The upper curve represents the spectrum of cluster distribution with sizes from 10 to 20 molecules. Those on the two top rows correspond to the prism isomer used by Sadlej *et al.* [18].

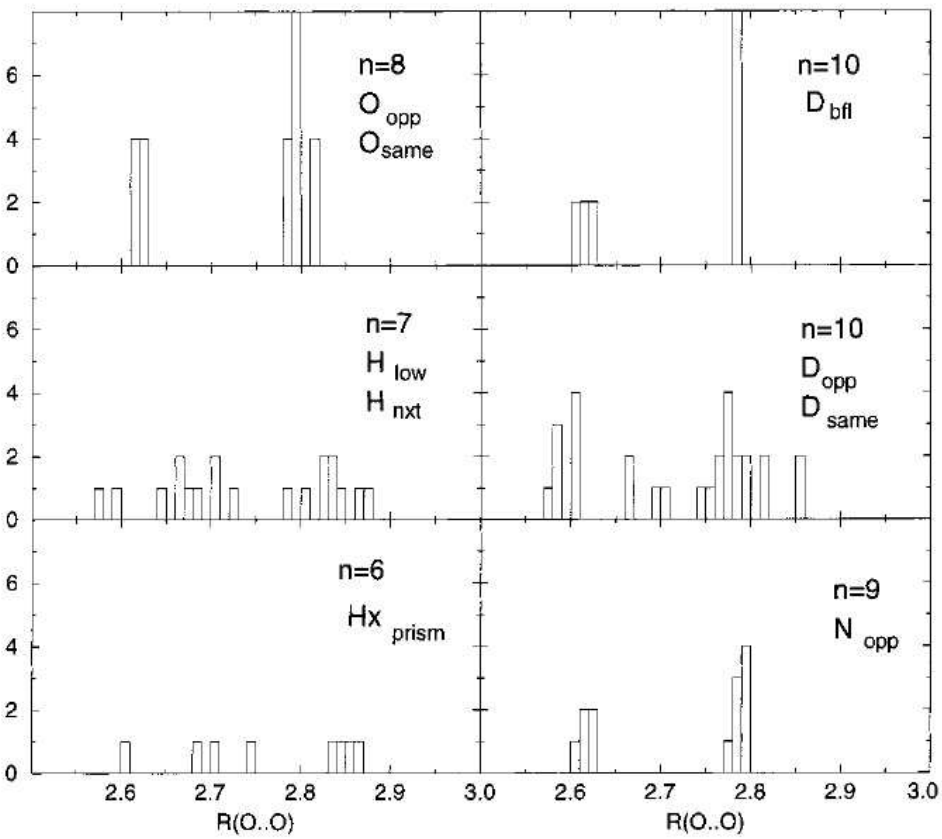

Figure 4.1.9. The histogram of nearest neighbor O···O distances between pairs of hydrogen bonded molecules in the 6-10-mer clusters at *MP2* level. Reproduced from Sadlej et al. [18]. The number of water molecules in the clusters is labelled by n, whereas particular configurations of clusters are labelled by subscripts to capital letters Hx, H, O, D, N standing for hexamer, heptamer, octamer, decamer and nonamer, respectively. The structures of these clusters are shown in Fig. 1, 2, and 3 in the Sadlej *et al.* report [18].

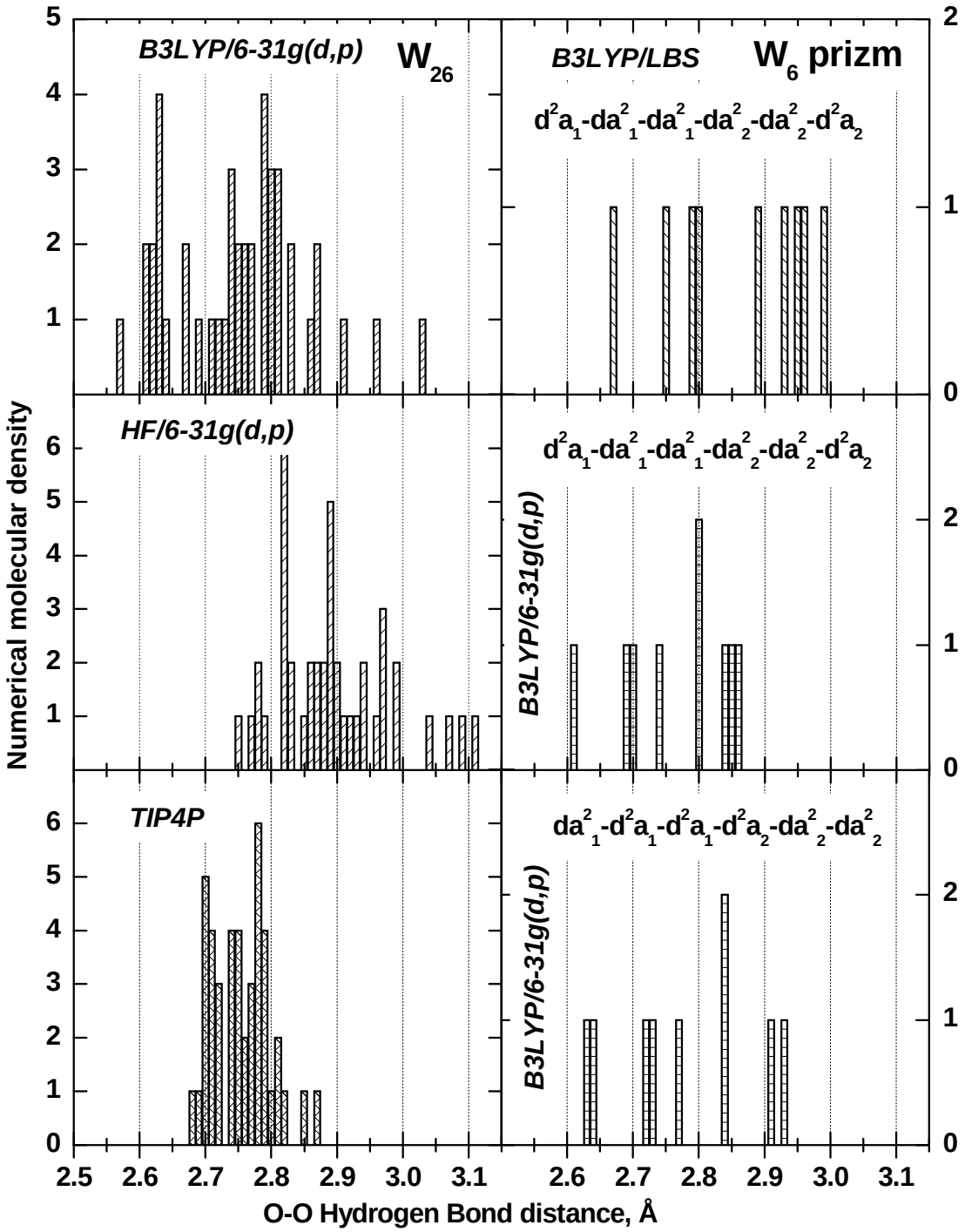

Figure 4.1.10. The histogram of nearest neighbour O···O distances between pairs of hydrogen bonded molecules in the 26-mer and 6-mer water clusters at *HF*, *B3LYP* and *TIP4P* levels.

The left column includes the histograms for a 26-mer cluster (W_{26}) at different levels of theory, whereas the right column includes the histograms for two different W_6 prism isomers calculated at *B3LYP* level with *6311++g(3df, 3pd)* and *631g(d,p)* basis sets. For the prizm structures, the following notations are used for labelling the hydrogen bond configurations of each water molecule: d and a stands for a donor and for an acceptor of hydrogen bond; the superscript indicates the number of donor or acceptor valences used by a molecule in question; the subscript enumerates either of the two tri-molecule ring in the prizm structure.

Sadlej *et al.* [18] clearly demonstrates that the O−H stretch peaks below 3000 cm^{-1} in the heptamer correspond to short hydrogen bonds with O^{*}−H···O^{*} (superscript stars indicate the atoms in question) distances slightly below 2.6 Å. This is in qualitative agreement with the present calculations on a 26-mer cluster. Sadlej's calculations show also that there are short *HB*'s in nonamer and decamer, but for these two clusters the range below 3000 cm^{-1} has been inaccessible to the experiment and, therefore, the computational results cannot be compared with the experiment below 3000 cm^{-1}. However, the experimental depletion spectrum for a set of clusters with the size range from 10 to 20 on upper panel of Figure 4.1.8 shows no distinct bands below 3000 cm^{-1}, while the presence of short *HB*'s in this set of water clusters could be expected on rather general basis. In this sense, the low frequency band experimentally observed at 2950 cm^{-1} for the heptamer is a unique experimental indication of the presence of short *HB*'s in isolated water clusters. The present author is not aware of any other experimental data which shows the distinct spectral features corresponding to the short hydrogen bonds in isolated water clusters or in continuous water media. Meanwhile, a few preliminary observations can be made on the basis of Figure 4.1.9 and Figure 4.1.10 regarding the distribution of the O···O hydrogen bonded pairs in different clusters and the effects of basis set quality and computational methods on these distributions. The *HF* calculations with a small *6-31g(d,p)* basis set apparently overestimate the intermolecular distances in comparison with the *B3LYP* results, which is in accord with the OO pair distribution functions shown in Figure 4.1.6. The *TIP4P* cluster exhibits the narrowest distribution in comparison with both *HF* and *B3LYP*. For a prism isomer, the small basis set *6-31g(d,p)* (referred as *SBS*, an abbreviation of small basis set) leads to shorter intermolecular distances in comparison with

much more flexible large basis set *6-311++g(3df, 3pd)* (referred as *LBS*, an abbreviation of large basis set) basis set at *B3LYP* level, which is in accord with significant overestimation of the *HB* pairwise energy with *SBS*. A comparison of the intermolecular distance distribution for the same prism isomer calculated at *MP2*/*DZ1P* (*(9s5p1d)/[3s2p1d]* for O, *(4s1p)/[2s1p]* for H and the single set of *p* polarization functions for H and O) by Sadlej *et al.* [18] and in the present studies at the *B3LYP/LBS* level shows that the cluster is significantly more contracted in the former case. This contraction apparently results in the appearance of short *HB*'s with stretching modes below 3000 cm^{-1}, whereas a utilization of more flexible basis sets could lead to relaxed structures with no spectral bands below 3000 cm^{-1}.

Therefore, there are grounds for speculating that employment of "restricted" basis sets could cause an additional contraction of water clusters in comparison with the real structures in the same configuration. One obvious consequence of such an event would be the underestimation of frequencies of the O−H stretching modes. In principle, this hypothesis could be verified or discarded by systematic studies of the influence of the basis set quality on the properties of water clusters but the present author is not aware of any such an attempt for cluster sizes beyond six molecules.

An examination of the symmetric hydrogen bond with a double-minimum potential reveals that the polarizability of such a hydrogen bond is two orders of magnitude larger than that of their separated counterparts, which leads to a continuous IR absorption (Zundel continuum) as shown by Zundel in an example of $H_5O_2^+$ cation at the *SCF* level [19]. In the case of non-symmetric *HB*'s with discernible covalence, the polarizability is still high enough to cause a very extensive broadening. Instead of strong peaks generated by static models (such as quantum mechanical harmonic computations), very broad features are expected at frequencies below 3000 cm^{-1} for the protonated systems with highly polarizable hydrogen bonds [19 b]. The characteristic feature of protonated water clusters is the presence of strong and short hydrogen bonds, which in the static model correspond to intense peaks red shifted with respect to the main OH stretching band. A particular structure of the protonated 26-mer is shown in Figure 4.1.11, which clearly reveals the presence of H_3O^+ cation coordinated in the water matrix (Eigen structure). The O−H distances between covalently bonded three hydrogen atoms and the central oxygen atom are close to each other (this justifies the

definition of H_3O^+ structural unit), yet it is evident that the O−H distances are modulated by the hydrogen bonding with neighboring water molecules. The shorter the HB the longer the corresponding O−H bond, which is in accord with a general view on the properties of hydrogen bond network. The three *HB*'s donated by the H_3O^+ cation belong to a category of short and strong hydrogen bonds whereas the accepted *HB* is evidently very long and weak, which again is in accord with general properties of hydrogen bond.

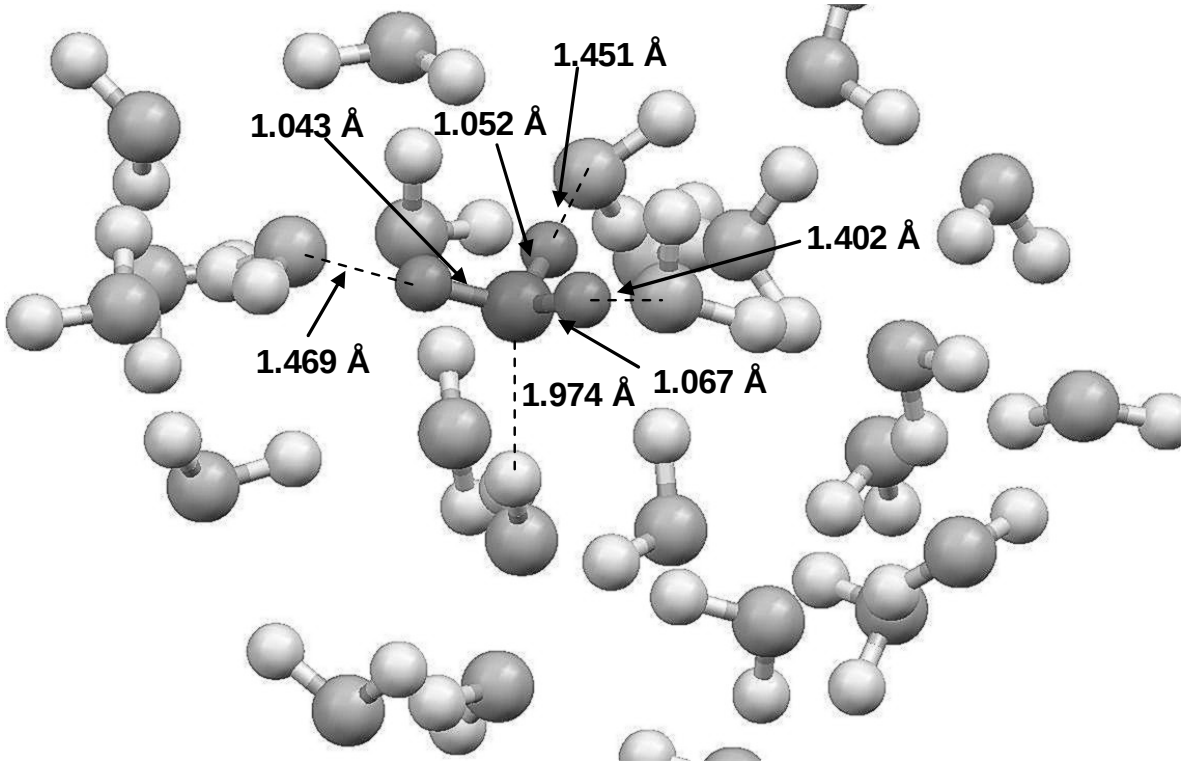

Figure 4.1.11. The structure of protonated O center in the 26-mer cation at *B3LYP* level. The calculations were performed with *6-31g(d,p)* basis set. The H_3O^+ fragment coordinated with the water matrix is clearly visible.

Figure 4.1.12 compares the IR spectra for a protonated 26-mer cluster ($H_{53}O_{26}^+$) obtained at the *B3LYP/SBS* level and that of a neutral cluster of the same configuration. Similar to Figure 4.1.7 (a), there are very intense red-shifted absorption bands associated with the stretching modes of $[O-H]^+\cdots O$ strong bonds around a protonated oxygen center. The hydrogen bond environment around the hydronium cation H_3O^+ within 26-molecule cluster is

evidently not symmetric within the framework of a static picture and, therefore, a continuous absorption is not expected.

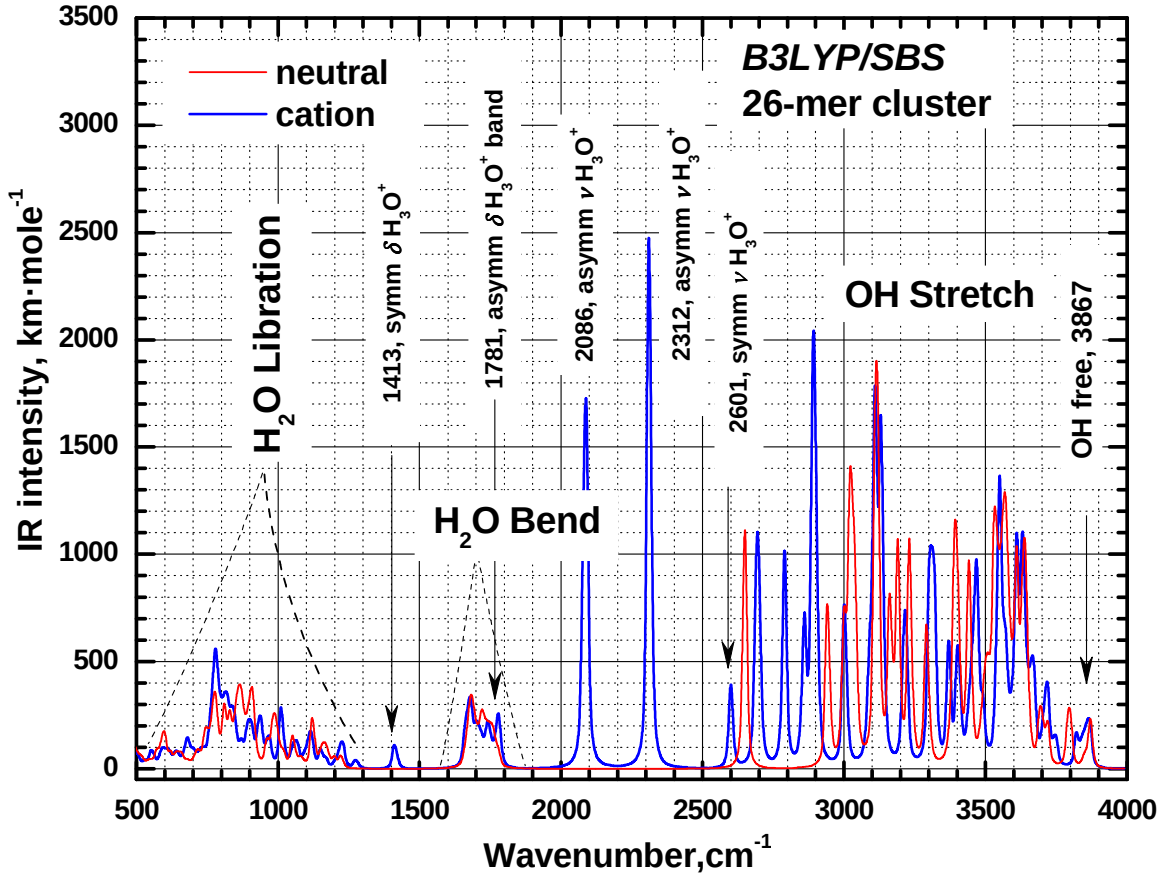

Figure 4.1.12. Calculated IR spectra of the 26-mer $H_{53}O_{26}^{+}$ cation (blue curve) and neutral 26-mer $H_{52}O_{26}$ (red curve) clusters optimized at *B3LYP/6-31g(d,p)* level.
The frequency lines are given with Lorentzian profile of 10 cm^{-1} width generated by the Gaussian View program. The spectral features at 2601 cm^{-1}, 2312 cm^{-1} and 2086 cm^{-1} correspond to the stretching modes of H_3O^{+} coordinated with the rest of cluster. The length of O−H bonds around the protonated oxygen atom are 1.0425 Å, 1.0522 Å, 1.0674 Å and 1.974 Å, whereas the corresponding O···O distances are 2.5118 Å, 2.5029 Å, 2.468 Å and 2.884 Å, respectively.

In contrast to the static picture, in the real system the vibrational modes are coupled to each other through anharmonic forces, which could lead to a potentially strong coupling

between the stretching modes and librational or/and translational motion. Depending on the magnitude of anharmonic forces, such a coupling could result in a considerable broadening of the stretching modes. Moreover, the cluster interacts with its environment, which affects the vibrational motion in the cluster. If this or another *HB* in the cluster is highly polarizable then it will be especially sensitive to the electrical fluctuations in the environment, which results in a further broadening of the vibrational band [19 (a)]. It is instructive to compare the differential harmonic spectra between a 26-mer cation and a neutral cluster with the differential spectra between 1.0 M solutions of HCl and HBr acids and pure water reported by Kim *et al.* [20] and reproduced in Figure 4.1.13 (b). Kim *et al.* [20] have performed instantaneous normal mode analysis for a variety of different configurations comprising the hydronium cation and its immediate neighbourhood and attributed, in particular, a positive differential peak at 2700-2950 cm^{-1} to a linear combination of the O−H stretch normal modes of symmetrically hydrated hydronium cation (see Figure 4.1.11). The present normal mode analysis of 26-molecule cation and neutral clusters strongly disagrees with Kim's assignment. The presence of the positive peak at 2700-2950 cm^{-1} in Figure 4.1.13 is due to the contraction of the cluster caused by protonation and does not include the stretching vibration of hydronium cation *per se*. The positive peak includes the stretching vibrations of short hydrogen bonds, the number of which has been increased by the protonation. This conclusion is supported by histograms of the distribution of distances between the hydrogen-bonded water molecules in neutral and protonated clusters. Indeed, as evident from Figure 4.1.14 (upper panel) for the neutral cluster, the number of pairs with O···O distances below 2.6 Å is *1*, whereas the same value for the protonated cluster rises to *8*. Among these *8* pairs only *3* are due to the hydronium cation while the remaining *5* pairs correspond to short *HB*'s among those water molecules, which are not bound directly to the hydronium species. On the other hand, the region between 2.6 and 2.65 Å (especially bins 2.62 and 2.63) is denser in the neutral cluster, which presumably is responsible for the negative peak at 3100-3200 cm^{-1}observed in the experimental IR spectra of dilute acids by Kim *et al.* [20]. The shape of the main OH stretch band directly depends on the distribution of the O···O *HB* distances (the *HB* angles are also important but as a less significant factor). The same statement remains valid for the spectra of diluted protonated aqueous systems including the immediate region below 3000 cm^{-1}. As seen

in Figure 4.1.13 (a) the main spectral contribution of the stretching modes of hydronium cation is located below 2500 cm^{-1}. The comparison with experimental spectra of acidic solution indicates that in this region there are no distinct spectral bands, but there is a clear signature of continuous absorption. The interpretation of positive peak at 2700-2950 cm^{-1} by Kim *et al.* [20] is primarily restricted to the vibrations of hydronium or diaquohydrogen cations. The vibrational analysis is limited to only *6* water molecules, which are surrounding the hydronium cation and are not interconnected. Any computational observation of a collective response of the water structure on the protonation is, therefore, precluded at the very beginning. The OH stretching band clearly shows the collective response on protonation rather than a localized reaction. It should be noted that the appearance of a positive peak at 2700-2950 cm^{-1}, if the latter is indeed produced by the collective response of the water media, is a manifestation of a significant increase in the transition dipole moments of corresponding vibrations upon the contraction of *HB* contacts. Without such an enhancement in the oscillator strength, this positive peak most likely would not be observed because the density of those low-frequency oscillators is relatively small in diluted systems (see Figure 4.1.14). The positive peak at 1700 -1800 cm^{-1} corresponds most likely to the asymmetric deformational band of hydronium cation in the water matrix.

Let us further illustrate Zundel's findings with a relevant example of the hydrochloric acid on ice, selected spectra of which collected in the present studies are shown in Figure 4.1.15. A practically continuum absorption beginning from the low-frequency side of the main OH stretching mode at 3389 cm^{-1} is evidently observed along with the peaks attributed to the vibrations of protonated water species and that of $Cl^{-}\cdots H{-}Cl$ species at 2115 cm^{-1}. These IR-RAS spectra are in good accord with the transmission IR spectra from the ice particles covered with HCl reported recently by Devlin *et al.* [21] and presented for the comparison in Figure 4.1.16. As temperature increases the continuum absorbance strengthens, which is interpreted by Devlin *et al.* [19] following the Zundel's approach as a signature of $D_5O_2^+$ ionic species formed by the dissociation of adsorbed DCl molecules. Accordingly, a Zundel profile observed in the IR-RAS spectra of HCl/noncrystalline H_2O in Figure 4.1.15 could be attributed as well to the $H_5O_2^+$ or, perhaps, to the protonated water clusters of different sizes (most likely larger than diaquohydrogen cation).

(a) *B3LYP/SBS* differential IR spectra between those of W_{26} and its cation

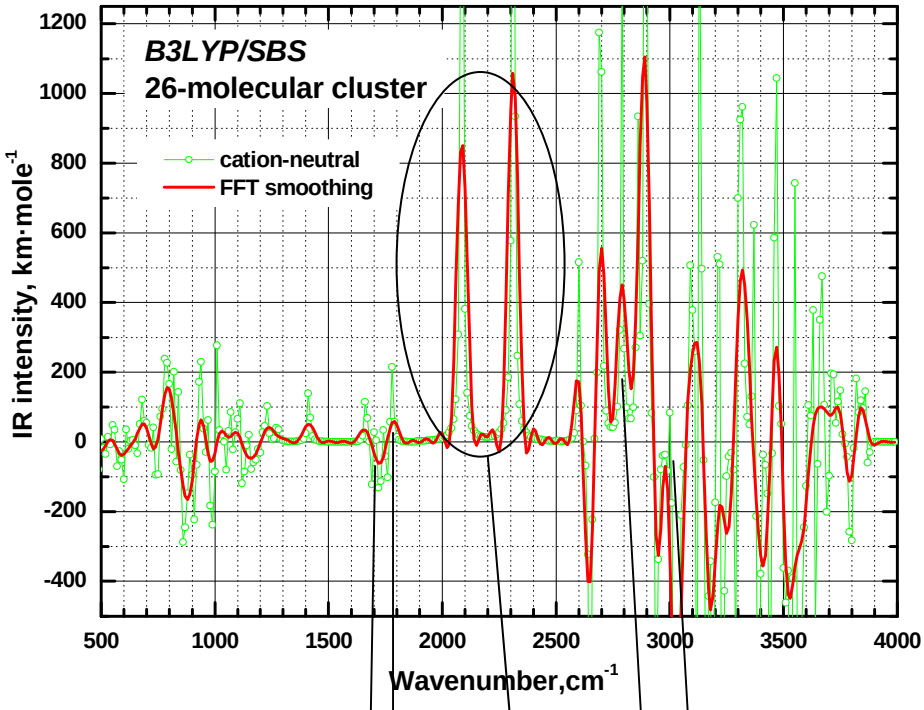

(b) Experimental differential spectra between 1.0 M of HCL, HBr and water [20]

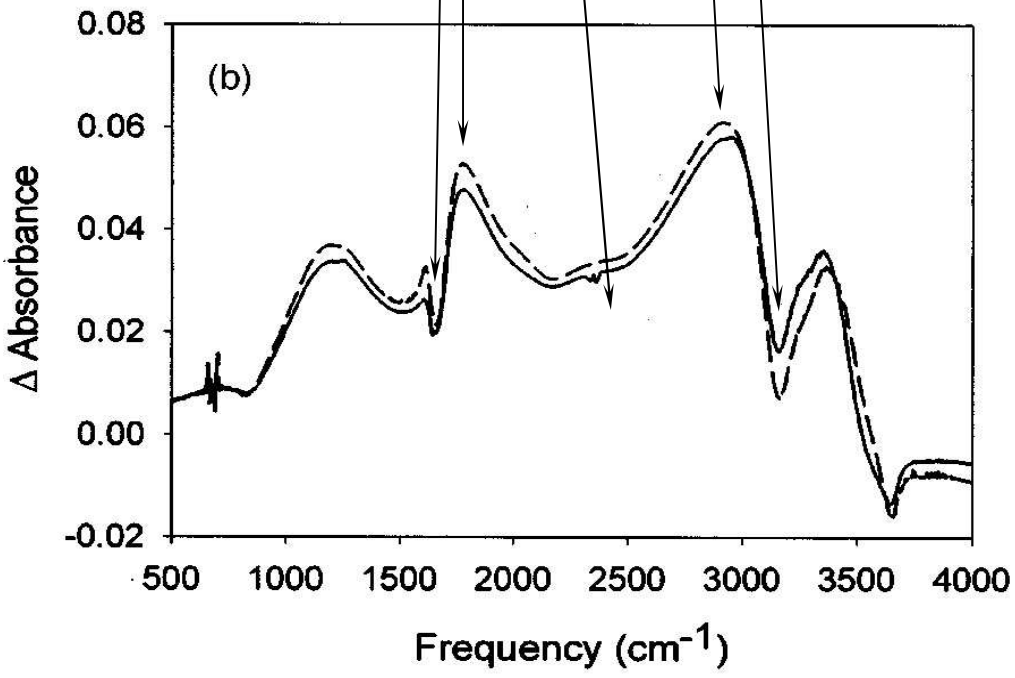

Figure 4.1.13. Computed and experimental (reproduced from Kim *et al.* [20]) differential IR

spectra between protonated 26-mer $H_{53}O_{26}^{+}$ and pristine, $H_{52}O_{26}$, water clusters.

The difference (a) between computed harmonic IR spectra of cation and neutral 26-mer clusters at *B3LYP/SBS*, i.e. $IR_{Calc}(H_{53}O_{26}^{+}) - IR_{Calc}(H_{52}O_{26})$ and (b) between the experimental IR absorption spectra of 1.0 MHCl (solid line), HBr (dashed line) and pristine water, i.e. $IR_{exp}(HX_{aq}) - IR(H_2O)$. Reproduced from Kim *et al.* [20].

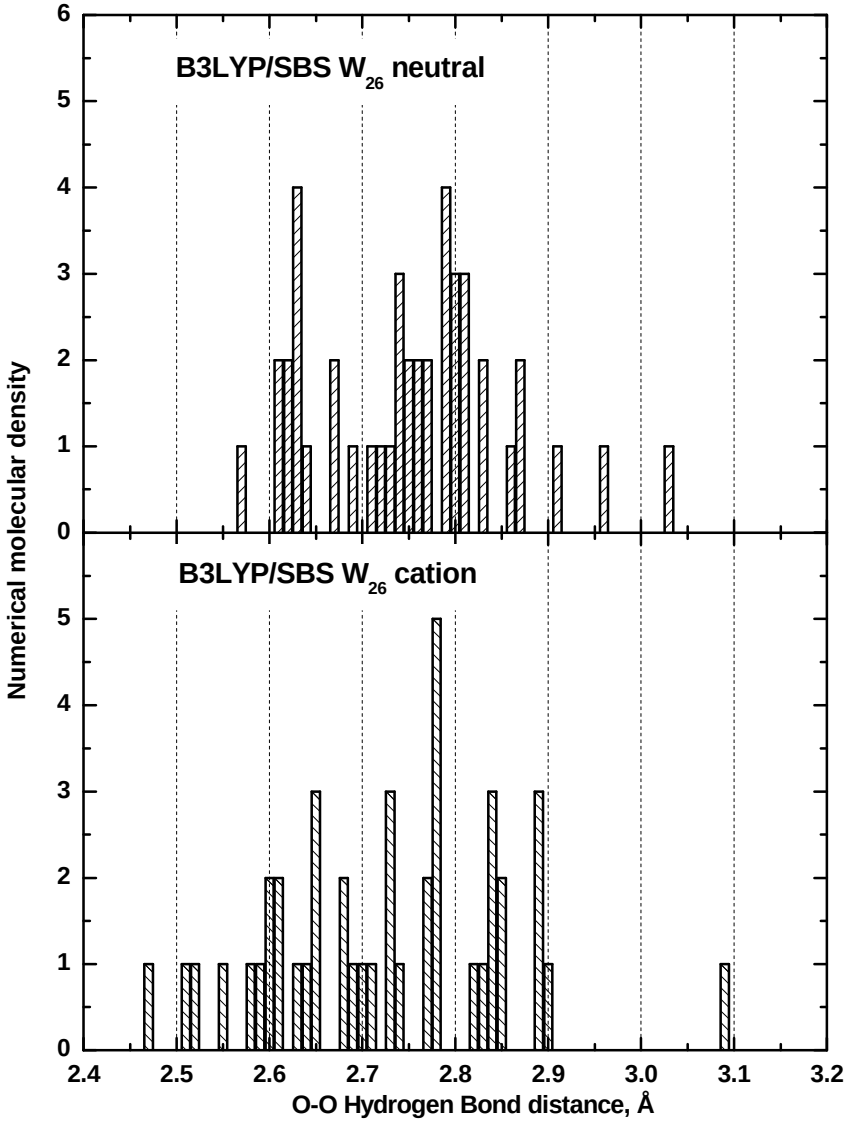

Figure 4.1.14. The histograms of nearest neighbour O···O distances between pairs of hydrogen bonded water molecules for 26-mer neutral and protonated cluster at *B3LYP/6-31g(d,p)*.

Evidently, the IR absorption by the stretching modes of ionic water clusters leads to very broad features, which could be difficult for the spectral detecting especially when the concentration of such species is small. However, in those cases when the protonated water species or short *HB*'s are abundant, a Zundel's profile should be discernible.

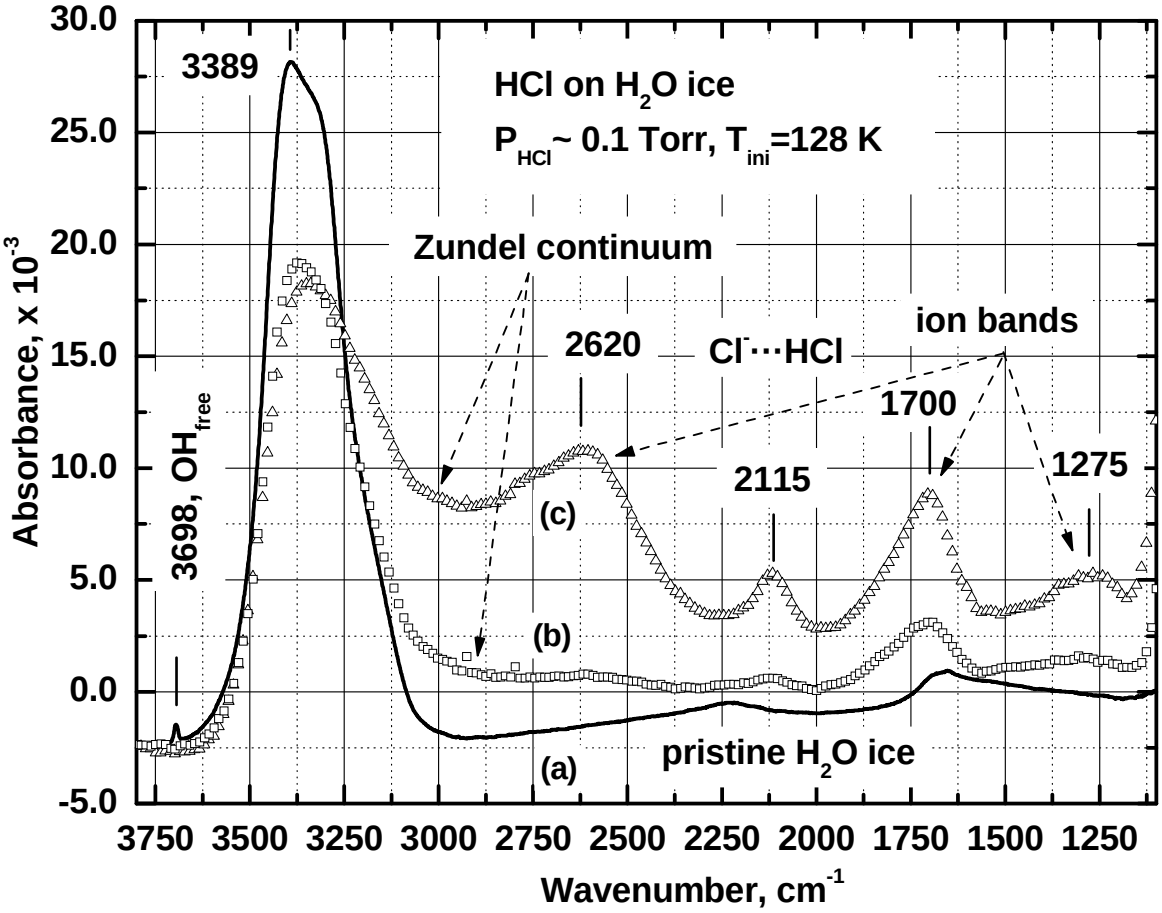

Figure 4.1.15. FTIR-RAS spectra of the HCl-ice films in comparison with that of pristine ice. (a) pristine thin ice film vapour deposited at 128 K (solid line); (b) 3.5 min into the exposure to ~ $1 \cdot 10^{-2}$ Torr of HCl (squares); (c) 4 min into pumping after the 5-minutes exposure to ~ $1 \cdot 10^{-2}$ Torr of HCl (triangles). In should be noted that in order to show clearly a Zundel continuum the spectra were artificially shifted on the ordinate scale to coincide at approximately 3750 cm^{-1}.

(a)

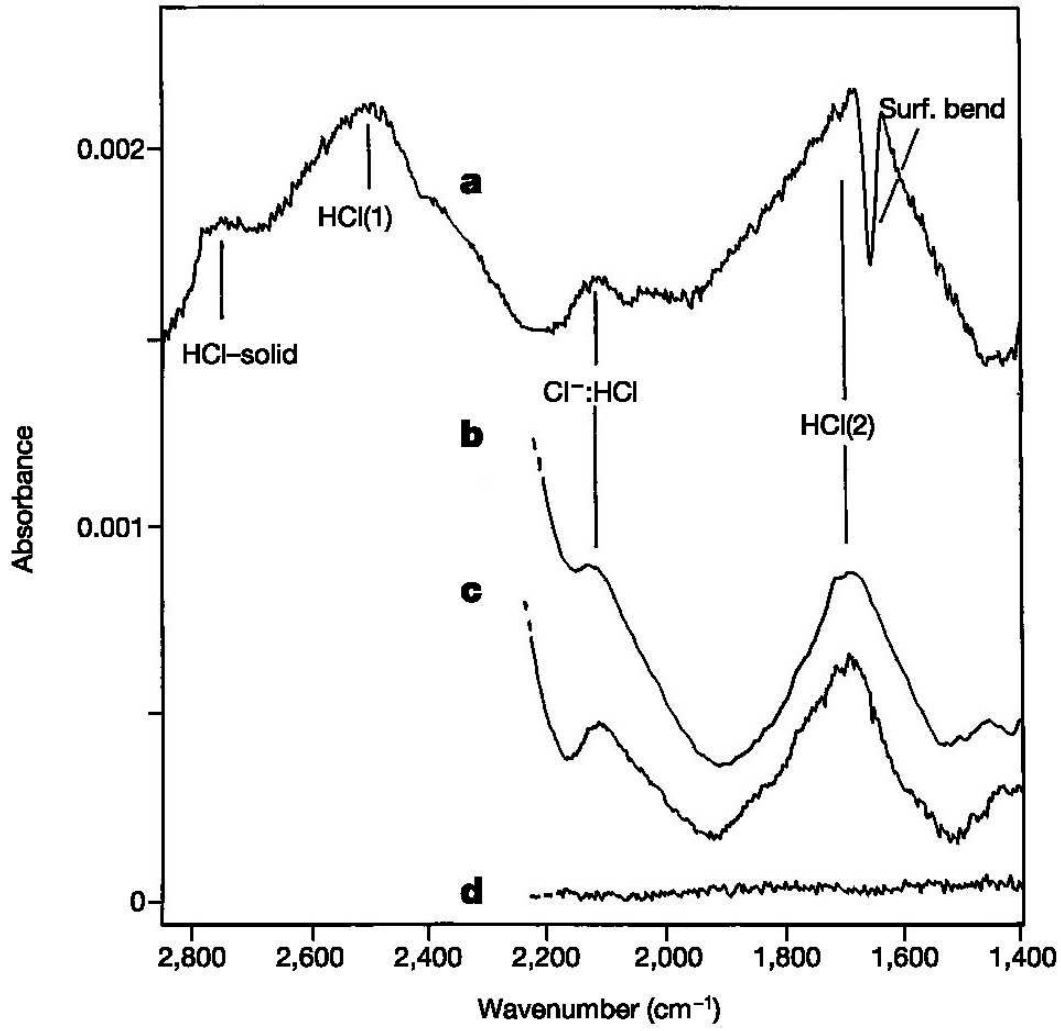
Surf. bend
0.002
a
HCl(1)
HCl–solid
Cl⁻:HCl
HCl(2)
b
Absorbance
0.001
c
d
0
2,800
2,600
2,400
2,200
2,000
1,800
1,600
1,400
Wavenumber (cm⁻¹)

(b)

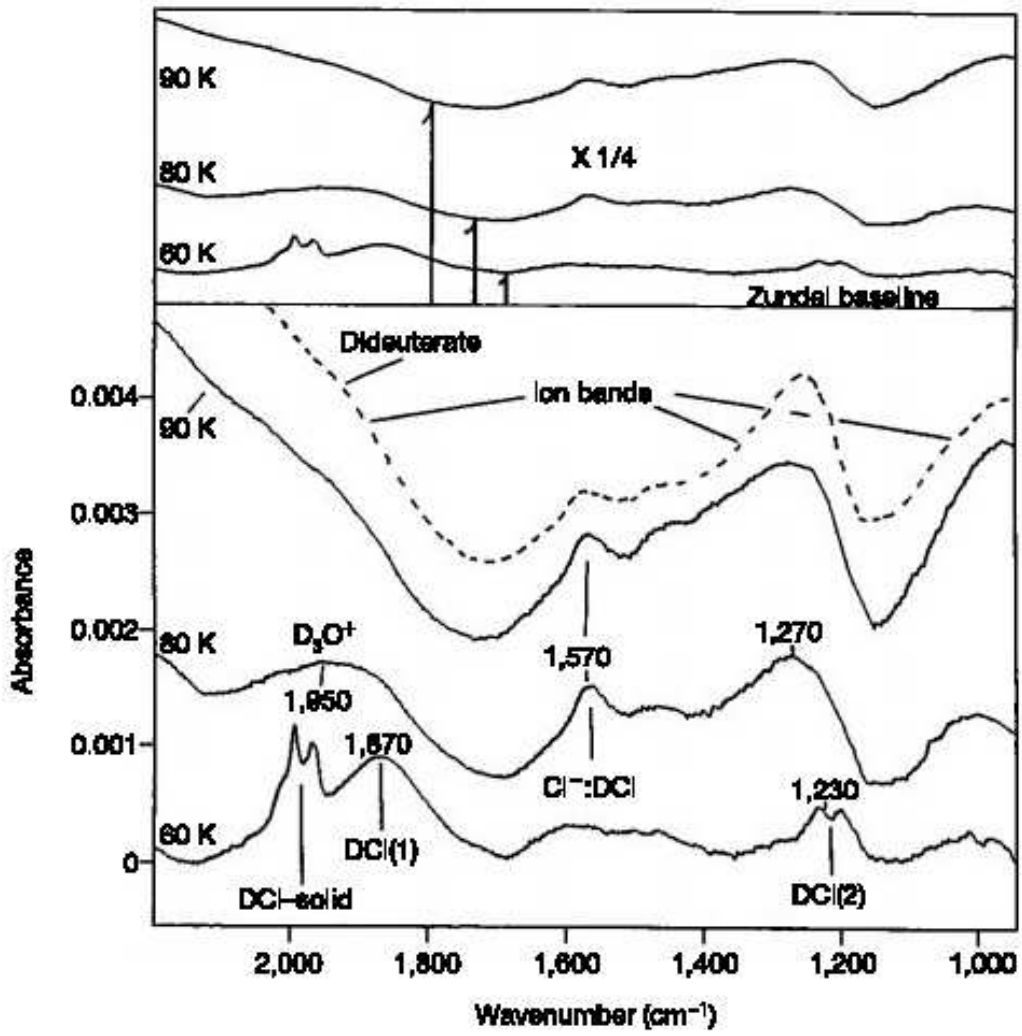

Figure 4.1.16. Differential IR spectra of H/DCL on ice. Reproduced from Devlin et al. [21]. The upper panel shows the FTIR difference spectra of HCl on ice particles at 50 K and ~ 15% coverage: (a) HCl on H_2O, (b) and (c) HCl on D_2O (d) background spectrum. The lower panel shows the FTIR difference spectra for the DCl adsorbate on D_2O at ~ 30% coverage for different temperatures.

The present quantum mechanical calculations of $H_5O_2^+$ cation show extremely large red shift in the $O\cdots H^+\cdots O$ stretch mode with respect to that in water dimer due to 20-fold decrease in the force constant of corresponding vibrations. The following Figure 4.1.17 and

Figure 4.1.18 represent these computational results.

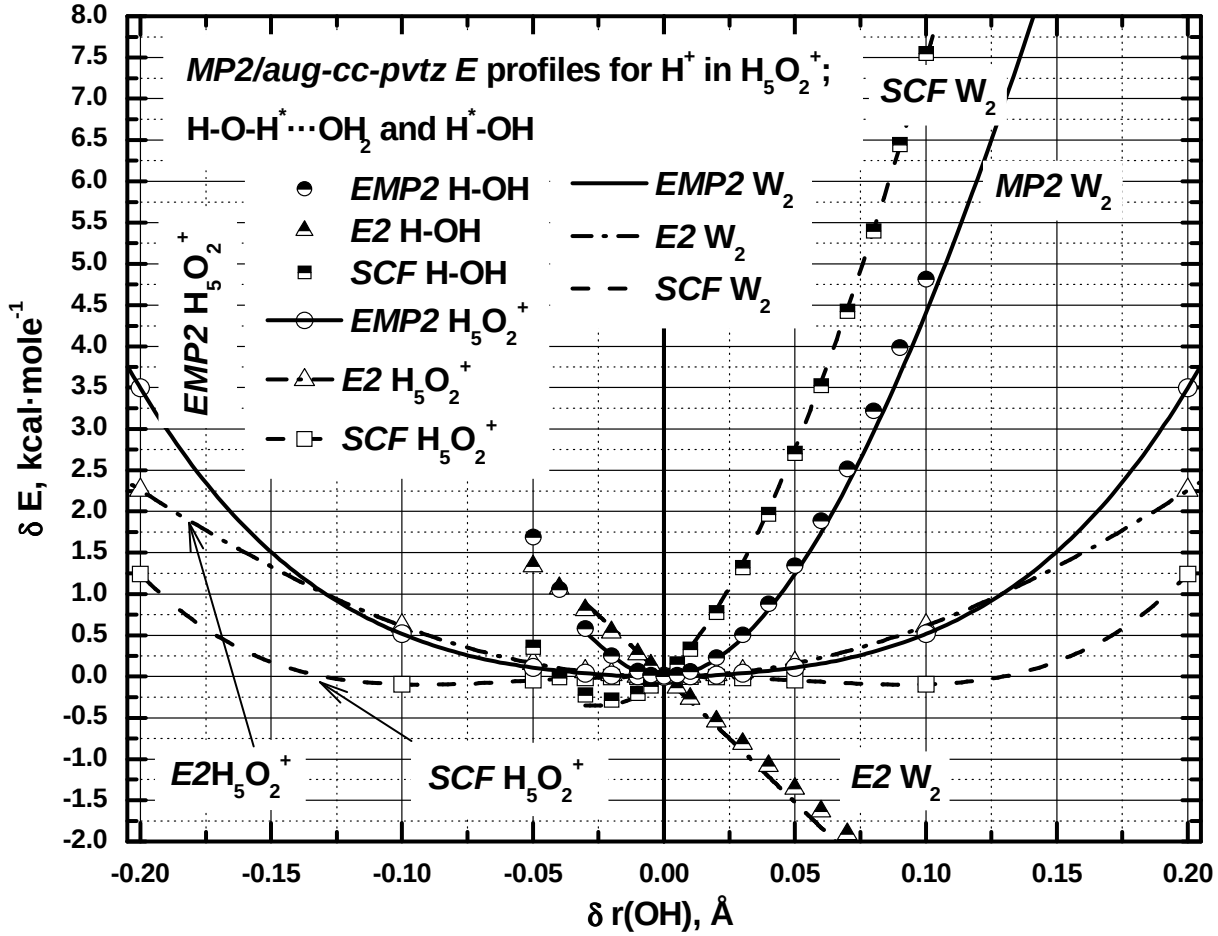

Figure 4.1.17. Potential energy profiles along the O−H coordinate for H_2O, $(H_2O)_2$ and $H_5O_2^+$. The calculations were performed on *MP2/aug-cc-pvtz* level. In the case of $H_5O_2^+$ all interatomic distances were fixed except two angular variables for H^+ whereas in the cases of water monomer and dimer all variables were allowed to vary with exception of a dihedral angle preserving the C_s symmetry in the dimer case. *SCF*, *E2*, and *EMP2* designate the *HF* energy, the second order MP correction to the *HF* energy and the sum of these values, i.e. the total MP2 energy, respectively.

(a) Harmonic spectrum of H_3O^+

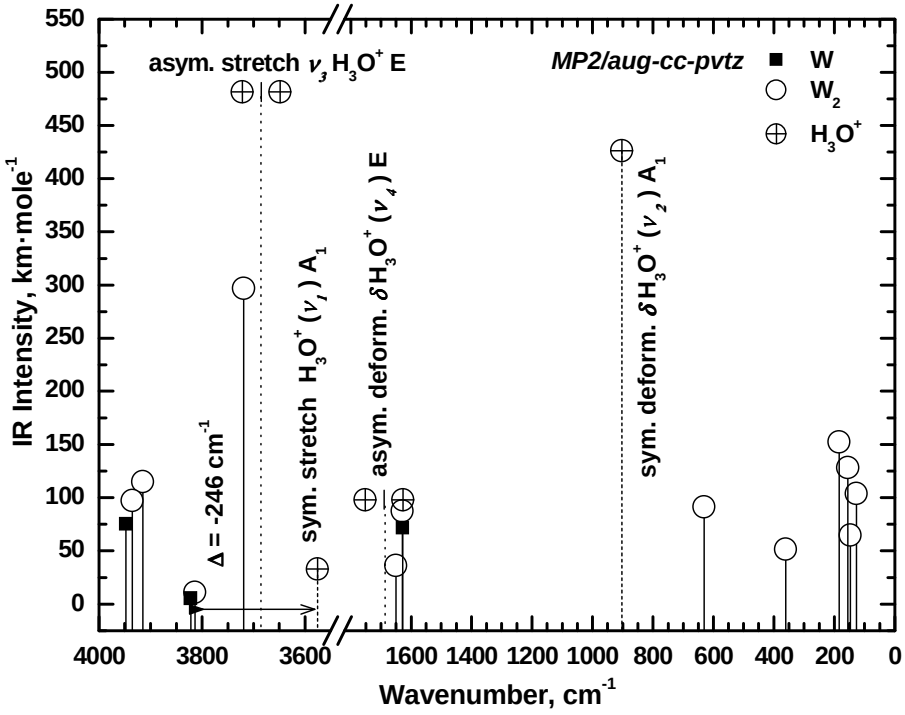

(b) Harmonic spectrum of $H_5O_2^+$

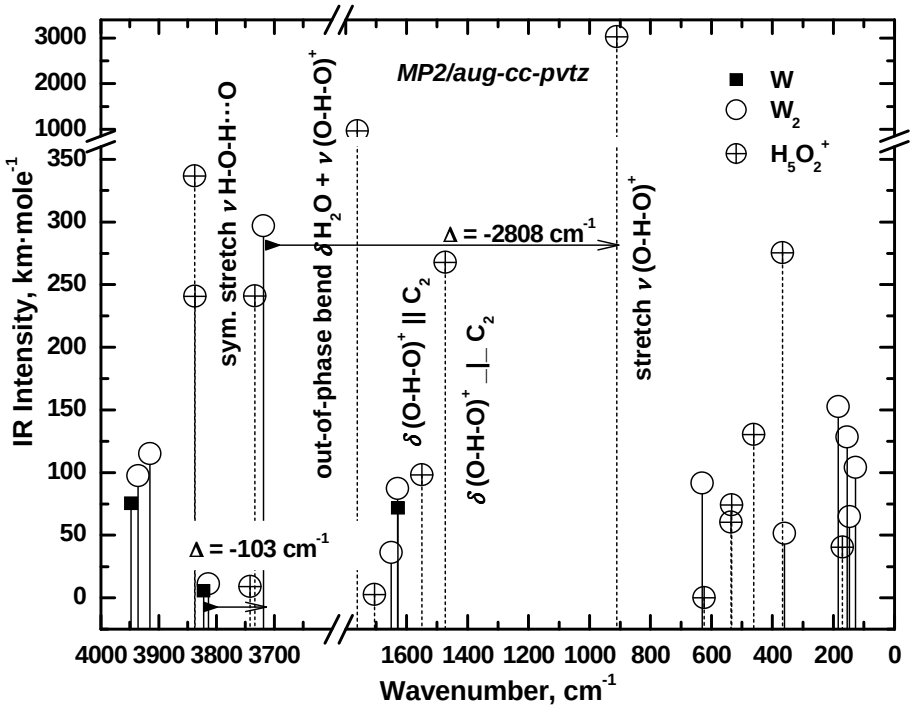

Figure 4.1.18. Comparison of the harmonic frequencies of water monomer and dimer with that

of (a) H_3O^+ and (b) $H_5O_2^+$ cations at the *MP2/aug-cc-pvtz* level.

Table 4.1.1. IR frequencies of single water molecule, dimer and water in condense state. The intensity of calculated IR bands are given in [10^3 m·mole^{-1}]. *MI*, D, M, G.P. stands for matrix isolation IR experiments, dimer, monomer, and gas phase.

Method	Gas Phase Monomer	Gas Phase Dimer	Δ(D.-M.)	Liquid State	Δ(L-G.P.)	Solid State, I_h	Δ(I_h-G.P.)
			v_3				
Exper.	3755.79			3490 {62.7} 3280 {54.5}	−266 −377	*v_3 (LO)+ v_1 out-of-phase* 3380	−376
						v_3 (TO) 3220	−536
Exper., *MI*	3725.7 {s}	3714.4_a {m} 3697.7_d {m}	−11.3 −28.0				
MP2-aug	3947.71 {75}	3935.28_a {97} 3915.15_d {115}	−12.4 −32.6				
B3LYP/LBS	3912.56 {59}	3903.03_a {82} 3885.66_d {81}	−9.5 −26.9				
B3LYP/SBS	3912.85 {20}			*D.B.* 3872-3852 3847 *tri-HB*			
				3795 (3.03, 2.96 Å) 3718-3692 (2.87-2.90 Å)			
				3650-3632 (*v_3*) 3615-3607			
			v_1				
Exper.	3656.65			3490 {62.7} 3280 {54.5}	−266 −377	*v_1 in-phase* 3150	−507
Exper., *MI*	3632.5 {m}	3625.6_a {w} 3547.5_d {m} *HB*	−6.9 −85.0				
MP2-aug	3821.88 {6}	3813.93_a { 11} 3718.74_d {297} *HB*	−8.0 −103.1				
B3LYP/LBS	3813.48 {5}	3807.02_a {10} 3695.96_d {329} *HB*	−6.5 −117.5				
B3LYP/SBS	3799.61 {2}						
			v_2				
Exper.	1594.59			1645 {20.8}	+50	$(2v_{Lib}+v_2)$ 1560	
Exper., *MI*	1596.9 {s}	1618.1_d {w} *HB* 1600.3_a {w}	+21.2 +0.4				
MP2-aug	1628.37 {72}	1650.27_d {36} *HB* 1629.31_a {87}	+21.9 +0.9				
B3LYP/LBS	1626.54 {72}	1648.42_d {39} *HB* 1626.92_a {90}	+21.9 −0.4				
B3LYP/SBS	1665.26 {70}						

The formation of symmetric *HB* in the diaquohydrogen cation with O···O and O···H distances at 2.39055 Å and 1.19716 Å, (the < O···H···O is 173.57 °) respectively, causes a dramatic change in the potential well for the hydrogen atom vibration with respect to those in H_2O and $(H_2O)_2$, as evident from Figure 4.1.17. At the *MP2* level, a potential well for the diaquohydrogen cation is extremely flat as the result of two equivalent bonds between the central hydrogen atom and the two oxygen atoms, the covalence of which is about half of the "normal" O−H bond. This potential profile originates from the merging of two potential minima where the hydrogen atom is allocated closer to that or another oxygen atom. Indeed, on the *SCF* level there is a small barrier that separates these two minima, whereas the barrier is evidently absent on the *MP2* level. As a consequence of the C_2 symmetry, the potential curve is nearly harmonical in the vicinity of the minimum. However, due to the relaxed shape of the potential the central hydrogen atom participates in an oscillation with the amplitude much larger than that of a typical covalent O−H bond. At relatively large distances from a minimum the potential profile for $H_5O_2^+$ deviates discernibly from the harmonical shape, which not only affects the numerical value of the frequency of the vibrational band but also provides the path for vibrational perturbation due to anharmonic coupling. The "normal" O−H potential profiles for water monomer and dimer are much sharper and appear to be very similar to each other, which leads to only minor frequency shift for the O−H stretch modes upon the dimer formation. Indeed, in the matrix isolation experiments [22] the following shifts are observed: ν_3 of H_2O monomer: 3756 $cm^{-1}_{G.P.}$ → 3725.7 cm^{-1}_{MI} (G.P. and *MI* stands for gasphase and matrix isolated species); ν_1 of H_2O monomer: 3657 $cm^{-1}_{G.P.}$ → 3632.5 cm^{-1}_{MI}; ν_3 of $(H_2O)_2$ *HB*-donor in *MI* is at 3697.7 cm^{-1}, i.e. there is a 28 cm^{-1}-shift from the monomer value; ν_1 $(H_2O)_2$ *HB*-donor in *MI* is at 3547.5 cm^{-1}, i.e. there is a 85 cm^{-1}-shift from corresponding *MI* monomer value. The frequency shift for the ν_1 mode upon dimer formation computed at the *MP2/aug-cc-pvtz* level amounts to 103 cm^{-1}, which is in a reasonable agreement with the experiments. These frequency shifts indicate that the potential well of the $(O-H)_{donor}$ bond is only slightly perturbed by the dimer formation. The bond order parameters and atomic charges show discernible changes upon a dimer formation. For instance, the Mayer and Wiberg bond order parameters change from 0.96 and 0.74 for O−H in H_2O to 0.87 and 0.7, respectively, for $(O-H)_{donor}$ in the dimer, which represent 9% and 5 % decrease in the covalence of this bond.

On the other hand, the Mulliken charge on the hydrogen atom involved in the *HB* bonding changes from +0.21 to +0.29, which together with decrease in the covalence indicates that the O−H bond becomes more ionic and less covalent being involved in the hydrogen bonding. This trend in the bond character is in accord with the frequency red shift and intensity rise exhibited by stretching modes of H_2O upon dimerization. The protonation of H_2O modifies the character O−H bonds in a similar way, they become more ionic and less covalent as represented by Mayer (*M.B.*) and Wiberg (*W.B.*) bond indexes (0.86 in H_3O^+ vs. 0.96 in H_2O (10% decrease in *M.B.*) and 0.63 in H_3O^+ vs. 0.74 in H_2O (15% decrease in *W.B.*)), which causes red frequency shifts and significant intensification of the stretching modes (the frequency shift is −246 cm^{-1} for the ν_1). The oxonium cation exhibits also a new spectral feature at ~900 cm^{-1}, which corresponds to a symmetric bending mode ν_2 (A_1). It appears that protonation of water molecules perturbs the O−H bonds in a stronger fashion in comparison with that upon a dimer formation. The bond indexes tentatively provide a quantitative description of these perturbation events although they are not absolute. The diaquohydrogen cation exhibits apparently unique spectral characteristics because of the vibrational profile corresponding to the symmetric hydrogen bond with a single minimum on the *MP2* level. Within the framework of static approach (when there are no external perturbations applied and an isolated harmonic system is at minimum) the stretching band of O←H→O^+ vibration appears at ~ 900 cm^{-1}, i.e. is red-shifted from a standard location by ~2800 cm^{-1} as evident from Figure 4.1.18. Such a low vibrational frequency is again associated with a very broad profile of the potential well at its minimum as shown in Figure 4.1.17. The bond indexes for the ordinary O−H bonds and those in a symmetric *HB* minimum are significantly different: *M.B.*s are 0.96 for H_2O, 0.86 for H_3O^+, 0.87 for *HB* in the dimer, 0.99 for OH_{free} in the dimer, 0.53 for the symmetric *HB* in $H_5O_2^+$, 0.93 for the rest of O−H bonds in $H_5O_2^+$; *W.B.*s are 0.74 for H_2O, 0.63 for H_3O^+, 0.70 for *HB* in the dimer, 0.74 for OH_{free} in the dimer, 0.34 for the symmetric *HB* in $H_5O_2^+$, and 0.67 for the rest of O−H bonds in $H_5O_2^+$. The Mayer bond index decreases by 45 % upon formation of the symmetric *HB* in comparison with the water monomer, while the Wiberg index decreases by 54 %. In other words, the covalence of a symmetric *HB* is about half of that for typical O−H bond. The excess of positive electric charge is not concentrated on the central hydrogen atom but is redistributed on two

neighbouring oxygen atoms as it is indicated by the Mulliken and *NBO* charges in accord with donor-acceptor interaction of H_3O^+ and OH_2.

It should be noted that in the original work on $H_5O_2^+$, Zundel and coworkers [19] have used the *HF* method, which produces a double-minimum potential well, whereas in the present work the potential profile for isolated diaquohydrogen cation shows only a single minimum at the *MP2* level (see Figure 4.1.17). The quantum motion of a proton depends on the potential profile and in this respect the presence of barrier plays a fundamental role in the vibrational properties of this system. The dynamical properties of the symmetric *HB* in a diaquohydrogen cation with a double minimum are unique, which lead to the Zundel profile described above. The underlying reasons for appearance of continuous absorption reside in the extremely high polarizability of the double-minimum *HB.* In the presence of small energy barrier separating the two proton minima, the solution of the vibrational Schrödinger equation for proton motion comprises, in particular, two lowest levels energetically close to each other, which are described by symmetric and asymmetric wave functions:

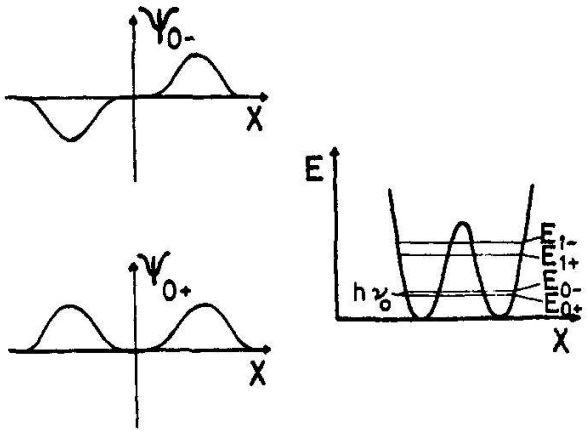

Figure 4.1.19. Double minimum proton potential and wave functions Ψ_{0+} and Ψ_{0-} of the two lowest states of Zundel ion. Reproduced from Janoshek *et al.* [19 a].

An external perturbation, imposed on the present system, causes a mixing of these two states, which, in turn, leads to the localization of a proton into the left or right minima, i.e. the system becomes polarized by a small perturbation. The central proton bears a discernible positive charge and its localization will cause positive charging of that or another water counterpart. In other word, the $H_5O_2^+$ can be represented by the following polarized resonance

structures: $\{H_3O^+\cdots OH_2 \leftrightarrow H_2O\cdots H_3O^+\}$, each of which shows asymmetric charge distribution. The high polarizability is responsible for the following consequences: (i) the symmetric *HB* is sensitive to the electric perturbations imposed by the neighbouring molecules; (ii) these bonds strongly affect each other, i.e. the resonance energy transfer is highly probable in these systems; and (iii) the stretching O−H···O mode is strongly coupled with the low-frequency intermolecular vibrations. It should be noted again that in a truly symmetric single minimum well the vibrational potential is nearly harmonical and therefore this oscillation will be uncoupled from the rest of system. Although the *MP2* calculations show that the isolated diaquohydrogen cation exhibits a single potential well minimum, the relative oscillation of water molecules or external force field could lead to the double-minimum potential and to continuous absorption. In the case of symmetric *HB* with a single minimum such as in the $(FH\cdots F)^-$ anions, the polarizability is still large, which causes extreme broadening of the stretching mode in the KHF_2 crystal [23]. On the other hand, stretching and deformational bands become much sharper and less intense upon dilution in a potassium chloride crystal matrix as shown by Salthouse and Waddington [23], who attributed this phenomenon to the electrostatic coupling between oscillators. In the case of KHF_2 crystal the broadening is caused by the resonance energy transfer between strongly coupled oscillators, while the dilution of the system break this relaxation path. It appears that the coupling of the $(FH\cdots F)^-$ stretching mode with the low-frequency vibrations is not effective in this case [23].

The IR spectra of diaquohydrogen cation measured by the infrared multiphoton photodissociation technique by Asmis *et al.* [24] are reproduced below in Figure 4.1.20 together with the Lorentzian profiles of the harmonic spectra obtained in the present work and shown in Figure 4.1.18. Let us first compare the experimental results of Asmis *et al.* [24] with the harmonic picture. There is an apparent agreement between the experimental and calculated spectra with respect to the two experimental bands *b* at 921 cm^{-1} and *e* at 1741 cm^{-1}, which appear to correspond to the *v* $(O\cdots H\cdots O)^+$ stretch at 911 cm^{-1} /*MP2* or 920 cm^{-1}/*B3LYP* and out-of-phase bending mode of the two water molecule at 1761 cm^{-1}/*MP2* or 1742 cm^{-1}/*B3LYP*, respectively.

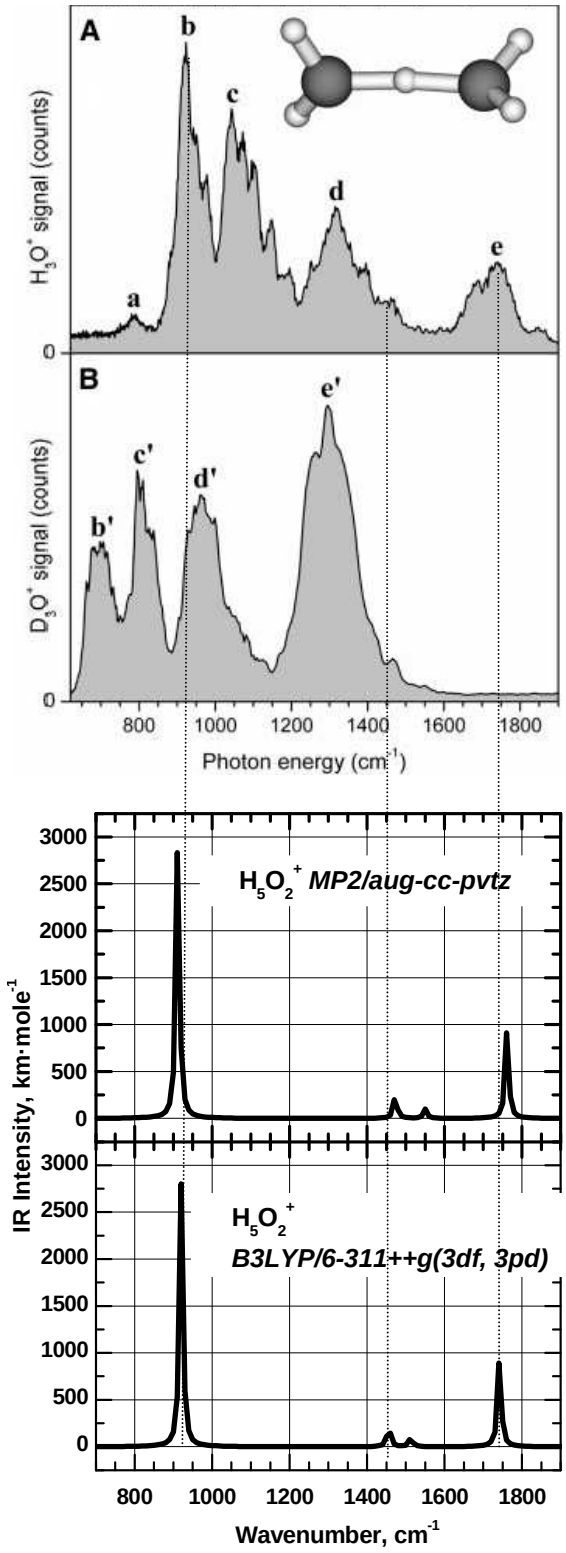

Figure 4.1.20. Experimental [24] and computed IR spectra of $H_5O_2^+$. The experimental *d*

band could include both bending modes of $\delta\,(O\cdots H\cdots O)^{+}$ unit, whereas there is no fundamental band at the *MP2* or *B3LYP* level that would correspond to the experimentally observed *c* band.

The IR spectra of acidic aqueous systems are characterized by the Zundel profile. For instance, the transmission IR spectra from H_2SO_4/H_2O films at different temperatures by Middelbrook *et al.* [25] show continuous absorption associated with the protonated water species. Caused by the changes of concentration of an acid and temperature, the evolution of the OH stretch mode and all spectral profile at lower frequencies of the water/sulphuric acid hydrogen-bond network is closely associated with Zundel absorption and, therefore, reflects the ionic vibrational dynamics in the protonated medium. Ritzhaupt and Devlin [26] have reported the spectra of different crystalline and amorphous hydrates of HNO_3 and amorphous hydrates of HCl , where the frequency region below 3600 cm^{-1} is determined by Zundel profiles, which could again be due to protonated water clusters with short *HB*'s. Even for a monohydrate of HNO_3, i.e. $HNO_3{\cdot}H_2O$, a signature of nearly continuous absorption below the main OH stretch band at 3300-3200 cm^{-1} is observed [26].

The ability of quantum mechanical calculations of providing detailed information about the normal modes, intensities and the spectral features associated with the structure of the given local minimum is evident. In resuming this part, let us suggest that a quantum mechanical analysis of small water clusters is useful for disclosing the underlying structure of the water network, which often remains hidden in the course of molecular dynamic simulations. The analysis of a water structure at a local minimum, when the atoms are located at their equilibrium positions, is indeed important for discosing unique structural and spectral features in the hydrogen bond network. The quantum mechanical calculations of clusters provide the frequencies and intensities of the available vibrational bands and, therefore, allow a direct comparison with the experimental spectral data. Such an analysis not only provides the structural details of a particular local minimum but with a proper design of cluster configurations it can also bring a valuable information about the structure and properties of infinite aperiodic water media. Suggested by Chaplin, such an algorithm for designing the initial configurations of water clusters that could simulate the inifiniter water media has been discussed in Chapter 2.

4.2 Theoretical Background of the *Ab Initio* and Density Functional Theory Calculations

4.2.1 Computational Methods and Supermolecular Approach to the Multimolecular Complexes

The computational methods of the formation (binding) energy are classified among supermolecular and perturbation techniques. Within a supermolecular technique the formation or binding energy is defined as: $E_{formation} = E_{AB} - (E_A + E_B)$, where E_{AB}, E_A and E_B designate the ground-state energies of subsystems A, B and united complex AB. For typical interactions between close-shell subsystems, E_{form} is a factor of four to seven orders of magnitude smaller than the total energy of either the united complex or the subsystems [28]. Moreover, the deviation of the calculated energy of the ground states for A, B and AB from their real values could be much larger than the formation energy E_{form}. Therefore, a reliable approximation for the formation energy can be obtained only if a fortunate cancellation of large numerical errors happens. Such a cancellation has been observed for the following computational methods: Möller-Plesset perturbation theory and the density functional theory [28]. However, there is no rigorous proof that the cancellation of errors should occur. A computational method should obey the following necessary conditions in order to provide reliable approximations for the formation energy: (i) size extensiveness and size consistence [27]; (ii) an adequate description of the electron correlation; and (iii) the electronic energies of subsystems A and B should be calculated with the basis set of the entire complex AB [38]. The alternative to the supermolecular approach is a perturbation technique, which computes the formation energy directly as a sum of physically distinct terms: $E_{form} = E^1_{pol} + E^1_{exch} + E^2_{pol} + E^2_{exch} + ...$, where E^1_{pol} is a classical electrostatic interaction, E^2_{pol} is a sum of the classical induction and quantum mechanical dispersion energies and E^1_{exch} and E^2_{exch} terms represent exchange contributions [28].

The computational results presented in the *ab initio* part of the present studies are based on the supermolecular approach, upon which a united complex *ABC…Z* is considered to consist of the interacting subsystems *A, B, C, …Z*. The total energy of the united complex *ABC…Z* can be defined within the supermolecular approach and, in particular, within the

Möller-Plesset (abbreviated as usually by *MP*) perturbation method as follows:

$$E^i_{ABC\ldots Z;G(ABC\ldots Z)} = \sum_X E^i_{X;G(X)} + \sum_X \Delta E^i_X + \sum_{X>Y} \Delta E^i_{XY} + \sum_{X>Y>W} \Delta E^i_{XYW} + \ldots\ldots + \Delta E^i_{ABC\ldots Z} \quad (4.1)$$

where *X, Y, W = A, B, C…Z*; and superscript *i* denotes the particular order of the Möller-Plesset perturbation theory, maximum of which is 2 in the present studies. *G(X)* (*X* stands for any particular subsystem) indicates that isolated subsystem *X* is considered in its own equilibrium geometry, whereas *G(ABC…Z)* indicates that subsystem is considered in the geometry it assumes in the united complex. The one-body term ΔE^i_X in eq. (4.1) is associated with the relaxation of a subsystem X upon the complex formation and is defined by the following equation:

$$\Delta E^i_X = E^i_{X;G(ABC\ldots Z)} - E^i_{X;GX}, \quad (4.2)$$

where $E^i_{X;G(ABC\ldots Z)}$ denotes the energy evaluated at the equilibrium complex geometry, in which a subsystem X exists in the complex *ABC…Z*. The two-body term ΔE^i_{CD} represents the pairwise interaction between two monomers *C* and *D* in the configuration they assume within the complex *ABC…Z*.

$$\Delta E^i_{CD} = E^i_{CD;G(ABC\ldots Z)} - \sum_{X=C,D} E^i_{X;G(ABC\ldots Z)}, \quad (4.3)$$

Higher order many-body terms are defined recursively, for example a three-body term is defined by the following equation:

$$\Delta E^i_{CDF} = E^i_{CDF;G(ABC\ldots Z)} - \sum_{X=C,D,F} E^i_{X;G(ABC\ldots Z)} - \sum_{X>Y;X=C,D,F} \Delta E^i_{XY} \quad (4.4)$$

where the ΔE^i_{CDF} term represents a three-body contribution arising from the three relaxed-geometry monomers arranged in the same configuration as in the complex *ABC…Z*. The four- and higher order terms are evaluated recursively according to the formula (4.4). This multi-body decomposition procedure could also be formally performed at the *DFT* level of calculations (while apparently ignoring the superscript in the energy components).

The exact spinless Born-Oppenheimer Hamiltonians for isolated subsystems A and B and for a united complex AB can be decomposed in the spirit of the *MP* theory on a Fock operator, F_X, and a fluctuating operator, W_X, as follow:

$H_X^{Total} = F_X + W_X$; where X = A, B, or AB. (4.5)

The Fock, F_X, and fluctuating, W_X, operators for the spin-orbits $\chi_i(r,\sigma) = \varphi_i^{\alpha}(r)\alpha(\sigma) + \varphi_i^{\beta}(r)\beta(\sigma)$ (where $\varphi_i(r)$ stands for the space orbital, and $\alpha(\sigma)$, $\beta(\sigma)$ are the spin wave functions of σ spin-coordinate for an electron) are defined as usually by the following equations [41]:

$$
\begin{aligned}
&F_X = \sum_{i \in X} h(i) + \sum_{i \in X}\left[\sum_{b \in X}^{occ} J_b(i) - \sum_{b \in X}^{occ} K_b(i)\right]; \text{ X = A, B or AB, where}\\
&J_b(i)\chi_a(1) = \int d x_2 \chi_b^*(2)\left[1/r_{i2}\right]\chi_b(2)\chi_a(i) = \left\langle \chi_b(2)\left| 1/r_{12} \right| \chi_b(2)\right\rangle \chi_a(i);\\
&K_b(i)\chi_a(1) = \int d x_2 \chi_b^*(2)\left[1/r_{i2}\right]\chi_a(2)\chi_b(i) = \left\langle \chi_b(2)\left| 1/r_{12} \right| \chi_a(2)\right\rangle \chi_b(i);\\
&\left\langle \chi_a(i)\chi_j(j)\left| 1/r_{ij} \right| \chi_j(j)\chi_i(i)\right\rangle = \left\langle \chi_a \left| J_j \right| \chi_i \right\rangle;\\
&\left\langle \chi_a(i)\chi_j(j)\left| 1/r_{ij} \right| \chi_j(i)\chi_i(j)\right\rangle = \left\langle \chi_a \left| K_j \right| \chi_i \right\rangle;\\
&W_X = \tfrac{1}{2}\sum_{i,j \in X} 1/r_{ij} - \sum_{i \in X}\left[\sum_{b \in X}^{occ} J_b(i) - \sum_{b \in X}^{occ} K_b(i)\right];
\end{aligned}
\qquad (4.6)
$$

while the Hartree-Fock potential is defined as:

$$V^{HF(i)} = \sum_{b \in X}^{occ} J_b(i) - \sum_{b \in X}^{occ} K_b(i);$$

b runs over the occupied spin-orbitals, i indexes the electrons.

J and K are the Coulomb and exchange operators, respectively. The *MP2* correction to the total energies of subsystem A or B and the united complex AB introduced by the fluctuating operator W_X is a small perturbation to the corresponding *HF* energies. For example for the water molecule on the *MP2/aug-cc-pvtz* level, $\langle \Phi_{H2O} | F_{H2O} | \Phi_{H2O} \rangle = -76.0602820$ Hartree whereas the second-order correction $\sum_{i<j}^{N}\left[\sum_{a<b} \frac{\left\langle \Phi_{ij}^{ab} \left| W_{H_2O} \right| \Phi_0 \right\rangle}{\varepsilon_i + \varepsilon_j - \varepsilon_a - \varepsilon_b}\right]$ is only −0.2687104 Hartree. On the other hand, the contribution of the second-order correlation to the formation energy of a complex can be very significant as shown below in Table 4.2.1. The interaction energy at the *MP2* level between two subsystems A and B that form the united complex AB is given by the following equations:

$$
\begin{aligned}
&\Delta E_{Int}^{SCF} = E_{AB}^{MP0} - \left(E_A^{MP0} + E_B^{MP0}\right) + E_{AB}^{MP1} - \left(E_A^{MP1} + E_B^{MP1}\right);\\
&\Delta E_{Int}^{MP2} = E_{AB}^{MP2} - \left(E_A^{MP2} + E_B^{MP2}\right);
\end{aligned}
\qquad (4.7)
$$

Further analysis of the interaction energy of subsystems A and B is based on the intermolecular *MP* perturbation (*IMPT*) theory [29], which employs a partitioning scheme of the exact Hamiltonian for a dimer comprising monomers A and B, H_{AB}, which is different from the *MP* theory (eq. **(4.5)**):

$$\begin{aligned} &H_{AB} = F_A + F_B + W_{intra} + V; \\ &W_{intra} = W_A + W_B; \\ &V = H_{AB} - \left(F_A + F_B + W_{intra}\right); \end{aligned} \tag{4.8}$$

Introduction of the formal expansion parameters t for V and s_A and s_B for W_A and W_B, respectively, leads to: $H_{AB} = F_A + F_B + tV + s_A W_A + s_B W_B$.

The W_X operators are defined in the spirit of Möller-Plesset perturbation theory according to eq. (4.6) for the subsystem units. This paritioning is based on an observation that the intra-molecular or intra-atomic *E2* correlation corrections are often much larger than the binding energy (which certainly the case for van der Waals complexes and *HB* systems). With this form of Hamiltonian paritioning (4.8), the total interaction energy between molecular units A and B combined in the united complex AB can be expressed formally by [29]:

$$E_{Total} = \sum_{n=0} \sum_{i=0} \sum_{j=0} t^n s_A^i s_B^j \varepsilon^{nij} \tag{4.9}$$

In particular, a corresponding equation at zero-order on V and $W_{A;B}$ reads:

$$\begin{aligned} &\left(F_A + F_B\right)\left|\Phi_{AB}^{HF}\right\rangle = \varepsilon^{000}\left|\Phi_{AB}^{HF}\right\rangle; \\ &\text{where } \left|\Phi_{AB}^{HF}\right\rangle = \left|\Phi_A^{HF}\right\rangle\left|\Phi_B^{HF}\right\rangle \text{ and} \\ &\varepsilon^{000} = E_{AB}^0 = \sum_{Aa} E_a + \sum_{Bb} E_b \text{ is a sum of the energies of the occupied HF orbitals} \\ &\text{in A and B obtained for the infinitely separated units.} \\ &\text{It is convenient for the later use to label } \left|\Phi_X^{HF}\right\rangle \text{ as } \left|0_X\right\rangle. \end{aligned} \tag{4.10}$$

The first-order (first-order on V and zero-order on subsystem fluctuating potential) interaction energy in the symmetry adapted perturbation theory (*SAPT*) approach [28, 29] is given by:

$$\varepsilon^{100} = \frac{\left\langle \Phi_{AB}^{HF}\middle|VA\middle|\Phi_{AB}^{HF}\right\rangle}{\left\langle \Phi_{AB}^{HF}\middle|A\middle|\Phi_{AB}^{HF}\right\rangle}; \text{where } A \text{ is antisymmetrizer} \tag{4.11}$$

and can be represented with a framework of the *HF* theory as a sum of the electrostatic and exchange contributions as follows:

$\varepsilon^{100} = \varepsilon^{100}_{pol} + \varepsilon^{100}_{exch}$, where the electrostatic part ε^{100}_{pol} is defined by $\left\langle \Phi_0^{HF} \middle| V \middle| \Phi_0^{HF} \right\rangle$. (4.12)

Therefore, the $\varepsilon_{\text{pol}}{}^{100}$ term describes the electrostatic interaction between undeformed *HF* A and B subsystems, and represents primarily the dipole-dipole interaction energy (for electrically neutral systems). Furthermore, a sum of the terms that are zero-order on *V* and the first order on W_A and W_B, ε^{000}, ε^{010}, and ε^{001}, equals to the sum of the *HF* energies of the isolated subsystems. The terms ε^{020} and ε^{002} that are second order on W_A and W_B are equal to $E^{MP2}{}_A$ and $E^{MP2}{}_B$, respectively. Indeed,

$$\varepsilon^{010} = \langle W_A \rangle \text{ and } \varepsilon^{001} = \langle W_B \rangle, \text{where} \langle W_A \rangle = \left\langle \Phi_A^{HF} \middle| W_A \middle| \Phi_A^{HF} \right\rangle =$$

$$= \left\langle \Phi_A^{HF} \middle| 1/2 \sum_{i,j \in A} 1/r_{ij} - \sum_{i \in X} \left[\sum_{b \in A}^{occ} J_b(i) - \sum_{b \in A}^{occ} K_b(i) \right] \middle| \Phi_A^{HF} \right\rangle = 1/2 \sum_{ab \in A}^{occ} \langle ab \| ab \rangle - \sum_{a \in A} \langle a | v^{HF} | a \rangle =$$

$$= -1/2 \sum_{ab \in A}^{occ} \langle ab \| ab \rangle, \text{where} \langle op \| kl \rangle = \langle op | kl \rangle - \langle op | lk \rangle \text{ and}$$

$$\langle op | kl \rangle = \int d x_1 d x_2 \chi_o^*(1) \chi_p^*(2) r_{12}^{-1} \chi_k(1) \chi_l(2) \quad (4.13)$$

$$E_A^{SCF} + E_B^{SCF} = \sum_{Aa} E_a - 1/2 \sum_{ab \in A}^{occ} \langle ab \| ab \rangle + \sum_{Bb} E_b - 1/2 \sum_{cd \in B}^{occ} \langle cd \| cd \rangle = \varepsilon^{000} + \varepsilon^{010} + \varepsilon^{001}$$

It is convenient to introduce the reduced resolvent of the unperturbed Fock operator defined in eqs. (4.6) and (4.10)for the ground state of the AB united complex or for those of subsystems A or B treated separately:

$$R_{X0} = \sum_{n=1} \frac{|n_X\rangle\langle n_X|}{E_{X0} - E_{Xn}}, \text{where } X \text{ stands for AB, A, or B.} \quad (4.14)$$

In particular,

$$R_{X0} = 1 - |0_X\rangle\langle 0_X| \quad (4.15)$$

Consider the ε^{020} term, which describes the correction to the *HF* energy of a subsystem A due to the second order perturbation of the *MP* fluctuation operator W_A defined in eqs. (4.6) and (4.8):

$$\varepsilon^{020} = \langle 0_A | W_A R_{A0} W_A | 0_A \rangle \text{ or just } \langle W_A R_{A0} W_A \rangle \quad (4.16)$$

which is the second-order *MP2* correction to the *HF* energy of subsystem A. Exactly the same result holds for its B counterpart, ε^{002}.

The next very important term at the *MP2* level of theory is the second-order on *V*, ε^{200}

term, which can be calculated as usual for the one-dimensional *RS* perturbation theory without considering perturbations introduced by W_A and W_B *MP* operators:

$$\varepsilon^{200}=\sum_{n=1}\frac{\langle 0_{AB}|V|n_{AB}\rangle^2}{E_{AB0}-E_{ABn}}=\langle V R_{AB0} V\rangle,$$

where E_{AB0} is a sum of the ground state *HF* energies of the noninteracting subsystems A and B, and E_{ABn} is accordingly the *n*-excited state for the noninteracting A and B *HF* systems. (4.17)

Evaluated at the uncoupled Hartree-Fock level, i.e. ignoring electron exchange between subsystems A and B, the ε^{200} term can be decomposed into three parts in accord with the decomposition of the $|n_{AB}>$ in eq. (4.17) onto the following terms: $|0_A>\cdot|n_B>$, when subsystem A is the ground *HF* state while B is in excited states; $|n_A>\cdot|0_B>$, when subsystem B is in the ground state while A is excited; and finally $|n_A>\cdot|n_B>$ when both A and B are in excited *HF* states.

$$\varepsilon^{200}=\sum_{n=1}\frac{\langle 0_{AB}|V|n_{AB}\rangle^2}{E_{AB0}-E_{ABn}}=\sum_{\substack{n_A=1\\ \langle n_B=0\rangle}}\frac{\langle 0_A|V_B|n_A\rangle^2}{E_{A0}-E_{An}}+\sum_{\substack{n_B=1\\ \langle n_A=0\rangle}}\frac{\langle 0_B|V_A|n_B\rangle^2}{E_{B0}-E_{Bn}}+\sum_{\substack{n_{AB}=2\\ \langle n_A\neq 0\rangle\\ \langle n_B\neq 0\rangle}}\frac{\langle 0_{AB}|V|n_{AB}\rangle^2}{E_{AB0}-E_{ABn}} \quad (4.18)$$

Therefore, in accord with the decomposition (4.18) the following equality takes place:

$$\varepsilon^{200}=\varepsilon^{200}_{indA}+\varepsilon^{200}_{indB}+\varepsilon^{200}_{disp} \quad (4.19)$$

The induction energy terms $\varepsilon^{200}{}_{\text{indA}}$ and $\varepsilon^{200}{}_{\text{indB}}$ represent an important attractive component of the interaction energy. The induction attraction originates from the electrostatic interaction of the permanent multipoles (if they exist) of one subsystem with the induced miltipoles of another subsystem. The long-range induction interaction vanishes asymptotically as r^{-4} or r^{-6} for the ion-molecule or the dipole-molecule systems, respectively. The dispersion term $\varepsilon^{200}{}_{disp}$ is attractive for the subsystems in their ground states and the leading term in the decomposition of $\varepsilon^{200}{}_{disp}$ into the power of r vanishes as r^{-6}.

Another group of the perturbation terms that should be taken in account at the *MP2* level of supermolecular perturbation theory includes the ε^{120} and ε^{102} terms of the second-order on the fluctuation potentials W_A and W_B and the first order on the interaction potential V. This is an intramolecular correction to the electrostatic interaction between undeformed subsystems A and B.

Summarizing the aforementioned results and considering the results of Chałasiński and Szeczęśniak [30,31], the Hartree-Fock energy of the united complex AB is expressed by the following equation:

$$E_{AB}^{HF} = E_A^{HF} + E_B^{HF} + \varepsilon^{100} + \varepsilon_{indA}^{200} + \varepsilon_{indB}^{200} + \sum_{n>2} \varepsilon_{ind}^{n00} + exch - def. \tag{4.20}$$

The "exch-def" stands for the exchange-deformation effects. According to Chałasiński and Szeczęśniak [31] no satisfactory definition nor evaluation of these exchange-deformation effects have been achieved.

The expression for the second order *MP2* correction to the *HF* energy of the AB complex can be expressed by the following formal equation:

$$E_{AB}^{MP2} = E_A^{MP2} + E_B^{MP2} + \varepsilon_{disp}^{200} + \varepsilon^{120} + \varepsilon^{102} + \sum_{\substack{n\geq 2 \\ i,j\geq 1}} \varepsilon_{ind-corr.}^{nij} + exch - def. \tag{4.21}$$

Eq. (4.21) provides a good approximation for the origin of the second order *MP2* correction at large separation distance R (i.e. a distance between centers of mass of A and B). In the case of the spherically-symmetric, neutral interacting subsystems, the dispersion energy term $\varepsilon^{200}{}_{disp}$ dominates over others. In the case of systems with permanent multipoles, the leading term is a sum of the ε^{120} and ε^{102} ($\varepsilon^{120} + \varepsilon^{102}$ is labelled by ε^{12}), which is an intramolecular correction to the electrostatic interaction energy ε^{10} due to the correction of the multipoles introduced by the *MP* perturbation.

Concerning the exchange terms in eqs. (4.20) and (4.21), it should be noted that these terms vanish exponentially with *R*. At those distances, where the overlap of the electron clouds is significant, i.e. near the potential minimum, the exchange corrections to the induction and dispersion energies become important but the exchangeless induction and dispersion energies remain useful approximations.

In order to decompose the supermolecular interaction energy within the framework of the intermolecular perturbation theory, the ΔE^0 and ΔE^1 terms in equations (4.1)-(4.4) should be considered in their combination by defining the self-consistent field (*SCF*) interaction energy ΔE^{SCF} as follows:

$$\Delta E^{SCF} = \Delta E^0 + \Delta E^1 \tag{4.22}$$

By intermolecular perturbation theory (eqs. (4.5)-(4.13)), the ΔE^{SCF} can be decomposed as

follows:

$$\Delta E^{SCF} = \Delta E^{HL} + \Delta E^{SCF-def} \tag{4.23}$$

where ΔE^{HL} is the Heitler-London interaction energy between mutually undeformed *SCF* subsystems, whereas the $\Delta E^{SCF\text{-}def}$ describes the *SCF* deformation contribution. The former ΔE^{HL} term can be further divided following eqs. (4.10)-(4.13) into the electrostatic term, $\varepsilon^{10}{}_{elst}$ and exchange term, $\varepsilon^{10}{}_{exch}$, and zero-order exchanged terms, the latter two of which are combined together into the $\Delta E^{HL}{}_{exch}$ term as follows [30, 31]:

$$\Delta E^{HL} = \boldsymbol{\varepsilon}^{10}_{elst} + \Delta E^{HL}_{exch} = \boldsymbol{\varepsilon}^{10}_{elst} + \boldsymbol{\varepsilon}^{10}_{exch} + \Delta \tag{4.24}$$

It turns out that the Δ term is small comparatively with the others if the basis set of the entire system is employed for the calculations of the *SCF* energies of the isolated subsystems and therefore it is included into the Heitler-London exchange interaction. The first-order (with respect to the perturbation operator *V*) electrostatic energy $\varepsilon^{10}{}_{\text{elst}}$ (see eqs. (4.10)-(4.13))can be interpreted as the energy of electrostatic interaction between isolated subsystems with unperturbed charge distribution, which is a direct analog to the classical electrostatic energy of the interaction between permanent muiltipoles associated with the unperturbed subsystems. The latter term $\Delta E^{SCF\text{-}def}$ in eq. (4.23) represents those effects that originate from the relaxation of electron orbitals in the Coulomb field created by the subsystems under the restriction imposed by the Pauli exclusion principle. This term is determined asymptotically by the classic induction effects and can be formally expressed in accord with eqs. (4.17)-(4.20) as follows [31]:

$$\Delta E^{SCF}_{def} = \sum_{n=2}^{\infty} \boldsymbol{\varepsilon}^{n0}_{ind,relax} + (exch - def) \tag{4.25}$$

in which case the latter exchange-deformation term is originated from the Pauli exclusion principle, whereas the first sum accounts for the induction effects regardless of the Pauli principle violation. In other words, the first sum mathematically represents the classic induction effects, which ignore the overlap between electron densities of two subsystems and the electron exchange, whereas the second term appears in this equation in order to account for the effects caused by the electron overlap and exchange between electrons of two subsystems.

The second order correction in the supermolecular perturbation theory is given in

accord with eq.(4.21) by the following formal expression [31]:

$$\Delta E^{MP2} = \varepsilon^{20}_{disp} + \varepsilon^{12} + \Delta E^{2}_{exch-disp-corr.} + \Delta E^{2}_{exch-ind-corr.} \quad (4.26)$$

where the term $\Delta E^{2}_{exch\text{-}disp\text{-}corr}$ combines the exchange-correlation and exchange-dispersion effects and $\Delta E^{2}_{exch\text{-}disp\text{-}corr}$ term corresponds to the induction correlation terms.

According to the perturbation theory of the intermolecular interaction, a nonadditivity of the multi-body interaction (i.e. $E_{Inter.}(ABC) \neq E_{Inter.}(AB) + E_{Inter.}(AC) + E_{Inter.}(CB)$) comprises of three components: exchange, polarization, and dispersion. Firstly, the polarization nonadditivity will be discussed because it is apparently among the most important factors for the *HB* systems. In the case of a trimer, the presence of the third subsystem C modifies the charge distribution on the other two subsystems A and B that, in turn, changes the AB pairwise interaction. This effect is accounted for by eq. (4.25), and, therefore, it constituents the *SCF*-deformation nonadditivity, which is detectable already on the *HF* level of calculations.

The dispersion nonadditivity can be interpreted in terms of the instantaneous multipole electrostatic interaction, which resulted from the intersystem electron correlation [31]. In order to reproduce this nonadditivity effect in the ab initio calculations, a highly correlated treatment is required. The minimum level of the theory necessary for its reproduction is at the *MP3* level. Therefore, the dispersion nonadditivity remains beyond the scope of the present studies, which were conducted at the *MP2* level.

The exchange nonadditivity could be associated with the electron density redistribution on the subsystems caused by a quantum exchange effect, which decreases the overlap of the electron clouds in the intermolecular region [30, 31]. The *SCF* and *MP2* levels of theory account for the exchange nonadditivity as evident from the eqs. (4.25) and (4.26). The additivity of the first-order electrostatic interaction energy ε^{10}_{elst} ensures that the nonadditivity being observed at the *SCF* level is due to the exchange and induction effects.

Along with the *ab initio* methods at the *MP2* level of theory, the *DFT* technique with the Becke's three parameters hybrid exchange-correlation semiempirical functional using the Lee-Yang-Parr correlation functional (*B3LYP*) was extensively used in the present studies for an investigation of the properties of the model *HB* systems, which include water clusters and those with acetone, acetaldehyde, and methanol molecules attached [32].

The *B3LYP* exchange-correlation functional, E_{XC_B3LYP}, as it has been implemented in

the G98 and G03 packages, is expressed by the following equation [32, 33]:

$$E_{XC\_B3LYP} = A \cdot E_X^{Slater} + (1-A) \cdot E_X^{HF} + B \cdot \Delta E_X^{Becke88} + \\ + (1-C) \cdot E_C^{VWN} + C \cdot E_C^{LYP}; \quad (4.27)$$

where $E^{Slater}{}_X$ is the Slater exchange functional and $E^{VWN}{}_C$ is the Vosko-Wilks-Nasar correlation functional within the Local Density approximation; $E^{HF}{}_X$ is the Hartree-Fock exchange operator (see eq. (4.6)); $\Delta E_X{}^{Becke88}$ is the Becke's gradient correction to the LSDA for the exchange, and, finally, $E_C{}^{LYP}$ is the gradient correction for the correlation after Lee, Yang, and Parr. As it follows from the eq. (4.27), the widely used *B3LYP* hybrid functional combines the exact exchange correlation given by the exchange energy of the Slater determinant with the Kohn-Sham orbitals with the density functional approximation for the correlation effects of dynamical nature. Three empirical coefficients *A*, *B*, and *C* in eq. (4.27) were determined by fitting sets of the atomization energies, the ionization potentials and the proton affinities of atoms and molecules in the Pople's G1 database [33]. A specific feature of this *B3LYP* functional form resides in the value of constant A, 0.2, which determines the contribution of "exact" exchange to the total exchange-correlation potential. The parameter *B* and *C* are set to 0.72 and 0.81, respectively [32, 33]. The accuracy of computation results obtained with this potential apparently depends on the value of that or another empirical constant. While a majority of the functionals performs reasonably well on the calculation of total exchange energy, the results in the calculations of the binding energies and the contribution of the exchange-correlation energy to the binding energy, especially in the cases of weakly bounded multimolecular complexes, were found to be less accurate [34]. In part, it was related to the structure of databases, to which the empirical constants of the *DFT* functionals have been adjust. As Lacks and Gordon pointed out, these databases include usually strongly bound molecular systems, in which the driving force of bonding is the electrostatic first-order energy (eqs.(4.12) and (4.20)), whereas in the weakly bound van der Waals systems, the bonding is driven by weak exchange-correlation effects in the space region of low electron density and large density gradient, located far from the nuclei [34]. However, recent results with the *B3LYP* and other similar hybrid functionals indicate an acceptable performance in comparison with the *ab initio* correlated treatments in those cases when the calculations were performed on the complexes of molecules with permanent dipoles [35]. Let

us again recall that this family of functionals was found to fail in the prediction of bonding between atoms of inert gases [34]. By consideration of these data (which will be reviewed in necessary details below in this Chapter), one can assume that the *B3LYP*-based calculations should accurately reproduce major components of the interaction energy in the case of *HB* complexes with polar molecules such as water molecules considered in the present work.

The Dunning's correlated *aug-cc-pvtz* basis set [36] for water molecule contains *92* atomic basis functions (*127* Gaussian primitives): *46* functions are localized on oxygen atom and *23* functions on each hydrogen atom. The oxygen set includes: *5 s*-orbitals (*4+1* diffus.), *4* sets of $p_{\{-1,0,1\}}$-orbitals (*3+1* diffus.), *3* sets of *5* $d_{\{-2,-1,0,1,2\}}$-orbitals (*2+1* diffus.) and *2* sets of *7* $f_{\{-3,-2,-1,0,1,2,3\}}$-orbitals (*1+1* diffus.). The hydrogen set includes: *4 s*-orbitals (*3+1* diffus.), *3* sets of $p_{\{-1,0,1\}}$-orbitals (*2+1* diffus.) and *2* sets of *5* $d_{\{-2,-1,0,1,2\}}$-orbitals (*1+1* diffus.). Although smaller than this *aug-cc-pvtz* but still flexible, the Frisch-Pople *6-311++g(3df, 3pd*) basis set [37] for a water molecule contains *75* atomic basis functions (*100* Gaussian primitives): *39* atomic basis funcitons are localized on oxygen atom (*5* sets of *s*-orbitals: $1\times1s$; $3\times2s$; $1\times3s$ (diffuse function); *4* sets of *p* -orbitals: $3\times2p_{\{x;y;z\}}$, $1\times3p_{\{x;y;z\}}$ (diffuse function); *3* sets of *d*-orbitals: $3\times3d_{\{-2;-1;0;1;2\}}$; and a single set of *f* orbitals: $1\times4f_{\{-3;-2;-1;0;1;2;3\}}$) and *18* atomic basis functions on each hydrogen atom (*4 s*-orbitals, *3* sets of *p*-orbitals and a single set of *d*-orbitals). In comparison with the *6-311++g(3df, 3pd)*, the *aug-cc-pvtz* basis set contains formally an extra set of *7 f*-orbitals for carbon and oxygen atoms and an extra set of *5 d*-orbitals for hydrogen atom. The *SCF* and *MP2* density matrixies for water molecule were found to be very different for these two basis sets, which results in different Mulliken atomic populations and bond order parameters.

The electronic energies of formation of H_2O and OH radicals, their dipole moments and vibrational frequencies exhibit strong dependence upon the method of calculations: *SCF*, *MP2* or *B3LYP*, which clearly demonstrates the significance of electron correlation in computing the molecular properties. As demonstrated in Table 4.2.1, a few observations regarding the effects of electron correlation on the properties of water molecule and OH radical can be made. Evidently, the *E2* or *B3LYP* exchange-correlation corrections to the *HF-SCF* energies amount to only a small fraction of the total molecular energy. The *E2* is only ~0.35% of the total internal energy for water at *MP2/aug-cc-pvtz* and the *B3LYP* exchange-correlation correction

is ~0.53% of the total energy for water at *B3LYP/aug-cc-pvtz*, being themselves very large values on the absolute scale, i.e. −168.62 kcal·mole^{-1} and −254.82 kcal·mole^{-1}, respectively. Evidently, the semi-empirical Becke's exchange-correlation stabilizing correction to the Hartree-Fock energy is significantly larger than the second-order Möller-Plesset perturbation term. It should also be noted that *B3LYP* gives −0.5022597 Hartree as the electronic energy of hydrogen atom, which is apparently significantly lower than the exact solution of Schrödinger equation, −0.5 Hartree. The latter can be attributed to the self-interaction error corresponding to the inbalance between the *HF* exchange and other terms in the *B3LYP* exchange-correlation potential. The contribution of correlation corrections to the formation energies of water molecule and OH radical becomes very significant and amounts to more than a third of the energy of formation. For instance, the computed enthalpies of formation for water molecule are −141.564 kcal·mole^{-1}, −218.779 kcal·mole^{-1}, and −217.281 kcal·mole^{-1} at the *SCF/aug-cc-pvtz*, *MP2/aug-cc-pvtz*, *B3LYP/aug-cc-pvtz* levels (Table 4.2.1), respectively, whereas the experimental value is approximately −222 kcal·mole^{-1}, which clearly indicates the deficiency of the Hartree-Fock results. Both *MP2* and *B3LYP* techniques with *aug-cc-pvtz* and *LBS* sets appear to give a surprisingly good agreement (within a few percents) with the experimental values (see for more details Table 4.2.1). This is indeed astonishing because the absolute electronic energies of water molecule computed with these two techniques are different by ~86.1 kcal·mole^{-1}, corresponding to 40 % of the formation energy. It is also obvious that the formation energies for the water molecule and the OH radical, being large values on the absolute scale, −222 kcal·mole^{-1} and −102 kcal·mole^{-1}, are only small fractions of the corresponding total electronic energies of O and H_2O themselves. The values of intra-atomic or intra-molecular correlations are (typically much) larger than the formation energy. Similar observations are perhaps in the foundation of the perturbation approach to the binding energy (*SAPT* for instance), which otherwise is obtained as a difference of very large numbers, which are more or less precise approximations to the electronic energies of subsystems. The computation of the binding or formation energy in the supermolecular approach relies on the cancellation of errors, i.e. the computed electronic energies of subsystems and united complex are different from the real energies in the same degree. From an observation that the *HF* method significantly underestimates the formation energy of water and OH radical while the

MP2 significantly improves the results, it is possible to conclude that the *E2* correction to the *HF* energy increases as two subsystems becomes united. In other words, the correlation strengthens with the size of a system of interacting particles, which is intuitively clear.

Table 4.2.1. Properties of H_2O, H, O, and OH radicals at different levels of theory. There are reported optimized geometries; dipole moments (μ); the total (Hartree), and formation energies (Hartee and kcal·mole^{-1}), the second order *E2* correction to the *SCF* energy (Hartree) and the difference between *B3LYP* and *SCF* energies (Hartree); vibrational frequencies (absolute intensities are given in parenthess in km·mole^{-1} units) and zero-point vibrational energies (*ZPVE* in kcal·mole^{-1} units); enthalpies ΔH (at 0K in kcal·mole^{-1} units) of corresponding entities at the *SCF*, *MP2* and *B3LYP* levels. Two basis sets are employed: (a) *aug-cc-pvtz* (*TZ*) and (b) *6-311++g(3df, 3pd)(LBS)*. The notation 2^{-4} stands for 2×10^{-4}.

(a) *aug-cc-pvtz* basis set

	SCF (Hartree)	*E2* (Hartree) *B3LYP* (Hartree)	Total (Hartree)	Frequencies, cm^{-1} ΔH, kcal·mole^{-1}
H_2O *HF/aug-cc-pvtz* : *r*(OH)= 0.94102 Å ^HOH= 106.315° μ_{SCF}= 1.9394 D	−76.0612031		−76.0612031	1745 (96) 4120 (15) 4222 (92) *ZPVE* = 14.421
HF/TZ: H + O → OH			*HF/TZ* : 2H+ O→H_2O	
OH *r*(OH)= 0.9517Å μ_{SCF}= 1.7467 D	$E_{(H)}$= −0.4998212 $E_{(O)}$= −74.8129822 $E_{(OH)}$= −75.4219669 $\Delta E_{el(OH)}$= −0.1091635 −68.501 kcal·mole^{-1}		ΔE_{el} (2H+ O→H_2O) $\Delta E_{el(OH)}$= −0.2485785 −155.985 kcal·mole^{-1}	ΔH_{H2O}= −141.564 ΔH_{exp}~ −222
H_2O *MP2(fc)/TZ*: *r*(OH)= 0.96137 Å ^HOH= 104.109° μ_{MP2}= 1.8594 D μ_{SCF}= 1.9926 D	−76.0602820	−0.2687104 −168.62 kcal·mole^{-1} (~0.35%)	−76.3289924	1628_{MP2} (72) 3822_{MP2} (6) 3948_{MP2} (76) *ZPVE*= 13.435
MP2/TZ : H + O → OH				
OH *r*(OH)= 0.9694 Å μ_{MP2}= 1.6664 D μ_{SCF}= 1.7608 D	$E_{(H)}$= −0.4998212 $E_{(O)}$= −74.8129822 $E_{(OH)}$= −75.4216531 $\Delta E_{el(OH)}$= −0.1088497 −68.304 kcal·mole^{-1} (~65%)	$E2_{(O)}$= −0.1463119 $E2_{(OH)}$= −0.2046843 $\Delta E2$=−0.0583724 −36.629 kcal·mole^{-1} (~35%)	$E_{MP2\ (O)}$= −74.9592941 $E_{MP2\ (OH)}$=−75.6263374 $\Delta E_{MP2(OH)}$=−0.1672221 −104.933 kcal·mole^{-1}	3795_{MP2} (20) *ZPVE*= 5.425 ΔH= −99.509 ΔH_{exp} ~ −102

BSSE:MP2/TZ : H + O → OH				
$\mu_{(H)}^{SCF}$= 0.0003 D $\mu_{(O)}^{SCF}$= 0.0043 D	$E^{BSSE}_{(H)}$= −0.4998362 $E^{BSSE}_{(O)}$= −74.8131960 $E^{BSSE}_{(H)} - E_{(H)} = -1.5^{-5}$ −0.00941 kcal·mole^{-1} $E^{BSSE}_{(O)} - E_{(O)} = -2.1^{-4}$ −0.134 kcal·mole^{-1}	$E2^{BSSE}_{(O)}$= −0.1481146 $E2^{BSSE}_{(O)} - E2_{(O)} = -1.8^{-3}$ −1.131 kcal·mole^{-1}	$E^{BSSE}_{MP2\,(O)}$=−74.961311 $E^{BSSE}_{MP2\,(O)} - E_{MP2\,(OH)} = 2.0^{-3}$ −1.267 kcal·mole^{-1}	
MP2/TZ : 2H+ O→H_2O				
	$\Delta E_{el\,(H2O)}$= −0.2476574 −155.407 kcal·mole^{-1} (~67%)	$\Delta E2$=−0.1223985 −76.806 kcal·mole^{-1} (~33%)	$\Delta E_{MP2(H2O)}$=−0.3700559 −232.214 kcal·mole^{-1}	ΔH= −218.779
B3LYP/TZ: H_2O				
H_2O: *r*(OH)= 0.9619 Å ^HOH= 105.079° μ_{B3LYP}= 1.8473 D μ_{SCF} = 1.9770 D	−76.0602926	Δ_{BLYP} −0.4059041 −254.709 kcal·mole^{-1} (~0.53%)	−76.4661967	1627 (76) 3796 (5) 3899 (63) *ZPVE* = 13.327
E difference, $E_{MP2} - E_{B3LYP}$ (H_2O)	0.0000106 0.007 kcal·mole^{-1}	0.1371937 86.090 kcal·mole^{-1}	0.1372043 86.097 kcal·mole^{-1}	
B3LYP/TZ : H + O → OH				
OH *r*(OH)= 0.9753 Å μ_{B3LYP}= 1.6497 D μ_{SCF} = 1.7655 D	$E_{(H)}$ = −0.4998212 $E_{(O)}$ = −74.8129822 $E_{(OH)}$= −75.4214174 ΔE_{el} = −0.1086140 −68.156 kcal·mole^{-1} (~63%)	$BLYP_{(H)}$= −0.0024385 $BLYP_{(O)}$= −0.2811974 $BLYP_{(OH)}$= −0.3471819 $\Delta BLYP$= −0.0635460 −39.876 kcal·mole^{-1} (~37%)	$E_{B3LYP(H)}$= −0.5022597 $E_{B3LYP(O)}$= −75.0941796 $E_{B3LYP(OH)}$=−75.7685993 ΔE_{B3LYP}= −0.1721600 −108.032 kcal·mole^{-1}	3695 (13) *ZPVE*= 5.282 ΔH= −102.750
B3LYP/TZ : 2H + O → H_2O				
	ΔE_{el}= −0.2476680 −155.414 kcal·mole^{-1} (~67%)	$\Delta BLYP$= −0.1198297 −75.194 kcal·mole^{-1} (~33%)	ΔE_{B3LYP}=−0.3674977 −230.608 kcal·mole^{-1}	ΔH= −217.281

(b) *6-311++g(3df, 3pd)(LBS)* basis set

	SCF (Hartree) *E2* (Hartree) *B−LYP* (Hartree)		Total (Hartree)	Frequencies, cm^{-1} Δ*H*, kcal·mole^{-1}
H_2O: *HF/LBS* *r*(OH)= 0.9403 Å ^HOH= 106.257° μ_{SCF}= 1.9681D	−76.0593511		−76.0593511	1745 (93) 4132 (15) 4231 (89) *ZPVE*=14.450
HF/LBS : H + O → OH			*HF/LBS* : 2H + O → H_2O	
ΔE_{el} (H + O → OH) *r*(OH)= 0.9506Å μ_{SCF}= 1.7620 D	$E_{(H)}$= −0.4998179 $E_{(O)}$= −74.8093404 $E_{(OH)}$= −75.4193389 $\Delta E_{el(OH)}$= −0.1101806 −69.139 kcal·mole^{-1}		ΔE_{el} (2H+ O→H_2O) $\Delta E_{el(OH)}$= −0.2503749 −157.113 kcal·mole^{-1}	ΔH_{H2O}=−142.663 ΔH_{exp}~ −222

MP2(fc)/LBS:H_2O				
H_2O: *r*(OH)= 0.9589 Å ^HOH= 104.037° μ_{MP2}= 1.8992 D μ_{SCF}= 2.0193 D	−76.0585564	−0.2657301 −166.748 kcal·mole^{-1} (~0.35%)	−76.3242865	1624 (67) 3870 (6) 3989 (73) *ZPVE*= 13.556
$E_{aug}-E_{LBS}$ *(MP2)*	−0.0017362 −1.089 kcal·mole^{-1}	−0.0029803 −1.870 kcal·mole^{-1}	−0.0047059 −2.953 kcal·mole^{-1}	
MP2/LBS : H + O → OH				
OH: *r*(OH)= 0.9664 Å μ_{MP2}= 1.6853 D μ_{SCF}= 1.7744 D	$E_{(H)}$= −0.4998179 $E_{(O)}$= −74.8093404 $E_{(OH)}$= −75.4190866 $\Delta E_{el(OH)}$= −0.1099283 −68.981 kcal·mole^{-1} (~65%)	$E2_{(O)}$= −0.1430809 $E2_{(OH)}$= −0.2017211 $\Delta E2$= −0.0586402 −36.797 kcal·mole^{-1} (~35%)	$E_{MP2(O)}$= −74.9524213 $E_{MP2(OH)}$= −75.6208078 $\Delta E_{MP2(OH)}$= −0.1685686 −105.778 kcal·mole^{-1}	3850$_{MP2}$ (20) *ZPVE*= 5.505 ΔH= −100.273 ΔH_{exp} ~ −102
$\mu_{(H)}^{SCF}$= 0.0034 D $\mu_{(O)}^{SCF}$= 0.0138 D	$E^{BSSE}{}_{(H)}$= −0.4998226 $E^{BSSE}{}_{(O)}$= −74.8102230 $E^{BSSE}{}_{(H)}-E_{(H)}=-4.7^{-6}$ −0.003 kcal·mole^{-1} $E^{BSSE}{}_{(O)}-E_{(O)}=-8.8^{-4}$ −0.554 kcal·mole^{-1}	$E2^{BSSE}{}_{(O)}$= −0.1459534 $E2^{BSSE}{}_{(O)}-E2_{(O)}=-2.9^{-3}$ −1.803 kcal·mole^{-1}	$E^{BSSE}{}_{MP2\,(O)}$=−74.95618 $E^{BSSE}{}_{MP2\,(O)}-E_{MP2\,(OH)}=3.8^{-3}$ −2.356 kcal·mole^{-1}	
MP2/LBS : 2H + O → H_2O				
	ΔE_{el}= −0.2495802 −156.614 kcal·mole^{-1} (~67%)	$\Delta E2$= −0.1226492 −76.964 kcal·mole^{-1} (~33%)	ΔE_{MP2}= −0.3722294 −233.578 kcal·mole^{-1}	ΔH= −220.022 ΔH_{exp}~ −222
B3LYP/LBS				
H_2O: *r*(OH)=0.96114Å ^HOH=105.041° μ_{B3LYP}= 1.8897 D μ_{SCF} = 2.005 D	−76.0584308	Δ_{BLYP} −0.4060808 −254.820 kcal·mole^{-1} (~0.53%)	−76.4645116	1627 (72) 3813 (5) 3913 (59) *ZPVE*= 13.370 kcal·mole^{-1}
E difference, $E_{MP2}-E_{B3LYP}$ (H_2O)	−0.0001256 −0.079 kcal·mole^{-1}	0.1403507 88.071 kcal·mole^{-1}	0.1402251 87.993 kcal·mole^{-1}	
B3LYP/LBS : H + O → OH				
ΔE_{el} (H + O → OH) *r*(OH)= 0.9742 Å μ_{B3LYP}= 1.6739 D μ_{SCF}= 1.7805 D	$E_{(H)}$= −0.4998179 $E_{(O)}$= −74.8093404 $E_{(OH)}$= −75.4187878 $\Delta E_{el(OH)}$= −0.1096295 −68.794 kcal·mole^{-1} (~63%)	$BLYP_{(H)}$= −0.0024391 $BLYP_{(O)}$= −0.2815744 $BLYP_{(OH)}$= −0.3474571 Δ_{BLYP}= −0.0634436 −39.811 kcal·mole^{-1} (~37%)	$E_{B3LYP(H)}$= −0.5022570 $E_{B3LYP(O)}$= −75.0909148 $E_{B3LYP(OH)}$=−75.766245 ΔE_{B3LYP}= −0.1730731 −108.605 kcal·mole^{-1}	3714 (12) *ZPVE*= 5.310 kcal·mole^{-1} ΔH= −103.295 kcal·mole^{-1}
B3LYP/LBS : 2H + O → H_2O				
ΔE_{el} (2H+ O→H_2O)	ΔE_{el}= −0.2494546 −156.535 kcal·mole^{-1} (~68%)	$\Delta BLYP$= −0.1196282 −75.068 kcal·mole^{-1} (~32%)	ΔE_{B3LYP}= −0.3690828 −231.603 kcal·mole^{-1}	ΔH= −218.233 kcal·mole^{-1}

4.2.1.1 Counterpoise Procedure for the Basis Set Superposition Error

Common chemical approach of partitioning the chemical matter on molecules leads to difficulties within the framework of the *ab initio* calculations, which in their *MO-LCAO* versions do not recognize the division of the whole system into individual parts. If for the sake of simplicity, we consider the system AB to be composed of two molecules A and B, each of which is stable, when isolated, then the binding energy could be defined as the difference

between energy of the complex, AB, and the combined energy of molecules A and B at infinite separation. This definition, of course, should be further clarified with respect to whether the binding energy is restricted to the electronic energy of the potential well, or the binding energy also includes the difference of zero-point vibrational energise between the complex and isolated monomers. Furthermore, the energy change in the vibrational, rotational and translational degrees of freedom upon the complex formation should be taken in account if the binding energy is treated as a thermodynamical entity. If the latter energy can be measured experimentally (as the enthalpy of complex formation), the electronic binding energy, in a majority of experimental cases, can only be approximated because it is very difficult to determine or calculate precisely the zero-point vibrational energy. On the other hand, the electronic *ab initio* or semi-empirical calculations provide the electronic energy of the potential well defined as the difference between directly computed energies of the complex AB at its optimum geometry and molecules A, and B in their optimum geometries. Following the idea of partitioning the complex AB into subunits A and B, it appears logical to define another entity, an interaction energy between molecules A and B when they assume together the equilibrium positions within the complex, by subtracting the energies of A and B calculated separately at their equilibrium geometry in the complex from the total energy of the complex. The intermolecular perturbation theory considers explicitly the presence of interacting separate units within the complex by implementing the specific perturbation partitioning scheme of the total Hamiltonian given by eqs.(4.8)-(4.9) above (i.e. by introducing explicitly the Hamiltonian of each monomer unit defined in eq.(4.8) and the system perturbation operator V defined in eq.(4.8). Therefore, the *SAPT* (symmetry adopted perturbation theory) version of the intermolecular perturbation theory provides directly the interaction energy components unlike the supermolecular approach, in which numerically small interaction energy appears from the subtraction of two large numbers corresponding to the electronic energies of monomer units from the total energy of the complex, which is also a large number. Technically, in the calculation of the interaction energy using the supermolecular approach the electronic energy of the individual monomers A and B is computed with the inclusion of the basis set of counterpart. Since the electronic energy, being a variational property, decreases with increasing the number of the basis functions, the computed electronic energy of the monomer

A (or B) within the complex AB depends on whether the basis set of entire complex is used or just the basis set of the monomer itself. In the former case the calculated energy (of the negative sign) will be larger by the absolute value than in the latter. On the other hand, the binding energy is defined with respect to the electronic energies of individual molecules A and B, parameters of which are usually optimized in their individual basis sets. However, if the molecule A in its equilibrium monomer geometry will be brought into the contact with molecule B similarly to that in the complex AB and the basis set of entire complex will be employed (but the interaction with B is set to zero, i.e. A does not fill physically the presence of B), then the electronic energy of monomer A will decrease. The reason for the energy lowering for physically the same molecule is entirely due to the expansion of the basis set employed. This artificial stabilization of the monomers upon the inclusion of the basis set of counterpart is called basis set superposition error (*BSSE*). In other words, monomer unit A and B attains additional non-physical stabilization in the complex comparatively to their individual states due to the inclusion of the basis set of counterpart in the calculation of its own energy. The same problem apparently presents during the optimization procedure. However, if the entire complex is considered as a whole without attempting to partition the system on the molecular parts then, of course, the *BSSE* does not exist because the basis set of entire complex is always used. Therefore, the *BSSE* appears as a result of employing the supermolecular approach to the chemical system under the question. Depending upon the size of basis set used for the calculations, the *BSSE* could numerically amounts to a significant fraction of the binding energy itself, which, of course, invites the correction procedure.

The commonly used method of avoiding this computational artefact, which, otherwise, will cause significant overestimation of the binding energy, is to add to the binding energy the combined difference of the energies of A and B at their equilibrium complex geometries computed without and with the basis set of counterpart, respectively. This widely accepted procedure known as a counterpoise correction was originally proposed by Boys and Bernardi [38]. From a practical point of view, the binding energies for the water and water-organic molecule *HB* complexes calculated in the present studies at *ab initio* or *DFT* levels are corrected according to the counterpoise procedure, which can be expressed mathematically by the following commonly accepted scheme [39, 40] (superscript and subscript indicate the basis

set and the geometry, respectively):

$$\text{(i)}\quad \Delta E(AB) = E_{AB}^{AB}(AB) - \left[E_A^A(A) + E_B^B(B)\right] \text{- classical Binding Energy (B.E.)}$$

$$\text{(ii)}\quad \Delta E_{INT}(AB) = E_{AB}^{AB}(AB) - \left[E_{AB}^{AB}(A) + E_{AB}^{AB}(B)\right] \text{- Interaction Energy (I.E.)}$$

$$\text{(iii)}\quad CP = \left[E_{AB}^{A}(A) + E_{AB}^{B}(B)\right] - \left[E_{AB}^{AB}(A) + E_{AB}^{AB}(B)\right] \text{- counterpoise correction} \qquad (4.28)$$

$$\text{(iv)}\quad \Delta E_{BSSEcorr}(AB) = E_{AB}^{AB}(AB) - \left[E_A^A(A) + E_B^B(B)\right] + CP =$$
$$= \Delta E_{INT}(AB) + \left[E_{AB}^{A}(A) + E_{AB}^{B}(B)\right] - \left[E_A^A(A) + E_B^B(B)\right] =$$
$$= \Delta E_{INT}(AB) + D.E. \text{(Deformation Energy)}$$

$$\text{(v)}\quad D.E. = \left[E_{AB}^{A}(A) + E_{AB}^{B}(B)\right] - \left[E_A^A(A) + E_B^B(B)\right]$$

As follows from eq.(4.28), the counterpoise-corrected (BSSE-corrected) binding energy is different from the interaction energy by a term, which can be physically interpreted as the deformation energy of monomers upon the dimer formation. Both, the interaction and deformation terms, are *BSSE* independent unlike their combination, the binding energy. A water dimer or Acetone-W_1 complexes can serve as a typical example of the weak *HB* complexes, where the deformation energy terms are usually very small comparatively to the interaction energy. The detailed analysis of these terms using the example of water dimer indicates that even numerically small terms could effect the minimum location in those situations when the potential energy surface is flat (this circumstance realises in the weak *HB* complexes, and water clusters are excellent example of that). Moreover, in the case for relatively large water complexes (such as water hexamers, W_6) calculated at the *B3LYP* level of theory, the deformation energies of a single water molecule can be as large as ~1 kcal·mole^{-1}. Though small comparatively to the total O−H binding energy in H_2O at ~120 kcal·mole^{-1} [41], these values are nearly comparable with the pairwise interaction energies in these clusters, which indicates the general importance of the deformation terms and the fundamental difference between the binding and interaction energies. Indeed, for particular mono-hydrogen bonded complex of acetone and water hexagon, the interaction energy between the acetone molecule and the water ring hexagon at the *B3LYP/6-311++G(3df, 3pd)* level of theory is found to be −6.513 kcal·mole^{-1} whereas the binding energy is only −3.439

kcal·mole^{-1}. This notable difference between the two values, the interaction and the binding energies, originates from the deformation of a hexagon ring. Large values of the deformation energy upon adsorption of the guests could be viewed as a characteristic feature of the water clusters and could be further associated with the general flexibility of the water media. Returning to the case of water dimer, it should be noted that the difference between the interaction and the binding energies is almost negligible numerically at the *MP2*/*aug-cc-pvtz* level but perceptible at the *SCF* level. Furthermore, the inclusion of the counterpoise correction on the stage of the potential energy profiling along the O−O coordinate leads to a shift of the minimum to a larger separation distance and, surprisingly, to the deepening of the potential well. The latter observations indicate that *CP* or other similar methodology affect not only the numerical values of the binding energy at a given minimum but also the location of that minima and, more generally, the *PES* (potential energy surface) of a complex in question.

4.2.2 Cooperativity Effects in the Water Media

In the *QM* analysis of the *HB* systems with multiple hydrogen bonds, the multi-body contributions to the total interaction energy can be used for elucidation of the cooperative nature of the *HB* network. The cooperativity in the *HB* network resides in those effects that make the "whole system to be larger than the sum of the parts" (in terms of interaction energy). The network of *HB*'s is bound more strongly together than any of individual links in the absence of the others due to contribution of the multi-body corrections to the pairwise interactions as it is represented by eqs.(4.1)-(4.4). In particular, Table 4.4.2 compares calculated in the present work bonding energies in the water dimer (C_S) and cyclic sequential hexamer (S_6) at the *MP2* and *B3LYP* levels with different basis sets. The cooperativity effect in cyclic hexamer leads to the following energetic and structural effects in transition from dimer to hexamer. The partial bonding energy between hydrogen bonded pair (obtained by division of the total binding energy on the number of hydrogen bonds in the system) is significantly larger in hexamers than the dimer: *B.E./HB* (binding energy per hydrogen bond) = −4.710 kcal·mole^{-1} (dimer) vs. −7.112 kcal·mole^{-1} (hexamers) at *MP2/aug-cc-pvtz* and −4.524 kcal·mole^{-1} (dimer) vs. −7.033 kcal·mole^{-1} (hexamers) at the *B3LYP/LBS* level. Furthermore, the O···O distance between pair of hydrogen bonded neighbors decreases significantly on transition from dimer to hexamer: 2.90719 Å (dimer) vs. 2.70686 Å (hexamers) at *MP2/aug-*

cc-pvtz and 2.91484 Å vs. 2.71299 Å at *B3LYP/LBS* levels. The increase in the length of O−H bond also reflects the cooperativity effect in the sequential chain of water hexamers. If in the dimer the length of O−H bond increases by 0.00721 Å and 0.00776 Å on the *MP2/aug-cc-pvtz* and *B3LYP/LBS* levels, respectively, in the hexamers the same values rise to 0.02222 Å and 0.02384 Å. It is possible to assume that relatively short intermolecular distances in the hexagonal ice (~ 2.7 Å) are originated from the cooperativity effect of hydrogen bond. Indeed, as Table 4.2.3 shows, the intermolecular distance in the water dimer is substantially underestimated while the bonding energy is significantly overestimated by those classical water potentials, which is optimized for the proper description of a bulk water medium. The classical potentials apparently cannot handle the cooperativity effects in finite water clusters, which lead to artefacts in the dimer properties.

The *HB* cooperativity leads to the common occurrence of the long chain or more complex arrangements of the *HB*'s in the organic crystal structures. Moreover, the cooperativity is a powerful enough to cause the formation of the stable molecular aggregates in the liquid phases such as six-member rings in the liquid formamide [42]. It should be noted that one could observe a correlation between the cooperativity and the topology of the *HB* network. Following a discussion in the Scheiner's book on the hydrogen bonding [43], let us consider a pair of molecules AH and CH, each of which contains a proton to donate (in order to form a hydrogen bond) and one or more lone electron pairs located on the A and the B moieties, which makes them to be appropriate for accepting a proton. In the case of linear arrangement H−C···H−A, an electron density shifts from the region of H−C bond to the region of *HB* between C and H, and then further, from the H−A bond towards A moiety. As the result of the HB formation between HC and HA moieties, the electron density on A increases whereas the electron density on H−C bond decreases. The dimer HC···HA can potentially act as a *HB* donor or acceptor, and, therefore, another molecule HD could be attached to HC moiety of the dimer leading to a trimer with the following structure H−D···H−C···H−A, which will be referenced thereinafter as a sequential configuration. Since the electron density on the proton of HC subsystem is lower in the dimer than in HC monomer, the *HB* between HD and HC is expected to be stronger due to the induction effect of HA part. Similarly, if HD acts as a *HB*-donor and interacts with the H−A part of the dimer, the *HB* bond in the trimer

H−C···H−A···H−D is stronger than that in the dimer complex H−A···H−D because the electron density on A is higher in the trimer's case due to the dative effect of HC part, which is apparently absent in the dimer H−A···H−D. The calculations confirm this reasoning, indicating that the induction effects are primarily accounted for the cooperativity in the *HB* network. The presence of carbonyl group in acetone (Ac) and acetaldehyde (AcAl) molecules creates a possibility of forming bifurcated W_2−Ac and W_2−AcAl complexes, in which oxygen atom acts as a double proton acceptor. This configuration is relatively unfavorable from the prospective of cooperative enhancement because the formation of first *HB* causes a depletion of the electron density on the oxygen atom of carbonyl group, which, therefore, is expected to weaken the second *HB* in accord with the above stated reasons. On the other hand, the 2:1 complexes are expected to be energetically (not thermodynamically because of the entropy reduction) more stable than W + W−Ac or W+ W−AcAl (water molecule and 1:1 complexes), and the present *QM* calculations indeed confirm this general expectation. The effect of cooperativity has been in particular investigated on the *SCF* and *MP2* levels for the *HB* linear chain containing up to seven HCN molecules by King and Weinhold [44]. Their calculations clearly show a progressive increase in the average *SCF* (with rather small *6-31+G(d)* basis set) binding energy from 4.2 kcal·mole^{-1} for the dimer to 7.68 kcal·mole^{-1} for the combination of two trimers, and a concomitant decrease in the frequency and very large intensity increase of the ν (C−H) stretch bands with number of the monomer units in the chain. It should be noted that the observed cooperativity effect causing significant enhancement in the individual *HB*'s was found to exhibit relatively slow saturation with the chain length that suggests the presence of even stronger *HB*'s in larger molecular associates with a distribution of the energy of individual *HB*'s along the chain. The strongest bonds are expected to be located at the central part of the chain whereas the weaker *HB*'s are expected to be at the edges. Natural bond orbital analysis performed by King and Weinhold [44] demonstrated that the cooperativity effect in the $(HCN)_n$ system can be qualitatively rationalized on the basis of a simple $n\mathrm{N}\rightarrow\sigma^*\mathrm{CH}$ charge transfer picture of the *HB*, which is part of the exchange-deformation included in the *SCF* deformation energy ΔE^{SCF}_{def} given by eq.(4.23). The interesting feature of the $(HCN)_n$ *HB* complexes is a character of the changes in the CN bond lengths and corresponding frequencies: an act of donating of a proton makes the CN bond longer and

causes red shift in the ν(CN) frequency while it becomes shorter if molecule acts as acceptor with concomitant blue shift in the frequency. The latter tendency is opposite, in particular, to a water-acetone complex, in which C=O bond becomes longer with concomitant red shift in frequency upon HB bonding. The changes in the carbonyl group upon *HB* bonding have been explained by Nyquist [45] in terms of increasing weight of the ionic $C^{+}-O^{-}$ resonance form, which weakens the C=O bond. It appears that this explanation does not work in the case of $(HCN)_n$ system. King and Weinhold further argued that the cooperativity effects in the *HB* network systems, which have been observed experimentally and confirmed by the theoretical calculations, appear to be in a contradiction with the electrostatic picture on the *HB* (i.e. due to primarily $\Delta E^{HL} + \Sigma\varepsilon^{n00}_{ind}$ terms, eqs. 4.20), which must, therefore, be augmented by the exchange-deformation terms in order to account for the cooperativity phenomenology. The discussion on the cooperativity could be viewed as logical continuation of the earlier contradictions between two approaches to the *HB*, one of which stresses the electrostatic nature of *HB* and is due to Pauling followed, in particular, by Bauer and Magat, and Lennard-Jones and Pople, and later Morokuma [46]. The opposite view stresses an importance of the charge-transfer or, more generally, exchange-correlation effects as a key element of the *HB*, and it is due to Mulliken followed, in particular, by Ratajczak, Orville-Thomas [47], and recently advocated by Weinhold [44]. The nonadditivity of multibody interaction energy resides in the non-additivity of polarization, dispersion, and exchange components, the cooperativity in the *HB* networks of water molecule. For instance, Table 4.2.4 and Table 4.2.5 represent a multibody contribution to the binding energy of the sequential water hexamer on the *MP2* and *B3LYP* levels. It appears that the pairwise interaction energy decreases in transition from dimer to hexamers, i.e. −4.749 kcal·mole^{-1} (dimer) vs. −4.013 kcal·mole^{-1} (hexamers) on the *MP2* level or −4.566 kcal·mole^{-1} vs. −3.908 kcal·mole^{-1} on the *B3LYP* level. On the other hand a strong three-body effect, which reflects the significance of induction in the sequential array of *HB*'s, is evident. Indeed, it amounts to −12.938 of total −42.196 kcal·mole^{-1} in the hexamers on the *MP2* level. Therefore, the cooperativity effect in the sequential array could be primarily associated with the induction interaction on the three-body level.

Table 4.2.2. Binding energies of the water dimer W_2 (Cs) and cyclic hexamer W_6 (S_6). The calculations were performed on the *MP2(fc)* (frozen core approximation) and *B3LYP* levels with the *aug-cc-pvtz* (TZ)and *6311++g(3df, 3pd)(LBS)* basis sets. Θ_C stands for the inclination angle of acceptor with respect to the O---O line. *L*(O-O) and ΔL (O_D-H) designate intermolecule distance and the change in the O-H distance upon hydrogen bonding. *SCF*, *E2* and *EMP2* designate the *HF* energy, second order *MP* correction and the total *MP2* energy.

		Dimer (C_s), kcal·mol^{-1}				Hexamer (S_6), kcal·mol^{-1}		
		MP2		*B3LYP*		*MP2*		*B3LYP*
Basis set		*TZ*	*LBS*	*TZ*	*LBS*	*TZ*	*LBS*	*LBS*
B.E.	*SCF*	−3.482	−3.777			−29.899	−31.536	
	E2	−1.699	−1.528			−16.473	−15.521	
	EMP2	−5.181	−5.305	−4.571	−4.832	−46.372	−47.057	−44.232
B.E. BSSE corr.	*SCF*	−3.406	−3.419			−29.287	−29.128	
	E2	−1.303	−1.149			−13.382	−12.020	
	EMP2	−4.710	−4.568	−4.518	−4.524	−42.669	−41.148	−42.196
		Expt. −5.44 (−5.5)						
B.E. BSSE corr. + ΔZPVE		−2.607	−2.346	−2.393	−2.350			−29.421
		Expt. ΔH^*_{373K} = −3.59 (-3.63)						
B.E. BSSE corr. per *HB*		−4.710	−4.568	−4.518	−4.524	−7.112	−6.858	−7.033
ΔL $(O-H)_{donor}$		0.00721	0.00704	0.00787	0.00776	0.02222	0.02177	0.02384
L (O−O)		2.90719	2.90384	2.91724	2.91484	2.70686	2.70395	2.71299
		Expt. 2.976						
Θ_C, º		56.6	56.1	56.8	58.0			
		Expt. 58						
HB ang., º		171.7	173.0	172.1	172.6	179.2	179.2	178.6
Dipole Moment, D		2.6201	2.6820	2.6337	2.6341	0		
		Expt. ~ 2.6						

Table 4.2.3. Optimized geometry and dimerization energy for the linear water dimer for the selected classical potentials [59].

Potential	O···O distance, Å	Θ_C, deg°	B.E., kcal·mol^{-1}
SPC	2.75	26	6.59
TIP3P	2.74	27	6.50
BF	2.72	47	6.06
ST2	2.85	52	6.84
TIPS2	2.79	46	6.20
TIP4P	2.75	46	6.24

Table 4.2.4. Multi-body decomposition of the binding energy for the water dimer W_2 (C_s) and the water cyclic hexamer W_6 (S_6) at the *MP2(fc)/aug-cc-pvtz* level. *SCF*, *E2* and *EMP2* designate the *HF* energy, second order *MP* correction and the total *MP2* energy.

			Dimer (C_s)		Hexamer (S_6)	
			μHartree	kcal·mol^{-1}	μHartree	kcal·mol^{-1}
B.E.		*SCF*	−5549	−3.482	−47647	−29.899
		E2	−2707	−1.699	−26252	−16.473
		EMP2	−8256	−5.181	−73899	−46.372
B. E. BSSE corr.		*SCF*	−5428	−3.406	−46673	−29.287
		E2	−2077	−1.303	−21325	−13.382
		EMP2	−7505	−4.710	−67998	−42.669
Deformation E. per molecule		*SCF*	162	0.102	1288	0.808
		E2	−130	−0.082	−787	−0.494
		EMP2	32	0.020	501	0.314
Pairwise Terms	1-2	*SCF*	−5752	−3.610	−3671	−2.304
		E2	−1816	−1.140	-2724	−1.710
		EMP2	−7569	−4.749	-6396	−4.013
	1-3	*SCF*			−1369	−0.859
		E2			−28	−0.017
		EMP2			−1396	−0.876
	1-4	*SCF*			−748	−0.469
		E2			23	0.015
		EMP2			-724	−0.454
	Σ total	*SCF*			−32482	−20.383
		E2			−16442	−10.317
		EMP2			−48924	−30.700
Three-body Terms for W_6			1-2-3		1-2-4	
		SCF	-2422	-1.520	-347	-0.218
		E2	38	0.024	1	0.001
		EMP2	-2383	-1.496	-346	-0.217
			1-2-5		1-3-5	
		SCF	-406	-0.255	-77	-0.048
		E2	1	0.001	-1	-0.001
		EMP2	-404	-0.254	-78	-0.049
			Σ total			
		SCF	-19203		-12.050	
		E2	245		0.154	
		EMP2	-18958		-11.896	
Four-body terms for W_6			1-2-3-4		1-2-3-5	
		SCF	-290	-0.182	-61	-0.038
		E2	-38	-0.024	-11	-0.007
		EMP2	-328	-0.206	-72	-0.045
			1-2-4-5		Σ total	
		SCF	-124	-0.078	-2478	-1.555
		E2	-15	-0.009	-338	-0.212
		EMP2	-139	-0.087	-2816	-1.767

				Σ total	
Five-body term for W_6	*SCF*	-38	-0.024	-228	-0.143
	E*2*	-10	-0.007	-63	-0.039
	E*MP2*	-49	-0.030	-291	-0.183
Six-body term for W_6	SCF	10	0.006		
	E*2*	3	0.002		
	E*MP2*	134	0.008		

Table 4.2.5. Multi-body decomposition of the binding energy for the water dimer W_2 (C_s) and the water cyclic hexamer W_6 (S_6) at the *B3LYP* level with *6-311++g(3df, 3pd)* basis set.

		Dimer (C_s)		Hexamer (S_6)	
		μHartree	kcal·mol^{-1}	μHartree	kcal·mol^{-1}
B.E.		-7700	-4.832	-70488	-44.232
B. E. $_{BSSE\ corr.}$		-7209	-4.524	-67244	-42.196
Deformation E.		34	0.021	553	0.347
Pairwise terms	1-2	-7277	-4.566	-6228	-3.908
	1-3			-1191	-0.748
	1-4			-644	-0.404
	Σ total			-46461	-29.154
Three-body terms for W_6	1-2-3			-2597	-1.630
	1-2-4			-378	-0.237
	1-2-5			-433	-0.271
	1-3-5			-86	-0.054
	Σ total			-20618	-12.938
Four-body terms for W_6	1-2-3-4			-358	-0.225
	1-2-3-5			-79	-0.050
	1-2-4-5			-143	-0.089
	Σ total			-3050	-1.914
Five-body term for W_6				-69	-0.043
	Σ total			-415	-0.260
Six-body term for W_6				26	0.017

4.3 Ab Initio and Semi-Empirical Analysis of the Hydrogen Bonding in the Small Water Clusters $(H_2O)_n$, n=2-6.

The small water clusters constitute a subject of special interest for the science on water because their relative simplicity allows one to perform a detail analysis of the topological and energetic features of the *PES* (potential energy surface) in these model systems on the *ab initio* or semi-empirical levels. The knowledge of *PES* features for relatively simple clusters could be used for modeling a large scale realistic water media. One possible approach to the molecular topological description of the large-scale water systems is to consider a dynamic equilibrium between small unstrained water clusters dispersed throughout the distorted and

irregular HB network of water molecules. This picture, conforming most closely to the liquid water at near-freezing temperatures and at the supercooled region, when the probability of forming the ordered unstrained clusters is expected to be significantly higher than at more elevated temperatures, is consistent with the cluster model of the liquid water, which originates from the studies of Frank [48], and Nemethy and Scheraga [49, 50]. In the search for plausible structurally recognizable local forms of liquid water, the cluster approach naturally turns to those water polyhedra, which have been observed in the crystalline water phases and in the clathrate-hydrate crystalline lattices. In particular, the building block of many of the clathrate-hydrate structures, pentagonal dodecahedron, appears among potential elementary units for the cold liquid water, whereas another plausible candidate, bicycle octagon, occurs over the structure of the hexagonal ice, *Ih*. Considered as isolated structures, these bulky unstrained water polyhedra exemplify most likely the global minima on the *PES* for a given number of the water molecules. The relative configuration of the water molecules determines the possible sequences and geometries of the hydrogen bonds throughout the cluster according to the Bernal-Fowler and Pauling ice rules [51, 6]. The latter states that in the *HB* network each participant can donate at most two hydrogen bonds to the closest neighbours and receive at most two bonds from another two closest neighbours, or in other words, a tetra-coordinated water molecule act as a double donor and as a double acceptor of *HB*'s. These ice rules play a key role in the understanding of the topological and energy properties of cubic, *Ic*, and hexagonal, *Ih*, ices by providing an elegant classification tool for the assignment of different *HB* configurations and by explaining the origin of an energy degeneration of allowed *HB* configurations.

Regarding the hydrogen bond topology, the notations of configuration and conformation are adopted from the general language of organic chemistry and employed in the present discussion. The relative position of hydrogen-bonded water molecules in the cluster and the sequence of hydrogen bonds connecting these molecules together constitute a configuration as shown below in on the example of water tetragons. In particular, in the present studies there are found the following configurations: sequential ring and tetrahedron. A transition from one configuration to another should involve, therefore, the creation and/or disruption of some *HB*'s participating in the initial and final networks. The OH groups that are

not involved in the *HB* network within the given configuration, form the dangling bonds (labelled as $(OH)_d$). An important property of these resides in the potential of becoming employed in the *HB* network. In the studies on isolated water clusters, in which the ratio of highly coordinated molecules to the low coordinated molecules is necessarily small (unlike the real water media, where the bulk to surface ratio is usually very large) the dangling bonds often play one of the leading roles in the reconfiguration of a cluster. For example, the transition from sequential ring to the tetrahedron occurs if W^1 becomes a double acceptor with 2 *DB*s and W^3 becomes a double donor (see Table 4.3.2). Analysis of the water tetramer family reveals the main structural and energetic features, which characterize the small water clusters W_3-W_6. The most noticeable structural feature of isolated water cluster, which controls the existence of particular configuration, resides in double donor (d^2) local arrangement. The double donor water molecule bears significant negative charge due to the donation from two *HB* neighbors. This negative charge attracts the non-compensated positive charge on OH *DB* located on the remote water molecules. As a consequence of this attraction the configuration changes such that additional *HB* will be established between the d^2 and OH *DB* by "internal reaction": d^2 + OH (*DB*)→*HB*. The sequential configurations are found to be the most stable among all others possible local minima for the water clusters of a given size as shown in particular in Table 4.3.2 for W_4. If an initial configuration includes the d^2 and the OH *DB*, such a configuration is found unstable. This unstable configuration will convert to another configuration with a larger number of *HB*'s, which belongs to a different configurational class as discussed below in section 4.3.3. Therefore, distorted *HB*'s originate from a collapse of the d^2 and the OH *DB* structural features of finite water clusters.

Figure 4.3.7 demonstrates the effect of cluster geometry on the energy properties for a W_1-W_4 set, calculated on *B3LYP* and *TIP4P* levels. It is evident that the binding energy of the sequential tetramer rings is the largest among all other clusters. The different orientation of dangling bonds within a given configuration does not significantly influence the total binding energy despite the apparent dipolar repulsion between OH bonds (see Table 4.3.2). The binding energy for the non-sequential configurations such as tetrahedron is discernibly larger as well as for those, which include multiple double donors and double acceptors. Another example is given by the transition from a bifurcated hexagonal ring configuration, comprising

a double donor in the first position and a double acceptor at the forth position in the ring, to the book configuration due to 1-4 hydrogen bonding. The former configuration appears therefore to be metastable with respect to that particular book configuration, in which it transforms during the minimization trial with the *B3LYP/6-311++G(3df, 3pd)* level of theory. Apart from the role that a dangling bond plays as a structure-forming element, this example also demonstrates a potential structural significance of the non-coordinated lone pairs on the oxygen atom of a water molecule (labelled as O_d). In other words, the OH_d and O_d moieties should be considered as a potential donor and acceptor of the hydrogen bond, respectively. These structural features are assumed to constitute the surface of water media. In the studies on ice surface [52], Fletcher has considered the preferential orientation of the incompletely coordinated water molecules on the surface of ice and found that the preferential orientation depends on the relative polarity of the OH_d and O_d molecular parts. Fletcher shown that the dipole-quadrupole interaction is a major contributor to the energy difference between two imaginary surface configurations with the OH_d or O_d outwards and concluded, based on the static values of the quadrupole tensor for water molecules, that the configuration with OH_d outward is more stable (latter [53], however, he has reversed this assignment because the earlier derivations erroneously included the spherical part of the quadrupole tensor [52], which should be ignored). The experimental evidence, primarily from the spectroscopic area [54], indicate the OH *DB*'s as the dominant species on the water medium surface, in accord with the conclusion of main Fletcher's work (despite the mathematical error involved [52, 53]). Of course, the polarity of the OH *DB*'s or O_d moieties depends on the nearest molecular environment, which makes this property to be a structure-dependent and dynamic feature. The lone pairs on the O_d moiety occupy two molecular orbitals, which within the framework of natural bond orbital approach are at −0.91948 Hartree with the *sp*-hybridization directed along bisector of the H−O−H angle and at −0.50561 Hartree with the *p*-hybridization directed perpendicular to the molecular plane whereas two nearly identical bond OH orbitals are found at −0.97481 Hartree with nearly sp^3-hybridization (*MP2(fc)*/*aug-cc-pvtz*). The high energy of the *p*-hybridized lone pair on O atom indicates the relatively high polarizability, which in turn could lead to potentially significant dependence of the dipole and quadrupole moments on the neighborhood.

Among many possible configurations with a given number of the water molecules, a special case comprises monocyclic arrangements, which often could be characterized by a high symmetry and an optimal conformation of the hydrogen bonds. Irrespectively to the size of the ring and the conformational arrangement of the *HB*'s, a key characteristic of this class of *HB* network resides in the hydrogen bonding only among the nearest neighbours, which leads therefore to the general equivalence between a number of molecules, hydrogen bonds and dangling groups. The monocyclic class can be further divided on two subclasses: sequential and non-sequential. In the sequential subclass, each water molecule donates hydrogen bond to the next closest neighbour and accepts a hydrogen bond from the nearest neighbor. The combination of a single donor (d) and single acceptor (a) coordination of a doubly bonded water molecule will be abbreviated as (*da*) thereinafter. The non-coordinated OH group of each molecule in the sequential arrangement appears in the dangling position usually above or below the plane of ring. In the non-sequential subclass, in contrast with the sequential subclass, some water molecules acts as a double donor of the hydrogen bonds whereas some other molecules act accordingly as a double acceptor. The double donor is labeled by d^2 whereas double acceptor is labelled by a^2, respectively. From the perspective of structural stability, the sequential monocyclic class has been found among the most stable configurations including those with a higher number of the hydrogen bonds involved. As it is shown below in this Chapter, the origin of this exceptional stability of sequential monocyclic arrangement can be attributed to the strong tri-body contribution (non-additive) to the total binding energy and the optimum relative orientation of the next-neighbor dipoles leading to the significant negative 1-3 pairwise contribution.

The non-sequential subclass has been found to be generally unstable and convert either to sequential configuration or to the multi-cyclic class of configurations. In contrast to the monocyclic class of configurations, in those cases when the *HB* network contains multiple cycles, a number of the *HB*'s becomes larger than the number of molecules involved, which causes an appearance of triply- and/or tetra-coordinated water molecules. In these cases, a water molecule at branching points acts as a double acceptor and/or as a double donor in accord with the ice rules. On the other hand, the sequence of *HB*'s, i.e. the number of donor and acceptor sites within the structure, will be considered as an attribute of the configuration

although it is possible that non-sequential unstable configuration will produce on minimization a stable sequential configuration but in the non-optimal conformation. With respect to the hydrogen bond between a pair of water molecules, the relative position of hydrogen atoms not involved in this hydrogen bond will be referred to as a conformation. For the isolated sequential *HB* rings different conformations includes "up" ($^{+}$) and "down" ($^{-}$) axial orientations of the non-coordinated free OH groups, i.e. OH dangling bonds. In addition to the axial conformations there are local minima associated with the nearly equatorial orientation of the dangling bonds such those found for pentagonal and hexagonal rings. The existence of equatorial minima is in accord with the flexibility of hydrogen bonds. Conformation ↔ configuration regrouping due to the molecular rotation is referred to as the Bjerrum's transitions. With respect to a water tetramer, two configurations are theoretically possible: a ring and a tetrahedron. The ring configuration can be characterized by the sequential cyclic arrangement of four *HB*'s: 1*d*→ *a*2*d*→*a*3*d*→*a*4*d*→*a*1. In particular, the cyclic arrangements of the *HB* systems are stabilized by the cooperative effect exemplified primarily on the tri-body level. On the other hand, in the tetrahedral configuration of four water molecules that has been also found to be a true local minimum of higher energy, there is an additional hydrogen bond acting as a bridge between the first and the third molecules and consequently increasing the total number of *HB*'s to five. Of course, this additional *HB* coordination causes the weakening of those *HB*'s that constitute the bonding in the cyclic part, such that the potential energy of this tetrahedral complex appears to be higher than that of a ring despite a larger number of the *HB*'s. The possibility of attaining different configuration should be viewed as a representation of the flexibility in the HB network because a smooth relaxed potential of the individual bond allows such degree of deformation, which is necessary for the transition to another local minimum. Furthermore, the energy of a given geometric arrangement of water molecules depends not only on their relative position associated with the position of oxygen atoms, but also to in a certain degree on the relative position of hydrogen atoms not involved in the hydrogen bonding (dangling bonds in the case of cyclic configuration), or, in other words, on the *HB* conformation. Therefore, it can be assumed that for a given number of water molecules, the relative stability of a particular H_2O-configuration depends on the *HB* conformation attained by the hydrogen atoms. Within the given configuration, the system can

transfer from one *HB* conformation into another by the Bjerrum's mechanism, which assumes that the transport over rotational transition states could violate the ice rule in the case of 4 *HB*-coordinated water molecules, become possible at certain temperature. In the case of tetragonal sequential ring configuration with 2 *HB*-coordinated arrangement, a transition from the lowest-energy sequential S_4-symmetry $(da)^{4[+-+-]}$ axial arrangement into the next C_i $(da)^{4[++--]}$ conformation of slightly higher energy requires the rotation of two neighbouring water molecule whereas a transition to the $(da)^{4[+++-]}$ conformer requires the rotation of only a single water molecule without breaking the sequential *HB* ring arrangement. Unlike the *B3LYP* results, the minimization of these axial conformers in the sequential tetramer configuration at classical *TIP4P* potential leads to the most stable S_4 conformer indicating small energy barrier for the molecular rotation in the open cyclic structures. An observation that different HB conformations in the small water clusters appear at different energies invites re-examining Pauling's hypothesis on an energetic equivalence of the HB conformations attained in the Ih according to the ice rule. In part this energy difference is due to Coulomb repulsion between positively changed hydrogen atoms, which is stronger in the *cis*- than in *trans*-conformations.

4.3.1 Water Dimer: Ab Initio and Semi-Empirical Results

The water dimer is the elementary hydrogen-bonded water complex with a single hydrogen bond between two water molecules. Microwave spectroscopy [55] has clearly established the C_s symmetry for the equilibrium geometry of the following general form:

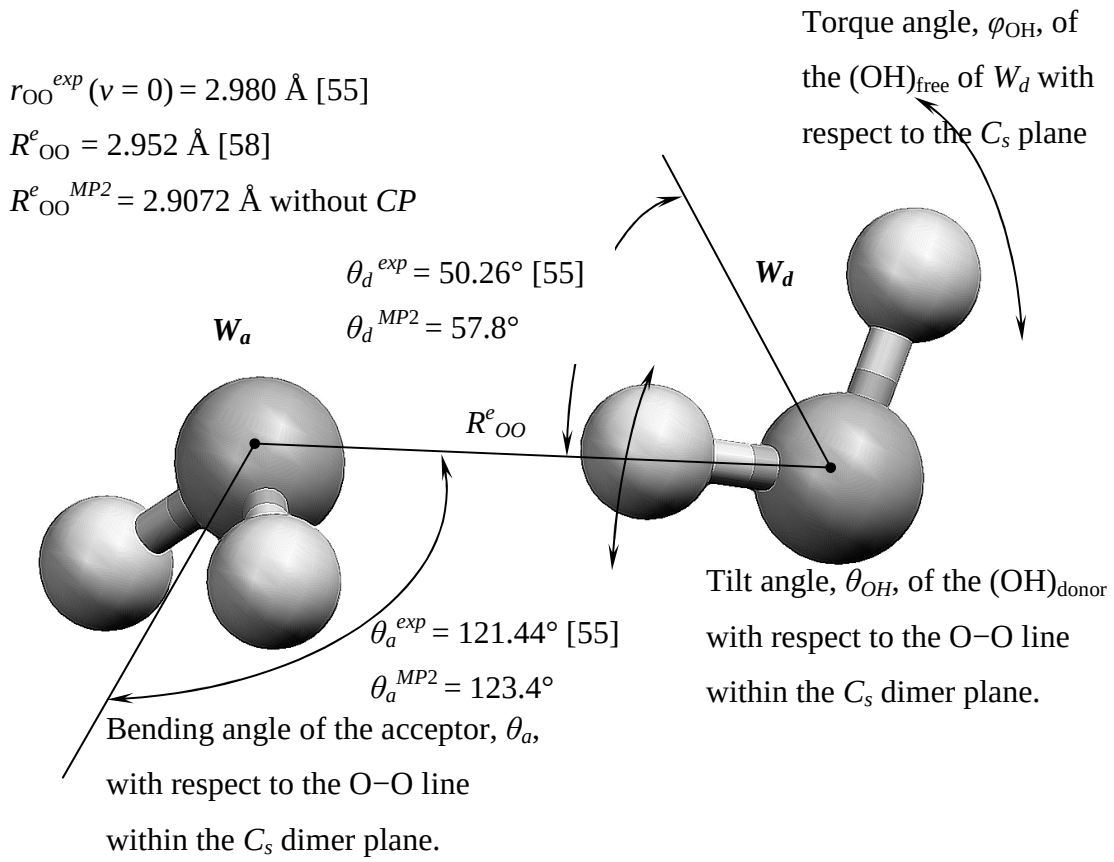

Figure 4.3.1. The geometry of the water dimer at C_s minimum.

Topological properties of the *PES* of the water dimer are important for understanding the structure and dynamics of more complex water aggregates, which could in turn serve as models for the noncrystalline water phases as discussed in Section 4.1. Experimental and theoretical studies evidently show that there are eight structurally equivalent configurations for the dimer, which can be obtained by the permutation of hydrogen atoms separately in the two water molecules, each of which acts in turn as the donor or the acceptor of the hydrogen bond (

the intermolecular permutations are not allowed) [56, 57]. All *8* forms assume the geometry given above in accord with the presence of a single global minimum on the dimer *PES* (with the C_s symmetry). In the present studies, the cross-sections of the *PES* were determined at the *MP2(fc)/aug-cc-pvtz* level of theory without correcting on the basis set superposition error, which is consistent with the minimization procedure implemented in the Gaussian program, because the latter ignores the *BSSE* effects on the location of minimum. Although it is straightforward to perform the *PES* mapping with the counterpoise correction (see section 4.2.1.1) for the basis set superposition error, we have not undertaken this task in the present studies with the exception of an O−O distance scan, which is of the primer importance for allocating the potential well and for determining the potential depth. Indeed, different results were obtained with and without the counterpoise correction. The equilibrium geometry of water dimer has been experimentally determined by Dyke *et al*. [55] using microwave spectroscopy with the equilibrium O−O distance at 2.980 Å and the bending angles for the acceptor and donor at 121.44° and 50.26°, respectively. A correction for the effects of anharmonicity performed by van Duijneveldt-van de Rijdt and van Duijneveldt [58] reduces the intermolecular distance to a value of 2.952 Å, which in this numerical representation can be directly compared with the *ab initio* calculations. The empirical potential well depth is found at −5.4 ±0.2 kcal·mole^{-1} by Reimers *et al*. [59], who extrapolated the results of semi-empirical analysis of the second virial coefficient of steam, and at −5.44 ±0.7 kcal·mole^{-1} by Curtiss *et al*. [60] from the data on the thermal conductivity of water vapor. The empirical potential well depth is obtained by subtracting the energy changes in the translational, rotational and vibrational degrees of freedom upon dimer formation from the experimental enthalpy of dimerization. Therefore, empirical well depth appears to be dependent on the zero point vibrational energy of dimer, which in the calculations of potential well depth was estimated at 2.25 kcal·mole^{-1} on the basis of *SCF/4-31G* level of theory [60, 61]. Regarding the anharmonicity influence on the empirical depth, Mas and Szalewicz argued that introduction of accurate zero-point vibrational energy in the calculation of the empirical well depth will bring the value up to −5.2 kcal·mole^{-1} [62]. Complete optimization by Frisch *et al*. [63] at the *MP2* (*fu*) (i.e. all electrons are included in Möller-Plesset calculations) level with the *6-311++G(2d, 2p)* basis set led to the equilibrium distance of 2.911 Å and to the *BSSE*

corrected binding energies at −3.43 kcal·mole^{-1} (*SCF*) and −4.57 kcal·mole^{-1}(*MP2*) obtained with larger *6-311++G(3df, 3pd)* 150-function basis set and frozen core approximation. In the present studies (Table 4.3.1), the calculations at *MP2*(*fc*) (i.e. *1s* electron pairs on oxygen atoms were excluded from *MP2* calculations) level with the *6-311++G(3df, 3pd)* basis set lead to 2.90384 Å (R_{OO}), −3.419 kcal·mole^{-1} (*SCF*), −4.568 kcal·mole^{-1} (*MP2*),respectively, which closely correlates with the results of Frisch *et al*. [63]. Utilization of a relatively larger *aug-cc-pvtz* 184-*AO*'s basis set in the present studies at *MP2(fc)* level leads to 2.90719 Å (R_{OO}), −3.406 kcal·mole^{-1} (*SCF*), −4.710 kcal·mole^{-1}, respectively, with the full energy for the global minimum at −152.66624093383 Hartree. With the same computational settings, Xantheas et al. [64] have reported a value of −152.66624091 Hartree for the global minimum whereas the equilibrium distance and BSSE corrected binding energy was found at 2.91 Å and −4.71kcal·mole−1 in a good agreement with the present result. Concerning the complete basis set limits for the binding energy of the water dimer at the *MP2(fc)* level of theory with the Dunning's *aug-cc-pvxz* basis sets, Xantheas [65] recommends a value of −4.9 kcal·mole^{-1}, which is noticeably smaller than the accepted experimental value of −5.4 ±0.2 kcal·mole^{-1} but in somewhat better agreement with the corrected value, −5.2 kcal·mole^{-1} [62]. With a very large 262-function [13*s*,8*p*,4*d*,2*f*/8*s*,4*p*,2*d*] basis set Kim *et al*. [66] have obtained at the *MP2* level the following values: −152.79031 Hartree (total energy), 2.925 Å (R_{OO}), 122.3°(θ_a), −3.69 kcal·mole^{-1} (*SCF*), −4.66 kcal·mole^{-1} (*EMP2*), respectively, with the approximated value of ~ −5.0 kcal·mole^{-1} for the complete basis set limit, which is approaching the experimental value.

Table 4.3.1. The comparative table for the *ab initio* and *B3LYP* data for water monomer and dimer.

Parameter	Expt.	H_2O The *HF* limit is at −76.0675 [73]		
Electronic energy, Hartree	−76.4802 [66]	*MP2 (fc)/aug-cc-pvtz* (*C*$_{2V}$) E_{MP2} = −76.3289924 E_{SCF} = −76.0602820 *MP2(fc)/LBS* (*C*$_{2V}$) E_{MP2} = −76.3242865 E_{SCF} = −76.0585564	*B3LYP/aug* (*C*$_{2V}$) *E* = −76.4661967 *B3LYP/LBS* (*C*$_{2V}$) *E* = −76.4645116	*MP2(fc)/LBS at MP2(fu)/6-311++g(2d, 2p) Frisch* geom. [63]: $E_{MP2(fc)}$ = −76.32428 $E_{MP4(fc)}$= −76.33868 ; *MP2/aug-cc-pvtz* : E_{MP2} = −76.3289924 *MP2/aug-cc-pv5z* E_{MP2} = −76.3602282 ; [28,18,8,3/18,8,3] [67]: E_{MP2} = −76.40404 E_{SCF} = −76.06742 ; [13,8,4,2/8,4,2] [65]: E_{MP4} = −76.40706 E_{MP2} = −76.39118 E_{SCF} = −76.06756 ; *(fc) aug-cc-pvtz* at *Frisch* geom. [73]: E_{SCF}= −76.0606 E_{MP2} = −76.3290 E_{MP4} = −76.3436
ZPVE, kcal·mole^{-1}	13.18 [4]	13.4351$_{aug}$ 13.5560$_{LBS}$	13.3267$_{aug}$ 13.3702$_{LBS}$	[13,8,4,2/8,4,2] [65] 13.50$_{MP2}$
L(O−H), Å	0.957 [68] 0.9576257 [69]	0.96137$_{aug}$ 0.95887$_{LBS}$	0.96185$_{aug}$ 0.96114$_{LBS}$	*Frisch* geom.[63]: 0.9571 ; [13,8,4,2/8,4,2] [65]: 0.959$_{MP2}$
<H−O−H, °	104.50 [68] 104.51 [69]	104.11$_{aug}$ 104.04$_{LBS}$	105.08$_{aug}$ 105.04$_{LBS}$	*Frisch* geom.[63]: 104.34 ; [13,8,4,2/8,4,2] [65] 104.2$_{MP2}$
Dipole, D	1.855 [55]	1.8595$_{aug}$ 1.8993$_{LBS}$	1.8473$_{aug}$ 1.8897$_{LBS}$	[13,8,4,2/8,4,2] [65] 1.850$_{MP2}$
		Dimer		
		MP2/aug-cc-pvtz (*C*$_{2V}$) E_{el} = −152.666241 Hartree	*B3LYP/LBS* (*C*$_{2V}$) E_{el} = −193.2323224 Hartree	*B3LYP/LBS* (*C*$_{2V}$) [20] E_{el}=−193.232326 Hartree

By implementing the partial optimization (with the nonoptimized geometric parameters of individual water molecules) at the *MP2* level with the *BSSE* counterpoise correction and progressively improved basis sets with the basis functions located at the middle of the O−H bonds, van Duijneveldt and van Duijneveldt [58] have obtained the following data: −152.643549 Hartree (total energy at *MP2* level), 2.949 Å (R_{OO}), 124.8°(θ_a), 57.6°(θ_d), −3.69

kcal·mole^{-1} (*SCF*), −4.73 kcal·mole^{-1} (E*MP2*), respectively. Using the *SAPT* approach and the partial optimization of dimer (both monomer units assume the same vibrationally averaged geometry different however from the monomer equilibrium geometry by small extension of the O−H bond), Mas and Szalewicz [62] have estimated the interaction energy in the dimer at −5.05 kcal·mole^{-1}, which is in a very good agreement with the anharmonicity-corrected experimental value for the binding energy. Indeed, the vibrationally averaged geometry of the water monomer used by Mas and Szalewicz [62], r(O−H) = 0.9716257 Å and 104.69° for the ^H−O−H angle, appears to be reasonably closed to that obtained by a complete optimization in the present work on the *MP2(fc)/aug-cc-pvtz* level, W_{Donor}: $r(O-H)_{donor}$ = 0.96858 Å, $r(O-H)_{free}$ = 0.96041 Å, $W_{Aceptor}$: $r(O-H)_{ac}$ = 0.96227 Å and ^H−O−H at ~104.5° although shorter O−H distances in the present geometry are noted. A key difference between these two geometries resides in the optimal O−O distance, which is 2.953 Å in the Mas and Szalewicz geometry and 2.907 Å in the present geometry. It is obvious that the monomer units are different from each other, and exist in the geometries different from that of isolated water molecule especially with the respect to the length of $(O-H)_{donor}$ bond, which is larger than the equilibrium O−H distance in the isolated water molecule. Moreover, since the elongation of the $(O-H)_d$ bond appears as an essential attribute of the *HB* systems (at least from the spectroscopic point of view), it is logical to perform a complete optimization of the dimer including the optimization of the internal coordinates of both water molecules. From the viepoint of binding energies, the results of van Duijnevent and van Duijnevent [58], and Mas and Szalewicz [62] neglect the deformation energy of the monomers (see eqs.(4.2) and (4.28) above), which is usually a very small positive value at the *MP2* level, although it could be negative at either *SCF* or second-order correction levels. *MP2/aug-cc-pvtz* calculations using the Mas and Szalewicz geometry [62] reveal that the total deformation energy of both molecules is +0.271 kcal·mole^{-1} (+1.250 kcal·mole^{-1} at *SCF* level) measured with respect to the optimized monomer geometry at the *MP2/aug-cc-pvtz* level of theory or +0.237 kcal·mole^{-1} (*MP2*) and +1.630 kcal·mole^{-1} (*SCF*) using the monomer obtained by Polyanski *et al*. geometry [69]. On the other hand, the combined deformation energy at the minimum of the dimer, obtained in the present studies at the *MP2/aug-cc-pvtz* level, was determined to be +0.040 kcal·mole^{-1} for the *MP2* and +0.203 kcal·mole^{-1} for the *SCF* levels, respectively (see

Figure 4.3.5.). If the deformational energy at the *MP2* level is indeed negligible, the *SCF* deformation part is discernible and could play a role in the location of minimum, and contribute to the *SCF* limit of the binding energy. In this sense, the Mas and Szalevicz [62] and van Duijnevent and van Duijnevent [58] results are associated with the interaction energy rather than with the binding energy as discussed in the section 4.2.1.1. Regarding the *SCF* complete basis set limit for the interaction energy, Rybak *at el*. [70] and Szalewicz *et al*.[71] have reported the value of −3.73±0.05 kcal·mole^{-1} at the near-equilibrium geometry determined at the *SCF* level of theory with a very large basis set by Popkie *et al*.[72] while Feller [73] has reported a value of −3.55 kcal·mole^{-1} using the Frisch's geometry [63]. These were reported in literature with no further explanations for such significant differences in the *SCF* limit of the interaction energy in the water dimer. Feller extrapolated his *MP2* level results using the *aug-cc-pvxz* basis sets to the value of −4.95 ±0.05 kcal·mole^{-1} as the complete basis set limit, which appears to be identical with Xantheas's estimate of the binding energy [65].

An investigation of the influence of the basis set on the components of the interaction energy [58, 74, 75] (eqs.(4.20)-(4.24) above) reveals that ΔE^{HL}, or the interaction energy between undeformed *SCF* subsystems that includes the attraction of permanent dipoles (as a leading term) and the Heitler-London exchange repulsion, is very sensitive to the basis set and, in particular, to the exponent of the polarization function. This strong basis set dependence of the electrostatic component of the binding energy is primarily due to the sensitivity of the dipole moment of the monomer units to the basis set. Smaller basis sets such as the standard *6-31G(d,p)* (10*s*4*p*1*d*/4*s*1*p*) [*321/21*] split valence basis poorly describe the electrostatic part of the binding energy because of the significant overestimation of the dipole moments of monomer units [74]. Despite this unfavorable feature, the computationally efficient *6-31G(d,p)* basis set is utilized in the present studies for the calculations of the large water clusters. On the other hand, the basis sets constructed by Sadlej [75, 76] and White and Davidson [77] for the purposes of computationally effectiveness while preserving necessary accuracy should be definitely considered as better candidates for the calculations of larger-size water clusters. In contrast to the $\varepsilon^{10}_{\text{elst}}$ component of ΔE^{HL} (eq. 4.23), both the Heitler-London exchange energy $\Delta E_{exch}{}^{HL}$ and *SCF* deformation energy $\Delta E^{SCF-def}$ (eq. 23) contributions to the

binding energy appears weakly dependent on the basis-set quality [58]. Mas and Szalewicz [62] have reported the following partitioning of the interaction energy at the approximate optimum geometry: $\Delta E^{HL} = -1.76$ kcal·mole^{-1} decomposed into $\varepsilon^{10}_{\text{elst}} = -7.73$ kcal·mole^{-1} and $\varepsilon^{10}_{\text{exch}} = +5.97$ kcal·mole^{-1}; $\Delta E^{SCF-def} = -2.03$ kcal·mole^{-1} decomposed on $\varepsilon^{20}_{\text{ind,relax}} = -2.50$ kcal·mole^{-1}, $\varepsilon^{20}_{\text{exch-def}} = +1.29$ kcal·mole^{-1} and higher order exchange-deformation terms at −0.82 kcal·mole^{-1}, which brings the *SCF* ($\Delta E^{HL} + \Delta E^{SCF-def}$) interaction energy to −3.79 kcal·mole^{-1}. The higher order perturbation corrections within the *SAPT* approach add −1.26 kcal·mole^{-1} to the interaction energy while the second order correction on the *MP2* level was found at −1.13 kcal·mole^{-1} with the large *243*-function basis set bringing the total *MP2* level interaction energy to −4.92 kcal·mole^{-1}. The similarity in the values of the *SAPT* and *MP2* corrections indicate that the second-order *MP2* correction to the *SCF* energy provides a reasonable approximation to the total interaction energy. The largest attractive contributor to the *MP2* correction is the dispersion energy (see eqs.(4.19) and (4.20)), which was found by Mas and Szalewicz at −2.35 kcal·mole^{-1}. The *MP2/aug-cc-pvtz* (with the *184*-function basis set) calculations with the Mas and Szalewicz geometry give values of −3.750 kcal·mole^{-1} for the *SCF* interaction energy accompanied with the −1.039 kcal·mole^{-1} *MP2* correction, which brings the total *MP2* level interaction energy to −4.789 kcal·mole^{-1}. It is interesting to note that the induction term counterbalanced by the exchange-deformation appears as the largest contributor to the interaction energy in the water dimer closely followed by the Heitler-London interaction and the dispersion energy. Being three times larger than the induction attraction (associated with the $\varepsilon^{200}_{\text{indA}} + \varepsilon^{200}_{\text{indB}}$ terms in eq. (4.19)) and at nearly the same proportion of the dispersion attraction, $\varepsilon^{200}_{\text{disp,}}$ the electrostatic $\varepsilon^{10}_{\text{elst}}$ term is the leading component among the purely attractive terms. Therefore, the dispersion interaction is a significant component of the interaction energy in the water dimer.

In the following section the partial cross-sections of the *PES* of the dimer are discussed starting from the variation of the binding and the interaction energies along the O−O coordinate.

4.3.1.1 Cross-section of the Potential Energy Surface of Water Dimer along the O−O Coordinate

Firstly, within the framework of the supermolecular approach, the dependence of the total electron energy as a function of the O−O coordinate was determined relative to the minimum of the total electronic energy of fully optimized dimer on the *MP2/aug-cc-pvtz* level (without the BSSE correction). At each point along the O−O coordinate the dimer is optimized with respect to all other degrees of freedom. The computational results represented in Figure 4.3.2 (a, b) clearly shows that the *MP2* minimum at ~2.907 Å is shifted to a shorter O−O distance by ~ 0.1 Å with respect to the *SCF* minimum, which appears to be very flat in accord with the notation of the weak hydrogen bond in the dimer. It should be noted that the present *MP2* energy profile over the entire region of simulations can be fitted by the following Morse function, $4.562 \cdot [1 - \exp(1.556 \cdot (2.90719 - r))]^2$. The relative flatness of the *SCF* profile originates from the balance of the electrostatic and induction attractive effects on one side and the corresponding exchange and exchange-induction repulsive terms on another side (see the *SAPT* data of Mas and Szalewicz [62]). Therefore, the theoretical minimum and the shape of the potential energy curve near the minimum is determined by the second order correction on the *MP2* level with the main attractive contributor being the dispersion energy. In other words, since the *SCF* profile is flat at minimum (as expected), the location of latter on the O−O coordinate is defined primarily by the distance dependence of the dispersion energy and other higher order perturbation corrections, the leading attractive term of which varies proportionally to the r^{-6} within the framework of London oscillation model [28]. Another non-negligible component of the second order correlation part of the interaction energy, ε^{12} corresponding to the intramolecular correlation correction to the electrostatic interaction (see eq. (4.26)) was found to be repulsive near the minimum at the level of ~6% of the electrostatic attraction, $\varepsilon^{10}_{\text{elst}}$. Figure 4.3.2 (b) clearly shows that the *MP* second-order correction moves the minimum by ~ 0.1 Å towards the repulsive part of the *SCF* curve, which is defined primarily by the exchange repulsion. It is interesting to observe, however, that the experimentally determined value for intermolecular distance in the dimer (2.952 Å [58]) appears to be between the *MP2* and *SCF* minima, which presumably indicates the deficiency of the *MP2* correction, assuming that the *SCF* profile is reproduced more precisely. Rybak *et al.* [70] have

found that only $\varepsilon^{20}_{\text{exch-disp}}$ and $\varepsilon^{22}_{\text{disp}}$ terms are discernable, which are both at comparable absolute value but with the former being repulsive while the latter attractive. The latter term, $\varepsilon^{22}_{\text{disp}}$, does not present on the *MP2* level of theory, which therefore indicates the deficiency of the *MP2* correction.

(a)

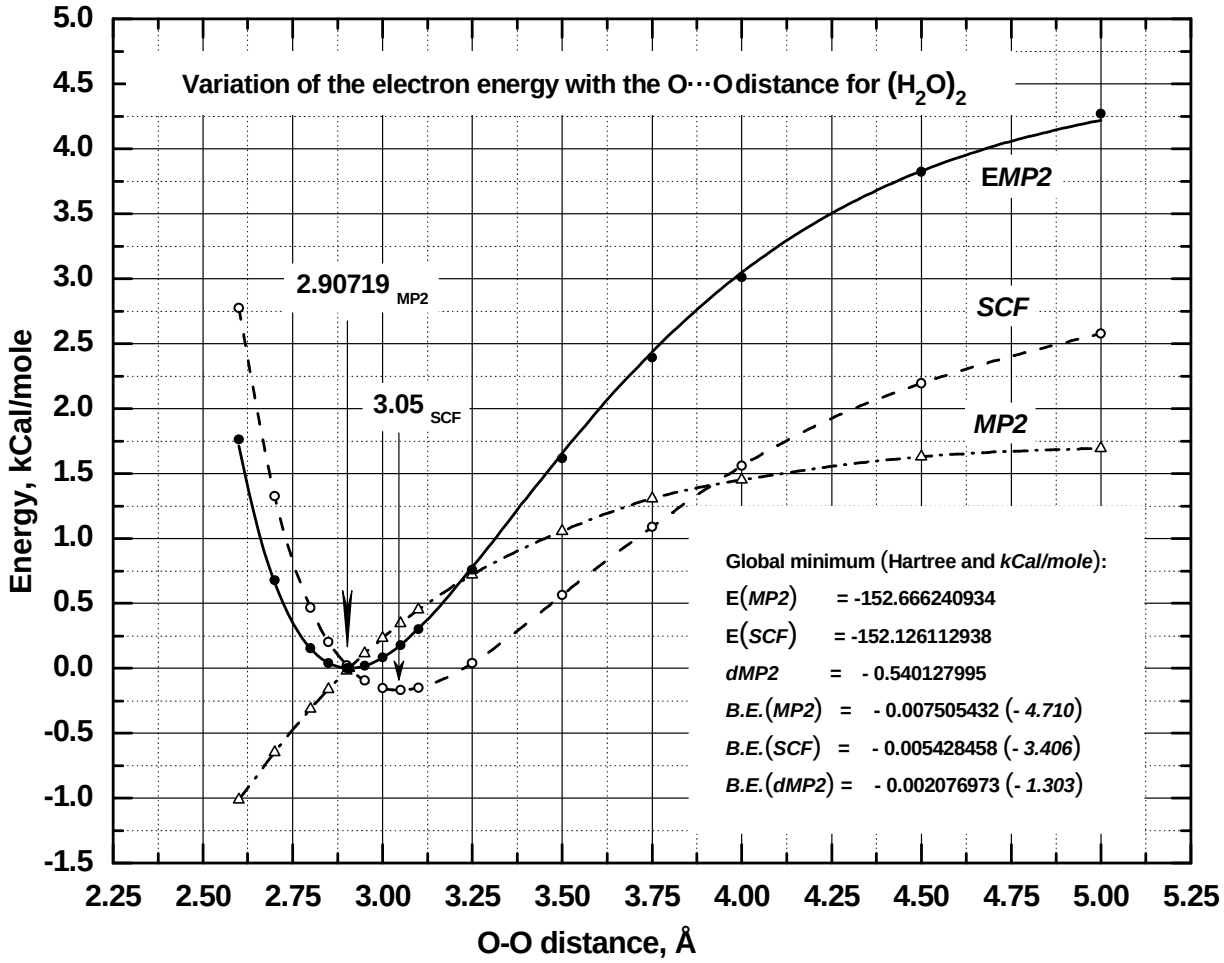

(b)

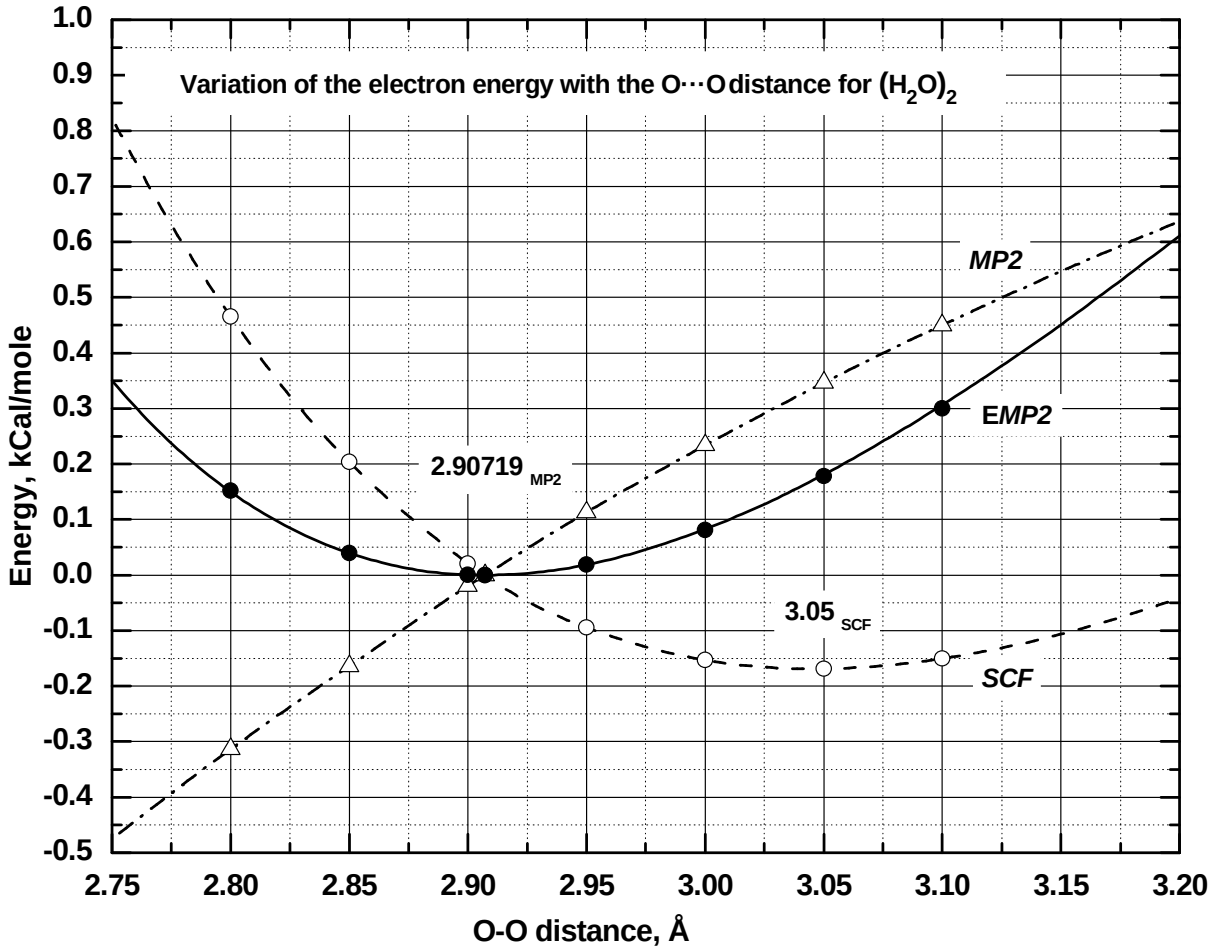

Figure 4.3.2. Potential energy profile for the water dimer along the O−O coordinate. The calculations were performed at the *MP2/aug-cc-pvtz* level of theory. The data points are shown without the *BSSE* correction. (a) Wide and (b) narrow range of the O−O distances. SCF, MP2 and EMP2 designate the *HF* energy, second-order *MP* correction and total *MP2* energy.

If the previous discussion has considered the variation of the total electron energy of the complex with respect to the minimum (i.e. no partitioning the system on the monomer units was considered), the next Figure 4.3.3 represents the variation of binding and interaction energies along the O−O coordinate with respect to the combined energy of the two monomers separated infinitely (i.e. with respect to the total energy of a single monomer taken twice). The binding and interaction energies of dimer were calculated in accord with eq.(4.28), in other

words the counterpoise correction has been employed in the calculation of the binding energy, which is given with respect to the electronic energy of the monomers at their optimum geometry. Firstly, a substantial difference between the binding and interaction energies at the *SCF* level should be noted, which is due to the discernible contribution of the deformation energy to the *SCF* binding energy.

(a)

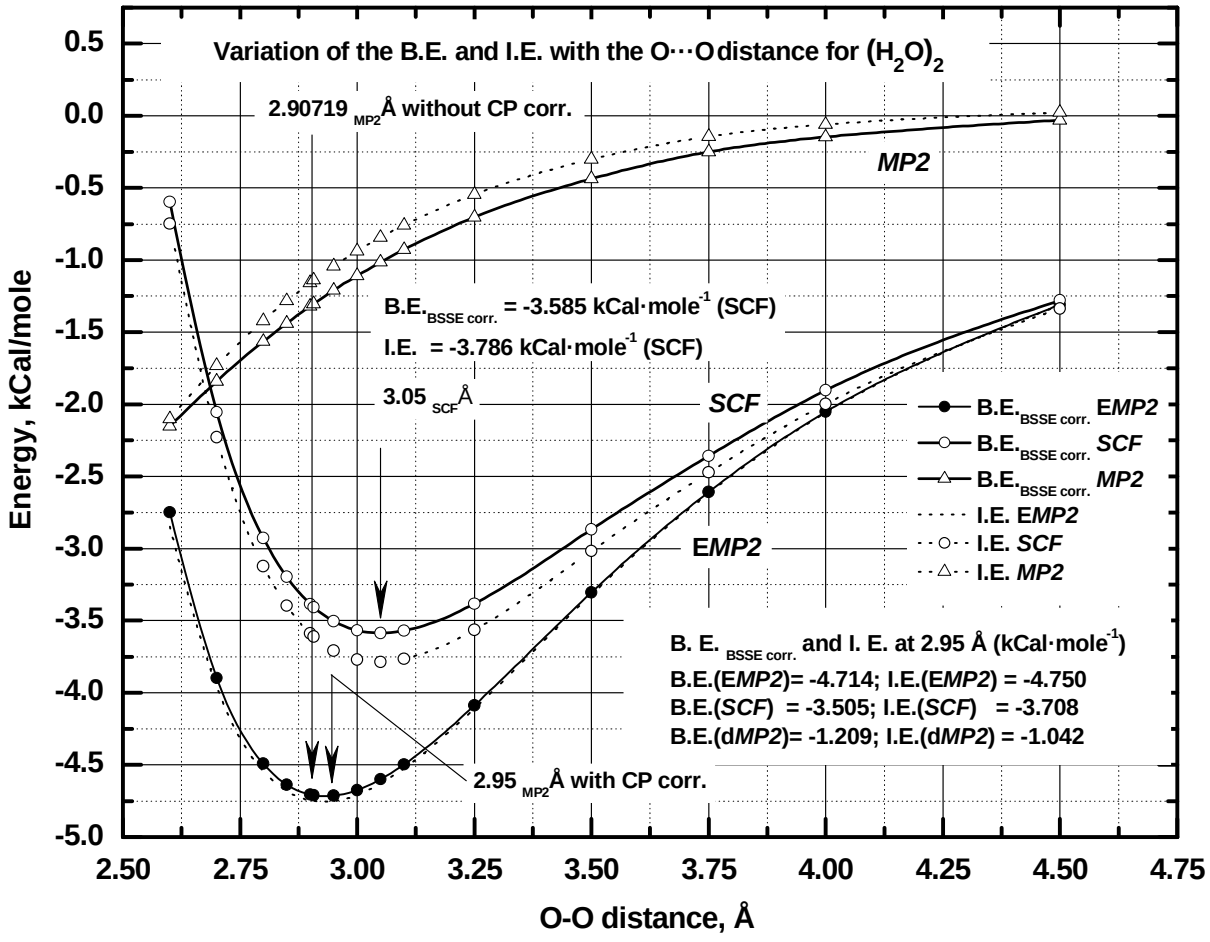

(b)

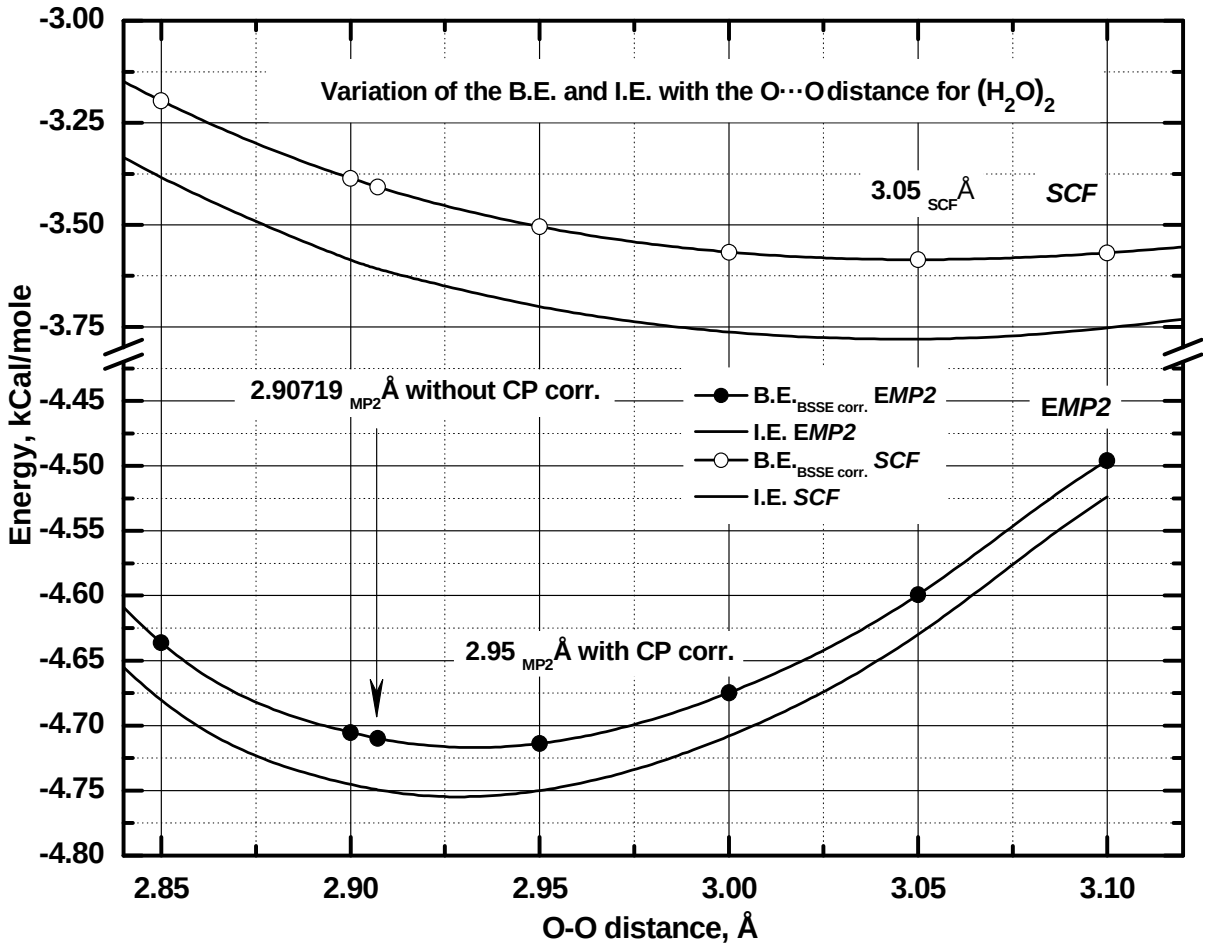

Figure 4.3.3. Profile of the *BSSE* corrected binding and interaction energies of water dimer along the O···O coordinate at the*MP2/aug-cc-pvtz* level of theory. (a) Wide and (b) narrow range of the variation of O−O distance.

On the other hand, it appears that this difference become smaller at the *MP2* level (Figure 4.3.3 (b)) due to the opposite sign contribution of the deformation energy to the second-order correlation correction, as it is evident from the Figure 4.3.3 (a). Indeed, if, at the minimum near ~2.95 Å, the *MP2* binding energy (−4.714 kcal·mole^{-1}) is found to be relatively close to the *MP2* interaction energy (−4.750 kcal·mole^{-1}). The *SCF* binding (−3.505 kcal·mole^{-1}) and interaction (−3.708 kcal·mole^{-1}) energies are found to be discernibly different. Secondly, the transition from the O−O profile of the *PES* obtained by the optimization of the

energy of entire complex (Figure 4.3.2) to the O−O profiles of the binding and interaction energies leads to a shift of the minimum to a larger separation distance as it appears in Figure 4.3.3 (b). The minimum of the total electron energy found at 2.90719 Å can be associated with the *BSSE*-corrected value of binding energy (−4.710 kcal·mole^{-1}) and the interaction energy (−4.7493 kcal·mole^{-1}) whereas the O−O profiling of the binding and interaction energies reveals that their respective minima should be allocated at the larger separation distance because at 2.95000 Å these values are at −4.714 kcal·mole^{-1} and at −4.750 kcal·mole^{-1}, respectively. The main reasons for such a shift could be attributed to the flatness of the potential surface in the region of minimum and to the dependence of *BSSE* correction on the separation. Indeed, Figure 4.3.4 shows that the counterpoise correction to the binding energy is not small near the minimum and more importantly it varies with the O−O separation distance. Therefore, the equilibrium geometry of the system depends on the *BSSE* correction that becomes (physically atificaial) force variable in the minimization procedure. It is evident from Figure 4.3.4 that the gradient of the *BSSE* correction is not zero at the point of the classical minimum (2.90719 Å), where the electron energy of the system is at minimum and the gradients along all spatial coordinates are zeros. If, as in the present case, the classical minimum is flat, i.e. the gradients are close to zero over a discernible spatial region, the gradient of the *BSSE* correction could become a non-negligible factor creating an additional force on the particle constituting the system in question. The origin of this force resides in the incompleteness of the mathematical basis used for the wave function expansion, and from this prespective is purely a computational factor. To the best of the present author knowledge, there is no straightforward way to include this spatial dependence of the *BSSE* correction directly in the minimization subroutine within the Gaussian set of programs. From a physical point of view, the minimum of the electron energy of the system would be the only meaningful representation of the properties of real system. However, the mathematical incompleteness of the basis leads to the different computational reality when the minimization of the total energy of the complex provides only one possible representation of the properties of the multimolecular complex whereas the minimization of the *BSSE* corrected binding energy or minimization of the interaction energy provides different computational representation of the system.

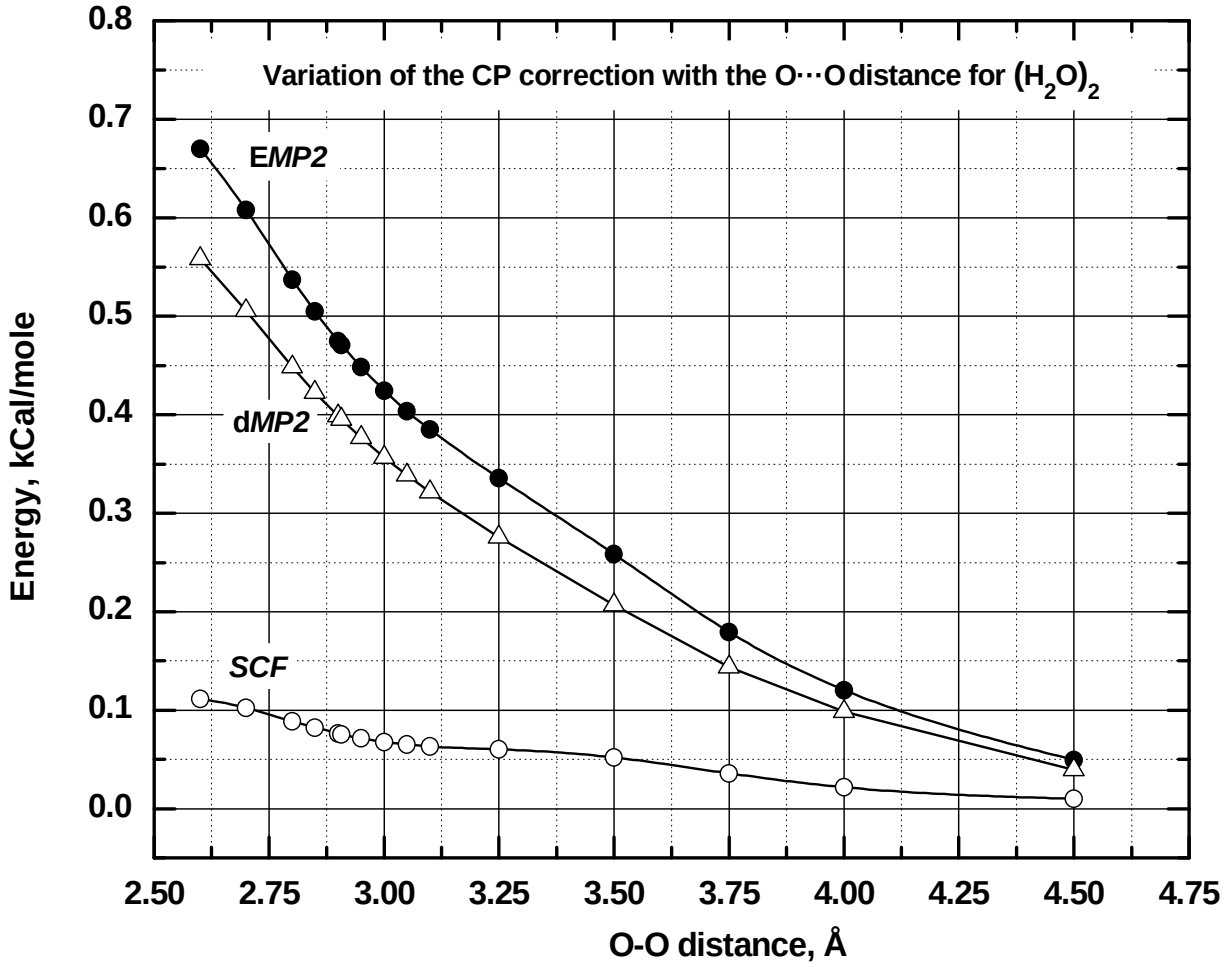

Figure 4.3.4. Profiles of the *BSSE* counterpoise correction for the water dimer along the O−O coordinate at the *MP2/aug-cc-pvtz* level.

Conventionally, the preference of one representation over another is established by comparing the computational and the experiment results, which appears favoring in many cases the counterpoise correction approach [38, 40, 62, 66, 70]. In the case of the water dimer, such a comparison does not lead to the definitive resolution taking in consideration a large uncertainty in the experimental and computational data. Furthermore, the mismatch between minima of the binding and interaction energies is expected according to eq. (4.28). This expectation is associated with the dependence of the deformation energies of two water molecules on the separation distance shown in Figure 4.3.5

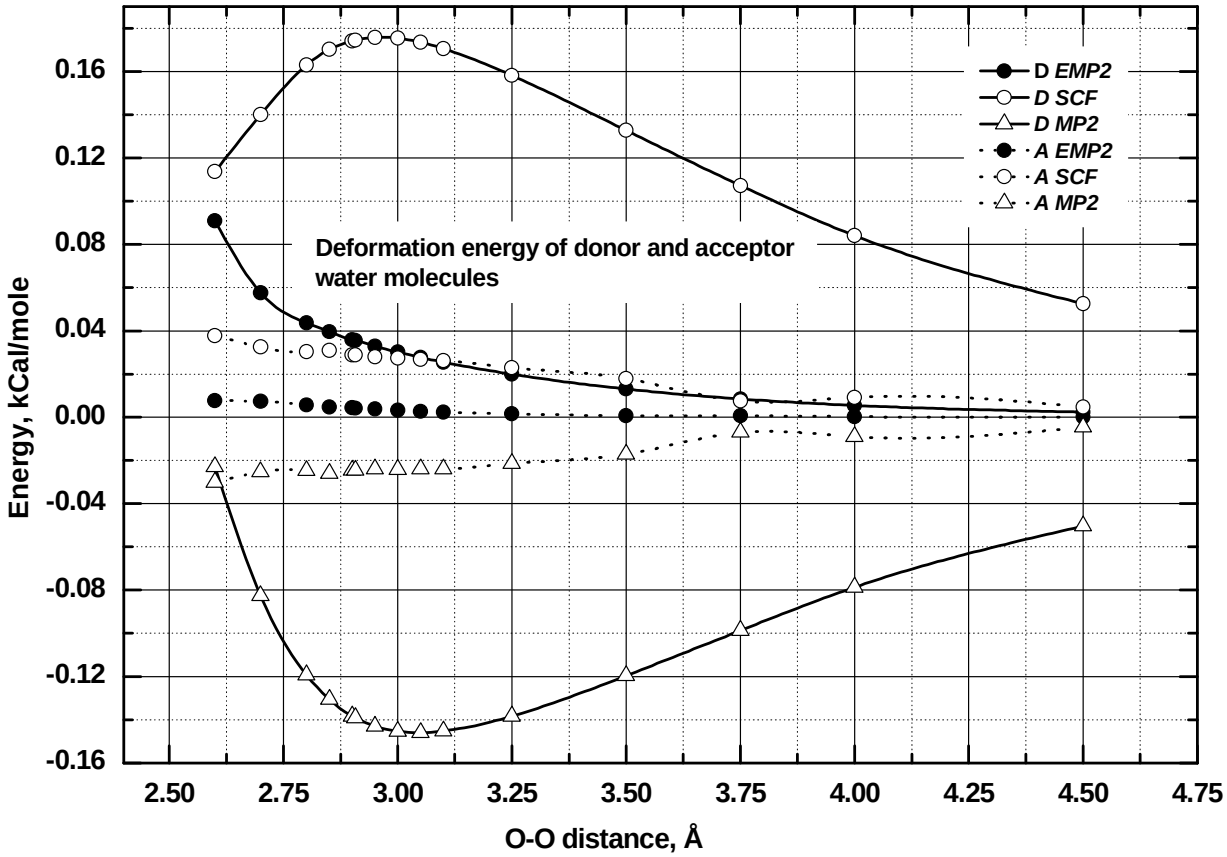

Figure 4.3.5. Profiles of the deformation energies of two water monomers in the dimer along the O···O coordinate at*MP2/6-311++g(3df, 3pd).*

It appears that the deformation of the donor is not negligible in the area of minimum and diminishes with the distance. The latter could contribute to the shift of the binding energy minimum further to a larger intermolecular distance relative to the minimum of the interaction distance. The contribution of the deformation energy to the *CP* corrected binding energy according to eq. (4.28) is physically meaningful, because the deformation of monomers as a physico-chemical molecular process should accompany the formation of multimolecular systems. It appears that the shift in the potential minimum from smaller to a larger separation distance upon the inclusion in computational analysis of the *CP* leads to a better apparent agreement with the experimental value. Furthermore, the comparison of the corrected and non-corrected values for the potential well depth also favours the counterpoise procedure, although there is no general agreement on this issue. In this sense, the computational results

are also subject of the errors and uncertainties that are difficult to estimate and correct.

Finally, the change in the geometry of the dimer as a function of the O−O distance is shown in Figure 4.3.6. Firstly, it should be noted that the relative orientation of two water molecules changes with the O−O distance from that shown in Figure 4.3.1, where the oxygen atom of acceptor is located outside the openings of H−O−H angle of the donor, to the arrangement where O atom of the acceptor is within the opening of HOH angle of the donor. This tendency is in agreement with the observation that C_{2V}-symmetry configuration of the dimer with double *HB* is a transition state. The rearrangement takes place when the molecules with the almost linear $O_{acceptor}\cdots(H-O)_{donor}$ arrangement are separated by 3.75-4 Å. As molecules moves closer than 3.75 Å, the linear *HB* arrangement becomes unstable and H atom of the donor is pushed out from the O−O line. The Van der Waals (VdW) minimum for the water dimer according to the *TIP4P* model is located at ~3.540 Å indicating that the deviation of the *HB* bond from the linear configuration at short distances is due to the VdW repulsion, which originates from the exchange effects. Accordingly, the bending angle of acceptor decreases with the shortening of separation. The present calculations confirm that the extension of the $(H-O)_{donor}$ bond of donor is an importance signature of the *HB*. Indeed, as Figure 4.3.6 shows that the length of $(H-O)_{donor}$ bond increases with the shortening of separation until it reaches maximum near the potential minimum.

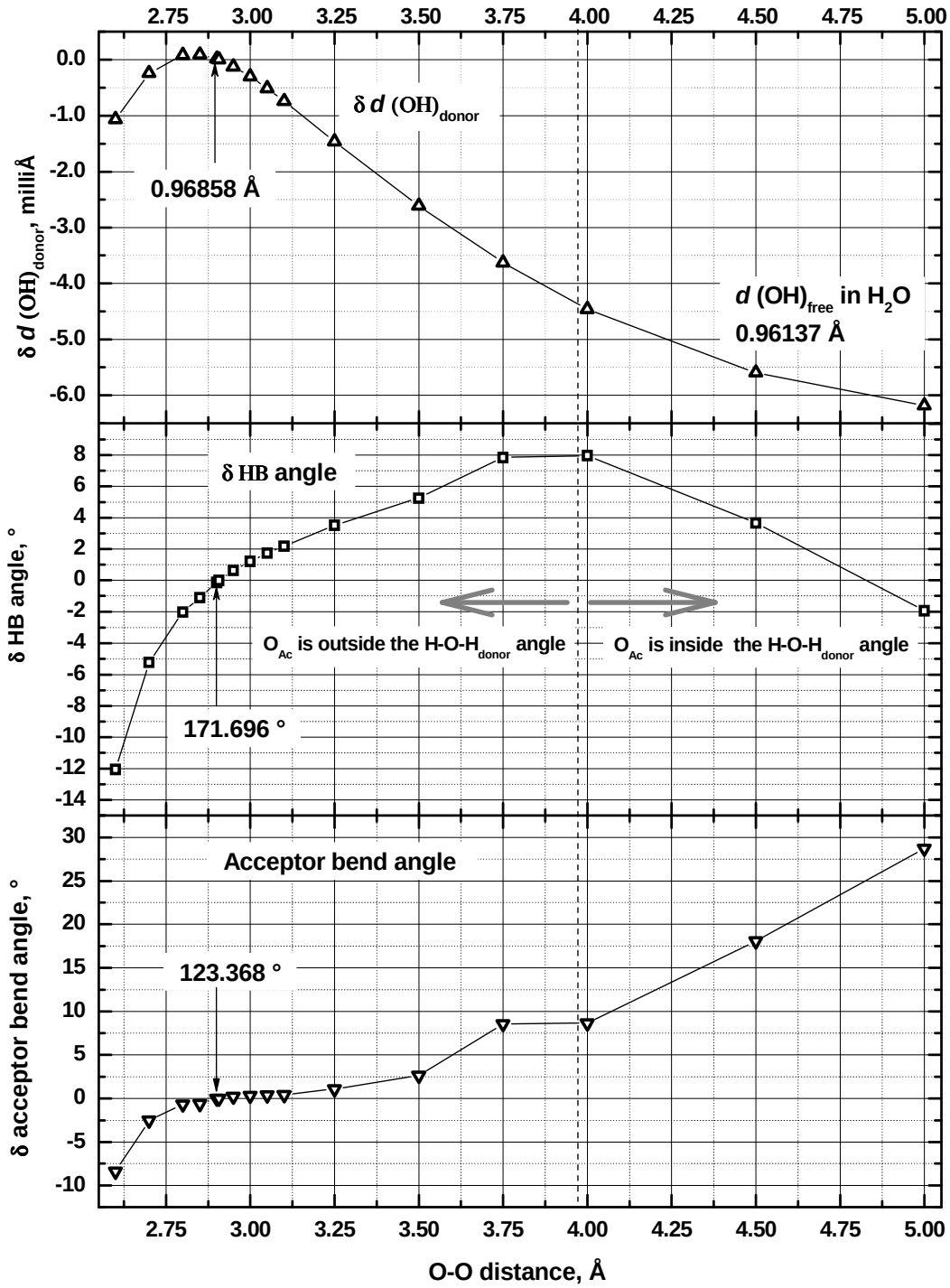

Figure 4.3.6. The dependence of the $(O-H)_d$ distance, the O···H−O *HB* angle, and the acceptor bending angle in the water dimer on the intermolecular O···O distance.

4.3.2 Water Tetramers

An analysis of the water tetramer family reveals the main structural and energetic features that are also found in the small water clusters W_3-W_6. The most noticeable structural feature of isolated water clusters, which controls the existence of particular configuration, resides in double donor (d^2) local arrangement. The double donor water molecule bears significant negative charge due to the donation from two *HB* neighbors. This negative charge attracts the non-compensated positive charge on OH *DB* (OH dangling bond) located on the remote water molecules. As a consequence of this attraction the configuration changes such that additional *HB* will be established between the d^2 and OH *DB* by "internal reaction": d^2 + OH (*DB*)→*HB*. The sequential configurations are found to be the most stable among all others possible local minima for the water clusters of a given size as shown in Table 4.3.2 for W_4. If the initial configuration includes the d^2 and OH *DB* such configuration is found unstable. This latter configuration converts to that with a larger number of *HB'*s. Therefore, the distorted *HB'*s are formed by joint of d^2 and OH *DB*. For example, a tetragonal configuration *T-HB5* with a distorted network of the *HB'*s shown in the second row of Table 4.3.2 is formed as a result of the excitation of a stable sequential configuration *Ring I SR4-HB4* if the molecule W^3 attains the d^2 configuration. This W^3 reconfiguration triggers a structural collapse: the d^2 W^3 will be approached by the dangling bond of W^1 forming the tetragonal compact structure.

It is appropriate to clarify the notation of the conformational space for a given configurational minimum. A sequential tetragonal ring could serve as a simple example of this notation. Indeed, both complexes a *Ring I SR4-HB4* $(da)^{4[-+-+]}$ and a *Ring II SR4-HB4* $(da)^{4[+--+]}$ belong to the same configuration, which defines a sequence of the hydrogen bonds. On the other hand, it is obvious that these structures do not coinside because the *DB*s are oriented differently with respect to each other and to the ring plane. A specific orientation of the *DB*s with respect to each other and to the ring is called a conformation. The conformational space "diffuses" the energy of a particular configuration over a range of energies, which depends on the dipole-dipole interaction of these *DB*s.

Figure 4.3.7 demonstrates the effect of cluster geometry on the energy properties of the W_1-W_4 set calculated at the *B3LYP* and *TIP4P* levels. It is evident that the binding energy of a

sequential ring configuration is the largest. The different orientation of dangling bonds within a given configuration does not significantly influence the total binding energy despite apparent dipolar repulsion between OH bonds (see Table 4.3.2). The binding energy for the non-sequential configurations such as a tetrahedron is discernibly smaller as well as that for the configurations with multiple double donors and double acceptors.

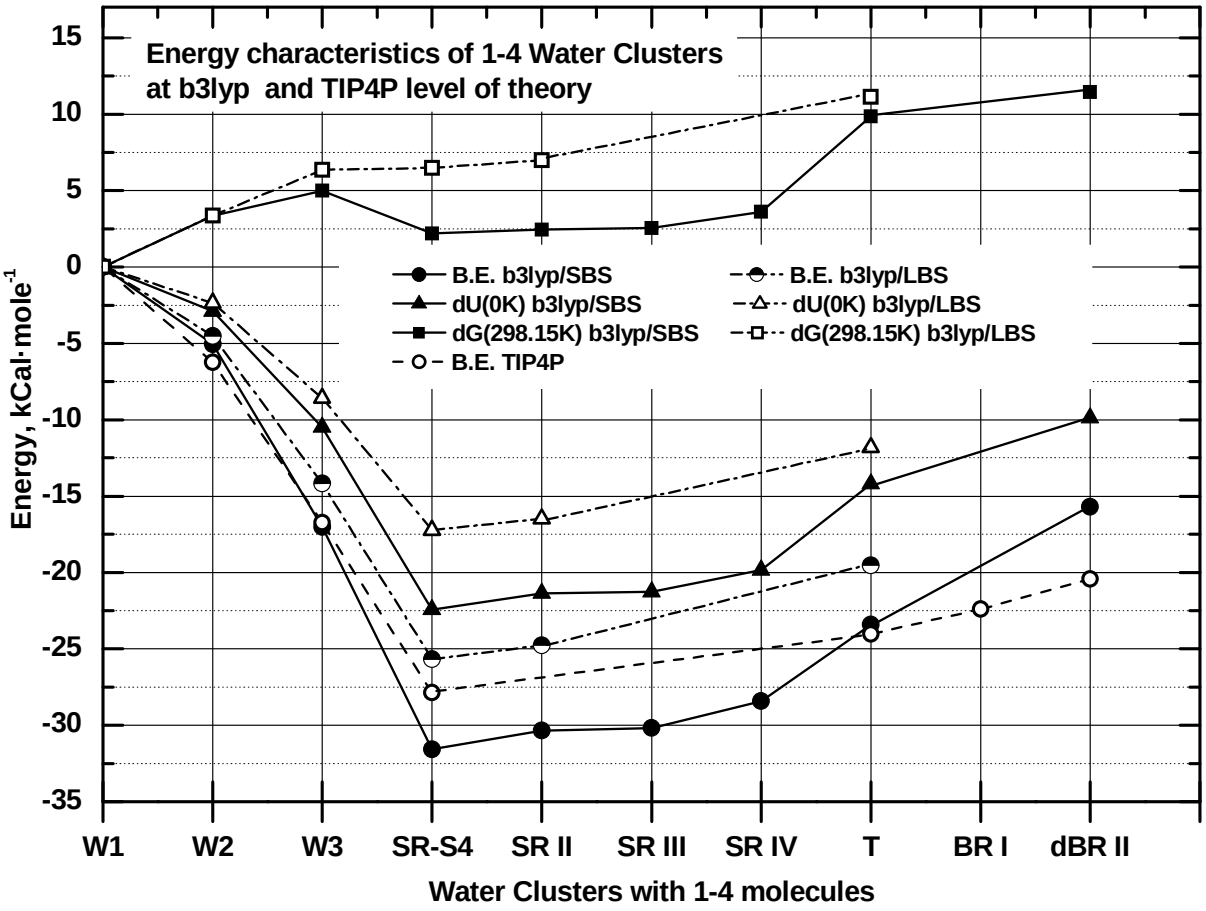

Figure 4.3.7. Binding energies and thermodynamic functions for the water tetramer clusters. Binding energies with BSSE corrections, ΔU*0K (the thermodynamic energy of the formation of a complex at 0 K), and ΔG*298.15K (the standard Gibbs energy of the formation of a complex at 298.15K) for the water clusters of 1-4 molecules at their local minima and transition states calculated at *B3LYP/6-31G(d,p) (SBS), /6-311++G(3df, 3pd) (LBS)* and classical *TIP4P* levels of theory.

The notations for the cluster's states are given in Table 4.3.2. The energetic for the W2 cluster at *B3LYP/SBS* in Figure 4.3.7 is given for the *Cs* distorted geometry, which appears to be a first order transition state (*TS*) with this basis set.

Table 4.3.2. Local minima and transition states in the *HB* systems with *4* water molecules. The computations are performed at the *B3LYP* level of theory with the *6-31G(d,p) (SBS)* and the *6-311++G(3df, 3pd) (LBS)* basis sets and with the classical *TIP4P* potential. The energies, distances and angles are given in [kcal·mole^{-1}], [Å] and [°] units. L and ΔL designate the distance and the change of the distance between entities in question. ΔZPVE stands for the zero-point vibrational energy contribution to the binding energy, B.E.. $\Delta G^{*}_{298.15}$ represents the standard Gibbs energy of the complex formation at 289.15 K. $HB_{ang.}$ and /O−O−$O_{ang.}$ designate the hydrogen bond angle O^{*}-H···O^{*} and the angle between three oxygen atom connected by the chain of *HB*'s. The interaction energy, pairwise, tri and multibody contributions to the interaction energy are indicated by appropriate subscripts. For classical TIP4P calculations the total interaction energy and electrostatic interaction energies are reported.

Structure / Symmetry	B.E.$_{BSSE\ corr.}$	B.E. $_{BSSE\ corr.}$ + ΔZPVE /$\Delta G^{*}_{298.15}$	TIP4P	L (O_1−O_2) /L(O_1−O_3) /L(O_2−O_4)	ΔL (O−H)$_{Donor}$	$HB_{ang.}$ /O−O−$O_{ang.}$
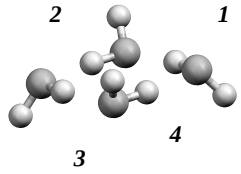 Sequential Ring / *SR4-HB4* (*da*)$^{4[-+-+]}$ / S_4 distorted	−31.57$_{SBS}$ −4.87 $_{W1W2}$ −1.67 $_{W1W3}$ −22.80$_{Pair}$ −9.87$_{Tri}$ −0.76$_{Tetra}$	−22.42$_{SBS}$ / +3.805$_{SBS}$	−27.87$_{Total}$ −36.07$_{Electr}$ W_1W_2 −6.06$_{Total}$ −8.18$_{Electr}$ W_1W_3 −1.80$_{Total}$ −1.67$_{Electr}$	2.69624$_{SBS}$ /3.81067$_{SBS}$ 2.74086$_{LBS}$ /3.87604$_{LBS}$ 2.722$_{TIP4P}$ /3.840 $_{TIP4P}$	0.02785$_{SBS}$ 0.02194$_{LBS}$	169$_{SBS}$ / ~90$_{SBS}$ 168$_{LBS}$ / ~90$_{LBS}$ 171$_{TIP4P}$ / ~90 $_{TIP4P}$
	−25.67$_{LBS}$ −4.18 $_{W1W2}$ −1.36 $_{W1W3}$ −19.43 $_{Pair}$ −6.84 $_{Tri}$ −0.63 $_{Tetra}$	−17.23$_{LBS}$ / +8.102$_{LBS}$				

Structure / Symmetry	B.E.$_{BSSE\ corr.}$	B.E. $_{BSSE\ corr.}$ + ΔZPVE /$\Delta G^{*}_{298.15}$	TIP4P	L (O_1−O_2) /L(O_1−O_3) /L(O_2−O_4)	ΔL (O−H)$_{Donor}$	HB$_{ang.}$ /O−O−O$_{ang.}$
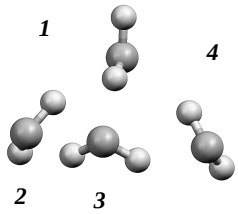 Tetrahedron *I* *T-HB5* (da^2−da−d^2a−da) / C_S distorted at *B3LYP* / C_1 at *TIP4P*	−23.41$_{SBS}$ −4.81$_{W1W2}$ −4.07$_{W1W3}$ −3.91$_{W2W3}$ 1.45$_{W2W4}$ −20.06$_{Pair}$ −4.56$_{Mutli}$ −19.54$_{LBS}$ −4.06$_{W1W2}$ −3.66 $_{W1W3}$ −3.24 $_{W2W3}$ 1.03 $_{W2W4}$ −17.22$_{Pair}$ −2.99$_{Mutli}$	−14.20$_{SBS}$ / +11.484$_{SBS}$ −11.80$_{LBS}$ / +12.743$_{LBS}$	−24.02$_{Total}$ −31.29$_{Electr}$ W_1W_2 −4.96$_{Total}$ −6.28$_{Electr}$ W_1W_4 −5.38$_{Total}$ −6.49$_{Electr}$ W_1W_3 −5.45$_{Total}$ −7.83$_{Electr}$ W_2W_3 −4.99$_{Total}$ −6.18$_{Electr}$ W_3W_4 −3.97$_{Total}$ −5.39$_{Electr}$ W_2W_4 0.73$_{Total}$ 0.88$_{Electr}$	2.80919$_{SBS}$ /2.64482$_{SBS}$ /4.01829$_{SBS}$ 2.88874$_{LBS}$ /2.71183$_{LBS}$ /4.27095$_{LBS}$ 2.800$_{TIP4P}$; 2.826$_{TIP4P}$ /2.703$_{TIP4P}$ /3.591$_{TIP4P}$	W_1 0.03221$_{SBS}$ 0.02444$_{LBS}$ W_2 0.01129$_{SBS}$ 0.00864$_{LBS}$ W_3 0.01251$_{SBS}$ 0.00819$_{LBS}$	W_1W_2 147 $_{LBS}$ / 95$_{W2W1W4}$ / 62$_{W2W1W3}$ /56$_{W1W2W3}$ 150 $_{TIP4P}$ / 79$_{W2W1W4}$ / 61$_{W2W1W3}$ /58$_{W1W2W3}$ W_1W_3 154 $_{LBS}$ 158 $_{TIP4P}$ W_2W_3 142 $_{LBS}$ / 94 $_{W2W3W4}$ 146 $_{TIP4P}$ / 80$_{W2W3W4}$
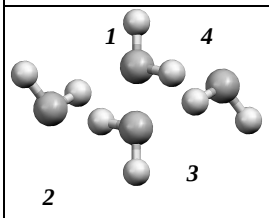 Sequential Ring *II* *SR4-HB4* (da)$^{4[+\,+\,-\,-]}$ / C_i distorted	−30.35$_{SBS}$ −4.09$_{W1W2}$ −4.88 $_{W1W4}$ −2.00 $_{W1W3}$ −1.93$_{W2W4}$ −21.86$_{Pair}$ −10.33$_{Mutli}$	−21.37$_{SBS}$ / +4.075 $_{SBS}$	converts to (da)$^{4[-\,+\,-\,+]}$	2.70363$_{SBS}$ /2.69776$_{SBS}$ /3.81106$_{SBS}$ /3.82756 $_{SBS}$ 2.75207$_{LBS}$ /2.74225$_{LBS}$ /3.88560$_{LBS}$ /3.88456$_{LBS}$	W_1 0.02744 $_{SBS}$ W_2 0.02720$_{SBS}$ W_1 0.02170$_{LBS}$ W_2 0.02101$_{LBS}$	W_1W_2 168$_{SBS}$ // $5^d{}_{SBS}$ W_1W_4 170$_{SBS}$ / ~90$_{SBS}$ W_1W_2 166$_{LBS}$ // $7^d{}_{LBS}$ W_1W_4 169$_{LBS}$ / ~90$_{LBS}$
	−24.76$_{LBS}$ −3.67$_{W1W2}$ −4.19$_{W1W4}$ −1.49$_{W1W3}$ −1.47$_{W2W4}$ −18.69$_{Pair}$ −7.26$_{Multi}$	−16.48$_{LBS}$ / +8.622$_{LBS}$				

Structure / Symmetry	B.E. $_{BSSE\ corr.}$	B.E. $_{BSSE\ corr.}$ + ΔZPVE /$\Delta G^{*}_{298.15}$	TIP4P	L (O_i−O_j)	ΔL (O_D−H)	$HB_{ang.}$ /O−O−$O_{ang.}$ /Dihedral H−O−O−H
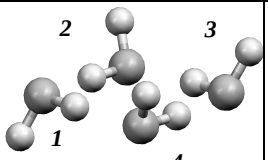 Sequential Ring *III* *SR4-HB4* $(da)^{4[-+++]}$ / C_1	−31.18$_{SBS}$ −4.91$_{W1W2}$ −4.83$_{W1W4}$ −4.18$_{W2W3}$ −4.12$_{W3W4}$ −1.96$_{W1W3}$ −1.67$_{W2W4}$ −21.67$_{Pair}$ −10.34$_{Multi}$	−21.25$_{SBS}$ / +4.168 $_{SBS}$	converts to $(da)^{4[-+-+]}$	W_1W_2 2.69814$_{SBS}$ W_1W_4 2.69581$_{SBS}$ W_2W_3 2.70558$_{SBS}$ W_4W_3 2.70493$_{SBS}$ W_1W_3 3.81763$_{SBS}$ W_2W_4 3.82085 $_{SBS}$	W_1 0.02756 $_{SBS}$ W_2 0.02754 $_{SBS}$ W_3 0.0268 $_{SBS}$ W_4 0.02677 $_{SBS}$	W_1W_2 170 $_{SBS}$ W_2W_3 168$_{SBS}$ W_3W_4 168$_{SBS}$ W_1W_4 170$_{SBS}$ / ~90$_{SBS}$
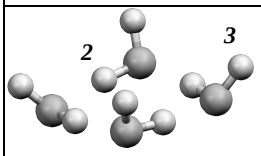 Sequential Ring *IV* *SR4-HB4* $(da)^{4[++++]}$ / C_i distorted	−28.42$_{SBS}$ −4.14$_{W1W2}$ −4.31$_{W1W4}$ −1.71$_{W1W3}$ −1.61$_{W2W4}$ −20.22$_{Pair}$ −9.98$_{Multi}$	−19.82$_{SBS}$ / +5.236$_{SBS}$	converts to $(da)^{4[-+-+]}$	2.70374$_{SBS}$ /2.71076$_{SBS}$ /3.79147$_{SBS}$ /3.84444$_{SBS}$	W_1 0.02577$_{SBS}$ W_2 0.02620$_{SBS}$	W_1W_2 168$_{SBS}$ W_1W_4 168$_{SBS}$ / 89$_{SBS}$; 90$_{SBS}$ W_1W_2 // 5^{d}_{SBS} W_1W_4 // 23^{d}_{SBS}
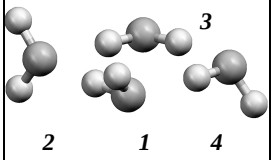 Bifurcated Ring *I* *BR4-HB4* $(da)^{+}(a)^{2+-}(d)^{2}(da)^{-}$ / C_1 at *TIP4P*	converts to *SR4-HB4* $(da)^{4[+++-]}$		−22.39$_{Total}$ −28.72$_{Electr}$ W_1W_2 −5.60$_{Total}$ −7.08$_{Electr}$ W_1W_4 −6.14$_{Total}$ −8.11$_{Electr}$ W_2W_3 −5.95$_{Total}$ −7.44 $_{Electr}$ W_3W_4 −4.28$_{Total}$ −5.93$_{Electr}$ W_1W_3 +0.25$_{Total}$ +0.40$_{Electr}$ W_2W_4 −0.65 $_{Total}$ −0.55$_{Electr}$	 2.781 2.735 2.782 2.763 3.702 4.108		

Structure / Symmetry	B.E. $_{BSSE\ corr.}$	B.E. $_{BSSE\ corr.}$ + ΔZPVE /$\Delta G^{*}_{298.15}$	TIP4P	L (O_i−O_j)	ΔL (O_D−H)	$HB_{ang.}$ /O−O−$O_{ang.}$ /Dihedral H−O−O−H
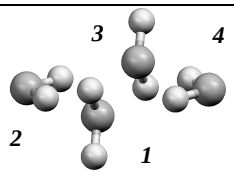 Doubly Bifurcated Ring *II* *dBR4-HB4* $(a)^2$−$(d)^2$−$(a)^2$−$(d)^2$ / D_{2h} Transition State of the second order at *B3LYP/SBS*	−15.69$_{SBS}$ −5.20 $_{W1W2}$ +1.60 $_{W2W4}$ +1.74$_{W1W3}$ −17.47$_{Pair}$ +1.62$_{Multi}$	−9.87$_{SBS}$ / +13.069$_{SBS}$	−20.42$_{Total}$ −25.79$_{Electr}$ W_1W_2 −6.15$_{Total}$ −7.55$_{Electr}$ W_2W_4 +2.67$_{Total}$ +2.81$_{Electr}$ W_1W_3 +1.50$_{Total}$ +1.59$_{Electr}$	 W_1W_2 2.98206$_{SBS}$ 2.790$_{TIP4P}$ W_2W_4 4.21424$_{SBS}$ 3.695$_{TIP4P}$ W_1W_3 4.22030$_{SBS}$ 4.182$_{TIP4P}$	W_2 0.00394$_{SBS}$	W_1W_2 170$_{SBS}$ 174$_{TIP4P}$ / ~90$_{SBS}$ ~83$_{W2W1W4}$ ~97$_{W1W2W3}$

4.3.3 Comparative Analysis of Small Water Clusters

After a detail review of the water tetramers configurations in the preceding section, let us compare the structural and energy properties of two classes of the water clusters: open monocyclic sequential clusters shown in Figure 4.3.8 and closed compact water clusters shown in Figure 4.3.9. A regular hexagon of *S6* symmetry is shown in the left column of Figure 4.3.8 is a basic structural element of the hexagonal, *Ih*, and cubic, *Ic*, ices, ice *II* and low-density noncrystalline media. A puckered form of regular pentagon of C_1 symmetry shown in the central column of Figure 4.3.8 appears to be a structural element of the ice *III/IX*.
The hydrogen bond length show a characteristic contraction in a sequence tetragon-pentagon-hexagon due to the multi-body induction effects in the hydrogen-bond network discussed in section 4.2.2. A main bonding factor among multi-body terms is a tri-body interaction in the sequential 1-2-3 *HB* chain: *da-da-da*. As evident from Figure 4.3.8, the tri-body contribution can reach up to 30% of the total interaction energy. The hydrogen bond is strongest and shortest in the hexagon because of the longest sequential chain: *6 da* units. This noticeable contraction of the hydrogen bond length is a direct consequence of the cooperation effect. Indeed, the pairwise 1-2 interaction energy decreases from a tetramer to hexamer, i.e. a W_2

dimer isolated from the rest of the cluster attains larger intermolecular separation distance. However, the presence of neighboring molecule causes the contraction of the water *HB* network.

The 1-3 distances show a characteristic geometric dependence on the number of apexes in polygon. A tetragonal configuration becomes a good candidate for the structural element of the high-density noncrystalline media. This result follows directly from the cosine theorem as shown in Figure 4.3.8 (bottom row).

The presence of double donor in the open polygonal structure will lead to the collapse of the network towards multicycle 3-dimentional configurations. This property of water clusters provides a "natural" path for the transition from one class of the clusters to another.

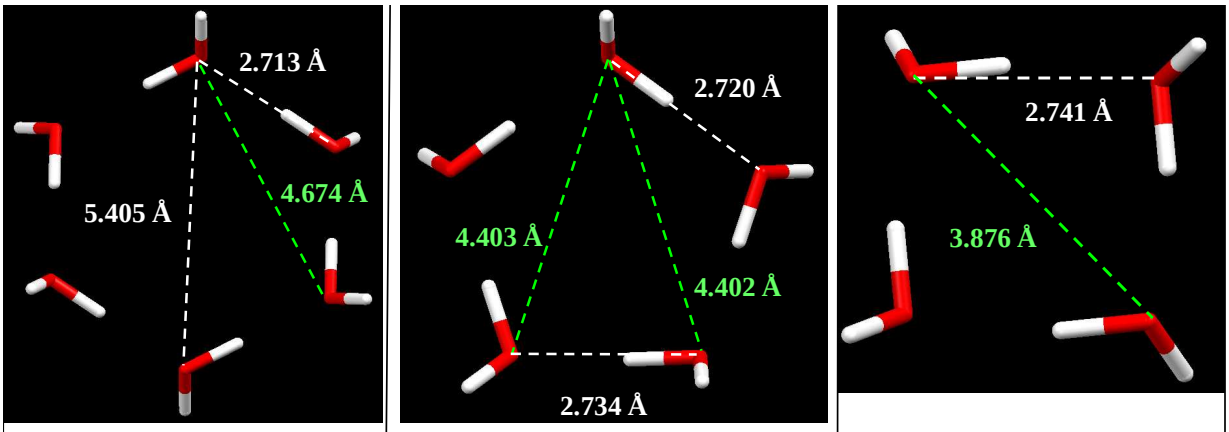

E_{Form}(*EL.*)= −42.196
(−29.421 / −4.904$_{HB}$)
Inter. E= −44.279 / −7.380
Pairwise IE= −29.154 / −3.908$_{12}$
3-body IE= −12.938
4-body IE= −1.914
5+6-body IE= −0.273

E_{Form}(*EL.*)= −34.016
(−23.448 / −4.690$_{HB}$)
Inter. E= −35.755 / −7.151
Pairwise IE= −24.209 / −3.931$_{12}$
3-body IE= −10.750
4+5-body IE= −0.796

E_{Form}(*EL.*)= −25.670
(−17.225 / −4.306$_{HB}$)
Inter. E= −26.903 / −6.726
Pairwise IE= −19.434 / −4.867$_{12}$
3-body IE= −6.838
4-body IE= −0.631

L(1-3) = 2 · L(1-2) · cos(180/n) →
n=6; 4.7
n=5; 4.4
n=4; 3.85

L(1-2)=2.720Å

Figure 4.3.8. Properties of cyclic regular tetramer, pentamer and hexamer water structures. The calculations were performed on the *B3LYP/6-311++g(3df, 3pd)* level. There are reported electron formation energies, corresponding *ZPVE* corrected values and those per hydrogen bond (in parantheses *E.F.+ΔZPVE / E.F.+ΔZPVE* : n *HB*'s) and the interaction energies with pairwise and multibody components are reported. L(x-y) designates the distance between corresponding atoms.

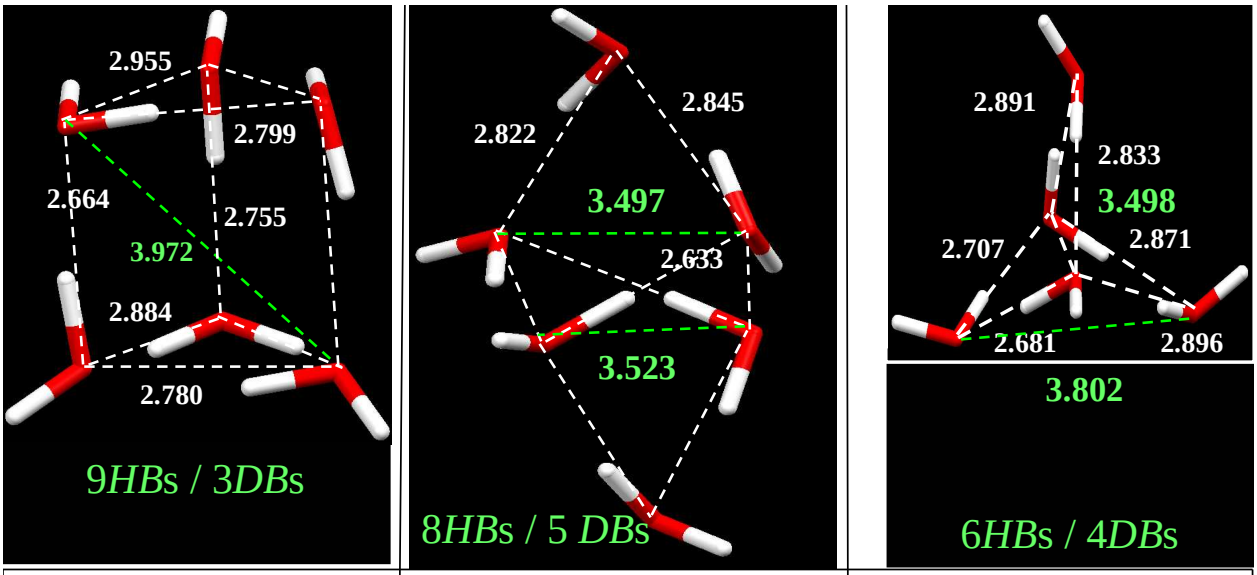

E_{Form}(*EL.*)= −40.587 (−26.811 / −4.469$_{Mol}$ / −2.979$_{HB}$) Inter. E= −42.492 / −7.082$_{Mol}$ / −4.721$_{HB}$	**E_{Form}(*EL.*)= −39.065 (−25.712 / −4.286$_{Mol}$ / − 3.214$_{HB}$) Inter. E= −41.067 / −6.845$_{Mol}$ / −5.133$_{HB}$**	**E_{Form}(*EL.*)= −30.881 (−20.143 / −4.029$_{Mol}$ / − 3.357$_{HB}$) Inter. E= −32.343 / −6.469$_{Mol}$ / −5.390$_{HB}$ Pairwise IE= −24.633 / $\underline{-3.615}_{12}$ Multi-body IE= −7.710**

Figure 4.3.9. Compact water clusters:prism and cage for hexamer and tri-leaf for pentamer. The calculations were performed on the *B3LYP/6-311++g(3df, 3pd)* level. There are reported electron formation energies, corresponding *ZPVE* corrected values and those per hydrogen bond (in parantheses *E.F.+ΔZPVE / E.F.+ΔZPVE* : n molecules / *E.F.+ΔZPVE* : n *HB*'s) and the interaction energies with pairwise and multibody components are reported. The configurations are labelled as follows from left to right: prism, cage configurations for water hexamer and tri-leaf configuration for water pentamer.

Figure 4.3.9 compares the *B3LYP/LBS* computational results for the prism and cage configurations of water hexamer and for the tri-leaf configuration of water pentamer. The electronic energies of these clusters as well as the energies corrected for the vibrational part are higher than those for corresponding open analogs despite a larger number of the hydrogen bonds in the compact structures. In the present case, therefore, the electronic energy of clusters is not directly related to the number of formal hydrogen bonds whereas the structural parameters of the clusters are still determined primarily by the hydrogen bonds. The comparison of pairwise and multi-body terms for the open and closed pentameric configurations reveals that the pairwise interaction energy increases by a very small fraction upon transition from the open to the compact structure, i.e. −24.209 kcal·mole^{-1} versus −24.633 kcal·mole^{-1} whereas a multi-body term exhibits a discernible decline, i.e −11.546 kcal·mole^{-1} versus −7.710 kcal·mole^{-1}. This result is an additional evidence for the significance of the cooperativity (induction) effects in the water network.

It appears that the 1-3 distances in a tri-leaf and in a cage are in good agreement with the scattering data reported by Finney *et al.* [12] for the high-density noncrystalline media. On the other hand, in the prism configuration the 1-3 distances are larger than those in the *HDA* and appear to be more appropriate for the *LDA*. It is, therefore, possible to assume that compact closed clusters such as a hexamer cage or a pentamer tri-leaf are responsible for the short 1-3 distances in high-density amorphous media as displayed in Figure 4.1.4 (Finney *et al*. neutron diffraction data on LDA and HAD [12]). It should be noticed that Ice *II* also contains short 1-3 pairs but does certainly not comprises the closed structural units.

The lengths of hydrogen bond exhibit a characteristic trend in accord with the electon density distribution. The shortest hydrogen bonds are found between such a pair of water molecules where one of the counterparts is a da^2 (donor and double acceptor) molecule. All configurations in Figure 4.3.9 provide evidence to support this statement.

4.4 Acetone-Water Clusters: *MP2* and *B3LYP* Studies

A molecule of acetone (Ac) exhibits interesting intramolecular electronic effects associated primarily with the hyperconjugation between *p*-lone pair of oxygen atom of the carbonyl group and the σ-bonds of the carbon skeleton. Analysis of these intramolecular effects performed within the *NBO* framework appears to be useful for estimating the collective molecular response on the carbonyl group perturbation induced by water molecules. Furthermore, the correlated changes in the IR absorption bands of such fundamental molecular vibrations as carbonyl and carbon-carbon stretching modes can be viewed as a manifestation of the collective electronic response on the perturbation induced by *HB*-ed water molecules coordinated against carbonyl group. The electronic response on the perturbation of carbonyl group hyperconjugated with the carbon skeleton leads to the weakening of the carbon-oxygen double bond ant to the strengthening of the carbon-carbon σ-bonds, which in turn can be observed as a red shift of carbonyl mode and corresponding correlated blue shift in the carbon-carbon stretching mode. The *MP2(fc)* and *B3LYP* calculations of free acetone molecule show that at relevant local minimum in Figure 4.4.1, which is expected to be the deepest one if the other minima exist or, otherwise, the global minimum, the symmetry group of molecule is C_2 (*B3LYP*/*LBS* optimization has been performed under the C_1 symmetry but the final geometry definitely belongs to the C_2 point group). In the literature [78, 79], acetone molecule is often classified among a C_{2V} symmetry group but present calculations indicate that two perpendicular symmetry planes are definitely lost because two methyl groups turn away from the perfect eclipsed conformation such that the dihedral angles become: $H^{'\text{in-plane}}{}_{\alpha}C_{sp3}C_{sp3}H^{''\text{in-plane}}{}_{\alpha} = 0.044°$ at *MP2/aug-cc-pvtz* and 7.396° at *B3LYP/LBS* (two H'_{α} and H''_{α} are the methyl protons closest to the molecular plane); $H^{\text{out-of-plane}}{}_{\beta}C_{sp3}C_{sp3}H^{\text{out-of-plane}}{}_{\beta} = 0.028°$ at *MP2/aug-cc-pvtz* and 4.801° at *B3LYP/LBS*. If the *MP2* geometry is indeed very close to C_{2V}, the *B3LYP* geometry in contrary is distinctly different, which rises a question on the origin of this noticeable difference in connection with possible intra-molecular hydrogen bonding between the H'_{α} and H''_{α} protons and the oxygen atom of the carbonyl group.

Table 4.4.1. Geometrical, bond (Wiberg, W.B., and Mayer-Mulliken, M.M.) and population parameters for the acetone molecule model at the *MP2/aug-cc-pvtz* and the *B3LYP/LBS*. *L* and *C* stand for the distance and the atomic charge of corresponding entity. The structure of acetone molecule is shown on Figure 4.4.1.

Parameter	Expt. [80a]	*MP2/aug-cc-pvtz* (C_2) *MP2* density matrix E_{el} = −192.7901428 Hartree	*B3LYP/LBS* (C_1) Present work E_{el} = −193.2323224 Hartree	*B3LYP/LBS* (C_{2V}) [79] E_{el}=−193.232326 Hartree
$L(C{=}O)_{vib=0}$	1.222 Å	1.21972 Å	1.20863 Å	1.2088 Å
$L(C{=}O)_{z.p.}$ [81]	1.210±4^{-3}Å	*W.B.*= 1.6895; *M.M.*= 1.3145	*W.B.*= 1.8166; *M.M.*=+1.4647	
		$C^{NBO}(O)$= −0.51254	$C^{NBO}(O)$= −0.55987	
		$C^{Mull}(O)$= −0.628283	$C^{Mull}(O)$= −0.702619	
		$C^{NBO}(C_{sp2})$= +0.56489	$C^{NBO}(C_{sp2})$= +0.58467	
		$C^{Mull}(C_{sp2})$= +0.418028	$C^{Mull}(C_{sp2})$= +0.746161	
Freq. [82] - gas ph.	1731 cm^{-1}	1756 cm^{-1}	1790.5 cm^{-1}	
$L(C'_{sp3}{-}C_{sp2})$	1.507 Å	1.50866 Å	1.51398 Å	1.5137 Å
$L(C''_{sp3}{-}C_{sp2})$		*W.B.*= 0.9462; *M.M.*= 0.8705	*W.B.*= 1.0096; *M.M.*= 0.7005	
		$C^{NBO}(C_{sp3})$= −0.67966	$C^{NBO}(C_{sp3})$= −0.66919	
		$C^{Mull}(C_{sp3})$= −0.839865	$C^{Mull}(C_{sp3})$= −0.169331	
Freq. [82]	1215.5cm^{-1}	1254.5 cm^{-1}	1234 cm^{-1}	
$<C'_{sp3}{-}C_{sp2}{-}C''_{sp3}$	117.02°	116.282°	116.524°	116.60°
$<C'_{sp3}{-}C_{sp2}{-}O$	121.49	121.859°	121.738°	121.70°
$<C'_{sp3}{-}C_{sp2}{-}C''_{sp3}{-}O$		180.000°	180.000°	180.000°
Dipole moment	2.86 D	2.9820 $_{MP2}$ D	3.0806 D	3.0813 D
		3.4770$_{SCF}$ D		
$L(C'_{sp3}{-}H'_{\alpha})$		1.08567 Å	1.08630 Å	
$L(O{-}H'_{\alpha})$		2.52500 Å	2.52425 Å	
$<H'_{\alpha}{-}C'_{sp3}{-}C_{sp2}$		110.065°	110.145°	
		W.B.= 0.8945; *M.M.*= 0.8968	*W.B.*= 0.9372; *M.M.*= 0.9931	
		W.B.(OH'_{α}) = 0.0025	*W.B.*(OH'_{α}) = 0.0038	
		M.M. (OH'_{α})= 0.0225	*M.M.* (OH'_{α})= 0.0019	
		$C^{NBO}(H'_{\alpha})$= +0.22240	$C^{NBO}(H'_{\alpha})$= +0.22270	
		$C^{Mull}(H'_{\alpha})$= +0.296034	$C^{Mull}(H'_{\alpha})$= +0.016004	
$L(C'_{sp3}{-}H'_{\beta})$		1.09069 Å / 1.09070 Å	1.09182 Å / 1.09222 Å	
$L(C'_{sp3}{-}H''_{\beta})$		*W.B.*= 0.8852; *M.M.*= 0.8512	*W.B.*= 0.9265; *M.M.*= 0.9762	
		W.B.= 0.8852; *M.M.*= 0.8512	*W.B.*= 0.9243; *M.M.*= 0.9783	
$\wedge H'_{\alpha}{-}C'_{sp3}{-}C''_{sp3}{-}H''_{\alpha}$		0.044°	7.396°	0.000°
$\wedge H'_{\beta}1{-}C'_{sp3}{-}C''_{sp3}{-}H''_{\beta}2$		0.028°	4.801°	0.000°

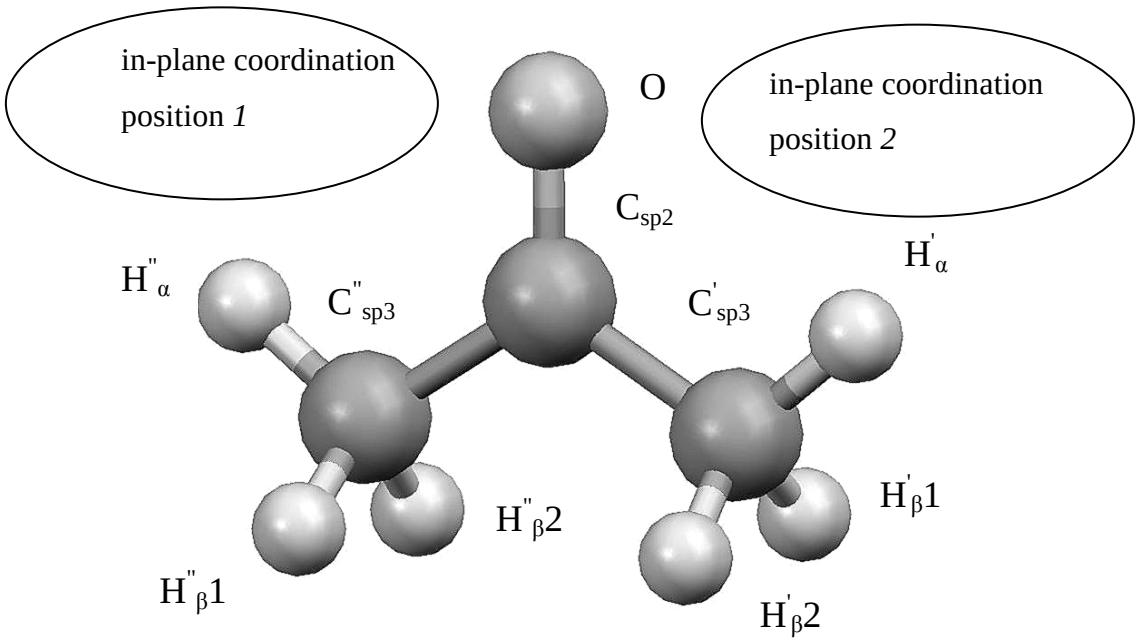

Figure 4.4.1. Atomic labelling and molecular structure of the acetone molecule. There are shown two coordination positions for accepting *2 HB*'s. The Wiberg bond indexes for C=O, $C_{sp2}-C'_{sp3}$, $C'_{sp3}-H'_{\alpha}$ and $C'_{sp3}-H'_{\beta1}$ ($C'_{sp3}-H'_{\beta2}$) are 1.8166, 1.0096, 0.9372, and 0.9265 (0.9243), respectively.

Evidently, Table 4.4.1 shows that a good general agreement is found between the geometric parameters obtained in the experiment [80a] and those calculated by both methods, which indicates a general capacity of both computational methods, *MP2* and *B3LYP*, to predict geometric parameters of carbonyl compounds. In the present case, a surprisingly good agreement is found between the computed values for the C_{sp2}=O bond length at 1.21972 Å (*MP2/aug*) and 1.20863 Å (*B3LYP/LBS*) and experimental value at $1.210 \pm 4\times10^{-3}$ Å [81]. Secondly, the computed dipole moment of acetone molecule is discernibly larger than the experimental value (Table 4.4.1), which leads to the overestimation of intermolecular interaction energy in the acetone-water clusters. The *MP2* value for the dipole moment is in better agreement with experiment than that obtained by the *B3LYP* calculations.

If the carbonyl group C=O is a characteristic feature of the acetone molecule, a tautomeric form, enol, contains the hydroxyl group with neighboring carbon-carbon double

bond: $(CH_3)_2$−C=O (Ac)↔CH_3−C(OH)=CH_2 (En). The electronic energy of enolic structure was found to be +11.493 kcal·mole^{-1} and +11.359 kcal·mole^{-1} with respect to the acetone form at the *B3LYP* and the *MP2* levels, respectively. This large energy excess indicates that the anticipated abundance of the enolic form is very small. However, in the water media, where the hydrogen bonding between the organic and water molecules is highly probable, the enolic form could be stabilized by additional donor coordination as follows:

$(CH_3)_2$−C=O (Ac) + nH_2O ↔ [$(CH_3)_2$−C=O (Ac)·2H_2O]$_{HB}$ + (n−2)H_2O + ΔH_{Ac}

CH_3−C(OH)=CH_2 (En)+mH_2O ↔ [CH_3−C(OH)=CH_2 (En)·3H_2O]$_{HB}$ + (m−3)H_2O + ΔH_{En}

It is possible to assume that the enolic tautomer will form *3HB*'s with water molecules: *2* acceptor-type coordination + *1* donor-type coordination; whereas the carbonyl tautomer is expected to form only *2* acceptor-type *HB*'s. Therefore, a simple estimation could be made for the enthalpies of hydration of both tautomers: if ΔH_{Ac} (Ac·2H_2O) = −6.704 kcal·mole^{-1} (*B3LYP/LBS*) then $\Delta H_{En} \sim 3/2 \cdot \Delta H_{Ac}$ = −10.056 kcal·mole^{-1}. It appears therefore that a plausible gain in the hydration energy is not sufficient for making enolic form energetically comparable with its carbonyl counterpart (of course, the above values for ΔH_{Ac} and ΔH_{En} are just zero-order approximations). An isolated acetone molecule and the acetone dimer with anti-parallel orientation of the carbonyl groups represent a γ-class of the acetone-water network structures. A characteristic feature of this class is the absence of hydrogen bond between acetone species and water network. The acetone-water interaction is limited to the electrostatic and van der Waals forces. Specific spectral examples of these complexes are given in Chapter 5.

In order to correlate the experimentally observed frequencies for acetone/water system the following complexes were designed and optimized on the *B3LYP*/*LBS* and *TIP4P* (and for simple complexes on *MP2/aug*) level of theory the following complexes: (i) Ac·*W*- single *HB* complex with in-plain coordination of water molecule; (ii) two different Ac·*2W* complexes: bifurcated complex with *2 HB*'s between the carbonyl group and water molecules and sequential complex with *1 HB* between water molecule and carbonyl group of acetone (structure of this complex is given in Figure 4.4.3);(iii) two different Ac·*3W* complexes with *2 HB*'s between water molecules and carbonyl group; the difference between these two

complexes resides in the *HB* sequence of the hydrogen bonds within water network (Table 4.4.2 and Table 4.4.3); (iv) three different Ac·W_6 (cyclic hexagon)- two complexes comprise bifurcated double hydrogen-bonded acetone with the first and third water molecules; the difference between this pair resides in the sequence of hydrogen bonding network; the third complex is constructed from acetone molecule bounded to a hexagone with single hydrogen bond, structure of which is given in Figure 4.4.6. Table 4.4.3 provides a detail structural and energy partitioning information for the above listed complexes whereas Table 4.4.4 demonstrates the vibrational frequency response of acetone molecule on the coordination in the different complexes.

The present quantum mechanical calculations reveal that the global minimum for the coordination of water molecules around acetone molecule includes two in-plane positions for the acceptor hydrogen bonded (see Figure 4.4.1). No local minima for the back-side or for the perpendicular to the carbonyl group coordinations have been found in the present studies in contrast to a previous report of Liao *et al*. [78], who obtained the local minima for the water molecule coordination with the CH_3 group from the back side of acetone molecule at *B3LYP/6-311g(d,p)* level. Moreover, the present author has undertaken the optimization of these latter complexes (laballed as *1b* and *2b* in the Liao *et al.* work) at *B3LYP/6-311++g(3df,3pd)* level starting from the geometries provided by Mebel *et al.* [83] and has found no minima corresponding to the suggested geometries. This result clearly indicates that the existence of the back-side minima depends on the quality of the basis set and, therefore, could be a computational artefact. It should be noted that in order to provide convincing evidences for the existence of the back-side local minima the *ab initio MP2* level calculations are required. To the best of the present author's knowledge, these *MP2* calculations have not yet been performed. However, at the present moment there are sufficient evidences for suggesting that the back-side minima (if indeed exist) are very shallow and depend strongly on the global configuration of water molecules around the acetone molecule. The global configuration is controlled by the hydrogen bonding of water molecules in the in-plane positions as shown in Figure 4.4.1.

An interesting example of the acetone-water hydrogen bond coordination is given by a pair of the local minima, in both of which the acetone species acts as an acceptor of a single

hydrogen bond in the in-plane configuration. The structures and other parameters of these complexes are given in Figure 4.4.2 and Figure 4.4.3. The acetone-water dimer (Figure 4.4.2) represents a characteristic *HB* in-plane arrangement, where the acetone molecule accepts a hydrogen bond from its counterpart. In other words, the lone pairs on the oxygen atom of acetone molecule donate the electron density towards the spatial region between O_{Ac} and H_W as represented by the Wiberg index value of 0.0306. This value is much smaller than typical values for a "normal" covalent bond, which points out the weak covalence of the hydrogen bond interaction in general and of the present *HB* interaction, in particular. The discernible reduction of the Wiberg index for O−H bond in the water molecule from 0.7923 for the isolated molecule to 0.7342 in the acetone-water dimer provides a convincing evidance of the orbital interaction between the two lone pairs of acetone molecule, n_O1 and n_O2, and the antibonding σ^*(O−H) orbital of the OH group. The reduction of electron density in the OH group that is involved in the *HB* coordination is compensated by the increase of the electron density on the adjacent OH bond. Regarding the carbonyl group of acetone molecule, it is evident that the *HB* coordination leads to a significant reduction of its covalence, which follows from the comparison of corresponding Wiberg indexes: 1.8166 for the isolated acetone and 1.7725 for the acetone-water dimer. In contrast, the carbon-carbon bond gains the covalence as a result of the *HB* coordination as indicated by the corresponding Wiberg index, which increases from 1.0096 for the isolated molecule to 1.0207 (1.0173 for the second C-C bond) for the acetone-water dimer. The electrostatic attraction between hydrogen atom H_α of acetone and the oxygen atom of water molecule is also evident from a specific location and the orientation of water molecule with respect to the acetone framework. However, no evidences of the *HB* character of this interaction are found in the present studies. Indeed, a Wiberg parameter for the $O_W\cdots H_{\alpha\,Ac}$ atomic pair is vanishingly, i.e. 3.1×10^{-3} versus 3.1×10^{-2} for the $H_W\cdots O_{Ac}$. The localization and orientation of the water molecule around acetone moiety is controlled primarily by the hydrogen bond coordination with the carbonyl group. This orientation is, however, modulated by the electrostatic and van der Waals interaction with the remainder of the acetone molecule. The above discussion further strengthens the partition scheme for polar organic molecules suggested in Chapter 2 (section 2.5). The anchoring interaction of small polar molecules with water is due to the hydrogen bond coordination while

the overall intermolecular interactions could be significantly "perturbed" by the less specific forces. This simple classical scheme forms the general foundation for the structural part of the present studies and provides reliable chemical orienteers for the interpretation of the spectral data on an intuitive level.

The insertion of second water molecules that which is hydrogen-bonded to the former water molecule causes strengthening of the water-acetone hydrogen bond. Indeed, the Wiberg index for the $H_W\cdots O_{Ac}$ pair rises from 0.0306 to 0.0416 whereas those for C=O and $O-H_{HB}$ bonds decrease from 1.7725 to 1.7474 and from 0.7342 to 0.7095, respectively. The origin of this strengthening effect resides in the induction electron effect of the second water molecule on the first molecule as described above in section 4.2.2.

In terms of the intermolecular interation energy a comparion of two complexes $Ac\cdot H_2O$ and sequential $Ac\cdot(H_2O)_2$ also provides interesting information. The acetone-water intraction energy rises significantly upon addition of the second molecule from −5.727 kcal·mole^{-1} to −9.046 kcal·mole^{-1}. Peculiarly, a tri-body term, −2.069 kcal·mole^{-1}, is larger than the pair-wise interaction energy, −1.650 kcal·mole^{-1}, of acetone and non-hydrogen-bonded water molecule, W^2 in Figure 4.4.3. This numerical result highlights the significance of the cooperativity effects on the coordination of polar organic species and the water network. Specific spectral examples of the effects of the water network configuration on acetone-water hydrogen bonding are given in Chapter 5 (section 5.5.1). The $Ac\cdot(H_2O)_2$ sequential complex could be considered as comprising the acetone molecule and the water dimer. It turns out that the intermolecular WW interaction is only slightly weakened by the attachment of acetone species (see Figure 4.4.3), which could be viewed as a manifestation of the flexibility of water *HB* network. In the present terminology, these two complexes are part of the β class of the acetone-water coordination network. A characteristic feature of this class is a single hydrogen bond between the acetone species and the water network.

A bifurcated $Ac\cdot 2H_2O$ complex with 2*HB*'s represents a parent structure for the α-class of the acetone-water coordination network. This class is characterized by two hydrogen bonds between a carbonyl group of acetone and two water molecules located in the in-plane positions as shown in Figure 4.4.1 and Figure 4.4.4. Pairwise interaction energy between an acetone molecule and a hydrogen bonded water molecule appears to be nearly identical in the mono

and bi-coordinated structures. This numerical result underscores that a carbonyl group of acetone is suited for accepting one or two hydrogen bonds.

In the present studies on the ab initio and semi-empirical levels, no evidence for a triple acceptor capacity of the carbonyl group of acetone was found. Therefore, the present studies tentatively suggest that the α- (bi-coordinated acetone species), the β- (mono-coordinated species) and the γ- (non-coordinated species) classes exhaust the possibilities of acetone-water coordination. Although the previous statement is only a tentative preposition at present moment (a *TIP4P* optimization leads in some cluster configurations to a triply-coordinated acetone species, and the enolic tautomeric form of acetone could become a non-negligible factor in the coordination of acetone-water species), as long as there are no direct experimental and theoretical evidences for higher-order acetone-water coordination, this preposition on the bi-coordination of acetone species remains a valid working model for the description of experimental spectral data.

It is found that the frequencies of carbonyl and carbon-carbon skeleton vibrations are directly related to the coordination of water molecules around acetone. The perturbation effect depends on two different coordinations in the acetone-water network (see Figure 4.4.2 and Figure 4.4.3): the acetone-water coordination involving hydrogen bonding of water molecules to the carbonyl group and the coordination within a network of water molecules. The frequency shift in acetone molecule can be used as an indicator of a specific sequence of the hydrogen bonds in the water network due to the induction effect in the chain of hydrogen bonds. Figure 4.4.5 provides a simple Lewis resonance form interpretation of the perturbation effect of hydrogen bonding on the acetone framework. It is evidently that the relative weight of the carbonyl resonance form (the parent covalent resonance form where all electron pairs are fully localized on corresponding atoms or pairs of atoms is used as a reference with the weight of 100 %) decreases while the relative weigth of the enolic resonance form increase on the hydrogen bond coordination. The frequency of stretching mode dependces strongly on the covalence character of the bond involved in a vibrational motion. The decrease of the contribution of a carbonyl resonance form manifests the "weakening" of the carbonyl group with the concomitant frequency decrease. In contrast, the increase of the enolic form weight suggests the strengthening of the carbon-carbon skeleton with the concomitant rise of a

frequency. Indeed, as Table 4.4.2 and Table 4.4.3 show, the length of C=O bond increases by 4.82×10^{-3} (*MP2/aug*) or 5.68×10^{-3} Å (*B3LYP/LBS*) on mono- *HB* coordination and by 9.59×10^{-3} (*MP2/aug*) or 1.14×10^{-2} Å (*B3LYP/LBS*) on bi- *HB* coordination, i.e. the linear deformation of carbonyl group doubles in transition from a mono- to bi- coordination. Therefore, one could expect that a frequency red shift would be twice larger on transition from a mono- to bi- *HB* coordination. Indeed, the experimental and computational results summarized in Table 4.4.4 clearly show that frequency shifts of the carbonyl stretching vibration and carbon-carbon asymmetric stretching vibration exhibits a trend expected on the basis of the present model. These results form the background for the spectrum-structure correlation in the acetone-water media, which is employed in Chapter 5 for the prediction of the structure of acetone-water complexes on the basis of the IR spectra.

F.E. BSSE Corr.	−5.58090	*F.E.BSSE. Corr.+ZPVE*	−3.71543
I.E.	−5.72664		

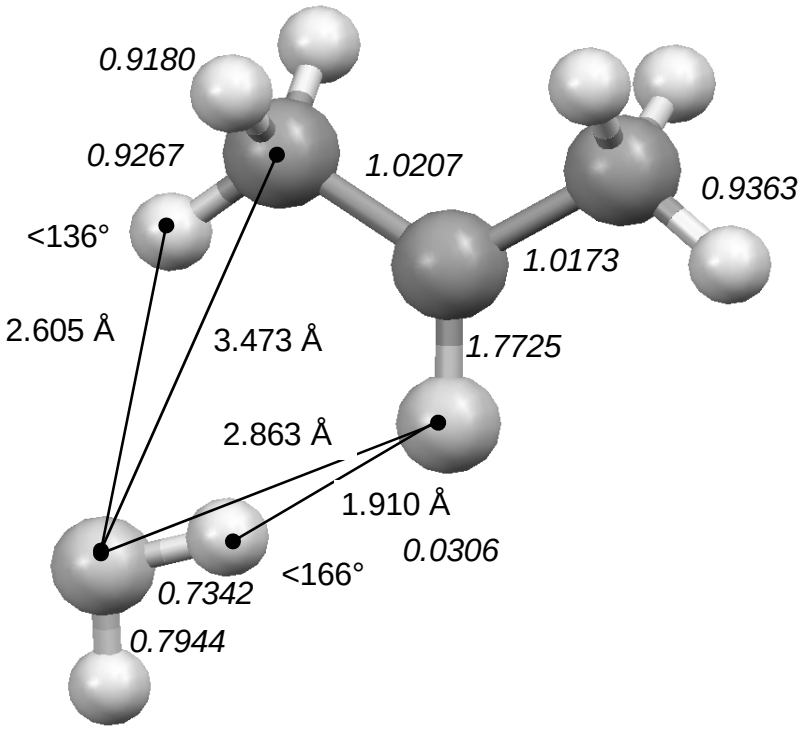

Figure 4.4.2. Acetone (Ac)·H_2O / 1*HB* complex is a parent structure for the *β*-class. The computations were performed at the *B3LYP 6-311++G(3df, 3pd)*; D.M. = 3.2433 D. The Wiberg bond indexes are given in italic. There are reported the electronic and *ZPVE* corrected formation energy (*F.E.*) and the interaction (*I.E.*) energies in the kcal·mole^{-1} units.

B.E. / W_2 dimer	−7.73646	*B.E.* / W_2 dimer *+ZPVE*	−5.58482
F.E. BSSE Corr.	−12.56842	*F.E.BSSE. Corr.+ZPVE*	−8.24264
Total *I.E.*	−13.37816	Pairwise *I.E.* (Ac−W_2)	−6.97645
I.E. (Ac−W_2)	−9.04560	Tri-body term	−2.06915
I.E. (Ac−W^1)	−5.33 (76%)	*I.E.* (Ac−W^2)	−1.65 (24%)
I.E. (W_2 dimer)	−4.56622	*I.E.* (W_2)	−4.33257

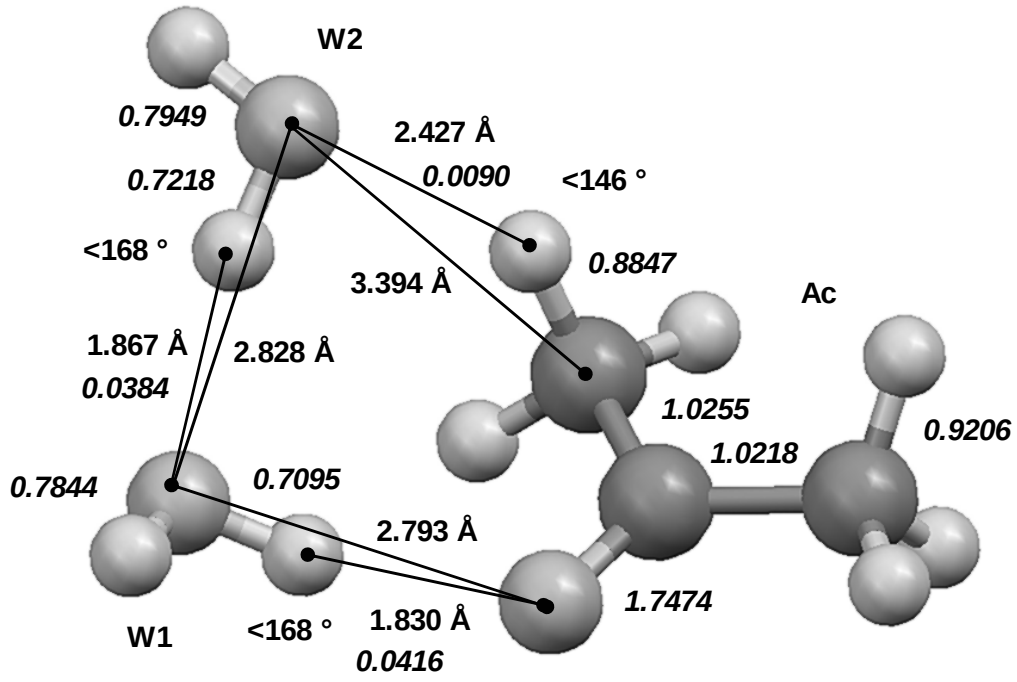

Figure 4.4.3. Acetone (Ac)·$2H_2O$ sequential / 1*HB* complex from the *β*-class.
The computations were peformed at the *B3LYP 6-311++G(3df, 3pd)*; D.M. = 1.8960 D. The Wiberg bond indexes are given in italic. The formation and interaction energies are given in the kcal·mole^{-1} units. There are reported the binding energy of the acetone molecule to the water dimer (*B.E./*W_2), the electronic and *ZPVE* corrected formation energy of the entire complex and the interaction energies and their components. For comparison, the interaction energy of water molecules in the isolated water dimer W_2 (I.E. W_2 dimer) is also provided.

F.E. BSSE Corr.	−10.34439	*F.E.*$_{BSSE.\ Corr.}$+*ZPVE*	−6.70434
Total *I.E.*	−10.67958	*I.E.* (W_2)	0.70885
I.E. (Ac−W_2)	−11.38843	Tri-body term	0.09385
I.E. (Ac−W^1)	−5.74114	*I.E.* (Ac−W^2)	−5.74114

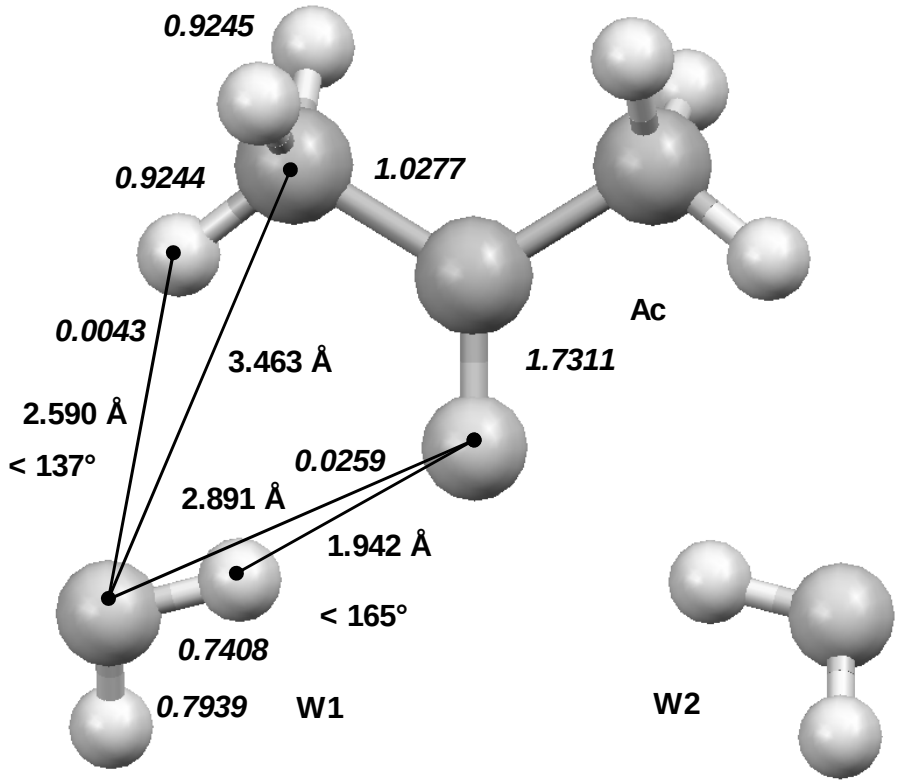

Figure 4.4.4. Acetone (Ac)·2H_2O (C_2)/2*HB* complex is a parent structure for the α-class. The computations were performed at the *B3LYP 6-311++G(3df, 3pd)*; D.M. = 1.8960 D. The Wiberg bond indexes are given in italic. The formation and interaction energies are given in the kcal·mole^{-1} units. There are reported the electronic and *ZPVE* corrected formation energy of the entire complex, the interaction energies and their components. In the present case, W_2 designates the pair of non-hydrogen-bonded water molecules, whereas each separate molecule is labelled by superscript.

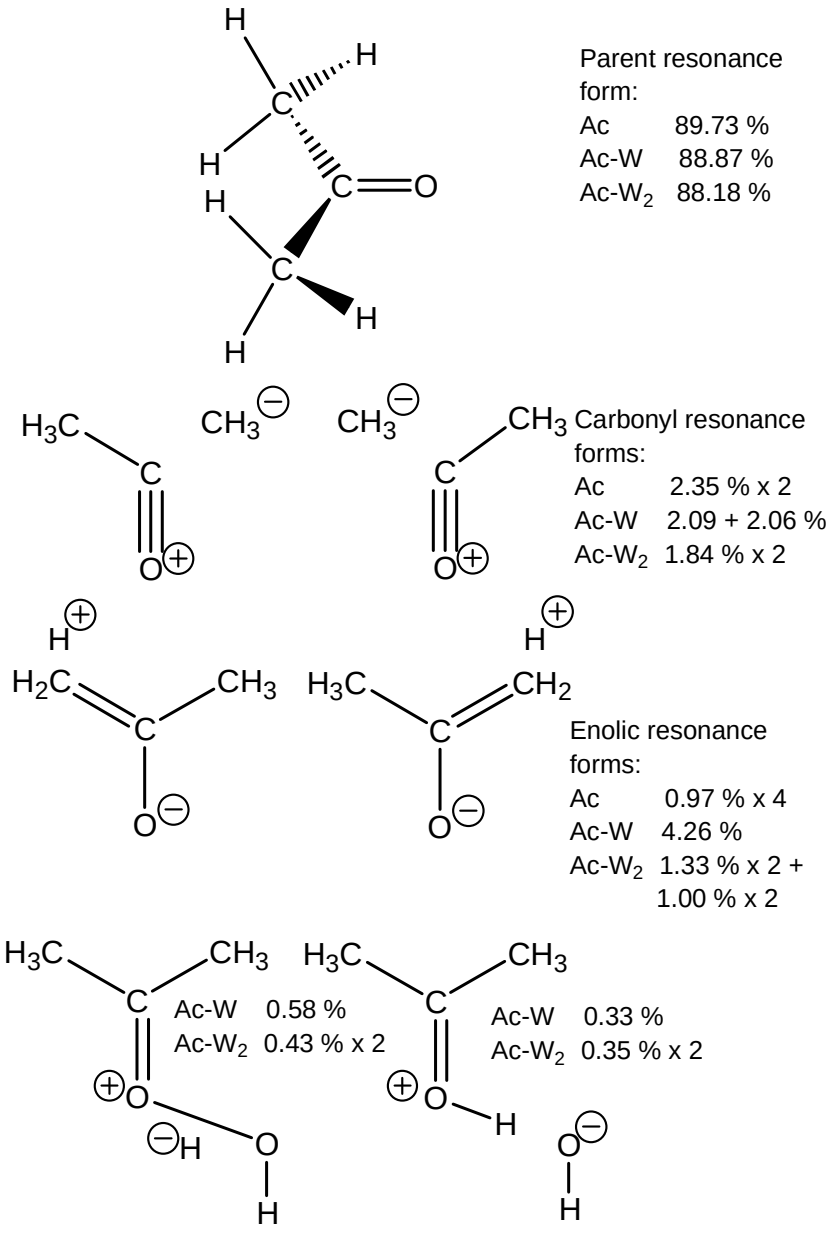

Figure 4.4.5. Resonance Lewis forms for Ac, Ac-W, and Ac-W_2 complexes were obtained by *NBO* program on the bases of the *SCF* density matrix for the optimal geometries.
The computations were performed at the *MP2/aug-cc-pvtz*. There reported the relative weights of corresponding resonance forms. The parent structure would gain a weight of 100% if the electron delocalization will be ignored.

Table 4.4.2. *MP2(fc)* comparative analysis of the Ac-W and Ac-W_2 complexes.
The calculations are performed with the *aug-cc-pvtz* basis set. The subscript indexes SCF, 2, and MP2 stand for the *SCF*, seconds order *MP* correction to the *SCF* energy and total *MP2* energy. The energy values are given in kcal·mole^{-1}, the linear and angular geometric parameters are given in Å and degress ° units, respectively. *L* and Δ*L* stands for the distance and the change of the distance between corresponding entities. *ΔZPVE* designates the contribution of zero-point vibrational energy. W and W_2 designate single water molecule and two water attached to the acetone molecule; W^1 and W^2 label the first and second molecules in Ac-W_2 complex.

Complex	Geometry			*B.E.*		*B.E.* BSSE. corr. */MP2+ΔZPVE*		ΔE^i_X Deformation E.		ΔE^i_{XY} Pairwise	ΔE^i_{XYZ}
	$\Delta L C_{Ac}-O_{Ac}$ /ΔL O_W-H	L O_W-O_{Ac} / L H_W-O_{Ac}	*HB* Ang.	*SCF*	*MP2*	*SCF*	*MP2*	Ac	W_1 / W_3		
Ac···W C_1	0.00482 / 0.01078	2.8387 / 1.8927	163.6	−4.106	−6.966	−4.007	−6.304 /−4.388	0.352_{SCF} -0.281_2 0.070_{MP2}	0.294_{SCF} -0.207_2 0.086_{MP2}	-4.652_{SCF} -1.808_2 -6.460_{MP2}	
Ac ···W_2 C_2	0.00959 / 0.00925	2.8597 / 1.9201	162.2	-7.559	-13.237	-7.356	−11.887	0.779_{SCF} -0.580_2 0.199_{MP2}	0.237_{SCF} -0.165_2 0.072_{MP2}		0.023_{SCF} 0.051_2 0.074_{MP2}
Ac···W^1 Ac···W^2										-4.742_{SCF} -1.770_2 -6.512_{MP2}	
W^1···W^2										0.853_{SCF} -0.133_2 0.720_{MP2}	

Table 4.4.3. *B3LYP* comparative analysis of the the Ac-W, Ac-W_2 and Ac-W_3 complexes. The *B3LYP* calculations are performed with the *6-311++g(3df, 3pd)*basis set. The short notations are described in preceding Table 4.4.2.

Complex	Geometry Å, deg.			B.E.	B.E. BSSE. corr. /+ΔZPVE	ΔE^i_X Deformation E.		ΔE^i_{XY} pairwise	ΔE^i_{XYZ} ΔE^i_{UXYZ}
	ΔLC_{Ac}-O_{Ac} /ΔL O_W-H	L O_W-O_{Ac} / L H_W-O_{Ac}	HB Ang.			Ac	W1 / W3		
Ac - W *E* symm.	0.00568 / 0.0105	2.8629 / 1.9101	166.1	-5.836	−5.581 / −3.715	0.069	0.076	−5.727	
Ac - W_2 C_2 symm. 1. Ac - W1 Ac - W2 2. W1-W2	0.01138 / 0.00886	2.8907 / 1.9424	165.1	−10.885	−10.344 / −6.704	0.220	0.058	 −5.741 0.709 Σ Total −10.773	0.094
Ac-W_3 C_2 symm. 1. Ac - W1 Ac - W2 2. Ac - W3 3. W1-W3 W2-W3 4. W1-W2	0.00959 / 0.00843	2.9087 / 1.9443	172.7	−16.786	−15.698 / -9.464	0.162	0.049 / 0.042	 −4.781 −1.520 −2.962 0.781 Σ Total −16.227	3-body Ac-W1-W2 0.403 Ac-W1-W3 −0.470 W1-W2-W3 0.592 Σ Total 0.524 4-body 0.172

Table 4.4.4. Experimental and computed frequencies for the Ac-W_n *HB* complexes. The spectral data are from [1][82], [84](S&R for Shaff and Roberts) and from the present studies[2]. *MI* stands for the matrix isolation; the intensities of IR bands are designated as s, m, w,vw for strong, moderate, weak and very weak; sh stands for shoulder. The relative intensities of the computated IR bands are given as superscript. The acetone dimer is a transition state labeled as T.S. The water cyclic hexagone is labeled by Hex.

Sym.	N	Mode	Gas ; Liquid[1]; /Liquid[2];	Ac and Ac-W *MI* experiment [85] *[86]*		$Ac_{(Ad)}$-ice: Ac RA differ. peaks			QM Calculations						
						Chem. states		S&R	DFT B3LYP/6-311++g(3df,3pd)						
				Ac	Ac-W	pc	nc	nc (D_2O)	Ac $_{C1\rightarrow C2}$	Ac-W_{C1}	Ac-$2W_{C2}$	Ac-3W	Ac-Hex 1:2	Ac-Hex 1:1	2Ac T.S.
A_1	1	ν_{as}CH	3018.5^{G}s 3004.8[2]				3012$_{vw}$		3143$^{3.2}$	3148$^{0.2}$	3148$^{0.02}$	3148$^{0.7}$	3145$^{3.6}$	3144$^{2.5}$	3141^{0} 3141$^{4.0}$
	2	ν_s CH	2937^{G}s 2924[1] / 2926[2]					2922 $_{w}$	3034$^{3.6}$	3035$^{3.2}$	3035$^{2.8}$	3038$^{0.7}$	3028$^{3.4}$	3031$^{2.5}$	3036^{0} 3036 $^{3.0}$
	3	ν C=O	1731^{G}s 1710[1] / 1714[2]	1721.3 *1721.5*	1715.9 *1716.6*	1708$_{sh}$ 1701 $_{s}$	1711$_{sh}$ 1703 $_{s}$	1716$_{s\ Ph.}$ 1703 $_{Ch.}$	1790^{100}	1771^{100}	1751^{100}	1758^{100}	1732^{100}	1765^{100}	1781^{100} 1771^{0}
	4	$\delta_{as}CH_3$ In	1435^{G}s 1434[1]	1429.1 *1429.4*	1420.9 *1420.8*	1428 $_{vw}$		1441 $_{m}$	1471$^{14.5}$	1473$^{8.7}$	1478$^{3.5}$	1474 $^{7.5}$	1474$^{9.5}$	1475$^{6.3}$	1472$^{21.7}$ 1472 ^{0}
	5	$\delta_{s}CH_3$ In	1363.5^{G}s 1364[1] / 1361[2]	1353.9 *1354.0*	1358.7 *1359.0*	1362			1388$^{10.3}$	1392^{16}	1398^{13}	1396 $^{8.8}$	1397^{11}	1389^{19}	1387$^{17.2}$ 1387 ^{0}
A_2	9	$\nu_{as}CH_3$ out							3080$^{0.1}$	3082$^{0.5}$	3084$^{1.3}$	3087 $^{0.4}$	3089$^{1.7}$	3083$^{2.8}$	3086 $^{0.2}$ 3086 ^{0}
	10	$\delta_{as}CH_3$ out							1465$^{1.0}$	1466$^{2.9}$	1463$^{8.0}$	1461$^{5.7}$	1471$^{3.5}$	1469$^{3.3}$	1469 $^{0.4}$ 1465 ^{0}
B_1	13	ν CH	3018.5s 3004[1] / 3005[2]	3016.3			3012$_{vw}$	3003 $_{m}$	3142$^{6.0}$	3145$^{3.4}$	3148$^{0.2}$	3147$^{1.8}$	3137$^{3.6}$	3139$^{4.3}$	3139 $^{7.2}$ 3139^{0}
	14	ν CH	2937^{G} s 2937[1]						3027$^{0.5}$	3029$^{0.3}$	3028$^{0.6}$	3031$^{0.1}$	3004^{12}	3022$^{4.8}$	3029 ^{0} 3029$^{0.6}$
	15	$\delta_{as}CH_3$	1410 s 1418[1] / 1419[2]					1419 $_{m}$	1460$^{0.3}$	1461$^{1.6}$	1463$^{0.7}$	1461$^{0.4}$	1463$^{4.3}$	1462$^{7.0}$	1462 ^{0} 1460 $^{0.3}$
	16	$\delta_{s}CH_3$ out	1363.5^{G} s 1361[1] / 1361[2]	1361.6 *1361.8*	1368.3 *1368.2*	1372 $_{m}$	1374 $_{m}$	1372 $_{vs}$	1388$^{26.9}$	1398^{18}	1399^{21}	1398^{18}	1393^{16}	1403^{15}	1388 $^{31.9}$ 1387 ^{0}

Sym.	N	Mode	Gas ; Liquid[1]; /Liquid[2];	Ac and Ac-W MI		$Ac_{(Ad)}$-ice: Ac RA differ. peaks			QM Calculations						
				Ac	Ac-W	Chem. states		S&R	DFT B3LYP/6-311++g(3df,3pd)						
B_1	17	ν_{as}CC	1215.5^{G} s 1221^{1} / 1222^{2}	1216.5 *1216.4*	1230.4 *1230.2*	1239_{m} 1242_{m}	1239_{m}	1238_{vs}	$1234^{37.3}$	1249^{29}	1261^{26}	1259^{20}	1259^{20}	1247^{38}	$1242^{31.4}$ 1237^{0}
B_2	20	ν CH	2972^{G} s 2964^{1} / 2967^{2}	2972.4					$3088^{8.4}$	$3090^{4.8}$	$3090^{2.9}$	$3094^{1.7}$	$3096^{1.7}$	$3089^{3.1}$	3094^{0} $3094^{7.0}$
	21	δ_{as} CH_3in	1454^{G} s						$1488^{9.8}$	$1490^{8.0}$	$1493^{6.8}$	$1488^{5.6}$	$1493^{5.1}$	$1492^{7.5}$	1492^{0} $1488^{10.2}$
	22	ρ CH_3	1090.5^{G} s 1092^{1} / 1092^{2}	1091.6 *1091.6*	1094.5 *1095.8*				$1120^{1.4}$	$1124^{1.6}$	$1125^{1.8}$	$1124^{1.4}$	$1125^{4.7}$	$1120^{2.2}$	1123^{0} $1122^{3.7}$

Figure 4.4.6 shows the *QM* models of acetone coordination in different water hexagone configurations, which are used to simulate the ice surface: a β-complex, a mono-coordinated acetone and two different α-complexes, a bi-coordinated acetone: symmetric and asymmetric. The asymmetry of the carbonyl group coordination in the two latter complexes is caused primarily by differences in the *HB* coordination of those water molecules, which are directly bounded to the carbonyl group. In the central unit, the left *HB* water molecule is a single donor and double acceptor, whereas the right water molecule is a double donor and single acceptor. The induction effect in a chain of hydrogen bonds causes either the additional polarization or depolarization of a particular OH bond. The acceptor coordination increases the polarization of an OH bond whereas the donor coordination decreases the polarization. The presence of two acceptors attached to the left water molecule (Figure 4.4.6, central panel) decreases the electron density on hydrogen atom and, therefore, facilitates its penetration capacity.

The interaction energies of acetone molecule with different water *HB* networks are shown in Figure 4.4.7. Evidently, the interaction energy is two/three times larger for the complexes from α-class in comparision with the complexes from β-class. The total interaction energy increases proportionally to the cluster size. The interaction energy within the water *HB* network depends on a sequence of hydrogen bonds. The presence of double donor in a

finite water network significantly destabilizes a *HB* structure. Indeed, the intermolecular interaction energy in the water network of the asymmetric α-complex (central structure in Figure 4.4.6) is noticeably smaller than that in the β-complex with sequential arrangement. It should be noted that the presence of acetone molecule stabilizes the water network in the α-asymmetric configuration, which otherwise would collapse to the book configuration. This example supports the Devlin-Buch conlcusion [87] that the adsorption of polar organic molecules induces ordering in the disordered near-surface region. The adsorption of such polar molecules as acetone prevents the open d^2 cyclic configurations on ice surface from a collapse towards the compact structures.

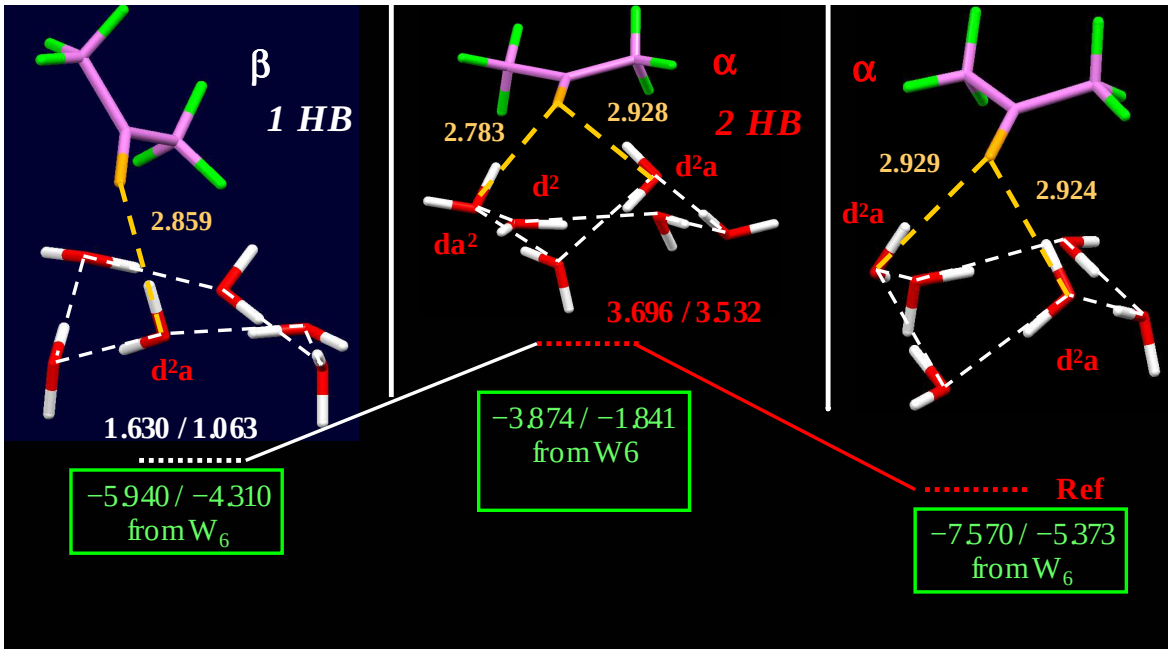

Figure 4.4.6. Different coordination of acetone on the water cyclic hexamer.
The computations were performe at the *B3LYP 6-311++G(3df, 3pd)* level. The left panel shows a *β*-structure with mono-coordinated acetone molecule, whereas the central and right panels show *α*-structures: asymmetric and symmetric complexes, respectively. The relative electronic and *ZPVE* corrected energies (E.E./ E.E.+Δ*ZPVE* in red and wight colors) are given with respect to the most stable symmetric configuration. In addition, the electronic and *ZPVE* corrected energies (in green color) of the present complexes are given with respect to the isolated acetone and water cyclic hexamer species.

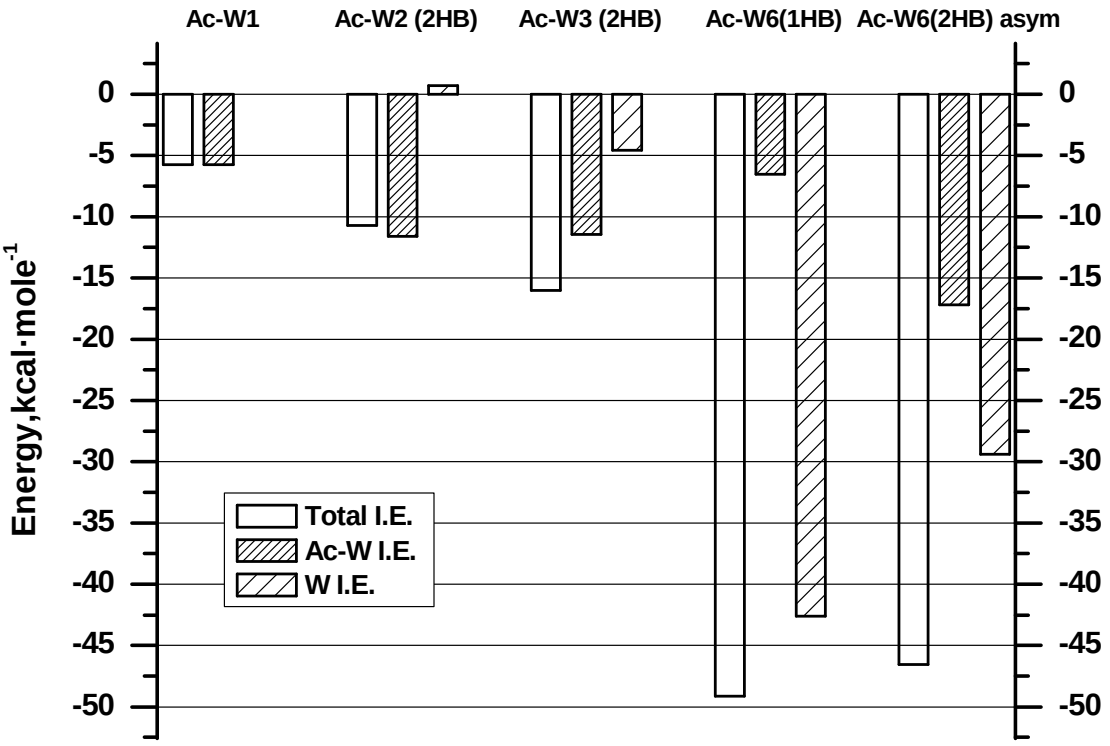

Figure 4.4.7. The interaction energy parameters for acetone-water clusters from the β- and the α-classes at the *B3LYP/6-311++g(3df, 3pd)* level.

The frequencies of the carbonyl and carbon-carbon asymmetric stretching modes for selected acetone-water complexes along with the corresponding Wiberg covalence bonding indexes are shown in Figure 4.4.8. Firstly, the frequency of carbonyl vibrations decreases in the sequence of $\gamma \rightarrow \beta \rightarrow \alpha$ class whereas the frequency of carbon-carbon stretch increase in the same sequence. This trend is in good accord with the resonance analysis presented above in Figure 4.4.5. The decrease of the carbonyl group frequency is nearly proportional to the increase in the bond length. The Wiberg indexes appear to be useful for predicting the general trend in the frequency change upon hydrogen bonding between acetone and water species. It should be noted that the the α-asymmetric complex (central structure in Figure 4.4.6) exhibits the strongest frequency shift, which correlates with a maximum value of the total acetone-water interaction energy found for this complex.

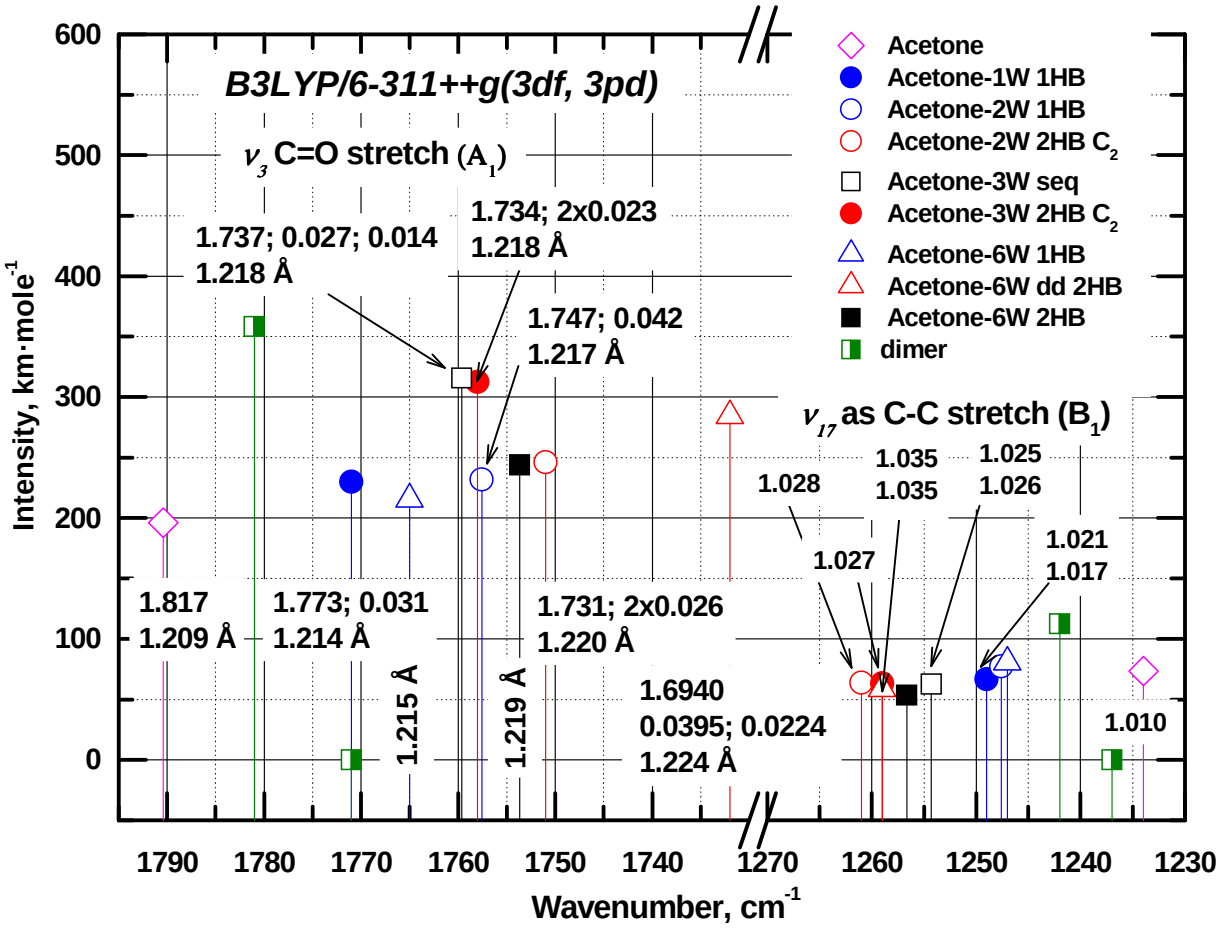

Figure 4.4.8. The frequencies of the carbonyl and the carbon-carbon stretching vibrations for selected acetone-water clusters at the *B3LYP/6-311++g(3df, 3pd)* level.

The Wiberg bond indexes for the C=O and C-C bonds and the $O_{Ac}\cdots H_W$ atomic pair are reported together with the length of the C=O bond.

Resuming this section devotied to a quantum mechanical investigation of the acetone-water complexes the following should be stated: (i) the coordination of carbonyl group in the water media comprises double hydrogen bond (α-class) and single hydrogen bond complexes (β-class), in which water molecules assume the in-plane coordination around the carbonyl group; (ii) the higher order hydrogen bond coordination around the carbonyl group of acetone is of low probability - no evidences have been found so far for these configurations (except a specially designed complex in the *TIP4P* potential); (iii) it is possible that a triply-coordinated carbonyl group will transform into the enolic form; (iv) the vibration frequencies of carbonyl and carbon-carbon asymmetric stretch motions are sensitive to the hydrogen bond coordination with water molecules and can be used as fingerprints for a specific hydrogen bond configuration of acetone species in the water media; (v) the cooperativity effect in a chain of hydrogen bond water network strongly affects the global coordination of water molecules around organic molecules with carbonyl functional group. Although a primary coordination of the carbonyl group is given by the class, each class of the acetone-water clusters include different complexes because the electronic properties of water molecules directly attached to the carbonyl group are modulated by their hydrogen bond environment.

References:

1. G. C. Pimentel, A. L. McClellan, “The Hydrogen Bond”, 1960, W.H. Freeman &CO, San Francisco and London.
2. L. Pauling, J. Am. Chem. Soc., ***57*** (1935) 2680.
3. J. D. Bernal, R. H. Fowler, J. Chem. Phys., ***1*** (1933) 515.
4. D. Eisenberg, W. Kauzmann, “The Structure and Properties of Water”, 1969, Clarendon Press, Oxford.
5. P. V. Hobbs, “Ice Physics”, 1974, Clarendon Press, Oxford.
6. V. F. Petrenko, R. W. Whitworth, "Physics of Ice", 1999, Oxford University Press, Oxford.
7. G. Albrecht, R. B. Corey, J. Am. Chem. Soc. ***61*** (1939) 1087.
8. M. Folk, O. Knop, Chapter 2 in "Water. A comprehensive treatise", vol. 2, ed. F. Franks, 1973, Plenum Press, New York.
9. P. A. Giguer, J. Chem. Phys. ***87*** (1987) 4835.
10. A. Geiger, P. Mausbach, "Molecular Dynamics Simulation Studies of the Hydrogen Bond Network in Water", in "Hydrogen-Bonded Liquids", v. 329, 1989, ed. J. C. Dore, J. Teixeira, NATO ASI Series (C), Kluwer Academic Publisher, London.
11. (a) E. D. Glendening, J. K. Badenhoop, A. E. Reed, J. E. Carpenter, J. A. Bohmann, C. M. Morales, F. Weinhold, NBO 5.0, Theoretical Chemistry Institute, University of Wisconsin, Madison, 2001; (b) F. Weinhold, NBO 5.0 Program Manual, Department of Chemistry University of Wisconsin, Madison, Wisconsin, 1996-2001.
12. J. L. Finney, A. Hallbrucker, I. Kohl, A. K. Soper, D. T. Bowron, Phys. Rev. Lett. ***88*** (2002) 225503-1.
13. OriginPro 7.5 SR0, v. 7.5714, OriginLab Corporation, Northampton, USA.
14. J. P. Devlin, V. Buch, J. Phys. Chem. ***99*** (1995) 16534.
15. B. Rowland, N. S. Kadagathur, J. P. Devlin, V. Buch, T. Feldman, M. J. Wojcik, J. Chem. Phys. ***102*** (1995) 8328.
16. W. S. Benedict, N. Gailar, E. K. Plyler, J. Chem. Phys. ***24*** (1956) 1139.
17. U. Buck, F. Huisken, Chem. Rev. ***100*** (2000) 3863.

18. J. Sadlej, V. Buch, J. K. Kazimir, U. Buck, J. Phys. Chem. ***103*** (1999) 4933.
19. (a) R. Janoshek, E. G. Weidemann, H. Pfeiffer, G. Zundel, J. Am. Chem. Soc. ***94*** (1972) 2387; (b) G. Zundel, Adv. Chem. Phys. ***111*** (2000), 1.
20. J. Kim, U. W. Schmitt, J. A. Gruetzmacher, G. A. Voth, N. E. Scherer, J. Chem. Phys. ***116*** (2002) 737.
21. J. P. Devlin, N. Uras, J. Sadlej, V. Buch, Nature ***417*** (2002) 269.
22. A. J. Tursi, E. R. Nixon, J. Chem. Phys. ***52*** (1970) 1521
23. J. A. Salthouse, T. C. Waddington, J. Chem. Phys. ***48*** (1968) 5274.
24. K. R. Asmis, N. L. Pivonka, G. Santamrogio, M. Brümmer, C. Kaposta, D. M. Neumark, L. Wöste, Science ***299*** (2003) 1375.
25. A. M. Middlebrook, L. T. Iraci, L. S. McNeill, B. G. Koehler, M.A. Wilson, O. W. Saastad, M. A. Tolbert, D. R. Hanson, J. Geophys. Res. ***98*** (1993) 20473.
26. G. Ritzhaupt, J. P. Devlin, J. Chem. Phys. ***95*** (1991) 90.
27. R. J. Bartlett, Ann. Rev. Phys. Chem. ***32*** (1981) 359.
28. B. Jeziorski, R. Moszynski, K. Szalewicz, Chem. Rev. ***94*** (1994) 1887.
29. K. Szalewicz, B. Jeziorski, Mol. Phys. ***38*** (1979) 191.
30. G. Chałasiński, M. M. Szczęśniak, Mol. Phys. ***63*** (1988) 205.
31. G. Chałasiński, M. M. Szczęśniak, Chem. Rev. ***94*** (1994) 1723.
32. A. D. Becke, J. Chem. Phys. ***88*** (1988) 1053.
33. A. D. Becke, J. Chem. Phys. ***98*** (1993) 5648.
34. D. J. Lacks, R. G. Gordon, Phys. Rev. ***47*** (1993) 4681.
35. P.R. Rablen, J.W. Lockman, W.L. Jorgensen, J. Phys. Chem. A ***102*** (1998) 3782.
36. T. H. Dunning, J. Chem. Phys. ***90*** (1989) 1007.
37. M. J. Frisch, J. A. Pople, J. S. Binkley, J. Chem. Phys. ***80*** (1984) 3265.
38. S. F. Boys, F. Bernardi, Mol. Phys. ***19*** (1970) 553.
39. Prof. J. D. Goddard, private communications, University of Guelph, 2003.
40. P. S. Sedano, Ph.D. Thesis "Implementation and application of basis set superposition error-correction schemes to the theoretical modeling of weak intermolecular interactions", Department of Chemistry, University of Girona, Girona, Spain, 2001.

41. S. Huzinaga, "The Method of Molecular Orbitals", on Russian, 1983, Moscow, Publisher "World", Russia.
42. R. Ludwig, F. Weinhold, T. C. Farrar, J. Chem. Phys. ***102*** (1995) 5118.
43. S. Scheiner, "Hydrogen Bonding. A Theoretical Perspective", Topics in Physical Chemistry, 1997, Oxford University Press.
44. B. F. King, F. Weinhold, J. Chem. Phys. ***103*** (1995) 333.
45. R. A. Nyquist, Vib. Spect. ***7*** (1994) 1, and Ref. therein.
46. K. Morokuma, K. Kitaura, "Variational approach (SCF *ab-inito* calculations) to the study of molecular interactions: the origin of molecular interactions", in 47.
47. H. Ratajczak, W. J. Orville-Thomas, "Molecular Interactions", v. 1, 1980, Wiley&Sons, Chichester.
48. H. S. Frank, Proc. Royal. Soc. London, Ser. A ***247*** (1958) 481.
49. G. Nemethy, H. A. Scheraga, J. Chem. Phys. ***36*** (1962) 3382.
50. G. Nemethy, H. A. Scheraga, J. Chem. Phys. ***41*** (1964) 680.
51. J. D. Bernal, R. H. Fowler, J. Chem. Phys. ***1*** (1933) 515.
52. N. H. Fletcher, Phil. Mag. ***18*** (1968) 1287.
53. N. H. Fletcher, "The Surface of Ice", p. 132 in the "Physics and Chemistry of Ice", ed. E. Whalley, S. J. Jones, L.W Gold, 1973, Royal Society of Canada, Toronto University Press, Ottawa.
54. G. L. Richmond, Chem. Rev. ***102*** (2002) 2693.
55. T. R. Dyke, K. M. Mack, J. S. Muenter, J. Chem. Phys. ***66*** (1977) 498.
56. T. R. Dyke, J. Chem. Phys. ***66*** (1977) 492.
57. B. J. Smith, D. J. Swanton, J. A. Pople, H. F. Schaefer III, L. Radom, J. Chem. Phys. ***92*** (1990) 1240.
58. J. G. C. M. van Duijneveldt-van de Rijdt, F. B. van Duijneveldt, J. Chem. Phys. ***97*** (1992), 5019.
59. J. R. Reimers, R. O. Watts, M. L. Klein, Chem. Phys. ***64*** (1982) 95.
60. L. A. Curtiss, D. J. Frurip, M. Blander, J. Chem. Phys. ***71*** (1979) 2703.
61. L. A. Curtiss, J. A. Pople, J. Mol. Spect. ***55*** (1975) 1.

62. E. M. Mas, K Szalewicz, J. Chem. Phys. ***104*** (1996) 7606.
63. M. J. Frisch, J. E. Del Bene, J. S. Binkley, H. F. Schaefer III, J. Chem. Phys. ***84*** (1986) 2279.
64. S. S. Xantheas, C. J. Burnham, R. J. Harrison, J. Chem. Phys. ***116*** (2002) 1493.
65. S. S. Xantheas, J. Chem. Phys. ***104*** (1996) 8821.
66. K. S. Kim, B. J. Min, U-S. Choi, K. Lee, J. Chem. Phys. ***97*** (1992) 6649.
67. E. Clementi, G. Gorongui, O.G. Stradella, in "Modern Techniques in Computational Chemistry: MOTTEC-91, ed. E. Clementi, 1991, ES-COM, Leiden, Netherlands.
68. W. S. Benedict, N. Gailar, E. K. Plyler, J. Chem. Phys. ***24*** (1956) 1139.
69. O. L. Polyansli, P. Jensen, J. Tennyson, J. Chem. Phys. ***101*** (1994) 7651.
70. S. Rybak, B. Jeziorski, K. Szalewicz, J. Chem. Phys. ***95*** (1991) 6576.
71. K. Szalewicz, S. J. Cole, W. Kołos, R. Bartlett, J. Chem. Phys. ***89*** (1988) 3662.
72. H. Popkie, H. Kistenmacher, E. Clementi, J. Chem. Phys. ***59*** (1973) 1325.
73. D. Feller, J. Chem. Phys. ***96*** (1992) 6104.
74. S. M. Cybulski, G. Chałasinski, R. Moszyński, J. Chem. Phys. ***92*** (1990) 4375.
75. M. M. Szczęśniak, R. J. Brenstein, S. M. Cybulski, S. Scheiner, J. Phys. Chem. ***94*** (1990) 1781.
76. A. J. Sadlej, Coll. Czech. Chem. Commun. ***53*** (1988) 1995.
77. J. C. White, E. R. Davidson, J. Chem. Phys. ***93*** (1990) 8029.
78. D-W. Liao, A. M. Mebel, Y-T. Chen, S-H. Lin, J. Chem. Phys. A ***101*** (1997) 9925.
79. W. O. George, B. F. Jones, Rh. Lewis, J. M. Price, J. Mol. Struc. ***550-551*** (2000) 281.
80. (a) E.Bloom, C. Altona, Mol. Phys. ***31*** (1976) 1377; (b) K. B. Wiberg, Y. Thiel, L. Goodman, J. Leszczynski, J. Phys. Chem. ***99*** (1995) 13850.
81. T. Iijima, Bull. Chem. Soc. Japan ***45*** (1972) 3526.
82. G. Dellepiane, J. Overend, Spectrochimica Acta ***22*** (1966) 593.
83. (a) A. M. Mebel, Private communication, 2005.
(b) D-W. Liao, A. M. Mebel, Y-T. Chen, S-H. Lin, J. Chem. Phys. A ***101*** (1997) 9925.
84. J. E. Schaff, J. T. Roberts, J. Phys. Chem. ***98*** (1994) 6900.
85. X. K. Zhang, E.G. Lewars, R. E. March, J. M. Parnis, J. Phys. Chem. ***97*** (1993) 4320.

86. A. Engdahl, Chem. Phys. ***178*** (1993) 305.

87. V. Buch, J. P. Devlin,eds., "Water in Confining Geometeries", 2003, Springler, Berlin.

CHAPTER 5

Experimental Results and Interpretations

5.1 The IR spectral Examination of the Ice Films Vapor Deposition at 125-185 K: Ice Spectral Bands and Dangling Bonds

The polycrystalline and non-crystalline ice films vapor-deposited at 128-185 K were investigated by grazing-angle FTIR RAS. The polycrystalline (pc-ice) phase was found above 155 K while the non-crystalline (nc-ice) phase was formed below 145 K. The nature of the polycrystalline and non-crystalline ice phases can be differentiated by comparing the respective RA spectra with spectral simulations based on the Fresnel reflection method. The OH stretching band, ν_1 and ν_3 at 3800-2800 cm^{-1} exhibits complex behavior as a function of film thickness (from less than 10 nm to 1500 nm), which can be simulated and attributed primarily to the physics of absorption-reflection based on the Fresnel equations for reflection coefficients for π- and σ-polarized light in a vacuum-dielectric film-metal system. The spectral evolution of the OH stretch with the film thickness is found to be similar for both polycrystalline and non-crystalline phases. In addition, spectral features of the incompletely coordinated OH groups at 3700-3690 cm^{-1} have been observed for a majority of nc- and pc-ice samples grown under different deposition conditions over the entire temperature range, which shows that these OH dangling bonds are an integral part of the surfaces of both non-crystalline and polycrystalline ice phases. For thin films less than 200 nm thick, both kinds of ice are found to have a comparable amount of OH dangling bonds. In contrast, the thicker films (with thickness greater than 700 nm) of the non-crystalline phase contain a noticeably larger amount of OH dangling bonds than the polycrystalline films of comparable thickness. This thickness dependence of the OH dangling bond feature suggests that the OH dangling bonds are located most likely on the external surfaces of the crystalline grains and/or of the ice film itself at larger thickness for polycrystalline phase and on the tracery external surface in the case of non-crystalline phase.

5.1.1 Polycrystalline Ice at 155-185 K

Figure 5.1.1a shows the experimental FTIR-RA spectra of the initial stage of water

deposition at 5×10^{-7} Torr with the Cu substrate held at 160 K, which correspond approximately to 10 seconds (Figure 5.1.1a, Curve A) and 30 seconds (Figure 5.1.1a, Curve B) into the phase formation. These spectra are compared with the Fresnel spectrum for pc-ice with film thickness of 0.5 nm (Figure 5.1.1a, Curve C). Evidently, there is a significant difference between the experimental and Fresnel spectra. In particular, the OH stretch band for the Fresnel spectrum (Figure 5.1.1a, Curve C) is blue-shifted by ~ 45 cm^{-1} and has a different shape from the experimental spectra (Figure 5.1.1a, Curves A-B), which suggests that the ice deposit is heterogeneous and consists predominantly of small particles that scatter the IR light. For the initial steps of the ice phase formation, the production of crystalline nuclei, instead of a uniform film, is therefore confirmed. This observation is consistent with the general tendency to minimize the surface area of a newly forming phase. As suggested by Mayer and Pletzer [1], the formation of the primary crystalline ice nuclei may have already occurred, at least partially, in the gas phase near the cold substrate surface.

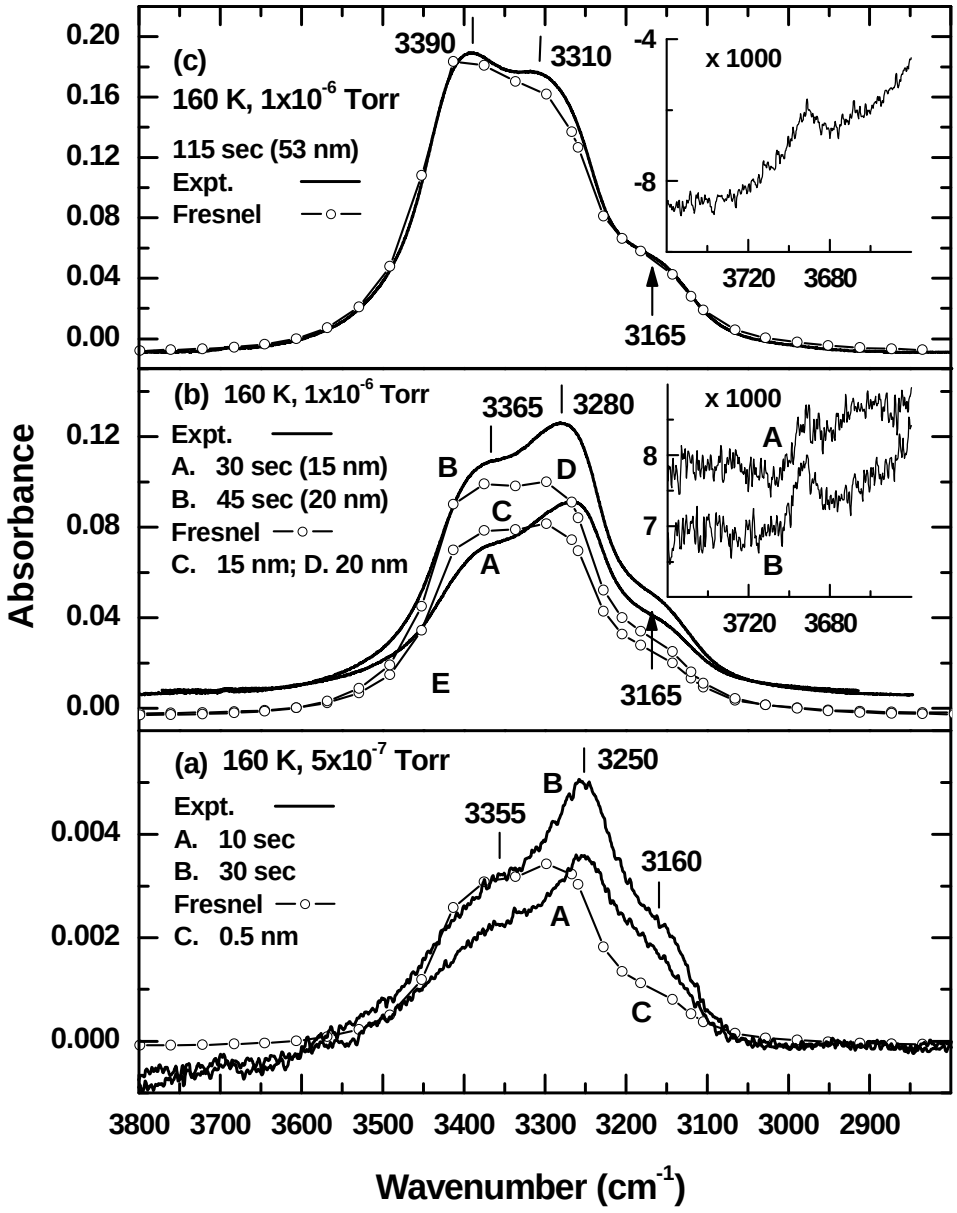

Figure 5.1.1. Comparison of experimental IR-RA spectra of the OH stretch region at 160 K for the early stage of formation of a polycrystalline ice (pc-ice) film with Fresnel simulations. (a) Experimental spectra (at 2 cm^{-1} resolution) for an ice film obtained by vapour deposition at 5×10^{-7} Torr for (A) 10 and (B) 30 seconds are compared with (C) the Fresnel spectrum of a 0.5-nm-thick pc-ice film (using optical constants obtained for films deposited at 163 K [2]). (b) Experimental spectra (at 2 cm^{-1} resolution) for an ice film obtained by vapour deposition at 1×10^{-6} Torr for (A) 30 and (B) 45 seconds (corresponding to estimated thicknesses of 15 and 20 nm respectively) are compared with the Fresnel spectrum of pc-ice with film thicknesses of

(C) 15. (c) Experimental spectra (at 0.5 cm^{-1} resolutions) for an ice film obtained by vapour deposition at 1×10^{-6} Torr for 115 seconds (corresponding to an estimated film thickness of 53 nm) is compared with the Fresnel spectrum of a pc-ice film of the same thickness. Inserts in (b) and (c) show expanded views (with the ordinate expanded by 1000) of the OH dangling bond region (3760-3640 cm^{-1}) for the respective films.

Continued deposition would result in the emergence of a polycrystalline film with RA spectra corresponding to intermediate scattering and Fresnel spectra (Figure 5.1.1b) and ultimately to the Fresnel spectra (Figure 5.1.1c). In particular, Figure 5.1.1b and Figure 5.1.1c show the experimental RA spectra for water deposition at 1×10^{-6} Torr with the substrate held at 160 K corresponding approximately to 30 and 45, and 115 seconds, respectively, into the phase formation. Fresnel spectra are generated with the appropriate film thicknesses that closest approximate the respective experimental spectra. At the 115-second deposition, the experimental spectrum evolves into that best described by the Fresnel model (Figure 5.1.1c). The ice phase as depicted in Figure 5.1.1b therefore corresponds to an intermediate state between the Fresnel thin-film and ensemble of ice particles. In this intermediate state, accumulation of a sufficient amount of crystalline nuclei on the substrate surface would eventually accelerate deposition in the inter-grain region. Figure 5.1.1b and Figure 5.1.1c also reveal the presence of a weak OH *DB* feature at 3693 cm^{-1} in the ice phase deposited at 160 K, with the observed frequency corresponding to a 3-coordinated OH group [3]. It is of interest to note that these OH *DB's* exist even at the early stage of ice formation and presumably on the surfaces of the crystalline grains that give rise to the scattering spectra.

By using proton-ordered and disordered Ic and Ih ice models, Buch and Devlin made use of four oscillating dipoles tetrahedrally arranged around a central O atom as the basis to calculate the OH stretching band [4]. They attributed the central peak of the OH stretching band at 3220 cm^{-1} to the zero wave-vector modes of two transversal (*TO*) branches and a longitudinal (*LO*) branch (which corresponds to two dipoles moving "in" with the other two diploes moving "out" in a way that correlates with the asymmetric stretching character of the v_3 molecular mode of an isolated water molecule). The asymmetric v_3 character of the OH central peak is in agreement with the spectral assignment made by Whalley [5]. The shoulder located at the lower-frequency side of the central peak appears to originate from the transversal

modes strongly perturbed by intramolecular interactions and was therefore attributed to the in-phase v_1 *TO* branch by Buch and Devlin [4], again in accord with Whalley's earlier assignment [5]. The state with the lowest OH stretch frequency corresponds to the globally in-phase v_1 vibration, which dominates in the Raman spectra obtained with parallel polarization [6]. In the higher-frequency region of the OH stretching band, an intermediate branch (i.e., one that exhibits no systematic variation in the angle between the dipole moment of the lattice and the wave-vector) and non-zero wave-vector modes of the aforementioned longitudinal branch were found [4]. Originated from the higher-frequency out-of-phase v_1 vibration of the four dipoles surrounding the O atom, the intermediate branch was characterized by a small dipole moment near the center of the Brillouin zone, in marked contrast to the longitudinal modes (with origin from the v_3 molecular vibration), which carry a significant dipole moment over the entire Brillouin zone [4].

Buch and Devlin further demonstrated that the OH stretch absorption band can be strongly affected by the shape of the ice medium and by the polarization of the electric field [4]. In particular, in the case of an ice slab, the modes of the higher-frequency intermediate and longitudinal branches are stimulated with surface-perpendicular polarization while the lower-frequency transversal modes of the v_1 branch are preferentially excited with surface-parallel polarization. The dependence of the absorption spectra on the shape is caused by the long-range dipole-dipole interaction, which was found to include a shape-dependent component associated with the surface polarization charge [7]. The oscillating surface charge creates an electric field inside the sample that changes the energy gap between the ground and excited vibrational levels [7], and consequently the corresponding vibrational frequencies become shape-dependent. However, the shape-dependent effect predicted by the model was found to be considerably stronger than that observed experimentally [4]. This discrepancy was attributed to a limitation on the spatial extent of the vibrational excited states imposed by the imperfections in the pc-ice medium.

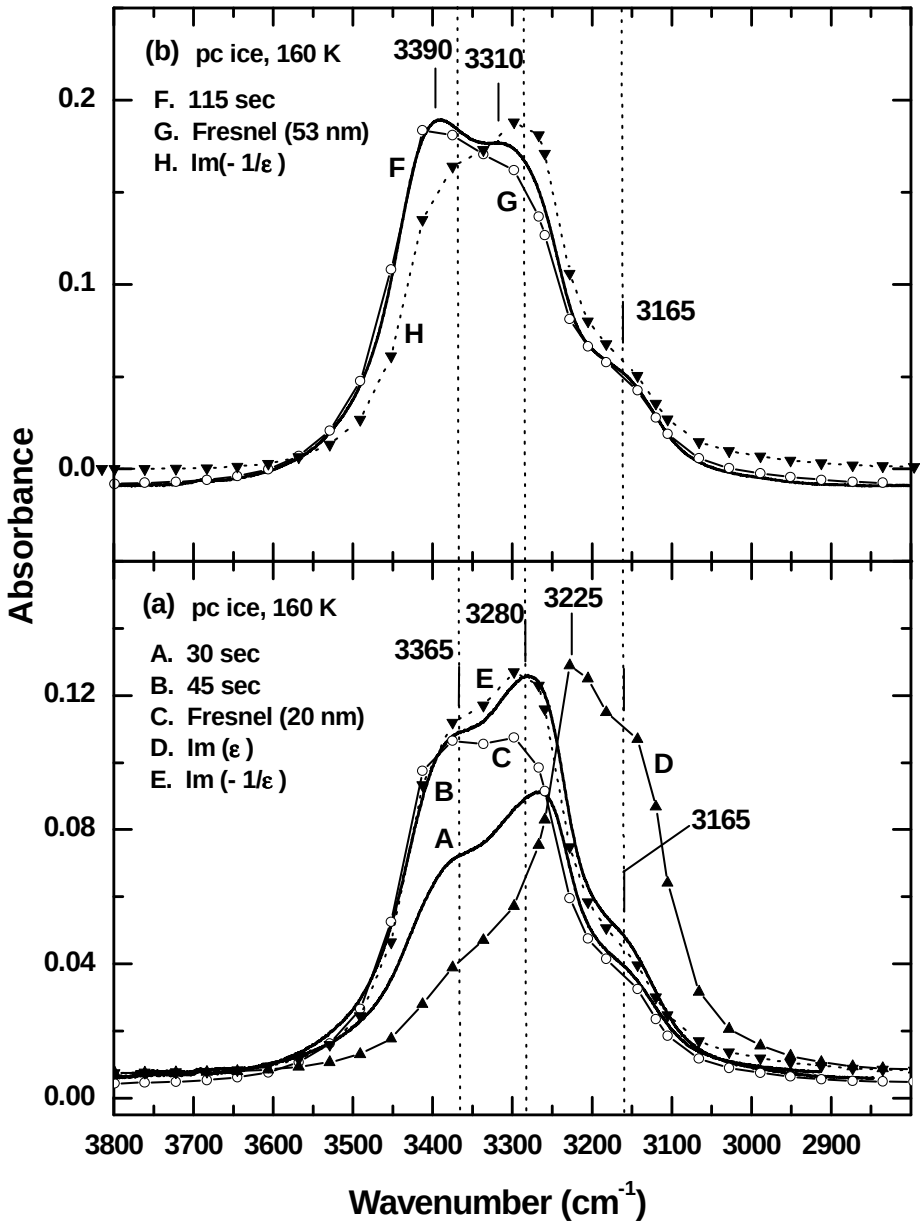

Figure 5.1.2. Comparison of the OH stretching band of the experimental FTIR-RA spectra of polycrystalline (pc) ice deposits with simulated Fresnel and Berreman profiles.
The pc-ice film was obtained by vapour deposition at 160 K and 1×10^{-6} Torr for 30 (A), 45 (B) and 115 seconds (F) and compared with the Fresnel spectra of 20-nm (C) and 53-nm (G) thick pc-ice films and the Berreman (E, H) and transmission profiles (D), all arbitrarily normalized.

The Buch-Devlin simulation of IR absorption by an ice slab for the surface-perpendicular polarization [4] could be directly compared with the experimental RA spectra of ultrathin ice films on a metal surface at grazing-angle illumination with π-polarized or non-polarized light. Upon reflection on a highly conductive metal, the σ-polarized component of the incident electric field is almost completely eliminated near its surface and only the π-polarized component of the electric field remains, which provides the physical justification for comparing the experimental RA spectra with the simulated spectrum for excitation of an ice slab by just the (surface-perpendicular) π- polarization. In particular, the Buch-Devlin model [4] predicts that the absorption spectra of the ice slab for the surface-perpendicular polarization are primarily originated from excitation of the intermediate and ν_3 *LO* branches, of which the former is of a higher frequency. Figure 5.1.2 compares our experimental RA spectra of the OH stretching band obtained for ultrathin pc-ice deposits (with an estimated thickness below 50 nm) with the corresponding Fresnel spectra and with the Berreman and transmission profiles [8] (arbitrarily normalized to the band maxima of the respective experimental spectra). The Berreman profile corresponds to the energy loss function defined as $Im(-\varepsilon^{-1}) = \varepsilon''/(\varepsilon'^2 + \varepsilon''^2)$, where the dielectric function $\varepsilon = \varepsilon' - i\,\varepsilon''$ (with its real ε' and imaginary ε'' parts), while the transmission profile is given by $Im(\varepsilon)$ (i.e., ε''). The Fresnel spectra and both of these profiles are generated based on the spectral data reported by Toon et al. [2]. Evidently, the spectra for pc-ice deposited at 160 K and 1×10^{-6} Torr for 30 sec and 45 sec (Curves A and B, Figure 5.1.2a) are in good accord in shape with the Buch-Devlin spectrum for the ice slab (see Figure 5.1.2c in Ref. [4]), supporting the assignment of the higher-frequency shoulder at 3365 cm^{-1} to the intermediate branch and of the 3280-cm^{-1} feature to the ν_3 *LO* band. The band maximum for the 3280-cm^{-1} peak is also found to be in good agreement with that of the ν_3 *LO* band (3299 cm^{-1}) predicted by Whalley [5]. Furthermore, the 45-sec spectrum (Curve B, Figure 5.1.2a) closely follows the energy loss function as represented by the Berreman profile (Curve E, Figure 5.1.2a), which again indicates that the blue shift of the central OH stretch peak with respect to the transmission profile (Curve D, Figure 5.1.2a) is due to stimulation of the longitudinal modes of the ν_3 branch. The apparent enhancement of the higher-frequency part of the OH stretch with the corresponding weakening of the lower-frequency part could be associated with the blue shift of the most intense ν_3 branch alone and not to the actual changes in their own respective intensities. As expected for thicker deposits, the 115-sec RA spectrum

shown in Figure 5.1.2b (Curve F) evidently begins to deviate from the Berreman profile (Curve H, Figure 5.1.2b) and converge to the Fresnel spectrum (Curve G, Figure 5.1.2b), indicating the onset of the formation of a stratified ice film with smooth interfaces. The continual blue shift of the OH stretch and the apparent changes in the relative intensities of the band components (band shape deformation) with increasing thickness are likely caused by optical effects in the film on a metal substrate [9]. Accordingly, at the initial stage of pc-ice film formation the ice deposit exists in the form of crystallites, which causes the experimental spectra to deviate from the Fresnel model. This is illustrated by the differences between the 30-sec and 45-sec spectra (both with a common shape, Curves A and B in Figure 5.1.2a) and the corresponding Fresnel spectrum. In this case, the frequency position of a band associated with the v_3 *LO* modes becomes dependent upon the particle shapes of the crystallites [6,7].

Further water deposition leads to the formation of a relatively thick film and a smooth vacuum-ice interface, and the corresponding spectra would be expected to be more similar to the Fresnel spectra. Figure 5.1.3 shows the experimental spectra for relatively thick films obtained by water vapour deposition at 1×10^{-6} Torr with the substrate held at 160 K for 3.5 (Figure 5.1.3a), 20 (Figure 5.1.3b), 33.5 (Figure 5.1.3c) and 52.5 minutes (Figure 5.1.3d). In addition to the OH stretch features at 3410, 3325 and 3180 cm^{-1} shown in Figure 5.1.3a, the features near 1630 cm^{-1} and 2240 cm^{-1} have been attributed to the OH bending band (v_2) possibly coupled with the first overtone ($2v_R$) of the hindered rotational lattice mode ($v_R \approx 850$ cm^{-1} [10]) and to the combination band of the OH bending and hindered rotational mode and/or the second overtone ($3v_R$) of the hindered rotational mode, respectively [11].

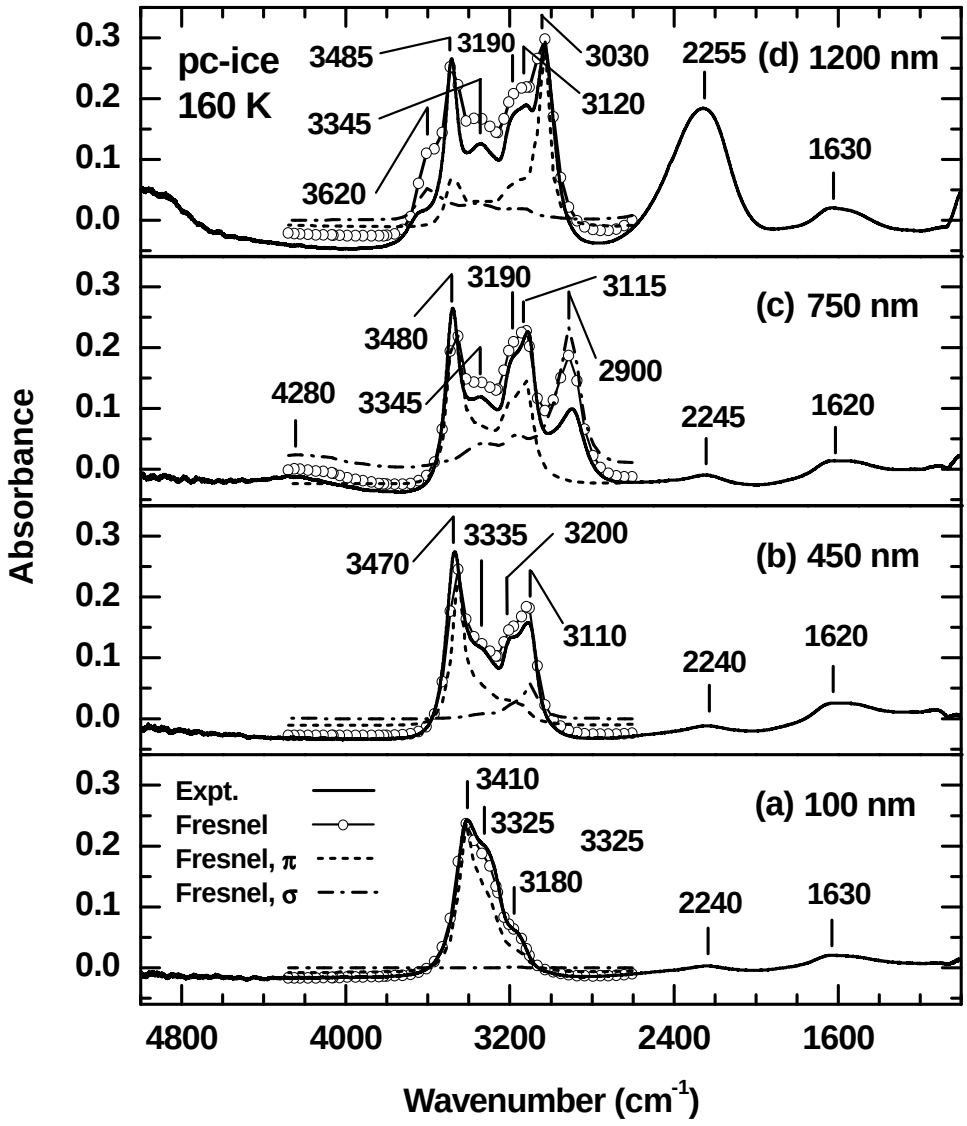

Figure 5.1.3. Comparison of experimental IR-RA spectra of thick polycrystalline films with the corresponding Fresnel spectra for non-polarized light and their σ- and π- components. The films were obtained by vapour deposition at 160 K and 1 ×10-6 Torr for (a) 3.5, (b) 20, (c) 33.5 and (d) 52.5 minutes. The IR-RA spectra (at 0.5 cm-1 resolution) are compared with the corresponding Fresnel spectra for non-polarized light and their σ- and π- polarized components (arbitrarily normalized) involving 100-, 450-, 750- and 1200-nm-thick films, respectively.

With the exception of the feature at 2255 cm^{-1} for the 1200-nm-thick film, these two vibrational bands are found to be essentially stationary with a general increase in the spectral

intensity with increasing film thickness (Figure 5.1.3). Furthermore, there is excellent agreement in the OH stretch region between the experimental spectrum and the corresponding Fresnel spectrum of a pc-ice film with thickness of 100 nm (Figure 5.1.3a). Indeed, the good accord between the experiment and the Fresnel simulation for even thicker films allows the thickness parameter in the Fresnel calculation to be used as a semi-empirical estimate of the thickness of the as-grown film. We have also performed optical interference measurements of the as-grown film and the film thickness so obtained is found to be in good accord with the corresponding Fresnel thickness parameter (depicted in Figure 5.1.3).

With increasing film thickness from 20 nm (Figure 5.1.1b) to ~50 nm (Figure 5.1.1c), the experimental band maximum is shifted to a higher frequency, with a concomitant increase in the intensity of the high-frequency shoulder near 3390-3400 cm^{-1}. The absorbance of the OH stretch feature appears to level off at ~70 integrated *AU*'s with increasing film thickness up to 100 nm (Figure 5.1.3a). Further film growth from 100 nm to 250 nm does not change the spectral intensity and band shape significantly. As the water deposition continues, the OH stretch region becomes considerably more complex, as depicted in Figure 5.1.3b-d. In particular, at least three spectral features are evident near 3410, 3325 and 3180 cm^{-1} for the 100-nm-thick pc-film (Figure 5.1.3a), which originate from the three corresponding features at 3375, 3300 and 3180, respectively, identified previously for the Fresnel spectrum of a 1-nm thick film. The shoulder feature at 3180 cm^{-1} for the 100-nm-thick film becomes a more prominent peak at 3200 cm^{-1} for the 450-nm-thick film, while the more intense features at 3325 and 3410 cm^{-1} shift to 3335 and 3470 cm^{-1}, respectively (Figure 5.1.3b). These three observed features remain relatively "stationary" in frequencies with increasing film thickness above 450 nm (Figure 5.1.3c-d).

To investigate the evolution of the remaining OH features in Figure 5.1.3 with increasing film thickness, we have evaluated the σ- and π-components of the Fresnel spectra, which are arbitrarily normalized to the corresponding maxima of the overall calculated spectra. It is important to note that the absorbance of the overall Fresnel spectrum of an ice film is not a simple linear combination of their constituent σ- and π-components. The present discussion is therefore limited to the identification of the contributing features of individual σ- and π-components to the overall spectrum by their respective peak locations. Evidently, the frequency position, shape, and intensity of the OH stretch are determined almost entirely by

the π-polarized component of the IR light for films with thickness below ~250 nm (Figure 5.1.3a), where the contribution of the *σ*-component is seen to be negligible. Similar results have also been reported for very thin films, with thickness below ~10 nm, in earlier theoretical studies by Greenler [12] and McIntyre and Aspens [13]. For film thickness above 250 nm, there is a general increase in the overall intensity of the σ-polarized profile. The low-frequency shoulder in the σ-polarized profile is seen to travel from 3110 cm^{-1} (for the 450-nm-thick film in Figure 5.1.3b) to 2900 cm^{-1} (for the 750-nm-thick film in Figure 5.1.3c), which contributes to the corresponding feature at 3110 cm^{-1} and at 2900 cm^{-1} in the respective experimental spectra. Further increase in the film thickness to 1200 nm causes this σ-polarized feature to move further towards the lower frequency, giving rise to the strong enhancement to the spectral intensity of the feature observed at 2255 cm^{-1} (Figure 5.1.3d). As illustrated in Chapter 3, this phenomenon is evidently caused by destructive interference of the σ-polarized IR light in a uniform film. Furthermore, a second *σ*-polarized feature near 4280 cm^{-1} appearing in the spectrum for the 750-nm-thick film (Figure 5.1.3c) is also found to migrate to 3620 cm^{-1} for the 1200-nm-thick film (Figure 5.1.3d). This migration of interference peaks is believed to be responsible for the intensity enhancement of the OH *DB* (at 3693 cm^{-1}) for the film thickness between 850 nm and 1200 nm. Similar interference peak movement is also evident for the π-polarized feature at 3115 cm^{-1} for the 750-nm-thick film (Figure 5.1.3c), which travels to 3030 cm^{-1} as the film thickness is increased to 1200 nm (Figure 5.1.3d). The observation of destructive interference peak movements generally reflects the quality of film uniformity obtainable for pc-ice by vapour deposition.

In the case of grazing-angle incidence, there is an opportunity to qualitatively categorize three different regions of thickness according to the spectral behaviour of the OH stretch mode. The extent of each region is a function of the incident angle and is therefore relative in value. In our case of 83º angle of incidence, the OH stretch band intensity is proportional to the film thickness in the first thickness region of approximately below 50 nm, and the shape of the band reflects the absorbance profile without being affected by the frequency profile of the vacuum-ice reflectance. In the intermediate thickness region of 50-250 nm, the intensity of the OH stretch is saturated, in this case, at 70 integrated *AU*s (this limit depends on the incident angle) and remains unchanged despite further increase in the film thickness. Instead, a gradual blue shift in the maximum of the OH band towards the high-

frequency minimum of the vacuum-ice reflection curve in the region of the OH stretch resonance (the so-called Christiansen effect [14]) is observed. The OH stretch band and the entire spectrum in the first two regions of film thickness can be principally described by the interaction of the π-polarized component of the IR light with the film. In the third thickness region starting at ~300 nm, the optical behaviour of the OH stretch band with increasing film thickness is determined primarily by the reflectance of the incoming IR light from the vacuum-ice interface, because the refracted beam is completely absorbed by the ice in the frequency range of the OH stretch band. The splitting of the OH stretch observed in Figure 5.1.3b-d takes place due to the reflective character of the OH band. Unlike thinner films, the RA spectrum in this third region of thickness is the result of contributions from both π- and σ-polarized components.

Although we have presented glancing-incidence FTIR-RAS data for ice films deposited at 160 K, similar data have also been obtained for ice films deposited at temperature as low as 155 K and as high as 185 K. These films have been classified as pc-ice based on similar Fresnel simulations discussed above. Our present data for pc-ice are found to be in good accord with the RA spectra for films deposited at 165 K over the 100-1000-nm thickness range reported by Zondlo *et al.* [15]. Our spectrum for a 20-nm-thick pc-ice film (Figure 5.1.1b) is also similar to that observed by Horn *et al.* for a pc-ice film obtained by crystallization at 155 K of an amorphous film grown at 80 K [16]. Figure 5.1.4a compares our spectrum for a 70-nm-thick pc-ice film (obtained at 83° incidence) with the RA spectrum obtained at 75° incidence by Jenniskens *et al.* [17] for an ice film deposited at 80 K followed by annealing at 160 K for 175 seconds. The spectrum by Jenniskens *et al.* is found to be in good agreement with a Fresnel spectrum calculated for an 80-nm-thick pc-ice film at 75° incidence and is consistent with the present work. Furthermore, Barone *et al.* has reported a RA spectrum for an ice film deposited at 140 K followed by annealing to 160 K, which is found to be in good agreement with our present data, and further attributed the observed dramatic change in the RA spectrum after annealing above 150 K to ordering of the amorphous ice to a more crystalline lattice [18]. The good agreement of our spectra with the spectra reported in these early studies [10, 15, 18] therefore confirms the polycrystalline character of the ice films prepared by direct vapour deposition at temperature above 155 K.

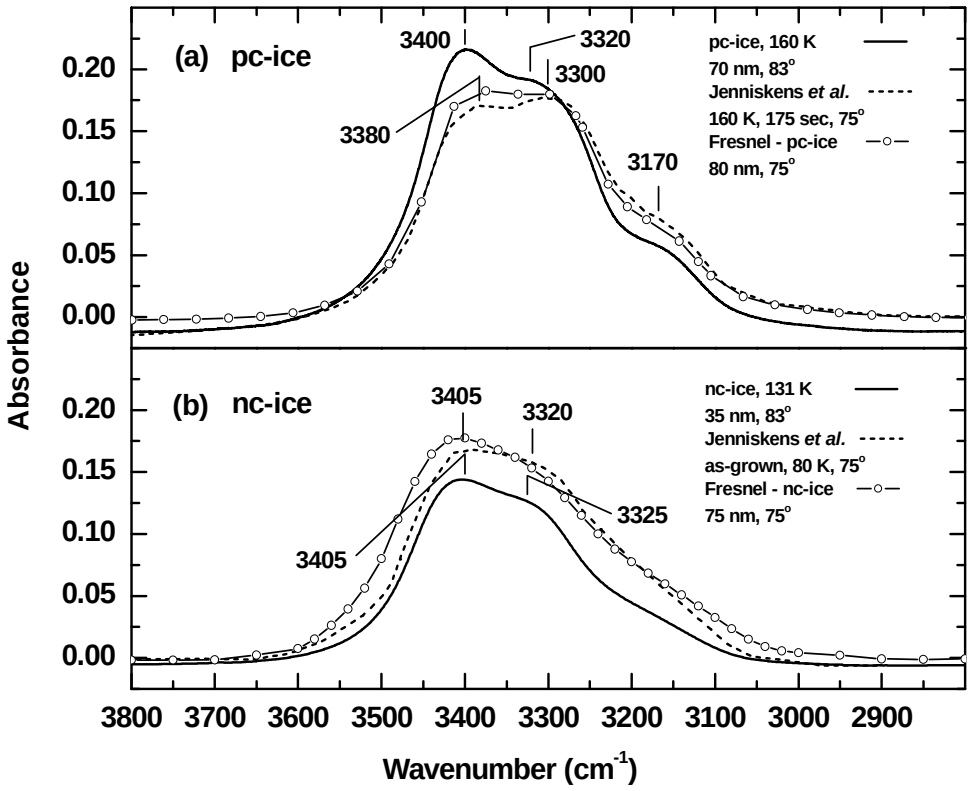

Figure 5.1.4. Comparison of the present experimental IR-RA spectra obtained at 83º of incident with the corresponding RA spectra reported by Jenniskens *et al.* at 75º incidence [17]. The present spectra for (a) a 70-nm thick polycrystalline ice (pc-ice) film deposited at 160 K (recorded at 0.5 cm^{-1} resolution) and (b) a 35-nm-thick non-crystalline ice (nc-ice) film deposited at 131 K (recorded at 2 cm^{-1} resolution) are compared with the corresponding RA spectra reported by Jenniskens *et al.* [17] at 75º incidence for ice films deposited at 80 K followed by annealing at 160 K for 175 sec, and as-grown at 80 K, respectively. The latter spectra are also compared with the respective Fresnel spectra for an 80-nm-thick pc-ice film and a 75-nm-thick nc-ice film calculated at 75º incidences.

5.1.2 Noncrystalline Ice at 128-145 K

Figure 5.1.5 compares the experimental spectra of thin nc-ice films deposited at 1×10^{-6} Torr for 40, 65, and 90 seconds with the substrate held at 131 K with Fresnel spectra for nc-ice with corresponding film thicknesses of 6, 18 and 35 nm, respectively. As expected with

increasing film thickness in this range, the overall OH stretch band increases in intensity. The small blue shift in the peak maximum from 3395 cm^{-1} (Figure 5.1.5, Curve A) to 3402 cm^{-1} (Figure 5.1.5, Curve C) along with a slight increase in the relative intensity of the high-frequency shoulder with increasing film thickness is due principally to the physical optical effects as illustrated in the Fresnel simulations and not to structural changes in the nc-ice network during film growth. The Fresnel spectra are evidently in reasonable agreement with the experiment for the nc-ice film in this thickness range, with notable discrepancies found in the width and the higher-frequency part of the band. The difference in the deposition temperature could lead to the formation of different water networks that could exhibit an OH stretch band with a different frequency position and shape. In particular, Hagen *et al.* have shown that annealing an amorphous ice sample deposited at 10 K to 130 K leads to a red shift of the OH stretch in the transmittance IR spectrum, along with narrowing of the spectral line and an increase in the peak intensity [19]. These irreversible spectral changes were attributed to structural reconstruction in the water network that occurs below the temperature of phase transformation to Ic (135-140 K) during the annealing process [19]. In addition, reversible spectral changes in the OH feature involving red shift, band narrowing and enhanced peak intensity with decreasing sampling temperature were also observed, which therefore indicates that the optical constants of the nc-ice films also depend on the temperature of the film (at which measurement is made). In keeping with the observations by Hagen *et al.* [19], these discrepancies could be attributed to the differences in the structures of the water network at different deposition temperatures. The stronger higher-frequency part of the Fresnel spectra obtained with optical constants at 77 K than the experimental spectra collected at 131 K suggests that stronger hydrogen bonding and more structural uniformity in the water network could be obtained at a higher deposition temperature. Moreover, the OH stretch band in the Fresnel spectrum for the nc-ice film is blue-shifted and wider in comparison with that of the corresponding Fresnel spectrum for a pc-ice film (and with the experimental pc-ice spectrum), consistent with the aforementioned temperature behavior observed by Hagen *et al.* [19].

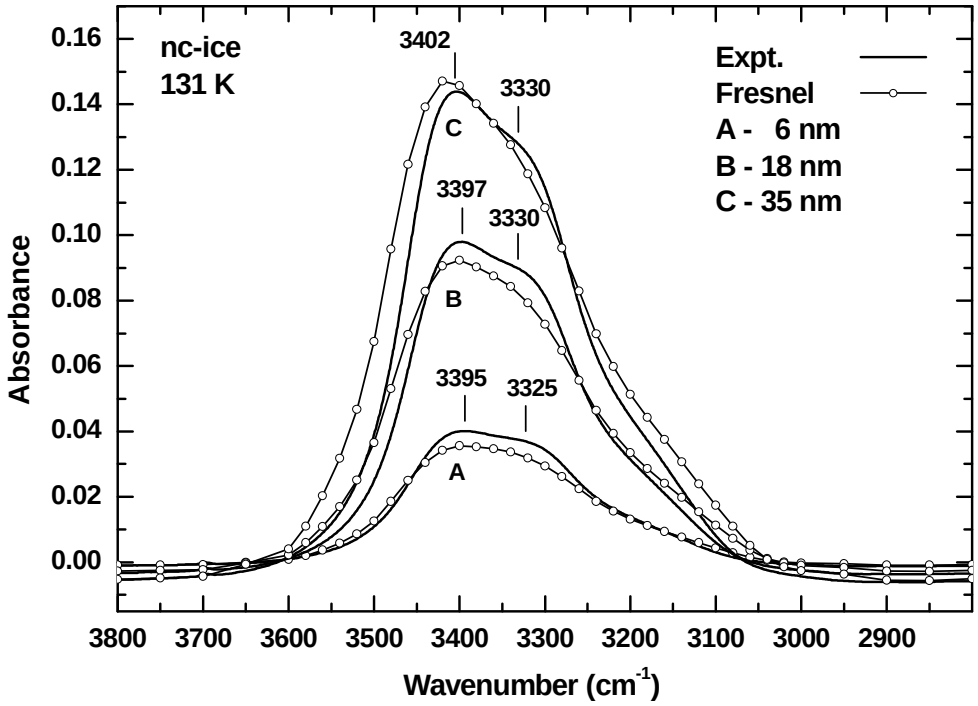

Figure 5.1.5. Comparison of experimental IR-RA spectra (at 2 cm^{-1} resolution) for non-crystalline ice (nc-ice) films deposited at 131 K and 1×10^{-6} Torr for (A) 40, (B) 65, and (C) 90 seconds with the corresponding Fresnel spectra for film thicknesses of 6, 18, and 35 nm, respectively.

Figure 5.1.6 compares the experimental and the corresponding Fresnel spectra of nc-ice and pc-ice films of three different thicknesses: 18-20 nm, 50-60 nm and 90-100 nm. Like the nc-ice film of a smaller thickness (Figure 5.1.5), the FTIR-RA spectra of the thicker nc-ice films are also found to be in general accord with the corresponding Fresnel spectra. Unlike pc-ice, discrepancies are clearly notable in the shape and the higher-frequency part of the Fresnel spectra when compared with the experiment for nc-ice. For films with a larger thickness, there is an apparent blue shift in the OH stretch band maximum for nc-ice relative to that for pc-ice [e.g., 3410 cm^{-1} vs 3385 cm^{-1} for 50-60 nm (Figure 5.1.6b), and 3425 cm^{-1} vs 3410 cm^{-1} for 90-100 nm (Figure 9c)] and in the frequency position of the band center of the OH stretch [e.g., 3320 cm^{-1} vs 3300 cm^{-1} for 50-60 nm (Figure 5.1.6b) and 3330 cm^{-1} vs 3310 cm^{-1} for 90-100 nm (Figure 5.1.6c)].

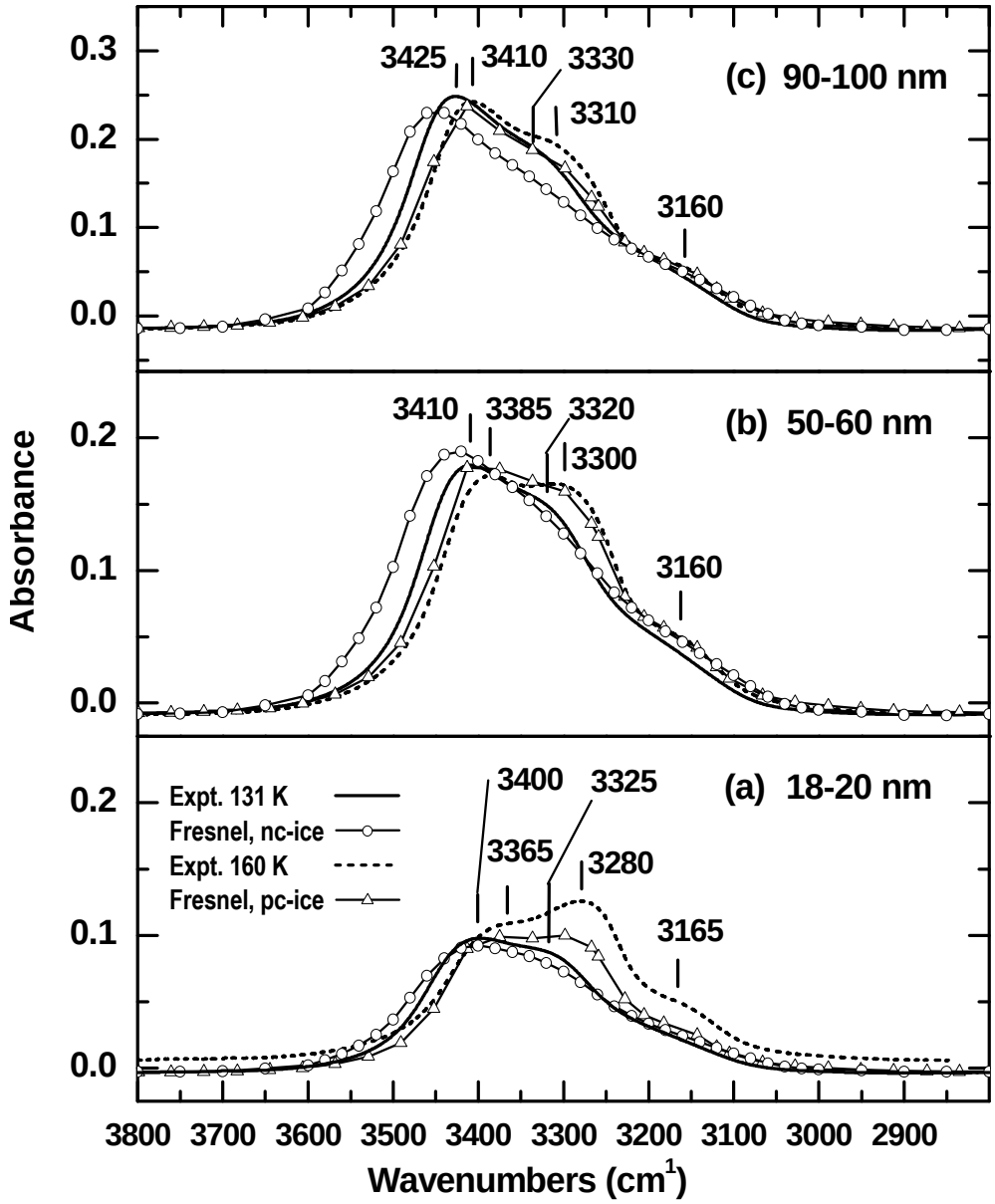

Figure 5.1.6. Comparison of experimental IR-RA spectra and the corresponding Fresnel spectra in the OH stretch region for non-crystalline ice (nc-ice) and polycrystalline ice (pc-ice) deposited at 1×10^{-6} Torr and 131 K and 160 K, respectively.

The corresponding thickness parameter used for the Fresnel simulations are (a) 18 (20) nm for 45 seconds of deposition for nc-ice (pc-ice), (b) 60 (50) nm for 120 (115) seconds of deposition for nc-ice (pc-ice), and (c) 90 (100) nm for 220 (240) seconds of deposition for nc-

ice (pc-ice). The nominal spectral resolution is 2 cm^{-1} for nc-ice spectra and 0.5 cm^{-1} for pc-ice spectra. The low-frequency shoulder clearly observable at 3160-3165 cm^{-1} in the spectra of pc-ice is less prominent in the nc-ice spectra (Figure 5.1.6a).

The blue shift and the less discernible shape of the entire OH stretching mode for nc-ice reflect the structural differences in the organization of the water networks between nc-ice and pc-ice, indicating the weaker hydrogen bonding system with a larger variation in such structural parameters as the nearest-neighbour separation and the OH-O angle. In the case of the 18-20-nm-thick film, the corresponding spectrum for nc-ice can best be approximated by the Fresnel model (Figure 5.1.6a), which suggests that the structure of the nc-ice film is more homogeneous.

Figure 5.1.7 further demonstrates the spectral differences in the bending and combination bands between nc-ice and pc-ice for the same film thicknesses. In particular, the OH bending band for nc-ice spectra is blue shifted to 1665 cm^{-1} from 1650 cm^{-1} for pc-ice (Figure 5.1.7a) and appears to be narrower without the weak low-frequency shoulder at 1570-1550 cm^{-1} characteristic of pc-ice. The small but discernible red shift in the band maximum of the combination band of nc-ice (2230 cm^{-1}) in comparison with that for the pc-ice (2240 cm^{-1}, Figure 10a) is in qualitative spectral agreement with the transmittance spectrum reported by Hardin and Harvey [10]. These spectral differences are manifested more clearly with increasing film thickness (Figure 5.1.7b-c). The difference in the frequency positions and relative intensities of the spectral features of the OH stretching and bending modes can therefore be used to identify the nature of the ice film deposited below 145 K as nc-ice. However, it is not straightforward to determine the magnitude and nature of the structural differences between nc-ice and pc-ice based on FTIR-RAS data alone. Figure 5.1.8 shows the experimental spectra for relatively thick films obtained by water vapour deposition at 1×10^{-6} Torr for 3.5, 20.5 and 33.5 minutes and at 5×10^{-6} Torr for 11 minutes with the substrate held at 131 K, which correspond to nc-ice film thicknesses of 110, 450, 750 and 1250 nm, respectively, as estimated by the optical interference method. As before, the features near 1655 cm^{-1} and 2230 cm^{-1} (Figure 5.1.8a) can be assigned, respectively, as the OH bending band and the combination band of the OH bending and hindered rotation modes [11]; and these features remain essentially “stationary” in peak positions with increasing film thickness.

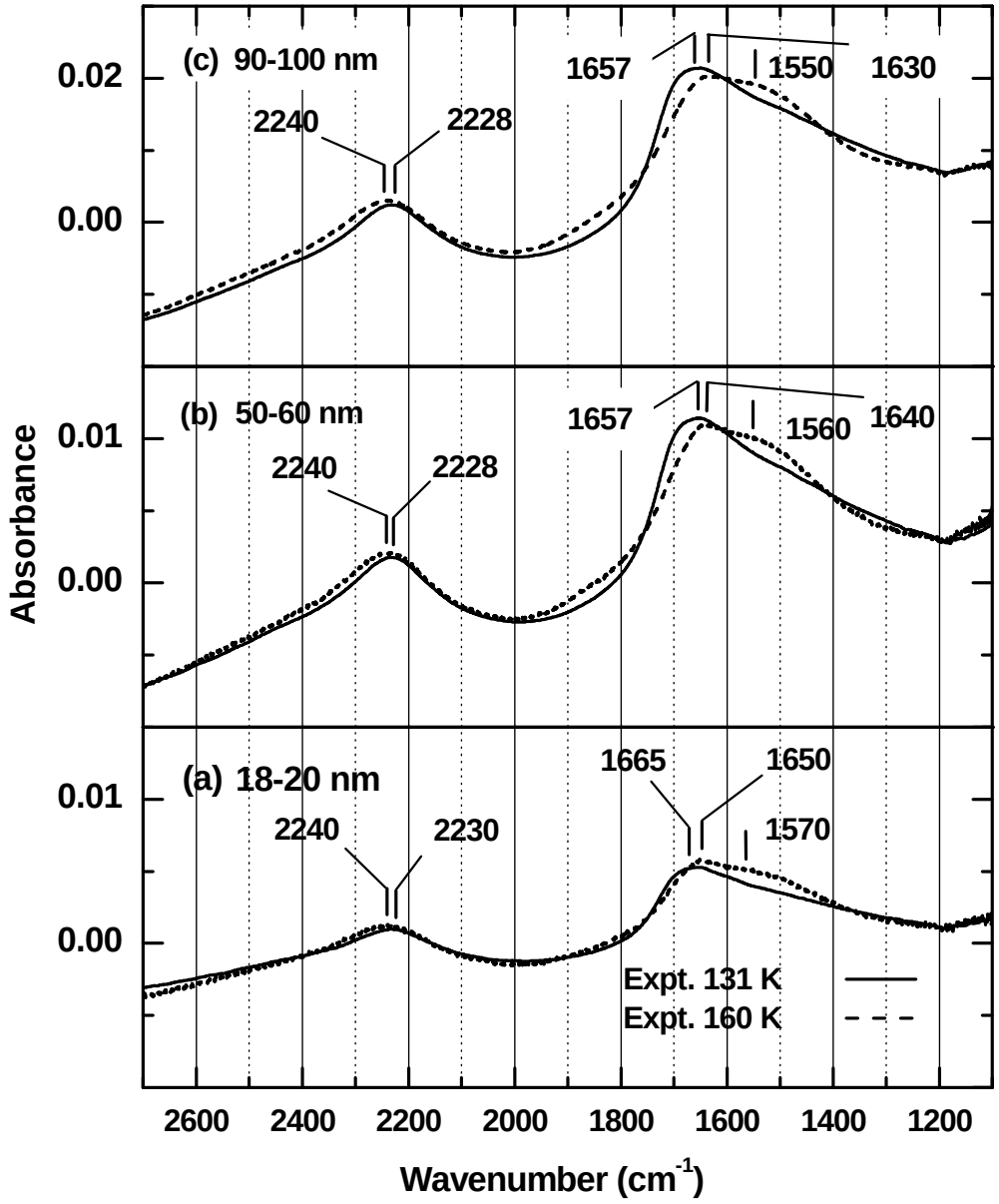

Figure 5.1.7. Comparison of experimental IR-RA spectra and the corresponding Fresnel spectra in the OH bending and combination band region for non-crystalline ice (nc-ice) and polycrystalline ice (pc-ice) deposited at 1×10^{-6} Torr and 131 K and 160 K, respectively. The corresponding thickness parameter estimated in the Fresnel simulations of the OH stretch region (Figure 5.1.6) are (a) 18 (20) nm for 45 seconds of deposition for nc-ice (pc-ice), (b) 60 (50) nm for 120 (115) seconds of deposition for nc-ice (pc-ice), and (c) 90 (100) nm for 220 (240) seconds of deposition for nc-ice (pc-ice). The nominal spectral resolution is 2 cm^{-1} for

nc-ice spectra and 0.5 cm^{-1} for pc-ice spectra.

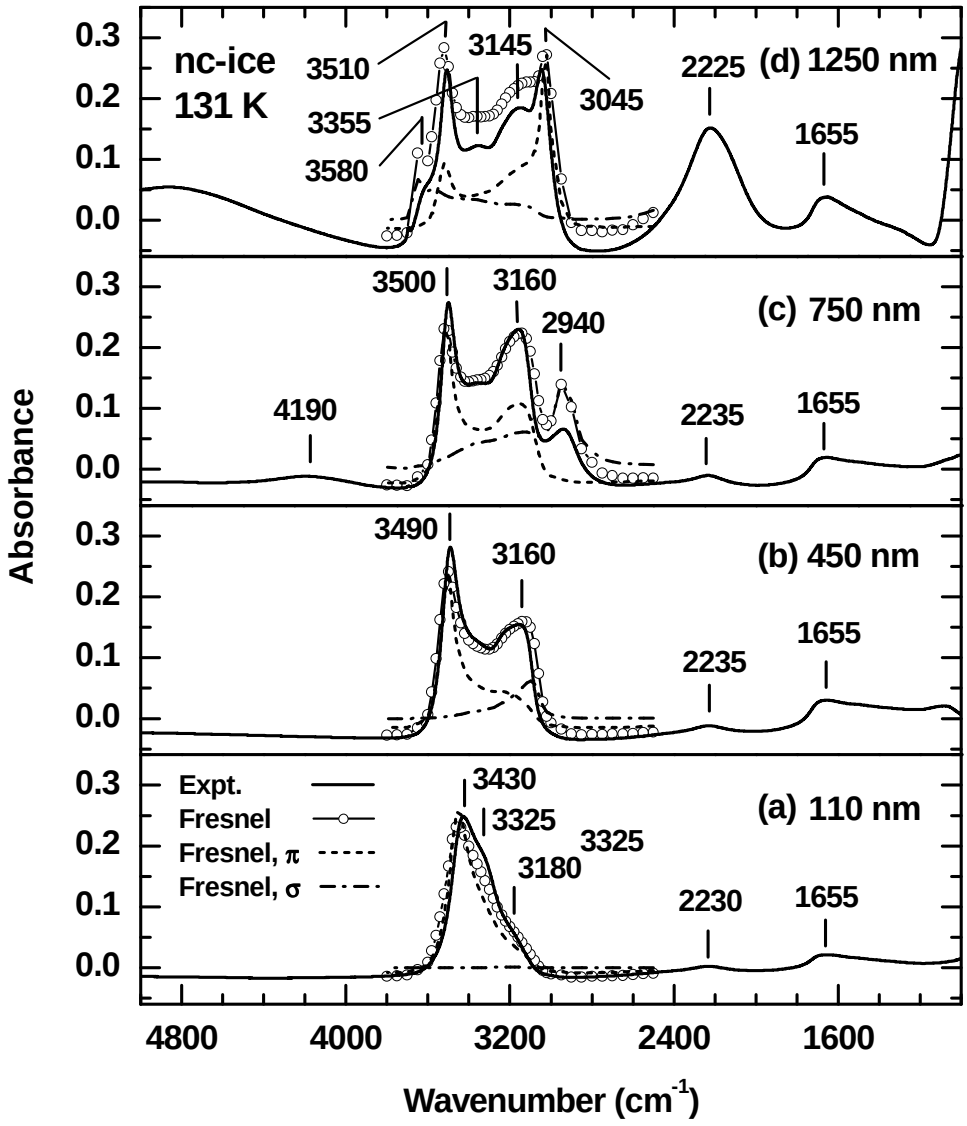

Figure 5.1.8. Comparison of experimental IR-RA spectra of noncrystalline ice (nc-ice) films obtained (at 0.5 cm^{-1} resolution) by vapour deposition at 131 K.
(a) 3.5, (b) 20.5 and (c) 33.5 minutes at 1×10^{-6} Torr and (d) 11 minutes at 5×10^{-6} Torr with the corresponding Fresnel spectra. Fresnel spectra are shown for non-polarized light, and their σ- and π- polarized components (arbitrarily normalized) involving 110-, 450-, 750- and 1200-nm-thick films, respectively. Nominal spectral resolution is 2 cm^{-1} for spectra (a-c) and 0.5 cm^{-1} for spectrum (d).

The spectral evolution of the OH stretch (near 3430 cm^{-1} for the 110-nm-thick film shown in Figure 5.1.8a) with growth of the nc-ice film is also similar to that observed for the pc-ice film growth (Figure 5.1.3). In particular, three relatively "stationary" features at 3490-3510 (band maximum), 3355, and 3160-3145 cm^{-1} can be resolved for film thickness greater than 450 nm (Figure 5.1.8b-d). The band maximum for nc-ice is seen to shift to a higher frequency (Figure 5.1.8), and the integrated intensity of the absorption band becomes saturated at ~ 70 integrated *AU* at film thickness near 120 nm, as observed similarly for pc-ice. We also show in Figure 5.1.8 the σ- and π-polarized components arbitrarily normalized to the maximum of the overall Fresnel spectrum. For film thickness below 250 nm, the shape of the OH stretch band is predominantly determined by reflection-absorption of the π-polarized component of the incident light (Figure 5.1.8a), with negligible contribution from the σ-polarized component. For film thickness greater than 250 nm, the σ-polarized component generally strengthens with the emergence of an interference feature travelling from ~3160 cm^{-1} at 450 nm (Figure 5.1.8b) to 2940 cm^{-1} at 750 nm (Figure 5.1.8c) and to 2225 cm^{-1} at 1250 nm (Figure 5.1.8d). Another σ-polarized interference feature near 4190 cm^{-1} for film thickness of 750 nm (Figure 5.1.8c) is also seen to travel to 3580 cm^{-1} for the 1250-nm-thick film (Figure 5.1.8d). The passage of this second interference feature through the spectral window of the OH *DB* causes amplification of the OH *DB* signal for nc-ice films with thickness of 800-1400 nm (as shown later in Figure 5.1.9). It is evident that the π-polarized components contribute prominently to the three aforementioned "stationary" OH stretch features over the film thickness range covered in Figure 5.1.8. The movement of the main π-polarized feature (near 3430 cm^{-1} for the 110-nm-thick film in Figure 5.1.8a) to a higher frequency with increasing film thickness gives rise to the observed blue shift of the band maximum. As noted earlier, this shift is related to the physics of reflection-absorbance and not to possible structural changes in the nc-ice network with an increase in the film thickness. For thicker films, the π-polarized interference feature observed at ~3160 cm^{-1} for the 750-nm-thick film (Figure 5.1.8c) is also found to travel to a lower frequency with increasing film thickness, e.g. 3045 cm^{-1} for the 1250-nm-thick film (Figure 5.1.8d). The evolution of the underlying σ- and π-polarized Fresnel contributions to the overall spectrum of nc-ice with increasing film thickness (Figure 5.1.8) is therefore similar to that found for pc-ice (Figure 5.1.3).

It is important to note that we have also performed FTIR-RAS experiments on ice

grown at a different temperature between 128 K and 145 K. Similar spectral results have been obtained, therefore suggesting that the ice films obtained by vapour deposition over 128-145 K can be characterized as nc-ice as discussed above.

There have been numerous earlier studies exploring the nature of nc-ice and pc-ice. In particular, as it was shown by an earlier study of thermal evolution of the hyperquenched water droplets by using X-ray diffraction and differential calorimetry, an ice phase predominantly in the form of vitreous ice could be obtained at deposition temperature below 140 K [25]. It should be noted that the temperatures for glass-to-liquid transition and for crystallization to Ic are found to be 129-143 K and 165 K, respectively [20, 25]. The temperature of crystallization of amorphous ice to Ic is generally a function of the deposition temperature and post-deposition history of the amorphous sample, which reflects the complex heterogeneous nature of amorphous ice [21]. Furthermore, the thermal evolution data for hyperquenched solid water prepared at 130-150 K [25] suggests the formation of a mixture of cubic ice and glassy materials. Hyperquenching above 160 K was found to produce predominantly cubic ice with at most 20% amorphous component [25], which could persist up to the Ic-to-Ih phase transition temperature (230 K). Based in part on the time evolution of FTIR-RA spectra of thin ice films (vapour-deposited at 80 K with an estimated thickness of ~20 nm) post-annealed to 160 K, Jenniskens *et al.* [17] concluded that the amorphous ice so obtained, when annealed to above the glass-to-liquid transition temperature, becomes a “viscous” liquid that coexists with Ic in the temperature range 140-210 K.

In the present work, crystallization of nc-ice deposited at 131 K is found to occur upon annealing to temperature starting from ~160 K. The spectra of the samples deposited at 131 K followed by annealing to 165 K (not shown) are found to be essentially identical to the spectra of pc-ice prepared by direct deposition at 160 K. In light of these results, the character of pc-ice deposited at 160 K in the present experiment (Figure 5.1.1 and Figure 5.1.3) could be interpreted as predominantly cubic ice. Although the deposition temperature for pc-ice used in the present experiment is well below the Ic-to-Ih transition temperature (230 K), the present FTIR-RAS data does not exclude the possible presence of hexagonal ice because of the nearly identical optical properties of the Ic and Ih phases. Based on the analysis of the OH stretch, the present data does not reveal any spectral evidence for the presence of nc-ice for films deposited above 155 K. However, the presence of non-crystalline material in, e.g., the inter-

grain regions of pc-ice or the surface region of the film cannot be ruled out due particularly to the weaker absorption of nc-ice relative to pc-ice. For ice deposited below 145 K, we have not found any spectral evidence of the existence of polycrystalline fragments, based on the shapes and frequency positions of the OH stretching and bending modes. The nc-ice obtained at 131 K (Figure 5.1.8) could therefore be attributed predominantly to amorphous solid.

Figure 5.1.4b compares the present experimental spectrum recorded at 83° incidence for nc-ice deposited at 131 K with that collected at 75° incidence for nc-ice obtained at 80 K by Jenniskens *et al*. [17]. The latter spectrum was found to be in good accord with the Fresnel spectrum for a 75-nm-thick nc-ice film calculated at 75º incidence using the optical constants of amorphous ice at 77 K reported by Leger *et al.* [22]. Apart from the differences in the intensity caused by the different angles of incidence, the spectrum obtained in the present work at 131 K is similar that of the amorphous ice obtained at 80 K by Jenniskens *et al.* [17], suggesting that the nature of nc-ice obtained in the present work could be interpreted as amorphous solid. Furthermore, Jenniskens *et al.* observed no discernible spectral changes upon annealing the sample to 145 K and attributed the subsequent changes observed upon further annealing to 155 K to crystallization of amorphous ice to cubic ice, which was confirmed for thin ice films by electron diffraction. This observation is also in qualitative agreement with the temperature range (128-145 K) over which the nc-ice films have been prepared. However, in contrast to the time evolution of the OH band observed for the film post-annealed at 160 K by Jenniskens *et al.* [17]**,** no similar behavior for ice films grown in the present work was observed and therefore the presence of viscous liquid cannot be confirmed. Furthermore, the OH *DB* signal at 3692 cm^{-1} detected on the as-grown amorphous ice at 80 K was found to disappear after post-annealing the ice film to 160 K by Jenniskens *et al.*[17]. In contrast, the OH *DB* signal on nc-ice grown at 131 K in the present work (spectra not shown) is found to persist up to 160-165 K, during which crystallization occurs.

5.1.3 OH Dangling Bonds

The OH *DB* signal can be detected for ice films deposited over a wide range of temperature, from 128 K in the case of nc-ice to as high as 185 K for pc-ice film, which indicates the remarkable thermal stability of the elements of ice surface containing these OH dangling groups. The spectral intensity of the OH *DB* feature observed at 3700-3690 cm^{-1} [15]

as a function of film thickness for pc-ice (obtained at 160 K) and nc-ice (obtained at 131 K) is shown in Figure 5.1.9. Given that the OH *DB* feature is generally very weak relative to the OH stretch feature and could therefore be susceptible to spectral noise and baseline instability at these frequencies, only the general trend in the dependence of the OH *DB* signal on the film thickness can be inferred. According to the metal surface selection rule, only the OH *DB's* that have a dipole moment component perpendicular to the metal surface could contribute to the RA signal in the case of a thin ice film (below 200 nm), as shown in Chapter 3. The observation of the OH *DB* RA signal on thin nc-ice films by Zondlo *et al.* [15] shows that the OH *DB* band could be detected only with the π-polarized light. A significant amount of the OH *DB's* that have dipole moments oriented parallel to the metal surface would remain invisible at this thickness range (below < 200 nm) to the RAS technique. With the exceptions of complete randomization of the OH *DB* orientation and of a fixed angular geometry for all *DB's*, the observed RA signal is not necessarily proportional to the amount of OH *DB's* in the ice film.

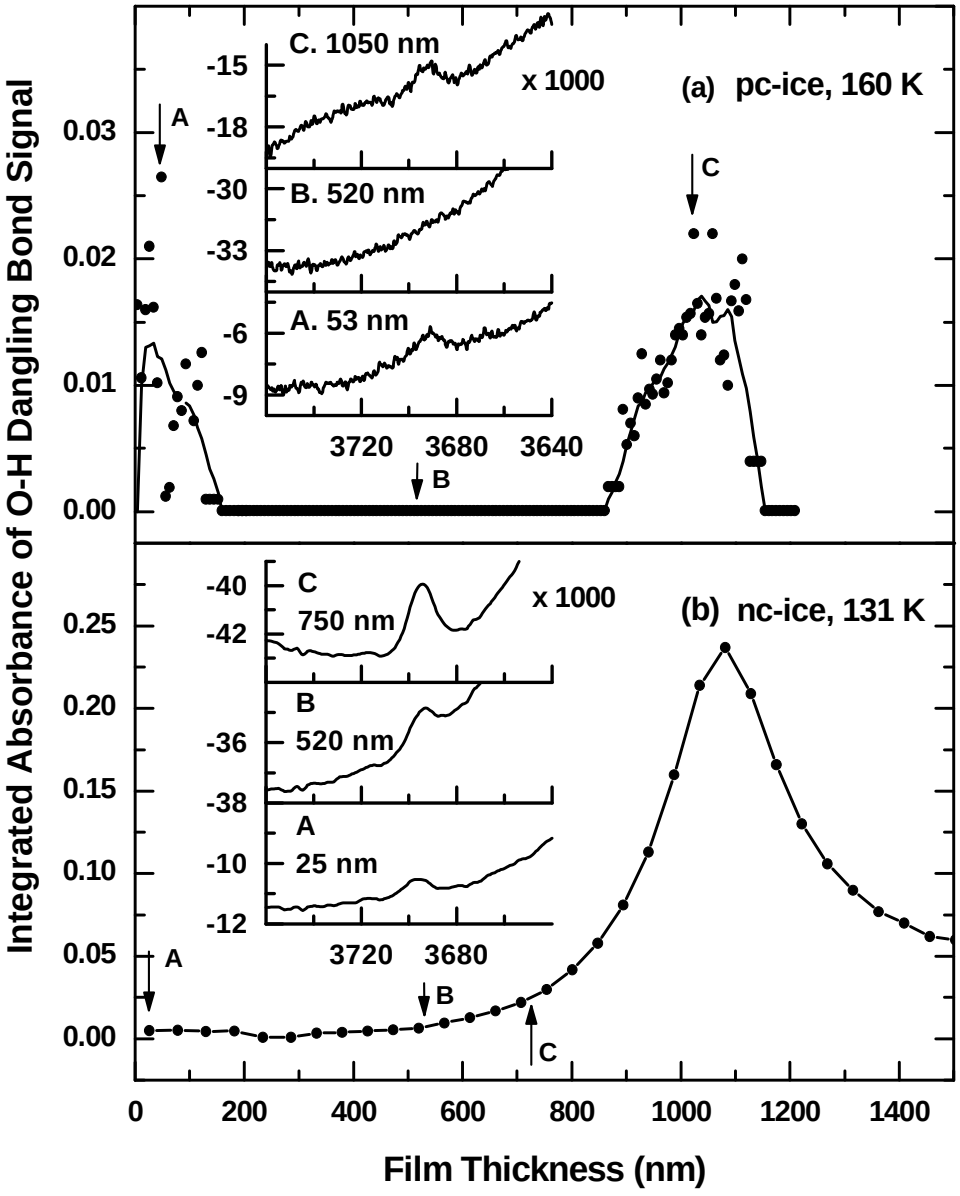

Figure 5.1.9. Integrated absorbance intensity of the OH dangling bond signal as a function of the film thickness for (a) polycrystalline ice (pc-ice) deposited at 160 K and 1×10^{-6} Torr, and (b) non-crystalline ice (nc-ice) deposited at 131 K and 5×10^{-6} Torr.

The curves are used to guide the eyes only. The film thickness is estimated by optical interference method and is found to be in reasonable agreement with the thickness parameter used in the respective Fresnel simulations. Insets (with the ordinate expanded by 1000) show the OH dangling bond feature at selected film thicknesses marked by arrows.

For film thickness smaller than ~200 nm, the OH *DB* signals for both pc-ice and nc-ice are found to be relatively weak and essentially independent of the film thickness (given the large uncertainty). The spectral intensity of the OH *DB* appears to diminish in the 150-850 nm thickness range for pc-ice but remains relatively constant up to a film thickness of 600 nm for nc-ice. For the 850-1200-nm-thick pc-ice and nc-ice films (Figure 5.1.9), the passage of the σ-polarized interference pattern over the optical window 3710-3680 cm^{-1} appears to significantly enhance the OH *DB* signal (by over 20 folds), which is in a good qualitative accord with the spectral simulation shown in Chapter 3. This strong optical amplification in the observed signal does not necessarily correspond to the increase in the total amount of the OH *DB's* in the material. The same phenomenon has also been observed for other absorption bands, most notably the combination band at 2255 cm^{-1} (Figure 5.1.3d). Apparently, the amplification is much stronger in the case of nc-ice (Figure 5.1.9b) than pc-ice (Figure 5.1.9a). Since the amplification is related to the passage of the *σ*-polarized interference pattern, the experimental observation of such an optical effect shows that the dipole moments of the OH *DB's* have surface-parallel components. For pc-ice films (Figure 5.1.9a), essentially the same magnitude of the OH *DB* signal for the 850-1150-nm-thick film as that for a thin film (< 200 nm) is observed. The lack of OH *DB* signal in the intervening thickness region therefore does not necessarily indicate the absence of the OH *DB*, but rather spectral interference that overwhelms the OH *DB* feature. This observation suggests that the total amount of the OH *DB* remains essentially the same with film growth, and the OH *DB* dipole moments are oriented more or less randomly with the respect to the metal surface. Accordingly, we attribute the spectral signal at ~3693 cm^{-1} to OH *DB* groups on the external surfaces of the crystalline grains in the early stage of pc-ice deposition (with film thickness below 50 nm), while for thicker films these OH *DB's* are thought to be located on the external surface of the pc-ice film itself. The OH *DB's* that exist on the outer surfaces of crystalline grains in the initial stage of pc-ice film formation would be effectively saturated by water molecules that fill the interstitial space during the film deposition process. Although the local nature of the water network in the inter-grain regions remains controversial, the present results suggest a near-crystalline structure for these regions in the water network.

The behavior of the OH *DB* signal is different in the case of nc-ice films. In particular, the intensity of the signal for nc-ice films thicker than 1400 nm is still significantly higher than

that for thin films (< 150-200 nm), unlike pc-ice films. This difference suggests that the total amount of OH *DB* in nc-ice may in fact increase with film growth, which is in general accord with the observation made by Zondlo *et al.* that the total amount of OH *DB's* in low-density ice (obtained at 94 K) increases with increasing film thickness [15]. In order to account for the proportionality of the abundance of the OH *DB's* with respect to the amount of ice, the latter work further concluded that the OH *DB's* are located on the surfaces of multiple micropores inside the amorphous solid ice network [15]. The existence of the OH *DB's* on the internal surfaces of open and close micropores has also been predicted for film growth of low-density ice under appropriate conditions by Zhdanov and Norton using Monte Carlo simulation [23]. The observed thickness profile of the OH *DB* signal shown in Figure 5.1.9b is similar to the simulated profile shown in Chapter 3, which confirms the increase in the total amount of OH *DB's* with increasing film thickness and the essentially random orientation of the OH *DB's*. The large difference in the deposition temperature between our experiment and that of Zondlo *et al.* is expected to cause some difference in the organization of the non-crystalline network that might result in a smaller amount of the internal micropores in the case of the higher-temperature deposit. The temperature dependence of the amount of micropores in nc-ice has been explained earlier by an increase in the surface mobility of incoming molecules with increasing temperature [15, 23]. We conclude therefore that the OH *DB's* are likely located on the highly convoluted external surface of the nc-ice film, which is in general accord with the studies by Callen *et al.* [24], Rowland and Devlin [3], Horn *et al.* [16], and Zondlo *et al*. [15]. We further suggest that the nc-ice vapour-deposited at 128 K or higher temperature may have a "tracery" organisation at least in the near-surface region that could give rise to the OH *DB* signal. In the case of thin nc-ice film, the OH *DB's* are most likely located on the external surface of the film, while with the increase in the film thickness the "openwork" character of the near-surface region (that would enhance the OH *DB* signal) is likely preferred. However, the presence of micropores at a higher temperature above 131 K cannot be ruled out.

Unlike the earlier studies, we have observed this OH *DB* signal to persist after annealing a <50-nm-thick nc-ice film from 131 K to 165 K, i.e. above the temperature of crystallization to cubic ice. This observation appears to support the aforementioned hypothesis that the OH *DB's* are localized on the external surfaces of thin nc-ice and pc-ice films, and suggests that the local structure of the surface of the nc-ice and pc-ice films are similar.

5.1.4 Summary

FTIR Reflection-Absorption Spectroscopy has been used to study the film growth of polycrystalline and non-crystalline ice obtained by vapour deposition over a range of film thickness from 10 nm to 1500 nm. Simulated spectra of the OH stretch region (3800-2800 cm^{-1}) based on the Fresnel reflection with the appropriate optical constants obtained from the literature [2, 22] are found to give good agreement with the experimental spectra. The intricate nature of the film growth process of ice at different temperatures can be qualitatively characterized as pc-ice or nc-ice, with their respective structures and properties (such as film thickness). Our experiment shows that pc-ice and nc-ice are most likely to form at deposition temperature above 155 K and below 145 K, respectively. Further analysis using the σ- and π-polarized components of the Fresnel spectra shows that the intensities and shapes of specific bands in a RA spectrum could be significantly affected by migration of interference peaks with increasing film thickness, which in turn complicates spectral identification and population analysis of the corresponding groups in the case of solid-state spectroscopy. The scattering character of the RA spectra for the early stage of film deposition of pc-ice and to a certain extent nc-ice generally confirms the heterogeneous character of the early deposit, which composes of nanoscale-sized water aggregates. The experimental confirmation of the Fresnel model upon further film growth illustrates the evolution to a more homogeneous film growth mechanism.

Weak RA peak at 3700-3690 cm^{-1} attributable to incompletely coordinated OH groups has also been observed for a majority of pc-ice and nc-ice films deposited under different conditions, indicating that the OH dangling bonds are an integral structural component of the surfaces of both pc-ice and nc-ice. Although the weak OH *DB* signals of both pc-ice and nc-ice are essentially independent of the film thickness below ~200 nm, the intensity of the *DB* feature for thicker films (particularly those of nc-ice) appears to be subjected to significant spectral amplification due to the passing of destructive interference patterns through the OH stretch spectral region over a specific film thickness range. Up to 20-fold enhancement has been observed in the case of the 1100 nm-thick nc-ice film. Furthermore, the OH *DB* signal has been found on pc-ice films deposited at temperature as high as 185 K, and on nc-ice deposited at 131 K and annealed to 165 K, which is above the temperature of crystallization to cubic ice. This behaviour of OH *DB* signal is consistent with the picture that the OH *DB's* are

most likely located on the external surfaces of the crystalline grains during the early stage of film growth and on the external surface of the film upon further film growth for pc-ice and on the openwork external surfaces in the case of nc-ice. The present work provides us with the basis for further studies of the interactions of volatile organic compounds with ice micro-phases.

5.2 Crystallization of Noncrystalline Ice Films at 160-165 K: IR Spectral Picture

Because nc-ice is considered metastable with respect to the crystalline ice form, annealing of an nc-ice deposit could promote crystallization to occur at a detectable rate above an appropriate temperature. Indeed, rapid changes in the OH stretch region are found at 153-163 K in the present work, in good accord with the earlier observations made by using different techniques [25]. In particular, Figure 5.2.1 shows the temporal evolution of the OH stretching band at 155 K for 30 minutes and at 163 K for 6 minutes for an nc-ice film deposited at 124 K and 1×10^{-6} Torr for 240 sec. In Figure 5.2.2, we compare selected experimental profiles with the appropriate calculated spectra. While no significant temporal spectral changes are found at 155 K (Curve B, Figure 5.2.1) relative to the as-deposited nc-ice spectrum at 124 K (Curve A, Figure 5.2.1), rapid dramatic changes in the shape of the OH stretching band are observed at 163 K (Curves C-K, Figure 5.2.1). By analogy with the assignment for pc-ice, the weak peak at 3694 cm^{-1} can be attributed to the OH dangling bonds, while the features at 3395 cm^{-1} and 3330 cm^{-1} and at 3165 cm^{-1} likely correspond to the out-of-phase ν_1 intermediate modes, the ν_3 LO branch, and the in-phase ν_1 branch, respectively. As shown in Figure 5.2.2, the OH stretch profiles for the nc-ice film as-deposited at 124 K and upon annealing to 155 K (Curve B, Figure 5.2.2) are well approximated by the Fresnel spectrum for a 14-nm-thick nc-ice film (Curve L, Figure 5.2.2), indicating the preservation of the smooth stratified film even upon annealing at 155 K for 30 minutes. On the other hand, discernible spectral changes near 3245 cm^{-1} are found upon annealing at 163 K for just 2 minutes (Curves C-E, Figure 5.2.1).

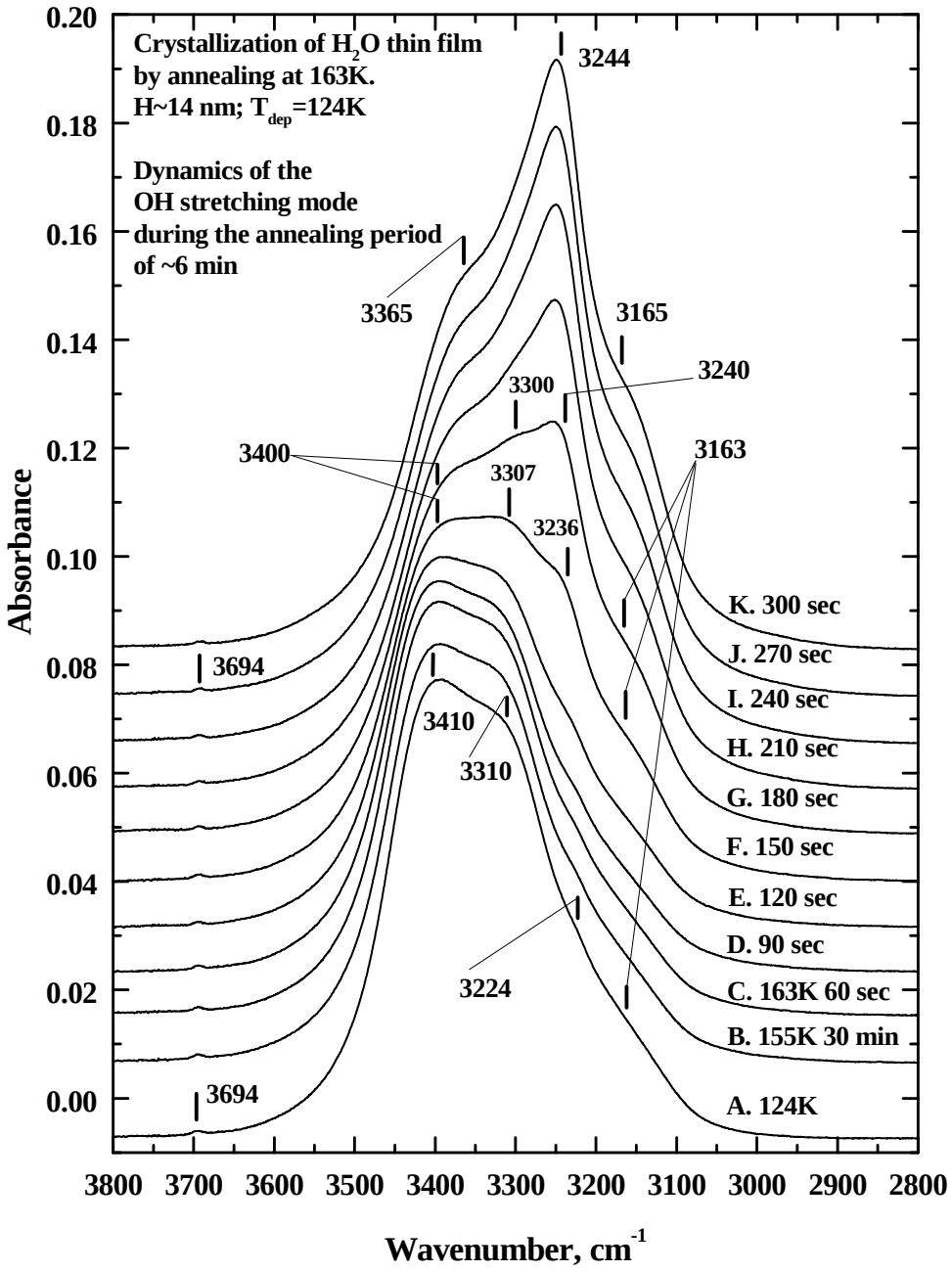

Figure 5.2.1. Typical evolution of the OH stretching mode of the nc-ice film upon annealing. A ~15-nm-thick H_2O ice film was prepared by vapor-deposited at 1×10^{-6} Torr × 2min and 124 K (A) and further annealed (B) at 155 K for 30 min and (C-K) at 163 K for 6 min. The spectral resolution is 1 cm^{-1}, and each spectrum is the result of averaging of 50 scans at 80 kHZ.

This feature develops into a strong, well-defined peak at 3250 cm^{-1} upon further annealing at the same temperature for 3 more minutes (Curves F-K, Figure 5.2.1). In contrast, the dangling-bond feature at 3694 cm^{-1} remains essentially unchanged except for the minor red shift during this anneal.

Figure 5.2.2 also compares selected spectra obtained during the 163-K anneal with the RA spectrum of the 30-sec pc-ice film deposited at 160 K and with the Berreman and transmission profiles for pc-ice films. Evidently, the major differences between the OH stretch profiles of the annealed nc-ice film (Curves G, H, and K, Figure 5.2.2) and that of the as-grown 30-sec pc-ice film (Curve O, Figure 5.2.2) are the location and relative intensity of the ν_3 LO manifold (at 3250 cm^{-1} vs 3270 cm^{-1}). According to the theoretical study by Wojcik *et al.* [26], the emergence of a prominent ν_3 LO band during annealing in the present work can be used as evidence of a rapid increase in the density of excited vibrational states in this narrow frequency region, which in turn indicates the onset of a crystallization process. The intensity increase of the overall OH stretching band during the anneal (Curves G, H, and K, Figure 5.2.2) is also consistent with the general chemical principle that crystallization leads to strengthening of the hydrogen bonds in the ice medium [27]. Furthermore, the peak maximum of the observed ν_3 band (3250 cm^{-1}) is found to be in between those of the Berreman profile (3300 cm^{-1}, Curve M, Figure 5.2.2) and the transmission profile (3225 cm^{-1}, Curve N, Figure 5.2.2). (It should be noted that the Berreman profile and the transmission profile are arbitrarily normalized to the experimental spectra shown as Curve G and Curve K, respectively.) The intermediate peak location is due to the presence of surface modes in the crystallites, as discussed by Englman and Ruppin [28] and Martin [29]. Moreover, the formation and growth of the crystallites introduce tension into the film and could lead to cracking in a sufficiently thin film.

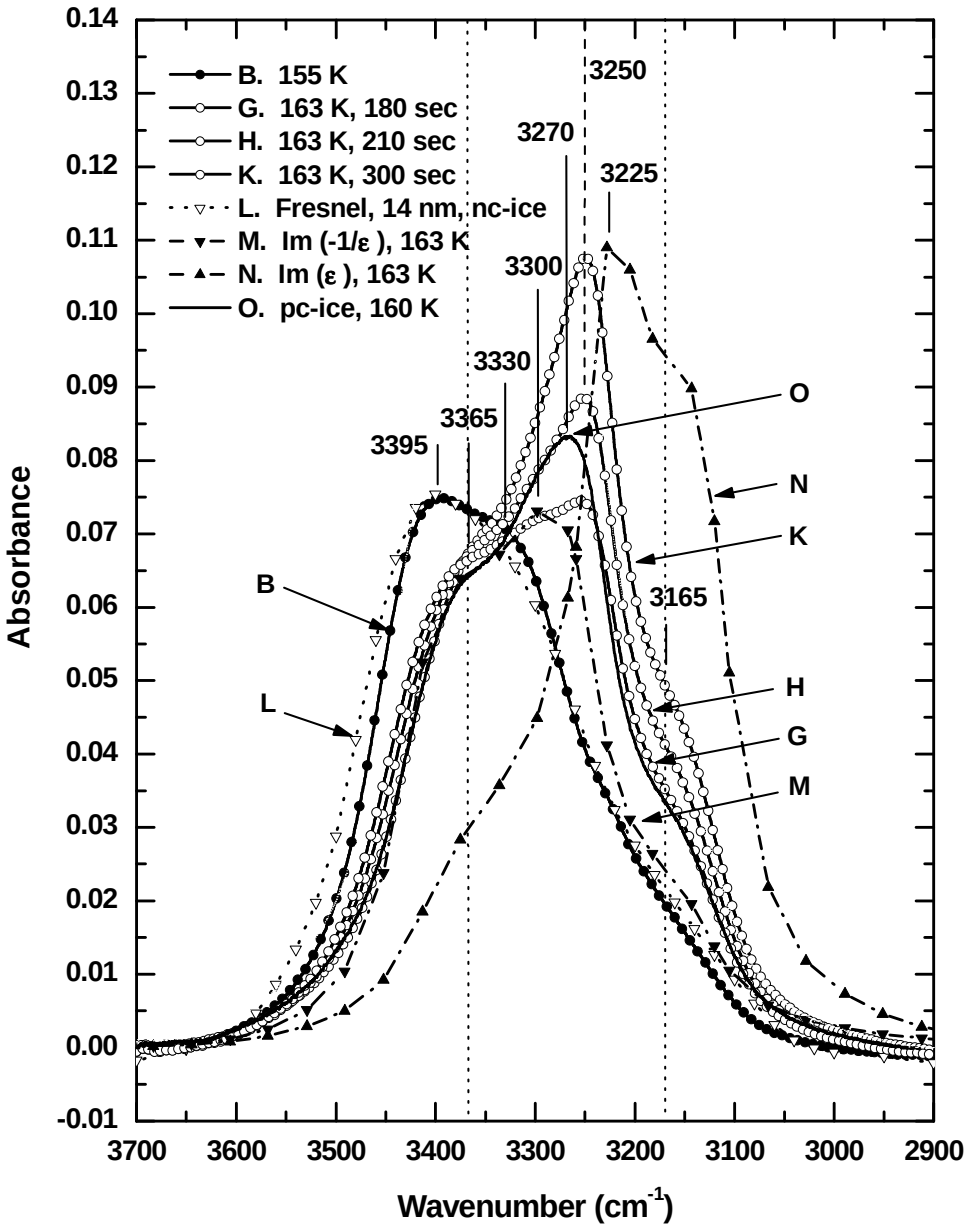

Figure 5.2.2. Comparison of the OH stretching band of the experimental FTIR-RA spectra of an early-stage noncrystalline (nc) H_2O ice deposit with those of annealed samples. The nc-ice sample was obtained by vapour deposition at 124 K and 1×10^{-6} Torr for 240 seconds followed by annealing to 155 K for 30 minutes (B) and to 163 K for 180 (G), 210 (H), and 300 seconds (K). The experimental spectrum of this sample is compared with that of a polycrystalline (pc) ice deposit obtained by vapour deposition at 160 K and 1×10^{-6} Torr for 30 seconds (O), and with the Fresnel spectrum of a 14-nm-thick nc-ice film (L) and the Berreman (M) and transmission profiles for the pc-ice (N), all arbitrarily normalized.

Figure 5.2.3 shows the temporal evolution of the OH and OD stretching modes of deuterated nc-ice as deposited at 120 K at 1.5×10^{-6} Torr for 9 minutes and during annealing to 162 K. Evidently, no discernible change is observed in the OD stretching mode upon annealing from 120 K to 162 K (Curves A-H, Figure 5.2.3a). Furthermore, the temporal evolution in the OD stretch features at 162 K for nearly 5 minutes (Curves H-N, Figure 5.2.3a) is found to be remarkably similar to that of OH stretch observed earlier in the undeuterated nc-ice sample (Figures 4 and 5), which again indicates the onset of rapid crystallization at this temperature. (Figure 5.2.3a also shows only minor changes in the dangling-bond signal of the OD surface groups at 2727 cm^{-1} during crystallization.) Moreover, the uncoupled OH stretching mode of HOD in the deuterated ice sample exhibits a red shift from 3300 cm^{-1} at 120 K (Curve A, Figure 5.2.3b) to 3280 cm^{-1} at 162 K (Curve N, Figure 5.2.3b) with concomitant narrowing of the peak, which is also consistent with the crystallization process. The changes in this vibrational mode are in excellent agreement with the transmission spectra for thick amorphous and polycrystalline ice samples obtained by Bergren *et al.* [30]. Between 120 K (Curve A, Figure 5.2.3b) and the crystallization onset at 162 K (Curve H, Figure 5.2.3b), there is a small but discernible blue shift of 7 cm^{-1} accompanied with peak broadening in this structure-sensitive mode, which could be argued as spectral evidence for further disordering of this nc-ice deposit immediately before crystallization. This spectral change might also be associated with an endothermic peak in the calorimetric upscan of an nc-ice medium often appearing just before the crystallization onset, which has been attributed to a glass-to-liquid transition in the earlier studies [25] because frequency shifts for the structure-sensitive modes (including, e.g., the aforementioned modes) are expected in the case of a supercooled liquid state. In particular, Jenniskens *et al.* have used this approach to interpret their FTIR-RAS data for the transition of nc-ice to pc-ice [17]. Smith *et al.* [31] also attributed the significant enhancement in the self-diffusivity of nc-ice over this temperature range to a glass-to-liquid transition. However, the observed blue shift for this nc-ice feature is also in remarkably good agreement with the blue shift of the corresponding feature for pc-ice solids upon annealing (from 3275.2 cm^{-1} at 120 K to 3280.5 cm^{-1} at 150 K) observed by Sivakumar *et al.* using Raman spectroscopy [32]. Indeed, we also observed a corresponding red shift in the OH stretch feature in the crystallized ice (Curve N, Figure 5.2.3b) upon re-cooling from 162 K to 120 K (not shown). The blue shift in the isolated OH stretch observed for nc-ice upon

annealing in the present work is therefore most likely just the natural consequence of thermal expansion of the ice medium. We favour the latter simpler explanation over the former explanation invoking the glass-to-liquid transition because such an equilibrium thermodynamic effect is expected to occur regardless of the existence of the glass-to-liquid transition. Together with the early spectroscopic studies on ice crystallization by Hardin and Harvey [10] and Hagen *et al.* [19], the present data therefore provides no conclusive spectroscopic evidence for the existence of a distinct glass-to-liquid transition in nc-ice in the 120-163 K range. Although any difference in the rates of relaxation processes is expected to manifest in the shape and width of the OH stretch band, we cannot rule out the possibility that the local structures of the water glass and supercooled liquid states happen to be almost identical, in which case the intermolecular interactions in both media are so close to each other that no spectral differences in the OH/OD stretching region could be resolved. In a separate experiment, we also obtained FTIR-RA spectra for an organic guest species, acetone or acetaldehyde, co-deposited with water to form a noncrystalline guest-ice matrix at 130 K. The temporal evolution of the spectral features of the embedded guest species upon annealing followed by crystallization of the ice at 165 K shows only steady escape of the guest species from the matrix. While spectral differences between the adsorption/absorption states of the guest species in the nc-ice and pc-ice samples were clearly resolved, no signature of the intermediate states in the guest-supercooled liquid water matrix in the 130-165 K temperature region could be observed. Similar spectral observations of a steady escape and the absence of any frequency shift for dimethylether in a dimethylether-water matrix at 130-160 K have also been reported recently by Schriver-Mazzuoli *et al.*, although the spectral changes for dimethylether have been found at 120-130 K and attributed to clathrate-hydrate formation [33]. These results further support our above observation of direct transition from nc-ice to pc-ice (i.e. without an intermediate glass-to-liquid transition). Furthermore, the results on crystallization kinetics of thin compact nc ice films by Dohnalek *et al.* [34] are also consistent with the direct solid-to-solid phase transformation.

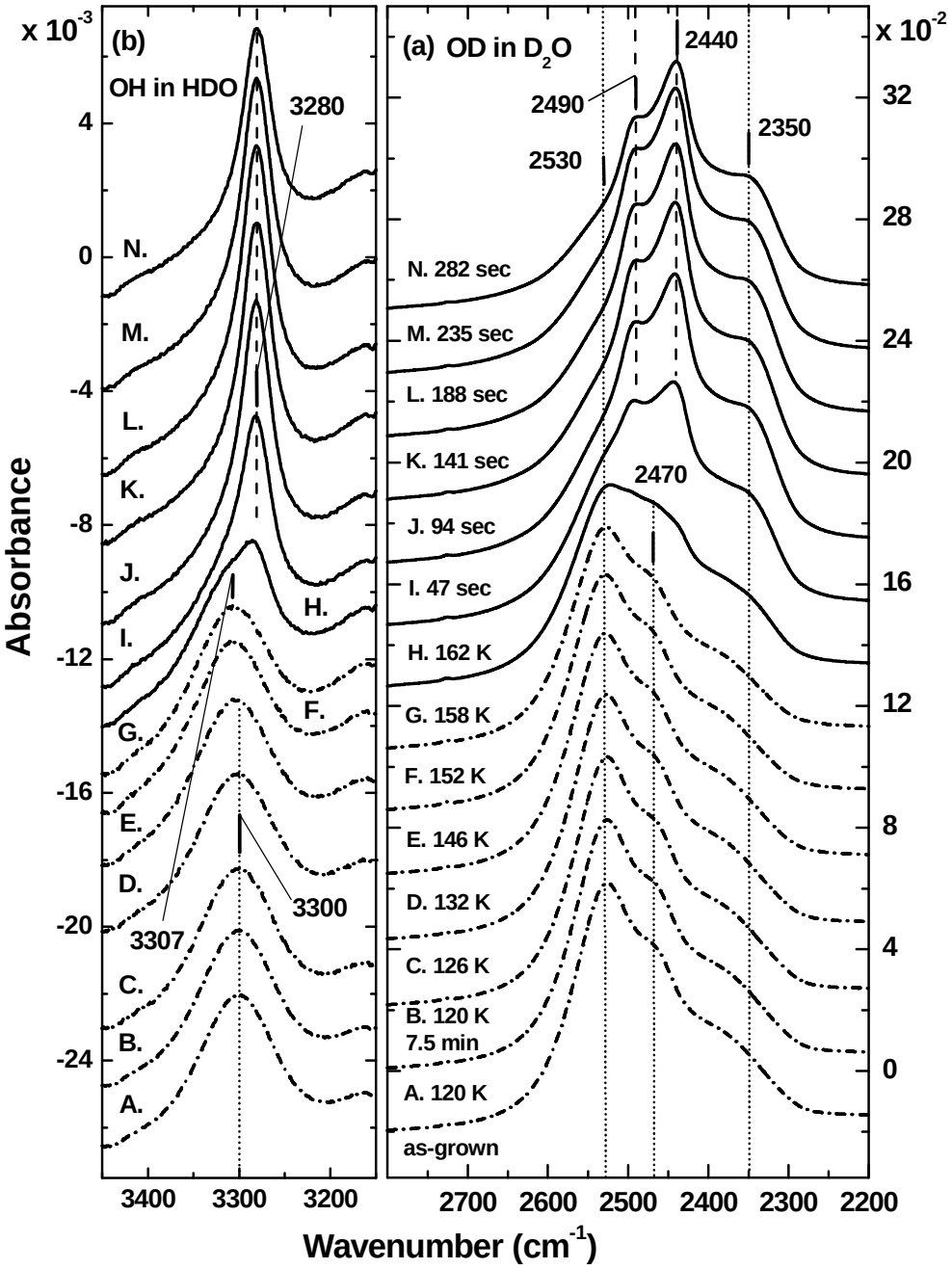

Figure 5.2.3. Evolution of (a) the OD stretching band (for D_2O) and (b) the OH stretching band (for HDO) in the experimental FTIR-RA spectra upon annealing of nc-ice film. An early-stage noncrystalline ice deposit was obtained by vapour deposition at 120 K and 1.5×10^{-6} Torr for 9 minutes (A), followed by annealing to 120 K for 7.5 minutes (B) and to 132 K (C), 146 K (E), 152 K (F), 158 K (G), and 162 K (H) for 47 (I), 94 (J), 141 (K), 188 (L),

235 (M), and 282 seconds (N).

Concerning the state of surfaces at nc-ice and pc-ice films investigated in the present studies, it should be noted that the amount of OH dangling bonds as estimated by the intensity of the corresponding spectral feature at 3694 cm^{-1} (Fig. 4) on the as-grown thin (and compact) nc-ice films is similar to that on pc-ice films prepared by crystallization of nc-ice films or by direct deposition. However, the present FTIR RAS data on acetone adsorption appear to indicate a dynamical difference in the surface states of the adsorbate on nc-ice and pc-ice films. This difference is clearly related not only to the "snap-shot" structure of the surface but also to the stability and dynamics of the surface and near-surface regions of nc- and pc-ice films as discussed by Buch *et al.* [35].

In summary, the temporal evolution of the OH (and OD) stretch manifold(s) in the (deuterated) nc-ice deposits upon annealing followed by crystallization has been investigated by using FTIR-RAS at grazing-angle incidence. The present section provides a microscopic interpretation of the spectral data using the theoretical results of Buch and Devlin [4] and Whalley's assignment [5]. For the ultrathin nc-ice deposits, crystallization near 160 K has been demonstrated for the first time to be marked spectroscopically by an abrupt enhancement along with a concomitant red shift in the longitudinal branch of the ν_3 OH (OD) stretching mode at 3250 (2440) cm^{-1}. These observations are consistent with strengthening of the hydrogen bonds in the molecular water network and with increased ordering of an ice medium during crystallization. Furthermore, the spectral dynamics of the OH and OD stretch manifolds and of the isolated OH stretching mode in a deuterated ice matrix near 160 K observed in the present work indicate that rapid crystallization proceeds directly from a noncrystalline to a crystalline state, i.e. without any long-lived intermediate state that involves hydrogen-bonded network structurally different from that of nc-ice at a lower temperature (120 K). While the present interpretation of the OH spectral dynamics does not favor the existence of a glass-to-liquid transition during crystallization, we cannot rule out the existence of a supercooled liquid state that happens to have a nearly identical local structure to glass. Further studies possibly involving non-spectroscopic data would be of great interest to resolve this intricate fundamental issue about ice.

5.3 The FTIR RA Spectral Analysis of Pristine Films of Organic Substances on Metal Surface at Cryogenic Temperatures

Crystals of acetone, acetaldehyde, methanol, and chloroform have been studied over the long history of spectral studies of organic crystals at cryogenic temperatures. The present work differs from the classical studies by the method of observation, i.e. a reflection-absorption method versus transmittance. In the case of vibrational modes with large transition moment the RAS mode provides a different perspectiv on the organic phase prepared by the vapor deposition. In the transmittance studies transversal modes are the major contributor to the spectra, and the appearance of longitudinal and/or surface modes is possible in a case of small-size crystals. In contrast, in the reflection-absorption studies, the longitudinal modes are always excited, whereas the transversal modes appear typically in the spectra of relatively thick films. In order to distinguish unambiguously between *TO* and *LO* modes in the reflection-absorption IR studies of organic crystals, a polarizer should be used.

An expected picture on the basis of the site group and factor group splitting in a crystalline solid could be significantly affected by the presence of strong *LO*/*TO* splitting for the modes of strong transition dipole moment. The *LO*/*TO* splitting is also expected for carbonyl band of solid acetone and acetaldehyde, and for the hydroxyl group band of solid methanol.

5.3.1 Solid Chloroform on the Cu Substrate at 125-165 K

A molecule of chloroform, $CHCl_3$, is considered to belong to a C_{3V} point symmetry group, which leads to the following symmetry species for the vibrational modes of isolated molecule:

$$\begin{aligned}\Gamma^{3N} &= 4\Gamma^{A_1} \oplus \Gamma^{A_2} \oplus 5\Gamma^{E} \\ \Gamma^{T} &= \Gamma^{A_1} \oplus \Gamma^{E} \\ \Gamma^{R} &= \Gamma^{A_2} \oplus \Gamma^{E} \\ \Gamma^{V} &= 3\Gamma^{A_1} \oplus 3\Gamma^{E}\end{aligned} \tag{5.1}$$

There are *9* ($3\times5-6=9$) vibrational modes for isolated chloroform molecule, three of which form a basis for the A_1 representation and other *6* from the *E* representation. The latter *6* vibrational normal modes appear as three sets of doubly degenerated vibrations. The reduction of molecular symmetry on transition from a gas to solid phase could cause the lifting of the

degeneracy and, therefore, the number of observed spectral transitions could rise from *6* in the gas phase to *9* in the condensed phase.

In the optical range between 5000 and 1000 cm^{-1} there are three fundamental modes: $v_1(A_1)$ stretching C−H mode and two degenerate v_4 (E) C−H bending modes, which are found in the liquid chloroform at 3019 cm^{-1} and 1216 cm^{-1}, respectively [36]. The transition dipole moments of these two vibrational manifolds are perpendicular to each other: the transition dipole of stretching modes is collinear with the direction of C_3 axis, whereas, in particular, the vectors of transitional dipole moments for bending modes are perpendicular to the C_3 axis. Together with these fundamental transitions, the present studies reveal the following overtones and combinational bands in the given spectral range: the combinational band of v_1+v_4 modes with the E symmetry, multiplet of which is found in the solid chloroform at the frequency range 4232-4201 cm^{-1} with π-polarization; the combinational band $v_1 + v_2$ of A_1 symmetry found in the liquid phase at 3683 cm^{-1} [36] and in the present studies at frequency range of 3692-3676 cm^{-1} with π-polarization ; the overtone of v_4 (E) of A_1+E symmetry found in the liquid phase at 2400 cm^{-1} [36] and in the present studies at frequency range of 2431-2393 cm^{-1} with π-polarization; the overtone of v_5 (E) of $A_1 + E$ symmetry found in the liquid phase at 1521 cm^{-1} [36] and in the present studies at 1533-1513 cm^{-1} with π-polarization; the combinational band of $v_4 + v_6$ of $A_1 + E$ symmetry found in the liquid phase at 1475 cm^{-1} [36] and in the present studies near 1482 cm^{-1} with π-polarization; the combinational band of $v_2 + v_5$ of E symmetry found in the liquid phase at 1423 cm^{-1} [36] and in the present studies in the frequency range of 1428-1419 cm^{-1} with π-polarization; and finally the overtone of v_2 (A_1) of A_1 symmetry found in liquid at 1334 cm^{-1} [36]and in the present studies also at 1334 cm^{-1} with π-polarization. The present studies are concentrated primarily on the fundamental modes v_1 and v_4, the combinational modes $v_1 + v_4$ and $v_1 + v_2$, and the overtone of v_4 because these modes are found to be sufficiently intense for the spectral observation during and after annealing.

The crystallographic studies by Fourme and Renaud [37] reveal that at 185 K chloroform crystalline structure belongs to a *Pnma* (D_{2h}^{16}) orthorhombic space group with *4* molecules in the crystallographic unit cell, occupying C_s-symmetry positions. A molecular packing in the solid chloroform is represented on Figure 5.3.1 with the following dimensions of the crystallographic unit cell: a = 7.485 Å; b = 9.497 Å; c = 5.841 Å [37]. The presence of a mirror plane populated by molecules creates a natural arrangement motif such that the

molecular structure could be regarded as consisting of layers oriented parallel to the (010) crystallographic plane. Within the layer there are 2 non-equivalent pairs of 2 nearest neighbors for each molecule such that the C−H group of one molecule is coordinated with two out-of-plane chlorine atoms of a molecule from the first pair, separated by 2.95 Å, and with an in-plane chlorine atom from a molecular nearest neighbor of the second pair with a separation distance of 3.12 Å. The former distance is equal to the sum of average van der Waals radii of hydrogen and chlorine atoms: 1.20 Å (H) + 1.77 Å (Cl) [38], whereas the latter is slightly larger. Therefore, the chloroform structure contains a network of oriented dipoles, in which a hydrogen atom of chloroform molecule is coordinated with three chlorine atoms of nearest neighbors: 2 out-of-plane and 1 in-plane.

The question on the contributions of electrostatic, induction, dispersion and exchange forces to the total interaction between nearest neighbors remains unanswered, and an assumption on the hydrogen bonding acting between chloroform molecules requires detail examination. The intensity of the C−H stretching mode, v_1 (A_1), rises by an order of magnitude upon transition from the gas in to liquid phase, which should be regarded as a signature of the hydrogen bond formation.

Each molecular layer is polarized along the [100] direction such that the collective dipole moments of two adjacent layers are anti-parallel. It is clear that the dipole-dipole attraction stabilizes the interlayer arrangement and also contributes to the interlayer interaction. It should be noted that the molecular localization at the C_s-symmetry site within the (010) plane prevents this layer from being closely packed. The dipole moments of the two nearest neighbors along the [001] direction are collinear such that it leads to electrostatic repulsion between them. Indeed, a in-plane chlorine atom of one molecule is in contact with two out-of-plane chlorine atoms of another molecule with an interatomic distance of 3.76 Å (see Figure 5.3.1). This latter distance is noticeably larger than the average van der Waals diameter of chlorine atom in polychloroalkyls at 3.54 Å [38] due to presumably a dipolar repulsion. Contacting by chlorine atoms, two adjacent layers interact by the electrostatic and van der Waals forces with the closest Cl···Cl contact at 360 Å. The closest interlayer $Cl_3C{-}H{\cdots}Cl{-}CHCl_2$ contact is at 3.70 Å, which is ~0.7 Å larger than the sum of average van der Waals radii of hydrogen and chlorine atoms: 1.2 Å (H) + 1.77 Å (Cl). A simple structural analysis given above allows predicting of the relative frequency positions of v_4 (E) modes due

to the site symmetry effect. Firstly, the close contact between hydrogen and chlorine atoms of neighboring molecules within the (010) *mirror* layer could be assumed to affect the frequency of the C−H bending mode in a degree prevailing over the similar effect of the hydrogen-chlorine contacts in the direction perpendicular to the layers. Therefore, an A' bending modes localized within the layer is expected to be at a higher frequency than that of A'' bending mode with transition dipole moment polarized in [010] direction.

The rows of centro-symmetric pairs of chloroform molecules with antiparallel dipoles (although the distance between the counterparts of the pair is not the shortest among all molecular pairs observed in the chloroform structure) are present in the crystalline arrangement, parallel to the [010] direction.

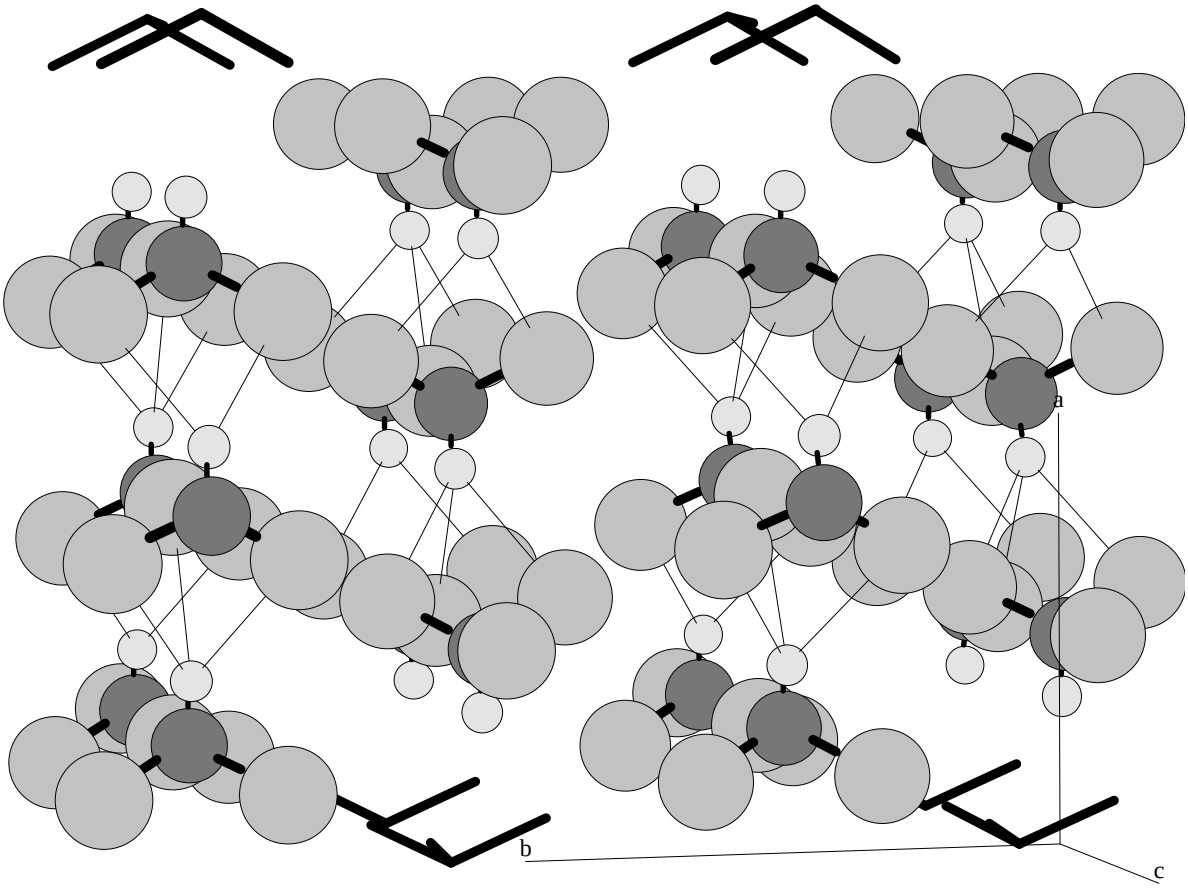

Figure 5.3.1. The crystallographic structure of chloroform. The structure belongs to the *Pnma*, D_{2h}^{16}, space group with the *4* molecules per crystallographic unit cell [37].
A molecule of chloroform occupies the C_s-symmetry position with the angle between the C−H bond and [100] axis of 14.36°. A hydrogen atom is coordinated with three chlorine atoms such that the H···Cl distances are 2.95 Å, 2.95 Å and 312 Å, which provides the anisotropic

bonding in the [100] direction within the (010) planes.

The correlation diagram for symmetry species of isolated molecule, the site and factor-group symmetry representation is given in Table 5.3.1.

Table 5.3.1. The correlation diagram for crystalline chloroform phase, space group *Pnma*, factor group D_{2h}.

Vibrational Modes	Molecule C_{3V}	Site C_s	Unit Cell D_{2h}	
$\nu_{1,2,3}$	A_1 (IR, R)	A'	A_g	R
			B_{1g}	R
			B_{2g}	R
	A_2		B_{3g}	R
			A_u	
$\nu_{4,5,6}$	E (IR, R)	A''	B_{1u}	IR, b
			B_{2u}	IR, a
			B_{3u}	IR, c

There are *4* molecules in the unit cell, which, therefore, leads to two IR-active modes for the ν_1 C−H stretching vibrations, polarized along *a* and *c* axes and to three IR-active modes for the ν_3 C−H deformational vibrations. Concerning the C−H stretch manifold it is possible to suggest that the B_{2u} (*a*) factor group mode should be significantly more intense than the corresponding B_{3u} (*c*) mode because the C−H vector is at an angle of 14.36° with the [100] direction. If the oriented gas model can be assumed, then the ratio of IR intensities for B_{2u} (*a*) and B_{3u} (*c*) species of ν_1 modes becomes: $I(B_{2u})$ (*a*)/ $I(B_{3u})$ (*c*)$=tan^{-2}(14.36°)\sim15$, i.e. the intensity of B_{2u} (*a*) is expected to be by the order of magnitude higher than that of B_{3u} (*c*). The opposite conclusion holds for the ratio of B_{2u} (*a*) and B_{3u} (*c*) components of the deformational C−H band ν_3, $I(B_{3u})$ (*c*)/ $I(B_{2u})$ (*a*) ~*15*, i.e. the intensity of *c*-polarized bending mode component is an order of magnitude higher than that of *a*-polarized component. We will

proceed to further analysis of the experimental RA spectra of chloroform based on the latter predictions of the gas oriented model.

The IR and Raman spectra of solid chloroform have been studied by Kimoto and Yamada [39], D'Alessio *et al.* [40], Andrews *et al.* [41], and Shurvell [42]. The relevant results can be summarized as follows: (i) the sample prepared by vapor condensation on the KRS-5 window at 100 K exhibits IR spectra, which change with time and on temperature rise; (ii) the IR spectra of the as-grown samples contain only sharp peaks, which indicates on the absence of amorphous phases; (iii) spectra stable with respect to time and a temperature change were obtained only after careful annealing of the pre-deposited sample to temperatures around 140-150 K; (iv) the differential thermo-analysis [39] and proton magnetic resonance [43] reveals no phase transition up to the melting point; (v) quadrupole resonance on Cl^{35} nuclei is detectable up to the melting point (209.7 K), which shows that the molecular reorientation is very slow, i.e. there is no molecular reorientation at frequencies above 1×10^4 Hz. The spectral studies of Kimoto and Yamada [39] indicate the existence of metastable crystalline phase in addition to stable phase in the solid chloroform rapidly deposited by gas spraying onto the N_2-liquid cool KRS-5 window. The present studies corroborate with that observation and further investigate the temporal evolution of the IR RA spectra of as-grown and thermo-annealed chloroform films. Figure 5.3.2 (I and II) show the two spectral manifolds of the C−H stretching and bending modes observed on the growing films with π- and σ-polarized IR beam. The ratio of intensities of at 1204 cm^{-1} deformation band and 3011 cm^{-1} stretch band (correspond to the stable crystalline phase *Pnma*) is 2.3 and 0.6 for π- and σ-polarized beam, respectively. In the polycrystalline chloroform the ratio of intensities of total deformation manifold to the stretch manifold was found to be 2.5 by Kimoto and Yamada [39] and given in Table 5.3.2.

Table 5.3.2. The IR spectral data on the C−H stretching and bending modes of chloroform. Present spectral data on solid film and bibliographic data on the gas, liquid and solid phases of chloroform ([39]) are compared. SP, MP, and AP stands for the stable crystalline phase, the metastable crystalline phase and amorphous phase, respectively. The absolute (integrated) intensities are shown in parentheses expressed in the nonstandard cm·millimole^{-1} units [39].

Band	Gas [39]	Liquid [39]	Solid
ν_1 (A_1)	3034 (44)	3015 (707)	3029_{MP} 3011_{SP} (1200 [39]) 3019_{AP}
ν_4 (E)	1221 (4200)	1216 (2900)	1223_{SP} 1208_{SP} (3000 [39]) 1204_{SP} 1223_{MP} 1219_{MP}
I (ν_4) / I (ν_1)	~ 100	4	2.5 [39] I(1204)/I(3011) = 2.3 (π) = 0.6 (σ)

I π-polarization

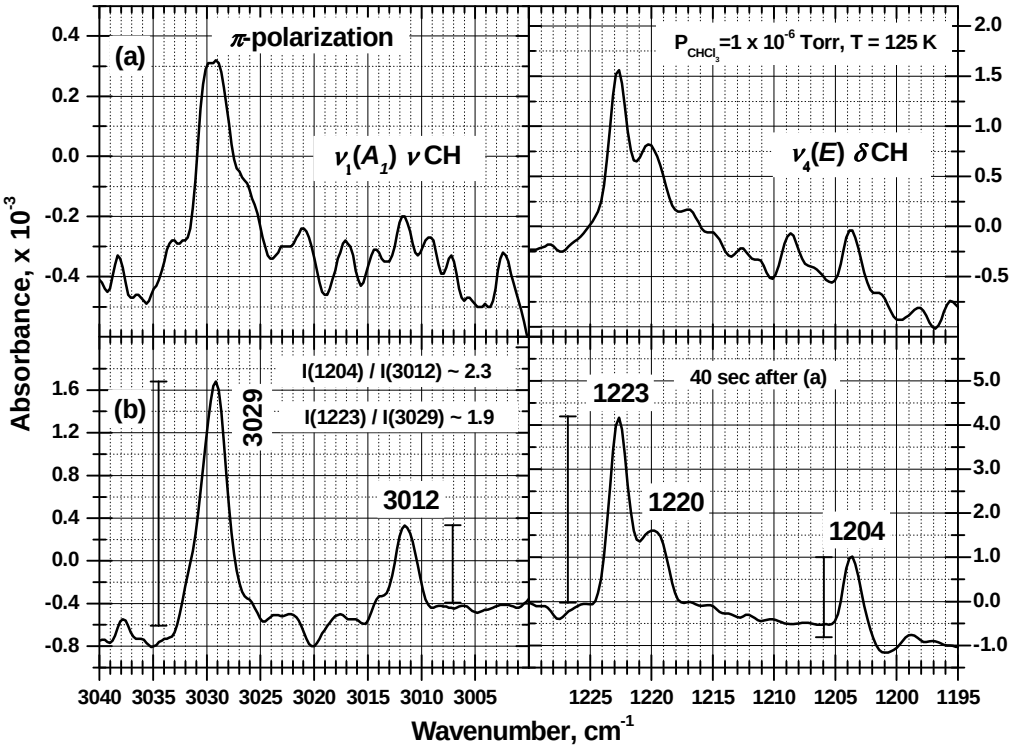

II σ-polarization

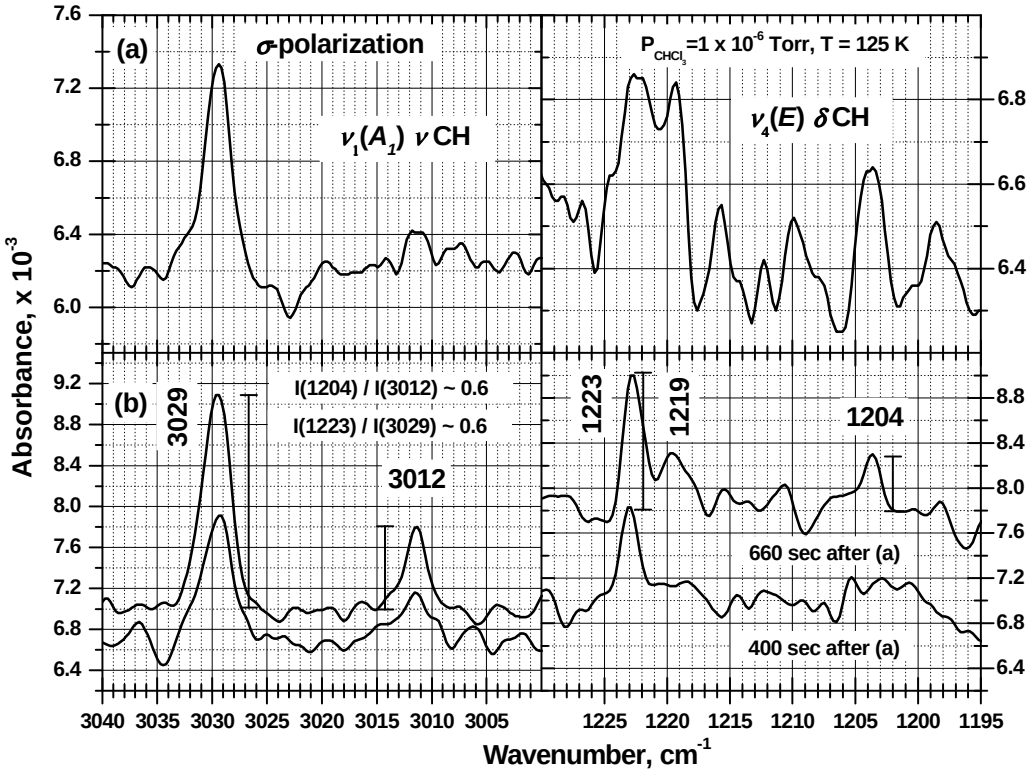

Figure 5.3.2. (I) π- and (II) σ- polarized spectral regions for (a) ν_1 (C−H) stretching and (b) ν_4 (C−H) deformation bands of growing $CHCl_3$ films at deposition temperature of 125 K. The ratios of intensity (approximated by the height of the corresponding band) of these bands shown on the graphs indicate that the C−H bond is oriented preferentially parallel to the metal surface.

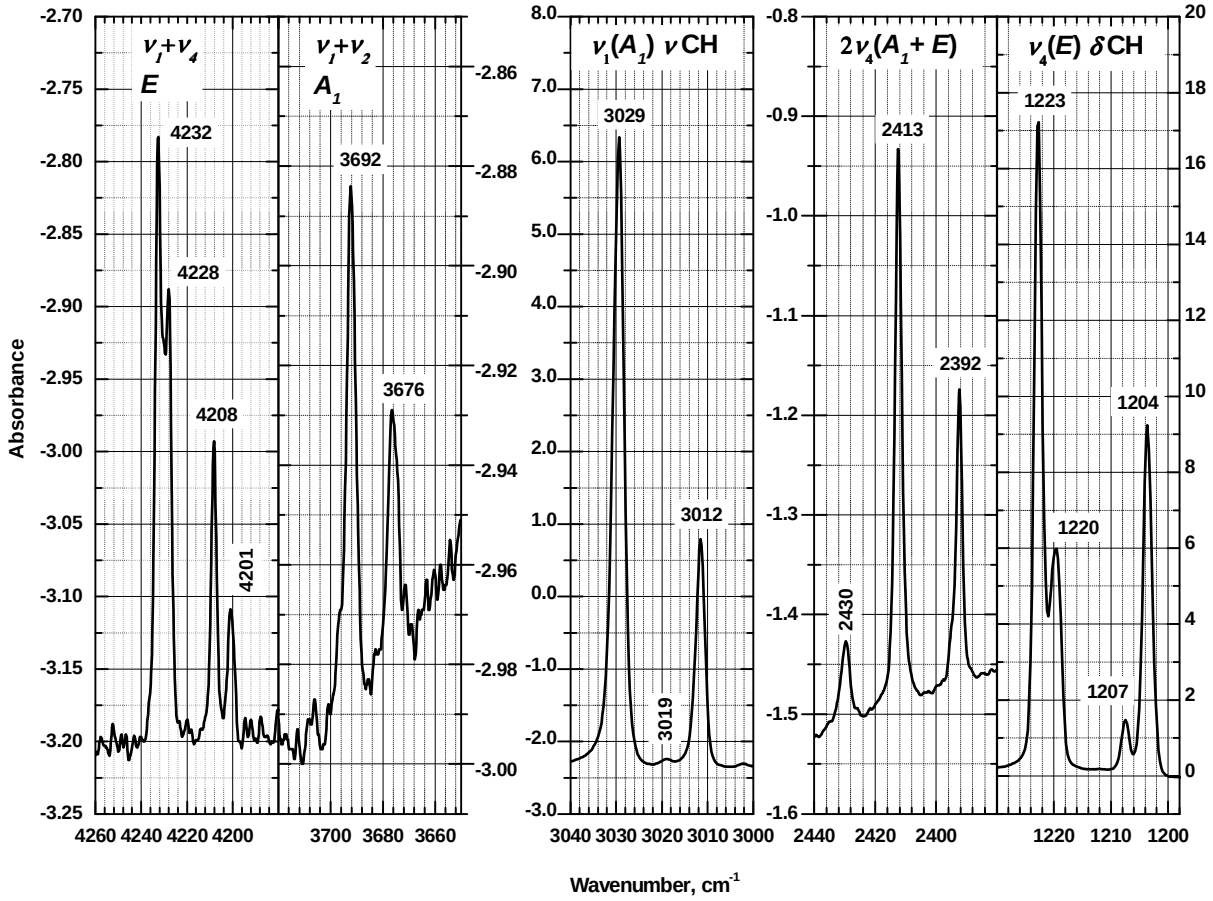

Figure 5.3.3. The π-spectrum of $CHCl_3$ film vapour deposited at P = 1×10^{-6} Torr and 125 K. The spectral signatures of two crystalline phases are evident.

These numerical values indicate that in the solid chloroform film deposited on the metal film in the present studies the molecular axis is oriented preferentially parallel to the metal surface. In other words, the axis *a*, [100] on Figure 5.3.1, is preferentially parallel to the metal surface. Figure 5.3.3 shows the π-spectrum of chloroform, which includes, apart from the fundamental modes, the overtone of the deformational band, $2\nu_4$, and the two

combinational manifolds of the C−H stretch and the bending mode as well as the C−H stretch and the C−Cl stretch modes. The correlation diagram shown on Table 5.3.1 indicates that C−H stretch could exhibit doublet whereas the deformational C−H mode could exhibit triplet upon the dynamic splitting. The stretching mode located at 3029 cm^{-1} was found to disappear converting to low-frequency peak at 3011 cm^{-1}, which remains the only peak of the stable *Pnma* chloroform phase. For the C−H deformational manifold, the annealing leads to significant decrease of the high-frequency peak at 1223 cm^{-1} and almost complete disappearance of 1220 cm^{-1} peak. The evolution of combinational $\nu_1 + \nu_4$ band and overtone $2\nu_4$ upon annealing supports this assignment: the high-frequency doublet at 4232 cm^{-1} and 4228 cm^{-1} and the overtone band at 2413 cm^{-1} completely disappear on annealing, which indicates that they are originated from the combination of 3029 cm^{-1} and 1223 cm^{-1} and from the 1223 cm^{-1} peaks. Therefore, peaks at 3029 cm^{-1}, 1223 cm^{-1}, and 1220 cm^{-1} belongs to the metastable phase, which transforms upon annealing to the crystalline stable phase. Resuming this part let us point out the present studies reveal that chloroform molecules are preferentially oriented with the molecular axis nearly parallel to the substrate surface.

5.3.2 Solid Acetone on the Cu Substrate at 125-165 K

This section provides a qualitative description of the main RA spectral features, which are characteristic to crystalline acetone solid phase/s and which can be used for the spectral identification of the acetone crystalline clusters in acetone-water systems and for distinguishing between different physisorption acetone states on the ice surfaces.

Twenty four fundamental vibrations of isolated acetone molecule form a basis for the irreducible representations of a C_{2V} molecular point group as follows: $8A_1 + 4A_2 + 7B_1 + 5B_2$. Six normal modes ($3A_1 + 2B_1 + 1B_2$) are associated with the motion of the acetone skeleton, whereas the remaining eighteen modes are primarily associated with the motion of hydrogen atoms. Among the skeleton vibrations, the carbonyl stretching fundamental ν_3 (A_1) found in the gas phase spectra at 1731 cm^{-1} and the asymmetric C−C stretching fundamental ν_{17} (B_1) at 1215.5 cm^{-1} [44] are of primarily interest for the present studies because their frequencies are found to be sensitive to the molecular neighborhood of acetone molecules [45, 46]. Moreover their relative intensities can be used for the prediction of the space orientation of acetone molecules in condensed state. Among the modes associated with a hydrogen atom motion, the

symmetric CH_3 deformation bands ν_5 (A_1) and ν_{16} (B_1) will be primarily used in the course of this paper for the identification purposes.

The crystallographic structures of two solid acetone phases, metastable orthorhombic *Cmcm* phase and stable *Pbca* phase prepared by the low temperature crystallization, have been determined by Allan *et al*. [47]. The crystals of both phases are composed from acetone molecules arranged in layers such that the carbonyl groups lie within (*Cmcm*) or closely to the layer (*Pbca*) while the carbon skeleton is oriented perpendicularly (*Cmcm*) or near perpendicularly to the layer (*Pbca*).

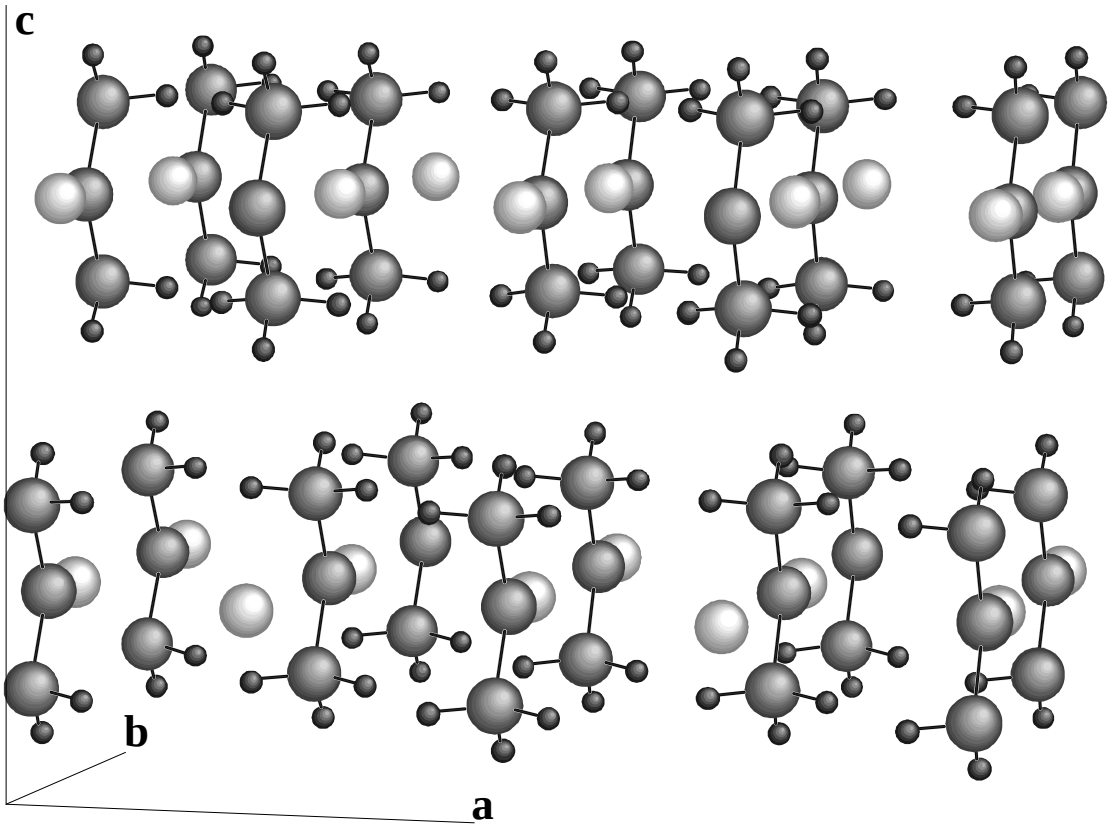

Figure 5.3.4. Molecular arrangement of the acetone molecules in a crystal of the metastable C-centered orthorhombic acetone phase *Cmcm*. a = 6.514, b = 5.4159, c = 10.756 Å, Z = 4 [47]. Coordination number of acetone in the layer is *4*. Carbon-carbon skeleton is in dark and oxygen atoms are in bright color.

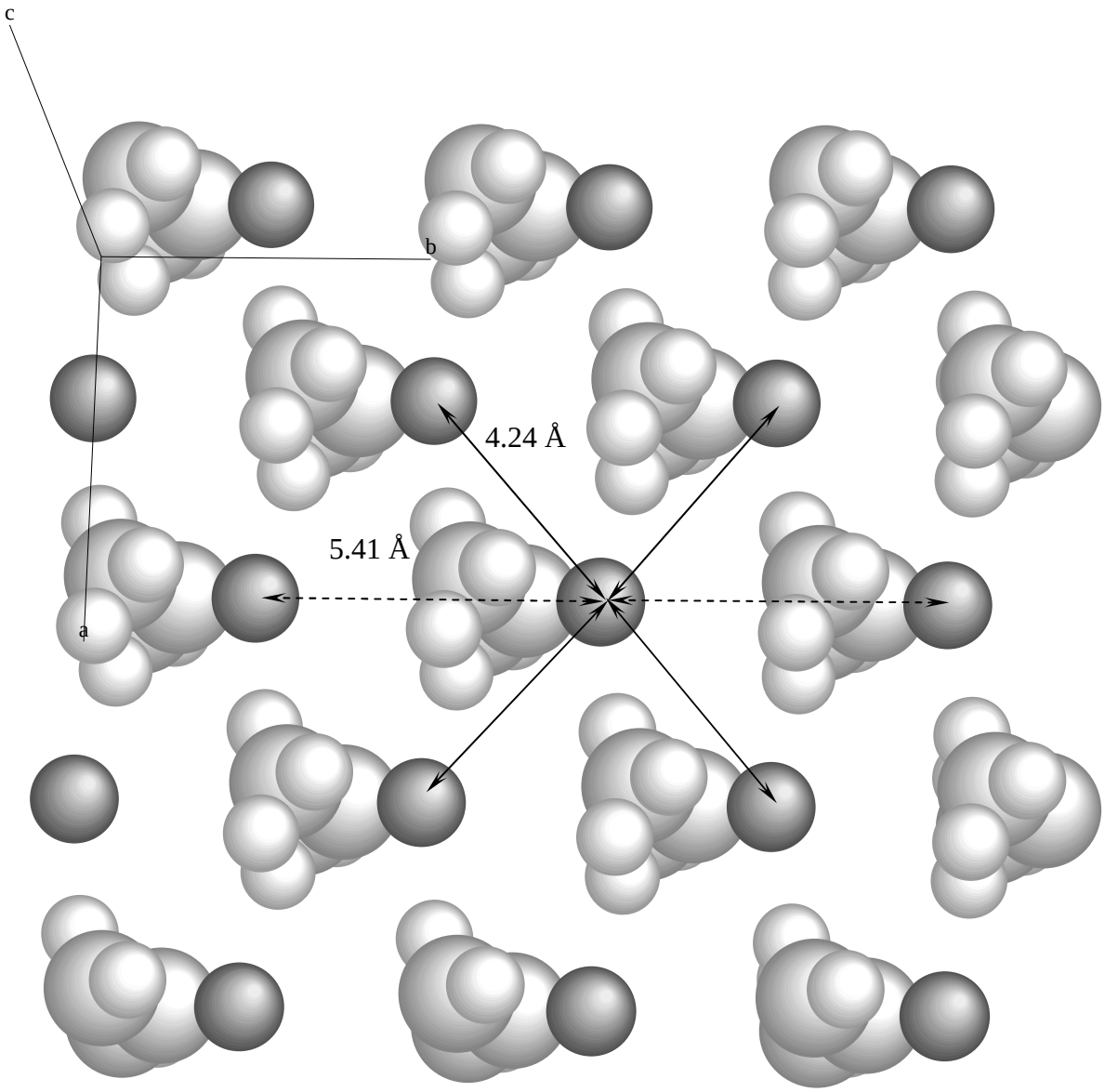

Figure 5.3.5. Structure of the *Cmcm* layer of acetone molecules in the *Cmcm* phase [47]. Within the (001) layer, a number of the nearest neighbours is *4* (O···O distance is 4.24 Å) with *2* additional close neighbours (O···O distance is 5.41 Å).

The molecular arrangement in the crystal of stable orthorhombic acetone phase (Pbca).
T = 150 K, a = 8.873, b = 8.000, c = 22.027 Å, Z = 16.
2a x 2b x 1c

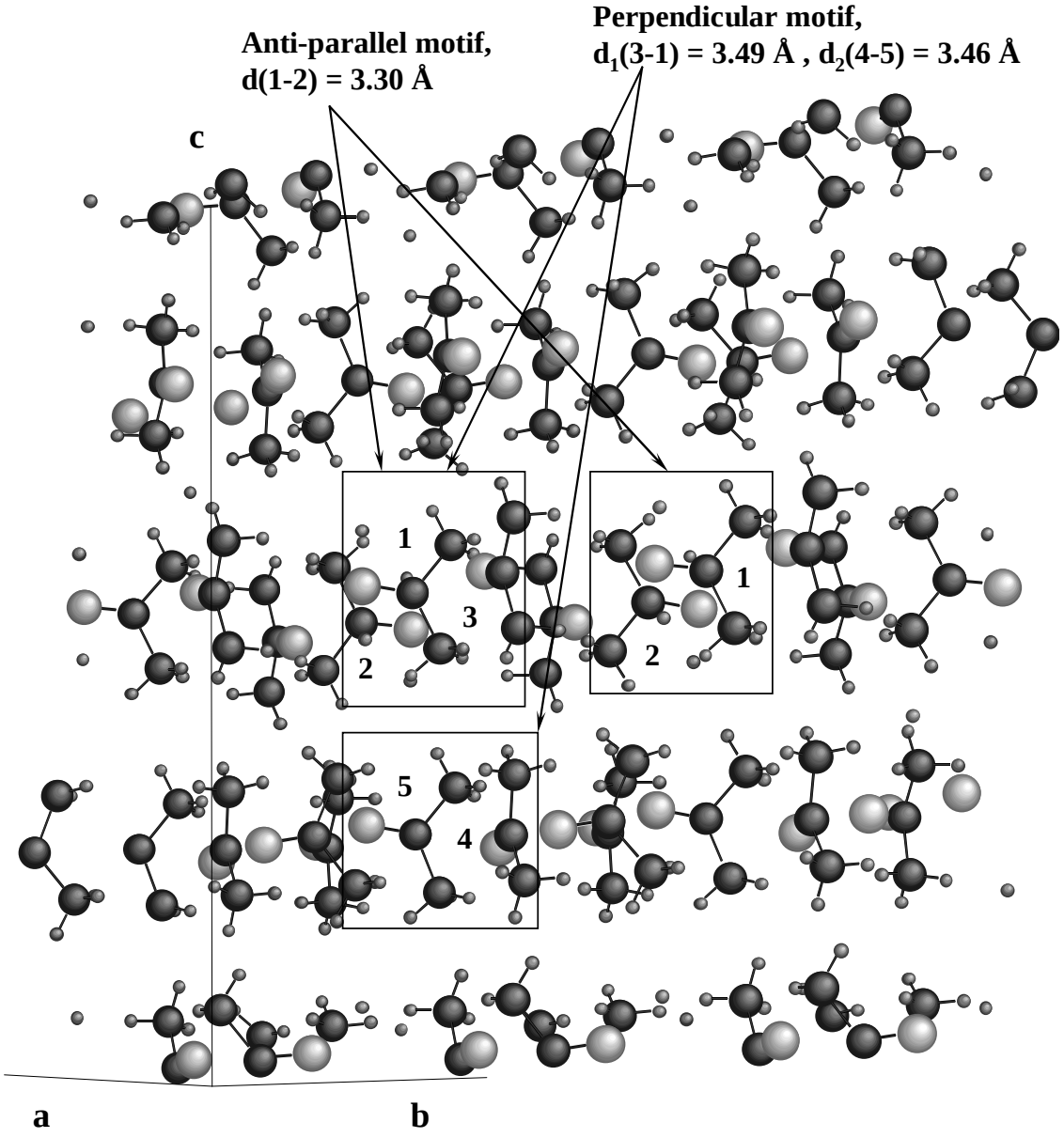

Figure 5.3.6. The molecular arrangement in the crystal of stable orthorhombic acetone phase (Pbca), T = 150 K, a = 8.873, b = 8.000, c = 22.027 Å, Z = 16 [47], dimensions 2a x 2b x 1c.

A metastable orthorhombic *Cmcm* phase can be prepared by slow cooling of the liquid through the melting point at ambient pressure; within a few hours it transforms into a stable primitive phase [47]. A characteristic feature of the *Cmcm* phase structure shown in Figure 5.3.4 is a skew-parallel motif of the acetone molecules arranged in the layer such that the first coordination sphere of acetone molecule contains *4* closest neighbors and *2* additional close molecules at a larger separation distance, which indicates that this structure is not close-packed (Figure 5.3.5). This structure is not close-packed because the molecular axis lies within the (001) layer as shown on Figure 5.3.5. Accordingly, this phase was found metastable and transforming slowly into a *Pbca* orthorhombic phase, the structure of which shown in Figure 5.3.6 [47]. This stable phase consists of two kinds of close-packed layers with coordination number 6, juxtaposed along the *c*-axis. The building block for one of the layers is a pair of closely touching acetone molecules mutually related by an inversion center, which in combination with the set of *b*-glide planes produces the close-packed centrosymmetric structure such that its projection on *ab*-plane forms *pgg* layer shown on Figure 5.3.7. The second layer is a closely-packed *pg* structure formed by the operation of a *b*-glide plane on the row of closely-packed acetone molecules such that molecules derived by its action from the initial molecules falls into a hollow between two molecules of the first row (Figure 5.3.8). The carbonyl groups are oriented such that the angles between carbon-oxygen bonds, which is the direction of intermediate principal axis I_B in isolated molecule, and crystallographic C-axis are bigger than 80º (~ 82º 44' for one of the layers and ~ 80º 27' for another). Accordingly, the minor principal axis I_A, along which the dipole moment of C-C asymmetric stretch is oscillating in isolated molecule, forms with the crystallographic C-axis angles less than 10º (~ 8º 11' for one of the layers and ~ 9º 7' for another).

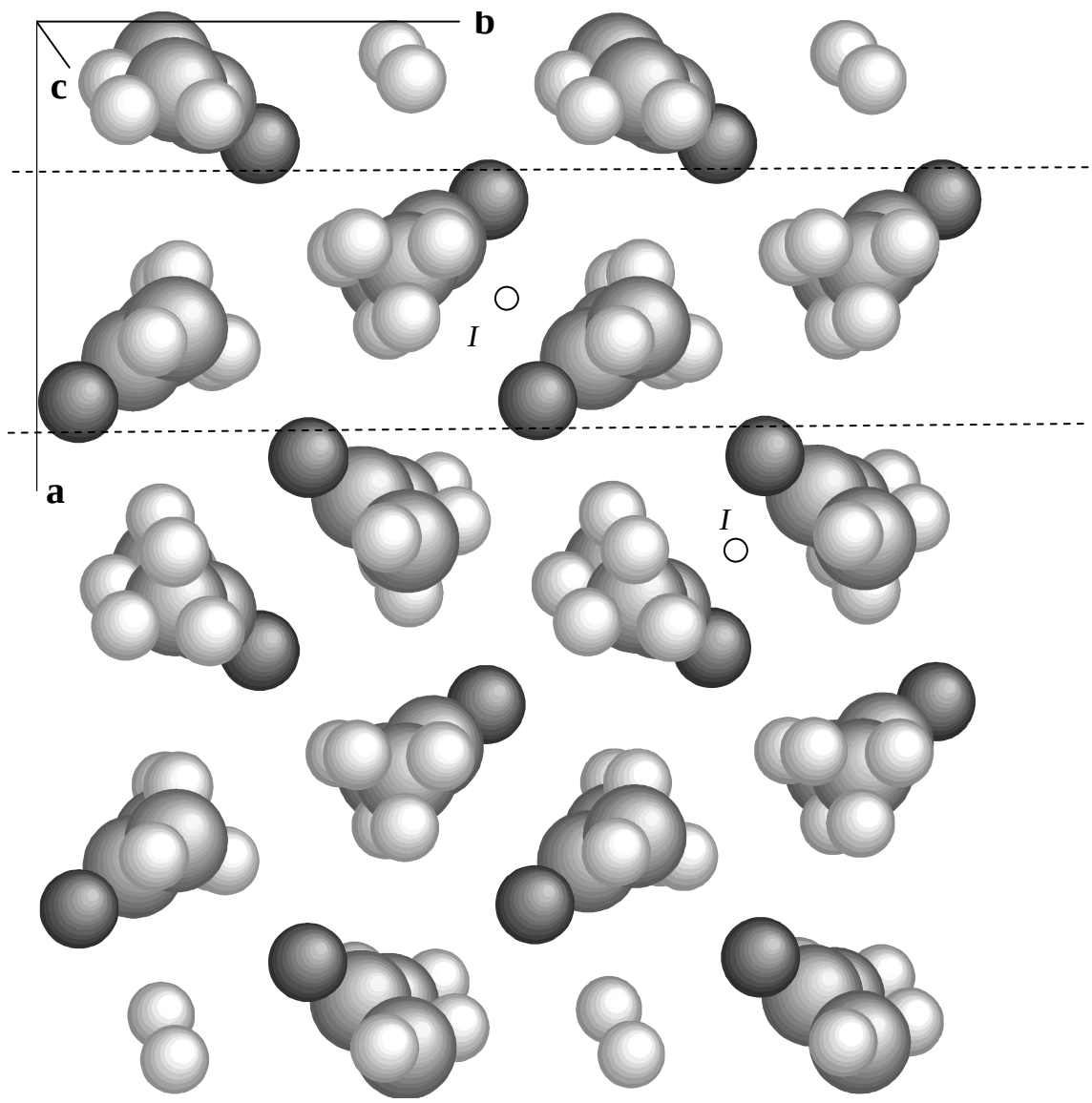

Figure 5.3.7. The *pgg*-layer in the *Pbca* stable acetone phase [47].

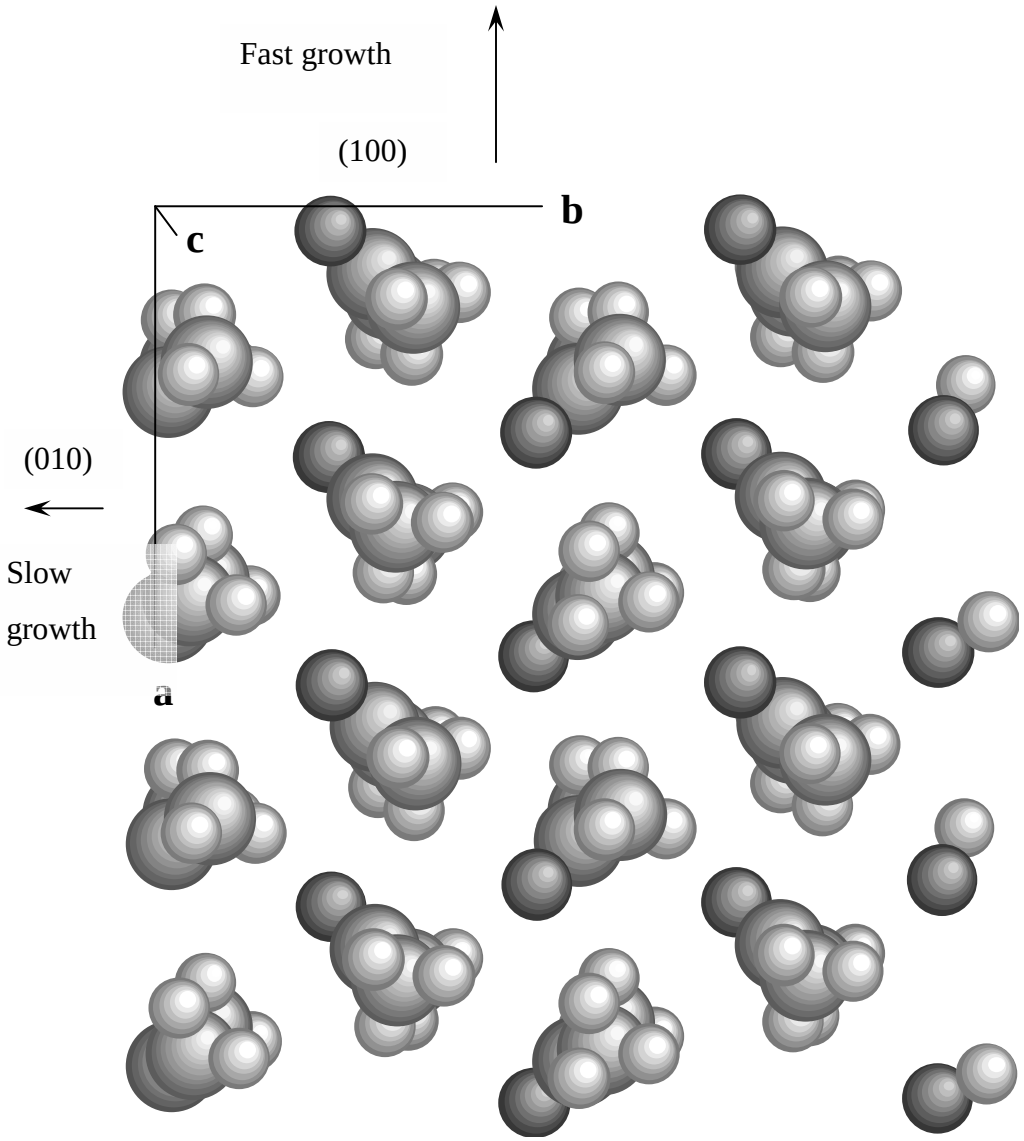

Figure 5.3.8. The *pg*-layer in the *Pbca* stable acetone phase [47].

The habitus and growth modes of the acetone crystals on a polycrystalline Cu substrate and on the ice films can be explored in some degree by FTIR-RA spectroscopy, and in turn, the information about crystal growth and an orientation on the surface is essential for an interpretation of the spectra. Quantitative analysis of the available crystal structures can provide some information about possible habitus and orientation of the acetone physisorbed films. Considering the possible habitus of the acetone crystal of *Pbca* phase, the fastest growth may be predicted for the (100) direction because an attachment of acetone molecule to the (100) plane would lead to establishing of three tight in-layer contacts (Figure 5.3.8) while the

slowest growth can be expected for the (001) plane (Figure 5.3.6). In such a case, the (001) and (100) faces would be the most and the least abundant faces of the *Pbca* phase crystal, respectively. The morphological significance of the (001) plane may be associated with a low interlayer attachment energy E_{att}, which is primarily due to van der Waals nature of the interlayer contacts, in combination with the relatively large layer energy E_L originating from close-packing of the *pg* and the *pgg*-layers [48].

Table 5.3.3. The correlation diagram for the *Cmcm* acetone phase.

Degrees of vibrational freedom per molecule	Degrees of vibrational freedom per Bravias cell (x 2)	Activity in isolated molecule	Molecular Symmetry Group C_{2V}	Site Group $C_{2V(Y)}$	Factor Group of Space Group (Cmcm) D_{2h}^{17}	Activity in crystal
8	16	IR R	A_1	A_1	A_g	R
					B_{1g}	R
4	8	R	A_2	A_2	B_{2g}	R
					B_{3g}	R
7	14	IR R	B_1	B_1	A_u	
					B_{1u}	IR(Z)
5	10	IR R	B_2	B_2	B_{2u}	IR(Y)
					B_{3u}	IR(X)

D_{2h}	N_{Tot}	N_{Acous}	N_{Trans}	N_{Rot}	N_{Vib}	Activity
A_g	9	0	1	0	8	R
B_{1g}	7	0	1	1	5	R
B_{2g}	5	0	0	1	4	R
B_{3g}	9	0	1	1	7	R
A_u	5	0	0	1	4	
B_{1u}	9	1	0	1	7	IR
B_{2u}	9	1	0	0	8	IR
B_{3u}	7	1	0	1	5	IR
Degrees of freedom	60	3	3	6	48	

Table 5.3.4. The correlation diagram for the *Pbca* acetone phase.

Degrees of vibrational freedom per molecule	Degrees of vibrational freedom per Bravias cell (x 16)	Activity	Molecular Symmetry Group C_{2V}	Site Group C_1	Factor Group of Space Group (Pbca) D_{2h}^{15}	Activity
8	128	IR R	A_1		A_g	R
					B_{1g}	R
4	64	R	A_2		B_{2g}	R
					B_{3g}	R
7	112	IR R	B_1	C_1	A_u	
					B_{1u}	IR(Z)
5	80	IR R	B_2		B_{2u}	IR(Y)
					B_{3u}	IR(X)

$$8 \times 16\ A_1 = 8 \times [2 \times (A_g + B_{1g} + B_{2g} + B_{3g} + A_u + B_{1u} + B_{2u} + B_{3u})]$$
$$4 \times 16\ A_2 = 4 \times [2x\ (A_g + B_{1g} + B_{2g} + B_{3g} + A_u + B_{1u} + B_{2u} + B_{3u})]$$
$$7 \times 16\ B_1 = 7 \times [2 \times (A_g + B_{1g} + B_{2g} + B_{3g} + A_u + B_{1u} + B_{2u} + B_{3u})]$$
$$5 \times 16\ B_2 = 5 \times [2 \times (A_g + B_{1g} + B_{2g} + B_{3g} + A_u + B_{1u} + B_{2u} + B_{3u})]$$

The crystallographic unit cell of the crystal structure of the metastable *Cmcm* phase contains four molecule units occupying C_{2V} symmetry positions, while the unit cell of the stable orthorhombic *Pbca* phase contains 16 acetone molecules in general symmetry positions. The symmetry correlation diagrams for the $k = 0$ vibrational modes of these crystal phases are given on Table 5.3.3and Table 5.3.4, respectively.

For the crystal of *Cmcm* group, the factor group analysis shows (Table 5.3.3) that there is one-to-one correspondence between the IR active vibrational modes of the isolated molecule and IR active vibrational modes of the crystal, therefore a factor group splitting in vibrational modes for this metastable phase is not expected and polarization of each mode is preserved. In contrast, for the crystal of *Pbca* group (Table 5.3.4), the correlation of the molecular (C_{2V}), site (C_1) and factor groups (D_{2h}^{15}) shows that each of *8* irreducible representations of the factor group holds two crystal vibrational modes originated from particular normal mode of the molecule. That is, the factor-group splitting causes each molecular mode to generate three pairs of the crystal IR-active vibrational modes polarized along three crystallographic axes, respectively. In particular, the appearance of multi-component absorption band can be expected for molecular non-degenerated modes such as carbonyl stretch ν_3 (A_1) and carbon-

carbon asymmetric stretch ν_{17} (B_1), along with lifting off the degeneracy of molecular modes such as methyl group symmetric deformation modes ν_5 (A_1) and ν_{16} (B_1) and C−H stretch ν_1(A_1) and ν_{13}(B_1) modes. For crystal structures with the centrosymmetric unit cells, to which the two acetone phases described above belong, the IR and Raman active vibration modes are expected to be at different frequencies with an exception of occasional coincidences for limited number of modes. The normal modes that correspond to the ungerade symmetry a species B_{1u}, B_{2u}, and B_{3u} of the factor group D_{2h}, are IR active, while all gerade modes are Raman active. The prediction of the mutual exclusion followed from correlation diagrams (Table 5.3.3and Table 5.3.4), however, appears to be in contradiction with the experimental IR data by Krause *et al.* [49] and Raman data by Harris and Levin [50] on solid acetone, a comparison of which shows that the frequencies for the majority of the IR and Raman bands coincide with one another. On basis of this observation, Krause *et al.* [49] have suggested that a unit cell of the acetone crystals is not centrosymmetric. Concerning a sensitivity of the techniques to spatial extent and arrangement of crystals, it is self-evident that IR and Raman spectroscopies provide information about short-range local molecular neighbourhood while X-ray diffractometry probes crystals on a long-range scale of an assembly of many molecular/atomic layers. In particular, considered as a dynamically independent from the closest layers, the intramolecular IR and Raman modes originated from the motion of acetone molecules in the *pg*-layer (Figure 5.3.8) could coincide. However, for the modes related to intramolecular motions in the *pgg*-layer, which was found to be composed of centro-symmetrical pairs of acetone molecules according to the X-ray diffraction data, frequency exclusion should take place. The break in the symmetry of unit cell of the acetone crystals and, specifically, the *pgg*-structure may be associated with a disorder in methyl-group positions, which has been mentioned by Ibberson *et al.* [51] in relation with the acetone phase transition taking place at ~ 150 K. In fact, instead of complete frequency exclusion: the lower frequency components (presumably belonging to A_1 factor-group component) of the carbonyl ν_3 (A_1) and the carbon-carbon asymmetric stretch ν_{17} (B_1) (Table 5.3.5) modes are found to be more intense in Raman spectra than corresponding high-frequency components, which is exactly opposite to a ratio of the same components in the IR spectra indicating that the symmetry of the *pgg*-layer is broken probably due to the methyl-group disorder.

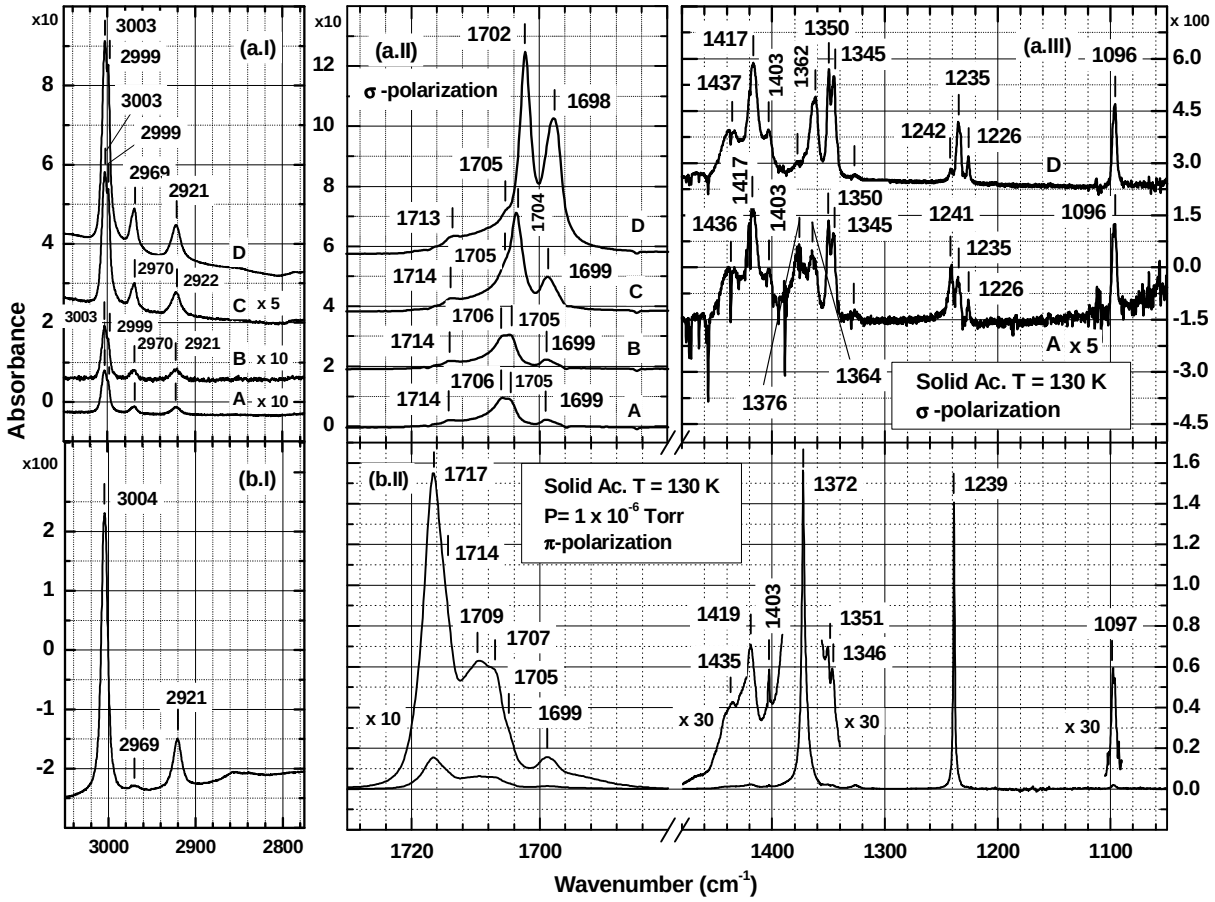

Figure 5.3.9. The (a) σ- and (b) π-polarized spectra of acetone films during fast condensation at 130 K and $P_{Ac}=5\times10^{-5}$ Torr and $P_{Ac}=1\times10^{-6}$ Torr, respectively. Spectra A through D on panel (a) correspond to the deposition time of 60 sec; 140 sec; 220 sec; 360 sec, respectively; the spectrum on panel (b) corresponds to the deposition time of 600 sec.

The acetone solid film deposited in our experiments is, certainly, a mixture of the crystalline and the noncrystalline fragments, which would be most likely classified by the X-ray diffraction method as a noncrystalline phase. However, the IR spectra of these solid acetone films appear to be comparable with the spectra of corresponding crystalline phase because IR spectroscopy probes a short-range molecular arrangement. Figure 5.3.9 shows the RA spectra obtained with σ- (Figure 5.3.9a) and π-polarized (Figure 5.3.9b) beams from solid acetone films vapour-deposited on Cu substrate at 130 K.

Table 5.3.5. The frequencies of fundamental vibrations of the acetone in solid crystalline state. The apparent peak positions (i.e. without deconvolution) are listed.

Sym	N	Mode	Vapor [44]	Raman (solid) [50]	Oriented solid [49]				Non-polarized beam		Polarization	
					Face1		Face 2		Deposit 1 T=150K, ν_3 A_1 is strong	Deposit 2 T=130 K ν_{as} (CC) B_1 is strong	π T=130K δ_s (CH_3) B_1 is strong	σ T=130K
					θ	θ + 90	θ	θ + 90				
A_1 (Z)	1	ν CH	3018.5 s	3004(49)	3005.1w	3005.1m	3008.6m	3008.3s	3002w		3004vw	3003s 2999s
	2	ν CH	2937s	2920(100)	2922.1w	2919.7w	2920.1w	2919.1m	2921vw	2921w	2921vw	2921m
	3	ν (C=O)	1731s	1717sh (14) 1697(72)	1712.9vs 1706.9vs 1698.3s	1715.6vs 1705.1s 1698w	1727.8s 1706.2 vs	1728.0s 1706.3 vs	1718vs 1711.3s 1699.2vw	1716.5m 1714sh 1709w 1707sh 1699vw	1717w 1714sh 1709w 1707w 1699vw	 1714vw 1706s 1705s 1699m
	4	δ_{as} (CH_3)	1435s	1431(31)	1418.2vs	1422.4vs	1420.7m	1420.6s	1419w		1419vw	1417vw
	5	δ_s (CH_3)	1363.5 vs	1351(12)	1351.1w 1346.4s	1350.5vs	1350.2m	1349.6s	1351m 1346w	1351vw 1346vw	1351vw 1346vw	1350w 1345w
	6	β (CH_3)		1072(7)	1070w		1070.8w					
	7	ν_s (CC)	785w	796(100)	795.3w	794.4w	797.5vw 790.7w	797.1w 790.7m				
	8	γ CC	385w	497(5)								
A_2	9	ν CH		2972(58)								
	10	δ (CH_3)		1426sh (29)	1428vw		1431w		1436w	1435sh	1435sh	1436sh
	11	β (CC)		872(4)	873.9vw	873.9w	874 vw	875.4 w				
	12	χ (CH_3)										
B_1 (X)	13	ν CH	3018.5 s	3004(49)	3005.1 wm	3005.1m	3008.6m	3008.3 ms		3004w		
	14	ν CH	2937s	2920(100)	2922.1w	2919.7w	2920.1w	2919.1m			2921vw	2921w
	15	δ_{as}(CH_3)	1410s	1408(3)	1402.4m	1403.4w	1393.3m	1393.4s	1405vw	1402vw	1403vw	1403vw
	16	δ_s (CH_3)	1363.5	1366sh(2)	1372.8w 1369.8m 1365.7w	1372vw 1368.6w 1364m	1364.5 vs	1364.8 vs	1371sh 1365.5m	1372vs	1372vs	1376vw 1364vw 1362vw
	17	ν_{as} (CC)	1215.5 s	1240sh(4) 1229(13) 1223sh (12)	1239.3w 1228.0 wm	1239.4s 1226.8w	1235.9w 1233.0w 1226.7 vw	1236.3s 1226.3w	1237sh 1234m	1238.5vs 1226sh	1239vs	1242vw 1235vw 1226vw
	18	ρ (CH_3)	891m	905(5)	908.6w	908.5m	904.5w	905.8s				
	19	β (CCO)	530s	533(19)	537.1wm 535.3	537.0m 533.0	535sh 532.3 wm	535sh 532.1s				
B_2 (Y)	20	ν (CH)	2972s	2972(58)	2971.6w	2972.1w	2977.5w	2977.9 vw			2969vw	2969m
	21	δ (CH_3)	1454s	1444sh (15)	1467.8w 1447.8w 1439.2m	1445.0s 1435.7w	1457.8s 1442.3s	1460.6w 1457.7m 1439.8m				
	22	ρ (CH_3)	1090.5 s	1098(4)	1098.9s	1098.7 ms	1100.6s	1100.1 wm	1096w	1097vw	1097vw	1096w
	23	γ (C=O)	484 w	402(12)	396.2wm	393.9w	391.9m	394.2 wm				

The following short forms are used: β- in-plane bend; γ- out-of-plane bend; δ- deformation; ν- stretch; ρ- rocking; χ- non-planar twisting. The relative intensities of IR bands are reported as s- strong, m- medium, w-weak, vw- very weak; sh designate a shoulder to the stronger peak.

Firstly, a self-evident conclusion following from Figure 5.3.9b.II at the π-beam is that, in the solid acetone films deposited at significant oversaturation, molecules are in such an average relative configuration that the molecular plane is perpendicular and the carbonyl group is near parallel to the metal surface. This conclusion is based on the observation, that, in contrast with the corresponding intensities in transmission IR spectra of gas and liquid phases [44], the RA peaks at 1372 and 1239 cm^{-1}, which originate from the CH_3 deformational v_{16} (B_1) and the C-C-C stretching v_{17} (B_1) molecular modes, are much stronger than the RA bands at 1716 cm^{-1} and at 1419 cm^{-1} originated from the carbonyl stretch v_3 (A_1) and the CH_3 asymmetric deformation v_4 (A_1) molecular modes, respectively. This particular ratio of the RA intensities of these modes in solid acetone phase is the result of metal surface selection rules, which cause the intensities of the modes with transition dipole moment perpendicular to the metal surface, specifically the v_{16} and the v_{17} (B_1), to be much stronger than the intensities of such modes as the v_3 and the v_4 (A_1) with transition dipole moment near parallel to the surface. In the IR spectra of acetone gas and liquid phases, the carbonyl stretch v_3 (A_1) is the most intense mode, the CH_3 symmetric deformational band v_{16} (B_1) and the C−C asymmetric stretch v_{17} (B_1) are close to each other by intensity and slightly less intense than the carbonyl stretch, while the CH_3 asymmetric deformational bands is the least intense in comparison with the bands mentioned above. The RA spectra of solid acetone phase obtained with σ-polarized light at Figure 5.3.9a also provide a clear support of this conclusion, because in contrast with the spectra obtained with π-polarized beam, the carbonyl stretch manifold at 1706-1702 cm^{-1} is the most intense band, whereas the CH_3 symmetric deformation band v_{16} (B_1) at 1362 cm^{-1} and C−C asymmetric deformation stretch v_{17} (B_1) at 1235 cm^{-1} are found to be at substantially lower intensity. This observation is in a good agreement with the RAS studies of the orientation of acetone molecules in multilayer films on Au (111) surface reported by Syomin and Koel [52]. This is in spite of the circumstance that in the present case the substrate is a polycrystalline Cu with a relatively rough surface, which could cause the acetone film to be a random polycrystalline deposit with an uncertainty in the relative orientation of crystallites. However, the apparent similarity of the RA spectra of solid acetone films, deposited on single-crystal Au(111) surface [52] and on polycrystalline Cu surface (Figure 5.3.9b), show that there is a preferential orientation of the acetone crystallites on a surface of the metal substrate, and the acetone phase growth mode at certain deposition conditions does not depend upon the

status of metal substrate.

A different molecular orientation was observed in the present studies at slow deposition at ~ 150 K, when a carbonyl group is preferentially oriented near to the perpendicular to metal surface while the molecular plane is oriented near to the parallel to metal surface. Taking into account that the oversaturation is apparently much less in this case, we could assume that the orientation of crystallites on the substrate (if the phase composition remains the same) depends on the deposition rate and, more generally, on the supersaturation .

Independently upon the phase structure of an acetone deposit, the spectral picture on Figure 5.3.9 is consistent with a crystalline structure, in which an average direction formed by C-C molecular skeletons is near perpendicular and an average plane formed by C=O groups is near parallel to a metal surface. Furthermore, considering the *Cmcm* and *Pbca* phase structures (Figure 5.3.5 and Figure 5.3.6), it is possible to conclude that crystallographic *C*-axis of crystallites is near perpendicular while the *AB*-plane is near parallel to a metal surface, which appears to be consistent with (001) plate-like morphological habitus of the crystallites. The morphological significance of the (001) plane of acetone crystals (*Pbca* phase) may be associated with low interlayer attachment energy E_{att}, which is primarily due to the van der Waals nature of the interlayer contacts, in combination with relatively high layer energy E_L originated from closely-packed *pg* and *pgg*-layers and substantial dipole-dipole intermolecular interaction [53].

The factor group and *LO/TO* splitting observed in the RA spectra of solid acetone deposit are inconsistent with the correlation diagram of *Cmcm* phase and, thus, will be analyzed on basis of the correlation diagram of the *Pbca* phase. It is instructive to begin spectral analysis from the crystal bands, which are originated from the B_1 molecular vibrations, because corresponding π-components are of high intensity in RA spectra showing no sign of the factor-group splitting, but with characteristic *LO/TO* splitting and thickness dependence of adsorption peaks. In particular, the very strong peaks at 1372 and 1239 cm^{-1} observed with π-polarized light (Figure 5.3.9b.II) are the *LO* components, which can be both classified as B_{1u} crystal modes originating from the CH_3 symmetric deformation ν_{16} and the C−C stretch bands ν_{17}, respectively. Accordingly, in the spectra obtained with σ-polarized light (obviously that in the experiment only incomplete polarization can be achieved) the peaks at 1376 and 1241 cm^{-1} (Figure 5.3.9a.III and Table 5.3.5) are *LO* components of these modes, while the

corresponding σ-polarized *TO* components are located at 1362 and 1235 cm^{-1}. The incompleteness of polarization and the very strong intensities of *LO* modes allow to observe them under σ-polarization. It should be noted that the B_{2u} and B_{3u} CH_3 symmetric deformation crystal modes were not identified among the observed RA peaks because, even if they present (*Pbca* group), the intensities are expected to be very low in accord with the crystal structure of *Pbca* phase. Therefore, these modes appear to be practically undetectable in the RA spectra being overwhelmed by corresponding B_{1u} peaks. The σ-polarized peak at 1364-1362 cm^{-1} (Figure 5.3.9a.III) is most likely multi-component but, at the present moment, we feel that its further decomposition would be neither useful nor reliable. For the crystal modes originating from molecular C−C asymmetric stretch, the additional σ-polarized adsorption band was found at 1226 cm^{-1} (Figure 5.3.9a.III). The weak adsorption peaks at frequencies 1228-1226 cm^{-1} have been also detected in transmission IR spectra by Krause *et al.*[49] for solid acetone at 18 K and classified among those vibrational modes that are originated from v_{17} molecular fundamental, while in the Raman spectra of polycrystalline acetone at 77 K two peaks at 1229 cm^{-1} and 1223 cm^{-1} (shoulder) were detected by Harris and Levin [50], who have assigned the peak at 1229 cm^{-1} to v_{17} fundamental (see Table 5.3.5). Accordingly, we tentatively attribute the low frequency very weak IR peak at 1226 $cm^{-1}$to the C−C stretch vibrational modes having origin in the centrosymmetric skeleton motion of the pairs of acetone molecules in *pgg*-layers (Figure 5.3.7), which appears in the IR spectra because of the symmetry break and otherwise would not be detectable. The vibrational mode that corresponds to asymmetric CH_3 deformation molecule mode v_{15} of B_1 symmetry was found to be a very weak feature at 1403 cm^{-1} in the RA spectra obtained with both polarizations (Figure 5.3.9b.II and a.III), though it is more distinct in the spectra obtained with π-polarization.

The crystal vibrations that are originated from following A_1 symmetry species of C_{2V} molecular point group including the carbonyl stretch v_3, CH_3 symmetric v_5 and asymmetric v_4 deformation modes and C-H stretch v_1 were detected in the IR-RA spectra of solid acetone. The two doublets at 1350 *TO*(1351 *LO*)/1345 *TO*(1346 *LO*) cm^{-1} and 3003 *TO*/2999 *TO* cm^{-1} (Figure 5.3.9 a.I, a.III and Table 5.3.5) can be tentatively attributed to the B_{2u} and B_{3u} crystal modes that correspond to CH_3 symmetric deformation band v_5 and C−H stretch v_1, respectively, in accord with correlation diagram for the *Pbca* space group. The δ_{sym} CH_3 mode exhibits most likely a factor-group splitting on doublet 1350/1345 cm^{-1} in the σ-spectra which

can be viewed as a spectral signature of *Pbca* phase. These modes are polarized in the *AB*-plane, while the 1362 *TO*/1372 *LO* cm^{-1} mode is polarized along the C-axis. The crystal modes corresponding to the CH_3 asymmetric deformation mode v_4 were found at 1417(1419) cm^{-1} with no sign of splitting (Figure 5.3.9 a.III, b.II). The complex carbonyl stretch band (v_3) shows splitting at both settings of the polarizer (Figure 5.3.9a.II and b.II, and Table 5.3.5), which is thought to be primarily the result of factor-group splitting affected by *LO/TO* splitting and by possible presence of different acetone micro-phases. The interpretation of this RA band observed with σ-polarized light is significantly complicated (and that is a typical case for thick films) due to the emergence of interference patterns in the spectral region of a particular absorption band. Clearly, the π-polarized complex band at 1716 cm^{-1} (Figure 5.3.9 b.II) could include the *LO* components of all B_{nu} crystal vibrational modes, while, tentatively, the *TO* components of B_{1u} (Z) mode can be found at 1713 cm^{-1} (Figure 5.3.9 a.II), and for B_{2u} and B_{3u} crystal modes at 1706/1705 cm^{-1} polarized in the AB crystallographic plane (Figure 5.3.9 a.II). The corresponding *LO* components could be tentatively allocated at 1709 and 1707 cm^{-1} in Figure 5.3.9b.II. Based on the present spectra, the low frequency RA band at 1699 cm^{-1} should be assigned to a fundamental mode resulting from a factor-group splitting, which could be in correlation with the strongest Raman C=O sub band at 1697 cm^{-1} (while the second less strong Raman C=O sub band was observed at 1717 cm^{-1} [50]) and with the IR transmission band at 1698 cm^{-1} [49].

Figure 5.3.10 displays the carbonyl group region of the Fresnel spectra (see Chapter 3) of acetone liquid films of 0.8 μ and 1 μ thickness with the optical constant of liquid acetone obtained from [54]. In transmittance mode, there is a single IR peak with maximum at ~1714 cm^{-1} as shown by the imaginary part of dielectric function (curve 1). For this disordered medium the π-component (*LO* mode) appears at 1727 cm^{-1} with discernible shoulder at 1714 cm^{-1} (the interference pattern, absent for thinner acetone films) whereas the σ-component (*TO* mode plus interference patters) at 1710 and 1705 cm^{-1} for 0.8 μ and 1 μ films, respectively. The non-polarized Fresnel spectrum of single fundamental vibration exhibits clearly a strong *LO/TO* splitting. The magnitude of this *LO/TO* splitting expected for a liquid acetone is ~ 20 cm^{-1}, which is as strong as the factor group splitting in the acetone crystal or even stronger. In addition the frequency position of both *LO* and *TO* modes depends on the film thickness. This general picture for carbonyl group vibration in liquid acetone was found reproduced precisely

in the experimental spectra of solid acetone deposit at 130 K. Indeed, for the non-polarized beam (Figure 5.3.10, curves 8 and 9) there is a clear σ-polarized *TO* manifold which travels from 1707 cm^{-1} to 1705 cm^{-1} as film thickness increases. At the same time, the π-polarized manifold at 1717 cm^{-1} achieves optical saturation (curve 8) and the peak shifts to ~1720 cm^{-1} (curve 9) and declines in the intensity as film thickness increases. Similar optical dependence of non-polarized RA spectra on the film thickness was found for pristine ice (see for instance Figure 5.1.3 in the present Chapter). Therefore, the observed experimental spectral evolution as function of acetone film thickness is clearly associated with the *LO/TO* splitting, which severely obscures the crystal structure-associated factor group or site group splitting of fundamental vibrations. The magnitude of the *LO/TO* splitting is proportional to the oscillator strength and to the transition dipole-transition dipole inter-vibrator coupling, which explains why this optical RA effect is so noticeable for all fundamental vibrations in solid acetone as it is shown on Figure 5.3.11. It is of interest to observe a significant amplification of the ν_5 (A_1) δ_s CH_3 *TO* mode factor-group doublet at 1349 and 1344 cm^{-1} upon a passage of the σ-interference pattern from neighboring strong ν_{16} (B_1) δ_s CH_3 at 1360 cm^{-1}, which confirms conclusion derived on basis of Figure 5.3.9. A small red-shift in their frequency positions is due to the dielectric effects in the thick acetone film. A conclusion that the pair of ν_{16} (B_1) δ_s CH_3 at 1372 (π, *LO*)-1362 (σ, *TO*) cm^{-1} and the pair of ν_{17} (B_1) ν_{as} C−C at 1242 (π, *LO*)-1235 (σ, *TO*) cm^{-1} on Figure 5.3.9 are *LO/TO* splits of the same fundamental vibrations is in accord with the spectra on Figure 5.3.11 and Fresnel model for carbonyl group on Figure 5.3.10.

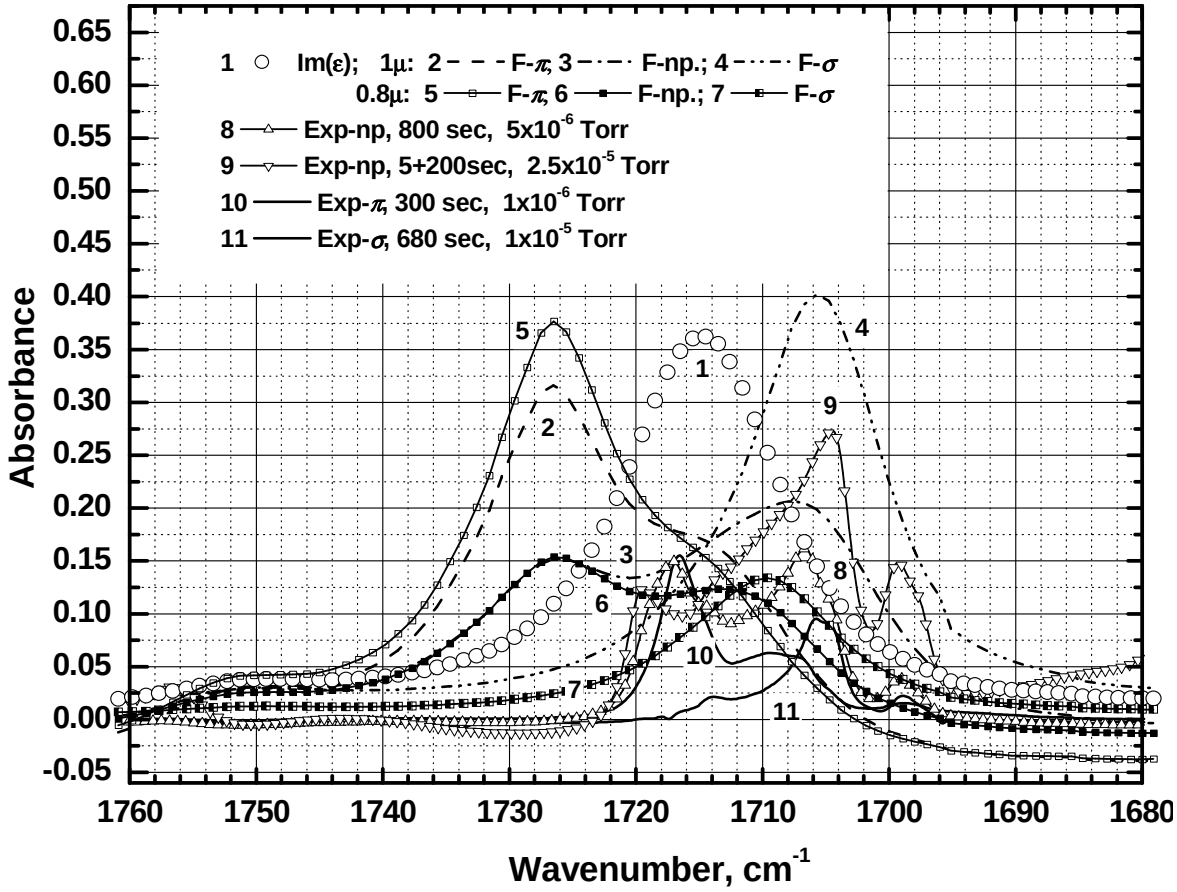

Figure 5.3.10. The RA spectra of the carbonyl group region of solid acetone.
The Fresnel spectra of liquid acetone film of 1 μ thickness (curves 2-4) and of 0.8 μ thickness (curves 5-7) and the imaginary part of the dielectric function of liquid acetone (curve 1, arbitrary scaled to fit the ordinate). Experimental RA spectra of acetone at 130 K with non-polarized beam (curves 8, 9) and with π- (curve 10) and σ- (curve 11) polarization.

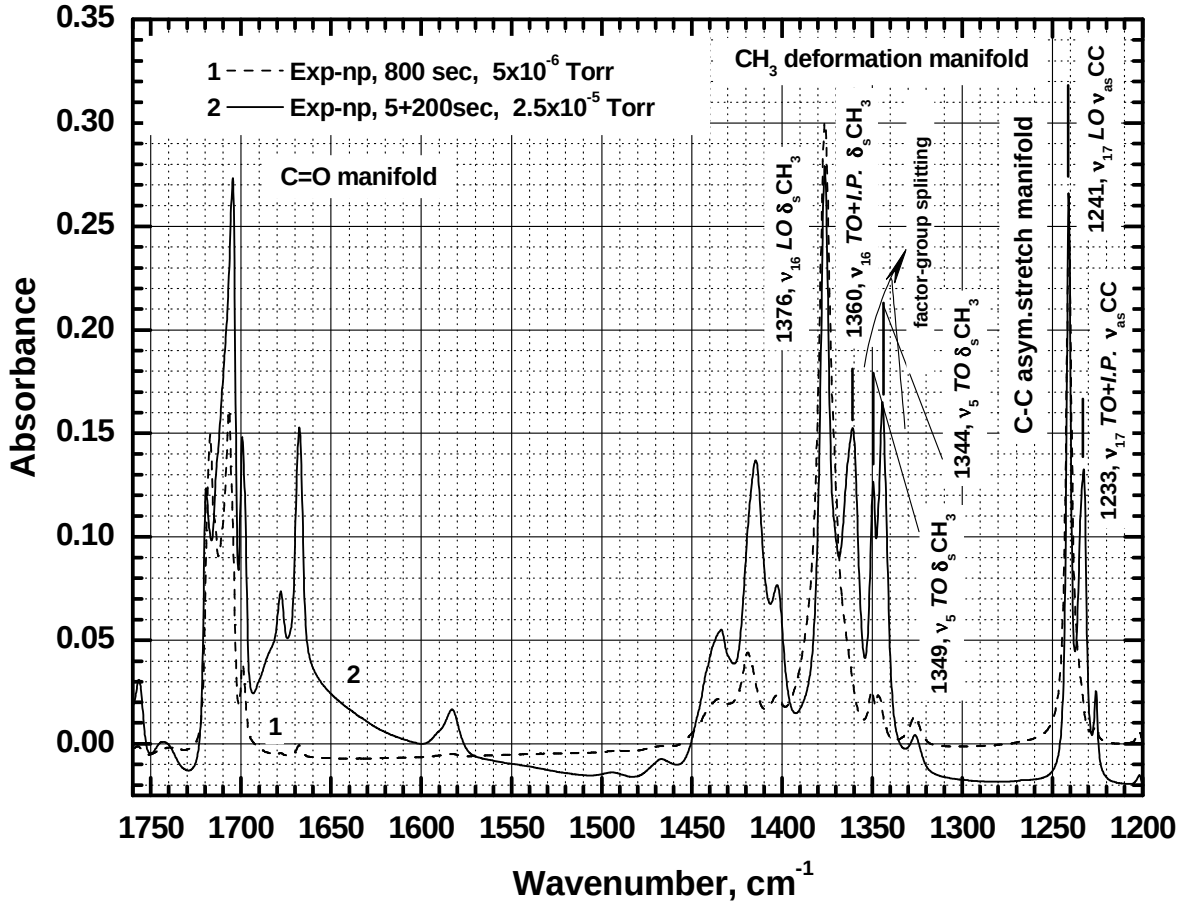

Figure 5.3.11. Experimental RA spectra of acetone at 130 K with non-polarized beam. The *LO/TO* splitting is evident for the CH_3 deformation and C−C asymmetric stretch modes.

Resuming this section on the spectral analysis of organic solids (chloroform and acetone) it is possible to suggest that the relative orientation of crystallites depends on the oversaturation or, in other words, on a combined effect of the substrate temperature and the pressure of the organic substance near the substrate surface. Further detailed studies are required in order to clarify these possible orientational effects of the combined action of substrate temperature and deposition pressure. If convincing evidence regarding preferential orientation will be obtained (the present studies provide a preliminary evidence for the existence of these effects) that provides a simple mean to control the average orientation of very small crystallites (nano-size) of organic solids on metal surface. For both chloroform and acetone, the deposition at high oversaturation was found leading to the orientation, where the molecular axis and the corresponding dipole moments are nearly parallel to the substrate.

5.4 The Interaction of Chloroform with Noncrystalline Ice

The adsorption of chloroform on the ice surface is accompanied with a red-shift of the frequency OH dangling bonds, which can be resolved in the FTIR RAS experiment. This circumstance is important for confirming that the interaction of adsorbate with the OH dangling bonds leads to surface complexes, where the adsorbate is indeed coordinated with the OH dangling bonds. Furthermore, the spectral observation of this new band of OH groups coordinated with the chloroform surface species can be used for monitoring the temporal or thermal evolution of the water-chloroform interface. Apart from the stretching mode of surface OH groups, the present spectral studies of the chloroform interaction with the ice surface are based on observation of C−H stretch and C−H deformational bands at frequency regions near 3015 cm^{-1} and 1220 cm^{-1}, respectively. To the best of the author's knowledge, the spectral evidences of the chloroform-oxygen function interaction, which would based on the direct observation of the chloroform fundamentals, are practically absent, in particular, because the frequency location of C−H stretching and bending modes appears to be insensitive to the complex formation [55, 56]. However, Szczepaniak [Ref. from 56, no numerical data of Szczepaniak's original work have been presented] has observed a considerable shift in the C−D deformation band upon complexation with acetone in n-hexane solution. On the other hand, the combinational bands and overtones of these fundamental modes were found to be sensitive to the complexation with the oxygen organic functions. Indeed, very early (and still unique) IR studies on the chloroform-oxygen function complexes by Buswell *et al.* [57] reveal that in the chloroform-acetone complex in CCl_4 the overtone ($2\nu_4$) of ν_4 (*E*) C−H deformation band located for chloroform/CCl_4 solution at ~2410 cm^{-1} exhibits a distinct peak at 2457 cm^{-1}. The latter indicates, with high probability, a hypsochromic shift of the deformational fundamental by approximately 20-25 cm^{-1} upon complexation, which would be in accord with the Szczepaniak's observation. For the saturated solution of water in chloroform, Choppin and Duwney [58] have observed a combinational band, $\nu_{1\ O-H} + \nu_{1\ C-H}$, which has been interpreted as a spectral signature of the hydrogen-bonded complex $Cl_3C-H\cdots OH_2$. By examining the C=O stretching mode, Whetsel and Kagarise [59] spectrally detected 1:1 and 1:2 hydrogen-bonded complexes between acetone and chloroform in cyclohexane solution. Therefore, there are numerous spectral evidences that chloroform can act as a *HB* donor in the complexes with oxygen functions including water species. While the frequency position of C−H stretching

mode, ν_1 (A_1), of chloroform species appears to be practically independent on the complexation, the C−H bending mode ν_4 (E) is most likely hypsochromically shifted. In a case of the coordination with water molecules chloroform can hypothetically act also as an acceptor of hydrogen bond from water molecule with the formation of a complex with structure HO−H···Cl−CCl_3H. By co-depositing the mixtures of halomethanes and D_2O vapour on cold (12 K) CsI window, Holmes and Sodeau [60] have determined the spectral location of the stretching modes of OH groups coordinated with corresponding halomethane species. For the chloroform species in D_2O matrix, the ν_3 mode of water molecule in the HO^*−H^*···$CHCl_3$ complex (of unknown structure) is found at 2690 cm^{-1}, which is consistent with 38 cm^{-1} red-shift with respect to the *DB* peak at 2728 cm^{-1} for pristine ice. The present spectral studies reveal that adsorption of chloroform on noncrystalline D_2O proceeds though the formation of hydrogen-bonded complex between an OD *DB* and a chloroform molecule as it is evident from Figure 5.4.1. The OD vibration in hydrogen bonded complex was found at 2690 cm^{-1} in excellent accord with Holmes and Sodeau [60]: the formation of *HB* complexes is accompanied by the depletion of OD *DB's* (a negative band in differential spectra on Figure 5.4.1). Moreover, a spectral signature is found for the hydrogen-bonded complex where the chloroform species acts as a donor and the oxygen subnetwork of ice as an acceptor as it is evident from a broad C−H deformation feature at ~1245 cm^{-1} (Figure 5.4.2). The lower frequency band at 1220 cm^{-1} corresponds to the physisorbed species in accord with the discussion in section 5.3.1.

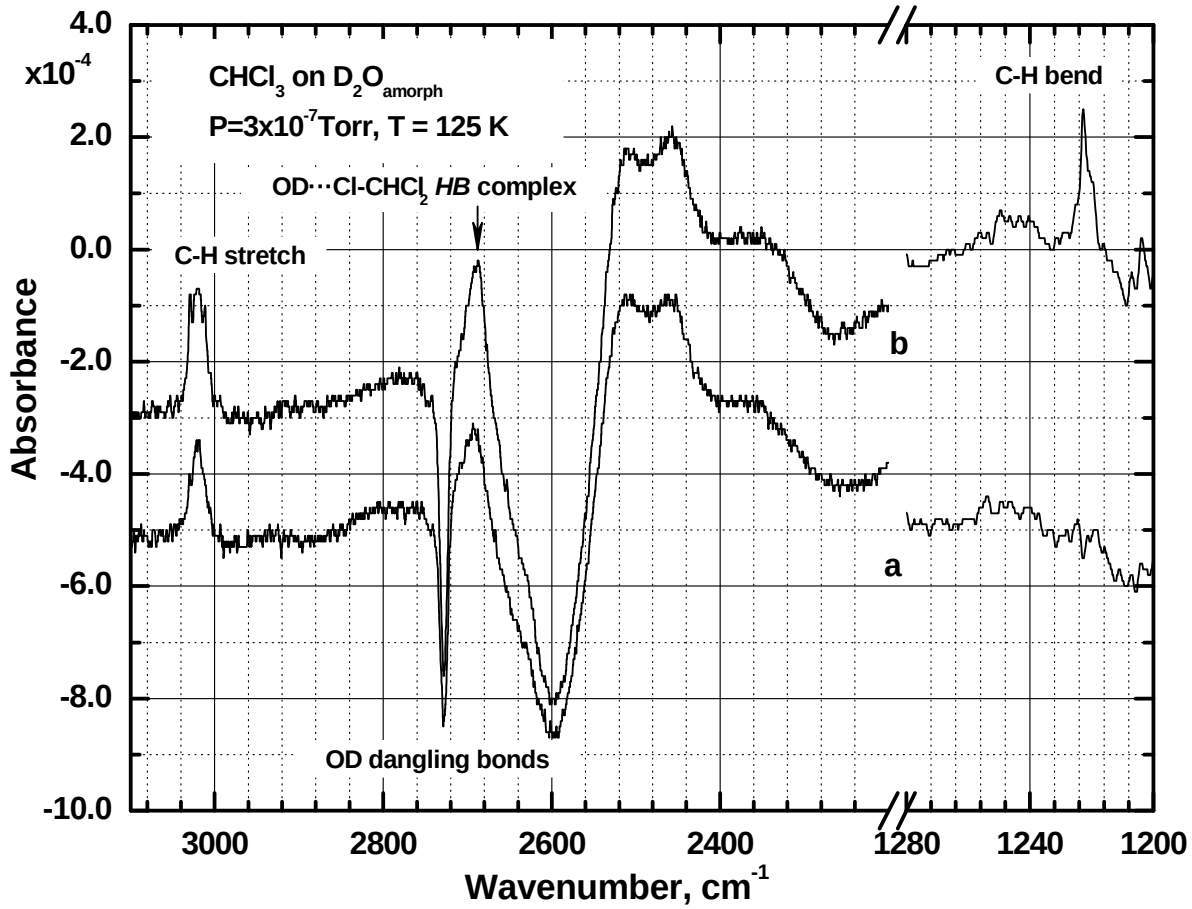

Figure 5.4.1. Differential RA spectra of chloroform adsorbed on noncrystalline ice at 125 K. Spectra (a) and (b) correspond to 13 min and 20 min into deposition, respectively. An acquisition time of a single spectrum is 40 sec. Spectral resolution is 1 cm^{-1}.

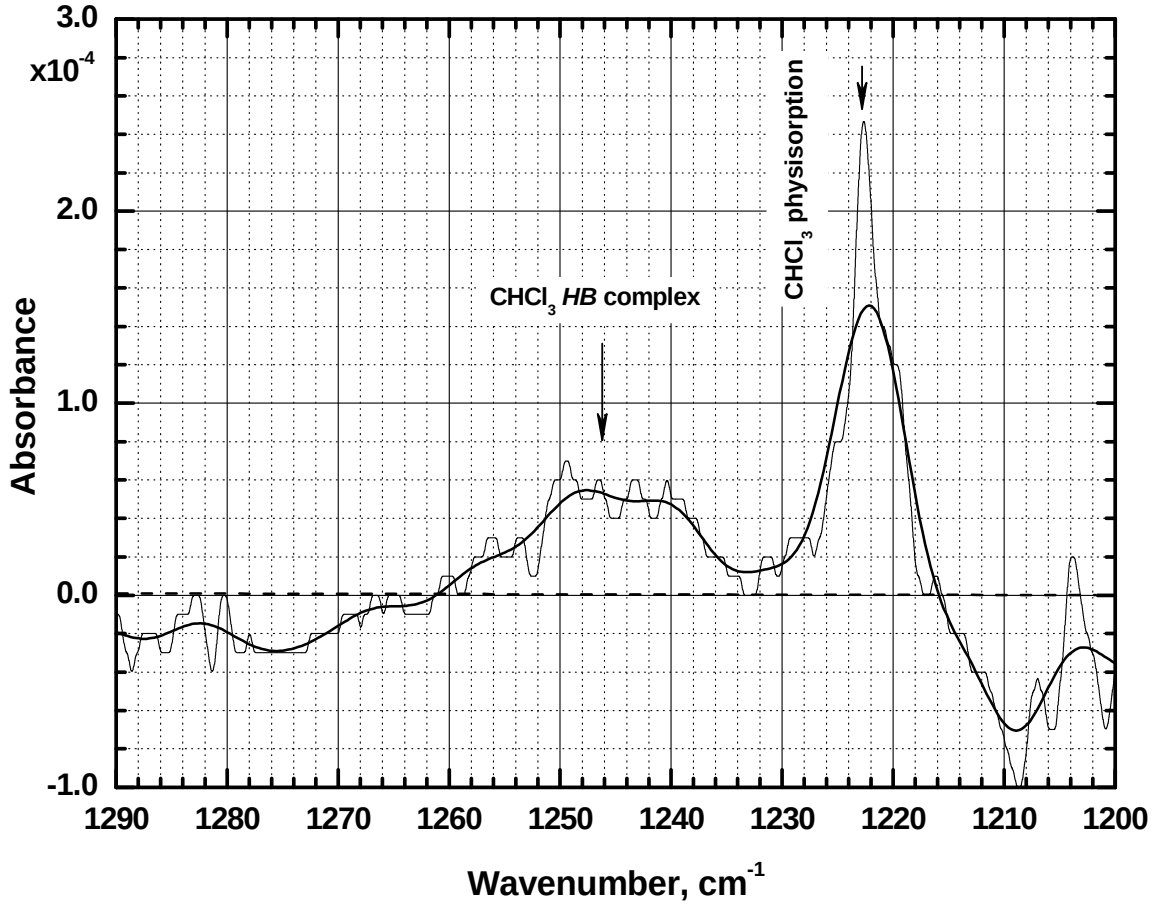

Figure 5.4.2. The spectral region of C−H deformational band for chloroform on ice at 125 K. This spectrum is the result of averaging of 10 consecutive spectra the first and the last of which are shown on Figure 5.4.1 above. The solid line represents the FFT smoothing of experimental data.

5.5 Interaction of Organic Substances with Oxygen-containing Functional Groups with Noncrystalline and Polycrystalline Ices

The present spectral studies of initial stages of adsorption of acetone, acetaldehyde, methanol and chloroform on the noncrystalline and polycrystalline ices reveals that hydrogen-bonded complexes between adsorbates and OH *DB's* play a leading role on the surface accommodation. We proceed to the detail analysis of the spectral features of acetone-water systems at cryogenic temperature.

5.5.1 The Interaction of Acetone with OH Dangling Bonds on Ice Films

In order to examine the role of the OH *DB's* in the surface chemistry of the ice micro-phases, the adsorption of acetone (a soft Lewis base) on pc-ice and nc-ice films is investigated by FTIR-RA spectroscopy. Based on temperature programmed desorption and FTIR-RA data of acetone adsorbed on thin nc-ice film (<20 nm thick) at 95 K, Schaff and Roberts proposed that the interaction between the adsorbate and the ice surface involves hydrogen bonding between the carbonyl group of acetone and the OH *DB's* in ice [61]. For the pc-ice prepared by crystallization of the nc-ice post-annealed at 160 K, no OH *DB* was observed and consequently neither was the acetone-H-O *DB* complex detected by Schaff and Roberts [61]. However, in the present studies the OH *DB* signals are observed for both pc-ice and nc-ice (Figure 5.2.1 above). Therefore, the formation of the acetone-H-O *DB* complexes involving hydrogen bonding is expected on these ice films. Figure 5.5.1 shows the RA difference spectra for various exposures of acetone under different exposure pressure conditions on a 30-nm-thick pc-ice film (obtained by vapour deposition at 160 K followed by soaking at the base pressure for 30 minutes). The difference spectra correspond to the difference of RA spectra for ice films with and without the acetone exposures and therefore should reveal spectral features corresponding primarily to the acetone-ice complexes.

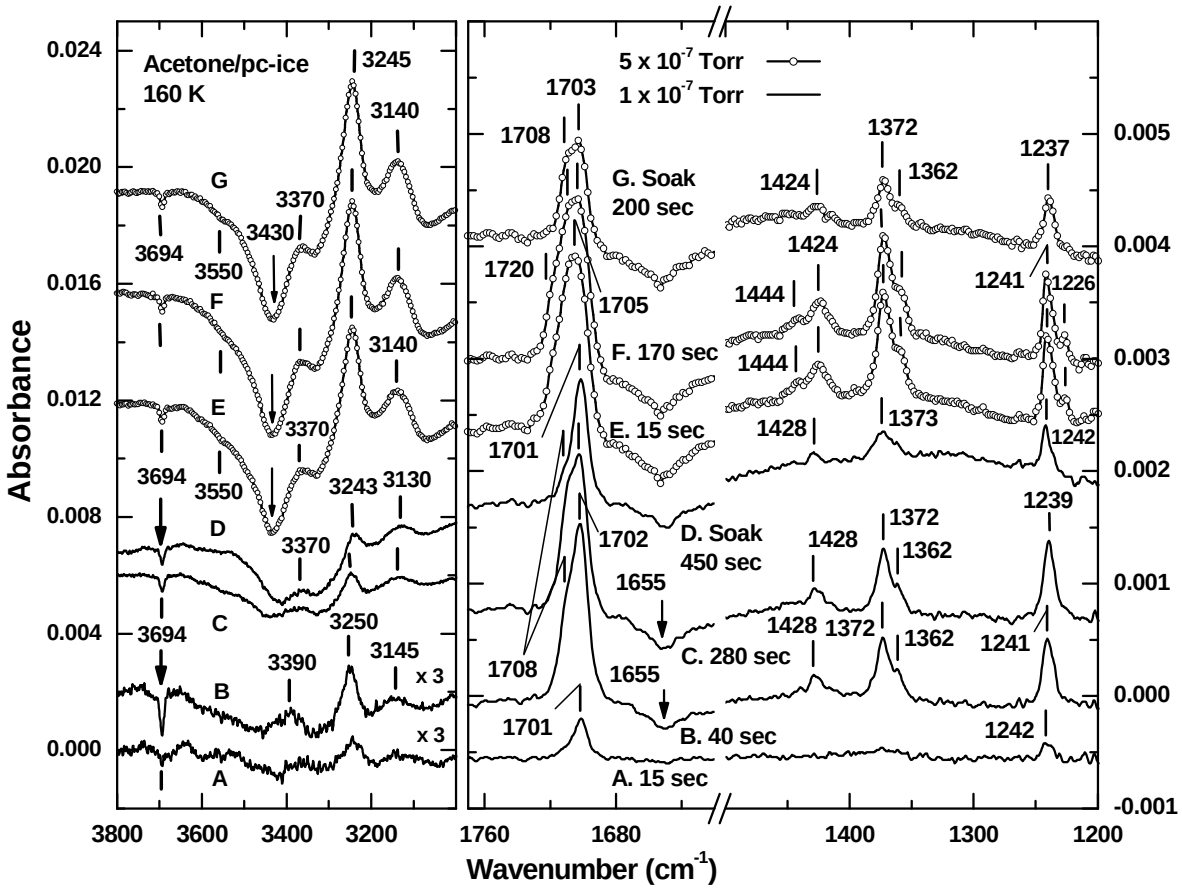

Figure 5.5.1. Experimental RA difference spectra of acetone obtained under different conditions on a polycrystalline ice (pc-ice) film deposited at 160 K and 5×10^{-7} Torr. The acetone exposures are performed at 160 K and 1×10^{-7} Torr for (A) 15, (B) 40 and (C) 280 seconds, and at 5×10^{-7} Torr for (E) 15 and (F) 170 seconds. A post-exposure soaking period at the ambient chamber pressure of 6×10^{-9} Torr for (D) 450 and (G) 200 seconds is performed after the acetone deposition in (C) and (F), respectively.

For the exposure pressure of 1×10^{-7} Torr, the adsorption of acetone is manifested in the difference spectra (Figure 5.5.1) by negative RA difference features in the OH *DB* and the O−H stretching and bending regions, and by the positive RA difference features that correspond to the fundamentals of acetone, including the carbonyl stretch, $\nu_3(A_1)$, at 1701 cm^{-1}, asymmetric, $\nu_{21}(B_2)$, $\nu_4(A_1)$ and symmetric $\nu_{16}(B_1)$, $\nu_5(A_1)$ CH_3 deformation bands at 1444, 1428, 1372 and 1362 cm^{-1} respectively, and asymmetric C−C stretch, $\nu_{17}(B_1)$ at 1242 cm^{-1}. The intensity of the carbonyl stretching band is found to saturate along with the negative

OH *DB* signal with increasing exposure, which provides strong evidence for the formation of a surface complex between acetone and the surface OH *DB*. The relative positions of the fundamental frequencies of the acetone-ice complex also support the hypothesis for the existence of hydrogen bonding in the adsorbate complex, given the red (blue) shift of the carbonyl stretch at 1701 cm^{-1} (asymmetric C−C stretch at 1242 cm^{-1}) found in the present case in comparison with that for pure liquid at 1710 cm^{-1}(1221 cm^{-1}) [62], isolated acetone matrix at 1725 cm^{-1}(1217 cm^{-1}) [62] and isolated acetone-water matrix at 1716 cm^{-1} (1230 cm^{-1}) [63]. These notable frequency shifts can therefore be attributed to the formation of strong hydrogen bonding between O of the carbonyl group in acetone and H of the OH *DB* (referred as α-complex in the present work). The definition and structural description of the α-, the β- and the γ- classes of the acetone-water network are provided in Chapter 4. The emergence of the high-frequency shoulder near 1708 cm^{-1} in the carbonyl stretch band (Figure 5.5.1, Curve B) at a higher acetone exposure indicates bonding of additional acetone molecules to surface water molecules by a single hydrogen bond (β-complexes). The interaction with other acetone molecules by electrostatic and van der Waals forces also contribute substantially to the spectral picture. The negative changes observed in the O−H stretching (3550 cm^{-1} and 3430 cm^{-1}) and bending (1655 cm^{-1}) regions indicate the loss of ice signal due to acetone adsorption, which could be attributed to the reconstruction of the near-surface region (consistent with the picture proposed by Devlin, Buch and coworkers [64, 65] and to possible sublimation of the acetone-ice complexes. The group of positive peaks at 3370 cm^{-1}, 3243 cm^{-1}, and 3130 cm^{-1} can be attributed to the bulk modes of crystalline ice, the intensity of which are enhanced by adsorbate-induced reconstruction in the near-surface region of ice (Figure 5.5.1, Curve C). The sublimation process of the acetone-water complexes exposes newly formed surface sites for further adsorption of incoming acetone molecules. The dynamic nature of the adsorption-desorption process is illustrated by the general reduction in the acetone fundamental features after the sample is left (soaking) at the ambient pressure of 6×10^{-9} Torr for a post-exposure period of 450 seconds (Figure 5.5.1, Curve D). Furthermore, the reduction in intensity for the high-frequency shoulder at 1708 cm^{-1} appears to be greater than that for the main carbonyl peak at 1701 cm^{-1}, suggesting a greater desorption rate for the β-complex (relative to the α-complex).

For acetone exposure at 5×10^{-7} Torr, the intensity of the carbonyl stretch saturates at a

higher level (Figure 5.5.1, Curve E) at 1.4 times of that for exposure at 1×10^{-7} Torr (Figure 5.5.1, Curve B). The saturation level is apparently not directly proportional to the exposure pressure that indicates the possible transition from Langmuir type adsorption driven by hydrogen bonding towards more complex adsorption mechanisms, which involve the multilayer adsorption and acetone trapping into the ice. The presence of a new feature at 1226 cm^{-1} attributable to asymmetric C−C stretch and an additional broad shoulder at 1720 cm^{-1} in the carbonyl band, along with enhancement in intensity of the asymmetric deformational band at 1444 cm^{-1} (Figure 5.5.1, Curves E and F), identify the emergence of a new acetone-ice complex (γ-complex), structure of which is thought to be close to the acetone clathrate-hydrate in the sense of the adsorbate-water network interaction based on the data of previous works [66, 67] and present observations. The present work assumes that the structures of γ-class include both the non-hydrogen bonded acetone species and the enclathrated acetone species. After the sample is allowed to soak at 160 K under an ambient pressure of 6×10^{-9} Torr for a post-exposure period of 200 seconds (Figure 5.5.1, Curve G), the spectral features of the γ-complex are found to disappear, leaving only the β- and α-complexes on the surface. The proposed enclathration of acetone molecules (γ-complex), which occurs in the surface structure of the pc-ice under the acetone exposure at certain temperature and pressure ranges (above ~160 K and 5×10^{-7} Torr of acetone), provides an additional indication of the existence of disordered fragments in the near surface structure of pc-ice. The dynamic formation of acetone clathrate-hydrate like intermediates is caused by rearrangement of these disordered fragments [66].

In order to obtain the structure of acetone species on the ice surface molecular dynamic simulations have been performed at 130 K with 6, 12, and 24 acetone molecules on an ice slab made up of 8 bilayers with 96 water molecules in each bilayer. In order to preserve the crystallinity of the ice structure, the four bottom bilayers (i.e., the 5*th* to 8*th* bilayers) were kept rigid during the simulations. The initial coordinates of the water molecules in the ice slab were obtained from Buch *et al.* [68]. For simulations the CHARMM program has been used employing the *TIP4P* model for the water molecules [69] and the CHARMM parameterization parameters for acetone-acetone and acetone-water interaction [70]. The system trajectorise have been collected typically over 500 ps of run time. The typical configuration of a 6Ac/ice model system reveals the presence of both the α- and the β- structures on the ice surface as

shown on Figure 5.5.2. The α-complexes prevail over the β-complexes at this concentration is excellent agreement with the spectral picture shown in Figure 5.5.1 curve A. There is an excellent agreement between the α-class topology of the hydrogen bond coordination of carbonyl group in the acetone-water system obtained in the present studies by the quantum mechanical and classical molecular dynamics methods.

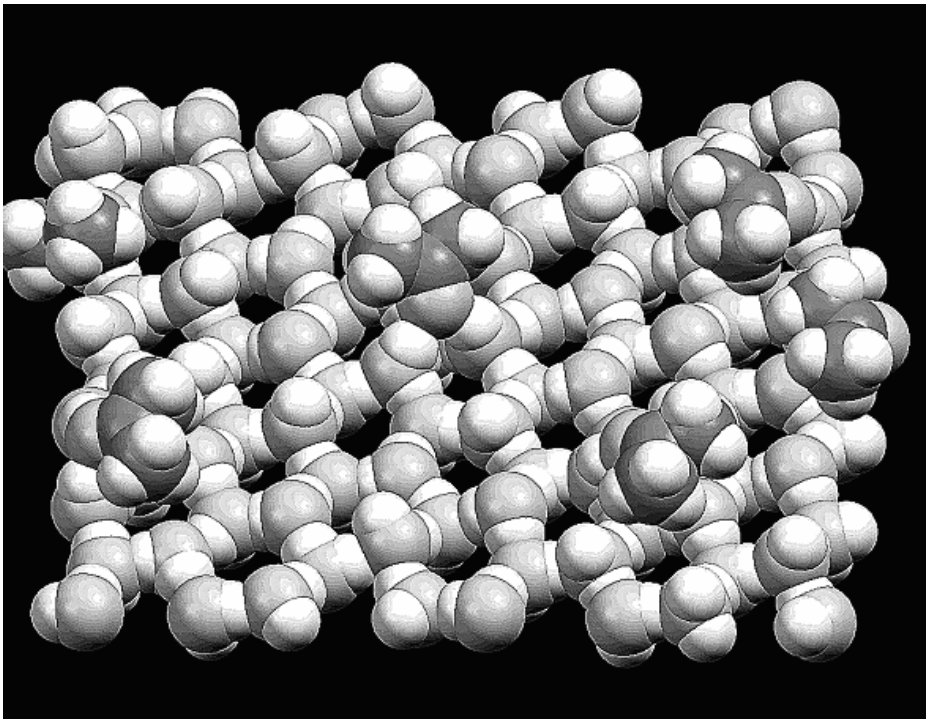

Figure 5.5.2. MDS snapshot of the acetone-ice surface at the molar ratio $Ac/H_2O = 6.25\times10^{-2}$. The molar ratio is defined as $N_{Ac}/96$, where N_{Ac} is a number of acetone molecules on the ice surface and there are 96 water molecules in the surface bylayer of initial ice configuration. The carbon skeleton of an acetone molecule is shown in dark.

At higher coverage of the surface of ice slab, i.e. when molar Ac/H_2O become 0.25, the β-structures prevail and the presence of non-coordinated γ-structures is evident from Figure 5.5.3 in an excellent agreement with spectral picture displayed on Figure 5.5.1, curves E-G.

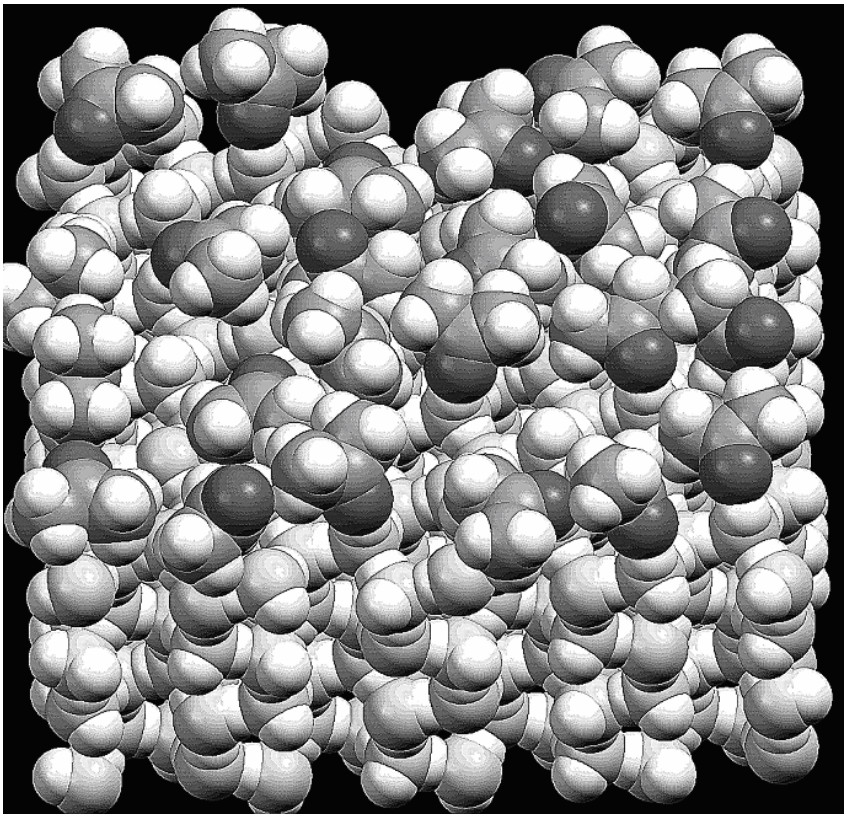

Figure 5.5.3. MDS snapshot of the acetone-ice surface at the molar ratio $Ac/H_2O = 0.25$. The carbon skeleton of an acetone molecule is shown in dark and the oxygen atoms of acetone molecules are shown in black to contrast with the rest.

The acetone adsorption experiments have also been performed on thin nc-ice films (with an estimated Fresnel thickness of 5 nm) deposited at 131 K. The corresponding differential RA spectra are shown on Figure 5.5.4. Despite the differences in the nature and film thickness of the ice film, similar behavior in the adsorption of acetone (to that on pc-ice), with gradual saturation of the OH *DB* signal along with a concomitant increase in the intensities of the acetone fundamentals, has been observed for acetone exposure pressure of 1×10^{-8} Torr. Furthermore, the saturation of the negative OH *DB* signal for nc-ice at essentially the same level as that for pc-ice provides further evidence that the OH *DB's* are located on the external surfaces of both thin pc-ice and nc-ice films. This result, together with the similarity in the FTIR-RA spectra for acetone adsorption on thin nc-ice and pc-ice films, suggests a similar surface structure for nc-ice and pc-ice in this thickness range (below 50 nm), consistent

with the conclusions of Devlin, Buch and coworkers [64, 65]. The initial adsorption of acetone species on the copper disk leads to the γ-complexes, which includes finite acetone islands comprising dimers and/or short oligomeric chains with an anti-parallel packing motif (see Figure 5.3.7 and Figure 5.3.8). The intermolecular interaction in these finite acetone clusters is weaker than in the crystalline acetone phase.

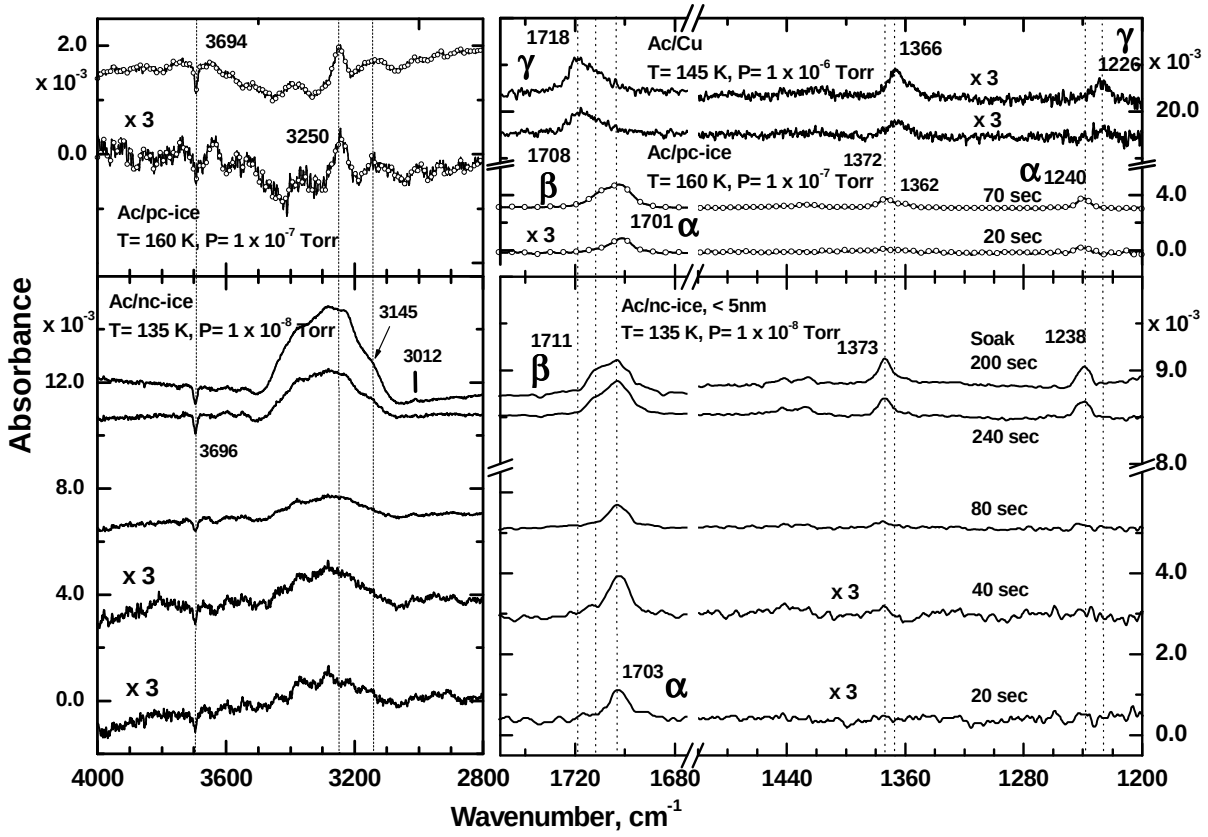

Figure 5.5.4. The FTIR-RA spectra of acetone species from the α-, the β- and the γ- classes on the thin nc- and pc-ice media, and on the bare Cu.

The metastable character of the non-crystalline ice is revealed in the temporal evolution of the O-H stretch main feature towards that, which is corresponding to pc-ice. The adsorption of acetone was found to promote this crystallization process, leading in same cases to the relatively deep reconstruction of the entire ice film.

In the case of pc-ice film 1100 nm thick deposited at 185 K, similar adsorption behavior of acetone is also observed, with the intensity of the negative OH *DB* signal after saturation by acetone found to be similar to those observed in the aforementioned cases. This

result again supports the conclusion that OH *DB's* are located on the external surface of thick pc-ice films, consistent with the dependence of the OH *DB* signal on film thickness shown in Figure 5.1.9.

To investigate the kinetic behavior of acetone adsorption on pc-ice and nc-ice films 1200-nm thick (grown at 160 K and 131 K, respectively), we expose acetone at 1×10^{-6} Torr on pc-ice and at 1×10^{-7} Torr on nc-ice at the respective substrate temperatures. Figure 5.5.5 shows the integrated absorbance of the OH *DB* feature (at 3694 cm^{-1}) and the carbonyl stretch (at ~1705 cm^{-1}) in the difference spectrum as a function of the acetone dosage (in units of 1×10^{-6} Torr second or Langmuir). It should be noted that the exposure pressure of acetone could significantly affect the composition of the acetone-ice complexes and the overall adsorbate coverage of the ice films. The nc-ice sample used in this experiment (Figure 5.5.5b) exhibits a similar OH *DB* intensity profile as a function of film thickness as that shown in Figure 5.1.9b. Moreover, Figure 5.1.9b shows the OH *DB* intensity to be ~0.15 integrated absorbance unit for a film thickness of 1200 nm, which corresponds approximately to the same value as the loss of the *DB* feature in the difference spectra at saturation (Figure 5.5.5b). Figure 5.5.5 shows that the amount of acetone adsorbed on both nc-ice and pc-ice films as approximated by the intensity of the respective carbonyl stretch bands is proportional to the amount of OH *DB's* present in the ice structure. This proportionality is present as long as there is no formation of solid acetone phase, which might be difficult to avoid for acetone exposure at the lower temperature range (e.g., the deposition temperature of nc-ice near 131 K). Indeed, the continual growth of the carbonyl stretch band intensity for acetone adsorption on nc-ice (Figure 5.5.5b) after OH *DB* band saturation might be caused by physiadsorption of acetone. However, the markedly more intense RA signals observed for acetone adsorption on the nc-ice sample in comparison with the pc-ice case for the same exposure (e.g. at 100×10^{-6} Torr second) indicates that nc-ice has a significantly larger surface area than pc-ice, in general agreement with the results by Stevenson *et al.* [71] and Zondlo *et al.* [15].

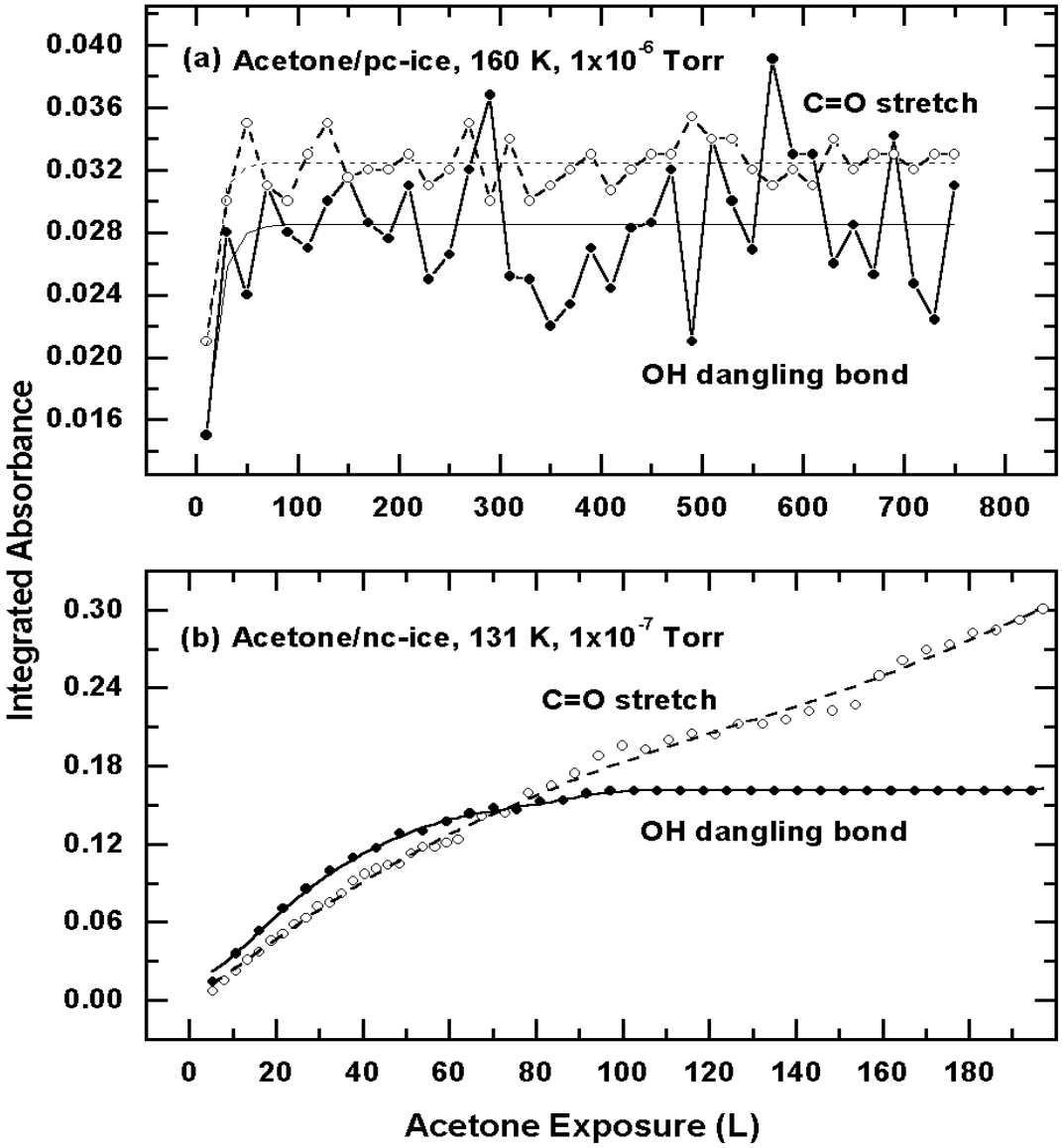

Figure 5.5.5. Integrated absorbance of OH dangling bond (solid circle) and C=O stretch (open circle) features in the RA difference spectra as a function of acetone exposure at (a) 160 K and 1×10^{-6} Torr on a polycrystalline ice (pc-ice) film 1200 nm thick, and (b) 131 K and 5×10^{-7} Torr on a non-crystalline ice (nc-ice) film 1200 nm thick.

The curves are used to guide the eyes only.

The OH *DB's* are located most likely on the external surface of nc-ice, which has a considerably higher convoluted tracery structure than pc-ice. The general increase in the intensity of the OH *DB's* from 700 nm to 1400 nm observed for nc-ice (Figure 5.1.9b) shows the evolution of the surface structure of nc-ice towards a more three-dimensional openwork structure that is accessible to gas exposure at the same time.

5.5.2 Concluding Remarks

In summary, the OH *DB's* (with characteristic features at 3700-3690 cm^{-1}) are an integral part of the nc-ice and pc-ice phases and they play a pivotal role in the surface chemistry of ice films. The surface structural elements containing these OH *DB's* are found to be stable over a wide temperature range of 128-185 K covered in the present work. Unlike the earlier work, we also observe the OH dangling bond signal originated on pc-ice films deposited at temperature as high as 185 K. The thin nc-ice and pc-ice films contain comparable amounts of OH *DB's*, which are located on the external surfaces of both phases with similar structures. The nature of the external surface (containing the OH *DB's*) remains unchanged upon film growth for pc-ice with a general increase in the amount of OH *DB's*, in contrast to film growth for nc-ice where the surface evolves into a more convoluted openwork structure. The acetone adsorption experiment shows that the $(CH_3)_2C{=}O\cdots 2(H{-}O)$ *DB* complex is formed first by hydrogen bonding between the O atom of carbonyl group in acetone and 2 hydrogen atoms of the hydroxyl cover in the ice film. In addition to the bi-coordinated *HB* α-complex, the mono-coordinated *HB* β-complexes and non-*HB*-coordinated γ-complexes, the latter of which involve interactions with other acetone molecules and substrate water molecules by electrostatic, van der Waals and other mechanisms including the intermediate formation of acetone clathrate-hydrate structures, can be observed at higher pressure exposures. The consequence of the presence of OH *DB's* on the surface of pc-ice at relatively high temperatures may have significant implications on the types of plausible atmospheric surface reactions that could occur on and in ice in the important 190-220 K stratospheric temperature range.

The combination of spectral and computational studies reported in the present work reveals that the acetone species on the surface and in the bulk of nc- and pc-ices exist as bi- (α-class), mono-(β-class) *HB*-coordinated and non-*HB*-coordinated (γ-class) species. The spectrum-

structure correlation scheme developed in the present work allows connecting the observed spectral features to the local configurations of acetone molecules on the ice surface or in the bulk of water condense phase.

References:

1. E. Mayer, R. Pletzer, J. Chem. Phys. ***80*** (1984) 2939.
2. O. B. Toon, M. A. Tolbert, B. G. Koehler, A. M. Middelebrook, J. Geophys. Res. ***99*** (1994) 631.
3. Rowland, J. P. Devlin, J. Chem. Phys. ***94*** (1991) 812.
4. V. Buch, J. P. Devlin, J. Chem. Phys. ***110*** (1999) 3437.
5. E. Whalley, Can. J. Chem. ***55*** (1977) 3429.
6. J. P. Devlin, J. Chem. Phys. ***90*** (1989) 1322.
7. D. Fox, R. Hexter, J. Chem. Phys. ***41*** (1964)1125.
8. D.W. Berreman, Phys. Rev. ***130*** (1963) 2193.
9. R. G. Tobin, Phys. Rev. ***45*** (1992) 12100.
10. A. H. Hardin, K. B. Harvey, Spectrochim. Acta ***29A*** (1973) 1139.
11. J. E. Bertie, E. Whalley, J. Chem. Phys. ***40*** (1964) 1637.
12. R. G. Greenler, J. Chem. Phys. ***44*** (1966) 310.
13. J. D. E. McIntyre, D. E. Aspens, Surf. Sci. ***24*** (1971) 417.
14. G. Turrell, “Infrared and Raman spectra of crystals”, Academic, New York (1972).
15. M. A. Zondlo, T. B. Onasch, M. S. Warshawsky, M. A. Tolbert, G. Mallick, P. Arentz, M. S. Robinson, J. Phys. Chem. B ***101*** (1997) 10887.
16. A. B. Horn, M. A. Chesters, M. R. S. McCoustra , J. R. Sodeau, J. Chem. Soc. Faraday Trans. ***88*** (1992) 1077.
17. P. Jenniskens, S. F. Banham, D. F. Blake, M. R. S. McCoustra, J. Chem. Phys. ***107*** (1997) 1232.
18. S. B. Barone, M. A. Zondlo, M. A. Tolbert, J. Phys. Chem. ***103*** (1999) 9717.
19. W. Hagen, A. G. G. M. Tielens, J. M. Greenberg, Chem. Phys. ***56*** (1981) 367.
20. A. Hallbrucker, E. Mayer, G. P. Johari, J. Phys. Chem. ***93*** (1989) 4986.
21. A. Kouchi, T. Yamamoto, Prog. Crystal Growth and Charact. ***30*** (1995) 83.
22. A. Leger, S. Gauthier, D. Deforneau, D. Rouan, Astron. Astrophys. ***117*** (1983) 164.
23. V. P. Zhdanov, P. R.. Norton, Surf. Sci. ***449*** (2000) L228.
24. B. W. Callen, K. Griffiths, P. R. Norton, Surf. Sci. Lett. ***261*** (1992) L44.
25. I. Kohl, E. Mayer, A. Hallbrucker, Phys. Chem. Chem. Phys. ***2*** (2000) 1579.

26. M. J. Wojcik, V. Buch, J. P. Devlin, J. Chem. Phys. ***99*** (1993) 2332.
27. A. V. Iogansen, Spectrochim. Acta A ***55*** (1999) 1585.
28. R. Englman, R. Ruppin, J. Phys. C. (Proc. Phys. Soc.) ***1*** **(**1968) 614.
29. T. P. Martin, Phys. Rev. ***177*** (1969) 1349.
30. M. S. Bergren, D. Schuh, M. G. Sceats, S. A. Rice, J. Chem. Phys. ***69*** 2(1978) 332.
31. R. S. Smith, Z. Dohnalek, G. A. Kimmel, K. P. Stevenson, B. D. Kay, ACS Symposium Series 820, American Chemical Society ***198*** (2002).
32. T. C. Sivakumar, S. A. Rice, M. G. Sceats, J. Chem. Phys. ***69*** (1978) 3468.
33. L. Schriver-Mazzuoli, J. M. Coanga, A. Schriver, P. Ehrenfreund, Vib. Spec. ***30*** (2002) 245.
34. Z. Dohnalek, R. L. Ciolli, G. A. Kimmel, K. P. Stevenson, R. S. Smith, B. D. Kay, J. Chem. Phys. ***110*** (1999) 5489.
35. V. Buch, L. Delzeit, C. Blackledge, J. P. Devlin, J. Phys. Chem. ***100*** (1996) 3732.
36. N. B. Colthup, L. H. Daly, S. E. Wiberley, "Introduction to Infrared and Raman Spectroscopy", 3^{d} Edition, Academic Press, Boston (1990).
37. R. Fourme, M. Renaud, C. R. Acad. Sc. Paris B ***263*** (1966) 69.
38. A. Bondi, J. Phys. Chem. ***68*** (1964) 441.
39. A. Kimoto, H. Yamada, Bull. Chem. Soc. Japan ***41*** (1968) 1096.
40. E. A. D'Alessio, E. Dodoero, C. Pomposiello, J. Chem. Phys. ***57*** (1972) 4136.
41. B. Andrews, A. Anderson, B. Torrie, Chem. Phys. Lett. ***104*** (1984) 65.
42. H. F. Shurvell, J. Chem. Phys. ***58*** (1973) 5807.
43. H. S. Gutowsky, D. W. McCall, J. Chem. Phys. ***41*** (1968) 548.
44. G. Dellepiane, J. Overend, Spectrochimica Acta ***22*** (1966) 593-614.
45. X. K. Zhang, E. G. Lewars, R. E. March, J. M. Parnis, J. Phys. Chem. ***97*** (1993) 4320.
46. L. Andrews, G. L. Johnson, J. Phys. Chem. ***88*** (1984) 5887-5893.
47. D. R. Allan, S. J. Clark, R. M. Ibberson, S. Parson, C. R. Pulham, S. Linsday, Chem. Comm. ***9*** (2000) 557-558.
48. I. Weissbuch, R. Popovitz-Biro, M. Lahav, L. Leiserovitz, Acta Cryst. ***B51*** (1995) 115.
49. P. F. Krause, B. G. Glagola, J. E. Katon, J. Chem. Phys. ***61*** (1974) 5331.

50. W. C. Harris, I. W. Levin, J. Mol. Spec. ***43*** (1972) 117.
51. R. M. Ibbreson, W. I. F. David, O. Yamamuro, Y. Miyoshi, T. Matsuo, H. Suga, J. Phys. Chem. ***99*** (1995) 14167.
52. D. Syomin, B. E. Koel, Surf. Sci. ***498*** (2002) 53.
53. I. Weissbuch, R. Popovitz-Biro, M. Lahav, L. Leiserovitz, Acta Cryst. ***B51*** (1995) 115-148.
54. T. G. Goplen, Ph. D. Thesis, 1976, University of Minnesota.
55. C. M.Huggins, G. C. Pimentel, J. Chem. Phys. ***23*** (1955) 896.
56. L. M. Fell, H. F. Shurvell, Can. J. App. Spec. ***41*** (1996) 90.
57. A. M. Buswell, W. H. Rodebush, M. F. Roy, J. Am. Chem. Soc. ***60*** (1938), 2528.
58. G. R. Choppin, J. R. Downey, Spectrochim. Acta ***30A*** (1974) 43.
59. K. B. Whetsel, R. E. Kagarise, Spectrochim. Acta ***18*** (1962) 329.
60. N. S. Holmes, J. R. Sodeau, J. Phys. Chem. A ***103*** (1999) 4673.
61. J. E. Schaff, J. T. Roberts, J. Phys. Chem. ***98*** (1994) 6900.
62. G. Dellepiane, J. Overend, J. Spectrochim. Acta. ***22*** (1966) 593.
63. X. K. Zhang, E. G. Lewars, R. E. March, J. M. Parnis, J. Phys. Chem. ***97*** (1993) 4320.
64. B. Rowland, N. S. Kadagathur, J. P. Devlin, V. Buch, T. Feldman, M. J. Wojcik, J. Chem. Phys. ***102*** (1995) 8328.
65. L. Delzeit, M. S. Devlin, B. Rowland, J. P. Devlin, V. Buch, J. Phys. Chem. ***100*** (1996) 10076.
66. D. Blake, L. Allamandola, S. Sanford, D. Hudgins, F. Freund, Science ***254*** (1991) 5.
67. K. Consani, J. Phys. Chem. **91**, 5586 (1987).
68. V. Buch, P. Sandler, J. Sadlej, J. Phys. Chem. B ***102*** (1998) 8641.
69. W. L. Jorgensen, J. Chandrasekhar, J. F. Madura, R. W. Impley, M. L. Klein, J. Chem. Phys. ***79*** (1983) 926.
70. B. P. Brooks, P. E. Bruccoleri, B. D. Olafson, D. J. States, S. Swaminathan, M. Karplus, J. Comput. Chem. ***4*** (1983) 187.
71. K. P. Stevenson, G. A. Kimmel, Z. Dohnálek, R. S. Smith, B. D. Kay, Science ***283*** (1999) 1505.

CHAPTER 6

Surface Adsorption and Trapping of Inert Gases on Hexagonal Ice by Molecular Dynamics Simulations

6.1 Introduction

Classical molecular dynamics (MD) simulations of Xe on the basal (0001) face of hexagonal ice at 180 K have been performed in order to investigate the mechanism of adsorption and the initial stage of absorption of a Van der Waals particle into crystalline ice. The potential of mean force (PMF) as a function of the relative position of the Xe atom perpendicular to the ice surface is found to increase abruptly as the particle propagates from the disordered outermost region to the deeper hexagonally ordered region. A set of local minima observed in the PMF appears to correspond directly to the layer-by-layer crystal structure of hexagonal ice. Along with the unbound state, the first two minima (with similar free energies) that correspond to the accommodation of the guest particle on and inside the disordered outermost bilayer, respectively, were found to be populated during the MD runs. The multiple transitions of the system among these three states were also observed in accord with the PMF profile, which also suggests that the penetration of any ordered hexagonal bilayer by the Xe atom is unlikely. Furthermore, MD simulations of pristine ice (i.e. without Xe) over a 3-ns simulation period show that the initially perfect-ordered hexagonal crystalline structure of the outermost bilayer undergoes transformation to a non-crystalline phase, in which fragmented domains with hexagonal ordering persist. Moreover, the accommodation of the Xe atom inside the outermost bilayer could facilitate further disordering of the hexagonal structure of this bilayer with the formation of a completely disordered Xe/Rn-ice surface phase.

Molecular mechanisms of adsorption, trapping, penetration and subsequent diffusion of different chemical species on ice are of fundamental importance to understanding a variety of physicochemical processes, including reactions of trace gases with ice and/or acid particles in the stratosphere and upper troposphere, interfacial chemistry on snowflakes, ice and other water-covered particles in the biosphere, clathrate hydrates formation, and compositional evolution of ice particulates in interstellar space [1,2,3]. To date, both experimental and

theoretical studies of the behaviour of different chemical species on ice have not revealed a universal molecular mechanism for adsorption and absorption [4], most likely due to an inherent complexity of the structure and the dynamics of the surface and the bulk of ice micro-phases. Of special interest is the adsorption and absorption behaviour of an "inert" Van der Waals (VdW) gas particle (such as Xe) on ice. In particular, Xe was reported to penetrate the ice structure to form clathrate hydrate experimentally first without an induction period by Pietrass *et al.* [5] but later with an induction period by Moudrakovski *et al.* [6]. However, the mechanism concerning enclathration of Xe into the ice structure remains controversial. According to Sloan and Fleyfel, the formation of clathrate hydrate should be accompanied by considerable reconstruction of the ice lattice, which includes the formation of a surface liquid layer generated by mechanical action (surface agitation) on the ice sample [7]. On the other hand, Pietrass *et al.* have shown that Xe clathrate hydrate can be formed at a temperature as low as 195 K and a pressure of only 0.3 MPa, and concluded the absence of liquid water layer on ice [5]. Furthermore, Moudrakovski *et al.* have demonstrated that the kinetics of clathrate hydrate formation depends on the microcrystalline structure of ice, in which the average size of crystallites depends on the history of the sample [6]. In any event, guest species must penetrate the interface of the ice structure at a considerable depth (100-1000 Å) in order to form clathrate hydrates. It is obvious that the penetration of a non-crystalline medium should be easier and involves a different mechanism than the penetration of crystalline ice [8]. For example, Jenniskens and Blake have associated the anomalous gas retention and release from the "water-rich ices" above 150 K with the presence of non-crystalline micro phases [9]. Given the early studies on this subject [5,6,7,8,10], Xe (Rn) therefore appear to be useful probes for further exploring the adsorption and absorption mechanisms of a prototypical VdW particle on ice.

The penetration of crystalline ice structure by "oversized" guest particles (with a VdW volume larger than the opening of a perfect water hexagon) is usually preceded by populating the adsorption sites. As it was demonstrated by Buch *et al.* for the CF_4/ice system [11] and by Kroes and Clary for the HCl/ice system [12], there are at least two types of accessible adsorption states on the disordered surface of crystalline ice: those on and inside the disordered outermost bilayer. In the present work, we are adopting the same terminology by referring to the sites on and inside the disordered outermost bilayer as on-layer and in-layer

adsorption states, respectively. However, as noted in the earlier studies [11,12], the guest-ice interaction energy for the in-layer adsorption state is larger than that of the on-layer adsorption state. The existence of these two types of adsorption states was also demonstrated by Girardet and Toubin in the MD simulations of HCl and HOCl on ice at 200 K [4]. Further penetration of the guest particles into the bulk was found to be accompanied by a significant increase in the free energy of the system [4], which is most likely caused by partial disruption of an initially perfectly ordered hydrogen-bonded structure of the second and inner bilayers. The energies and structural parameters of the adsorption states should depend on the equilibrium organization of the outermost bilayer of the ice surface, which inherently assumes that the temperature of the guest/ice system is an important parameter for the adsorption and absorption mechanisms. On the other hand, using a short (3 ps) MD simulation, Al-Halabi *et al*. [13,14] showed that for 110-190 K hyperthermal HCl molecules with energies exceeding 100 kJ/mol could either adsorb on or directly penetrate the ideal (0001) hexagonal surface through the openings of surface hexagons, leading to the absorption of the guest particle at an interstitial site between the water bilayers.

Of relevance to atmospheric chemistry is the temperature range of 180-270 K, over which surface melting of ice occurs with disordering of the outermost bilayer and then proceeds further in depth with the formation of a quasi-liquid layer at the higher temperature end (i.e., near 270 K) [4,15]. In particular, MD studies of the surface dynamics of TIP4P ice Ih by Bolton and Pettersson showed that already at 180 K the equilibrium organization of the outermost bilayer is non-crystalline with the emergence of different surface polygons (from pentagons to octagons) in dynamical coexistence [16], which is in accord with the early results of Kroes [17] at 190 K. Bolton and Pettersson further demonstrated that in the case of Ar impinging on ice the dynamics of the ice surface is responsible for the reversible adsorption-trapping-desorption cycle [18]. In particular, Ar was found to penetrate the disordered outermost bilayer quickly, visiting for a relatively short time (with an average life time of 120 ps) the absorption sites in the heptagon and octagon structures before leaving the ice surface [18]. This study has in effect suggested that Ar atoms cannot penetrate the ordered second bilayer of crystalline ice structure [18]. On the other hand, the enclathration of Ar into ice was observed experimentally by Hallbrucker and Mayer [19] at 200 K and 1 bar, at which conditions the formation of a quasi-liquid surface layer is not expected. It should be noted that

the process of direct penetration of the hyperthermal particle described by Al-Halabi *et al.* [13,14], in which dynamic rearrangement of the surface water hexagons plays little or no role, should be distinguished from that of trapping into the disordered outermost bilayer predicted by Buch *et al.* [11], Kroes and Clary [12], and Bolton and Pettersson [18]. These studies raise further questions about the absorption and trapping mechanisms of a VdW particle in crystalline ice. In the present work, we investigate the details of these fundamental surface processes on crystalline ice at 180 K by classical MD simulations using Xe as the probe atom.

6.2 Methods and Computational Details

MD simulations of Xe and Rn atom on the basal (0001) plane of a proton-disordered hexagonal ice slab were performed using the CHARMM program [20] employing the TIP4P model for the water molecules [21]. The VdW interactions between any pair of the non-bonded atoms for the Xe-Xe, Rn-Rn, and Xe-H_2O and Rn-H_2O systems were described by the Lennard-Jones (12,6) potential (LJ). The CHARMM program uses the arithmetic-mean combining rule for the $Rmin_{ij}$ ($Rmin_{ij}$= ½[$Rmin_{ii}$ + $Rmin_{jj}$]) LJ parameters and the geometric-mean combining rule for the ε_{ij} (ε_{ij}= [$\varepsilon_{ii}\cdot\varepsilon_{jj}$]^{½}) LJ parameters [70]. The LJ parameters for the Xe-Xe VdW interaction were adopted from Tanaka [22] with the following values for ε_{XeXe} = −0.4591 kcal·mole^{-1} and $Rmin_{XeXe}$ = 4.5426 Å. The LJ parameters for the VdW interactions for the Xe-O and Xe-H pairs are as follows: ε_{XeO} = −0.27026 kcal·mole^{-1} and $Rmin_{XeO}$ = 3.8712 Å, and ε_{XeH} = −0.15121 kcal·mole^{-1} and $Rmin_{XeH}$ = 3.0714 Å. The LJ parameters for the Rn-Rn VdW interaction were adopted form Lazaridis and Paulaitis [23] with the following values for ε_{RnRn}=−0.5760 kcal·mole^{-1} and $Rmin_{Rn}$= 4.8940 Å.

Periodic boundary conditions were imposed in the x and y directions of the basal surface of ice such that the rectangular MD simulation box with (x, y) size of (26.945 Å, 31.113 Å) contains one Xe atom and an ice slab made up of 8 bilayers with 96 water molecules in each bilayer. In order to preserve the crystallinity of the ice structure, the four bottom bilayers (i.e., the 5*th* to 8*th* bilayers) were kept rigid during the simulations. The initial coordinates of the water molecules in the ice slab were obtained from Buch *et al.* [24].

MD trajectories were generated using the leap-frog integrator with 1 fs integration step at a constant temperature of 180 K. The SHAKE algorithm was employed for keeping the water molecules rigid by constraining the distances between the atoms in a molecule [25]. The

cutoff distance for non-bonded interactions was set to 13 Å in order to be consistent with the simulation box size.

The free energy change can be obtained by calculating the potential of mean force (PMF) [26]. In particular, the PMF as a function of z coordinate of the Xe atom (along the perpendicular direction to the ice surface), *W(z)*, was obtained by carrying out the umbrella sampling [27], where the potential energy of the Xe-ice system was changed by applying an umbrella potential $V_s(z) = k_s(z-z_s)^2$ to the Xe atom in order to restrict the sampling range of z in a given run around a prescribed z_s value. Sixty separated MD runs were performed using a series of different z_s values chosen for each simulation, so that successive simulations sample overlapping regions in the range 17.5 Å < z < 32.5 Å. The force constants k_s in the umbrella potential were set to 5.2516 kcal/(mol·Å^2) and 2.6258 kcal/(mol·Å^2) in the simulations where the motion of the Xe atom was restricted outside and inside the ice, respectively. The first simulation run was started with the ideal hexagonal crystalline structure of ice (obtained from Buch *et al*. [68]), while the starting configuration for each subsequent run was taken from the previous one. For each run, the MD trajectory over a 150 ps period was collected for further analysis. The WHAM technique [28] adopted from Lemak and Gunn [29] was employed for calculating in a canonical ensemble the probability distribution of z-coordinate of Xe, P(z), which could in turn be used to determine the PMF according to the relation $W(z) = -k_BT\ lnP(z)$ (where k_B is the Boltzmann constant).

To study the surface dynamics of Xe and Rn, the MD simulations have been extended to 1, 2 and 4 Xe and 4 Rn atoms on the ice surface without applying an umbrella potential to the system at a constant temperature of 180 K. With the Xe/Rn atoms initially located randomly at the adsorption site ε_1 (and at z ~29 Å), the MD trajectories were propagated for a 3 ns period.

Structural evolution of the ice surface has been followed by observing the order parameter, which is an average of three translational order parameters introduced by Kroes [17], along the MD trajectories for the ice and Xe/Rn-ice systems. This order parameter S_T equals 1 for perfectly ordered hexagonal lattice while it is of the order 1/N (~ 0.02) for a structure without hexagonal order, where N = 48 is the number of water molecules in a half bilayer of ice structure in the simulation box.

6.3 Results and Discussion

6.3.1 Potential of Mean Force of Xe on Ice

The PMF for the Xe-ice system along the *z* direction shown in Figure 6.3.1a exhibits a set of minima of increasing free energy values at positions closely associated with the layer-by-layer structure of hexagonal ice. In particular, the minimum located outside the ice structure on the surface corresponds to the on-layer adsorption state ε_1 of the Xe atom. Existence of this minimum with respect to an unbound state is due to VdW attraction of Xe to ice, the outermost bilayer of which is a disordered and heterogeneous structure. The next local minimum is located inside the first disordered bilayer and it corresponds to the in-layer adsorption state ε_2. The existence of a continuous open path from the unbound state to the ε_2 state justifies its designation as an adsorption state. The subsequent local PMF minima localized inside the ice structure are identified as a set of Xe absorption states $\{\mu_i\}$. The sharp increase in free energy between subsequent absorption states is associated with partial disruption of the crystalline structure of the corresponding bilayer. Local disruption of the bilayer is necessary for the accommodation of the Xe atom because the VdW volume of Xe is larger than the free space available in the ideal hexagonal ice lattice. For example, transition of the system from the in-layer adsorption state ε_2 to the first absorption state μ_1 is accompanied by an increase in free energy of 9 kcal·mole^{-1} (Figure 6.3.1a) and local disruption of the initially ordered second bilayer. Evidently, this transition also causes a decrease in the translational order parameters S_T for the second bilayer shown in Figure 6.3.1b. In contrast to the transition to the first absorption state and between absorption states of higher order, there is a relatively small free energy difference (~1.8 kcal·mole^{-1}) between the two adsorption states ε_1 and ε_2, which are separated only by a small barrier (Figure 6.3.1a). Low degree of crystallinity of the outermost bilayer (Figure 6.3.1b) is therefore responsible for the PMF profile in this spatial region (Figure 6.3.1a). The significantly larger change in the free energy accompanying the $\varepsilon_2 \rightarrow \mu_1$ transition relative to that of the $\varepsilon_1 \rightarrow \varepsilon_2$ transition is consistent with the much higher degree of ordering of the second bilayer relative to the first (outermost) bilayer (Figure 6.3.1b).

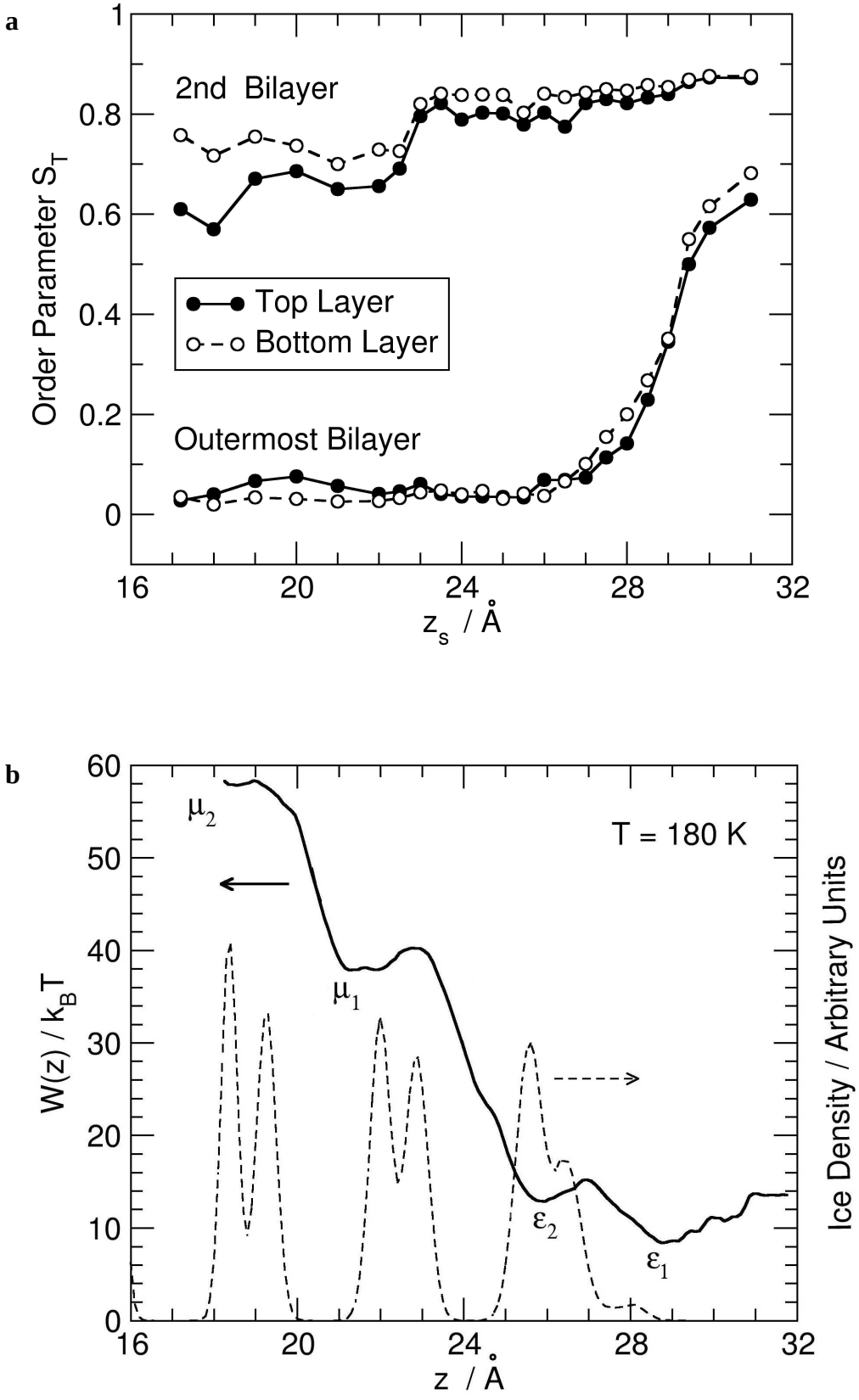

Figure 6.3.1. (a) Order-parameters and (b) Potential of mean force, W(z), as a function of the

z-coordinate (the direction perpendicular to the ice surface) for the Xe-ice system at 180 K. The broken lines show the relative density profile of the oxygen atoms for a pristine ice lattice. The two adsorption sites outside the ice surface and inside the outermost bilayer and the two absorption sites inside the ice slab are labeled by ε_1, ε_2, μ_1, and μ_2, respectively. (a) Translational order parameter S_T for the top (solid circles) and bottom (open circles) layers of the outermost and second outermost bilayers of the ice slab as a function of z_s, the constrained position of the Xe atom in the series of umbrella sampling simulations. The lines are drawn for eye guidance only.

The PMF profile of the Xe-ice system at 180 K (Figure 6.3.1a) appears to be qualitatively similar to the free energy profiles of HCl and HOCl on hexagonal ice at 200 K reported by Girardet and Toubin (see Fig. 18 in Ref. [4]). Although the VdW sizes of these molecules and Xe are larger than the opening of the hexagon of water molecules, the observed similarity in the PMF profiles is unexpected because the interactions of HCl and HOCl with ice include strong electrostatic potential in addition to the VdW potential. There are, however, notable quantitative differences between these systems. In particular, the free energy change for the $\varepsilon_2 \rightarrow \mu_1$ transition for the Xe-ice system at 180 K is about twice that for the HCl-ice and HOCl-ice systems at 200 K, which may be attributed either to a decrease in the activation energy of structural reconstruction of ice due to electrostatic interaction, or to an increase in the degree of disorder of the second bilayer with increasing temperature. It is also noteworthy that the PMF profiles for guest-ice systems considered in the present work and by Girardet and Toubin [4] represent the resistance of the ice structure against the disruption introduced by the guest particle penetration. Moreover, the similarities in the PMF profiles suggest that intermolecular interactions in the ice structure itself appear to be more important, at least at a qualitative level, for the determination of the PMF profile than a specific guest-ice interaction.

Finally, the present PMF profile for the Xe-ice system (Figure 6.3.1a) clearly shows that at 180 K there are relatively large probabilities of occupying an unbound state and the adsorption states (ε_1 and ε_2) of the Xe atom while those of occupying μ_1 and higher-order absorption states (such as μ_2) are very small. These results are connected to the order-disorder equilibrium in the ice surface and near-surface region.

6.3.2 Order-disorder of the Xe-Ice Surface

Earlier experimental and theoretical studies of the surface properties of ice [4,15,16,17,30,31] suggested that an equilibrium state of the pristine hexagonal ice surface below 170 K is dominated by a hexagonally ordered crystalline structure, while for 180-220 K it most likely involves significant disorder in the outermost bilayer but with nearly perfect crystalline organization for the inner bilayers. In particular, Nada and Furukawa [15] concluded from their MD simulations of TIP4P hexagonal ice that the relaxation time for this system at 185 K is less than 1 ns, within which the outermost bilayer is found to evolve into a disordered structure. Such a disordered structure is characterized by the presence of water admolecules that "jump out" from the outermost bilayer [15]. In addition, over the MD simulation time of tens of nanoseconds at temperatures above 180 K, Bolton and Pettersson [16] have observed inter-bilayer migration of water molecules with preferential motion into the inner layers, which leads to the appearance of non-zero density between the first and second outermost bilayers and an increase in the number of molecules in the second bilayer. However, it should be noted that there is no direct correspondence between the temperature used in the MD simulations and the experimental temperature because, for instance, the melting point of a proton-ordered TIP4P hexagonal ice was calculated by Volt *et al*. to be ~214 K at 1 atm [32], which is significantly lower than the experimentally observed value of 273 K.

In the present study, the translational order parameter S_T for pristine hexagonal ice at 180 K was monitored over a period of 3 ns along a MD trajectory started from a non-equilibrium configuration. In particular, S_T for both the top and bottom layers of the outermost bilayer are found to decrease from an initial value of ~0.5 and level off near 0.3 after 1 ns (Figure 6.3.2), which indicates the onset of a long-lived state of ice having a partially disordered first bilayer.

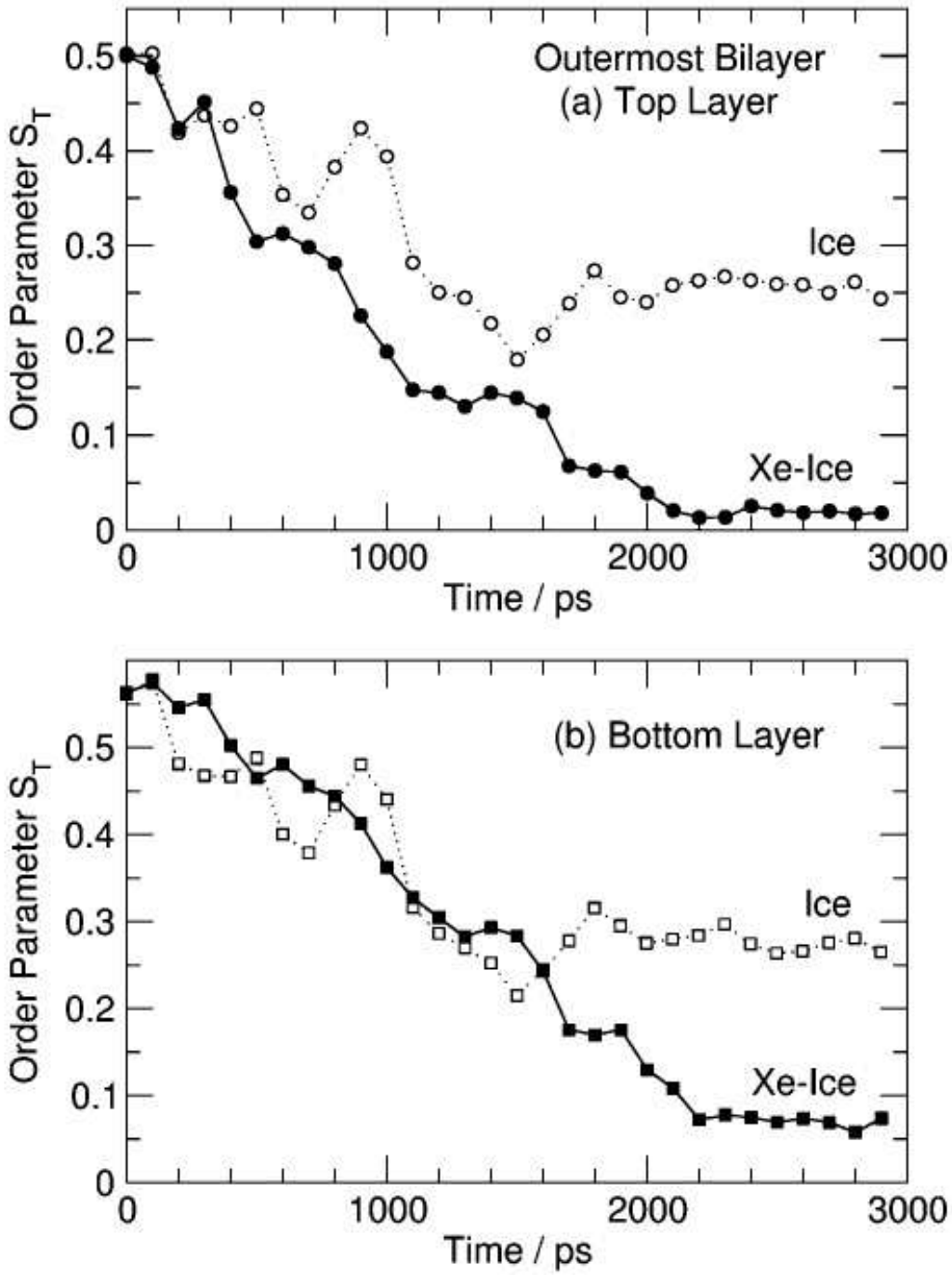

Figure 6.3.2. Translational order parameter S_T of (a) the top and (b) bottom layers of the outermost bilayer as a function of simulation time for two MD trajectories.
Open and solid symbols correspond to the trajectories of pristine ice and Xe-ice systems respectively. Each point represents the S_T value averaged over 100 ps.

Although molecules primarily from the top bilayer were occasionally observed in the interlayer region, no density in this region is found in the molecular density profile of ice shown in Figure 6.3.1a, which is consistent with the lack of significant inter-bilayer migration in this long-lived state. Figure 6.3.3a shows a typical configuration of the oxygen atoms of the water molecules in the first bilayer in this stable state, which evidently consists of a few admolecules and a set of different polygons formed by 5, 6 and 7 water molecules. The existence of admolecules also manifests itself as a shoulder near 28 Å in the density profile (Figure 6.3.1a), which is in agreement with the calculations by Nada and Furukawa [15]. Similar polygonal non-crystalline structure for the top bilayer of ice at 180 K was also reported by Bolton and Pettersson [16,18]. It should be noted that despite a significant overall disorder in the first bilayer, there are regions on the ice surface where the nearly perfect hexagonal structure is preserved (Figure 6.3.3a, lower right). The structural organization of the outermost bilayer of hexagonal ice at 180 K as revealed by the present MD simulations is therefore characterized by the coexistence of dynamical polygons, slightly distorted hexagonal fragments, admolecules, and occasional inter-bilayer water molecules. This structure exhibits uneven local distribution of molecular density inside the bilayer, and the areas of rarefied density provide the openings for guest particle trapping in the ε_2 adsorption state.

The present MD simulations show that the presence of a Xe atom on the ice surface promotes further disordering of the outermost bilayer and increases the number of molecules appearing in between the first and second bilayers. As shown in Figure 6.3.2, the S_T parameters for the Xe-ice system are found to level off at 0.025 and 0.05 for the top and bottom layers respectively. These S_T values are therefore notably smaller than the corresponding S_T values of 0.3 for the pristine ice system (Figure 6.3.2), indicating the formation of a long-lived disordered state for the Xe-ice system with a substantially lower concentration of hexagonally ordered fragments. Indeed, the snapshot of the outermost bilayer for the Xe-ice system (Figure 6.3.3b) clearly demonstrates the noticeably more disordering of the outermost bilayer relative to that for the pristine ice system

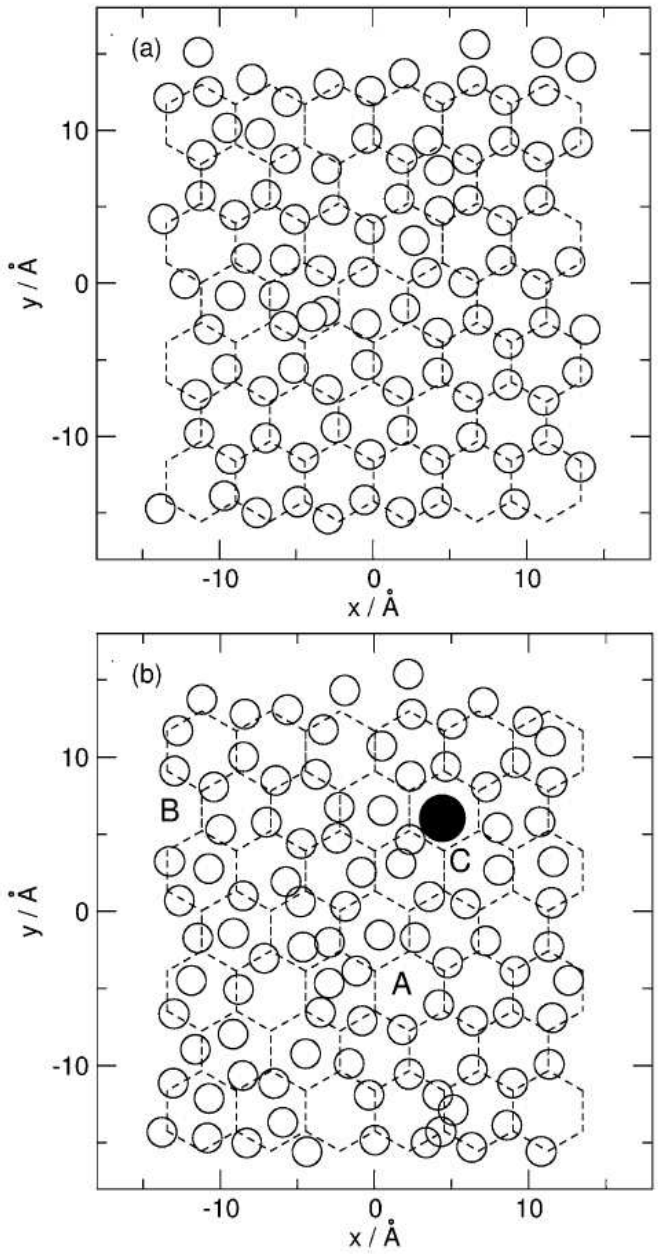

Figure 6.3.3. Snapshot of the positions of oxygen atoms in the outermost bilayer (open circles) for t = 3 ns on a typical trajectory of (a) the pristine ice, and (b) the Xe-ice system. The position of the Xe atom is shown as a solid circle. The positions A, B, and C correspond to the ε_2 adsorption sites in the outermost bilayer visited by the Xe atom. The oxygen positions of the ideal hexagonal ice structure are represented by the junction points of the honeycomb grid drawn with dashed lines in (a, b).

Kinetically, the disordering process in the outermost bilayer is found to proceed at a higher rate at those moments when the Xe atom is located in the in-layer adsorption state ε_2. It should be noted that the corresponding water density profile of the Xe-ice system is found to be nearly identical to that of the pristine ice system (Figure 6.3.1a). However, the presence of Xe in the ε_2 state enhances molecular motion in the inter-bilayer region of the ice lattice with barely discernible density in between the first and second bilayers. The formation of the Xe-containing phase on the ice slab surface is therefore not only much more laterally disordered from the hexagonal arrangement but also more diffuse in the z direction relative to the outermost bilayer of pristine ice at 180 K. In effect, the Xe-ice phase formation causes partial "fluidization" of the surface of the ice slab by facilitating a more fluid-like outermost bilayer, which is in accord with the model introduced by Molina [33]. In contrast to the Xe-ice system, the MD simulations of HCl adsorption on a 18 Å-thick Ih ice film supported by MgO at 190 K by Toubin *et al.* [34] have demonstrated that ordering of the outermost bilayer persists for the HCl adsorption and absorption processes at a coverage of 0.3 monolayer with a slight increase in the S_T parameter from 0.4 to 0.5. Similar S_T values for different HCl-ice adsorption /absorption complexes obtained by MD simulations were also reported by Kroes and Clary [12] and by Gertner and Hynes [35]. At higher HCl coverages of 0.6 and 1.0 monolayer, the S_T parameters for the outermost bilayer were found to decrease to the level of 0.2 and 0.1, respectively [34], which are still higher than that of the Xe-ice system after 2 ns of simulation. This notable difference in the S_T parameters for the Xe-ice and HCl-ice systems could be attributed to the effect of an electrostatic component of HCl-ice interaction. In particular, the presence of the hydrogen bonding between HCl and surface water molecules theoretically shown by Kroes and Clary [12] could account for the preservation of partial ordering of the ice surface. This picture is consistent with the Devlin-Buch model for the interaction of the chemically different adsorbates with ice [36,37].

6.3.3 Surface Dynamics of Xe

In order to illustrate the details of the molecular mechanism in populating the ε_1 and ε_2 adsorption states by the guest particle, the dynamics of 1, 2 and 4 Xe atoms on the ice surface at 180 K has been followed by MD simulation over a period of 3 ns [38]. In particular, the Xe atom impinging on a disordered ice surface is found to be accommodated either in the ε_1 state or directly in the ε_2 state, the latter of which is possible if the guest particle accidentally enters the openings in the outermost bilayer (Figure 6.3.3). Figure 6.3.4a shows a typical trajectory of a single Xe atom on the ice surface. Evidently, starting initially in the ε_1 state, the Xe atom has repeatedly visited the ε_2 state, penetrating the outermost disordered bilayer and being trapped at different locations (A, B and C), before finally accommodated in the ε_2 state for more than 1 ns (Figure 6.3.4b). In the ε_1 state, the Xe atom has high lateral mobility (Figure 6.3.4a), which allows it to probe an ensemble of dynamic polygons of different sizes and shapes and indeed to penetrate into, where appropriate, the accessible opening. In contrast, the ε_2 adsorption state is characterized by its limited lateral mobility, which constrains the Xe atom to a polygon site.

Figure 6.3.4c shows the corresponding interaction energy of Xe-ice along the same trajectory shown in Figure 6.3.4a. Evidently, the interaction energy for the ε_2 state appears to be larger by 2-3 kcal·mole^{-1} than that for the ε_1 state for positions A and C but remains unchanged for position B. The energy difference at B and C is caused by different specific configurations of the water molecules surrounding the Xe atom. In position C, the Xe atom is located directly above the center of the water hexagon of the second bilayer and is tightly surrounded by 10 water molecules of the first bilayer. On the other hand, the Xe atom at position B is found to be atop of a water molecule from the second bilayer with a loosely bound neighborhood in the first bilayer. For the ε_2 adsorption state, the preferred trapping site for the Xe atom therefore includes the center of hexagon of the second bilayer. The dynamics of a single Xe atom on the ice surface is similar to that observed for Ar by Bolton and Pettersson [18] with the important difference that the characteristic occupancy times of the ε_1 and ε_2 states for the Xe atom (over 1 ns) are an order of magnitude greater than that for the Ar atom (120 ps).

MD simulations of 2 and 4 Xe atoms on the ice surface demonstrate reversible

transitions of Xe atoms between three states: (a) unbound (gaseous) state, (b) on-layer adsorption state ε_1, and (c) in-layer adsorption state ε_2 on a time scale of 3 ns. The interaction among Xe atoms gives rise to interesting dynamical phenomena, including the formation of weakly bound pairs of Xe atoms (Xe dimers) in both the ε_1 and ε_2 states, and fast exchange of Xe atoms in these states. Break up of the Xe dimers could result in desorption of individual Xe atoms from the surface. These results will be presented in a follow-up paper [38]. The dynamics of the system observed in these simulations [38] is in good accord with the PMF for Xe-ice system represented in Figure 6.3.1a.

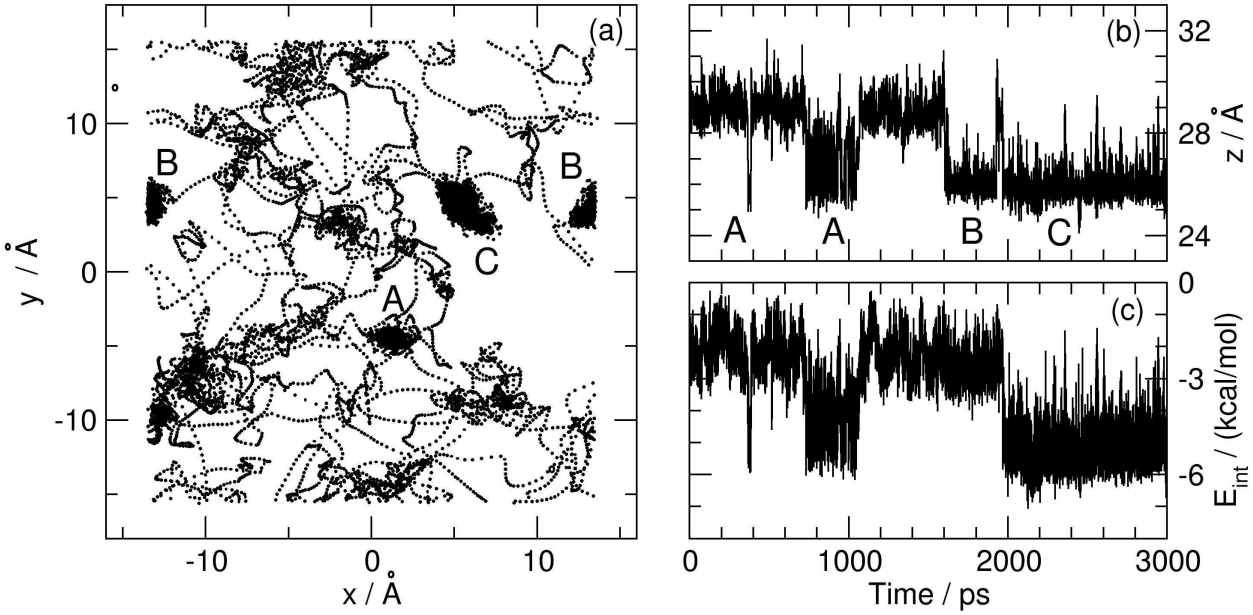

Figure 6.3.4. Typical trajectory of the Xe atom on the ice surface (a) in the (x, y) plane and (b) along the corresponding z-coordinate of the Xe atom.
The positions A, B, and C correspond to the ε_2 adsorption sites in the outermost bilayer visited by Xe atom. (c) Interaction energy (E_{int}) of Xe atom with the ice slab as a function of time for the same trajectory.

The present studies consider also the surface dynamics of the Rn-ice system at very similar simulation conditions. The surface and penetration dynamics of Rn appears to be in accord with that of Xe atoms. The MD simulations of acetone and methanol on ice surface are at the initial stage. It should be noted that typical snapshots of the surface state of acetone-ice system were found to provide interesting insight on the deposition dynamics (Chapter 5).

6.4 The Diffusive Transport in Systems comprising of the Gas and Liquid phases

In addition to the above-reported molecular dynamic studies, the diffusional transport of inert guests such as acetone from gas phase to liquid aqueous media has been studied on two theoretical levels: (i) mathematical solution of the mass balance equation for two phases separated by interface and (ii) kinetic modeling of the penetration process. The formulas obtained within the frameworks of these two different methods appear to be useful for analysis experimental and theoretical data on the penetration processes and mass accommodation coefficient.

In particular, the former analytical approach (i) shows that even at relatively low pressure of the ambient atmosphere gas diffusion plays often a leading role in controlling the overall guest transport from the gas to liquid phase. Furthermore, it is shown that the Fuchs-Sutugin [39] steady-state or Schwartz and Freiberg [40] time-dependent approximations are not applicable for the transport into aerosol particles of tens of microns in diameter at temperatures above 0 °C. These findings indicate that it is impossible to ignore the gas phase resistance in analysis experimental data on the aerosol transport. Moreover, the published experimental data obtained from microscopic aerosols do not allow making any conclusion regarding specifically interfacial resistance for the gas-to-liquid transport.

The latter kinetic method (ii), which follows the Langmuir approach, provides simple expressions for the interfacial contribution to the resistance in gas-to-aerosol transport as function of rate constants and surface accommodation activity. In particular, the total concentration of adsorption centers on the external interface or the absorption centers on the internal interface of liquid phase controls the interfacial transport.

References:

1. F. Domine, P. B. Shepson, Science ***297*** (2002) 1506.
2. M. A. Zondlo, P. K. Hudson, A. J. Prenni, M. A. Tolbert, Annu. Rev. Phys. Chem. ***51*** (2000) 473.
3. A. Kouchi, T. Yamamoto, Prog. Crystal Growth and Charact. ***30*** (1995) 83.
4. C. Girardet, C. Toubin, Surf. Sci. Rep. ***44*** (2001) 159.
5. T. Pietrass, H. C. Gaede, A. Bifone, J. A. Ripmeester, J. Am. Chem. Soc. ***117*** (1995) 7520.
6. I. L. Moudarkovski, A. A. Sanchez, C. I. Ratcliffe, J. A. Ripmeester, J. Phys. Chem. B ***105*** (2001) 12338.
7. E. D. Sloan, Jr., F. Fleyfel, AIChE J. ***37*** (1991) 1281.
8. D. Laufer, E. Kochavi, A. Bar-Nun, Phys. Rev. B ***36*** (1987) 9219.
9. P. Jenniskens, D. F. Blake, Science ***265*** (1994) 753.
10. G. Notesco, D. Laufer, A. Bar-Nun, T. Owen, Icarus ***142*** (1999) 298.
11. V. Buch, L. Delzeit, C. Blackledge, J. P. Devlin, J. Phys. Chem. ***100*** (1996) 3732.
12. G-J. Kroes, D. C. Clary, J. Phys. Chem. ***96*** (1992) 7079.
13. Al-Halabi, A. W. Klein, G. J. Kroes, J. Chem. Phys. ***115*** (2001) 482.
14. Al-Halabi, A. W. Klein, G. J. Kroes, Chem. Phys. Lett. ***307*** (1999) 505.
15. H. Nada, Y. Furukawa, Surf. Sci. ***446*** (2000) 1.
16. K. Bolton, J. B. C. Pettersson, J. Phys. Chem. B ***104*** (2000) 1590.
17. G-J. Kroes, Surf. Sci. ***275*** (1992) 365.
18. K. Bolton, J. B. C. Pettersson, Chem. Phys. Lett. ***312*** (1999) 71.
19. A. Hallbrucker, E. Mayer, J. Chem. Soc., Faraday Trans. ***86*** (1990) 3785.
20. B. P. Brooks, P. E. Bruccoleri, B. D. Olafson, D. J. States, S. Swaminathan, M. Karplus, J. Comput. Chem. ***4*** (1983) 187.
21. W. L. Jorgensen, J. Chandrasekhar, J. F. Madura, R. W. Impley, M. L. Klein, J. Chem. Phys. ***79*** (1983) 926.
22. H. Tanaka, Fluid Phase Equilibria ***144*** (1998) 361.
23. T. Lazaridus, M. E. Pauliatis, J. Phys. Chem. ***98*** (1994) 635.

24. V. Buch, P. Sandler, J. Sadlej, J. Phys. Chem. B ***102*** (1998) 8641.

25. J. P. Ryckaert, G. Ciccotti, H. J. C. Berendsen, J. Comput. Phys. ***23*** (1977) 327.
26. D. A. McQuarrie, “Statistical mechanics”, 1976, Harper and Row, New York.
27. G. M. Torrie, J. P. Valleau, J. Comput. Phys. ***23*** (1977) 187.
28. S. Kumar, D. Bouzida, R. H. Swendsen, P. A. Kollman, J. M. Rosenberg, J. Comput. Chem. ***13*** (1992) 1011.
29. A. S. Lemak, J. R. Gunn, J. Phys. Chem. B ***104*** (2000) 1097.
30. N. Materer, U. Starke, A. Barbieri, M. A. Van Hove, G. A. Somorjai, G.-J. Kroes, C. Minot, Surf. Sci. ***381*** (1997) 190.
31. F. M. Geiger, A. C. Tridico, J. M. Hicks, J. Phys. Chem. B ***103*** (1999), 8205.
32. M. J. Volt, J. Huinik, J. P. van der Eerden, J. Chem. Phys. ***110*** (1999) 55.
33. M. J. Molina, in “The Chemistry of the Atmosphere: Its Impact on Global Change”, 1994, Blackwell Scientific, Oxford, p. 27-38.
34. C. Toubin, S. Picaud, P. N. M. Hoang, C. Girardet, B. Demirdjian, D. Ferry, J. Suzanne, J. Chem. Phys. ***116*** (2002) 5150.
35. B. J. Gertner, J. T. Hynes, Faraday Discus. ***110*** (1998) 301.
36. L. Delzeit, M. S. Devlin, B. Rowland, J. P. Devlin, V. Buch, J. Phys. Chem. B ***100*** (1996) 10076.
37. L. Delzeit, K. Powell, N. Uras, J. P. Devlin, J. Phys. Chem. B ***101*** (1997) 2327.
38. S. Mitlin, B. Torrie, A. S. Lemak, K. T. Leung, to be published.
39. N. A. Fuchs, A. G. Sutugin, "Highly Dispersed Aerosols", 1970, Ann Arbor Science Publishers, London.
40. S. E. Schwartz, R. L. Freiberg, Atmos. Environ. ***15*** (1984) 1129.

CHAPTER 7

General Conclusions

1. For the analysis of the physico-chemical properties of condensed media comprising either pristine water or bi-component systems of water and polar organic substances of environmental significance there have been developed:

   a. An Ultra High Vacuum cryogenic apparatus.
   b. An experimental system comprising the Ultra High Vacuum chamber optically coupled to the Fourier Transform Infrared Spectrometer for conducting Reflection-Absorption Spectral studies of condensed films.
   c. Methods of spectral analysis of the processes of growth, aging and thermo-annealing in condensed films. It is found that analysis of IR RA spectra allows detailed characterization of (i) the intermolecular interaction in adsorbate-substrate systems; (ii) the physico-chemical state of ice surface and bulk; (iii) the morphology of pristine and mixed phases. With the help of time-dependent FTIR RAS the dynamics of these processes has been studied.
   d. Mathematical methods and a computer program for simulating IR RA spectra on the basis of the Fresnel optical model.

2. The experimental studies of pristine ice films reveal that:

   a. Condensed water exists either as noncrystalline porous media or as a polycrystalline medium. The formation of one form or the other is controlled by the deposition temperature.

   b. The surfaces of both noncrystalline and polycrystalline media contain non-coordinated hydroxyl groups, which act as adsorption centers for the accommodation of polar organic molecules. The adsorption and absorption properties of condensed water are found to depend on the surface area and the accessibility of a surface for the guest molecules. These characteristics depend directly on the crystallinity of condensed ice.

c. For very thin ice films (< 50 nm) the total surface area is the same for both types of ice media. In the case of thick films (> 100 nm), the surface area of noncrystalline porous media is substantially larger than that for polycrystalline ice films.

d. Upon annealing the noncrystalline structure undergoes a rapid crystallization into a polycrystalline phase at certain temperature range. The hydroxyl cover of the external surface of noncrystalline thin ice films exhibits no a discernible change on the crystallization. On the other hand, the isothermal soaking of thick noncrystalline ice films leads to a discernible reduction in the total amount of hydroxyl noncoordinated groups due to the decrease of the internal surface of pores.

3. The experimental studies of pristine organic solids reveal that:

a. The vapor deposition of chloroform leads to the formation of two crystalline phases: a stable orthorhombic *Pnma* (D_{2h}^{16}) phase and a metastable phase. The metastable phase is found to transform into the stable *Pnma* phase upon annealing.

b. The vapor deposition of acetone leads directly to the formation of crystalline orthorhombic *Pbca* or mixed *Pbca/Cmcm* phases with a discernible preferential orientation of the carbonyl group and carbon-carbon molecular skeleton relative to the substrate surface, which depends on deposition temperature.

4. The experimental studies of adsorption/desorption of organic molecules on ice reveal that:

a. At an initial stage of adsorption on the ice surface, the organic molecules in question interact directly with surface hydroxyl groups of ice forming hydrogen-bonded complexes. The structure of these complexes depends on: (i) the functional group of the organic molecule; (ii) the crystallinity of ice film; (iii) the surface concentration of organic species.

b. Subsequent adsorption leads to the formation of: (i) isolated non-crystalline nano-clusters of organic molecules; (ii) the solid phase of the corresponding organic substance at high exposure.

5. Condensation of a mixture of water and organic substances over a wide cryogenic temperature range forms noncrystalline solids, in which organic molecules in question are hydrogen bonded to the water network. The present studies reveal that thermo-annealing of water-organic mixtures leads to separation of chemical components such that the ice crystallization is accompanied by partial evaporation of organic component. The intermediate formation of of clathrate-hydrates of small organic molecules such as acetone could be suggested on the basis of present IR spectral data.

6. Computational analysis on quantum mechanical and classical molecular dynamics levels of isolated water clusters and those carrying proton or a organic component reveal that:

a. The structural parameters and the IR spectra of these clusters are mutually related to the intermolecular water network of hydrogen bonds.

b. The IR spectrum is primarily a function of the distribution of lengths of hydrogen bonds.

c. The existence and stability of certain configurations of water clusters depend on the distribution of hydrogen atoms across an oxygen carcass.

d. A unique topology in the hydrogen bond coordination between the organic and water molecules is found.

7. Diffusional and kinetic modeling of the gas-to-liquid diffusion of stable chemical species in the wide range of the external parameters reveals that: (i) the mass accommodation coefficient for small organic molecules on the water aerosols depends on the ration of diffusion coefficients in the rarefied and condensed phases; (ii) the experimental values for mass accommodation coefficients do not depend on the rate of surface process.

8. Classical dynamics simulations of adsorption and diffusion of inert guests inside the water media lattice reveal that:

a. For non-polar molecules such as Xe (Rn) there are two different sets of surface adsorption centers. A first set comprises on-layer adsorbates, which freely travel over entire available surface. A second set comprises in-layer adsorbates, for which the adsorption field is confined to small openings in the ice surface.

b. Penetration of the ice surface by guest molecules is accompanied by a significant local disruption in the network of hydrogen bonds. The hopping of water molecules between structural layers in the ice lattice could be a rate determining factor for non-polar guest molecule penetration.